WHOI-2003-03

Conceptual Models of the Climate

2001 Program of Study in Geophysical Fluid Dynamics

Course Lectures
Fellows Project Reports

PREFACE

In 2001, the Geophysical Fluid Dynamics Summer Study Program grappled with Conceptual Models of the Climate. Eli Tziperman (Weizman Institute), Paola Cessi (Scripps Institution of Oceanography) and Ray Pierre-Humbert (University of Chicago) provided the principal lectures. This introduction gave us all a glimpse into the complex problem of the climate, both in the present, past and future, and even on other planets. As always, the next weeks of the program were filled with many seminars from the visitors, and culminated in the fellow's reports.

Special thanks go to Eric Chassignet for dealing with the computers, and to Jack Whitehead for the year-long administration of the Program. In 2001, as in all summers, W.H.O.I. Education continued to provide the perfect atmosphere for the program, and I specially thank Janet Fields, our industrious coordinator, for her invaluable assistance.

Neil Balmforth, Director

TABLE OF CONTENTS

V FELLOW'S LECTURES (continued)

2001 GFD FELLOWS, STAFF AND VISITORS

Fellows

Helen C. Andersson	Goteborg University, Sweden
Fiona Eccles	Oxford University, United Kingdom
Edwin P. Gerber	Princeton University
Takamitsu Ito	Massachusetts Institute of Technology
Shreyas Mandre	Northwestern University
Lianke te Raa	Utrecht University, The Netherlands
Matthew S. Spydell	University of California, San Diego
Chiara Toniolo	Istituto di Cosmogeofisica/CNR, Italy

Staff and Visitors

James L. Anderson	Stevens Institute of Technology
Neil J. Balmforth	University of California, Santa Cruz
David Battisti	University of Washington
Andrew J. Bernoff	Harvey Mudd College
Joseph A. Biello	Rennselaer Polytechnic Institute
Sebastien Bigorre	Florida State University
Giulio Boccaletti	Princeton University
Gregory Buck	Saint Anselm College
John Bush	Massachusetts Institute of Technology
Sandro Calmanti	Istituto di Cosmogeofisica del CNR, Italy
Paola Cessi	University of California, San Diego
Eric P. Chassignet	University of Miami
Liam Clarke	University of Oxford, England
Arnaud Czaja	Massachusetts Institute of Technology
Agatha DeBoer	Florida State University
Paul J. Dellar	St. John's College, England
William K. Dewar	Florida State University
Henk Dijkstra	Utrecht University, The Netherlands
Abebech Dione	University of Miami
Charles Doering	University of Michigan
Russell Donnelly	University of Oregon
Kerry Emanuel	Massachusetts Institute of Technology
Alexey V. Federov	Princeton University
Dargan Frierson	Princeton University
Eric Gaidos	California Institute of Technology
Thomas W. N. Haine	Johns Hopkins University
Chris Hallstrom	Brown University
Louis N. Howard	Florida State University/M.I.T.
Thierry Huck	Universite de Bretagne Occidentale, France
Christopher Jones	Brown University
Joseph B. Keller	Stanford University
Yochanan Kushnir	Columbia University
Norman R. Lebovitz	University of Chicago

Dmitri Leonov	Florida State University
Willem V. R. Malkus	Massachusetts Institute of Technology
David Marshall	University of Reading, England
John Marshall	Massachusetts Institute of Technology
Igor Mezic	University of California, Santa Barbara
Philip J. Morrison	University of Texas, Austin
Joseph J. Niemela	University of Oregon
Francesco Paparella	University of Leece, Italy
Antonio Parodi	University of Genoa, Italy
Claudia Pasquero	Istituto di Cosmogeofisica del CNR, Italy
Giuseppe Passoni	Politechnico di Milano, Italy
Vinicio Pelino	Centro Nazionale di Meteorological e Climatologia Aeronautica (CNMCA), Italy
Raymond Pierre-Humbert	University of Chicago
Antonello Provenzale	Istituto di Cosmogeofisica del CNR, Italy
Alan W. Rempel	University of Washington
Claes G. Rooth	University of Miami
Tapio Schneider	New York University
Wayne H. Schubert	Colorado State University
Michael J. Shelley	New York University
Leonard Smith	London School of Economics, England
Edward A. Spiegel	Columbia University
Melvin Stern	Florida State University
Kevin Trenberth	National Center for Atmospheric Research
Eli Tziperman	Weizmann Institute of Science, Israel
Geoffrey K. Vallis	Princeton University
George Veronis	Yale University
Jeffrey Weiss	University of Colorado
John S. Wettlaufer	University of Washington
Philip A. Yecko	Columbia University
William R. Young	University of California, San Diego

Standing (left to right): Sebastien Bigorre, Dargan Frierson, Vitalii Sheremet, Philip A. Yecko, Takamitsu Ito, Wayne H. Schubert, Janet Pierrehumbert, Annalisa Bracco, Paola Cessi, Christopher N. Hill, Louis N. Howard, Jean-Michel Campin, Louis N. Howard, Vinicio Pelino, John Marshall, Janet Fields

Seated on porch (left to right): William R. Young, Francesco Paparella, Matthew S. Spydell, Giulio Boccaletti, Joseph B. Keller, Agatha DeBoer, George Veronis, Geoffrey K. Vallis, William K. Dewar, Helen C. Andersson, Eric P. Chassignet, Claes G. Rooth, Jack Whitehead, Neil J. Balmforth, Eli Tziperman

Seated on ground (left to right): Raffaele Ferrari, Abebech Dione, Chiara Toniolo, Sandro Calmanti, Raymond T. Pierrehumbert, Chris Hallstrom, Fiona J.R. Eccles, Lianke A. Te Raa, Edwin P. Gerber, Shreyas D. Mandre, Thierry Huck, Alexander Stein, Peter Huybers

Not Pictured: James L. Anderson, David Battisti, Andrew J. Bernoff, Joseph A. Biello, Gregory Buck, John Bush, Liam Clarke, Arnaud Czaja, Paul J. Dellar, Henk Dijkstra, Charles Doering, Russell Donelly, Kerry Emanuel, Alexey V. Fedorov, Eric Gaidos, Thomas W. N. Haine, Christopher Jones, Yochanan Kushnir, Norman R. Lebovitz, Dmitri Leonov, Willem V.R. Malkus, David Marshall, Igor Mezic, Philip J. Morrison, Joseph J. Niemela, Antonio Parodi, Claudia Pasquero, Giuseppe Passoni, Antonello Provenzale, Alan W. Rempel, Tapio Schneider, Michael J. Shelley, Leonard Smith, Edward A. Spiegel, Melvin Stern, Kevin Trenberth, Jeffrey Weiss, John S. Wettlaufer

2001 Principal Lecturers

Raymond Pierrehumbert, Paola Cessi, Eli Tziperman

Lecture 0
A very brief introduction

Eli Tziperman

Climate variability results from a very diverse set of physical phenomena and occurs on a very wide range of time scales. It is difficult to envision a single model, complex as it might be, which could explain, simulate or predict all sources of climate variability. It is therefore simple models, that concentrate on a single or a few phenomena and on some limited range of time scales, that have had the most success in explaining the physics of climate variability. We start these lectures with a very brief gallery of examples of climate variability from very long time scales to shorter ones, and of a few climate toy models that are displayed without much of a discussion, as an introduction to the fuller review in the following lectures.

After this introduction, the following lectures discuss conceptual (toy) models of the El Nino - Southern Oscillation phenomenon (lectures 1-3), of the thermohaline circulation (lectures 4-5), and of glacial cycles (lectures 8-9) preceded by some basic concepts of climate dynamics (lectures 6-7). We conclude with a brief discussion of toy models of very early earth and planetary climates (lecture 10).

Climate variability exists on all time scales from seconds to billions of years, as shown in the schematic spectrum of Fig. 1. The last 60 Million years (Myr) show a gradual slow cooling, and a strong increase in variability over the past few millions of years (Fig. 2). Continuing to the more recent past, the Quaternary (last 2.6 Myr) glaciation record shows the glacial cycles and a significant change in the nature of these oscillations some 1 Myr ago (Fig. 3).

Focusing on the past 150,000 years, one sees a full glacial cycle (Fig. 4). On shorter-yet time scales, and focusing on the past 90 kyr or so, we can see Heinrich events (major iceberg discharges on a 7-10 kyr time scale), and Dansgaard-Oeschger oscillations (warm events in Greenland ice core records, 1000-1500 yr time scale, Fig. 5). The variability is clearly very dramatic in terms of both amplitude and abruptness of the observed climate changes. A record of the past 10,000 yr shows the Younger Dryas cold event interrupting the last deglaciation (Fig. 6), while the record during the past 500 years shows the “little ice age” (Fig. 7). Finally, on a time scale of a few years to decades, we see the North Atlantic Oscillation record (Fig. 8) and an El Nino record for the past 50 years (Fig. 9).

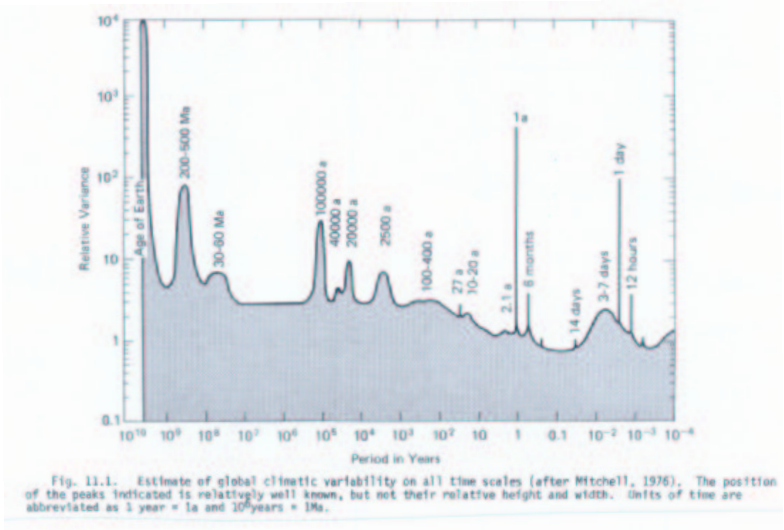

Figure 1: A schematic climate spectrum (Ghil and Childress Fig. 11.1).

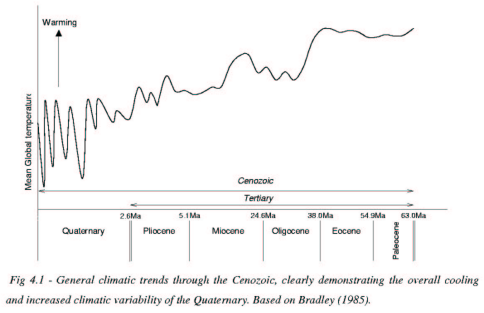

Figure 2: The past 60 Myr (Heslop 2001, http://www.geo.uu.nl/~forth/David/chapter4.pdf).

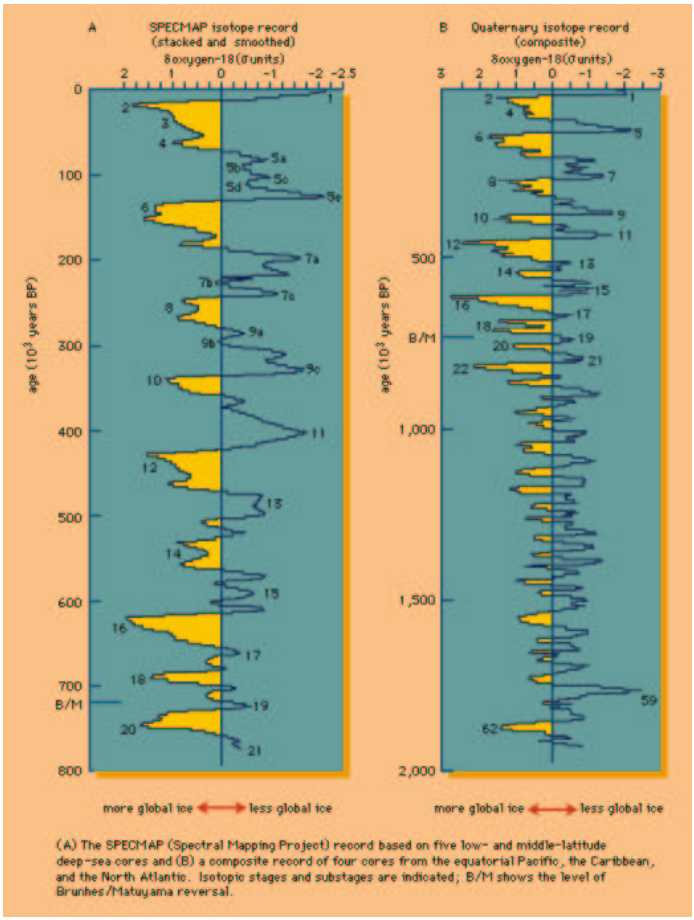

Figure 3: SPECMAP record of glacial cycles over the past 2Myr from ocean sediments.

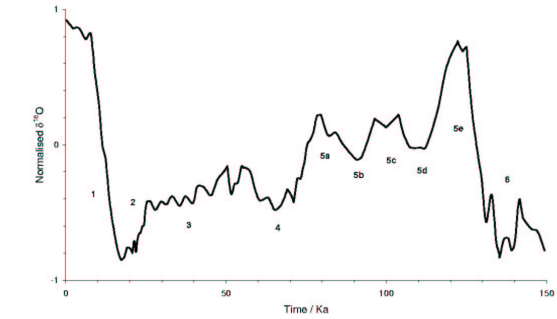

Fig 4.7 – Oxygen isotope stages for the past 150Ka in the Martinson et al (1987) stacked marine isotope record.

Figure 4: The past 150 kyr and isotopic stages (Heslop 2001, http://www.geo.uu.nl/~forth/David/chapter4.pdf).

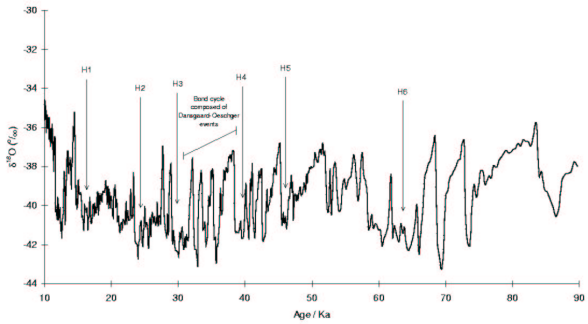

Fig 4.10 - d^{18}O record from the GISP2 record demonstrating the grouped interstadial cooling events defined as Bond cycles. Each cooling phase is composed of a number of Dansgaard-Oeschger events that produce the characteristic asymmetric saw-tooth shape and is terminated by a cold Heinrich event, which are marked H in the figure.

Figure 5: An ice core (GISP) record of the past 90 kyr, showing Heinrich events (10 kyr time scale), and Dansgaard-Oeschger oscillations (1 kyr time scale), (Heslop 2001, http://www.geo.uu.nl/~forth/David/chapter4.pdf).

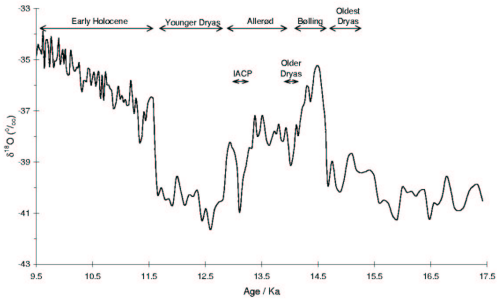

Fig 4.14 – Variations in O^{18} within the Lateglacial zone of the GISP2 ice-core. The resolution of this record is sufficient to show in detail all the chronozones previously defined by European pollen records. Based on Stuiver et al 1995.

Figure 6: A record of the period from 9 kyr before present (bp) to 17 kyr bp, and the Younger Dryas event (Heslop 2001, http://www.geo.uu.nl/~forth/David/chapter4.pdf).

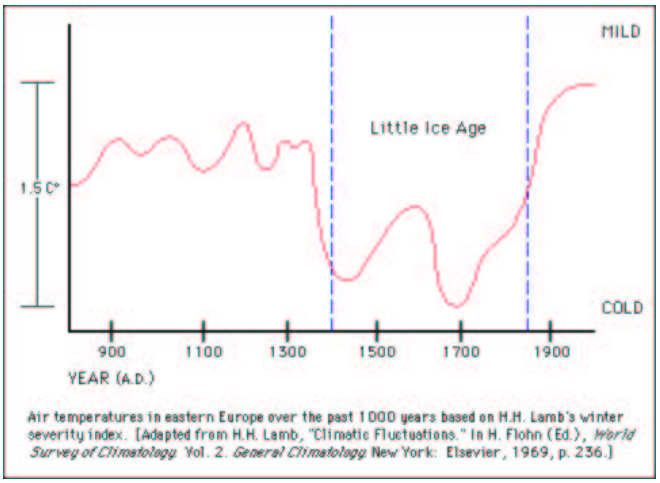

Figure 7: The little ice age...

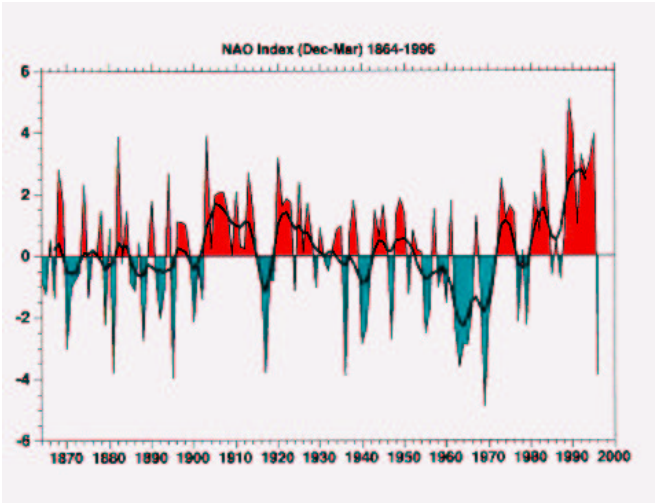

Figure 8: The NAO index from 1864 to 1996, defined as the difference in normalized pressure between Lisbon and Stykkisholmur, for the winter months, December-March. From “Atlantic Climate Variability” by Marshall and Kushnir, http://geoid.mit.edu/accp/avehtml.html.

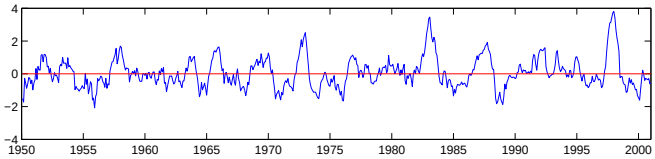

Figure 9: NINO3 record (averaged SST over the East Pacific: 5N-5S, 150W-90W), from 1950 to 2001.

The above gallery of climate variability examples, should make it clear that first, the climate system is tremendously complicated and second, that we are not likely to succeed in understanding it using a single model of all of the above phenomena and processes. Models used to study climate variability form a hierarchy, from general circulation models (GCMs) to toy models, roughly as follows:

1. General Circulation Models: 3D PDEs (based on the Navier-Stokes equations or similar) of the oceans and atmosphere, which require large computational resources and are not easy to decipher.

2. Intermediate models (Quasi Geostrophic, sometimes 2D; 2D continuous models in either longitude-latitude or latitude-depth; simplified reduced gravity layer models, etc):

3. Idealized toy (conceptual) models that highlight a single or a few physical mechanisms, and are more often than not derived heuristically, by guessing what the most dominant feedbacks are, rather than being derived rigorously from fuller models.

The focus of the following lectures is the third category, of toy models. These models, in spite of their heuristic derivation, have had a surprising success in explaining a variety of climate phenomena. Furthermore, the predictions of such highly simplified models have been confirmed numerous times by far more complex and realistic models. Let us briefly consider a few examples of such toy models in order to get an impression of the level of idealization they correspond to. Begin with a 0D energy balance model of the globally averaged temperature in which incoming radiation is partially reflected by the earth albedo and is balanced (at steady state) by long wave outgoing radiation

$$\frac{dT}{dt} = H_{\odot}^{\downarrow} \times (1 - \text{albedo}(T)) - \sigma T^4.$$

Some remarkable results may be obtained when considering specific dependences of the albedo on the temperature, as will be seen in lectures 6-9.

Proceed next to the Stommel two box [55] model of the thermohaline circulation (THC, Fig. 10). This model makes some simplifying assumptions that seem not only unjustified but possibly also unjustifiable. Yet, the model predictions of multiple equilibria and stability behavior of the THC have been confirmed by 3D ocean and coupled GCM results and have been shown to be remarkably robust (more in lectures 4-5).

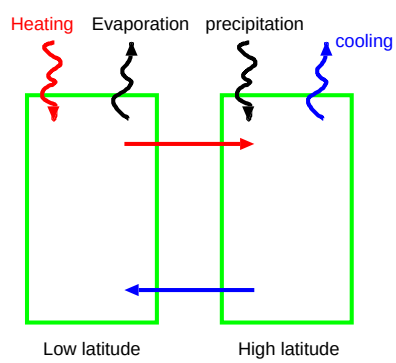

Figure 10: The Stommel two box model of the Thermohaline circulation

As a third and final example, consider a (nondimensional) delayed oscillator model of ENSO [56], to be further discussed in Lectures 1-3, in which the sea surface temperature of the East Pacific is affected by positive feedback term due to equatorial Kelvin wave propagation, by a delayed negative term due to equatorial Rossby waves, and using some simple cubic dissipation term

$$\frac{dT(t)}{dt} = T(t) - \alpha T(t - \delta_T) - T^3(t).$$

This simple model provides heuristic understanding of ENSO's dynamics that has led to many further interesting dynamical insights.

In general, toy models such as these, in spite of their lack of rigor, proved to be the most useful tool for understanding climate variability. Once a physical mechanism is understood within such an idealized toy model, the fuller intermediate models or GCMs may be used for a quantitative study of the proposed mechanism and for validation in a more realistic framework. Surprisingly, when the toy model results are checked using observations and fuller and more realistic models, the predictions of these toy models are often found correct as well as robust, making the study of such models worthwhile. That these trivial models are so successful in producing robust explanations for complex climate phenomena is nearly a miracle, possibly indicating that in spite of the complexity of the entire climate system, each separate time scale is governed by relatively simple low order dynamics.

Lecture 1

El Nino - Southern Oscillations: Phenomenology and dynamical background

Eli Tziperman

1.1 A brief description of the phenomenology

1.1.1 The mean state

Consider first a few of the main elements of the mean state of the equatorial Pacific ocean and atmosphere that play a role in ENSO's dynamics. For a more comprehensive introduction to the observed phenomenology see [47]; many useful pictures and animations are available on the El Nino theme page at http://www.pmel.noaa.gov/tao/elnino/nino-home.html.

The mean winds are easterly and clearly show the Inter-Tropical Convergence Zone (ITCZ) just north of the equator (Fig. 11); a vertical schematic section shows the Walker circulation (Fig. 12) with air rising over the "warm pool" area of the West Pacific and sinking over the East Pacific. The seasonal motion of the ITCZ and the modulation of the Walker circulation by the ENSO events are key players in ENSO's dynamics as will be seen below.

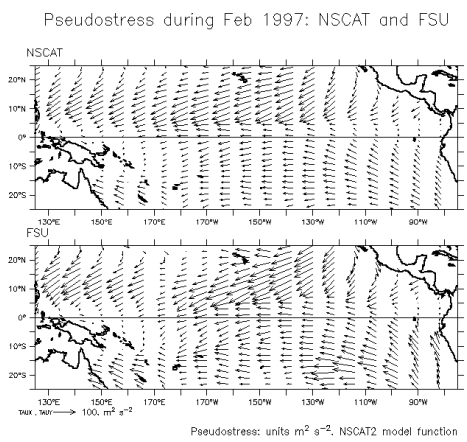

Figure 11: The wind stress showing the ITCZ in Feb 1997, using two different data sets (http://-www.pmel.noaa.gov/~kessler/nscat/vector-comparison-feb97.gif).

The mean easterly wind stress causes the above-thermocline warm water to accumulate in the West Pacific, causing the thermocline to slope as shown in the upper panel of Fig. 13. The thermocline slope induces an east-west gradient in the sea surface temperature (SST), creating the "cold tongue" in the east equatorial Pacific and the "warm pool" on the west (Fig. 14). This gradient, in turn, affects the Walker circulation and the mean wind stress as mentioned above.

1.1.2 ENSO variability

We now proceed to a brief description of the phenomenology of the ENSO variability about the mean climatology described above. The spatial structure of SST anomalies during La Nina, normal conditions and during El Nino are shown in Fig. 15. The slope in the equatorial thermocline varies quite dramatically between the El Nino, La Nina and normal conditions (Fig. 16).

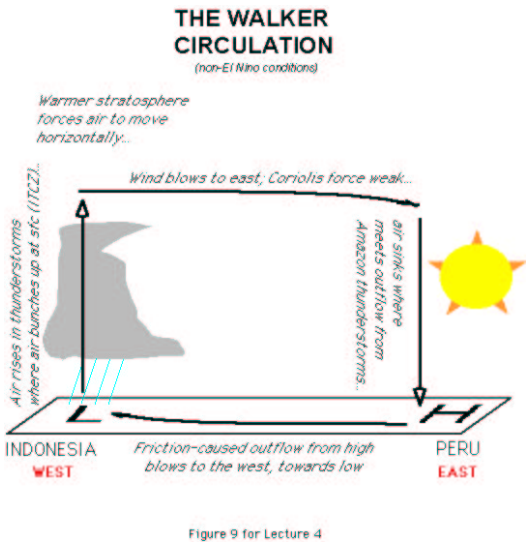

Figure 12: The Walker circulation (http://www.ldeo.columbia.edu/dees/ees/climate/slides/complete_index.html).

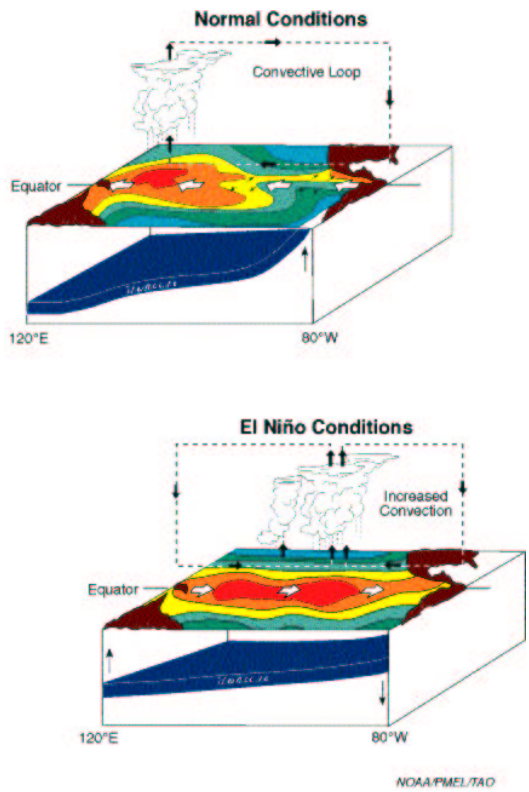

Figure 13: Schematic plot showing the equatorial thermocline slope during normal and El Nino conditions from the El Nino theme page http://www.pmel.noaa.gov/toga-tao/el-nino/.

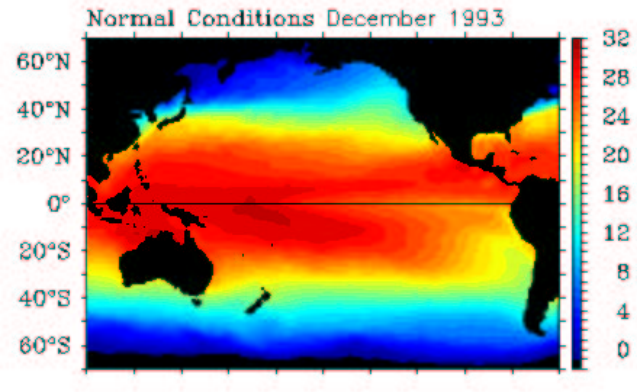

Figure 14: Normal SST conditions in the equatorial Pacific, showing the warm pool in the west and the cold tongue in the east (Reynolds data, from El Nino Theme page).

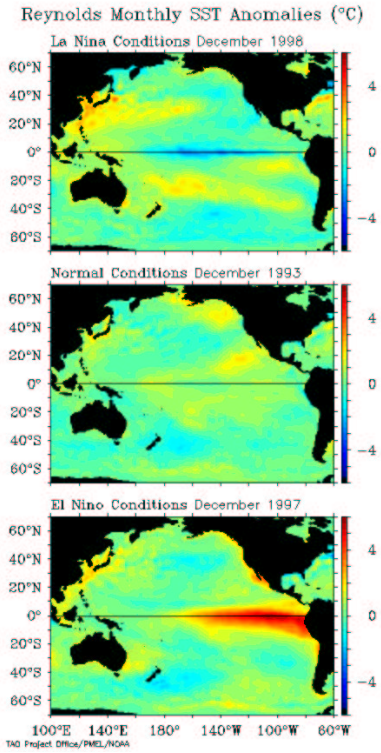

Figure 15: The anomalous SST field during typical La Nina, normal conditions and El Nino.

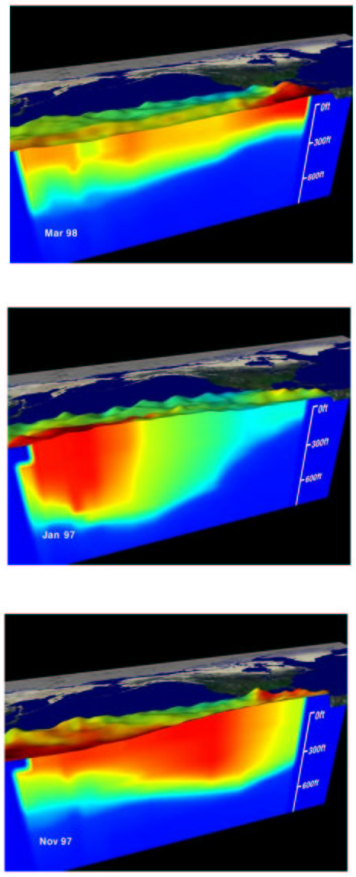

Figure 16: An east-west vertical section along the equatorial thermocline during normal, La Nina and El Nino conditions, from El Nino theme page http://www.pmel.noaa.gov/tao/elnino/nino-home.html.

The SST changes shown above during the ENSO cycle are accompanied by wind anomalies that cause the mean easterlies to weaken during El Nino events and strengthen during La Nina events. In order to obtain some feeling for the structure of the evolution in time during ENSO events, consider the equatorial SST as function of longitude and time, shown in Fig. 17. One can see the several-year time scale between El Nino events, and the irregular amplitude and time separation between the events. Also, note that El Nino events tend to reach their peak toward the end of the calendar year. For the implications of ENSO events on global weather etc see, for example, http://www.pmel.noaa.gov/toga-tao/el-nino/impacts.html. The purpose of the toy models to be considered below would be to explain the coupled ocean-atmosphere variability in the winds, thermocline slope and SST, as well as the time scale, the aperiodicity, and locking to the seasonal cycle of these events.

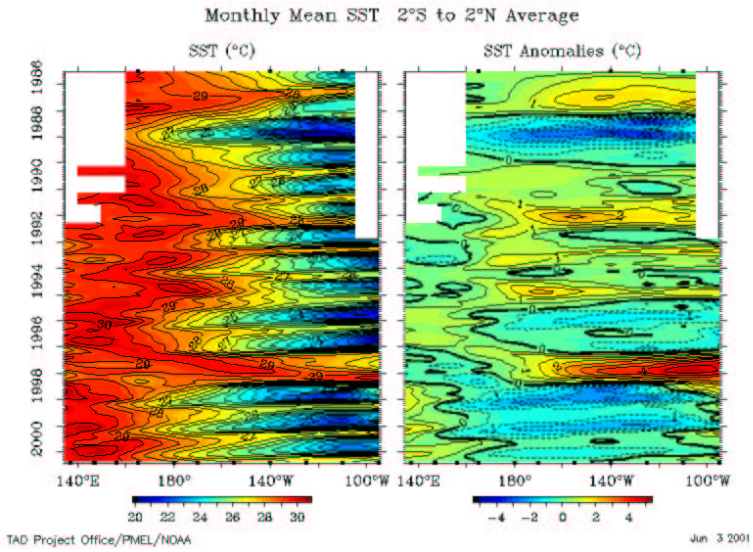

Figure 17: SST along the Equatorial Pacific as a Hovemoller diagram (plotted as function of longitude and time), for both the full SST and anomalies with respect to climatology. From El Nino theme page http://www.pmel.noaa.gov/toga-tao/el-nino/

1.1.3 Main issues

To summarize, the main questions to be addressed below regarding ENSO's dynamics using various conceptual models are

1. What is the mechanism of the El Nino cycle?
2. Why is the mean period quite robustly 4 years?
3. Is ENSO self-sustained or is it damped and requires external forcing by weather noise for example in order to be excited?
4. Why are ENSO events irregular: is it due to chaos? noise?
5. Why do ENSO events tend to peak toward the end of the calendar year (phase locking to the seasonal cycle)?

1.2 A brief equatorial dynamics background

1.2.1 Importance of thermocline dynamics and reduced gravity models

The phenomenology above indicates that motions of the equatorial thermocline are critical to ENSO's dynamics. We therefore start by deriving the simplest equations that describe the thermocline dynamics. Consider a two layer model, with the lower layer much thicker and thus assumed to be at rest (Fig. 18).

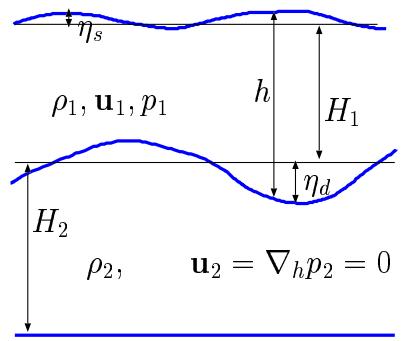

Figure 18: The $1\frac{1}{2}$ layer model

The momentum equations (Boussinesq approximation)

$$\frac{\partial \mathbf{u}}{\partial t} + \mathbf{u}\cdot\nabla\mathbf{u} + 2\Omega\times\mathbf{u} = -\frac{1}{\rho_0}\nabla p + \mathbf{g}\rho/\rho_0 + \nu\nabla^2\mathbf{u}$$

then imply that because the horizontal velocity in the lower layer is zero, $\mathbf{u}_{2H} = (u_2, v_2) = 0$, the horizontal pressure gradients are also zero in the lower layer, $\nabla_H p_2 = 0$, with $\nabla_H = (\frac{\partial}{\partial x}, \frac{\partial}{\partial y})$ being the two dimensional horizontal gradient, and where ∇ above stands for the three dimensional gradient operator. Assuming a hydrostatic vertical momentum balance (because $H \ll L$)

$$p_z = -g\rho$$

and integrating this balance in z, we can write the pressure at a depth z in the upper layer as

$$p_1(x,y,z,t) = g(-z + \eta_s(x,y,t))\rho_1$$

so that

$$-\frac{1}{\rho_0}\nabla p_1 \approx -g\nabla\eta_s.$$

In the lower layer, the pressure is

$$p_2(x,y,z,t) = g(H_1 + \eta_s - \eta_d)\rho_1 + g(H_2 + \eta_d - z)\rho_2$$

so that

$$\begin{aligned}\frac{1}{\rho_0}\nabla_H p_2 &= \nabla_H\left(\frac{\rho_1}{\rho_0}g\eta_s + \frac{\rho_2-\rho_1}{\rho_0}g\eta_d\right)\\ &\approx \nabla_H(g\eta_s + g'\eta_d)\end{aligned}$$

where $g' \equiv \frac{\rho_2-\rho_1}{\rho_0}g \approx \frac{\rho_2-\rho_1}{\rho_2}g$. That this deep horizontal pressure gradient vanishes gives

$$g\nabla_H\eta_s = -g'\nabla_H\eta_d$$

which, together with the observation that $g' \ll g$ so that $\eta_s \ll \eta_d$, implies

$$g\nabla_H \eta_s = -g'\nabla_H \eta_d \approx g'\nabla_H h.$$

Together with the above relations this finally allows us to write the horizontal pressure gradient in the upper layer as a function of the upper layer thickness

$$-\frac{1}{\rho_0}\nabla p_1 = -g'\nabla h.$$

1.2.2 The equatorial β plane

The objective now is to find a convenient representation of the effect of the earth rotation near the equator [43, 20]. We start with horizontal momentum equations for a $1\frac{1}{2}$ layer fluid as above, on a sphere, where we use

$$2\vec{\Omega} \times \mathbf{u} = 2\Omega \begin{pmatrix} w\cos\theta - v\sin\theta \\ u\sin\theta \\ -u\cos\theta \end{pmatrix}.$$

to find

$$\begin{aligned} \frac{du}{dt} + \frac{uw}{r} - \frac{uv}{r}\tan\theta + 2\Omega(w\cos\theta - v\sin\theta) &= -\frac{g'}{r\cos\theta}\frac{\partial h}{\partial\phi} + \mathcal{F}_\phi \\ \frac{dv}{dt} + \frac{wv}{r} - \frac{u^2}{r}\tan\theta + 2\Omega u\sin\theta &= -\frac{g'}{r}\frac{\partial h}{\partial\theta} + \mathcal{F}_\theta \end{aligned}$$

where

$$\frac{d}{dt} \equiv \frac{\partial}{\partial t} + \frac{u}{r\cos\theta}\frac{\partial}{\partial\phi} + \frac{v}{r}\frac{\partial}{\partial\theta} + w\frac{\partial}{\partial r},$$

and where $(\mathcal{F}_\phi, \mathcal{F}_\theta)$ represent the forcing and dissipation terms, and θ, ϕ the latitude and longitude. Next, assume linear momentum dynamics, and use the fact that $w \ll (u,v)$. Also, write the vertical coordinate as $r = r_0 + z$ where r_0 is the earth radius, so that within a thin layer of fluid (ocean thickness $\ll$ earth radius) we have $1/r = 1/(r_0+z) \approx 1/r_0$, and therefore,

$$\begin{aligned} \frac{\partial u}{\partial t} - 2\Omega\sin\theta v &= -\frac{g'}{r_0\cos\theta}\frac{\partial h}{\partial\phi} + \mathcal{F}_\phi \\ \frac{\partial v}{\partial t} + 2\Omega\sin\theta u &= -\frac{g'}{r_0}\frac{\partial h}{\partial\theta} + \mathcal{F}_\theta. \end{aligned}$$

Next, we restrict our attention to near-equatorial regions, where we can define local Cartesian coordinates around some central location (θ_0, ϕ_0)

$$\begin{aligned} x &\equiv r_0\cos\theta_0(\phi - \phi_0) \\ y &\equiv r_0(\theta - \theta_0), \end{aligned}$$

as well as expand the Coriolis force as

$$\begin{aligned} 2\Omega\sin\theta &\approx 2\Omega\sin\theta_0 + 2\Omega\cos\theta_0(\theta - \theta_0) \\ &= f_0 + \beta y \end{aligned}$$

with $\beta \equiv 2\Omega\cos\theta_0/r_0$. An expansion around the equator $\theta_0 = 0$ leads to $f_0 = 0$. Using a simple linear friction law and incorporating the wind stress forcing

$$\begin{aligned} \mathcal{F}_\phi &= \mathcal{F}_x = -\varepsilon u + \tau^x/(\rho_0 H) \\ \mathcal{F}_\theta &= \mathcal{F}_y = -\varepsilon v + \tau^y/(\rho_0 H) \end{aligned}$$

we obtain the final set of β-plane momentum equations for a $1\frac{1}{2}$ layer model

$$\frac{\partial u}{\partial t} - \beta y v = -g' \frac{\partial h}{\partial x} - \varepsilon u + \frac{\tau^x}{\rho_0 H} \tag{1}$$

$$\frac{\partial v}{\partial t} + \beta y u = -g' \frac{\partial h}{\partial y} - \varepsilon v + \frac{\tau^y}{\rho_0 H}. \tag{2}$$

and with three unknowns (u, v, h) we need a third equation which is provided by the linearized mass conservation equation (which also includes on the rhs a rough linear parameterization of entrainment (mixing) at the base of the water layer above the thermocline)

$$\frac{\partial h}{\partial t} + H\left(\frac{\partial u}{\partial x} + \frac{\partial v}{\partial y}\right) = -\varepsilon h. \tag{3}$$

1.2.3 Equatorial waves

The derivation here follows Gill [20]. Consider first the case of an equatorial Kelvin wave, which is a special solution of (1,2,3) for the case of zero meridional velocity ($v = 0$), no forcing and no dissipation. In this case, these equations reduce to

$$\begin{aligned} \frac{\partial u}{\partial t} &= -g' \frac{\partial h}{\partial x} \\ \beta y u &= -g' \frac{\partial h}{\partial y} \\ \frac{\partial h}{\partial t} + H \frac{\partial u}{\partial x} &= 0 \end{aligned}$$

Note the geostrophic balance in the y-momentum equation. Substituting $e^{i(kx-\omega t)}$ dependence for all three variables, we get from the first that $u = (kg'/\omega)h$, so that the third one gives the dispersion relation

$$\omega^2 = (g'H)k^2$$

which is the dispersion relation of a simple shallow water gravity wave. The second equation then gives $\beta y \frac{kg'}{\omega} h = -g' \frac{\partial h}{\partial y}$, or

$$\frac{\partial h}{\partial y} = -\frac{\beta k}{\omega} y h.$$

We are searching for equatorial-trapped solutions, and we note that the solution for the y-structure decays away from the equator only when $k > 0$. This implies that the wave solution we have found must be eastward propagating! Using the dispersion relation, with

$$c \equiv \sqrt{g'H} \approx (9.8 \times 10^2 * cm\, sec^{-2} \times 5 * 10^{-3} \times 100 \times 10^2 cm)^{1/2} \approx 2.2 m/sec$$

we finally have

$$h_{Kelvin}(x, y, t) \propto e^{-\frac{1}{2}(\beta/c)y^2} e^{i(kx-\omega t)}.$$

Note that the decay scale away from the equator is the equatorial Rossby radius of deformation defined as

$$L_{eq}^R \equiv \sqrt{c/2\beta} \approx (c/(2 \times 2.3 \times 10^{-11} m^{-1} sec^{-1}))^{1/2} \approx 220 km$$

Next is the derivation of the full set of equatorial waves, where we now do not assume that the meridional velocity v vanishes. Substitute $h(x,y,t) = h(y)e^{i(kx-\omega t)}$ dependence, and similarly for (u,v), and derive a single equation for h to find the parabolic cylinder equation (Gill, [20], section 11.6.1)

$$\frac{d^2v}{dy^2} + \left(\frac{\omega^2}{c^2} - k^2 - \frac{\beta k}{\omega} - \frac{\beta^2}{c^2}y^2\right)v = 0.$$

The solutions that vanish at $y \to \pm\infty$ occur only for certain relations between the coefficients, and these relations serve as the dispersion relation

$$\frac{\omega^2}{c^2} - k^2 - \frac{\beta k}{\omega} = (2n+1)\frac{\beta}{c}. \tag{4}$$

Note that the Kelvin wave dispersion relation is formally a solution of this dispersion relation for $n = -1$ (simply check that $\omega = ck$ satisfies (4) for $n = -1$). The meridional structure of the waves in this case of equatorially trapped solutions is expressed in terms of the Hermit polynomials

$$v = 2^{-n/2}H_n((\beta/c)^{1/2}y)\exp(-\beta y^2/2c)\cos(kx-\omega t)$$

and is shown in Fig. 19, where

$$H_0 = 1; \qquad H_1 = 2x; \qquad H_2 = 4x^2 - 2; \qquad H_3 = 8x^3 - 12x; \qquad H_4 = 16x^4 - 48x^2 + 12$$

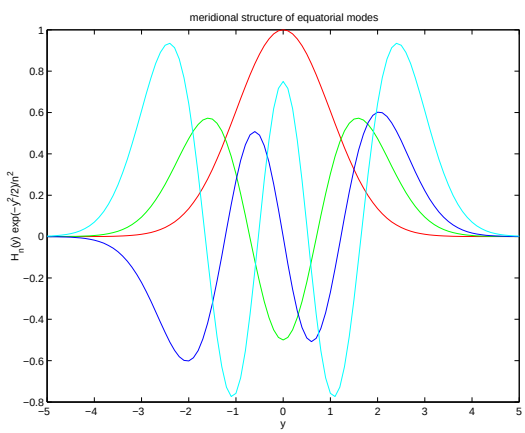

Figure 19: The latitudinal structure of the first few equatorial modes: $H_n(y)\exp(-y^2/2)/n^2$.

The dispersion relation is plotted in Fig. 20.

So, we have a complete set of waves, the Kelvin ($n = -1$), Yanai ($n = 0$), Rossby and Poincare ($n > 0$) waves. As seen in the plot, the dispersion relation includes two main sets of waves for $n > 0$. For high frequency, we can neglect the term $\frac{\beta k}{\omega}$, to find the Poincare gravity-inertial waves

$$\omega^2 \approx (2n+1)\beta c + k^2c^2,$$

while for low frequency, we can neglect the term ω^2/c^2 in the dispersion relation to find the westward propagating Rossby wave dispersion relation

$$\omega = \frac{-\beta k}{k^2 + (2n+1)\beta/c}.$$

Typical speeds of long Rossby waves would therefore be

$$\omega/k = \frac{-c}{2n+1}$$

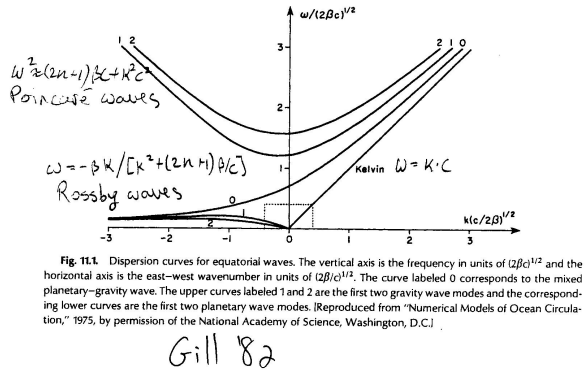

Fig. 11.1. Dispersion curves for equatorial waves. The vertical axis is the frequency in units of $(2\beta c)^{1/2}$ and the horizontal axis is the east–west wavenumber in units of $(2\beta/c)^{1/2}$. The curve labeled 0 corresponds to the mixed planetary–gravity wave. The upper curves labeled 1 and 2 are the first two gravity wave modes and the corresponding lower curves are the first two planetary wave modes. [Reproduced from "Numerical Models of Ocean Circulation," 1975, by permission of the National Academy of Science, Washington, D.C.]

Figure 20: The Equatorial wave dispersion relation, (Gill [20], p 438, Fig. 11.1)/

so that the first Rossby mode ($n = 1$) travels at a 1/3 of the Kelvin wave speed, implying a roughly 2.5 months crossing time for Kelvin and 8 months for Rossby waves (based on 15,000 km basin width).

Note (Fig. 19) that the first Rossby mode has a zero at the equator and two maxima away from the equator, while the Kelvin wave has a maximum at the equator. This tells us something about how a random initial perturbation will project on the different modes. That is, a forcing pattern or an initial perturbation that is centered at the equator may be expected to excite Kelvin waves, while a forcing or initial perturbation that has components off the equator will tend to excite Rossby waves. The above discussion centers on the first baroclinic mode, but may be generalized to higher vertical baroclinic modes, although for our purposes this is not essential.

1.2.4 Ocean response to wind perturbation

Consider first the mean state of the thermocline. The steady state ($\partial u/\partial t = 0$) momentum equation (1) in a reduced gravity model, at $y = 0$ ($\beta y v = 0$) in the presence of easterly wind forcing and neglecting frictional effects ($-\varepsilon u = 0$) is

$$0 \approx -g' \frac{\partial h}{\partial x} + \frac{\tau^x}{\rho_0 H}$$

so that an easterly wind stress is balanced by a pressure gradient due to a thermocline tilt, with the thermocline closer to the surface in the East Pacific. This mean state of the thermocline results in the cold tongue there, as observed, via the mixing of cold sub-thermocline water with the surface water, as will be discussed more quantitatively below.

Regarding the interannual equatorial thermocline variability, at this stage we just note that a wind perturbation that corresponds to a weakening of the mean easterlies in the central Pacific affects the thermocline depth in the central Pacific. It creates downwelling Kelvin waves (that is, waves that propagate a downwelling signal, which means a thermocline deepening signal; these are waves that propagate a warm water surplus above the thermocline, and may therefore be called "warm" waves) and upwelling (i.e. cold) Rossby waves. The excitation of these waves by a wind anomaly will be examined more rigorously below.

1.2.5 Atmospheric response to SST anomalies

We now need to describe the atmospheric response to SST perturbations. Use Gill's [19] model for this, whose equations are very much like the β plane ocean equations, except that the atmospheric time scales are much

shorter so that we assume the atmosphere to be in a steady state with the forcing by a specified heating Q,

$$-\beta y V = -\frac{\partial \Theta}{\partial x} - \varepsilon_a U \tag{5}$$

$$+\beta y U = -\frac{\partial \Theta}{\partial y} - \varepsilon_a V \tag{6}$$

$$c_a^2 \left(\frac{\partial U}{\partial x} + \frac{\partial V}{\partial y} \right) = -\varepsilon_a \Theta + Q. \tag{7}$$

where (U, V, Θ) stand for the zonal and meridional surface winds, and a geopotential ($dp = -g\rho dz = -\rho d\Theta$, Gill [20] section 6.17). The heating may be parameterized to be linear in the SST

$$Q = \alpha_T T.$$

We next need to use these equations to deduce the effect of an SST anomaly in the East Pacific on winds in the central Pacific. The above equations may be solved for a general heating function, and we only briefly outline the derivation of the solution (see Dijkstra, [9] p. 347). One first defines $S = \Theta + U$ and $R = \Theta - U$ and expands the heating and these two new variables in a series of parabolic cylinder equations, e.g.

$$Q(x,y,t) = \sum_{n=0}^{\infty} Q_n(x) D_n(y).$$

Next, these expansions are substituted into the Gill's model and equations are derived for $S_n(x)$ and $R_n(x)$ for each n. The solution of these equations for $n = 0, 1, 2$ is

$$\begin{aligned} R_0(x) &= \mu_0 \int_{x_w}^{x} e^{-\varepsilon_a (x-s)} Q_0(s) ds \\ R_1(x) &= 0 \\ R_2(x) &= \mu_0 \int_{x}^{x_e} e^{3\varepsilon_a (x-s)} (Q_2(s) + Q_0(s)) ds \end{aligned}$$

where $\mu_0 = \alpha_T \Delta T L / c_a^3$. Note that $R_0(x)$ is influenced by heating west of x, and thus represents the influence of atmospheric Kelvin waves that travel eastward, accumulate the influence of the heating, and thus influence the atmospheric state at x. The atmospheric Kelvin waves are damped (via the terms depending on ε_a) on their way, and therefore "remember" only the heating within a (nondimensional) distance $1/\varepsilon_a$ to the west of x. Similarly, $R_2(x)$ reflects the influence of atmospheric Rossby waves that travel westward toward x. In this case the waves travel slower, and thus by the time they arrive at x, they only "remember" the influence of the heating over a (nondimensional) distance of $1/(3\varepsilon_a)$.

Next, these solutions for R and S are transformed back to the physical variables U, V, Θ and truncated into the first 2-3 terms only in n, giving

$$U(x, y = 0) = \frac{3}{2} R_2(x) - \frac{1}{2} R_0(x)$$

Finally, we assume that the atmospheric heating occurs only over the east Pacific

$$Q(x) = \alpha_T \delta(x - x_e) T(x_e)$$

and perform the integrations over x in the above expressions for $R_{0,1,2}$ to find that only the atmospheric Rossby wave solution that propagates from x_e to x affects the wind speed at x

$$U(x,y) \propto -e^{(x-x_e)/(c_a/3\varepsilon_a)} T(x_e) e^{-\frac{1}{2} y^2/(L_R^a)^2} \tag{8}$$

where $c_a \approx 40 m/sec$; $\beta = 2.3 \times 10^{-13} cm^{-1} sec^{-1}$; $L_r^a = \sqrt{2c_a/\beta} \approx 2 \times 10^3 km$, and the decay scale of the influence of the east Pacific heating on the zonal wind west of that point is $(c_a/3\varepsilon_a) \approx 3500 km$ for $\varepsilon_a \approx 3 day^{-1}$.

1.2.6 On the atmospheric heating

As a simple entry point to this subject, it is convenient to consider the atmospheric heating parameterization used in intermediate El Nino models such as the Cane-Zebiak [66] model. This parameterization assumes that the anomalous atmospheric heating is dominated by diabatic heating that occurs via latent heat release due to moisture condensation. The heating is divided into a contribution due to condensation of water evaporated locally at the ocean surface (Q_s) and another contribution due to the condensation of the larger scale humidity field induced by upward air motion that results from a local wind convergence (Q_1),

$$\begin{aligned} Q &= Q_s + Q_1 \\ Q_s &= (\alpha T)\exp[(\bar{T} - 30^\circ C)/16.7^\circ C] \\ Q_1 &= \beta_*[M(\bar{c} + c) - M(\bar{c})] \\ c &= -[U_x + V_y]. \end{aligned}$$

The function $M(x)$ is defined as

$$M(x) = \begin{cases} x & x > 0 \\ 0 & x \leq 0 \end{cases}$$

The local evaporation parameterization is simply an empirical curve fitting of the Clausius-Clapeyron relation + linearization which together give the saturation vapor pressure (pressure at which vapor and liquid water can coexist) at a temperature T

$$q_w(\bar{T} + \delta T) = a\exp[-\frac{b}{T + \delta T}] \propto \delta T \exp[-\frac{b}{T}]$$

The dependence of the atmospheric heating on the mean SST, $\bar{T}$, is therefore exponential, hence quite strong. The increase in climatological monthly equatorial eastern Pacific mean SST from about 23°C in September to about 26.5°C in March-April corresponds to a 25% enhancement in the perturbation heating Q_s for the same SST perturbation.

The condensation of the larger scale humidity field due to the local wind convergence is again influenced by the mean conditions; in this case the mean convergence: only if the total convergence $\bar{c} + c$ is positive, is the local air motion upward. And only if the local motion is upward, does it induce condensation and therefore atmospheric heating. The mean convergence in the east equatorial Pacific is determined by the seasonal location of the ITCZ. When the ITCZ is near the equator, the mean convergence is positive, and anomalous atmospheric convergence is effective in causing atmospheric heating. When the ITCZ is away from the equator, the mean convergence is negative, and anomalous convergence does not cause diabatic heating.

Overall, it is important to note that the response of the atmospheric heating to a given SST anomaly depends on the mean atmospheric conditions which vary seasonally. As we shall see below, this dependence on the mean seasonal conditions introduces some interesting dynamical effects.

Lecture 2

ENSO toy models

Eli Tziperman

2.1 A heuristic derivation of a delayed oscillator equation

Let us consider first a heuristic derivation of an equation for the sea surface temperature in the East Pacific, which will be followed by a more rigorous derivation in the following sections. Assume that the East Pacific SST affects the atmospheric heating and thus the central Pacific wind speed. The resulting wind stress, in turn, excites equatorial Kelvin and Rossby ocean waves. These waves affect the East Pacific thermocline depth and hence the East Pacific equatorial SST, and the whole feedback loop may be quantified as follows. Let τ_K and τ_R be the basin crossing times of equatorial Kelvin and Rossby waves, correspondingly. Now, a positive central Pacific equatorial thermocline depth anomaly $h_{eq}(x_c)$ at time $t-\frac{1}{2}\tau_K$ excites an eastward propagating downwelling Kelvin wave at the central Pacific that arrives after about $\frac{1}{2}\tau_K \approx 1$ month to the eastern Pacific and deepens the thermocline there. Similarly, a negative off-equatorial depth anomaly (that is, a shallowing signal of the thermocline) in the central Pacific $h_{off-eq}(x_c)$ at a time $t-[\frac{1}{2}\tau_R+\tau_K]$ ($\frac{1}{2}\tau_R+\tau_K \approx 6$ months) excites a westward propagating Rossby wave at the central Pacific that is reflected off the western boundary as an equatorial Kelvin waves and eventually arrives to the eastern Pacific at time t, shallows the thermocline there and causes cooling of the SST. We add a nonlinear damping term that can stabilize the system, and write an equation for the eastern Pacific temperature that includes the Kelvin wave, Rossby wave and local damping terms as follows

$$\frac{dT(t)}{dt} = \hat{a}h_{eq}(x_c, t-\frac{1}{2}\tau_K) + \hat{b}h_{off-eq}(x_c, t-[\frac{1}{2}\tau_R+\tau_K]) - cT(t)^3$$

where $\hat{a}, \hat{b}, c$ are positive constants. Note that we assume that once the thermocline deepening or shallowing signal reaches the East Pacific it immediately affects the SST there. This actually neglects the SST adjustment time and we will include this time scale in the more rigorous derivation below. Note that because the mean thermocline depth is shallower in the East Pacific than in the West Pacific, a deepening or rise of the thermocline in the East Pacific is able to affect the mixing between cool sub-thermocline waters and surface waters, and thus affect the SST; in the West Pacific, the thermocline is deeper, so that even if it rises somewhat, it is still too deep to affect the SST. Now, the thermocline depth in the equatorial central Pacific is a response to the equatorial central Pacific wind. The off-equatorial thermocline depth in the central Pacific will be shown below to be a response to the wind curl off the equator, which will be shown to be negatively correlated with the wind stress at the equator. We can therefore write the above equation as

$$\frac{dT(t)}{dt} = \bar{a}\tau_{eq}(x_c, t-\frac{1}{2}\tau_K) - \bar{b}\tau_{eq}(x_c, t-[\frac{1}{2}\tau_R+\tau_K]) - cT(t)^3$$

where $\bar{a}\bar{b}$ are some new proportionality constants. Next, the wind stress in the Central Pacific is a pretty much simultaneous response to the East Pacific SST, so that we can actually write

$$\frac{dT(t)}{dt} = aT(t-\frac{1}{2}\tau_K) - bT(t-[\frac{1}{2}\tau_R+\tau_K]) - cT(t)^3 \tag{9}$$

where again the constants of proportionality a, b, c are all positive. The first term in this equation provides a positive feedback due to the Kelvin wave, with a short delay of about one month; the second term represents the Rossby wave with a longer-delayed negative feedback, and the last term is a nonlinear damping term. This last equation (9) is the desired delayed oscillator equation for El Nino.

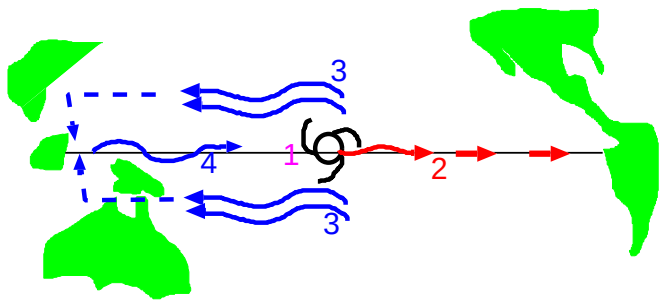

Figure 21: A schematic picture of the delayed oscillator mechanism

Based on the delayed oscillator model, the El Nino cycle may be described as follows (Fig. 21). A wind weakening (1 in Fig. 21)) creates an equatorial warm (downwelling) Kelvin wave (2) that travels to the East Pacific within 1-2 months, where the thermocline deepening induces an SST heating and starts an El Niño event. The SST heating further weakens the central Pacific winds and the event is therefore amplified by ocean-atmosphere instability. The original wind weakening also creates off-equatorial cold (upwelling) Rossby waves (due to the induced changes to the wind curl, as will be shown below) (3) that are reflected from the western boundary as cold Kelvin waves (4), arrive at the eastern boundary about 6 months later and terminate the event.

Note that we ignored reflection at the eastern boundary. Much of the energy of an eastward traveling equatorial Kelvin wave incident on the eastern boundary will be reflected as poleward traveling coastal Kelvin waves and will escape from the equatorial domain. In contrast, westward traveling Rossby waves incidenting on the western boundary are reflected as equatorward traveling coastal Kelvin waves. These, in turn, are reflected eastward at the equator as equatorial Kelvin waves, hence creating an efficient reflection process in which the wave energy ermains in the equatorial strip.

2.1.1 Analysis of the delayed oscillator equation

Battisti [2] and Suarez and Schopf [56] (see also Dijkstra [9] section 7.5.4.2) have used a slightly different delayed oscillator equation, basically ignoring the shorter Kelvin wave delay, which in a nondimensional form is

$$\frac{dT(t)}{dt} = T(t) - \alpha T(t-\delta_T) - T^3(t). \tag{10}$$

Note first that a delayed equation formally has an infinite number of degrees of freedom (it requires an infinite number of initial conditions corresponding to the times from $t = -\delta_T$ to $t = 0$, and is thus equivalent to an infinite number of ODEs). So formally this is not a "simple" equation. Only a few of these degrees of freedom are actually activated in reasonable parameter regimes (as measured by the dimension of the attractor in phase space). The various delayed oscillator equations result in El-Nino like oscillations whose periods may be tuned, by changing the coefficients, to about 4 years (Fig. 22).

Let us analyze the linearized stability behavior of 10. The equilibria of the above delayed oscillator equation are the zero solution, and then one warm solution and one cold solution

$$\bar{T} = 0, \pm\sqrt{1-\alpha}.$$

Considering a perturbation about these steady states by setting $T = \bar{T} + \tilde{T}$ and linearizing, we have

$$\frac{d\tilde{T}(t)}{dt} = \tilde{T}(t)(1-3\bar{T}^2) - \alpha\tilde{T}(t-\delta_T).$$

Letting $\tilde{T} = e^{\sigma t}$ where $\sigma = \sigma_r + i\sigma_i$, results in the linearized eigenvalue problem

$$\sigma = 1 - 3\bar{T}^2 - \alpha e^{-\sigma\delta_T}$$

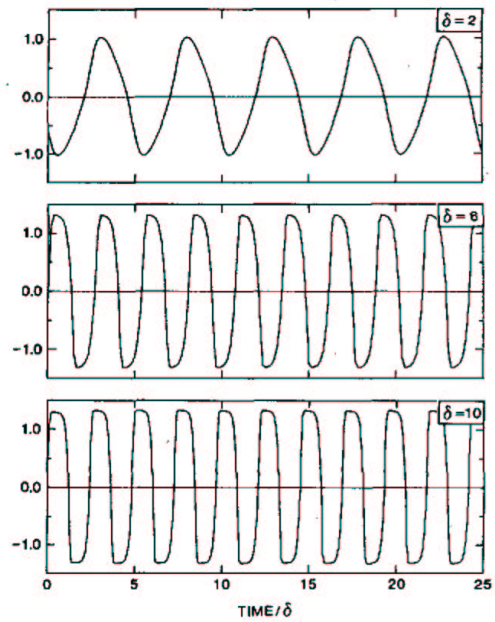

FIG. 4. Behavior of the nonlinear oscillator. (a) $\alpha = 0.75$, $\delta = 2$, (b) $\alpha = 0.75$, $\delta = 6$, and (c) $\alpha = 0.75$, $\delta = 10$. The time axis is scaled in units of the delay.

Figure 22: Results of the delayed oscillator of equation 10, from [56].

(note that this is a complex transcendental equation, with the real and imaginary parts of σ satisfying equations that involve sine and cosine functions) which can be solved for the frequency σ as function of the two nondimensional parameters α and δ_T. It turns out that the zero solution is unstable, with a non oscillatory exponential growth. The two other (warm and cold) equilibria may become oscillatory unstable, as shown in Fig. 23.

The behavior of the unstable modes is not completely simple nor intuitive: the unstable modes appear for larger values of the negative feedback (Rossby term) α, and for larger values of the delay time δ... The period of the oscillatory solutions in the delay model is shown by the light solid lines in Fig. 23, while the dashed contours give the period in multiples of the delay time. The period of the unstable modes is in the range of up to 2-3 times the Rossby delay time. Taking that delay time to be some 8 months, we get a 16-24 months period, which is significantly smaller than the observed period of 48 months. Clearly the period is not a well determined part of the picture, as it is not a robust outcome of this model, and has reasonable values for a fairly small range of model parameters. Other studies [36] also found that the period of ENSO may not be well determined by linearized theories, and may be due to some not understood nonlinear effects.

While the delayed oscillator model above is useful in providing us with a feeling of what the mechanism of ENSO is, it actually represents only a specific limit of the fuller dynamics. It assumes that once the waves arrive to the East Pacific, they immediately influence the SST. In reality, there is another time scale (delay) that accounts for the time it takes the sub-surface thermocline depth anomalies in the eastern Pacific to affect the eastern Pacific SST. To introduce this and other processes, it is useful to go through a more rigorous derivation, starting from the β plane equations.

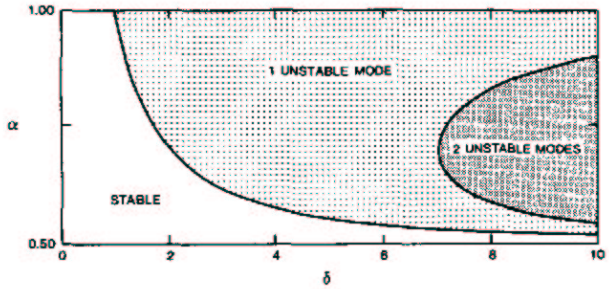

FIG. 2. Neutral stability curves of the outer stationary solution. Parameters lying below the lower line are stable. An infinite number of additional neutral curves exist to the right of the lines shown, but are only found for large δ.

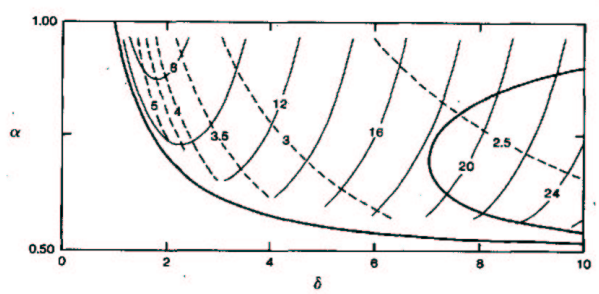

FIG. 5. The fundamental period of the nonlinear oscillator found numerically. The heavy solid lines are the neutral curves of the linear problem, reproduced from Fig. 2. The light solid contours give the period of the oscillation ($2\pi/\sigma_i$), while the dashed contours present the period in multiples of the delay.

Figure 23: Stability and period of the delayed oscillator of equation 10; Suarez & Schopf [56].

2.2 Fast SST, fast wave and mixed mode ENSO regimes

2.2.1 Ocean dynamics

Let us represent the equatorial dynamics using the two-strip approximation of Jin [27, 28] with an equatorial strip and an off-equatorial strip. The equations for the ocean wave dynamics for each strip are then solved by integrating them along wave characteristics following Galanti and Tziperman [12]. Further simplification is achieved by neglecting the meridional damping ($-\varepsilon_m v$) and the meridional wind stress ($\tau_y/\rho H$) terms. Yet another simplification is obtained by taking the long wave approximation, which results in dropping the time derivative from the y momentum equation. This occurs because the meridional velocity v scales like $C_o\frac{\lambda}{L}$ while the zonal velocity scales like C_o, where C_o, λ, L are the gravity wave speed, meridional scale (equatorial Rossby radius) and the long zonal scale of the wave, respectively, and because $\frac{\lambda}{L} \ll 1$. The resulting set of equations is

$$\begin{aligned}
\frac{\partial u}{\partial t} - \beta y v + g'\frac{\partial h}{\partial x} &= -\varepsilon_m u + \frac{\tau_x}{\rho H}, \\
\beta y u + g'\frac{\partial h}{\partial y} &= 0, \\
\frac{\partial h}{\partial t} + H\left[\frac{\partial u}{\partial x} + \frac{\partial v}{\partial y}\right] &= -\varepsilon_m h,
\end{aligned} \tag{11}$$

where ε_m is the oceanic damping coefficient. Eliminating u and v from (11), a single equation for h may be obtained,

$$\beta y^2(\partial_t + \varepsilon_m)h + \frac{g'H}{\beta}\left[\frac{2}{y}\partial_y - \partial_{yy}\right](\partial_t + \varepsilon_m)h - g'H\partial_x h + \frac{1}{\rho}(\tau_x - y\partial_y\tau_x) = 0. \tag{12}$$

Next, evaluate this equation at the equator ($y = 0$), and at a zonal band off the equator ($y = y_n$). This "two-strip" approximation assumes that the ocean dynamics in the equatorial region is well represented by a combination of equatorial Kelvin waves and off-equatorial long Rossby waves, both well represented by the two strips at latitudes $y = 0$ and $y = y_n$.

A Kelvin wave solution of the form

$$h(x,y,t) = h_e(x,t)\exp(-\frac{\beta}{2C_o}y^2), \tag{13}$$

satisfies equation (12), and therefore, taking advantage of the known meridional structure, we can get an equation for a forced and dissipated Kelvin wave at $y = 0$ of the form

$$(\partial_t + C_o\partial_x + \varepsilon_m)h_e = \frac{1}{C_o\rho}\tau_{ex}, \tag{14}$$

where τ_{ex} is the wind stress at the equator and $C_0 = \sqrt{g'H}$. The rhs forcing for the Kelvin waves is proportional to the wind stress, and we shall see below that this implies that a weakening of the easterlies results in the excitation of warm Kelvin waves. Next, integrate (14) over the trajectory of an eastward propagating Kelvin wave that starts from the western boundary at a time $t - \tau_2$ and reaches the eastern boundary at a time t, where $\tau_2 = L/C_o$ is the Kelvin crossing time of a basin of length L. The wave is assumed to be excited by the wind stress in the central part of the basin, from $x = x_W + .25L$ to $x = x_W + .75L$. The wind stress is evaluated at the middle of the basin, $x = x_w + L/2$, at a time $t - \tau_2/2$, which is the time when the Kelvin wave crosses the middle of the basin. We denote the equatorial thermocline depth anomaly at the western (eastern) edge of the basin by h_{eW} (h_{eE}), and the solution to (14) obtained by integrating along characteristics is then

$$h_{eE}(t) = h_{eW}(t - \tau_2)e^{-\varepsilon_m\tau_2} + \frac{1}{\rho C_o}dt\tau_2\tau_{ex}(\frac{L}{2}, t - \frac{\tau_2}{2})e^{-\varepsilon_m\frac{\tau_2}{2}}, \tag{15}$$

where $dt = 0.5$ is the fraction of crossing time during which the wind stress affects the oceanic waves.

Next, we wish to solve (12) at the off-equatorial band ($y = y_n$), in order to include the Rossby wave dynamics in the model. It can be shown that at $y_n \geq 2L_o$ (where L_o is the oceanic Rossby radius of deformation) the second term in (12) is negligible [27, 28], resulting in the off-equatorial equation for a forced and dissipated Rossby wave

$$(\partial_t - \frac{C_0^2}{\beta y_n^2}\partial_x + \varepsilon_m)h_n = \frac{1}{\beta\rho}\left[\frac{\partial}{\partial y}(\frac{\tau_x}{y})|_{y=y_n}\right]. \tag{16}$$

Note that the rhs forcing for the Rossby waves is the curl of the wind this time, and we shall use this below to show that a weakening of the easterlies results in the excitation of cold Rossby waves. Solving (16) again along characteristics, for a Rossby wave that starts from the eastern boundary at time $t - \tau_1$, where $\tau_1 = Ly_n^2\beta/c^2$ is the Rossby crossing time of a basin length L, at a latitude y_n, we find

$$h_{nW}(t) = h_{nE}(t-\tau_1)e^{-\varepsilon_m\tau_1} - \frac{1}{\beta\rho}dt\tau_1\left[\frac{\partial}{\partial y}(\frac{\tau_x}{y})|_{(y_n,\frac{L}{2},t-\frac{\tau_1}{2})}\right]e^{-\varepsilon_m\frac{\tau_1}{2}}. \tag{17}$$

The eastern and western boundary conditions represent the reflection of Kelvin waves into Rossby waves at the east, and the reflection of Rossby waves into Kelvin waves at the west. In terms of the thermocline depth at the boundaries, these boundary conditions are

$$h_{eW} = r_W h_{nW}, \qquad h_{nE} = r_E h_{eE}, \tag{18}$$

where r_W and r_E are reflection coefficients at the western and eastern boundaries, respectively. Using the above boundary conditions, (15) and (17) may be joined to give an expression for the equatorial thermocline depth anomaly at the eastern Pacific,

$$\begin{aligned} h_{eE}(t) &= r_W r_E h_{eE}(t-\tau_1-\tau_2)e^{-\varepsilon_m(\tau_1+\tau_2)} && \text{free RW reflected as KW} \\ &- \frac{1}{\beta\rho}dt\tau_1[\frac{\partial}{\partial y}(\frac{\tau_x}{y})|_{(y_n,\frac{L}{2},t-\tau_2-\frac{\tau_1}{2})}]e^{-\varepsilon_m\frac{\tau_1}{2}}] && \text{forced RW reflected as KW} \\ &+ \frac{1}{\rho C_o}dt\tau_2\tau_{ex}(\frac{L}{2},t-\frac{\tau_2}{2})e^{-\varepsilon_m\frac{\tau_2}{2}} && \text{forced KW} \end{aligned} \tag{19}$$

This form of equation manifests clearly the delayed dependence of $h_{eE}(t)$ on the wave dynamics. The first term represents the effects of a thermocline depth anomaly at the eastern boundary at a time $t - \tau_1 - \tau_2$. This anomaly is reflected poleward and then propagates as a free Rossby wave. This wave in turn, is reflected at the western boundary as a Kelvin wave at time $t - \tau_2$ and arrived at the eastern Pacific at time t. The second term represents the Rossby waves excited at a time $t - \tau_2 - \tau_1/2$ in the central Pacific, and the third represents the Kelvin waves excited at a time $t - \tau_2/2$. To calculate the forced RW terms explicitly, we need to discuss the SST and atmospheric dynamics now.

2.2.2 SST response to thermocline movements

The equation describing SST changes at the equator is based on that of Zebiak and Cane [66]. Following Jin [27, 28], we only keep the time rate of change, the advection by the mean upwelling $\overline{w}\frac{\partial T}{\partial z}$, and the damping terms,

$$\partial_t T = -\varepsilon_T T - \gamma\frac{\overline{w}}{H_1}(T - T_{sub}(h)), \tag{20}$$

where ε_T is a thermal damping coefficient, $T_{sub}(h)$ is the temperature anomaly at some specified constant depth H_1 (not to be confused with other H_1s appearing above...), and is a function of the thermocline depth anomaly h, typically taken as some hyperbolic tangent [66]. The parameter $0 < \gamma < 1$ relates the temperature anomalies entrained into the surface layer to the non local deeper temperature variations due to $T_{sub}(h)$.

2.2.3 Wind response to SST forcing

Based on the solution to Gill's model above (8), we take the wind stress to be a function of the SST at the equator (T_e) which decays in latitude according to the *atmospheric* Rossby radius of deformation L_a

$$\tau_x(x,y,t) = \mu A(T_e,x)\exp(-\frac{y^2\alpha}{2L_o^2}). \tag{21}$$

In this last formula, $\alpha = (\frac{L_o}{L_a})^2$, $A(T_e,x)$ is a non local function that relates the equatorial SST to the wind stress, and μ serves as a relative coupling coefficient. The wind stress terms in (19) may thus be expressed as

$$\begin{aligned} \tau_{xe} &= \mu A(T_e,x), \\ \partial_y(\tau_x/y)|_{y=y_n} &= -\mu A^* A(T_e,x), \end{aligned}$$

where

$$A^* = \left[\frac{L_o^2+\alpha y_n^2}{(y_n L_o)^2}\right] e^{-\frac{y_n^2\alpha}{2L_o^2}},$$

$A(T_e,x)$ is obtained by solving a Gill-type atmospheric model [19] using a long wave approximation (see section 1.2.5above, or Hao et al. [21]), resulting in a linear relation between the wind stress and the equatorial SST. As derived in (8), the wind stress in the central Pacific may be assumed to be proportional to the temperature anomaly in the East Pacific (this implies that the information about the East Pacific heating is propagated in the atmosphere by atmospheric Rossby waves to affect the wind stress in the central Pacific)

$$A(T_e, x = x_w + L/2) = b_0 T_{eE}(t), \tag{22}$$

where b_0 is the annual mean coupling strength. The assumption embedded in (22) is that most of the SST variability and thus atmospheric heating is in the eastern part of the equatorial Pacific. The resulting wind stress anomaly, according to the Gill model, will reach the central Pacific where it affects the ocean wave dynamics [27, 28].

2.2.4 Mixed mode ENSO model

The expression (19) for the East Pacific thermocline depth may now be written more explicitly, using the above equations as

$$\begin{aligned} h_{eE}(t) &= r_W r_E h_{eE}(t-\tau_1-\tau_2)e^{-\varepsilon_m(\tau_1+\tau_2)} \\ &- r_W \frac{1}{\beta\rho} A^* dt \tau_1 \mu b_0 T_{eE}(t-\tau_2-\frac{\tau_1}{2})e^{-\varepsilon_m(\frac{\tau_1}{2}+\tau_2)} \\ &+ \frac{1}{\rho C_o} dt \tau_2 \mu b_0 T_{eE}(t-\frac{\tau_2}{2})e^{-\varepsilon_m \frac{\tau_2}{2}}, \end{aligned} \tag{23}$$

expressing h_{eE} at time t as function of h_{eE} and T_{eE} at previous times. As before, the first term represents the free Rossby and Kevin waves, the second represents the excited Rossby wave, and the third represents the excited Kelvin wave. The thermodynamic equation (20) evaluated at the eastern side of the basin gives the dynamical equation in which the above $h_{eE}(t)$ is used

$$\partial_t T_{eE} = -\varepsilon_T T_{eE} - \gamma\frac{\overline{w}}{H_1}(T_{eE} - T_{sub}(h_{eE})). \tag{24}$$

Equations (23) and (24), together with an explicit expression for T_{sub}, form the mixed mode model originally derived in a slightly different format (no explicit delays) by Jin [27, 28], and then re-derived in the present form by [12]. The mixed mode dynamics and its fast wave and fast SST limits were originally investigated by Neelin and Jin [29, 30, 38]. Hereafter we denote T_{eE} by T and h_{eE} by h. Note that the nonlinearity in the model is due to the nonlinear function $T_{sub}(h)$.

The mechanism of the oscillation in this mixed mode model is similar to that of the above heuristic delayed oscillator, except that there is an additional explicit delay time due to the time it takes the SST in the East Pacific to adjust to changes in the thermocline depth there. An alternative description of the mechanism has been used by Jin [27, 28], emphasizing water transport rather than wave propagation, and is shown in Fig. 24.

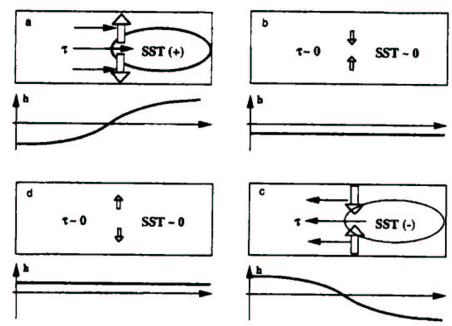

Figure 7.37. Sketch of the different stages of the recharge oscillator (Jin, 1997a).

Figure 24: The recharge oscillator mechanism (Jin, 1997).

2.2.5 The fast SST Limit

In the fast SST limit, the SST adjustment time is assumed to be much shorter than the ocean dynamics adjustment time, or in other words SST is assumed to respond instantaneously to thermocline depth changes [37, 29, 30, 38]. We obtain our model equations for this limit by taking the term $\partial_t T_{eE}$ in (24) to be zero, so that the SST equation becomes a diagnostic equation balancing the Newtonian cooling and the upwelling terms, and giving an instantaneous relation between the thermocline depth anomaly $h(t)$ and the SST $T(t)$

$$T(t) = \gamma \frac{\overline{w}}{H_1} \left(\varepsilon_T + \gamma \frac{\overline{w}}{H_1} \right)^{-1} T_{sub}(h). \tag{25}$$

The oscillation mechanism in this case is pretty much the same as of the heuristic delayed oscillator described above.

2.2.6 The fast wave limit

In the fast wave limit, the Rossby and Kelvin wave propagation times are assumed to be much shorter than the SST adjustment time of the SST to thermocline perturbations. The wave speeds are actually assumed to be infinite, resulting in an instantaneous adjustment of ocean thermocline depth and current velocities to wind stress anomalies [21]. Hence, the SST adjustment time to thermocline depth changes is the only delay and plays the central role in the physical mechanism of the oscillations obtained in this parameter regime. The fast wave limit results in somewhat unrealistic oscillations, in comparison to both ENSO's time scale and amplitude, as this is not a realistic ENSO regime. Nevertheless, it is still useful to analyze this regime, since it reveals some new aspects that are not considered in the previous two regimes.

The fast wave limit can be derived by taking the time derivatives in the ocean momentum equation to be zero. In the fast wave limit, the dynamics crucially depend on the east-west tilt of the thermocline. One variant of the fast wave limit is obtained by dividing the basin into two boxes, one for the East Pacific and one for the central Pacific. The full derivation of the model equations may be found in [12], and it is a simplification into a system of ODEs based on the PDE model of Hao et al. [21]. The two SST tendency equations for the two regions are

$$\partial_t T_c = -\varepsilon_T T_c - \gamma \frac{\overline{w}}{H_1} T_c + \gamma \frac{\overline{w}}{H_1} T_{sub}\left(h_c(T_c, T_e)\right), \tag{26}$$

$$\partial_t T_e = -\varepsilon_T T_e - \gamma \frac{\overline{w}}{H_1} T_e + \gamma \frac{\overline{w}}{H_1} T_{sub}\left(h_e(T_c, T_e)\right), \tag{27}$$

where T_c and T_e are the SST in the central Pacific and the East Pacific respectively, and the dependence of T_{sub} on T_c and T_e is via the thermocline depth anomalies h_c and h_e. The oscillatory mechanism of the eastward propagating fast wave oscillations is explained in Hao et al. [21]. Given the lack of wave delay time, the coupled system memory required for an oscillation resides in the different response rates of the SST to thermocline displacements at different longitudes. This may result in either westward propagation or eastward propagation (not in the above two box model, but in a continuous representation of the fast wave regime [21]). It is possible to obtain different time scales from 2 yr to much longer, as well as relaxation oscillations, and an example from Jin and Neelin [29, 30, 38] is shown in Fig. 25.

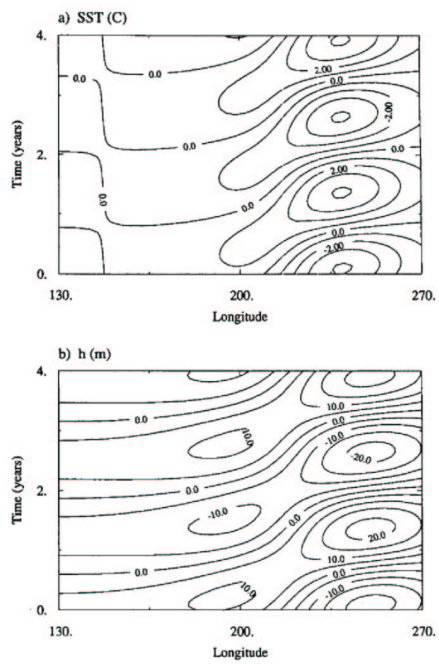

FIG. 8. Time–longitude plot of an eastward-propagating SST mode in the fast-wave limit: (a) SST, (b) thermocline depth anomalies along the equator constructed from the eigenvector for $\mu = 0.9$, $\delta_s = 0$, and $\epsilon_a = 4.0$ (units: °C and m, respectively, up to a normalization factor).

Figure 25: An oscillation of the equatorial Pacific in a model of the fast wave regime (Jin and Neelin, 1993)

Lecture 3

ENSO's irregularity and phase locking

Eli Tziperman

3.1 Is ENSO self-sustained? chaotic? damped and stochastically forced?

That El Nino is aperiodic is seen, for example, in a nino3 time series (Fig. 26). The ENSO delayed oscillator mechanism may result in either self-sustained oscillations, or in a steady state solution that has a damped oscillatory mode. In the later case, oscillations may be excited by external stochastic (weather) noise. In the scenario in which ENSO is self-sustained, it may be irregular due to low-order chaos. In the stochastically driven scenario, ENSO's irregularity is simply an outcome of the stochastic forcing. Whether ENSO is damped or self-sustained depends on the ocean-atmosphere coupled instability, also referred to as the coupling strength. For this purpose, the coupling strength may be defined for example as the response of the atmospheric wind stress per unit change in the thermocline depth. Note that this coupling is the product of (at least) three different coupling coefficients: the response of SST to thermocline depth changes, the response of the atmospheric heating to SST changes, and the response of the wind stress to the atmospheric heating. A stronger coupling implies self-sustained possibly chaotic oscillation, while a weak coupling implies damped oscillations.

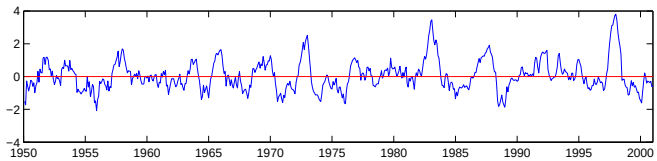

Figure 26: The observed irregular El Nino events (nino3 index of averaged east equatorial SST).

3.1.1 Strength and seasonality of ocean-atmosphere coupling

Some of the physical processes affecting the coupling strength are the mean (i.e. monthly climatological) upwelling strength, mean SST; ITCZ motion and its effect on the atmospheric heating parameterization, mean thermocline depth, thermocline outcropping, etc [23, 46, 62]. All of these fields vary seasonally (Fig. 27), and therefore so does the coupling coefficient.

To summarize only a few of the seasonal coupling factors:

1. Seasonal motion of ITCZ and its effect on atmospheric heating (via mean atmospheric convergence): results in stronger coupling when the ITCZ is near the equator.

2. Seasonal variations in upwelling amplitude: affects the efficiency of transfer of thermocline signal to surface.

3. Seasonal variations in the mean SST, and its effect on atmospheric heating: warmer mean SST makes a given SST perturbation more effective in inducing atmospheric heating.

4. Seasonal motion of thermocline in the East Pacific: when the thermocline outcrops, Kelvin Waves manage to transfer the sub-surface temperature signal to the surface and affect the SST more efficiently.

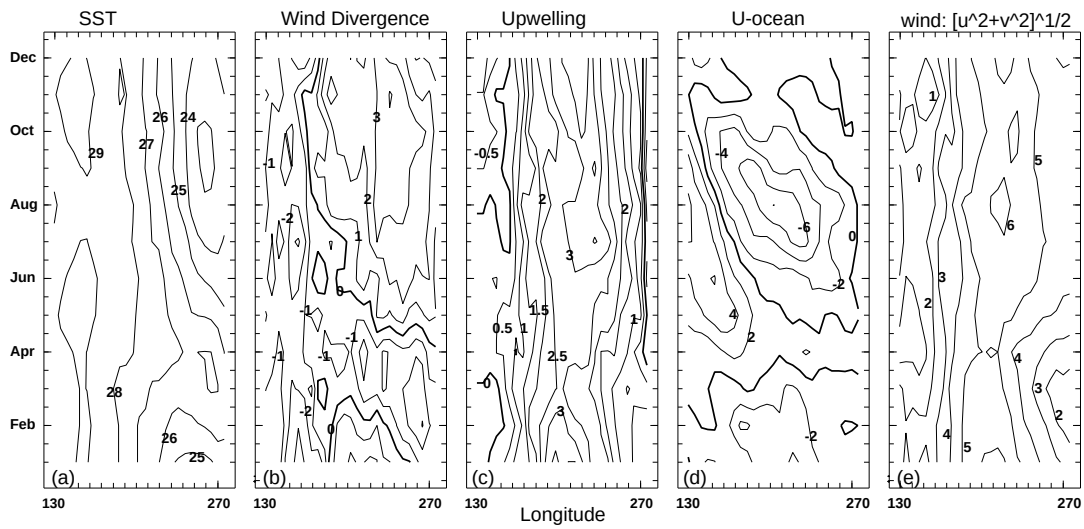

Figure 27: Monthly climatology of SST, wind divergence, upwelling, zonal ocean currents, and wind speed, at the equator, taken from the background fields in the CZ model.

Each of these factors results in a somewhat different time of maximal coupling. The combined effect is a seasonal coupling strength that is maximal during spring and early summer and minimal at the end of the calendar year.

Consider next the two possible mechanisms leading to ENSO's irregularity and limited predictability.

3.1.2 ENSO's irregularity: low order chaos

Consider first a pendulum driven by periodic forcing and affected by friction. For small amplitude, one may linearize the equation of motion, and when the forcing frequency equals the natural frequency of the pendulum, a linear resonance occurs. For larger amplitude motion, the governing equation is nonlinear. Because of the nonlinearity, the period of the pendulum depends on its amplitude. In this case a "nonlinear resonance" may occur when the pendulum frequency ω is related to the forcing frequency ω_F as two integers: $\omega/\omega_F = n/m$ rather than only when the two frequencies are equal, as in the linear case. When the nonlinearity is sufficiently strong, the pendulum tends to change its amplitude a bit so that its frequency would also change, such that the frequency is related to that of the forcing as the ratio of two integers and a nonlinear resonance occurs. This is also called "mode locking" to the external forcing, and is the same phenomenon as of the "Huygens clocks" shown in Fig. 28. For larger yet nonlinearity, the governing equation of the pendulum has several different solutions that correspond to different nonlinear resonances, all for the same physical parameters (friction, gravity, length of pendulum, forcing amplitude, etc). Each of these possible nonlinear resonances is unstable, so that the pendulum does not remain near these solutions indefinitely, but oscillates near one of these frequencies for a while, but then escapes and jumps to another such nonlinear resonance with a different integer ratio with ω_F. The resulting motion is an irregular jumping between the different nonlinear resonances. This is the mechanism of chaos for the damped nonlinear pendulum forced by external periodic forcing [1]. Check the pendulum Java applets at http://www.dartmouth.edu/~phys15/interact/pendulum.html or http://monet.physik.unibas.ch/~elmer/pendulum/spend.htm for a nice demo.

The above dynamics may also be demonstrated using the simple circle map

$$\theta_{n+1} = \theta_n + \Omega + \frac{K}{2\pi}\sin(2\pi\theta_n)$$

which is an iterative map roughly representing a periodically forced pendulum [54]. Here θ_n is the angle of the pendulum at iteration n, Ω represents the periodic forcing, and the nonlinear term with amplitude $\frac{K}{2\pi}$ corresponds

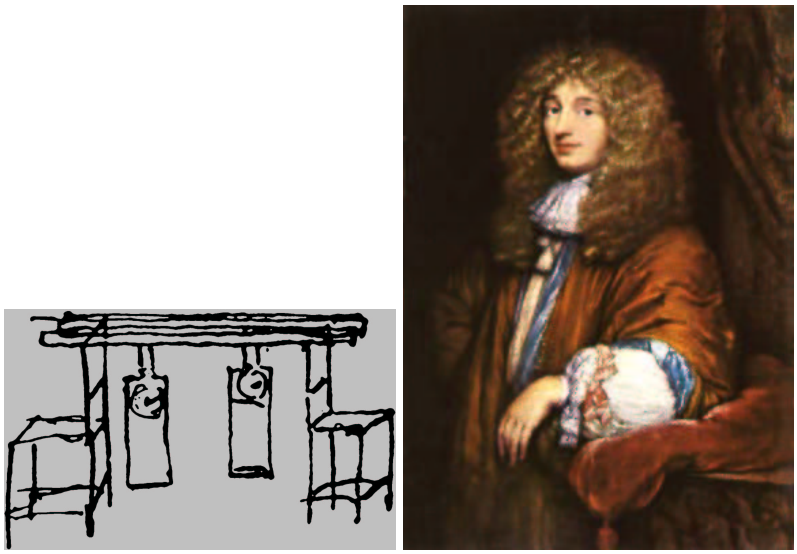

Figure 28: "While recovering from an illness in 1665, Dutch astronomer and physicist Christiaan Huygens noticed that two of the large pendulum clocks in his room (which he patented 8 years earlier) were beating in unison, and would return to this synchronized pattern regardless of how they were started, stopped or otherwise disturbed" (http://www.agnld.uni-potsdam.de/~mros/synchro.html).

to a similar term in the pendulum equation. As the nonlinearity in the map increases, the map displays a nonlinear resonance and then chaos for $K > 1$. The transition to chaos as the nonlinearity increases and as a function of Ω is called the quasi-periodicity route to chaos (Fig. 29); try playing with the following Matlab program to see the map behavior:

```
    clear; clf; pi=atan(1.0)*4.0; omega=0.5; K=2.0; I=20000; theta(1:I)=1.0e-17;
for n=1:I
  theta(n+1)=mod(theta(n)+omega+(K/(2*pi))*sin(2*pi*theta(n)),1);
end
plot(theta,'r+')
```

We finally proceed to the application of these ideas to ENSO's dynamics. The idea is very simple [61, 58, 31]: the nonlinear pendulum in the above discussion corresponds to the delayed oscillator in a self-sustained parameter regime. The periodic forcing is the seasonal cycle and especially the seasonal variations of the coupling strength discussed above. This may be demonstrated by considering the transition to chaos in a simple delayed oscillator model [61] where the seasonal forcing is added as an additive forcing term,

$$\frac{dh(t)}{dt} = a\mathcal{A}[h(t-\frac{1}{2}\tau_K)] - b\mathcal{A}[h(t-\tau_K-\frac{1}{2}\tau_R)] + c\cos(\omega_a t) \tag{28}$$

and where $\mathcal{A}(h)$ is a nonlinear tanh-like function. This function has a slope of κ at the origin ($h = 0$) which serves as the coupling coefficient in the sense discussed above. As the coupling coefficient is increased, this model shows exactly the same quasi-periodicity route to chaos discussed above (Fig. 30). The same transition to chaos occurs if the seasonal forcing is added, more realistically, as seasonal variations in the coupling strength, rather than as an additive forcing term.

The mechanism of irregularity of El Nino according to this scenario is thus low order chaos driven by the seasonal cycle in the Equatorial Pacific. The nonlinear delayed oscillator goes into a nonlinear resonance with the seasonal cycle forcing. For sufficiently strong nonlinearity and/ or seasonal forcing amplitude, several such resonances coexist and are destabilized. Such a nonlinear resonance corresponds to an ENSO cycle of a period T_{ENSO} that is related to the annual period as the ratio of two integers. T_{ENSO} could be for example 2, 3 or 4 years,

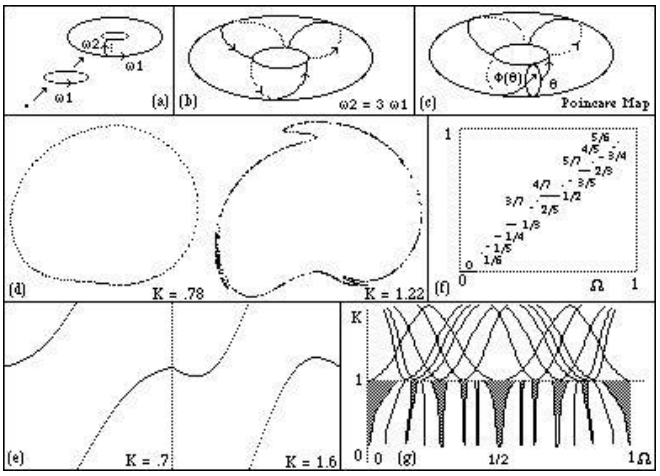

Figure 29: http://www.dhushara.com/book/paps/chaos/bchaos1.htm: "The quasi-periodicity route to chaos: (a) Repeated Hopf bifurcations result in tori. Creation of two oscillations results in a flow on the 2-torus. (b) Periodic flow on 2-torus results in closed orbits which meets themselves exactly. (c) Poincare map of a cross section maps each point in a cross section C to the corresponding point one cycle on along the flow. The flow illustrated is irrational and hence has orbits consisting of lines which do not meet themselves, but cover the torus ergodically passing arbitrarily close as time increases. (d) Breakup of the torus under the circle map as K crosses 1. The increasing energy thus disrupts the periodic relationships as chaos sets in. (e) f(q) versus q for the circle map. At K = .7 the function is 1 - 1 and hence invertible, but for K = 1.6 it is not. (f) The devils staircase of mode-locked states. These order the possible rationals assigning to each the interval of values for which such mode-locking occurs for K = 1. At this value the mode-locked states fill the interval, leaving only a Cantor set of irrational flows. (g) K - diagram of the circle map showing mode-locked tongues (K<1) and chaos densely interwoven with periodicity (K>1). The rational mode-locking exist only on the curves for K > 1."

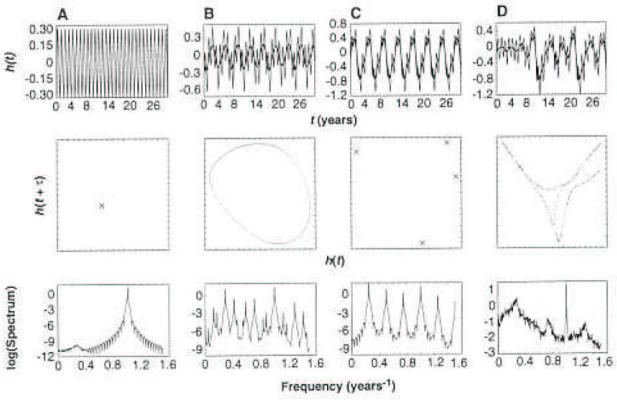

Figure 30: Transition to chaos in a simple delayed oscillator El Nino model [61].

or other period for which $T_{ENSO}/1yr = n/m$. The equatorial Pacific delayed oscillator therefore jumps irregularly between these nonlinear resonances, resulting in the observed irregularity. This scenario which was originally investigated using highly simplified toy models such as (28), was also found [58] to be the mechanism of chaos in the widely used El Nino prediction intermediate coupled model of Zebiak and Cane [66].

3.1.3 ENSO's irregularity: stochastically forced non-normal optimal modes

An alternative explanation to ENSO's irregularity is based on the idea of non normal transient growth [11, 10] and was examined in the context of ENSO for example by [45] and [32]. Consider first the simple linear system of two equations (thanks to Eyal Heifetz for his help with this example)

$$d\vec{\Psi}/dt = A\vec{\Psi}$$

where

$$A = \begin{pmatrix} -0.1 & -0.9\cot\theta \\ 0 & -1 \end{pmatrix}$$

so that its eigenvectors/ values are

$$\begin{aligned} \vec{P}_1 &= \begin{pmatrix} 1 \\ 0 \end{pmatrix} \\ \vec{P}_2 &= \begin{pmatrix} \cos\theta \\ \sin\theta \end{pmatrix} \\ \begin{pmatrix} \lambda_1 \\ \lambda_2 \end{pmatrix} &= \begin{pmatrix} -0.1 \\ -1 \end{pmatrix}. \end{aligned}$$

Note that both eigenvalues are negative, so that the solution to any initial conditions eventually decays to zero. The solution may be written as

$$\vec{\Psi} = a_1\vec{P}_1 e^{-0.1t} + a_2\vec{P}_2 e^{-t},$$

where the initial conditions are

$$\vec{\Psi}(t=0) = a_1\vec{P}_1 + a_2\vec{P}_2.$$

At a later time $t = 1$, the solution is therefore

$$\vec{\Psi}(t=1) = a_1\vec{P}_1 e^{-0.1} + a_2\vec{P}_2 e^{-1}.$$

Now, note that the two eigenvectors are not necessarily perpendicular, depending on the value of θ:

$$\begin{aligned} \theta &= 0 \Rightarrow \vec{P}_1 \parallel \vec{P}_2; \\ \theta &= \pi/2 \Rightarrow \vec{P}_1 \perp \vec{P}_2 \end{aligned}$$

choosing initial conditions such that

$$\vec{\Psi}(t=0) = (\sin\theta, -\cos\theta)^{\dagger} \perp \vec{P}_2 \Rightarrow (a_1, a_2) = (\csc\theta, -\cot\theta)$$

we find that at a later time the norm of the solution actually increased rather than decay

$$\theta = \pi/18_{rad} = 10^{\circ} \Rightarrow |\vec{\Psi}(t=1)|/|\vec{\Psi}(t=0)| \approx 3.2$$

This somewhat surprising result may be explained with the help of Fig. 31. Note that the initial conditions are a super position of the two eigenvectors in such a way that the two components proportional to the eigen vectors

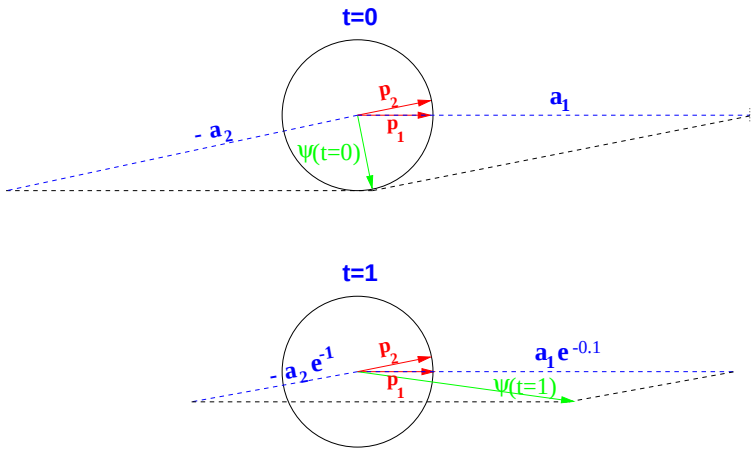

Non-modal transient growth: change in both amplitude and structure

Figure 31: non-normal system at i.c and at a later time

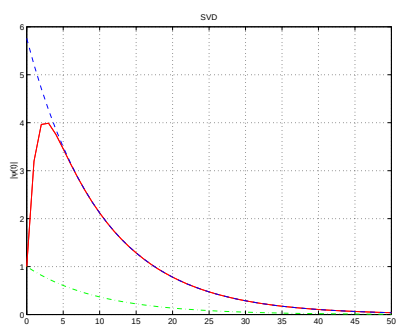

Figure 32: amplitudes as function of time for the projections on the eigenvectors (dash and dotted lines) and for the norm of the total solution (solid line).

are large-amplitude but cancel each other at $t = 0$. At a later time $t = 1$ one of the eigenvectors decays much faster than the other, so that the solution at that time remains basically equal to the large initial value of the remaining eigenvector, hence the initial amplification. This amplification is transient because at later times both eigenvectors must decay (Fig. 32).

Given a dynamical system as above, we could search for the initial conditions that maximize growth at some time $t = T_{opt}$, by solving the problem

$$\text{find}\,\Psi(t=0)\ \text{that results in}\ \max|\Psi(t=T_{opt})| \quad \text{subject to}\,|\Psi(t=0)| = 1.$$

The usual normal modes stability analysis is equivalent to taking $T_{opt} \to \infty$. Alternatively, we could ask what are the initial conditions that lead to a maximum initial growth trend at $t = 0$

$$\text{find}\ \Psi(t=0)\,\text{that results in}\ \max\left|\frac{d\Psi}{dt}|_{t=0}\right| \quad \text{subject to}\,|\Psi(t=0)| = 1.$$

In this last case, we search for the maximum of the norm of $(d\Psi/dt)|_{t=0} = A\Psi(t=0) = A\Psi_0$ subject to $|\Psi_0| = 1$. Writing this maximization problem using a Lagrange multiplier λ as

$$\begin{aligned} & \max\left((A\Psi)^T(A\Psi) + \lambda(\Psi^T\Psi - 1)\right) \\ = \ & \max\left(\Psi^T(A^TA)\Psi + \lambda(\Psi^T\Psi - 1)\right). \end{aligned}$$

and equating the derivative of the quantity to be maximized and to zero, we have

$$\begin{aligned} 0 &= \frac{d}{d\Psi_0}\left(\Psi_0^T(A^TA)\Psi_0 + \lambda(\Psi_0^T\Psi_0 - 1)\right) \\ &= (A^TA)\Psi_0 + \lambda\Psi_0. \end{aligned}$$

This implies that the optimal initial conditions Ψ_0 that maximize the growth rate at $t = 0$ are the eigenvector of the matrix A^TA. In more general cases the answer is derived by solving different and somewhat more complex eigen problems, typically using an adjoint model of the model whose optimal initial conditions are searched.

As a final comment before returning to ENSO, note that if the optimal transient growth exceeds the non–linearity threshold within the time scale of interest, then the linear stability nature of the system is irrelevant. Very often the growth rate due to non-normal effects is much larger than that of the normal modes even for a system that is unstable in the usual normal modes sense. What's considered "optimal" is subjective.

In the case of ENSO, it has been suggested that the optimal initial conditions (e.g. for the wind) which result in the fastest growth of El Nino conditions (happen to?) have the same structure as of westerly wind bursts occurring in the West Pacific warm pool area (these wind bursts may be related to the Madden-Julian 30-40 day oscillations in the tropical atmosphere). This implies that El Nino may be triggered by external factors rather than being a self-sustained oscillation that is at most randomized by external noise. Predictability may still be possible if the system needs to be preconditioned before the westerly wind bursts can excite an event. In any case, the structure of the optimals for El Nino seems very model dependent at the moment, and the issue is still being investigated.

There are clearly many possible mechanisms for ENSO's irregularity, according to which it might be: self-sustained and chaotic, self-sustained and randomly forced; damped and stochastically forced efficiently due to the non-normal structure of its linearized dynamics, etc. At the moment, it seems that the issue of whether ENSO is self-sustained and possibly chaotic or damped and stochastically forced (or one of the other alternatives) is still unresolved.

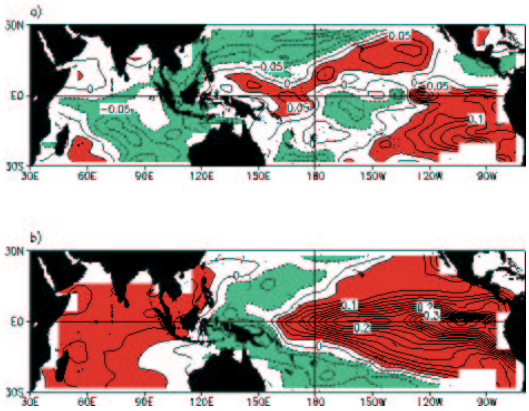

Figure 33: (a) The optimal initial structure for sea surface temperature anomaly growth. The pattern is normalized to unity. The contour interval is 0.025, and negative values are indicated by dashed contours. (b) The linear inverse model's 7-month prediction when (a) is used as the initial condition. Contour interval and shading are as in (a). (http://www.cdc.noaa.gov/review97/overview/chpt2/fig.2.1.html)

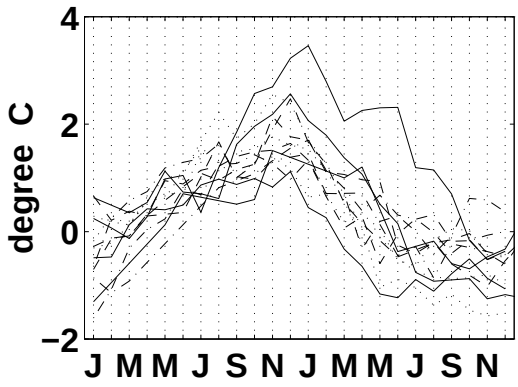

Figure 34: Super imposed nino3 time series from many observed events, showing the tendency of the events to reach a maximum toward the end of the year and therefore be phased locked to the seasonal cycle.

3.2 ENSO's phase locking to the seasonal cycle

El Nino events tend to reach their maximum toward the end of the year (Fig. 34). Given the importance of seasonal forcing via the seasonal ocean-atmosphere coupling strength to El Nino's dynamics it is not surprising that such phase locking occurs, but the mechanism of this phase locking still requires an explanation.

Some Previous explanations suggested that (1) Spring time is the most unstable time of year in the Equatorial Pacific, so that ENSO events start then & peak a few months later... (Philander [46], Hirst [23]). However, this explanation is clearly still a bit vague, summer is also unstable, and the delayed oscillator mechanism is not incorporated into the proposed mechanism. (2) End of year is most stable time of year, so that dissipation will overcome instability then, and events will peak and start decaying (Zebiak and Cane, [66]). However, this again does not use the equatorial waves and delayed oscillator ideas. (3) If El Nino's irregularity is due to seasonal forcing, one might expect nonlinear phase locking to the seasonal forcing. However, this is clearly not a sufficiently specific physical mechanism, and the locking actually seems to occur in linear models as well.

A linear mechanism based on equatorial wave dynamics for El Nino's phase locking has been proposed by [59, 12]. The mechanism may be demonstrated using a simple delayed oscillator equation

$$\begin{aligned} dh(t)/dt &= bF[K(t-\tau_1)h(t-\tau_1)] && \text{Warm Kelvin wave} \\ &- cF[K(t-\tau_2)h(t-\tau_2)] && \text{Cold Rossby Waves} \\ &- dh(t) && \text{Dissipation} \end{aligned} \tag{29}$$

where $h(t)$ = East Pacific thermocline depth, $K(t)$ = seasonal strength of ocean-atmosphere instability, $(\tau_1, \tau_2) = (1, 6)$ months, are the (Kelvin, Rossby+Kelvin) wave travel times, $F[K(t)h(t)]$ is a nonlinear function representing the thermocline $\rightarrow$ SST $\rightarrow$ wind connection, monotonously increasing with $K(t)h(t)$ and roughly shaped like a hyperbolic tangent function.

This model displays events that are aperiodic, but peak time of $h(t)$ (same as nino3), is always at the end of the year (Fig. 35).

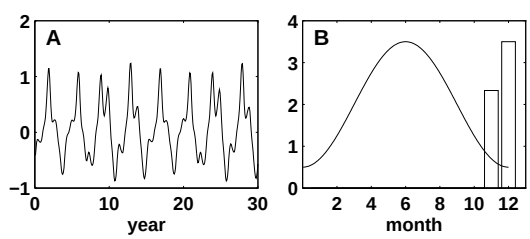

Figure 35: Results of the toy model described in the text for El Nino's phase locking. left: typical time series of model solution for $h(t)$; right: the seasonal coupling strength (line) and histogram of timing of peaks of the model time series showing that these peaks occur during November and December.

The end of year is also the time when the coupled ocean atmosphere instability strength (coupling strength) $K(t)$ is smallest in reality as well as in this toy model (solid line on right panel of Fig. 35). Given the simplicity of this model, we can try to use it to explain why the peak time is also time of minimum coupling. Note that at the peak time: $dh(t)/dt = 0$ so that warming due to the Kelvin wave term balances the cooling due to the Rossby and dissipation terms:

$$bF[K(t-\tau_1)h(t-\tau_1)] = cF[K(t-\tau_2)h(t-\tau_2)] + dh(t) \tag{30}$$

Next, we note that in the delayed oscillator picture, the ENSO cycle is viewed as a continuous succession of Kelvin and Rossby waves excited in the central Pacific. Also, the wave's initial amplitudes are related to that of the ENSO event at the time when the waves are excited. Finally, the waves are also amplified (during their excitation time) by the strength of the ocean-atmosphere instability at the season of their excitation.

Let us show now that the event peak cannot occur at a time of maximum ocean-atmosphere instability strength $K(t)$ (which is also summer time), using the schematic Fig. 36. If the peak time is indeed during summer, then warm Kelvin waves arriving during the peak time to the East Pacific are excited $\tau_1 = 1$ month before ENSO's peak-time with a large amplitude (because they are forced by a strong wind anomaly existing just prior to the peak time. These waves are also strongly amplified when they are excited by the strong coupling that exists during the summer. These strong waves cannot be balanced by the small-amplitude cold Rossby waves created $\tau_2 = 6$ months before the peak time, during the winter time, when the event was still weak, having also been only weakly amplified during winter by the weak coupled instability then. In other words, in equation (30), $K(t-\tau_1)$ and $h(t-\tau_1)$ are large, while $K(t-\tau_2)$ and $h(t-\tau_2)$ are small, so that the balance in that equation cannot be obtained, and therefore peak time cannot occur at the time of maximum couping $K(t)$.

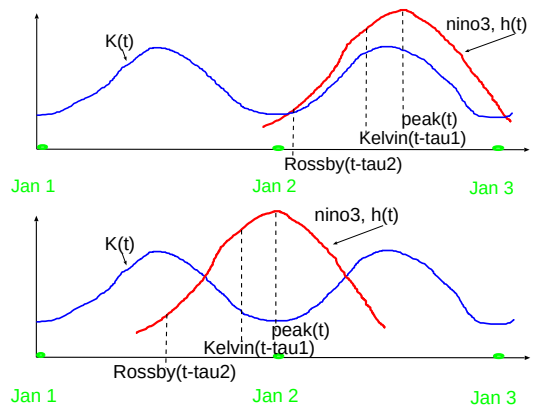

Figure 36: upper: can El Nino peak during summer time? lower: can El Nino peak during winter time? In both cases: the blue curve shows the seasonal coupling strength, and red curve the East Pacific SST.

Next, let us show that the peak can occur at a time of minimum ocean-atmosphere instability strength $K(t)$ (Fig. 36). In this case, the warm Kelvin waves arriving to the East Pacific at the peak time are Large amplitude because they were excited by the strong wind anomalies near the peak-time. But these waves were only weakly amplified during winter when they were excited. These waves may therefore be balanced by the cold Rossby waves excited with a small-amplitude when the event was still weak, but strongly amplified by the strong winter time coupled instability strength. In other words, in equation (30) we now have $K(t-\tau_1) = small$; $h(t-\tau_1) = large$, $K(t-\tau_2) = large$; $h(t-\tau_2) = small$, so that the balance in that equation may be obtained and peak time can occur at the time of minimum coupling $K(t)$. (Extension to mixed mode and other ENSO regimes were discussed by Galanti and Tziperman [12]).

The common bibliography for Eli Tziperman's lectures is at the end of Lecture 9, on page 131.

Lecture 4

Thermohaline Circulation Variability

Paola Cessi

1 A brief introduction

While the major surface oceanic currents are predominantly driven by the wind-stress, the dynamics of the deep circulation depends mostly on horizontal density gradients, established as a result of the combined effect of surface thermal and saline forcing.

The meridional inhomogeneity of radiative heating of the atmosphere produces horizontal density difference between the colder polar and the warmer equatorial sea surface temperature. The effect of this temperature gradient alone would be the generation of denser water at higher latitudes and of lighter water in tropical regions. However the excess of evaporation over precipitation towards the equator causes the mean salinity to decrease with latitude. The equation of state for seawater is approximately given by

$$\rho = \rho_0(1 - \alpha T + \beta S), \tag{1}$$

so that the thermal effect on density opposes that of salinity (α and β are the expansions coefficient of seawater).

In summary:

- temperature favors downwelling of dense water at high latitudes and upwelling at the equator;
- for salinity the opposite is true.

The net result of these competing effects is the establishment of a flow which extends to the deep oceanic layers, known as *thermohaline circulation*.

In the present climate, the North Atlantic deep circulation is dominated by two thermally direct cells, one with high-latitude sinking in the Northern Hemisphere and one with high-latitude sinking in the Southern Hemisphere. However, paleoclimatic data indicate that as recently as 11,000 years ago the deep circulation and the downwelling at high latitudes has been much weaker.

The two processes involved can in fact give rise to the existence of multiple steady states, with the possibility of transitions among the equilibria.

2 The Stommel-Arons model

The classical approach to the study of the buoyancy-driven circulation is Stommel-Arons model of the abyssal oceanic flow. One interpretation of the model regards the ocean as a box with a rigid lid and a two-layer approximation. The upper layer has depth h and density ρ_1 while the lower one has depth $H - h$ and density ρ_2.

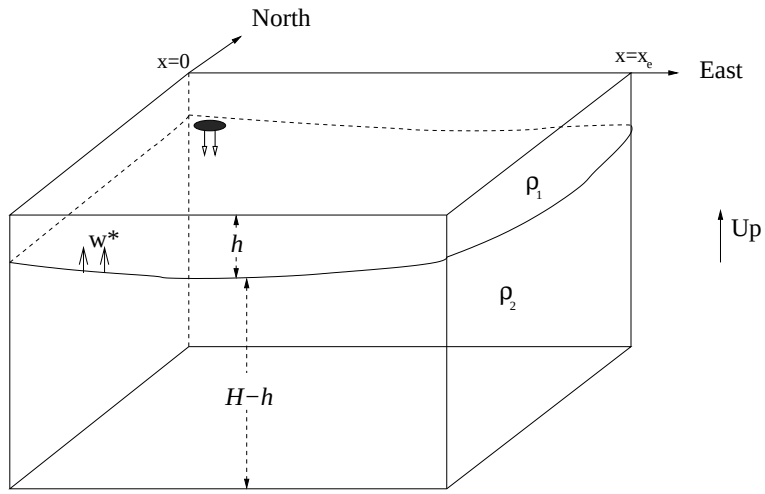

HIgh-latitude convection transforms water of density ρ_1 into water of density ρ_2, and this downwelling is assumed to be localised at the poleward edge of the box. In steady state there is a velocity, w^*, at the layers' interface that compensates for this high-latitude density exchange. This upwelling is assumed to be diffuse, and is constrained by:

$$\int_{Basin} dx\, dy\, w^* = \text{Deep water production rate.}$$

The Stommel-Arons model examines the flow driven by this large scale interfacial velocity. Specifically, the steady dynamics in the lower layer obeys

$$\begin{aligned} -fv &= -p_{2x}/\rho_0 - ru && (2)\\ fu &= -p_{2y}/\rho_0 - rv && (3)\\ p_{1,2z} &= -\rho_{1,2} g && (4)\\ [(H-h)u]_x &+ [(H-h)v]_y = -w^*. && (5) \end{aligned}$$

where $r \ll f$ is the dissipation rate. We now wish to find an expression for the dynamic part of the pressure of the lower layer in terms of the layer thickness, h. Firstly, using the hydrostatic relation, we find

$$\begin{aligned} p_1 &= -\rho_1 g z + \hat{p}_1(x,y)\,, \\ p_2 &= -\rho_2 g z + \hat{p}_2(x,y)\,. \end{aligned}$$

From continuity of pressure at the interface, $z = -h$, we have

$$\hat{p}_2 = -\rho_0 g' h + \hat{p}_1 \tag{6}$$

where $g' \equiv g(\rho_2 - \rho_1)/\rho_0$ is the reduced gravity.

If we integrate the continuity equation vertically over the whole box, applying the condition that there is no vertical velocity at the top and bottom we have

$$[hu_1 + (H-h)u_2]_x + [hv_1 + (H-h)v_2]_y = 0\,. \tag{7}$$

Away from the boundaries we can neglect dissipation and we use geostrophic balance in both layers. Multiplying the upper layer momentum equations by h and the lower layer momentum equations by $H - h$, and forming a vorticity equation we find

$$f\{[hu_1 + (H-h)u_2]_x + [hv_1 + (H-h)v_2]_y\} + \beta[hv_1 + (H-h)v_2] = \\ h_x(\hat{p}_2 - \hat{p}_1)_y + h_y(\hat{p}_1 - \hat{p}_2)_x\,. \tag{8}$$

Because $\hat{p}_2 - \hat{p}_1$ depends linearly on h [from (6)] the RHS of equation (8) vanishes as does the first bracketed term on the LHS [because of (7)]. Thus

$$hv_1 + (H-h)v_2 = 0 \tag{9}$$

$$hu_1 + (H-h)u_2 = 0, \tag{10}$$

and there is no vertically averaged flow. Because the interior velocities are geostrophic we must have

$$h\nabla\hat{p}_1 + (H-h)\nabla\hat{p}_2 = 0. \tag{11}$$

Finally, eliminating for $\hat{p}_1$ from (6) and integrating we have

$$\hat{p}_2 = -\frac{\rho_0 g' h^2}{2H}. \tag{12}$$

The vertically averaged lower layer equations thus satisfy:

$$f(H-h)v = P_x + r(H-h)u\,, \tag{13}$$

$$-f(H-h)u = P_y - r(H-h)v\,, \tag{14}$$

where we have defined the vertically averaged pressure in the lower layer

$$P \equiv g'(\frac{h^3}{3H} - \frac{h^2}{2}). \tag{15}$$

In the regime $r \ll f$, P obeys the potential vorticity equation [$\beta \equiv df/dy$]

$$\frac{\beta}{f^2}P_x = w^* - \nabla(r\frac{\nabla P}{f^2}). \tag{16}$$

Integrating the mass conservation equation (4) across the box from $x = 0$ to x_e, and assuming no normal flow at the boundaries we obtain the net meridional abyssal mass transport, $\psi(y)$,

$$\psi(y) \equiv \int_0^{x_e} dx\,(H-h)v = -\int_0^{x_e} dx \int_0^y dy'\, w^*(x, y'). \tag{17}$$

A relation between P and ψ is obtained integrating 14 across the width of the basin and neglecting dissipation, hence

$$f\psi(y) = P(x_e, y) - P(0, y). \tag{18}$$

In the ocean *interior* we can obtain P from (16) by neglecting dissipation and imposing $u = 0$ ($P_y = 0$) at $x = x_e$.

$$P_I(x, y) = -\frac{f^2}{\beta} \int_x^{x_e} dx'\, w^*(x', y) + P_0, \tag{19}$$

where P_0 is the (constant) value of P on the eastern boundary.

The *interior* mass transport, i.e. the mass transport that excludes the western boundary layer contribution is

$$\psi_I(y) \equiv f^{-1}[P_0 - P_I(0, y)] = \frac{f}{\beta} \int_0^{x_e} dx\, w^*(x, y) \geq 0.$$

A cross section shows that the interior flow is towards the source in the abyss!

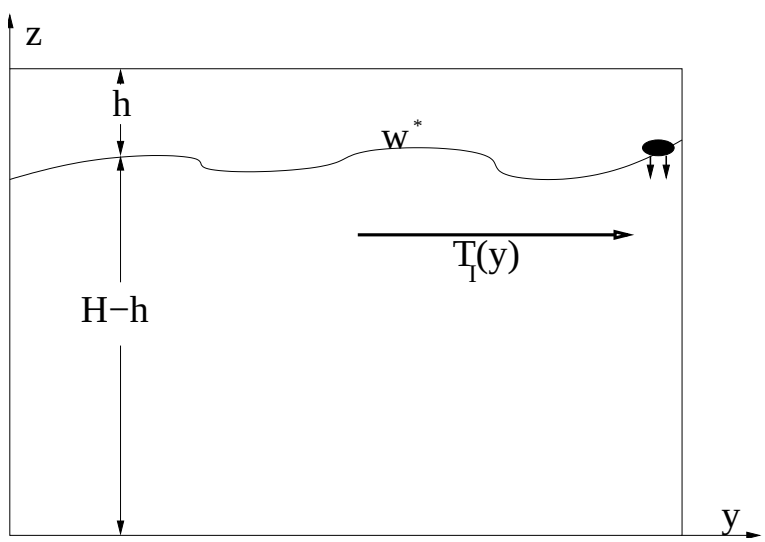

Thus there must be a flow in the western boundary layer, which returns the flow towards the source. Near the western boundary we rescale x such that it becomes small, of the same order of magnitude as r/β. Then, near the boundary we have

$$\frac{\beta}{f^2} P_x = -\frac{r}{f^2} P_{xx}.$$

The solution for the whole box then is

$$P = P_I + \underbrace{A(y) \exp(-\beta x/r)}_{\text{Boundary layer correction}} .$$

$A(y)$ is determined by mass conservation. If we take the continuity equation (4) and integrate it across the whole of the E–W direction and from $y' = 0$ to y then we obtain again equation 17. Substituting P gives

$$\int_0^{x_e} dx P_x = \int_0^{x_e} dx \int_0^y dy' w^*(x, y') \,. \tag{20}$$

The integral of the interior part of the streamfuntion P is just the interior mass transport (equation 19) and thus

$$\psi_I - A(y) = -\int_0^{x_e} dx \int_0^y dy' w^*(x, y') \tag{21}$$

which gives solution for $A(y)$

$$A(y) = f \int_0^{x_e} dx \left[f w^*(x, y)/\beta + \int_0^y dy' \, w^*(x, y') \right] .$$

It is useful to divide the transport into an interior part, ψ_I and a boundary contribution, ψ_{WB}, so that

$$\begin{aligned} \psi(y) &= f^{-1}[\overbrace{P(x_e, y) - P_I(0, y)}^{\psi_I} + \overbrace{P_I(0, y) - P(0, y)}^{\psi_{WB}}] \\ \psi_{WB} &= -A(y) \leq 0. \end{aligned}$$

This clearly shows that the transport in the western boundary is negative (equatorward) if w^* is positive, so that ψ_{WB} is away from the high-latitude convection source.

In the particular case when w^* is independent of y we have, $[f = \beta y]$,

$$\psi_{WB} = -2y \int_0^{x_e} dx \, w^*(x) = \mathbf{2}\psi(y).$$

The western boundary layer transports *twice* the zonally averaged transport: the flow from the convection source and the interior flow which is towards the source.

A contour of P for uniform w^* shows an interior poleward flow and an equatorward western boundary current.

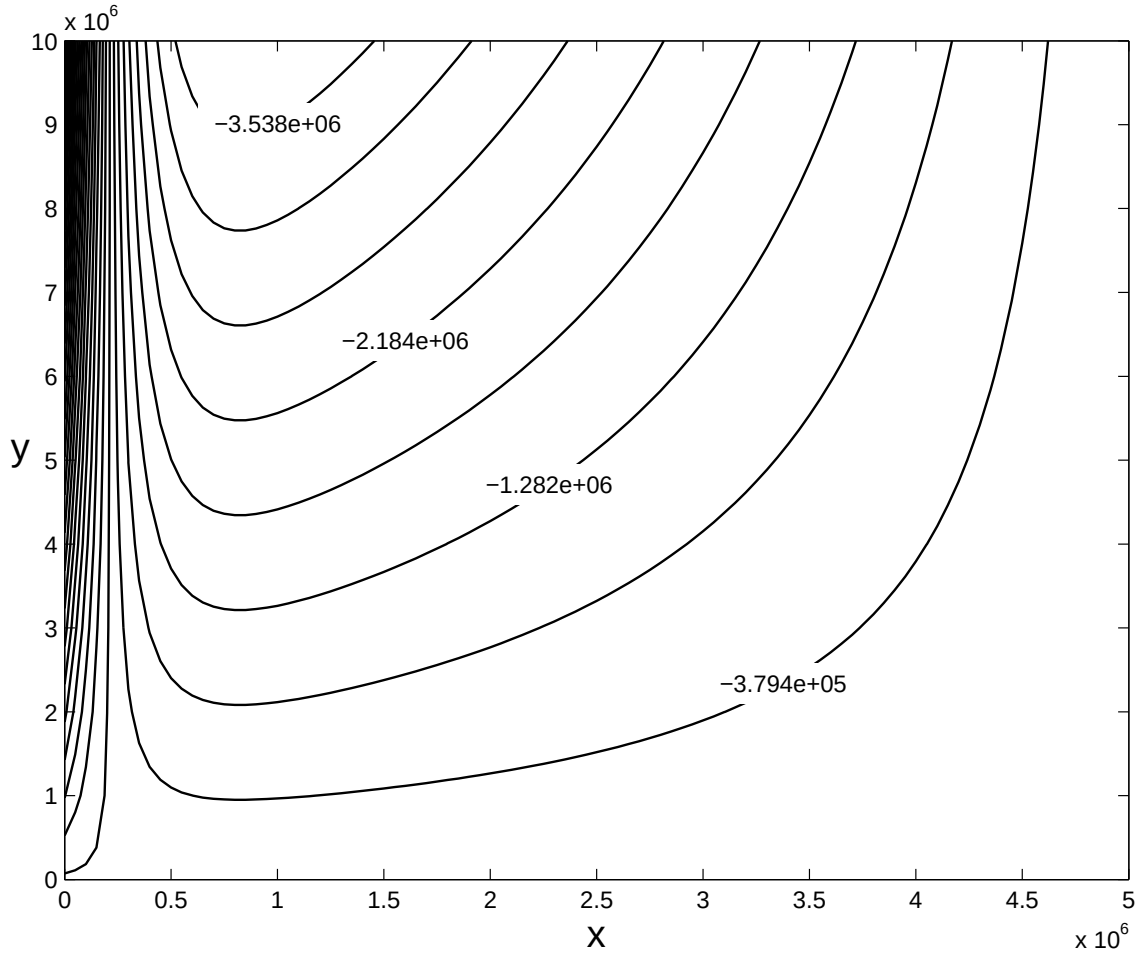

3 What determines w^*?

It is clear that the circulation in the Stommel-Arons model depends crucially on the interior upwelling, w^*, at the interface of the two layers, i.e. at the base of the thermocline. To estimate what determines the interior upwelling we use scaling arguments, which are confirmed by more detailed laminar calculations (e.g. Vallis, 2000).

The scenario is one where a bounded ocean is driven by surface buoyancy fluxes only, which are transmitted downward through diffusion. No time-dependent instabilities are considered. In this case, the interior vertical velocity satisfies the approximate balance:

$$w^* \rho_z \approx \kappa \rho_{zz}.$$

The thickness of the thermocline, (i.e. of the upper layer in Stommel-Arons model) is diffusive:

$$h = O(\frac{\kappa}{w^*}) \quad w^* = O(\frac{hV}{L}).$$

In the presence of walls that confine the flow to the East and West, a large scale East-West pressure gradient can be maintaned, so that we can assume that v is geostrophic and hydrostatic, i.e.

$$f v_z \sim g\rho_x/\rho_0.$$

We thus arrive at the following estimate for the depth of the thermocline:

$$h^3 = O(\frac{\kappa f L^2 \rho_0}{\Delta\rho g}).$$

For fixed surface density, $\Delta\rho$ is independent of κ, and therefore the depth of the thermocline satisfies

$$h = O\left(\frac{\kappa f L^2 \rho_0}{\Delta\rho g}\right)^{1/3} \sim \kappa^{1/3}, \quad w^* \sim \kappa^{2/3}.$$

For fixed surface flux, we estimate the *horizontal* density difference to be $\Delta\rho = O(Fh/\kappa)$:

$$h^4 = O(\frac{\kappa^2 f L^2 \rho_0}{Fg}).$$

In this case

$$h \sim \kappa^{1/2}, \quad w^* \sim \kappa^{1/2}.$$

These scalings have been confirmed by non-eddy-resolving numerical simulations of the primitive equations (Vallis, 2000 and Huang et al. 1994): density gradients are confined to a thin diffusive layer, while the abyssal layer is essentially homogeneous.

Essential to this scaling is the existence of an East-West pressure gradient that maintains a geostrophically balanced meridional flow.

It is therefore interesting to enquire what happens when such a balance fails because there are no boundaries at the East and West that can support a pressure difference.

4 Thermohaline flow in a reentrant geometry

In the next section we will discuss the thermohaline circulation in the specific case of a channel unbounded in the East-West directions, limited in latitude and with periodic boundary conditions at the ends. Because of the absence of meridional walls, this model could describe the circulation in the Antartic Circumpolar region.

We assume that the horizontal flow obeys the steady two dimensional equations of motion, and we neglect nonlinear advective terms:

$$\begin{aligned} -fv &= -\frac{p_x}{\rho_0} - ru \\ fu &= -\frac{p_y}{\rho_0} - rv \end{aligned} \tag{22}$$

The shape of the basin imposes periodic E-W boundary conditions for all fields so that the longitudinally averaged pressure gradient in the x-direction must vanish, i.e.:

$$\overline{p_x} = 0. \tag{23}$$

This restriction prevents the system from reaching a steady geostrophic balance and does not allow an efficient meridional transport of water. We can in fact consider the zonally averaged momentum balance:

$$\begin{aligned} -f\overline{v} &= -\frac{\overline{p_x}}{\rho_0} - r\overline{u} \\ f\overline{u} &= -\frac{\overline{p_y}}{\rho_0} - r\overline{v} \end{aligned} \tag{24}$$

and solve for the meridional velocity:

$$\overline{v} = -\frac{r}{f^2 + r^2}\frac{\overline{p_y}}{\rho_0}. \tag{25}$$

The spreading of warm water from the equator towards the polar regions is achieved only because of friction. For weak drag, $r \ll f$, the meridional flow is small.

For x-independent buoyancy forcing, and excluding the spontaneous generation of x-dependent instabilities we have $v = \overline{v}$. Thus the flow is two-dimensional and it is described by a streamfunction ψ:

$$\begin{aligned} \overline{v} &= -\psi_z \\ \overline{w} &= \psi_y \end{aligned} \tag{26}$$

hence:

$$\begin{aligned} \overline{p_z} &= -\overline{\rho}g \\ \psi_{zz} &= -\frac{rg}{f^2 + r^2}\frac{\overline{\rho_y}}{\rho_0} \end{aligned} \tag{27}$$

With density to be determined by temperature and salinity as stated in equation (1), the flow is then governed by the two evolution equations:

$$\begin{aligned} \overline{T_t} + J(\psi, \overline{T}) &= \kappa \overline{T_{zz}} + \nu \overline{T_{yy}} \\ \overline{S_t} + J(\psi, \overline{S}) &= \kappa \overline{S_{zz}} + \nu \overline{S_{yy}} \end{aligned} \tag{28}$$

where $J(A, B) = \partial_x A \partial_y B - \partial_y A \partial_x B$.

The boundary conditions at the top of the layer for the two variables are very different. Sea surface temperature can be thought as adapting instantaneously to variations in heat flux, giving rise to a prescribed distribution of *temperature* with respect to latitude. Instead, surface salinity plays a minor role in the balance between evaporation and precipitation, so that the surface *salinity flux* is imposed by the atmosphere. Thus, we impose the following boundary conditions at the surface $z = 0$ and at the bottom of the sea $z = -H$:

$$\begin{aligned} \bar{T} &= \Delta T \Theta(y), \quad \kappa \bar{S}_z = F \mathcal{F}(y) \quad \text{at} \quad z = 0 \\ \kappa \bar{T}_z &= \kappa \bar{S}_z = 0 \quad \text{at} \quad z = -H. \end{aligned}$$

We now adimensionalize the set of equations (28), choosing the following scalings for lenghts, temperature and salinity:

$$z = H\,\zeta, \quad y = L\,\eta, \quad T = \Delta T\,\theta, \quad S = \frac{\alpha \Delta T}{\beta}\,\sigma \tag{29}$$

while for density, stream function and time, we nondimensionalize (27) using:

$$\rho = \rho_0 \alpha \Delta T\,\pi, \quad \psi = \frac{H^2 r g \alpha \Delta T}{f^2 L}\,\phi, \quad t = \frac{\kappa}{H^2}\epsilon^2\,\tau. \tag{30}$$

Substituting the non-dimensional variables into the governing equations, we obtain:

$$\begin{aligned} \phi_{\zeta\zeta} &= (\theta - \sigma)_\eta \\ \epsilon^2 \theta_\tau + \epsilon J(\psi, \theta) &= \theta_{\zeta\zeta} + \delta \theta_{\eta\eta} \\ \epsilon^2 \sigma_\tau + \epsilon J(\psi, \sigma) &= \sigma_{\zeta\zeta} + \delta \sigma_{\eta\eta} \end{aligned} \tag{31}$$

with boundary conditions:

$$\begin{aligned} \phi &= 0; \quad \theta_\zeta = \sigma_\zeta = 0 \quad \text{at} \quad \zeta = 0 \\ \phi &= 0; \quad \theta = \Theta(\eta) \quad \text{at} \quad \zeta = 1 \\ \sigma_\zeta &= R\mathcal{F}(\eta) \quad \text{at} \quad \zeta = 1 \end{aligned} \tag{32}$$

There are three parameters governing the behavior, defined as:

$$\overbrace{\epsilon \equiv \frac{r g H^3 \alpha \Delta T}{\kappa f^2 L^2}}^{\text{Rayleigh-Ekman \#}}, \quad \overbrace{R \equiv \frac{\beta F H}{\kappa \alpha \Delta T}}^{\text{density ratio}}, \quad \delta \equiv \frac{\nu H^2}{\kappa L^2}.$$

- ϵ is the product of the Rayleigh number and the Ekman number square;
- R expresses the ratio between temperature and salinity contributions to density variation;
- δ weights the importance of meridional to vertical diffusivities for T and S.

For weak drag $\epsilon << 1$ and we can simplify the analysis by expanding the three variables above in power series of ϵ:

$$\begin{aligned}\phi &= \phi_0 + \epsilon\phi_1 + \epsilon^2\phi_2 + 0(\epsilon^3)\\ \theta &= \theta_0 + \epsilon\theta_1 + \epsilon^2\theta_2 + 0(\epsilon^3)\\ \sigma &= \sigma_0 + \epsilon\sigma_1 + \epsilon^2\sigma_2 + 0(\epsilon^3)\end{aligned}$$

We further assume that the density ratio is small, specifically

$$R = O(\epsilon^2);\ \delta = O(\epsilon^2) \tag{33}$$

As a preliminary observation, we note that with this ordering of the parameter R the forcing (32) on the surface salinity flux enters only at order ϵ^2:

$$\sigma_{0\zeta} + \epsilon\sigma_{1\zeta} + \epsilon^2\sigma_{2\zeta} = \epsilon^2 R\mathcal{F}(\eta), \tag{34}$$

nevertheless, σ is $O(1)$.

Solving for the various orders in ϵ we get a hierarchy of equations. Starting from the leading order, $O(1)$, the temperature and salinity equations are:

$$\sigma_{0\zeta\zeta} = \theta_{0\zeta\zeta} = 0,$$

with boundary conditions:

$$\begin{aligned}\sigma_{0\zeta} = \theta_{0\zeta} = 0 \quad &\text{at} \quad \zeta = 0\\ \sigma_{0\zeta} = 0, \quad \theta_0 = \Theta(y) \quad &\text{at} \quad \zeta = 1\end{aligned}$$

Thus the two fields are vertically homogeneous at leading order:

$$\sigma_0 = \sigma_0(\eta, \tau), \theta_0 = \theta_0(\eta, \tau). \tag{35}$$

Furthermore, because of the fixed temperature boundary condition, the temperature at leading order is determined and $\theta_0 = \Theta(y)$. However, the leading order salinity is determined by the balance at higher orders.

We can also now determine the leading order streamfunction, which satisfies

$$\phi_{0\zeta\zeta} = (\theta_0 - \sigma_0)_\eta$$

and the condition $\phi_0 = 0$ at the two boundaries. Integrating vertically we find:

$$\phi_0 = \frac{1}{2}\zeta(\zeta + 1)(\theta_0 - \sigma_0)_\eta \tag{36}$$

At next order, $O(\epsilon)$, the salinity equation is:

$$-\phi_{0\zeta}\sigma_{0\eta} = \sigma_{1\zeta\zeta}$$

which, when integrated vertically, gives:

$$-\phi_0\sigma_{0\eta} = \sigma_{1\zeta}, \tag{37}$$

because the meridional flow turns lateral gradients into stratification. Because both the top and bottom boundary conditions for σ_1 are automatically satisfied, we must proceed to the next order to determine σ_0.

The evolution equation for σ_0 is obtained by vertically averaging the evolution equation of the salinity at $O(\epsilon^2)$ which is given by:

$$\partial_\tau\sigma_0 + \partial_\eta(\phi_0\sigma_{1\zeta}) - \partial_\zeta(\phi_0\sigma_{1\eta} + \phi_1\sigma_{0\eta}) = \sigma_{2\eta\eta} + \frac{\delta}{\epsilon^2}\sigma_{0\eta\eta}.$$

We thus obtain:

$$\partial_\tau\overline{\sigma_0} + \partial_\eta\int_0^1 d\zeta(\phi_0\sigma_{1\zeta}) = \frac{R}{\epsilon^2}\mathcal{F}(\eta) + \frac{\delta}{\epsilon^2}\sigma_{0\eta\eta}.$$

Here we have used the result that the third term on the left hand side vanishes and we have applied the surface condition $\sigma_{2\zeta}|_{\zeta=0} = \frac{R}{\epsilon^2}\mathcal{F}(\eta))$. If we substitue the expression for $\sigma_{1\zeta}$ obtained from (37) we find:

$$\partial_\tau\sigma_0 - \partial_\eta\int_0^1 d\zeta(\phi_0^2\sigma_{0\eta}) = \frac{R}{\epsilon^2}\mathcal{F}(\eta) + \frac{\delta}{\epsilon^2}\sigma_{0\eta\eta}.$$

Finally, using the expression (36) for ϕ_0 we get:

$$\partial_\tau\sigma_0 = \frac{1}{120}\partial_\eta[(\theta_0 - \sigma_0)_\eta]^2\sigma_{0\eta} + \frac{R}{\epsilon^2}\mathcal{F}(\eta) + \frac{\delta}{\epsilon^2}\sigma_{0\eta\eta} \tag{38}$$

with $\theta_0 = \Theta(\eta)$.

It is also useful to write the dimensional forms of the equations, which are given by

$$\psi = \frac{rg}{2(f^2+r^2)}z(z+H)(\alpha T_{0y} - \beta S_{0y}),$$

$$T_0 = \Delta T\Theta(y),$$

$$S_{0t} = \frac{\epsilon^2 L^4\kappa}{120H^2}\left[\frac{(\beta S_{0y} - \alpha T_{0y})^2}{(\alpha\Delta T)^2}S_{0y}\right]_y + \frac{F}{H}\mathcal{F} + \nu S_{yy}. \tag{39}$$

The meridional circulation transports salt downgradient with a nonlinear "diffusivity" proportional to ρ_y^2.

For $r << f$, ψ is independent of κ and the density field is almost vertically homogeneous. Thus the qualitative picture of the circulation in a channel, in the limit where the friction is very small, is very different than that obtained in the presence of meridional walls. The circulation is also accompanied by a large east-west velocity, which is in thermal wind balance, which does not influence the meridional circulation.

5 The two-box model approximation

In this section a two-box approximation of (39) is considered, since this reduction illustrates the qualitative properties of the full partial differential equation. This approximation also leads to a model which is very similar to that original proposed by Stommel (1961) in the limit of rapid temperature relaxation.

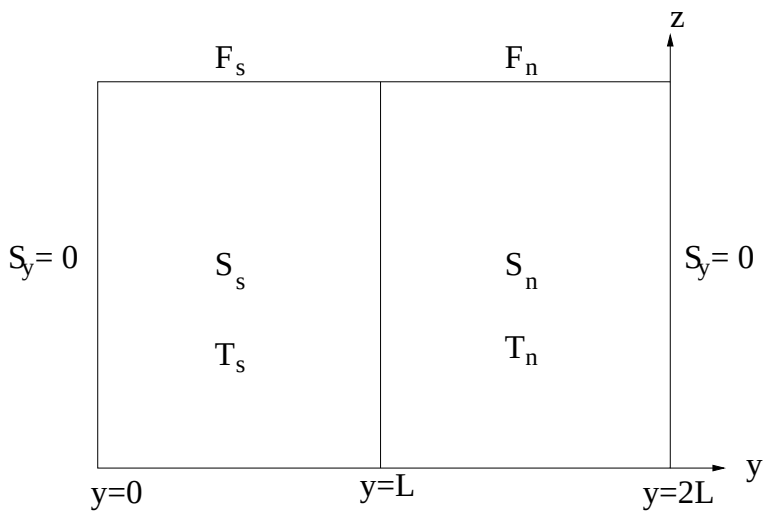

Figure 1: The box-model approximation to (39).

The left hand box in figure (1) is the equatorial box, denoted by subscript s, while the right hand is the polar box, denoted by subscript n. The salnity is assumed to be independent of latitude and depth within each box.

F represents the surface flux of salinity, S the salinity and T the temperature. There is no meridional flux of salinity at the sides. Integrating (39) in latitude over the equatorial and the polar box the salt equation we obtain the following two equations:

$$\begin{aligned} \dot{S}_s &= [\mu S_{0y}(\beta/\alpha S_{0y} - T_{0y})^2 + \nu S_{0y}]_{y=L} + \frac{F}{H}\mathcal{F}_s, \\ \dot{S}_n &= -[\mu S_{0y}(\beta/\alpha S_{0y} - T_{0y})^2 + \nu S_{0y}]_{y=L} + \frac{F}{H}\mathcal{F}_n. \end{aligned} \tag{40}$$

Notice that we need $\mathcal{F}_s + \mathcal{F}_n = 0$, in order to conserve the mean salinity of the system.

In order to determine the salinity gradient at the latitude $y = L$, S_{0y}, we use the following differentiation rule:

$$S_{0y}|_{y=L} = \frac{S_n - S_s}{L}, \quad T_{0y} = \frac{T_n - T_s}{L}.$$

Defining

$$\sigma \equiv \frac{\beta(S_n - S_s)}{\alpha(T_n - T_s)},$$

and rescaling time, the salinity difference satisfies

$$\dot{\sigma} = -\sigma(\sigma - 1)^2 + \gamma - \lambda\sigma. \tag{41}$$

In this equation γ is a parameter expressing the ratio between N-S salt flux effect and heat temperature gradient:

$$\gamma \propto \frac{F_n - F_s}{T_n - T_s} > 0$$

while λ is proportional to the lateral diffusion, ν. We expect stationary condition to be reached for compensating temperature and salinity effects. If $T_n - T_s < 0$, $F_n < 0$ and $F_s > 0$, the equilibria will correspond to positive values of γ.

Stommel (1961) used a slightly different box-model, which in the limit of rapid temperature relaxation is:

$$\dot{\sigma} = -\sigma|\sigma - 1| + \gamma - \lambda\sigma.$$

Both systems will reach a steady state, minimum of a potential, V because

$$\dot{\sigma} = -\frac{\partial V(\sigma)}{\partial \sigma} \;\Rightarrow\; V_\sigma \dot{\sigma} = \dot{V} = -(V_\sigma)^2 \leq 0.$$

The potential, V, associated with (41) is a function of σ given by

$$V(\sigma) = \frac{1}{4}\sigma^4 - \frac{2}{3}\sigma^3 + \left(\lambda + \frac{1}{2}\right)\sigma^2 - \gamma\sigma.$$

Depending on γ and λ, V can have one or two minima as illustrated in the following figure. Equilibria are associated with extrema of the potential, V: minima are stable and maxima are unstable.

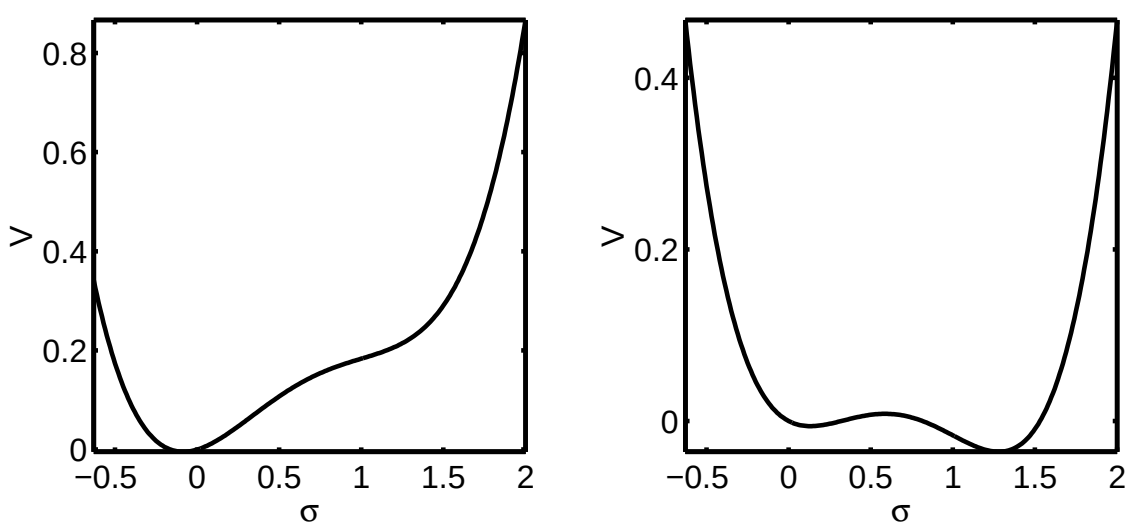

Figure 2: The potential V for two different values of λ.

Multiple equilibria (3) are obtained for:

$$(1-3\lambda)^{3/2} \geq |1 - \frac{27}{2}\gamma + 9\lambda|, \tag{42}$$

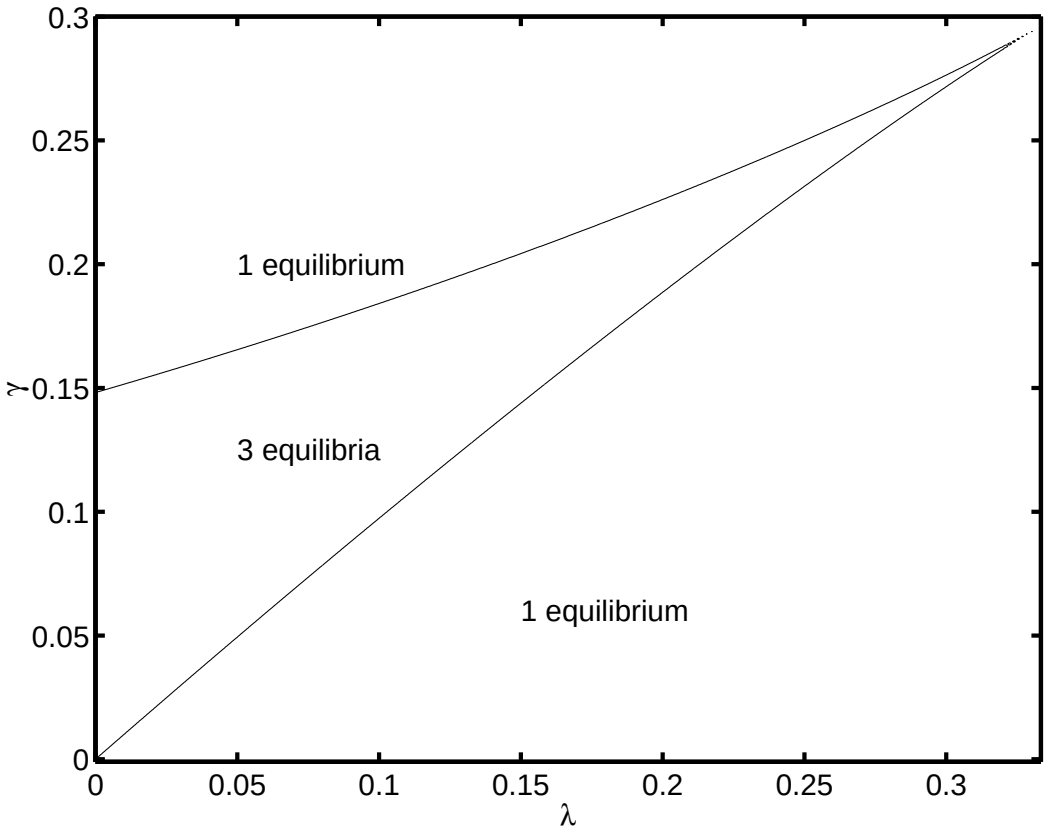

Figure 3: The region where multiple equilibria exist is bounded by the curve (refcusp:eqn) in the $\gamma - \lambda$ space.

In the limit $\lambda \ll 1$ (weak lateral diffusion) it is possible to find approximate expressions for the steady states, which are given by:

$$\sigma(\sigma-1)^2 = \gamma \ll 1.$$

There is a thermally-driven solution with small salinity gradient:

$$\sigma_a \approx \gamma \ll 1.$$

There is a salt-compensated solution with small density gradient:

$$\sigma_c \approx 1 + \sqrt{\gamma}.$$

The third solution, $\sigma_b \approx 1 - \sqrt{\gamma}$ is unstable.

Recalling that the meridional overturning circulation is given by $\psi \propto (1-\sigma)$, the meridional circulations associated with the two stable equilibria are:

$$\begin{aligned} \psi_a &\propto 1-\gamma \\ \psi_c &\propto -\sqrt{\gamma}. \end{aligned}$$

Thus ψ_a and ψ_c have opposite sign and the haline-driven circulation, ψ_c, is much weaker than the thermally driven flow.

The deterministic model does cannot lead to time-dependent variability of the thermohaline circulation, since it only admit (multiple) fixed points. Thus, the system cannot spontaneously jump from one equilibrium to the other: all initial states to the left (right) of the potential barrier end up in the same left-(right)hand well.

Notes by Fiona Eccles and Chiara Toniolo

References

Bryan, F., 1986: High-latitude salinity effects and interhemispheric thermohaline circulations. *Nature*, **323**, 301-304.

Cessi P. and W.R. Young, 1992: Multiple equilibria in 2-dimensional thermohaline circulation, *J. Fluid Mech.*, **241**, 291-309.

Huang, R.X. and R.L. Chou, 1994: Parameter sensitivity study of the saline circulation. *Climate Dyn.*, **9**, 391-409.

Manabe, S. and R.J. Stouffer, 1988: Two stable equilibria of a coupled ocean-atmosphere model. *J. Climate*, **1**, 841-866.

Stommel, H., 1961: Thermohaline convection with two stable regimes of flow. *Tellus*, **13**, 224-230.

Vallis, G.K.,2000: Large-scale circulation and production of stratification: Effects of wind, geometry, and diffusion. *J. Phys. Oceanogr.*, **30**, 933-954.

Lecture 5

Thermohaline Variability

Paola Cessi

1 Stochastic Forcing

The 2-box model analyzed in the prvious section (as well as Stommel's box-model) is governed by a deterministic equation, i.e. the time evolution of the salinity difference, σ, is completely determined by the model equation given an initial condition. Moreover, the system always reach one of two possible stable steady states. However, variability can be forced by a time-dependent forcing.

Now, let us consider a case where the salt flux, γ, has a component, γ', that is random in time, $\gamma = \bar{\gamma} + \gamma'(t)$. With the noise, σ is no longer a deterministic variable, but becomes a random variable. In this case, σ can be written as $\sigma = \bar{\sigma} + \sigma'(t)$.

Here, we consider two cases. For a weak agitation, or in a short time scale, the system oscillates near the stable steady states (See Figure 1). For a large agitation, it will shift from one stable point to another. In this section, we describe the behavior of the 2-box system using stochastic methods.

2 Rattle near stable points

For weak agitation, the system rattles almost linearly around each equilibrium. Assuming that the perturbation is small, we linearize the model equation around a stable solution, say $\bar{\sigma} = \sigma_c$. The time-dependendent perturbation satisfies

$$\frac{\partial \sigma'}{\partial t} = -\frac{\partial^2 V}{\partial \sigma^2}(\sigma_c)\sigma' + \gamma' \tag{1}$$

We use Fourier transforms to solve for the spectrum of σ'. The Fourier transform, $\tilde{\sigma}(\omega)$, of $\sigma'(t)$ is defined as:

$$\tilde{\sigma}(\omega) \equiv \frac{1}{2\pi}\int_{-\infty}^{\infty} \sigma'(t)\exp(-i\omega t)\,dt \tag{2}$$

$$\sigma'(t) = \int_{-\infty}^{\infty} \tilde{\sigma}\exp(i\omega t)\,d\omega \tag{3}$$

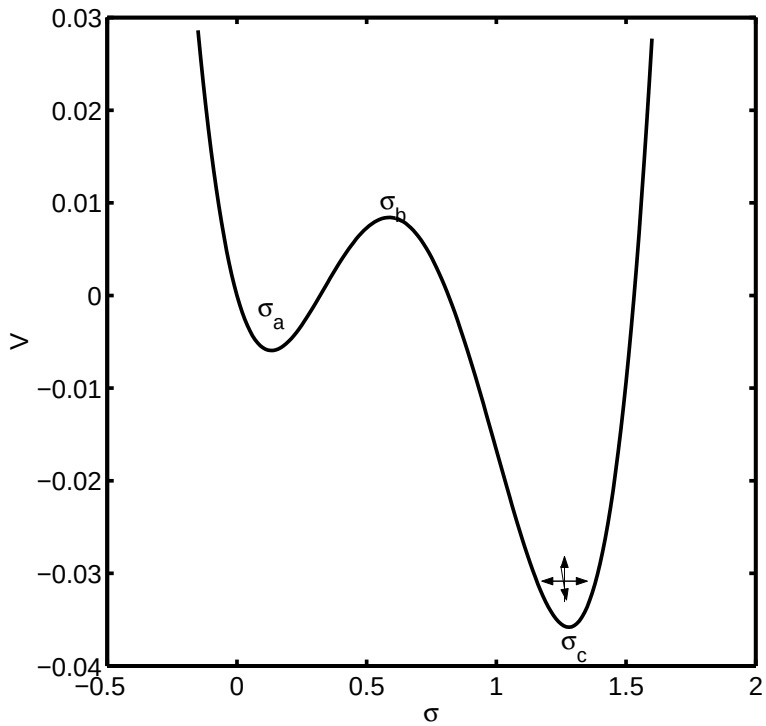

Figure 1: *Rattle near stable points:* Potential V is a function of σ. For weak noise, the system rattles around the steady states, σ_a, and σ_c.

And similarly, the Fourier transform pair of $\gamma'(t)$ is:

$$\tilde{\gamma}(\omega) \equiv \frac{1}{2\pi}\int_{-\infty}^{\infty}\gamma'(t)\exp(-i\omega t)\,dt \tag{4}$$

$$\gamma'(t) = \int_{-\infty}^{\infty}\tilde{\gamma}\exp(i\omega t)\,d\omega \tag{5}$$

Applying these relationship to (1), we obtain,

$$\tilde{\sigma} = \frac{\tilde{\gamma}}{V_{\sigma\sigma} + i\omega} \tag{6}$$

$\gamma'(t)$ is the stochastic noise, and is randomly picked at every timestep, dt, from a gaussian distribution with zero mean and variance ξ^2. The auto correlation of γ' is,

$$< \gamma'(t)\gamma'(t+\tau) > \approx \delta(\tau)dt\,\xi^2. \tag{7}$$

where $\delta(\tau)$ denotes a delta function in τ. The Fourier transform of a delta function is a constant, therefore, the spectrum (given by the ensemble average of the Fourier transform of the auto correlation function) $< |\tilde{\gamma}|^2 >$ is constant for all ω. Thus the spectrum of σ can be calculated by taking the product of (6) with its own complex conjugate and ensamble averaging to obtain:

$$< \tilde{\sigma}\tilde{\sigma^*} > = \frac{< \tilde{\gamma}\tilde{\gamma^*} >}{V_{\sigma\sigma}(\sigma_c)^2 + \omega^2} = \frac{dt\,\xi^2}{V_{\sigma\sigma}(\sigma_c)^2 + \omega^2}. \tag{8}$$

This spectrum is red since it decreases with increasing frequency, starting at a frequency of the order of the linear damping term.

3 Jumps between equilibria

On longer time scales or with larger variance of the noise, jumps between σ_a and σ_c can occur occasionally. To study the stochastic behavior of the model with the noise-induced jumps between equilibria, we go back to the nonlinear model equation with the noise term.

$$\dot{\sigma} = -\frac{\partial V(\sigma)}{\partial \sigma} + \gamma'(t). \tag{9}$$

The probability distribution function (hereafter, PDF), $\phi(\sigma, t)$, describes the probability of finding a particular value for σ at time t. The Fokker-Plank Equation (hereafter, FPE) describes the time evolution of the PDE of the stocastically forced system *[Gardiner 1990]*. The FPE of the 2-box model is,

$$\frac{\partial \phi}{\partial t} = (V_\sigma \phi)_\sigma + D\phi_{\sigma\sigma} \tag{10}$$

where $D \equiv \frac{\xi^2}{2}\,dt$. Taking the right hand side of the FPE to zero we obtain the steady state solution, ϕ_s, which is the probability of finding a state with a particular value of σ when time goes to infinity. The steady distribution is given by

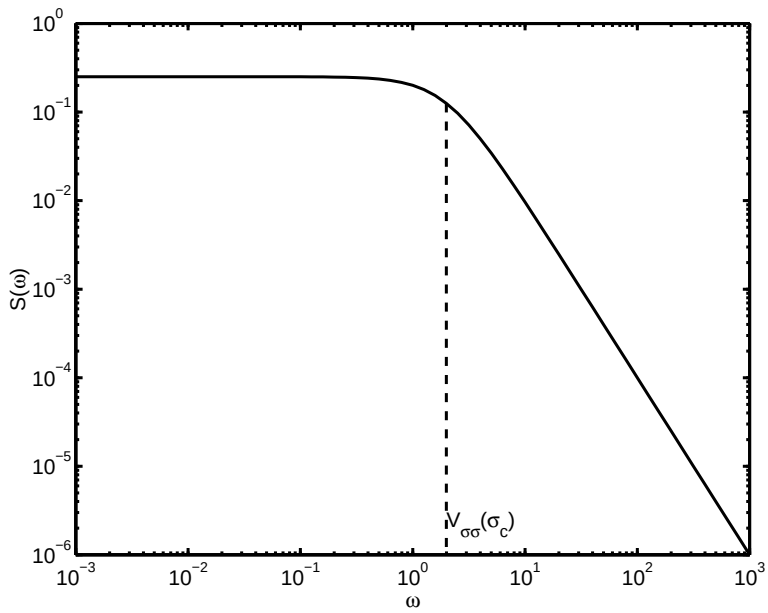

Figure 2: *Power spectrum of small perturbation around stable points*

$$\phi_s(\sigma) = N \exp(\frac{-V(\sigma)}{D}). \tag{11}$$

where N is a normalization constant which is determined by the constraint $\int_{-\infty}^{\infty} \phi_s \, d\sigma = 1$. Figure 3 shows an example of stationary distribution, ϕ_s, as a function of σ.

4 Average transit times

In this section, we calculate the average time for the system to shift from one stable equilibrium to another. First, let us calculate the probability, N_{ac}, of finding $\sigma_a \leq \sigma \leq \sigma_c$ at time t.

$$N_{ac} = \int_{\sigma_a}^{\sigma_c} \phi(x,t) \, dx \tag{12}$$

The probability N_{ac} can also be viewed as the probability that the time, τ, to exit the interval $[a, c]$, exceeds t. Indeed, finding σ in the range $[\sigma_a, \sigma_c]$ at time t implies that σ must leave the region after the time t. We define $q(\tau)$ as the PDF for the exit time, τ, from the region $[\sigma_a, \sigma_c]$.

$$N_{ac} = \int_{t}^{\infty} q(\tau) \, d\tau \tag{13}$$

Then, the average exit time is given as the first moment of the PDF, $q(t)$. Denoting with $T_{a \to c}$ the average time for σ to escape from the region $[\sigma_a, \sigma_c]$, we find:

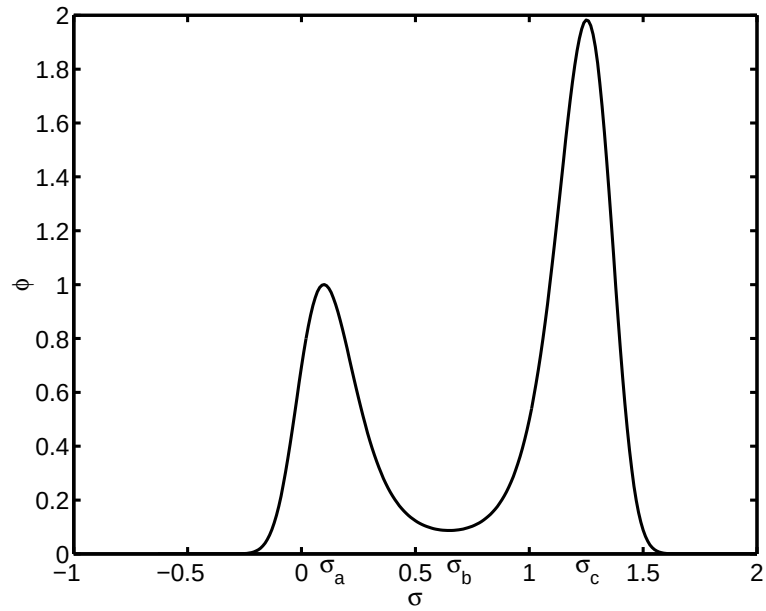

Figure 3: *Steady state of the PDF :* $\phi_s(\sigma)$

$$
\begin{aligned}
T_{a\to c} &= \int_0^\infty tq(t)\,dt \\
&= -\int_0^\infty t\frac{dN_{ac}}{dt}\,dt \\
&= \int_0^\infty N_{ac}\,dt. \qquad (14)
\end{aligned}
$$

To find $T_{a\to c}$ we integrate the FPE with boundary conditions in time and space. The mean escape time from σ_c to σ_a, denoted with $T_{c\to a}$ can be also find using a similar procedure. The boundary conditions will specify the direction of the shift between equilibria.

Here, consider a case where σ moves from σ_a to σ_c. We assume that at $t = 0$, the model state, σ, is at σ_a, so that the PDF is a delta function. We also assume that as time goes infinity, the PDF goes to zero. Defining the time-integrated PDF, $\bar{\phi} \equiv \int_0^\infty \phi(\sigma, t)\,dt$ and integrating (10) in time from 0 to ∞ we find

$$-\delta(\sigma - \sigma_a) = (V_\sigma \bar{\phi})_\sigma + D\bar{\phi}_{\sigma\sigma}. \qquad (15)$$

We also assume that $\bar{\phi} \to 0$ as $\sigma \to -\infty$ because σ moves from σ_a to σ_c, implying that once the particle has moved to σ_c, it should not return to the original location. This condition gives $\bar{\phi}(\sigma_c) = 0$. With these boundary conditions, one can solve equation (15), and obtain $T_{a\to c}$.

$$
\begin{aligned}
T_{a\to c} &= \frac{1}{D}\int_{\sigma_a}^{\sigma_c}\frac{dx}{\phi_s(x)}\int_{-\infty}^{x}\phi_s(y)\,dy \\
&\approx \frac{1}{D}\int_{\sigma_a}^{\sigma_c}\frac{dx}{\phi_s}\int_{-\infty}^{\sigma_b}\phi_s\,dy \qquad (16)
\end{aligned}
$$

We calculate $T_{c\to a}$ using the same equation with different boundary conditions. In this case, the model state, σ is initially concentrated at σ_c and the PDF is delta function there. We assume that $\bar{\phi}\to 0$ as $\sigma\to\infty$ because σ moves from σ_c to σ_a (with $\sigma_a<\sigma_c$ as in figure 1). Also we set $\bar{\phi}(\sigma_a)=0$, assuming that once particles arrive at σ_a they never come back. With these boundary conditions, we solve the equation (15), and obtain $T_{c\to a}$.

$$
T_{c\to a}\approx\frac{1}{D}\int_{\sigma_a}^{\sigma_c}\frac{dx}{\phi_s}\int_{\sigma_b}^{\infty}\phi_s\,dy \qquad (17)
$$

5 Random Telegraph Process

On long timescales we can assume that the system simply jumps between the two equilibria. We ignore the rattle around each equilibrium and only allow σ to be in one equilibrium or another. In this case, we can approximate the system with a Random Telegraph Process : σ is in σ_a with probability $\frac{N_a}{N}$ or in σ_b with probability $\frac{N_b}{N}$. The sum of $\frac{N_a}{N}$ and $\frac{N_b}{N}$ is unity. We can now use the average escape times $T_{c\to a}$ and $T_{a\to c}$ to estimate the rates of transitions between equilibria. Specifically we have

$$
\dot{N}_a = -\omega_a N_a + \omega_c N_c \qquad (18)
$$

$$
\dot{N}_c = -\omega_c N_c + \omega_a N_a \qquad (19)
$$

where $\omega_a = T_{a\to c}^{-1}$ and $\omega_c = T_{c\to a}^{-1}$. Steady solutions are found equating the right hand sides to zero, so that

$$
N_a = N\frac{\omega_c}{\omega_a+\omega_c} \qquad (20)
$$

$$
N_c = N\frac{\omega_a}{\omega_a+\omega_c} \qquad (21)
$$

We can compute the low frequency spectrum by taking the Fourier Transform of the auto-correlation function. First, we define the auto-correlation function of the Random Telegraph process.

$$
\mathcal{C}(\tau) =< \sigma'(t)\sigma'(t+\tau) > \qquad (22)
$$

where $\sigma' = \sigma - <\sigma>$. The average value for σ is $<\sigma>=\frac{1}{N}\sum_1^N\sigma = \sigma_a\frac{N_a}{N}+\sigma_c\frac{N_c}{N}$. We need the time-dependent equation for $\mathcal{C}(t)$. First, let us consider the equilibrium value at $\tau=0$,

$$\mathcal{C}(0) = \frac{1}{N}\sum_{1}^{N}\sigma'^2 \tag{23}$$

$$= \frac{N_a}{N}{\sigma'_a}^2 + \frac{N_c}{N}{\sigma'_c}^2 \tag{24}$$

$$= \frac{N_a N_c}{N^2}(\sigma_a - \sigma_c)^2 \tag{25}$$

$$= \frac{(\sigma_a - \sigma_c)^2\omega_a\omega_c}{(\omega_a + \omega_c)^2} \tag{26}$$

Next we consider the state of the system at time, $0 + dt$. We can calculate the auto-correlation, $\mathcal{C}(dt)$, by counting the expected number of jumps between the two states. During the time period, dt, the switch $\sigma_a \to \sigma_c$ occurs with a probability of $\frac{N_a}{N}\omega_a\, dt$. Similarly, the switch $\sigma_c \to \sigma_a$ occurs with a probability of $\frac{N_a}{N}\omega_c\, dt$.

We can count all the possible states of the system at time, $0+dt$. First, we can estimate the number of states where σ is at σ_a during the interval $[0, dt]$. The number of this particular state is $N_a(1 - \omega_a\, dt)$. Secondly, we can estimate the number of states where σ is at σ_c during $[0, dt]$. The number of this particular state is $N_c(1 - \omega_c\, dt)$. Finally, we can estimate the number of states in the transition between the equilibrium. The number of this particular state is $(N_a\omega_a + N_c\omega_c)\, dt$. Taking these together, we find

$$\mathcal{C}(dt) = \sum_{1}^{N}\sigma'(dt)\sigma'(0) \tag{27}$$

$$= \underbrace{\frac{N_a}{N}(1 - \omega_a dt){\sigma'_a}^2}_{\sigma_a \text{ at } 0 \text{ and } dt} + \underbrace{\frac{N_c}{N}(1 - \omega_c dt){\sigma'_c}^2}_{\sigma_c \text{ at } 0 \text{ and } dt} + \underbrace{(\frac{N_a}{N}\omega_a + \frac{N_c}{N}\omega_c)dt\sigma'_a\sigma'_c}_{\text{in transit}} \tag{28}$$

We can now form the differential equation for $\mathcal{C}$ at time, $t = 0$.

$$\frac{\partial\mathcal{C}}{\partial t}|_{\tau=0} = -\frac{1}{N}(\omega_a + \omega_c)(N_a{\sigma'_a}^2 + N_c{\sigma'_c}^2) \tag{29}$$

$$= -(\omega_a + \omega_c)\mathcal{C}(0) \tag{30}$$

The solution of this equation is $\mathcal{C}(\tau) = \mathcal{C}(0)e^{-(\omega_a+\omega_c)\tau}$, with $\mathcal{C}(0)$ given by (28).

Thus, the low-frequency end of spectrum for the box-model subject to noise is given by:

$$S(\omega) = \mathcal{C}(0)^2\frac{2(\omega_a + \omega_c)}{(\omega_a + \omega_c)^2 + \omega^2} \tag{31}$$

Given the dependence of the espace times on the noise variance, the amplitude of the spectrum increases as the noise variance decreases.

$$S(0) = \frac{2(\sigma_a - \sigma_c)^2\omega_a\omega_c}{(\omega_a + \omega_c)^3} \tag{32}$$

$$\propto \exp(A\xi^{-2}) \tag{33}$$

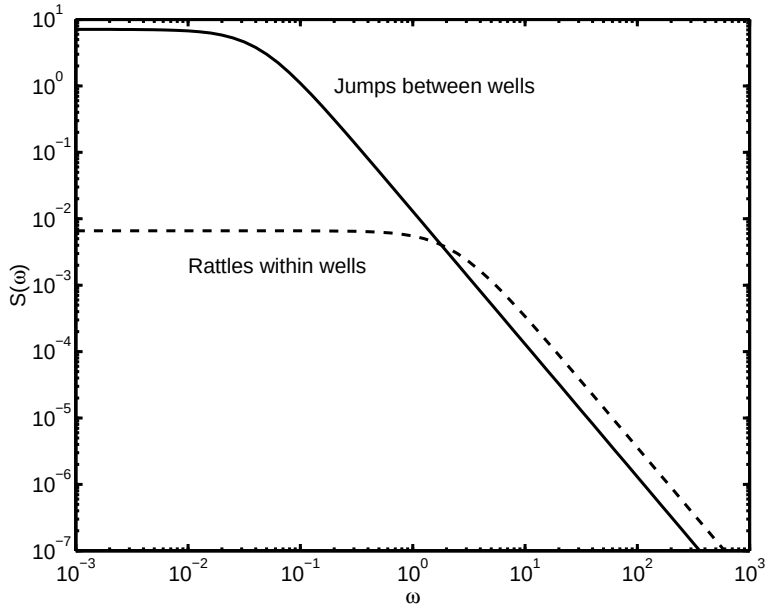

Figure 4: *The comparison of the short-time timescale and the long-timescale power spectrum*

Figure 4 compares the low-frequency and the high-frequency approximations. Note that the short-timescale spectrum represents the rattling around the stationary points, and saturates at higher frequency. The long-timescale spectrum approximates the jumps between the stationary points. Neither of the spectra show a peak because the associated deterministic system has only fixed points.

6 The Howard-Malkus-Welander loop

The next conceptual model that we will consider is the Howard-Malkus-Welander loop. A circular ring of fluid with temperature T and salinity S flows with angular velocity $\omega = \dot{\phi}$, with ϕ the angle to the vertical. The ring is immersed in a bath at constant temperature T_E and salinity S_E (see Fig. 5). The outer radius of the ring is r, the inner radius is a and g is gravity. For a thin loop with $(r - a) \ll a$, the fluid can be assumed to be well mixed in the radial direction, so that all variables become independent of r. In this case, the angular velocity satisfies the following equation

$$\dot{\omega} = -\frac{p_\phi}{\rho_0 a^2} - \frac{\rho g \hat{k} \cdot \hat{\phi}}{\rho_0 a} - \Gamma\omega. \tag{34}$$

Γ is the friction coefficient, $\hat{k}$ the unit vector in the vertical direction and $\hat{\phi}$ the unit vector in the tangential direction. Again we assume a linear equation of state, so that $\rho\hat{k} \cdot \hat{\phi} = \rho_0(\beta S - \alpha T)\sin\phi$.

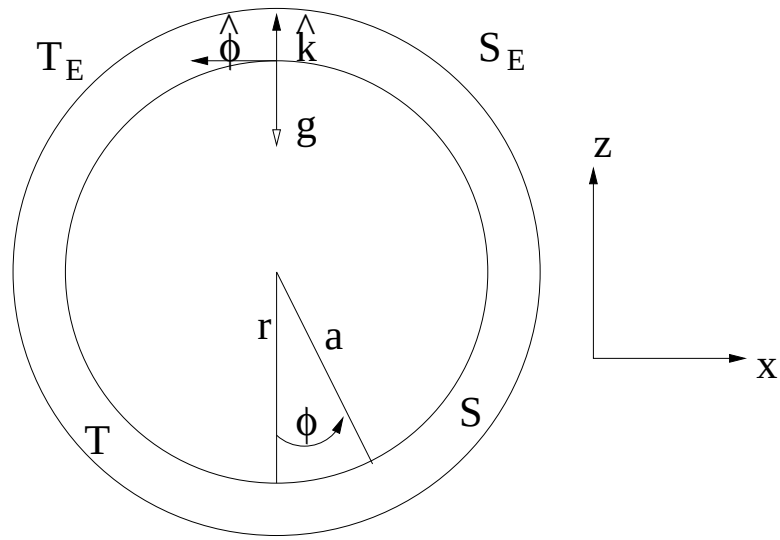

Figure 5: *Sketch of the Howard-Malkus-Welander loop.*

Equation (34) can be integrated around the loop to eliminate p and this yields

$$2\pi a\dot{\omega} = g\int_0^{2\pi} d\phi\,(\alpha T - \beta S)\sin\phi - 2\pi a\Gamma\omega \tag{35}$$

where we have used that, for a two-dimensional incompressible fluid, the angular velocity cannot depend on ϕ, if $\omega_r = 0$.

The temperature and salinity are determined through:

$$\begin{aligned} \dot{T} + \omega T_\phi &= r(T_E - T), \\ \dot{S} + \omega S_\phi &= r_s(S_E - S). \end{aligned}$$

where r and r_S are the diffusion rates of temperature and salinity, respectively. With antisymmetric forcing $(T_E, S_E) = (T_0, S_0)\sin\phi$ (heating and salting on the right side of the loop, cooling and freshening on the left side), we decompose temperature and salinity into a symmetric part and a antisymmetric part

$$T = T_1\cos\phi + T_2\sin\phi, \quad S = S_1\cos\phi + S_2\sin\phi.$$

Substitution of these relations in equation (36) yields

$$\begin{aligned} \dot{T}_1 + \omega T_2 &= -rT_1, \qquad & \dot{T}_2 - \omega T_1 &= r(T_0 - T_2), \\ \dot{S}_1 + \omega S_2 &= -r_s S_1, \qquad & \dot{S}_2 - \omega S_1 &= r_s(S_0 - S_2). \end{aligned}$$

For long time scales inertia will be much smaller than friction, $\dot{\omega} \ll \Gamma\omega$ and it follows directly from equation (35) that ω then satisfies

$$\omega = \frac{g}{2\Gamma a}(\alpha T_2 - \beta S_2). \tag{36}$$

In the limit where the relaxation rate of temperature is much greater than the relaxation rate of salinity, i.e. $r \gg r_s$, the temperature is clamped to the forcing, so that $T_1 \approx 0$, $T_2 \approx T_0$. The salinity evolves on a slower time-scale according to:

$$\begin{aligned} \dot{S}_1 + \frac{g}{2\Gamma a}(\alpha T_0 - \beta S_2)S_2 &= -r_s S_1, \\ \dot{S}_2 - \frac{g}{2\Gamma a}(\alpha T_0 - \beta S_2)S_1 &= r_s(S_0 - S_2). \end{aligned}$$

We introduce new variables $y_{1,2} = \frac{\beta S_{1,2}}{\alpha T_E}$ and $\hat{t} = \frac{g\alpha T_E}{2\Gamma a}t$, so that

$$\dot{y}_1 + (1 - y_2)y_2 = -\delta y_1 \tag{37}$$

$$\dot{y}_2 - (1 - y_2)y_1 = \delta(y_0 - y_2) \tag{38}$$

where a dot indicates now differentiation with respect to $\hat{t}$ with $\delta = \frac{2r_s\Gamma a}{g\alpha T_E}$.

The limit of a fixed salinity flux is given by $\delta \to 0$ with $\delta y_0 \equiv F$ finite. In this limit there is only one fixed point (the others are at ∞), given by

$$y_1 = -F, \quad y_2 = 0.$$

We can look at its linear stability by setting

$$y_1 = -F + \epsilon_1(t), \quad y_2 = \epsilon_2(t).$$

Neglecting $O(\epsilon^2)$ terms we find:

$$\dot{\epsilon}_1 + \epsilon_2 = 0, \quad \dot{\epsilon}_2 - \epsilon_1 - F\epsilon_2 = 0$$

These are the equations for an oscillator with damping $-F$:

$$\ddot{\epsilon}_2 + \epsilon_2 - F\dot{\epsilon}_2 = 0.$$

There is linear growth when $F > 0$, i.e. when the forcing is warm-salty and cold-fresh. When $F < 0$, the oscillations are damped out. Oscillations can only occur if the temperature and salinity forcing are opposing each other. Similarly, the Stommel 2-box model only admits multiple equilibria when there is competition between thermal and haline forcings.

The physical mechanism of the oscillation can be described as follows. As the fluid on the left flows downwards, it slows down due to the freshening. At the bottom it is now lighter and thus rises more rapidly on the right. Thus, it acquires less salt going up than it lost going down and at the next cycle it slows down even further. This leads to a growing alternation of slowing on the left and speeding on the right while going around the loop.

This oscillation occurs through a Hopf bifurcation at a certain value of the flux F, as illustrated in Figure 7: as the parameter F passes a certain value (in this case 0), the steady solution becomes oscillatory.

The period of this oscillation, $2\pi/\omega$, is the advection time around the loop and set by the thermally driven flow (see equation (36). For the North Atlantic, a similar advection time can be defined, which is about 100 years.

It is left to the reader to show that without salinity, but for general forcing, the steady state transport vanishes as $r \to 0$ when there is heating from above.

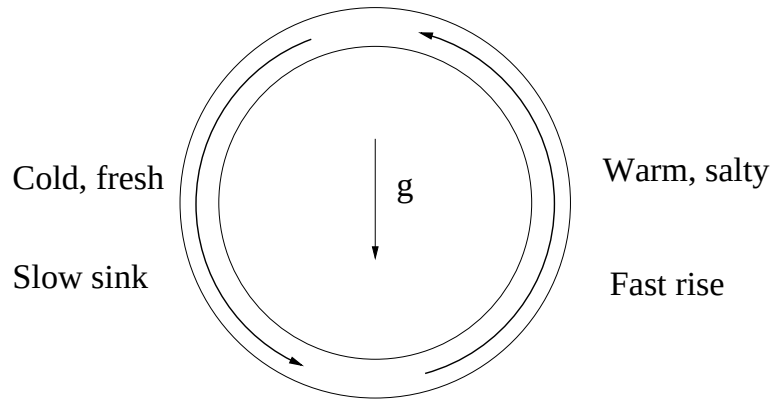

Figure 6: *Sketch of the oscillation mechanism.*

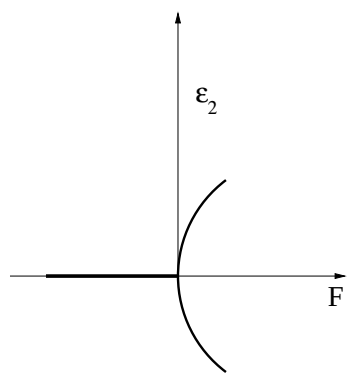

Figure 7: *Schematic plot of a Hopf bifurcation*

The effect of noise

Suppose now that the salinity flux consists of an average part $\bar{F}$ and a random part $F'(t)$, where the noise has variance $< F'^2 > dt = \sigma^2$. This noise can excite oscillations even when $\bar{F} < 0$, that is when the associated deterministic system has a stable fixed point. We compute again steady states and perform linear stability analysis to get

$$\ddot{\epsilon}_2 + \epsilon_2 - \bar{F}\dot{\epsilon}_2 = F'.$$

We can solve the system using Fourier Transforms, so

$$-(\omega^2 - i\omega\bar{F} - 1)\tilde{\epsilon}_2 = \tilde{F}'.$$

Then the spectrum is

$$< |\tilde{\epsilon}_2|^2 >= \frac{< |\tilde{F}'|^2 >}{(\omega^2 - 1)^2 + \omega^2\bar{F}^2} = \frac{\sigma^2}{dt[(\omega^2 - 1)^2 + \omega^2\bar{F}^2]}. \tag{39}$$

A typical spectrum is plotted in Fig. 8. Characteristic of the spectrum of such a system is that it peaks at the intrinsic frequency, which is $\omega = 1$ in this case, and that the height depends on the noise variance.

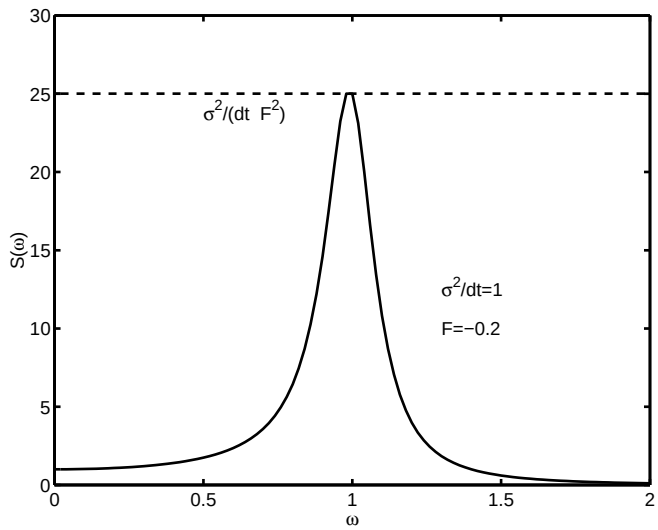

Figure 8: *A typical example of the spectrum of equation 39. Values that were used were* $f = -0.2$ *and* $\sigma^2/dt = 1$*. The height of the spectrum is* $\sigma^2/(dtF^2)$*.*

7 Welander's flip-flop oscillation

Another conceptual model of the thermohaline circulation is the so-called flip-flop model of Welander. It consists of a box of temperature T and salinity S that can exchange heat and salt vertically with a reservoir that is kept at temperature T_0 and salinity S_0 (see Fig 9).

The surface box is relaxed towards a temperature T_A and is forced by a freshwater flux

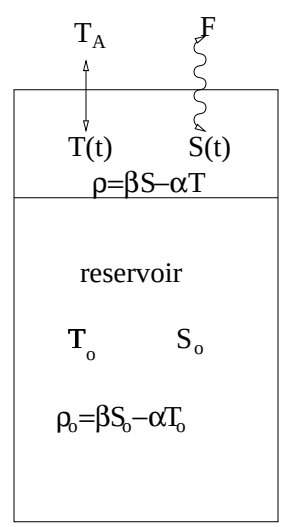

Figure 9: *Welander's flip-flop model*

F. Again, a linear equation of state is used for both boxes, so that $\rho = \beta S - \alpha T$ for the upper box and $\rho_0 = \beta S_0 - \alpha T_0$ for the reservoir. The equations that describe the evolution

of temperature and salinity in the upper box are given by

$$\begin{aligned} \dot{T} &= -\gamma(T - T_A) - \kappa(T - T_o), \\ \dot{S} &= F - \kappa(S - S_o). \end{aligned} \tag{40}$$

where γ is a relaxation coefficient, κ a mixing coefficient that is taken equal for heat and salt and H is the thickness of the upper box. The mixing coefficient is taken to be dependent on the density difference between the two boxes, to represent the effect of convection. Mixing with the reservoir is much faster if the stratification is unstable than if it is stable:

$$\kappa = \begin{cases} \kappa_1 & \text{if } \rho - \rho_o \leq \Delta\rho \\ \kappa_2 & \text{if } \rho - \rho_o > \Delta\rho. \end{cases}$$

with $\kappa_2 \gg \kappa_1$. Introducing new variables

$$x \equiv \frac{T - T_o}{T_A - T_o}, \; y \equiv \frac{\beta(S - S_o)}{\alpha(T_A - T_o)}, \; t' \equiv \gamma t,$$

we can rewrite 40 to

$$\begin{aligned} \dot{x} &= 1 - x - \nu x \\ \dot{y} &= \mu - \nu y. \end{aligned}$$

Here we have definex $\mu = \beta F/(\gamma\alpha H(T_A - T_0))$ and

$$\nu = \frac{\kappa}{\gamma} = \begin{cases} \nu_1 & \text{if } y - x \leq \epsilon \\ \nu_2 & \text{if } y - x > \epsilon, \end{cases}$$

with $\epsilon = \Delta\rho/(\alpha(T_A - T_0)$.

The steady states of the model are

$$x = \frac{1}{1+\nu}, \quad y = \frac{\mu}{\nu}.$$

Thus there are steady states if the density satisfies

$$\begin{aligned} \text{either} \;\; y - x &= \frac{\mu}{\nu_1} - \frac{1}{1+\nu_1} \leq \epsilon \\ \text{or} \;\; y - x &= \frac{\mu}{\nu_2} - \frac{1}{1+\nu_2} > \epsilon. \end{aligned}$$

In the first case, the stratification is stable and 'convection' never occurs, in the latter case the stratification is unstable and there will always be 'convection'. No steady states can *exist* if

$$\mu_1 < \mu < \mu_2$$

with

$$\mu_2 \equiv \epsilon\nu_2 + \frac{\nu_2}{1+\nu_2}, \quad \mu_1 \equiv \epsilon\nu_1 + \frac{\nu_1}{1+\nu_1}$$

For $\mu_1 < \mu < \mu_2$ the fixed point *disappears* and the system has relaxation-oscillations (Fig. 10). The system follows a slow relaxation towards the unstable, always convecting

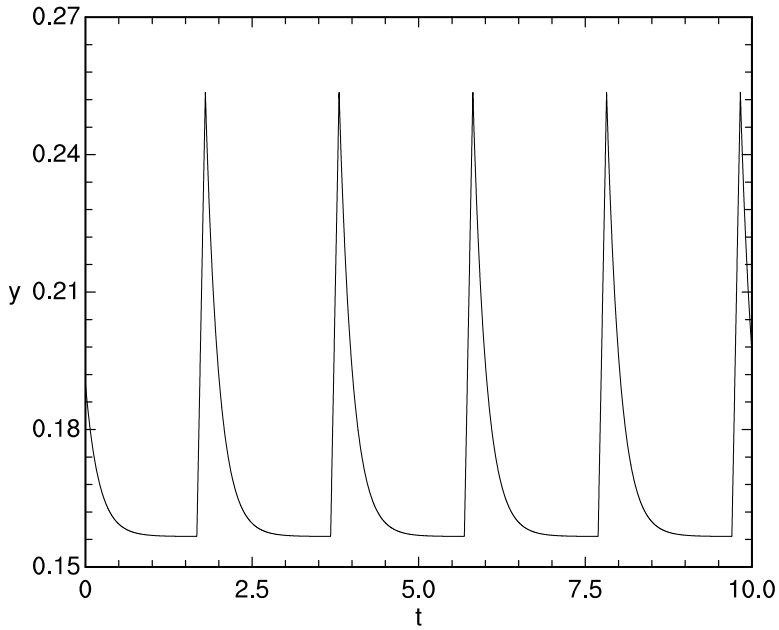

Figure 10: *Relaxation oscillations for Welander's flip-flop model.*

state, but before the steady state is actually reached the stratification becomes stable due to the strong mixing in the convecting state. As soon as a stable stratification is reached, the mixing coefficient becomes small (ν_1) and convection stops. Now the surface freshwater flux starts to increase the salinity of the upper box [this corresponds to $y \equiv \beta(S - S_0)/(\alpha(T_A - T_0))$ becoming larger], so that the density of the upper box increases strongly and the system evolves towards the stable, never-convecting state. However, before this equilibrium is reached, the stratification becomes unstable and convection will start again. The amplitude of this type of oscillations is finite and the period τ is given by

$$\tau = -\frac{\ln \delta}{\nu_2}.$$

where $\delta = \mu_2 - \mu$ and $0 < \delta \ll 1$. The period of the oscillation thus depends on the distance from the critical parameter (in this case μ_2). Note that type of oscillations differ fundamentally from the oscillations in the Howard-Malkus-Welander loop that arose as the system went through a Hopf bifurcation. Now the steady state does not become unstable, it simply ceases to exist. Another difference with the Hopf bifurcations is that there are no damped oscillations for $\mu > \mu_2 + \delta$, whereas damped oscillations exist in the case of the Hopf bifurcation.

The effect of noise

To study the effect of noise we suppose again that the salinity flux consists of an average part that is now called $\bar{\mu}$ and a random part $\mu'(t)$, where the noise has variance $< \mu'^2 > dt = \sigma^2$. This noise excites oscillations in the fixed point regimes, $\bar{\mu} < \mu_1$ and $\bar{\mu} > \mu_2$ (see Fig. 11). If there is no noise, the system goed to a stable, always convecting state (see the dashed

line in Fig. 11). If noise is added to the system, there will be fluctuations that make the fluid in the upper box light enough to give a stable stratification so that convection stops. At this moment the system goes towards the other equilibrium.

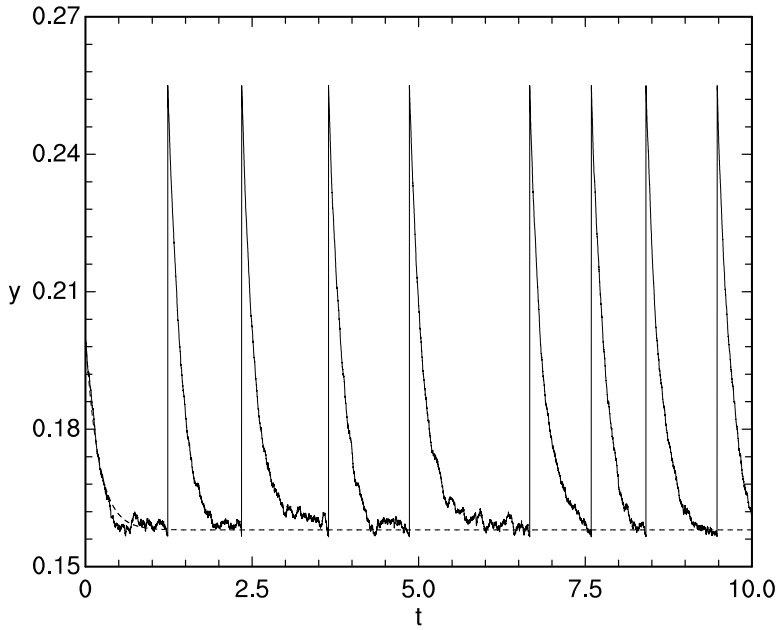

Figure 11: *The solid line gives the relaxation oscillations for Welander's flip-flop model in the stable regime $\bar{\mu} > \mu_2$ in the case with noise. The dashed line gives the solution for the same parameter values, but without noise.*

To make the computations easier, we now replace the fast relaxation to the convecting state with an instantaneous adjustment, so that the equations for the system with noise become

$$\begin{aligned} \dot{y} = \bar{\mu} + \mu' - \nu_2 y \quad &\text{if} \quad y \geq \mu_2/\nu_2 \\ y \to y_{max} \quad &\text{if} \quad y < \mu_2/\nu_2. \end{aligned}$$

where y_{max} is the value of y after the adjustment to the convecting state. Define now $\phi(y,t)dy$ as the probability that a certain realization of this experiment gives a salinity gradient between y and $y + dy$ at time t, so that $\phi(y)$ is again the probability distribution function (PDF). The average frequency of pulses is the probability flux $J(y_{max})$ through the point y_{max}. The PDF is governed by the Fokker-Planck equation (Gardiner, 1985):

$$\phi_t = J_y, \qquad J = (\nu_2 y - \bar{\mu})\phi + \sigma^2 \phi_y/2,$$

with boundary conditions

$$\phi(y < \frac{\mu_2}{\nu_2}) = 0$$

and

$$J(y = \frac{\mu_2}{\nu_2}, t) = J(y_{max}, t)$$

The first boundary condition says that y cannot take values under μ_2/ν_2, because as soon as $y < \mu_2/\nu_2$ we have $y \to y_{max}$. The second condition states the adjustment rule, which in turn corresponds to requiring that any member of the ensamble that goes through the threshold μ_2/ν_2 reappears with a value y_{max}. This is equivalent to say that the flux of states for these two values must coincide.

We can solve the steady Fokker-Planck equation using the normalization condition

$$\int_{\frac{\mu_2}{\nu_2}}^{y_{max}} dy\, \phi(y) = 1.$$

For weak noise and $\mu \approx \mu_2$ we obtain (Cessi, 1996)

$$J(y_{max}) \approx -\nu_2 \ln \frac{\sigma}{\sqrt{\nu_2}},$$

The average frequency of pulses is given by $\omega_{av} = 2\pi J(y_{max})$, and so this depends on $\sigma/\sqrt{\nu_2}$, which is the noise amplitude. The spectrum peaks at a frequency that depends on σ, but the height is independent of σ.

8 Summary

Both in the Howard-Malkus-Welander loop and in Welander's flip-flop model oscillations can be found that are either self-sustained, or that can be excited by noise. However, the characteristics of these two types of oscillations are quite different. Self-sustained oscillations in the Howard-Malkus-Welander loop occur through a Hopf bifurcation, the amplitude is proportional to the distance between the parameter and the critical value of that parameter and the period is finite.

The oscillations in Welander's flip-flop model instead occur because the steady state ceases to exist (global bifurcation). The oscillation arising through this global bifurcation are characterized by a finite amplitude even at onset and a period which depends logarithmically on the distance to the critical parameter value. Noise-induced oscillations in the Howard-Malkus-Welander loop have an amplitude that is proportional to the variance and a finite period, while noise-induced oscillations in the flip-flop model have finite amplitude and a period that depends logarithmically on the variance of the noise. This behavior is summarized in Table 1.

Notes by Taka Ito and Lianke te Raa

References

Cessi P., 1994: A simple box model of stochastically forced thermohaline flow. *J. Phys. Oceanogr.*, **2**, 1911-1920.

Cessi, P., 1996: Convective adjustment and thermohaline excitability. *J. Phys. Oceanogr.*, **26**, 481-491.

Self-sustained oscillations		
Dynamical behavior	Hopf bifurcation	Global bifurcation
Amplitude	$\propto \sqrt{\delta}$	finite
Period	finite	$\propto \ln \delta$
Example	HMW loop	Flip-flop model
Noise-induced oscillations		
Amplitude	$\propto \sigma$	finite
Period	finite	$\propto \ln \sigma$

Table 1: *Characteristics of the oscillations in the Howard-Malkus-Welander loop and in Welander's flip-flop model*

Dewar, W.K. and R.X. Huang, 1995: Fluid flow in loops driven by freshwater and heat fluxes. *J. Fluid Mech.*, **297**, 153-191.

Gardiner, C. W., 1990: Handbook of stochastic methods for physics, chemistry, and the natural sciences, 2nd ed., Springer-Verlag.

Huang, R.X. and R.L. Chou, 1994: Parameter sensitivity study of the saline circulation. *Climate Dyn.*, **9**, 391-409.

Mikolajewicz, U. and E. Maier-Reimer, 1990: Internal secular variability in an ocean general circulation model. *Climate Dyn.*, **4**, 145-156.

Tritton, D. J., 1988: Physical fluid dynamics, 2nd ed., Oxford University Press, 1988.

Welander, P., 1982: A simple heat-salt oscillator. *Dyn. Atmos. Oceans*, **6**, 233-242.

Welander, P., 1986: Thermohaline effects in the ocean circulation and related simple models. In *Large-scale transport processes in oceans and atmosphere*, J. Willebrand and D.L.T. Anderson, Eds., NATO ASI Series, Reidel, 163-200.

Lecture 6

Energy Balance Models

Raymond T. Pierrehumbert

How I learned to stop worrying, and taught myself radiative transfer...

1 Simple energy balance models

The Earth and other planets in the solar system are heated by radiation from the sun. In turn, the planets reprocess the radiation and emit energy into space, leading to a global radiative balance which plays a key role in determining the planetary climate. As a result, a detailed treatment of radiative transfer is a necessary ingredient in models of climate dynamics.

For terrestrial planets (those with a solid crust), the influx of solar radiation must balance the outflow from the surface and atmosphere. It was known to Aristotle that the source of energy on earth is the sun, but it took 20th century quantum mechanics (specifically Planck and his understanding of black body radiation) to understand how the earth loses energy back to space. Based on the notion that radiation comes in discrete bundles of energy, quanta, $\Delta E = h\nu$, where h is Planck's constant ($6.6262 \times 10^{-34} Js$) and ν is the frequency of the radiation in Hertz, Planck explained the Stefan-Boltzmann law, which states that $E = \sigma T^4$, where E is the energy output of a black body, $\sigma = 5.67 \times 10^{-8} Wm^{-2}K^{-4}$ is the Stefan-Boltzmann constant and T is the absolute temperature of the body. He expressed his result in form of the spectral energy density, $B_\nu(T)$, at frequency ν as

$$B_\nu(T) = \frac{2\pi h}{c^2} \frac{\nu^3}{\exp(h\nu/kT) - 1} [Jm^{-2}], \tag{1}$$

where $c = 2.998 \times 10^8 ms^{-1}$ is the speed of light and $k = 1.37 \times 10^{-23} JK^{-1}$ is Boltzman's thermodynamic constant. (B_ν gives the energy emitted outward per unit area and time over the frequency interval $[\nu, \nu + d\nu]$; an integration over frequency gives the black-body radiation law.) Planck's theory also explained Wien's Law which states that the frequency at which the radiation from the black body is maximal is proportional to the absolute temperature of the body:

$$\nu_{max} = \left(5.879 \times 10^{10} \frac{Hz}{K}\right) T \tag{2}$$

The simplest radiative-convective model is zero-dimensional in space: the entire planet is given one temperature, T. Such simple models are the first line of defense against the onslaught of complexity present in climate problems. We consider terrestrial planets, like the Earth and Mars, that have solid surfaces, as opposed to gaseous planets like Jupiter.

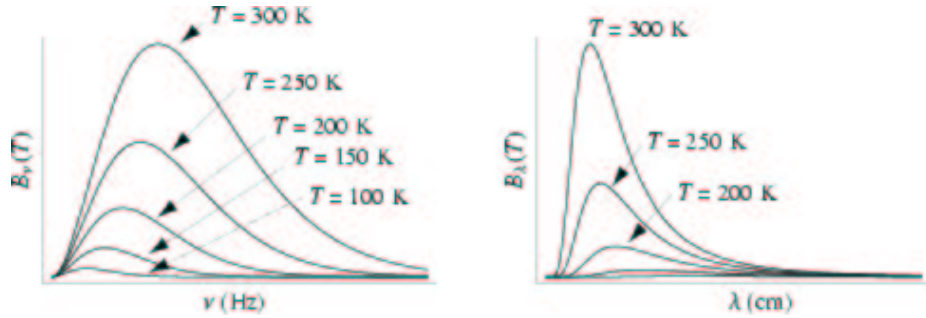

Figure 1: Emission spectra of black bodies at selected temperatures.

Standing on the shoulders of our scientific forefathers, we write a simple energy balance equation,

$$H_{sun}(1-\alpha) = \sigma T^4 \tag{3}$$

where H_{sun} is the radiation flux incident from the sun, averaged over time and over the planet's surface, α is the albedo, the fraction of the incident radiation that is reflected back into space, and hence never absorbed, and σ is the Stefan-Boltzmann constant. Thus we equate the net energy absorbed by the earth with the energy it loses to space as a black body. Given that H_{sun} is approximately 340 W/m^2, and taking $\alpha \approx 0.3$ (a crude estimate of the combined effect of sea, land, ice, clouds and so on), we find that $T = 255K$, much colder than the global average temperature we experience. Of course, we have here the grossest of models; the earth is basically treated as a metallic sphere. The more complicated models described next build on this model by incorporating the atmosphere. However, a key idea is clearly expressed in this model: the incoming radiation from the sun must be balanced by the outgoing radiation from earth.

2 Atmospheric structure

According to Wien's Law, a black body at 6000K, the temperature of the solar surface, emits the most radiation in the visible spectrum. We will assume that the atmosphere absorbs none of this incident radiation. This approximation is not too bad, the atmosphere actually absorbs less than 20% of incoming radiation. A fraction of the radiation incident on the earth, (1-α), is absorbed on the surface, causing the surface to warm. The warmed surface radiates energy back to space, primarily in the infra-red (IR) region of the spectrum, in accord with Wien's law for a black body near 300 K.

The atmosphere is, however, not transparent to IR radiation, and part of the outgoing radiation is absorbed; this upsets the energy balance, thereby increasing the surface temperature. How do we build such features into a radiative balance model? We start with the empirical data. The atmospheric radiation spectrum can be observed by looking directly upwards on a clear day with an infra-red interferometer. Spectra can also be taken from satellites, looking down, but one must then cancel out the radiation from the earth. Such spectra reveal a rough continuum interrupted by a immense number of molecular absorption lines. Fig. 2 shows the absorption spectrum for CO_2 in the IR region. Note that the

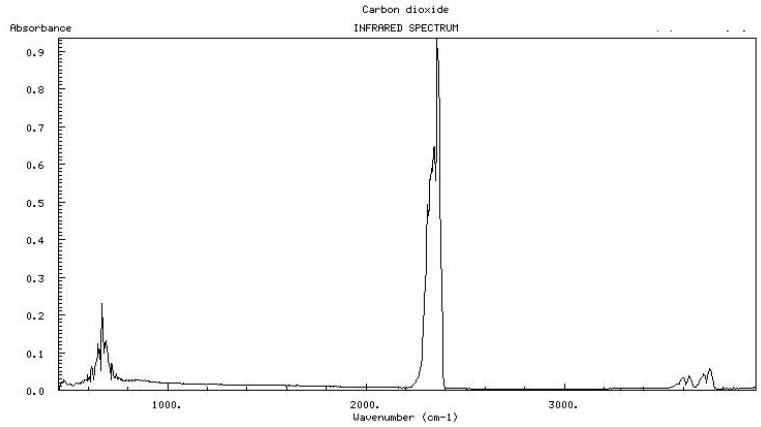

Figure 2: Absorption Spectrum of CO_2 (www.webbook.nist.gov).

wavenumber is the inverse of the wavelength measured in cm, and hence proportional to energy. It is through these spectral lines that certain molecules, such as CO_2, affect the atmospheric heat balance, and is how the greenhouse effect comes into play.

Now, according to quantum mechanics, molecules absorb light at discrete wavelengths. The so-called greenhouse gases are those that absorb in the IR, where photons are of the same energy as the translational, rotational, and bending modes of the molecules. A crude requisite to be a greenhouse molecules is to be polar and/or to support rotational or bending modes that create an oscillating dipole moment. Water and CFC's fall into the former category, while CO_2 and CH_4 satisfy the latter. An oscillating dipole moment is necessary to interact with the incoming electromagnetic radiation. Nonpolar molecules like N_2 and O_2 are transparent in the IR, but do play an indirect role in the greenhouse effect, as indicated below.

Under ideal conditions, the restriction of the absorption to narrow lines places severe limitations on the greenhouse effect: the absorption lines saturate quickly, so that the addition of more greenhouse gas does not result in a proportionate increase in absorption. In the atmosphere, however, conditions are far from ideal, and absorption lines can be broadened by molecular motion. As a result, the greenhouse effect is considerably extended by mechanisms that broaden the absorption lines. These mechanisms are:

1. Collisions with other molecules, which allow the absorber to take in a photon of smaller/larger energy, and transfer the energy difference to another molecule during the collision. This is how the greenhouse-neutral gases like N_2 and O_2 come into play. Because the collision frequency is proportional to the pressure of the gas, this broadening depends on the atmospheric pressure.

2. Doppler shifting of the absorbing molecule. If the molecule is moving towards/away from the source of radiation, it experiences a different frequency. Doppler broadening is a function of temperature (as temperature dictates the speed of the gas particles); the higher the temperature the broader the windows.

3. Ultimately, Heisenberg uncertainty puts a lower bound on the peak breadth.

The collisional effect dominates on earth. In fact, even though Mars has a pure CO_2 atmosphere, the warming effect is rather less than that of the CO_2 on earth due to our N_2 and O_2, even though the content of CO_2 on earth is far less. Collisional broadening decreases with air density, causing the absorption lines to narrow with height. At the top of our atmosphere the Doppler effect starts to dominate. However, the bulk of absorption takes place in the lower atmosphere, where the atmosphere is thickest, so that Doppler broadening can be neglected. In any case, the importance of line spectra in determining atmospheric absorption has the unappealing consequence that one needs a sophisticated treatment of radiative transfer in order to construct properly a model of the climatic energy balance.

To understand radiative transfer, we need more information about the atmosphere's vertical temperature structure. Roughly speaking the atmosphere is composed of the "troposphere" and "stratosphere." There is also a relatively shallow boundary layer just above the ground, which we will ignore. Inside the troposphere, the temperature decreases with height. The decline of temperature halts at a level referred to as the "tropopause," where the temperature is about $200K$, and then in the stratosphere above it, the temperature begins to increase. Some observed vertical temperature profiles for a location in the tropics are shown in figure 3. Crudely speaking, the reason why the globally averaged temperature is higher than the $255K$ expected from the simple energy balance argument above is that the effective "photosphere" of the Earth's emission into space is higher in the atmosphere than ground level. The earth must emit energy as a black body at $255K$ to maintain radiative balance with the sun. The surface, however, can be warmer as long as the radiation it loses is trapped by the colder atmosphere, which radiates at $255K$.

But why does temperature decline with height? The simplest argument, ignoring details such as the effect of water vapour, leads to what is called the "dry adiabat:" As a parcel of air rises off the ground, it expands as the pressure decreases. The gas does work as it expands, loses energy, and hence cools. We invoke the ideal gas approximation, which is quite accurate for the earth's atmosphere. On Venus, or in the protoclimate of Mars, however, increased pressures cause significant deviations from the ideal gas law. The potential temperature θ, a measure of the entropy of a gas, is defined by

$$\theta = T\left(\frac{p}{p_*}\right)^{-R/C_p}, \tag{4}$$

where p is the pressure, p_* some reference pressure (say 1 atmosphere), R the ideal gas constant, and C_p, the heat capacity of the gas at constant pressure. Quantum theory tells us that R/C_p is approximately $2/7$ for a diatomic gas, and this approximation works well for our atmosphere.

If we assume constant entropy (constant θ), a "dry" atmosphere's temperature should be a function of pressure according to

$$T = \theta\left(\frac{p}{p_*}\right)^{R/C_p}. \tag{5}$$

Constant entropy is a good assumption, as the timescale on which fluid motions mix up the atmosphere, homogenizing scalar invariants such as entropy, is shorter than the timescale on which radiation warms the atmosphere.

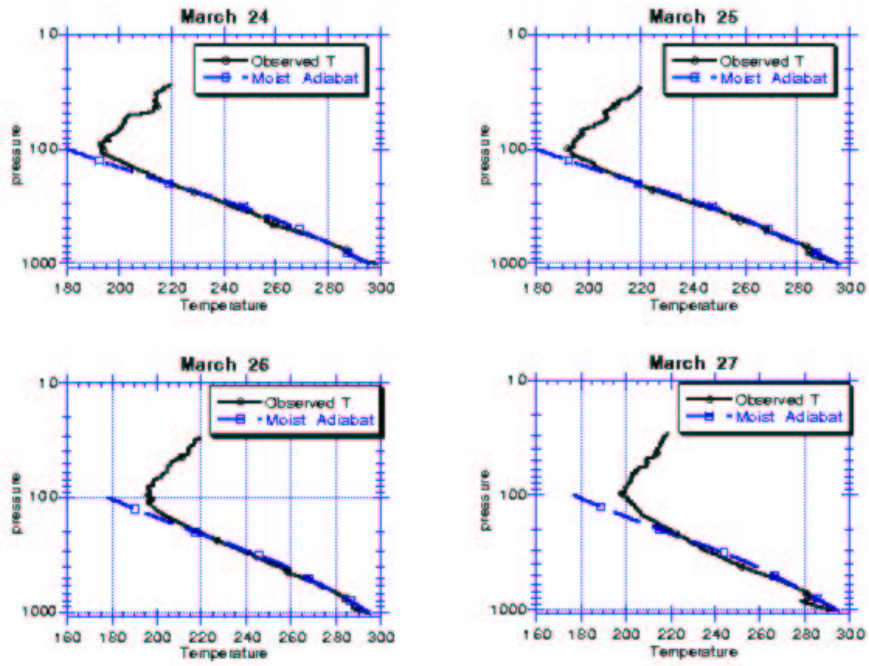

Figure 3: Air temperatures as function of altitude.

Equation (5) is the dry adiabat. The temperature of our atmosphere, however, does not fall as quickly as this relation predicts. The error stems from the fact that we have neglected the effect of water vapor, which can have a significant effect as a result of the release of latent heat. As the temperature cools with height, H_2O evaporated on the surface condenses, heating up the air and reducing the temperature gradient. Just 1 kg of water vapor releases 2.5 megaJoules when it condenses in the upper atmosphere. The moist adiabat is calculated by assuming that the air remains saturated with water vapour all the way up, that is, that there is no entrainment of dry air and thus the relative humidity is held constant at 100% once condensation starts. This gives a remarkably good fit for air in the tropics. This is shown in Fig. 3. Note we are only fitting the temperature in the troposphere. In the stratosphere absorption of solar radiation dominates, and the temperature deviates strongly from the moist adiabat.

The fit is quite remarkable in light of the fact that, outside the inter-tropical convergence zone (ITCZ) near the equator, the air in the tropics above the surface boundary layer is quite dry. The relative humidity is just 5-10%, "as dry as a desert." (See Fig. 4.) The Hadley circulation in the tropics explains why this dry air fits the moist adiabat, but we leave this until lecture 7. The mid latitudes do not follow the moist adiabat, but the temperature still falls with height up until the stratosphere.

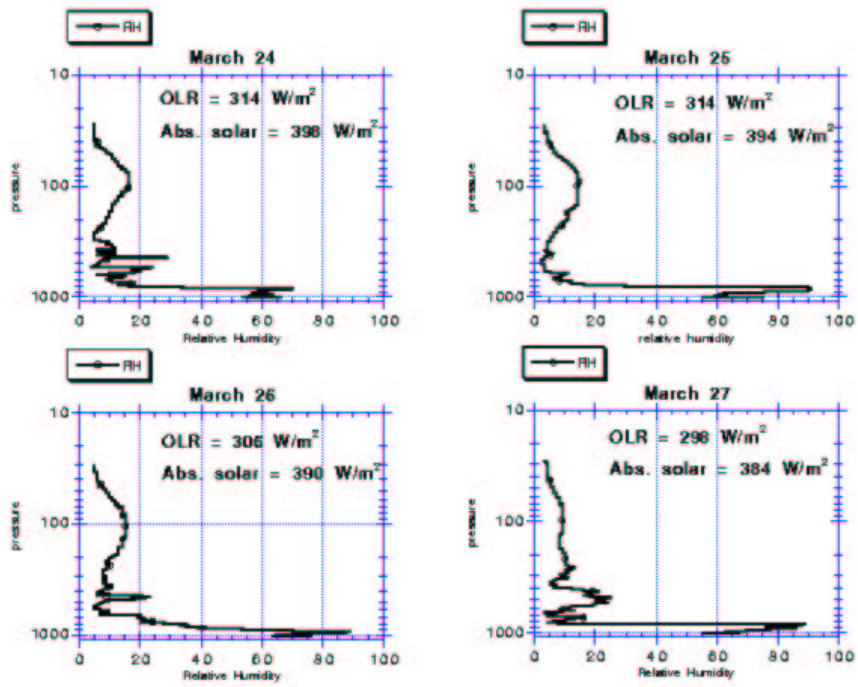

Figure 4: Relative humidity as a function of altitude.

3 The OLR curve

We now have the machinery needed to explain the greenhouse effect, which is most succinctly described in terms of the "OLR curve" – the dependence of the Outgoing Long-wave Radiation on surface temperature. This curve is also the key ingredient in a variety of toy climate models that will be described later.

In most places in the world the surface temperature is approxmately the same as the surface air temperature. Exceptions are deserts, where the surface can be 10 to 15 degrees warmer,and ice where the surface can be tens of degrees colder than the overlying air a few meters up. In simple models it is usually acceptable to equate surface temperature with surface air temperature.

Given the surface temperature, the thermal structure of the atmosphere above roughly follows the moist adiabat up to the tropopause. The stratosphere is ignored, as its overall effect is unimportant. The crucial step in constructing the climatic energy balance is then to determine the radiative transfer through the troposphere of the infra-red radiation leaving the surface. That transfer ultimately determines the total outgoing long-wave radiation (OLR), which must balance the incident solar energy flux. All told, this amounts to a complicated radiative transfer computation that approximates the collective effect of all the absorption and emission lines of every important molecule in the atmosphere. The computation involves thousands of lines of coding and a multitude of clever approximations

to meet the computational efficiency requirements dictated by climate modeling.

The result of the calculations is the total OLR emitted by the earth as a function of the surface temperature; sample computations of this function are shown in figure 5. The key to understanding global warming is predicting how the addition of CO_2 and other greenhouse gases change the OLR, which in turn force a change in surface temperature in order to bring the outgoing energy into balance with the solar heating. The trickiest part is predicting how the relative humidity, RH, changes as the temperature increases. Unlike CO_2, the concentration of water vapor is highly dependent on temperature. Manabe proposed that the relative humidity remains constant as the temperature increases. This assumption is widely employed in conceptual climate models, but has never really been justified on the basis of first-principals physical arguments.

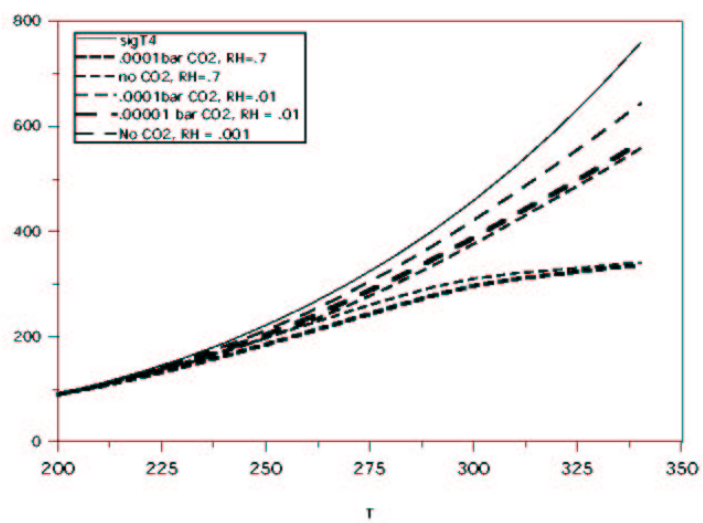

Figure 5: OLR as a function of surface temperature.

Fig. 5 shows the OLR as a function of surface temperature, for calculations based on different compositions of greenhouse gases and relative humidity. Recall that the OLR must be $340W/m^2$ to maintain radiative balance with the sun. To find the steady state surface temperature from the diagram, we draw a horizontal line at $340W/m^2$, and read off the surface temperature from where it intersects the OLR curve. The curves that do not reach $340W/m^2$ have no steady state and reveal a runaway greenhouse effect. Given an initially cool surface temperature, the OLR is below the incoming flux value, so the planet warms. The OLR thereby increases, and provided the OLR continues to increase with surface temperature, an equilibrium arrangement will eventually be struck. However, for the curves that flatten out, the OLR can never reach the input, so a runaway greenhouse ensues, at least if the physical input to the computation remains the same.

The specific mechanism for the runaway can be attributed largely to the effect of water vapour. Water vapour is a powerful greenhouse gas, there is plenty of it on earth, and the saturation pressure of water in air increases exponentially with temperature. The positive feedback of the runaway follows the route:

higher temperature $\Rightarrow$ more water vapor $\Rightarrow$ more global warming $\Rightarrow$ higher temperature

Once the feedback starts, the temperature keeps increasing without bound, and the OLR can never rise high enough to balance the incoming radiation. In such a situation, the energy continues to build up, leading to the melting of the ice caps, the evaporation of the oceans, and the eventual dissociation of H_2O. At this juncture, the hydrogen would escape into space, leaving an atmosphere much like that of Venus. Fortunately, the earth's atmosphere is much drier than that necessary for this doomsday scenario, at least for now.

4 A simple model of the greenhouse effect

According to the preceding arguments, the following phenomena are crucial to greenhouse effect on earth:

1. Decreasing atmospheric temperature with altitude.
2. Decreasing atmospheric pressure with altitude. This affects both the amount of greenhouse gasses and the peak broadening, and has its basis in the hydrostatic balance of the atmosphere, $dp/dz \approx -\rho g < 0$.
3. Presence of greenhouse gases in atmosphere, where the greenhouse gases are defined as the components of the atmosphere having absorption bands in the infra-red.

In this section, we build a simple model that illustrates the construction of the OLR, together with an implicit greenhouse effect.

The model consists of a plane-parallel atmosphere in which the pressure, $p(z)$, and temperature, $T(z)$, fall with height, z, from their values at ground level, p_0 and T_0 respectively. Since we are interested in only demonstrating how the ingredients add together to keep the earth surface warm, we will make some pretty crude idealizations. For one, the temperature and pressure fields will be specified by the piece-wise linear functions:

$$T(z) = T_0 \left(1 - \frac{z}{H}\right) \vartheta(H - z) \qquad p(z) = p_0 \left(1 - \frac{z}{H}\right) \vartheta(H - z), \tag{6}$$

where $\vartheta(x)$ is the step function; see figure 6.

The atmosphere is assumed to consist mainly of an inert gas except for small fraction of a greenhouse gas with a single absorption line at the frequency corresponding to maximum emission for a black body at temperature T_0 (see Wien's law in (2)).

$$\nu^* = \left(5.879 \times 10^{10} \frac{Hz}{K}\right) T_0. \tag{7}$$

The line is, however, broadened to a degree determined by the pressure. Let the width of the line be given by

$$\Delta\nu(z) = 2\delta_{\nu^*} p(z). \tag{8}$$

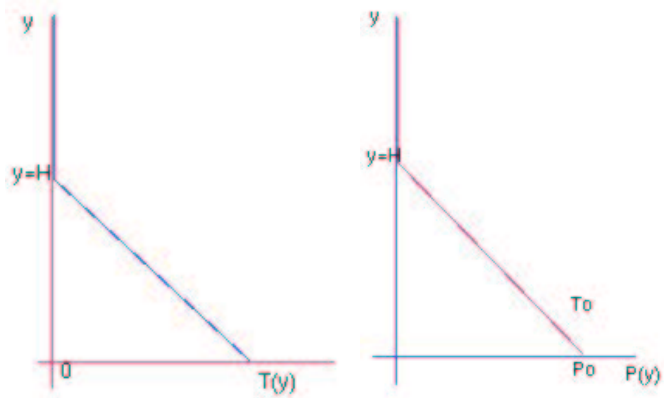

Figure 6: Temperature and pressure of a piece-wise linear toy model.

Thus the absorption depends on both frequency and height. We choose the simple model absorption coefficient shown in figure 7, in which constant absorption occurs within the broadened spectral line:

$$\epsilon_\nu(z) = \epsilon_0 \qquad \text{if } \nu^* - \delta_{\nu^*}p(z) < \nu < \nu^* + \delta_{\nu^*}p(z) \tag{9}$$

$$= 0 \qquad \text{otherwise.} \tag{10}$$

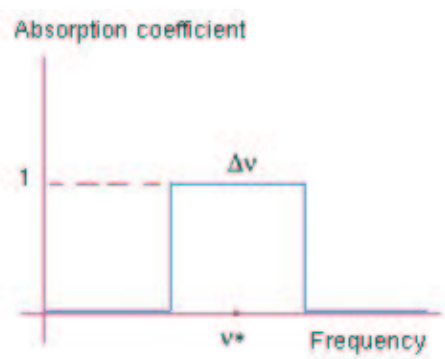

Figure 7: Model absorption coefficient for greenhouse gas.

The transfer of radiation is described by the intensity, $I_\nu(z)$, the upward energy flux density in the frequency interval $[\nu, \nu + d\nu]$, by a simple energy balance between layers, this satisfies

$$\frac{dI_\nu}{dz} = \frac{\epsilon_\nu(z)}{2} B_\nu\left(T(z)\right) - \epsilon_\nu(z) I_\nu(z). \tag{11}$$

That is, the change of intensity equals emission minus absorption, with the boundary condition,

$$I_\nu(0) = B_\nu(T_0), \tag{12}$$

which assures that the intensity at the base of the atmosphere is given by the emission from the ground.

Outside the greenhouse window on the ground, $[\nu^* - \Delta\nu(0), \nu^* + \Delta\nu(0)]$, the radiation is never affected by the greenhouse gas:

$$\frac{dI_\nu}{dz} = 0 \qquad \text{for } |\nu - \nu^*| > \Delta\nu, \tag{13}$$

and so $I_\nu(H) = B_\nu(T_0)$.

If the frequency lies inside the ground-level greenhouse window, radiation can be absorbed at certain heights. The decline in pressure with height narrows the window of absorbtion. For radiation of frequency ν we denote the height H_ν to be the point at which absorbtion of this frequency ceases. For our simplified model,

$$H_\nu = \left[1 - \frac{|\nu - \nu^*|}{\delta_{\nu^*} p_0}\right] H. \tag{14}$$

The governing equations for radiation flux then become

$$\begin{aligned} \frac{dI_\nu}{dz} &= -\epsilon_0 I_\nu + \frac{h\epsilon_0}{c^2}\frac{\nu^3}{\exp[h\nu/kT(z)] - 1}, \qquad \text{for } 0 < z < H_\nu \\ \frac{dI_\nu}{dz} &= 0 \qquad \text{for } H_\nu < z < H, \end{aligned} \tag{15}$$

with $I_\nu(z)$ continuous at $z = H_\nu$. Since $T(z)$ is an decreasing function of temperature, and $\exp[h\nu/kT(z)] > \exp[h\nu/kT(0)] \approx 16 \gg 1$, we may simplify still further:

$$\begin{aligned} \frac{dI_\nu}{dz} &= -\epsilon_0 I_\nu + \frac{h\epsilon_0}{c^2}\nu^3 \exp\left(-\frac{\chi_\nu}{1 - z/H}\right) \qquad \text{for } 0 < z < H_\nu \\ \frac{dI_\nu}{dz} &= 0 \qquad \text{for } H_\nu < z < H, \end{aligned} \tag{16}$$

where

$$\chi_\nu = \frac{h\nu}{kT_0}. \tag{17}$$

The radiation leaving the atmosphere, $I_\nu(H) = I_\nu(H_\nu)$, and is therefore given by the integral,

$$I_\nu(H) = e^{-\epsilon_0 H_\nu} B_\nu(T_0) + \frac{\epsilon_0 h\nu^3}{c^2}\int_0^{H_\nu} \exp\left(z - \epsilon_0 H_\nu - \frac{H\chi_\nu}{H - z}\right) dz). \tag{18}$$

The first term in this expression is the residual attenuated radiation from the earth's surface; the second term is the net radiation from the atmosphere, also suitably attenuated. Fig. 8 shows a representative spectrum as given by (18).

The expression (18) can be integrated over all frequencies to yield an OLR curve as a function of surface temperature; see figure 9. It can be seen that the OLR for the greenhouse system is always below the OLR curve for the black body, and so the surface temperature is always higher. The parameter values used are merely representative, and chosen chiefly to bring out the difference between the black-body law and our toy model. Real models of greenhouse effect incorporate absorption spectrum of all the greenhouse gases present in the atmosphere and use realistic stratifications for the temperature and pressure.

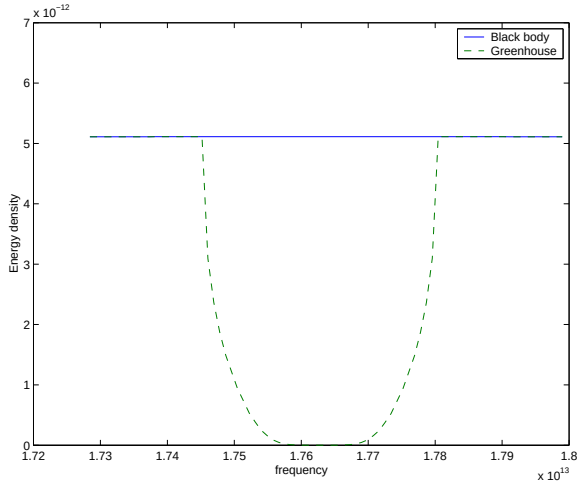

Figure 8: Intensity at the top of the atmosphere for the toy model.

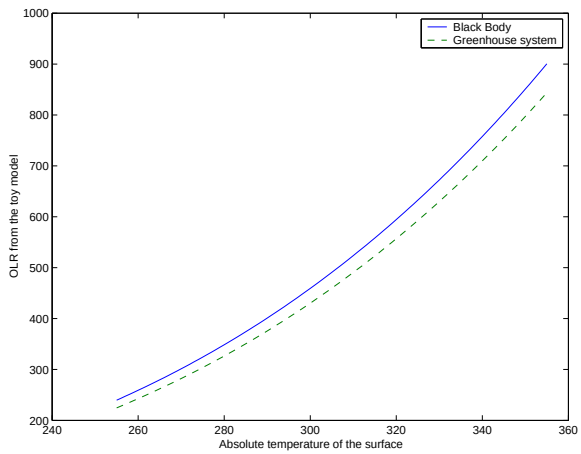

Figure 9: OLR curve for the toy model.

5 Radiative balance models

In general, the OLR curve as a function of surface temperature is the main ingredient in a radiative balance model. To compute this curve we follow the recipe outlined above, which requires as input the structure and composition of the atmosphere. With the balance of incoming and outgoing radiation, we then may infer surface temperatures. Often the procedure can be simplified by tabulating the OLR curve and fitting both its shape, the dependence on surface temperature, together with the dependence upon other significant variables, such as CO_2 concentration. One can then make relatively fast global warming calculations with the OLR curve and build conceptual climate models.

For example, consider CO_2 on earth. Once all the calculations are done, it turns out

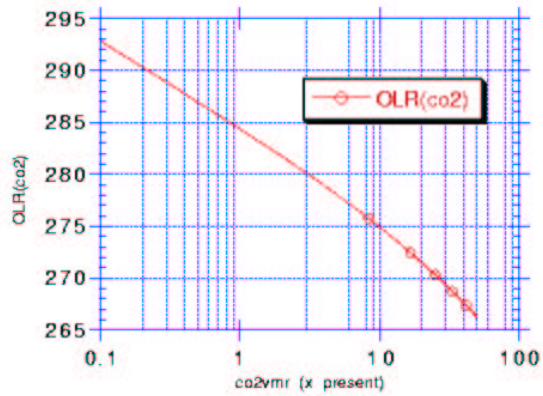

Figure 10: Effect of carbon dioxide concentration on OLR.

that the OLR response to CO_2 is roughly logarithmic, as shown in Fig. 10. Hence,

$$OLR(T, \ln CO_2) \approx OLR(T, \ln CO_{2*}) + D(T) \ln \left(\frac{CO_2}{CO_{2*}} \right), \tag{19}$$

where CO_{2*} is some reference value and the linear coefficient $D(T)$ may be a function of T. Here we see how important it is that absorption is limited to narrow bands – without saturation, the absorption would grow linearly with concentration, generating a much more pronounced sensitivity of the OLR to CO_2. The OLR exhibits the same kind of logarithmic dependence on concentration for most greenhouse gases.

From figure 10, we see that doubling the CO_2 concentration lowers the OLR by 4 W/m^2, assuming that the total water vapour content stays constant. In order to balance the incoming solar radiation, the surface temperature must then increase in order to raise the OLR. Based on the black-body curve, this amounts to an increase of about half a degree in surface temperature. If, however, the relative humidity (RH) remains the constant, more water vapour will enter the atmosphere, and the rise in temperature becomes as large as 2 $^\circ$ C.

Although, the effect of CO_2 on the OLR is significant, the effects of water vapour and clouds are even greater (figure 11). For example, doubling the RH from 10 to 20% causes a 10 W/m^2 shift in the OLR, equivalent to nearly tripling the CO_2 in the atmosphere. Clouds, on the other hand, constitute a very delicate climate variable. By adding the condensed substance, in this case water, the opportunities for molecular collisions are vastly increased, thereby leading to a significant broadening of the absorption lines. In this regard, clouds act like greenhouse gases and one expects a cloudy climate to have a lower OLR. The height and water mass of a cloud largely determine its radiative effect, because its temperature is given by the moist adiabat. Idealized computations suggest that the greenhouse warming effect of clouds is minimal at the surface, but at 10 km, they can lower the OLR by 150 W/m^2.

Clouds, however, also reflect the incoming short-wave radiation back into space, thereby increasing the albedo of the planet. Calculating cloud albedo is nontrivial exercise. For

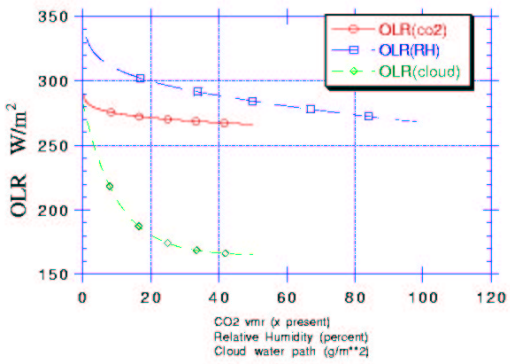

Figure 11: Relative effect of carbon dioxide, water vapor and clouds on OLR.

instance. the albedo dependends strongly on the size of the water droplets composing the cloud, so there is no simple correlation with the total mass of water. The average size of a cloud droplet is 10 micrometers. Changing from 8 to 12 micrometers, however, can result in albedo changes that are equivalent to a 20% reduction of the OLR.

Overall, clouds near the surface have a net cooling effect, while high clouds can be warming. Experimental evidence suggests that the net effect of clouds in the tropics is near zero, with a 100 W/m^2 jump in the OLR caused by increased absorption almost completely compensated by cloud albedo. In the extratropics (30° latitude and up) the net result is cooling, effectively lowering the OLR by approximately 15 W/m^2.

That the net effect of clouds must be computed from the close subtraction of two relatively large quantities makes the problem prone to severe error. The matter is complicated still further by the fact that cloud formation is also not particularly well understood: Nucleation sites are needed to begin condensation, creating a dependence on the concentration of airborne particles, such as dust and sulfate aerosols. (The dependence on sulfate aerosols is revealed in the higher rate of cloud cover over ship tracks, where aerosol pollutants are introduced to the atmosphere!) In the absence of nucleation centers, water vapor can become supersaturated in the atmosphere without forming any clouds. Suffice to say that clouds are the main uncertainty in climate modelling, from the toy system to the GCM. We need a theory of clouds if we are to make more progress in answering climate questions.

In summary, as the intensity of the OLR must balance incoming solar radiation, at least in the steady state climate, any change in the environment that lowers or raises the OLR will eventually manifest itself as a change in the surface temperature. The relationship between OLR and surface temperature is roughly linear over small variations, as shown in Fig. 12. All one needs therefore do is to calculate the linear coefficients and incorporate this into a model, as we do next.

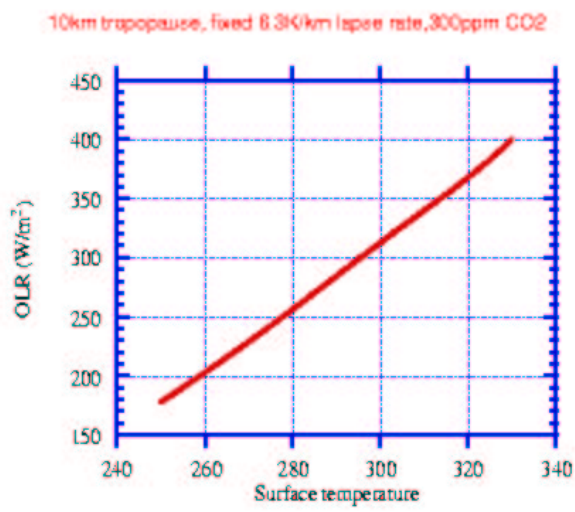

Figure 12: Dependence of OLR on Temperature

6 Ice albedo feedback

We are now ready to construct toy models; we illustrate with a simple model of the ice-albedo feedback effect. The albedo is quite complicated: Deserts have large albedos compared to forests and oceans, and fresh ice and snow is more reflective than older ice, on which dust and other debris may have collected. The average albedo of land and sea ice $\alpha_{ice} = 0.7$, whilst the average ice-free land/sea albedo $\alpha_0 = 0.1$. We consider just the average albedo of the entire surface of the Earth, $\alpha(T)$, as a function of the average surface temperature, T. The reflected light lies in the visible and so escapes immediately into space; the absorbed radiation is converted into the infra-red and percolates up through the atmosphere eventually providing the OLR. Thus the energy balance is

$$S_0 = \alpha(T)S_0 + OLR, \qquad \text{or} \qquad S(T) \equiv S_o[1 - \alpha(T)] = OLR, \tag{20}$$

where S_0 is the annual average incident radiation.

Let T_0 be the annual mean temperature necessary to sustain permafrost over the whole earth. Such a "snowball earth" may have existed in the neoprotozoic – about 600 million years ago (see lecture 10). We set T_1 to be the average temperature of a completely ice-free earth, as it was during the Eocene, about 55 million years ago, when lemurs roamed Spitzbergen and Crocodiles cavorted in the Hudson bay (as also discussed in lecture 10). We then make up a "plausible" function $f(T)$ to connect $\alpha(T)$ between its values for the

permafrost and temperate earths:

$$\begin{aligned} \alpha(T) &= \alpha_{ice}, \quad T < T_0, && (21) \\ &= f(T), \quad T_0 < T < T_1 && (22) \\ &= \alpha_0, \quad T > T_0 && (23) \end{aligned}$$

The interpolating function $f(T)$ should have the features that it decrease sharply for T just above T_0, but more slowly for T near T_1. This is because near T_0, the albedo declines when the equatorial region becomes ice free; this region has both the largest area, per degree latitude, and experiences the strongest, annual average incident radiation. But approaching T_1, a slowly increasing albedo reflects the shrinking polar ice caps that have least area and weakest annual radiation.

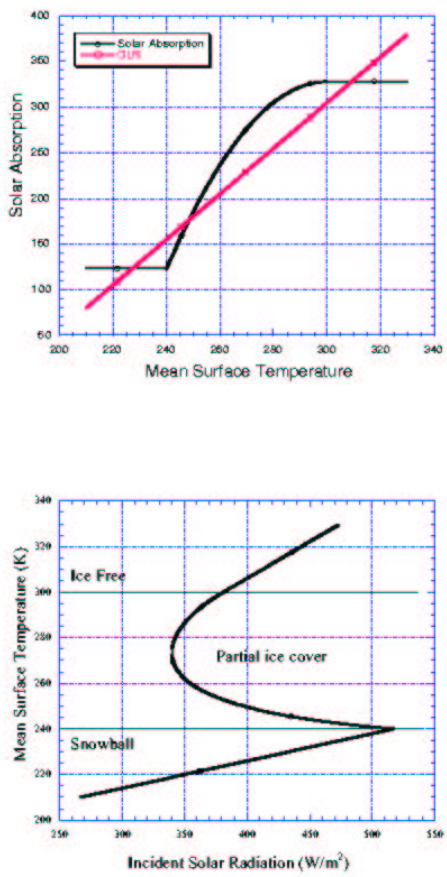

Figure 13: Top panel: absorbed solar radiation and the OLR. Lower panel: Bifurcation diagram.

In figure 13 we plot the OLR curve, which we approximate to be a straight line, and the net absorbed solar radiation $S_o(T)$. In this particular example, $T_o = 240K$, $T_1 = 300K$,

and the greenhouse gas content gives an OLR intersecting the net incoming radiation curve at three points. This reveals three possible steady states. At the far left, we have a stable snowball earth, while at the far right we have the ice-free eocene climate. If we shift the OLR over to the left by, for example, decreasing the CO_2, the warmer steady state becomes a world like today, with a small polar ice cap. In the middle we have steady state characterized by large ice sheets; this state is an unstable equilibrium, as indicated as follows.

Away from the steady states the earth is not in balance with the incoming radiation. If we let M be the "thermal mass" of the earth, a fuzzy constant meant to characterize earth's heat capacity and the energy needed to melt ice sheets, and so on, then

$$M\frac{dT}{dt} = -(A + BT) + S_0[1 - \alpha(T)], \tag{24}$$

where the first term is the linearization of the OLR curve, and the latter is the net incident radiation. If the planet were placed immediately to the right of the middle steady state, which would correspond to adding a small warm anomaly, $\mathrm{d}T/\mathrm{dt}$ becomes positive, pushing the earth toward the warmer state. Conversely, if the planet were pushed leftward by a small cold deviation, the climate becomes pushed all the way to a snow ball. This is the mechanism of the large ice-sheet instability.

If we allow the incident solar flux to vary in some way, we can find transitions between the other two, stable equilibria; this is the content of the bifurcation diagram in Fig. 13. On the $x-$axis we plot the solar radiation constant, S_0, and on the $y-$axis, the global mean surface temperature, T. The curve plots all possible equilibria. The upper curve above 270 K represents the stable warm climate equilibrium. The curve below it, stopping at 240 K, shows the unstable, partial ice cover equilibria. Below 240 K, we have the snowball earth. We see that if the output of the sun falls below 340 W/m^2, the earth can fall from a stable warm climate into a snowball. Similarly, at 520 W/m^2, a stable snowball climate evaporates into a simmering tropical earth.

Figure 13 plots the equilibria against the incoming flux and so models the effect of secular variations in the solar constant, which could be brought about by, for example, the evolution of the sun. One could rather vary the greenhouse gas content of the atmosphere, instead of the solar flux, and obtain a similar bifurcation diagram. As increasing the CO_2 is approximately equivalent to raising the sun's radiation, the $x-$axis could equally well read $\ln CO_2$.

Finally, we close this lecture with a few remarks on some of the missing pieces in the climate puzzle. We have already mentioned that clouds are one of the main unknown ingredients to models. But we have also neglected vegetation, which can have a significant effect on, amongst other properties, the surface albedo. Unlike tundra, trees can offset the reflective effect of snow cover. Also, the thermal stratification of the atmosphere, a crucial part of the recipe for constructing the OLR, has been tacitly assumed to be given by the moist adiabat. This is certainly true for the tropics, but is not an accurate approximation for the mid-latitude atmosphere. Here, a significant role is played by fluid motion in determining the mean stratification (in particular, transport by turbulent eddies may play a key role), and there could be some, as yet unexplored, interesting interactions between the mid-latitude greenhouse effect and the atmospheric fluid dynamics.

Notes by Ed Gerber and Shreyas Mandre

Lecture 7

Basic Principles of Climate

Raymond T. Pierrehumbert

One-dimensional climate models

Introduction

In zero-dimensional models, variations of temperature with latitude cannot be taken into account. This is potentially problematic because there is a significant pole-equator temperature difference, and because the surface properties of the pole can differ remarkably from those of the equator (due largely to ice). As a next step up in sophistication for simple climate models, we therefore turn to one-dimensional models, in which the temperature $T(\phi, t)$ depends both on latitude ϕ and time t.

An important first ingredient is the input solar heating: The amount of solar radiation per unit area that is received at the top of the atmosphere varies with latitude and with the time of the year. This is given by the solar constant S_0 (which is about $1370 Wm^{-2}$) times a flux factor $F(\phi, t)$ that gives the dependence on latitude and time, which is given in Fig. 1. There are two competing effects that determine this flux factor. First, the inclination of the surface relative to the incoming radiation gives greater weight to the regions where the sun is overhead (the tropics). This is offset by the second effect, that of the increase of the length of the day, which promotes solar heating at the poles in summer. For the present-day Earth's inclination, the effect of the day's length exceeds the inclination effect and as shown in figure 1, the polar region in the summer hemisphere receives more radiation than the equatorial region. Were it not for moderating influence of the ice, atmosphere and ocean, the hottest regions would therefore migrate from pole to pole through the year, and Antarctica would have the warmest summer on Earth.

Given that the climate moderates the annual variation of solar heating, the flux factor $F(\phi, t)$ is not the most useful characterization of the energy input for a watery planet like Earth. Instead, we turn to the annual average, shown in Fig. 2, which has a minimum at the poles and a maximum at the equator, and varies by a factor of about two. Also shown is the annual average for an Earth with zero obliquity, for which the variation between pole and equator is much larger (because the day's length is constant and there is only the inclination effect).

Based on the annual average, one expects that, if there were no latitudinal heat transport, the atmosphere would be in local radiative equilibrium at every position and the

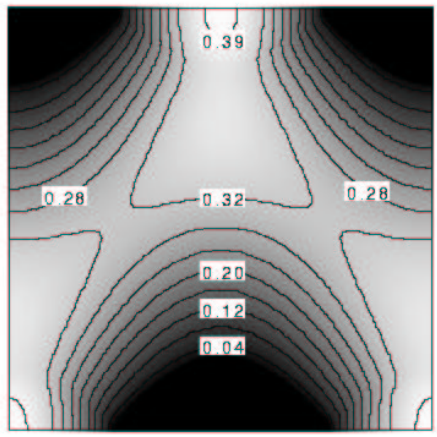

Figure 1: *Flux factor $F(\phi, t)$ as a function of time on the horizontal axis and latitude on the vertical axis. the time range is from January to December, the latitude axis from $90°S$ to $90°N$.*

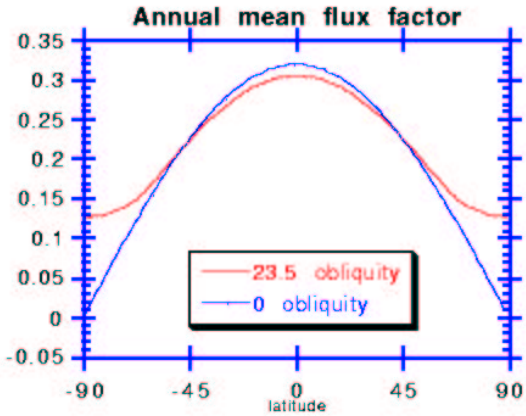

Figure 2: *Annual mean flux factor as a function of latitude.*

temperature difference between equator and pole would be very large. Because such a severe temperature drop is not observed, there must be a latitudinal transport of heat that reduces the variation. Satellite imagery of the actual energy budget at the top of the atmosphere (solar heating minus OLR) is shown in Fig. 3. The radiative imbalance is about 75 to 100 Wm^{-2} in the equatorial region, and about -100 to -150 Wm^{-2} at the poles. Also noticeable in the figure are the outlines of the continents (particularly South America) and the relatively light Sahara desert. The latter is a significant contributor to OLR due to the high cooling effect of sand, the dry atmosphere and because there are very few clouds. The

ice cover of Antarctica is also visible to the lower right.

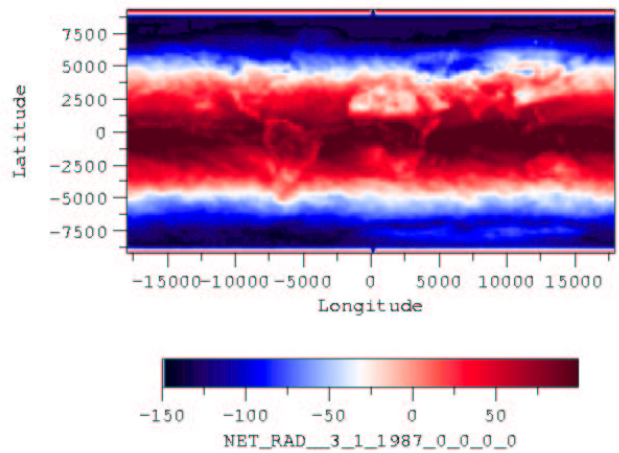

Figure 3: *Net energy budget in Wm^{-2} at the top of the atmosphere.*

The latitudinal heat transport occurs partly through the atmosphere and partly through the oceans. At $45°N$, the atmosphere is responsible for most of the heat transport, except locally in the North Atlantic (in the Gulf Stream region). A large amount of the atmospheric heat transport occurs through latent heat transport, as water evaporates in the tropical region and precipitates at higher latitudes. In the oceans, the heat transport is accomplished through both the wind-driven and thermohaline circulation.

The latitudinal distribution of the energy budget at the top of the atmosphere is compared with the sea surface temperature (SST) in Fig. 4. The temperature is relatively constant between about $20°S$ and $20°N$. A simple explanation for this flat temperature profile will be given later with the help of a conceptual model of tropical temperatures.

In addition to temperature, there is also a significant variation with latitude in the moisture content of the atmosphere; maps of monthly precipitation and specific humidity are shown in Figs. 5 and 6. Areas of large precipitation are found near the equator over the Intertropical Convergence Zone (the "ITCZ"), over the warm pool in the western Pacific ocean (labelled W) and above the storm tracks of the Atlantic and Pacific (labelled ST). There is also a significant amount over the rainforests of the Amazon basin and the Congo.

The specific humidity is high in a band between $20°S$ and the equator (Fig. 6) and there is a sharp gradient in relative humidity over the central Pacific. This latitudinal distribution of precipitation and specific humidity does not result from temperature variations, but can be understood from the mean circulation pattern of the atmosphere in the tropics, which is part of the low-latitude "Hadley Cell": Directly above the surface, air converges to the equator, where it rises in a relatively narrow band (the ITCZ), then spreads out again to the north and south at higher altitudes to create a compensating subsidence flow of a much larger scale. Evaporation seeds the surface flow with water vapour which condenses over the ITCZ as the rising air cools, to produce a large amount of rainfall over that area.

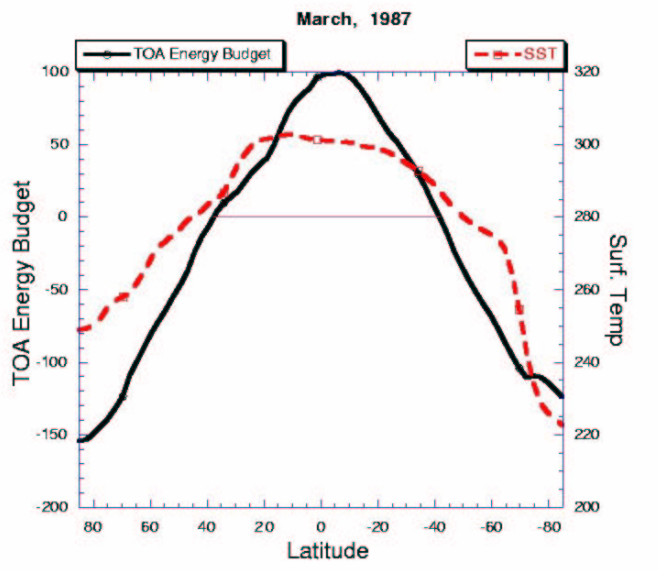

Figure 4: *Net energy budget at the top of the atmosphere (TOA) and surface temperature averaged over March 1987 as a fuction of latitude.*

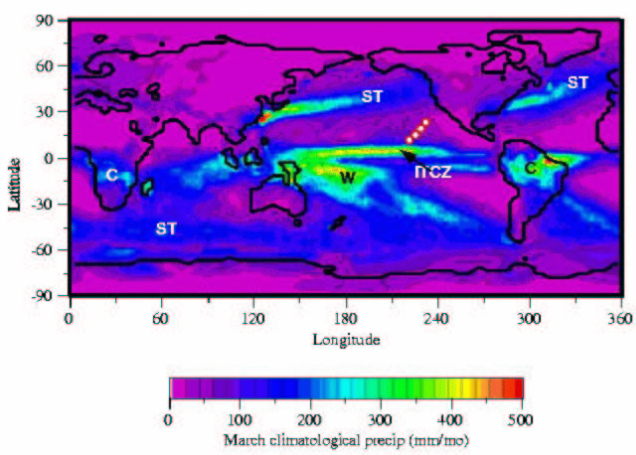

Figure 5: *Climatological precipitation in March in mm/month.*

The subsiding flow is much drier, and as it warms with descent, the relative humidity becomes even lower. Specific humidity is conserved as air subsides, and the air in the subsiding branch is dry because it is brought down from a cold, dry place. This action has the potential to create very strong humidity variations with latitude, variations that are, in fact, much stronger than those which are observed. The subsiding flow is wetter than this simple picture predicts because of latitudinal transport of moisture by turbulent

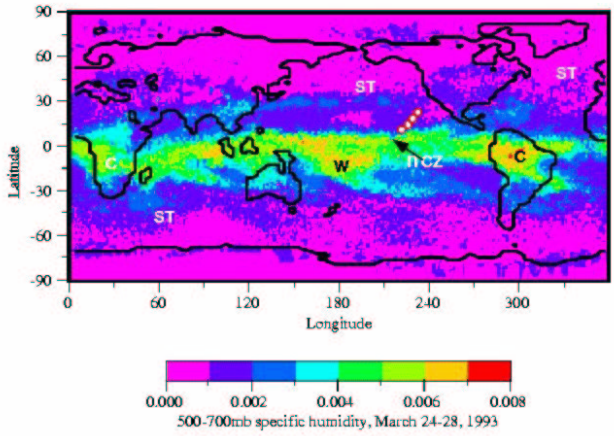

Figure 6: *Specific humidity of the 500-700 mb level, averaged over the period of March 24-28, 1993.*

eddies (the precise origin of these fluid motions is not completely understood, but possible candidates are tropical waves, baroclinic instability, westerly wind bursts and the "Madden-Julian Oscillation"). Although the subsidence region is still dry compared to the ITCZ, the increase in relative humidity due to the latitudinal eddy transport is important because of the logarithmic dependence of OLR on specific humidity. Dry as the subtropics are, it still matters precisely *how dry* they are.

The circulation of the Hadley cell is an essential element of the meridional heat transport. Between $20°S$ and $20°N$ the coriolis force is relatively weak and the circulation is dominated by the Hadley cell. In fact, the structure of the Hadley cell is more complicated than suggested above: The rising motions typically occur in the summer hemisphere, and the downward motions in the winter one. As a result, at a particular time, the circulation in the meridional-vertical plane is quite asymmetric, with rising air in one hemisphere and subsidence in the other. Moreover, during the year, the ITCZ moves only over a relatively short distance, whereas the subsidence region moves over a much greater distance. This makes the annually averaged Hadley circulation rather symmetric around the equator, in contrast to the instantaneous pattern.

From the perspective of energetics, the Hadley circulation is powered by two different mechanisms acting in the rising and subsiding parts of the flow. The rising flow is energized by sunlight, which through evapouration laces the upflow with water vapour ("liquid sunshine"); the vapour subsequently condenses to release latent heat on adiabatic cooling. The descending flow acts like a huge compressor, heating the air and generating upward infra-red radiation. Any imbalances between the two regions are rapidly communicated and equalized by pressure forces, which is why diffusive effects are secondary and strong water vapour gradients can be maintained. Overall, this relatively rapid pressure equalization sustains a fairly constant temperature throughout the tropics; the toy model described below illustrates these physical ideas.

Tropical heat transport

Since the total energy reaching the earth's surface arrives primarily in the equatorial regions, it's important to understand the mechanisms of heat transport there. We formulate this problem in terms of a one-dimensional model, in which all longitudinal variation is neglected. The model is based on work by Held & Hou (1980) and Lindzen & Hou (1988, *JAS*, **24**, 151).

The basic equations we start with are the zonal and meridional shallow-water equations on the equatorial $\beta-$plane:

$$\begin{array}{l} \partial_t U + U\partial_x U + V\partial_y U - \beta y V = -\partial_x h \\ \partial_t V + U\partial_x V + V\partial_y V + \beta y U = -\partial_y h \end{array},$$

where U and V are the zonal and meridional velocities respectively, and h is the depth of the atmosphere.

We consider relatively slow (linear), steady motions with no zonal structure, and so the shallow-water equations reduce to

$$\left\{ \begin{array}{r} V\partial_y U - \beta y V = 0 \\ \beta y U = -\partial_y h \end{array} \right.$$

Note that, in the tropical regions of interest, $f \approx 0$. Because there is then no Coriolis term to balance the longitudinal pressure gradient, the usual geostrophic balance cannot be attained. Also, the mass below a surface of constant potential temperature is roughly proportional to the mean temperature of the layer. In the following we will therefore use h as a proxy for temperature T in order to determine the thermodynamic state of the atmosphere.

This model is a fairly good representation of the upper branch of the Hadley cell (the high-altitude flow), where we can reasonably neglect dissipative effects. The lower branch of the cell (the flow just above the surface), however, is controlled in part by stronger dissipation, which one might try to model by adding friction terms to the equations.

The $x-$momentum equation can be re-arranged to give

$$V\partial_y \left(U - \frac{1}{2}\beta y^2 \right) = 0, \tag{1}$$

so that

$$\left(U - \frac{1}{2}\beta y^2 \right) = constant. \tag{2}$$

This is essentially a statement of angular momentum conservation. If we consider a equatorially-symmetric Hadley circulation, then $U = 0$ at $y = 0$ and we have:

$$U = \frac{1}{2}\beta y^2. \tag{3}$$

Integrating the $y-$momentum equation over y now gives the following relation for the meridional profile of the height of the tropopause:

$$h = h_{eq} - \frac{1}{8}\beta^2 y^4, \tag{4}$$

which is plotted in Fig. , and roughly corresponds to the meridional temperature distribution. The flatness of the curve near the equator comes from the dependence of h on the fourth power of y.

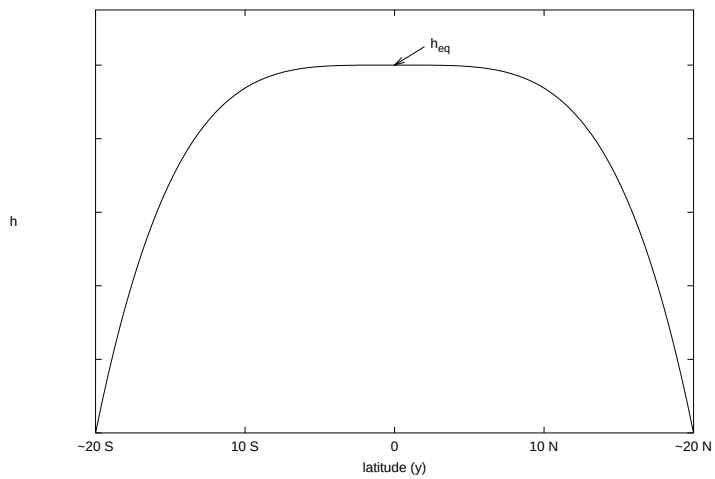

Figure 7: Layer depth (mean temperature) as a function of latitude

This profile is obtained with the assumption of zero zonal velocity, U, at the equator. On the other hand, we could have imposed the following, less restrictive, condition: $U(y = 0) = U_{eq}$, which case,

$$\frac{\partial h}{\partial y} = -\beta y \left(U_{eq} + \frac{1}{2}\beta y^2 \right) \tag{5}$$

and

$$h = -\frac{\beta^2 y^4}{8} - \frac{\beta y^2 U_{eq}}{2} + h_{eq}. \tag{6}$$

The quadratic term on the right-hand side of equation (6) may cause (for $U_{eq} < 0$) a depression of the height of the tropopause at the equator (see figure 8).

At this stage we have not introduced the solar heat input, and so the symmetry properties of the temperature profile are independent of the details of the solar forcing. Also, we have no way of determining the latitudinal extent of the Hadley cell, $[-y_{max}, y_{max}]$. Given that the cell must continuously match onto a mid-latitude atmosphere in which we might wish to prescribe the depth $h(y_{max}) = h_{mid}(y_{max})$ by the condition of radiative equilibrium (which determines the function $h_{mid(ymax)}$)), this is equivalent to having an arbitrary equatorial depth, h_{eq}. The cell size and equatorial depth are, however, related by

$$h_{eq} = h_{mid} + \frac{1}{8}\beta y_{max}^4 + \frac{1}{2}\beta U_{eq} y_{max}^2. \tag{7}$$

To complete the solution, we evaluate the global atmospheric meridional mass flux:

$$\frac{\partial}{\partial_y}(Vh) = -\frac{h}{\tau} + Q, \tag{8}$$

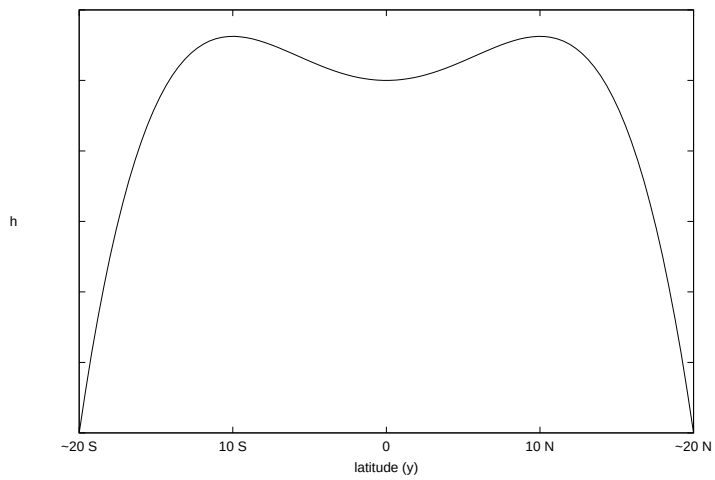

Figure 8: Layer depth as a function of latitude for a situation with non-zero zonal velocity at the equator

where the two terms on the right hand side represent the upper radiative cooling of the troposphere by long wave radiation (which is assumed to be proportional to the thickness of the layer, with a relaxation time τ) and the incoming source of heat $Q(y)$ (a known function). Integrating over the whole extension of the Hadley cell, we obtain

$$\int_{-y_{max}}^{y_{max}} \partial_y(Vh)dy = 0 = \int_{-y_{max}}^{y_{max}} \left(-\frac{h}{\tau} + Q\right) dy, \tag{9}$$

on using the boundary conditions $V(y_{max}) = V(-y_{max}) = 0$. This constraint determines the size of the cell (y_{max}) or, equivalently, the layer depth (i.e. temperature) at the equator, h_{eq}: we substitute our solution for $h(y)$ into the integral to find

$$\tau \int_{-y_{max}}^{y_{max}} Q(y)dy = y_{max}h_{mid} + \frac{3}{40}\beta y_{max}^5 + \frac{1}{6}\beta U_{eq} y_{max}^3 \tag{10}$$

(an implicit equation for y_{max}).

Although this simple model can produce a reasonable latitudinal temperature profile, it has evident limitations, particularly as it does not give the location of the ITCZ. For that, the problem must be closed by coupling the heating distribution Q to the flow and surface characteristics.

A diffusive energy balance model

As a second example of a one-dimensional model, we extend our discussion of the ice-albedo feedback, and consider the effect of the latitudinal structure of the ice cover and the meridional transport of heat, assumed to be given by a simple down-gradient diffusion. We adopt a local coordinate system on the earth surface, and define $y = sin(\varphi)$, where φ is the

latitude. In this coordinate system, the steady, zonally symmetrical heat equation is

$$\frac{d}{dy}\left[(1-y^2)D\frac{dT}{dy}\right] = OLR(T) - L_\odot[1-\alpha(y)]F(y), \tag{11}$$

where D is the diffusivity, and the two terms on the right-hand side represent, respectively, the loss of energy through outgoing long wave radiation and the solar forcing. The forcing depends on the solar constant $L_\odot = 1370Wm^{-2}$, the albedo, $\alpha(y)$, and the flux factor, $F(y)$. As a further simplification we use the linearized version of the OLR in the form,

$$OLR(T) = B(T - T^*) = BT', \tag{12}$$

where $T' = T - T^*$ is the deviation from the reference mean temperature, T^*. The response of the system to a perturbation from the equilibrium state is thus given by

$$\frac{d}{dy}\left[(1-y^2)\frac{dT'}{dy}\right] = \frac{B}{D}T' - \frac{L_0}{D}(1-\alpha)F. \tag{13}$$

As boundary conditions, we take $T_y = 0$ at the equator, $y = 0$, which enforces symmetry between the two hemispheres, and insist that T be regular at the pole, $y = 1$.

We may exploit Green's function to write the solution to this equation in the form,

$$T(y) = -\frac{L_0}{D}\int_0^1 G(y,y')[1-\alpha(y')]F(y')dy', \tag{14}$$

where the Green function involves the Legendre functions $P_\nu(y)$ and $Q_\nu(y)$ with $\nu^2 + \nu + B/D = 0$. However, for practical purposes, it is also straightforward to solve the differential equation numerically.

A complication in this equation is that the albedo is not simply a function of latitude, but also should depend on temperature. Nevertheless, for some simple models, we may still find the solution in the following way: consider the simple model for the albedo in which

$$\alpha = \begin{cases} \alpha_o & y < y_i \\ \alpha_i & y \geq y_i \end{cases}, \tag{15}$$

where α_i is the (constant) albedo of ice, α_o characterizes the albedo of unfrozen land and sea, and y_i is the latitudinal position of the edge of the ice cover (the ice margin). Then,

$$T_i = T(y_i) = -\frac{L_0}{D}\int_0^{y_i} G(y,y')(1-\alpha_o)F(y')dy' - \frac{L_0}{D}\int_{y_i}^1 G(y,y')(1-\alpha_i)F(y')dy'. \tag{16}$$

For consistency, T_i should be the temperature at which the ice cover first forms (273 degrees Kelvin), and so (16) determines y_i implicitly. From a practical perspective, we solve either (16) or the differential equation for given y_i, determine T_i, and then adjust y_i in order to bring T_i to the required value (such as by Newton iteration). Some sample computations are shown in figure 9. At $y_i = 0$, we find snowball Earth solutions (worlds with complete ice cover) provided $T_i < 273$. There are also solutions for ice-free worlds with $y_i = 1$ if $T_i > 273$. In between, and depending on the diffusivity, there are solutions for partially

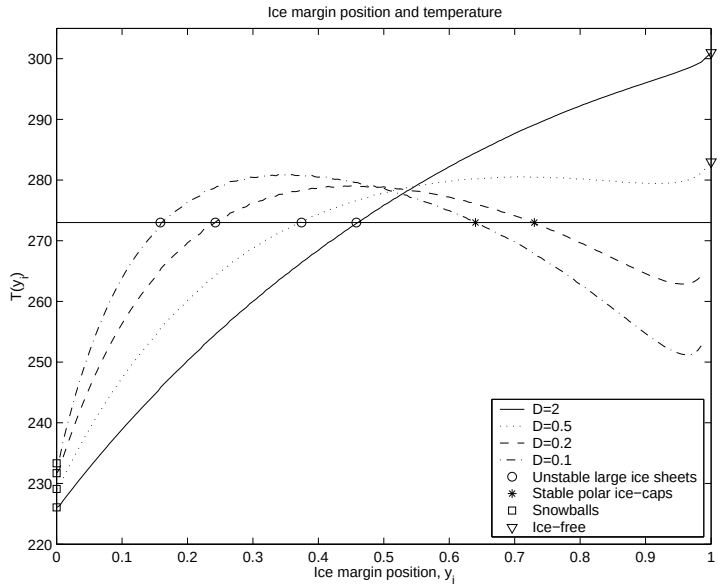

Figure 9: Ice margin position against temperature.

ice-covered worlds ($0 < y_i < 1$ and $T_i = 273$), of which one is prone to the large ice-sheet instability, and the other is a stable solution with a polar ice-cap.

Note that a natural lengthscale for the temperature variation is $\sqrt{D/B}$. In the limit that this scale is large, the temperature field has weak variations and we recover the zero-dimensional model described in lecture 6. Also, we need not strictly use the linearization of the OLR curve; in some problems (like greenhouse runaway), it is necessary to incorporate a nonlinear OLR curve. The numerical solution of the differential equation is no harder and proceeds in the same fashion.

Finally, we might also reinstate the time rate of change of T into the heat equation (a term like $M\partial T/\partial t$, where M is the "thermal mass"), in which case we could further explore the temporal rearrangements of temperature and ice cover with latitude during climate changes. This is the basis of the celebrated Sellers model (and the related Budyko model), often used by climate dynamicists.

Notes by Lianke te Raa and Chiara Toniolo

Lecture 8

Glacial-interglacial variability: phenomenology and dynamical background

Eli Tziperman

8.1 A brief description of the phenomenology

Information about climate history over the past two million years or so is obtained from two main sources [4]. The £rst is sediment cored from the ocean's bottom, where the isotopic compositions of buried plankton skeletons and other buried material are used as proxy indicators to past climate, and are related empirically to past ice land volume, paleo temperature, etc (Fig. 3). The second source is ice core records from Antarctica and Greenland, that contain again various isotopic records as well as trapped gas bubbles and atmospheric dust from the past 400,000 years or so (Fig. 37).

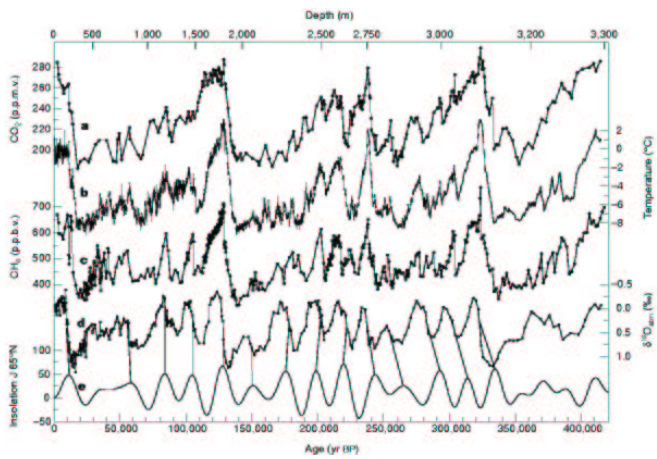

Figure 37: Vostok ice core record for atmospheric gasses.

A brief summary of some of the observed glacial cycle characteristics for the past 2 Myr follows:

1. Roughly a 100 kyr time scale between glaciations during the past 800 kyr.
2. Saw-tooth structure: long glaciations (Order 90,000 yr), short deglaciations (5-10,000 yr).
3. A transition from 41 kyr to 100 kyr glacial cycles about 800 kyr ago.
4. Atmospheric CO_2 variations during the glacial cycles.
5. Some phase locking to Milankovitch forcing (this forcing is explained in section 8.2.5).
6. Global extent of the glacial signal.

Besides the need for a theory that explains these observations, we also need to address the following questions regarding the cycles' dynamics:

1. Are the cycles externally forced? by what? or perhaps internally produced (self sustained) within the climate system?

2. Are the cycles produced by the physical climate components (i.e. excluding CO_2 variations that are likely due to a biogeochemical mechanism)? By the biogeochemical components? Both? Only ampli£ed by CO_2 variations that are, in turn, induced by the cycle in the physical system? Which components of the physical climate system participate in the glacial dynamics and on what time scales?

3. Are the cycles driven from the northern hemisphere, where most of the land ice volume changes occur, or from some other region? what phase lags should we expect between northern & southern hemispheres?

We proceed now with a description of some basic climate feedbacks that are likely to be important in glacial dynamics, and then describe a few of the toy models/ mechanisms for the glacial cycles which have been proposed over the years and that are based on these climate feedbacks.

8.2 Basics and relevant climate feedbacks

8.2.1 Energy balance, and the ice albedo feedback

As a crude simpli£cation, one may write a simple equation for a globally averaged temperature T in which incoming solar radiation $H^{\downarrow}$ is partially re¤ected by the earth albedo, and partially compensated by long wave modi£ed black body radiation $e\sigma T^4$ (see Lectures 6-7).

$$\frac{dT}{dt} = H^{\downarrow} \times (1 - \text{albedo}) - e\sigma T^4 \tag{31}$$

This equation implies, of course, that a higher albedo results in a cooling effect, which is a feedback that will play a signi£cant role in the followings due to the albedo effect of changing land and sea ice covers, as follows. Given the higher albedo of land and sea ice relative to that of the land or ocean, larger ice covered area results in larger albedo, and based on the above simple energy balance argument, in a lower temperature:

$$\begin{aligned} \text{albedo} &\propto \text{land ice and sea ice area} \\ \text{albedo} &\uparrow \implies \text{temperature} \downarrow \end{aligned}$$

8.2.2 Ice sheet dynamics and geometry

(Ghil and Childress, [15]; or Paterson, [42]). Glaciers ¤ow as non-Newtonian ¤uids. The ¤ow is governed by the stress-strain or stress-rate of strain relation. (The stress tensor $\tau = \tau_{ij}$, denoting force per unit area, could be shear stress for $i \neq j$ or normal stress for $i = j$. The strain tensor e_{ij} is the displacement or deformation per unit length). Some examples of stress-strain relations are (Fig. 38):

- Elastic materials (Hook's law, metals for low stress): $\tau = Be$
- Plastic materials (metals beyond their critical stress): no deformation below a critical yield stress, and then beyond that point arbitrarily large deformation with no increase in stress.
- Viscous Newtonian ¤uid: $\tau = \nu(de/dt)$.
- For ice, there is Glenn's law, $de/dt = A(T)\tau^n$, where $A(T)$ is exponential in the temperature (warm ice is softer...) and $n = 3$ is a typical value that £ts laboratory data etc. Note that $n \to \infty$ corresponds to plasticity. Extending Glenn's law from the 1d normal stress-strain relation to the relation between the full tensors τ_{ij} and e_{ij} is nontrivial, see [42]...

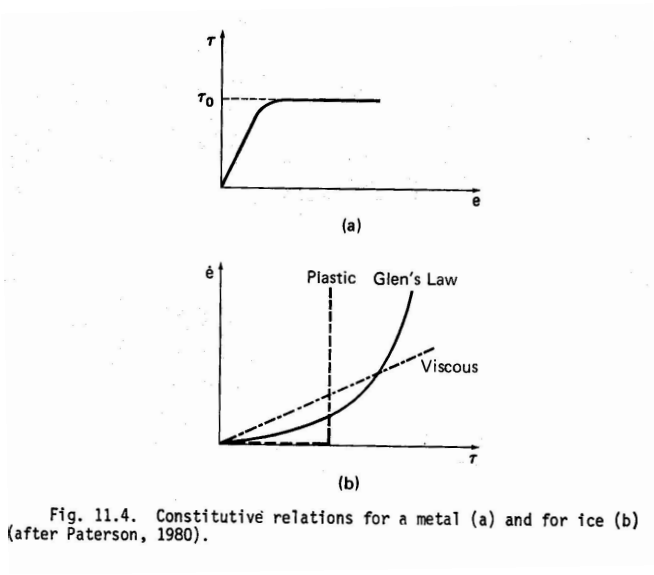

Figure 38: Strain-stress relations for ice and some other materials (Ghil and Childress Fig. 11.4).

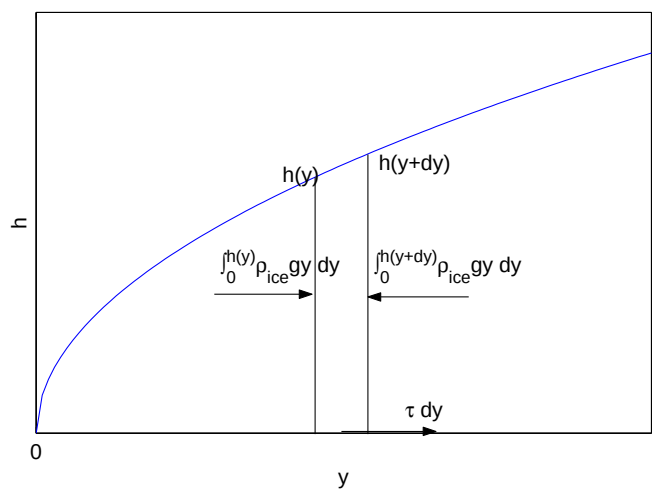

Figure 39: Force balance on a slice of an ice sheet, used to deduce the parabolic pro£le.

Parabolic pro£le of ice sheets: consider a balance of forces for a glacier that is symmetric in longitude x. The glacier height as function of latitude is $h(y)$. The balance of forces on a slice of the glacier between latitudes $(y, y+dy)$ is between hydrostatic pressure integrated along the face of the slice, and stress applied by bottom friction (Fig. 39)

$$\int_0^{h(y+dy)} \rho_{ice} g z dz - \int_0^{h(y)} \rho_{ice} g z dz = \tau(y, z=0) dy$$

or simply

$$h(y) \frac{dh}{dy} \rho_{ice} g = \tau(y, z=0) = \tau_0$$

where we assume that the bottom is at the yield stress τ_0 (i.e. glacier in a "critical" state). In other words, we assume perfect plasticity: glacier yields to the hydrostatic-induced stress at the above critical stress. The solution to the last equation gives the desired parabolic pro£le that is not a bad £t to observations (Fig. 40).

$$\frac{1}{2} h(y)^2 = \frac{\tau_0}{g \rho_{ice}} (y - y_0).$$

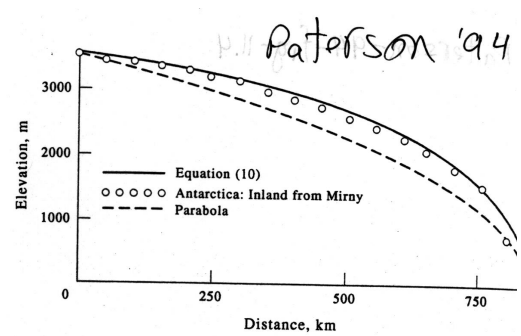

FIG. 11.4. Profile of Antarctic Ice Sheet inland from Mirny compared with theoretical profiles. Data from Vialov (1958).

Figure 40: Fit of parabolic pro£le for ice sheet geometry to observations. From Paterson [42].

Accumulation/ ablation: The area of an ice sheet is divided into an accumulation zone and an ablation zone. The net accumulation minus ablation depends on both the latitude and the height of the ice sheet surface. The interaction between the mass balance and the elevation is complex... On the one hand, there is the Elevation-desert effect: as the ice sheet surface reaches higher elevations, the amount of precipitation on it is reduced due to the decreased humidity content of the atmosphere with height. However, increased elevation also means colder temperatures and therefore decreased ablation. This effect is often assumed dominant. The line at which the net accumulation minus ablation is zero (equilibrium line, $E(y)$) starts at sea level at some northern latitude, and increases in elevation southward, to compensate for the increased surface temperature.

Given these considerations, the source term for an ice sheet mass balance is written as (Oerlemans, Pollard)

$$G = \begin{cases} a(h+h'-E(y)) - b(h+h'-E(y))^2 & h+h'-E < 1500m \\ c & h+h'-E > 1500m \end{cases} \tag{32}$$

Ice streams: The ice in ice sheets ¤ows from the accumulation to the ablation zones at an averaged velocity of meters to tens of meters per year (Fig. 42). However, some 90% of the discharge ¤ow in glaciers actually occurs in rapid and narrow ice streams (velocities can reach 4 km/yr, which is 100-1000 times that of a laminar ice sheet ¤ow) that occupy only a small area of the ice sheet. These ice streams are also transient in time rather

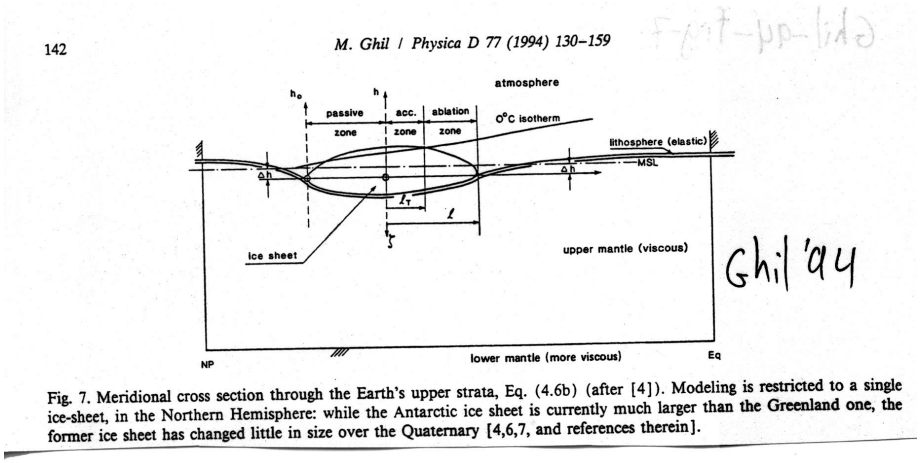

Figure 41: ice sheet geometry and the equilibrium line separating accumulation and ablation zones (Figure 7 from Ghil [14]).

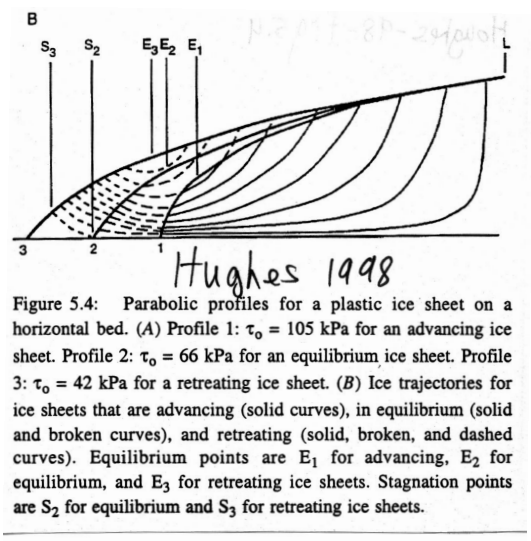

Figure 42: Schematic ice ¤ow in an ice sheet [24].

than in a slow uniform and steady ¤ow (Figs. 43, 44). The dynamics of ice streams are complex and not fully understood. Among the relevant feedbacks are some that involve the melting and deformation of the till below the ice stream. Another feedback is induced by the bottom topography and the internal heat of deformation: a ¤ow of a glacier over a bump induces larger ice velocities, and therefore in increased heating due to internal glacier deformation; this softens the ice and affects the coef£cient in Glenn's law ($A(T)$), therefore increasing the ice velocity again.

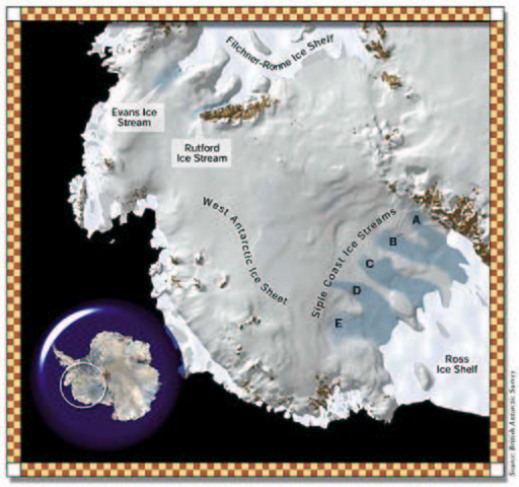

Figure 43: Ice stream locations in Antarctica (http://nsidc.org/NASA/RAMP/icestreamb_mapw.html, http://web.mit.edu/dabrams/www/).

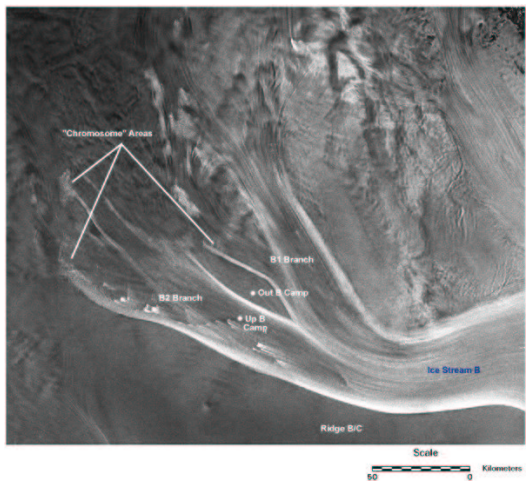

Figure 44: Ice stream b in Antarctica (http://nsidc.org/NASA/RAMP/icestreamb_mapw.html, http://-web.mit.edu/dabrams/www/).

Calving processes: (Pollard [50], Fig. 45) When the ice sheets are suf£ciently large and heavy, they deform the earth crust (see section 8.2.4), sink below sea level, and may be ¤oated by incoming sea water. This detaches them from the bedrock and may cause a rapid ice ¤ow/ sliding to the ocean. A simple parameterization of this calving process in the framework of the above 1D ice sheet model is to add the following term to the ablation parameterization [50, 48, 49]

$$G(x_{i+1}) = -20\,m\,yr^{-1} \qquad if\ \rho_{ice}h(x_i) < \rho_w(S - h'(x_i))\ and\ h'(x_{i+1}) < S \tag{33}$$

where S is the sea level, the £rst above conditions requires that sea level is large enough to be able to ¤oat the ice, and the second condition is that sea ice can reach point x_i (Fig. 45). The calving process may be triggered as follows: suppose that the ice sheet has reached a maximum size that causes a signi£cant bedrock depression, and that at that stage an increased summer radiation due to Milankovitch cycles caused some retreat of the southern ice tip into the depression formed by the isostatic adjustment (both Milankovitch cycles and isostatic adjustment are discussed below). Because the bedrock takes some time to respond to the new position of the ice sheet, the gap that is formed between the ice sheet and the depressed bedrock allows sea water to penetrate the empty depression and ¤oat the ice sheet, causing the calving process. There is also a positive feedback involved with the calving process (Watts and Hayder [65]): once some calving occurs, it raises the sea level, and therefore reinforces the ¤oating of more ice and induces yet more calving. Presently, 80% of the ablation in Greenland is due to calving, although Peltier and Marshal [44] £nd that this process is not suf£cient to eliminate the Laurentide ice sheet during the deglaciation stage in their model.

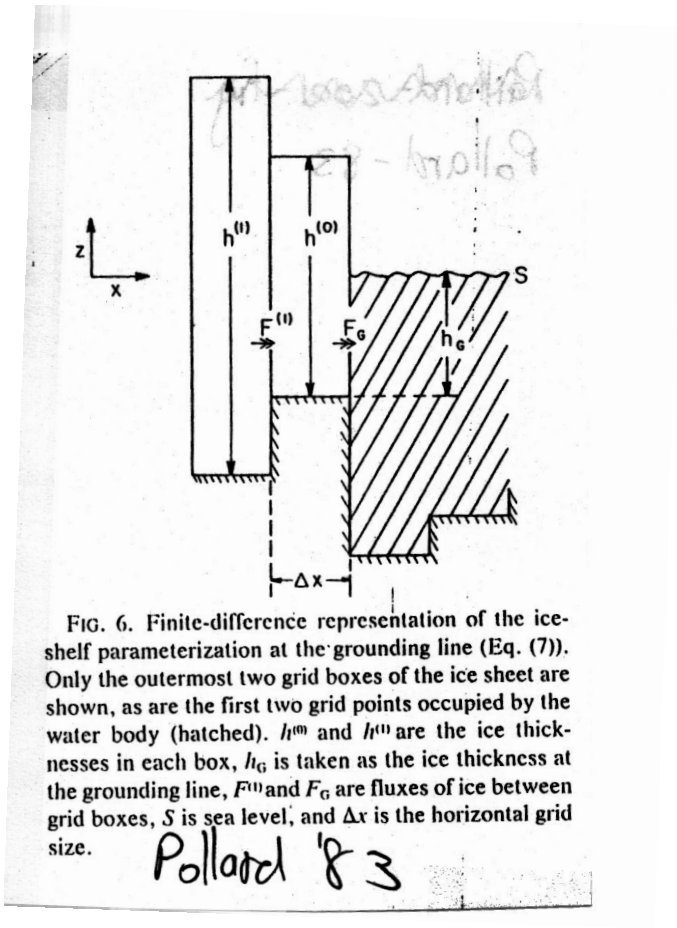

Figure 45: Calving parameterization, from Pollard 1983.

There are other instability processes that were used in various models as part of the ablation parameterization, such as specifying that when ice sheets get too large they collapse due to gravitational instability, etc...

Dust loading and enhanced ablation: (Peltier and Marshal [44]) The atmosphere during glacial periods, being drier, more windy (due to the larger meridional temperature gradient), and having larger exposed continental shelves, contains larger amounts of aerosols and dust. Continental dust is up to 10-30 times that during interglacials, and marine aerosols (salt) up to 3-4 times more. Dust loading could affect the albedo of ice sheets

in ablation areas, which are relatively narrow strips along the boundary of the ice sheet where ablation is larger than accumulation. The dust cover may reduce the surface albedo there, therefore causing the the ice sheet to absorb more solar radiation and enhancing melting. A reduction of the dirty snow/ ice albedo from 0.7 to 0.1-0.4 results in the surface absorbing 2-3 times more radiation, much of which causes enhanced ice melting. Peltier and Marshal [44] £nd that the dust loading effect is critical for getting rapid terminations in their ice sheet model. However, this is only an indirect indication of the importance of dust loading, as they parameterize the effects of dust on ablation directly, rather than deal with the effect of dust on the albedo, which then affects the radiation absorption and eventually the melting.

8.2.3 Temperature-precipitation feedback

Ice core proxy observations show that the rate of accumulation of snow over land ice sheets is signi£cantly higher during relatively warm periods (Fig. 46). GCM experiments indicate a similar trend. In particular, greenhouse scenarios show that as the temperature increases, accumulation increases initially faster than ablation, so that the net accumulation is larger for warmer temperatures. Once the warming passes some threshold, the increase in ablation surpasses that in precipitation, so that the net accumulation £nally decreases with temperature (Figs. 47, 48). The increase in net accumulation over land ice with increased temperature seems to have been quite robust during glacial-interglacial cycles, and has been termed the temperature-precipitation feedback [14].

There are several mechanisms that could be responsible for this feedback. First, higher temperature implies larger moisture content of the atmosphere based on the Clausius Clapeyron relation, and therefore a stronger hydrological cycle. Second, at least some of the precipitation falling on northern hemisphere land ice sheets is due to local evaporation from the polar and high latitude ocean. During suf£ciently cold periods, the high latitude ocean is covered by (perennial and seasonal) sea ice which signi£cantly reduces evaporation from the ocean, and therefore limits the precipitation of snow over the land ice. Finally, the presence of even seasonal sea ice may shift the storm track away from the land ice sheets, thus again reducing the precipitation brought by winter storms from falling on the ice sheets.

The temperature-precipitation feedback plays quite an important role in a number of glacial cycle theories as we shall see below.

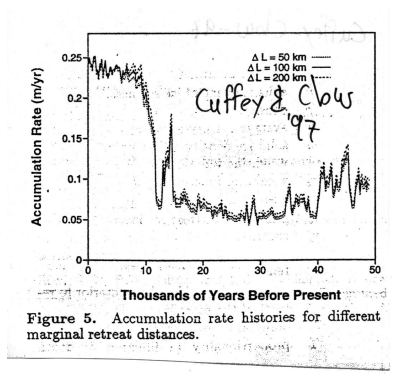

Figure 46: accumulation rate for warm and cold periods, showing the temperature-precipitation feedback. Fig. 5 from Cuffey and Clow [8].

8.2.4 Isostatic adjustment

Ice density is roughly a $\frac{1}{3}$ of the earth interior density. Ice sheets therefore sink into the crust roughly a $\frac{1}{3}$ of their height, and this process is referred to as the "isostatic adjustment" (Fig. 49).

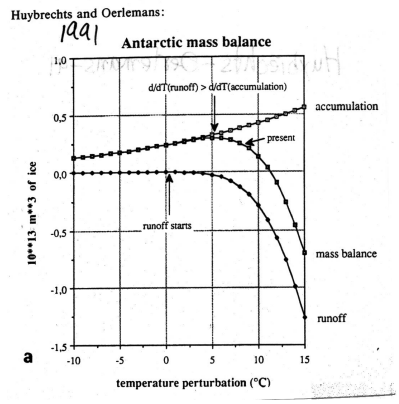

Figure 47: Mass balance of ice sheet as function of temperature, showing temperature-precipitation feedback for small temperature increases, and increased ablation dominating for a larger temperature increase. Fig. 5a from Huybrechts and Oerlemans [25].

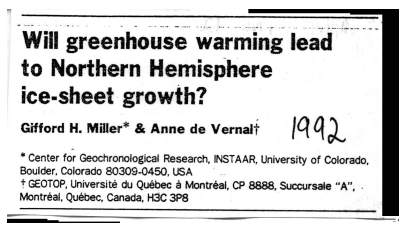
Will greenhouse warming lead to Northern Hemisphere ice-sheet growth?

Gifford H. Miller* & Anne de Vernal† 1992

* Center for Geochronological Research, INSTAAR, University of Colorado, Boulder, Colorado 80309-0450, USA
† GEOTOP, Université du Québec à Montréal, CP 8888, Succursale "A", Montréal, Québec, Canada, H3C 3P8

Figure 48: Temperature-precipitation feedback in the news... [35]

This adjustment process is not immediate and there is a time scale of a few thousands of years involved. Let us derive an equation for an ice sheet evolution including the isostatic adjustment effect (Oerlemans [39]; Pollard [50, 48, 49]). Start with a simple relation of a Glenn's law type between the vertical average velocity of the ice sheet and the shear stress at the bottom

$$\mathbf{u} = B\vec{\tau}_b^m$$

In principle, B is a function of the temperature, and m might change depending on sliding conditions at the base of the glacier (frozen/ melted), but let us assume they are both constant. We can show, based on similar arguments to those used for deriving the parabolic glacier geometry, that

$$\vec{\tau}_b = \rho_{ice} g h \frac{\partial h}{\partial y}$$

where h is the ice thickness and $h = h + h'$ is the ice surface elevation, and where h' is the elevation of the bedrock above some reference level (Fig. 50).

Now, the (1 dimensional) mass continuity of the glacier is simply

$$\frac{\partial h}{\partial t} = \frac{\partial}{\partial y}(hu) + G(h,y,t)$$

where $G(h,y,t)$ is the net accumulation-ablation. Substituting the above expression for the velocity

$$\begin{aligned} \frac{\partial h}{\partial t} &= \frac{\partial}{\partial y}(hB(\rho_{ice} g h \frac{\partial}{\partial y}(h+h'))^m) + G \\ &= A \frac{\partial}{\partial y}(h^{m+1}(\frac{\partial}{\partial y}(h+h'))^m) + G \end{aligned}$$

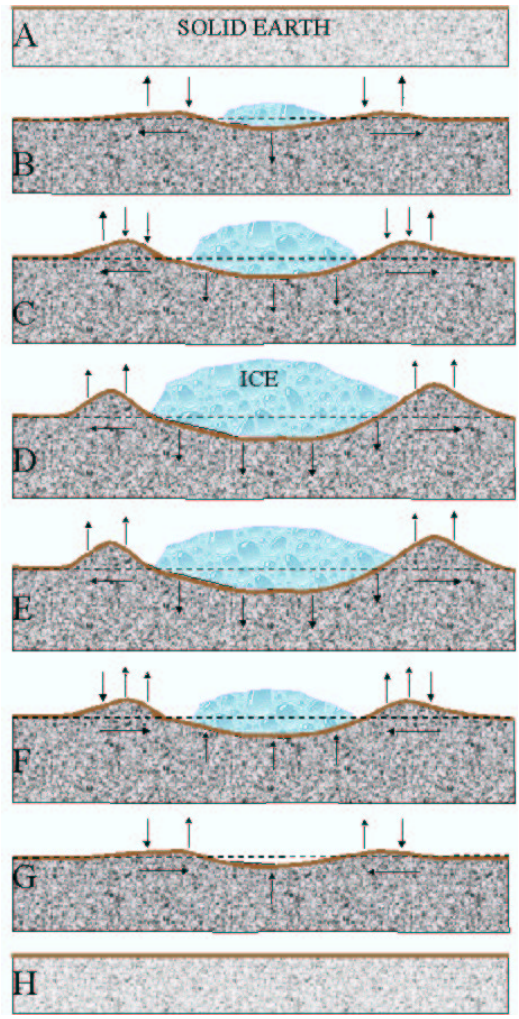

Figure 49: Schematic plot of isostatic adjustment for changing ice sheet volume, from http://rgalp6. harvard.edu/background.html.

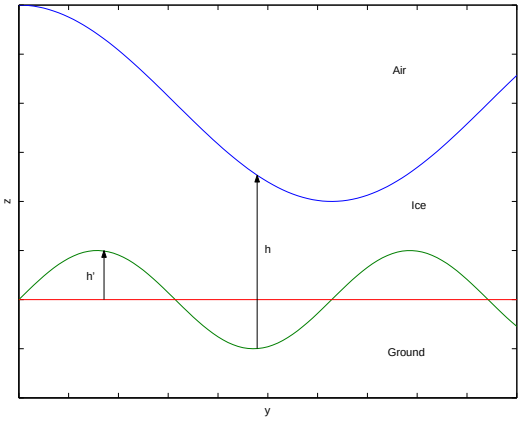

Figure 50: Ice sheet geometry and variables for the isostatic adjustment model.

which may be written as a nonlinear diffusion process

$$\begin{aligned} \frac{\partial h}{\partial t} &= \frac{\partial}{\partial y}(D(h)\frac{\partial}{\partial y}(h+h')) + G(h,y,t) \\ D(h) &= h^{m+1}(\frac{\partial}{\partial y}(h+h'))^{m\ \ 1} \end{aligned} \tag{34}$$

Now, the ¤ow within the upper part of the earth interior (lithosphere...) can be modeled as an adjustment to perturbations introduced due to the ice sheet load that penetrates down into the lithosphere to a depth rh where $r = \frac{1}{3}$, plus an inherent topography of the crust $h_0'(y)$. The adjustment could be modeled using a simple time scale $T_{isostatic}$,

$$\frac{\partial h'}{\partial t} = (h' - h_0'(y) + rh)/T_{isostatic}$$

or using a scale selective adjustment using a simple diffusion law

$$\frac{\partial h'}{\partial t} = \nu \frac{\partial^2}{\partial y^2}(h' - h_0'(y) + rh) \tag{35}$$

The typical time scale for the isostatic adjustment seems to be about 3000 yr. Equations (34, 35) provide us with an ice sheet model based on the isostatic adjustment feedback, where in order to solve for the glacier distribution history we still need to specify the ice source/ sink (accumulation/ ablation) G, as in (32) and (33), for example.

8.2.5 Milankovitch forcing

One of the main ingredients for many glacial cycle theories is the temporal changes in the solar radiation arriving to the earth surface due to changes in orbital parameters of the earth around the sun. A useful recent review is given by Paillard [41]. The commonly used orbital parameters and the corresponding time scales at which they change are as follows, following Paillard [41]. (Figs. 51, 52). **Eccentricity**, e, with a time scale of about 100kyr: corresponds to changes in the elongation of the ellipse along which earth circles the sun; affects the annual mean, global mean radiation (though only by a very small factor of about, has a negligibly weak climatic effect. Note that Earth's trajectory was nearly spherical 400 kyr ago. **Obliquity**, ε, 41 kyr: the tilt of earth's axis, varies due to the torque acting on the earth by the sun and moon because of its equatorial bulge, that is, because the earth is not perfectly spherical; the corresponding amplitude in solar radiation changes is a few (5-15) $watt/m^2$, and the effect is on the annual mean contrast between the poles and the equator, as well as on the contrast between the seasons, and is of the same magnitude in both hemispheres. **Precession**, γ, has time scales of 19 kyr and 23 kyr. It corresponds to the circular motion of the earth's rotation axis in space, and has a climatic effect only when the earth orbit is not exactly spherical. The amplitude of changes in solar radiation is of the order of 20% ($O(100)\,watt/m^2$), and the effect is antisymmetric with respect to seasons and hemispheres. Because it does not have any climatic effect when earth's trajectory is exactly spherical, the climatic precession parameter is de£ned to be proportional to e. NO effect on annual mean radiation or globally mean radiation.

The main effect of Milankovitch forcing is not due to the direct effect of changes in the solar radiation on the atmospheric energy balance and therefore on the atmospheric temperature, but rather due to its effect on glacier ablation (Held, [22]): ice is a very poor heat conductor, and the heating by solar radiation therefore remains near the ice sheet surface. Thus a 25% variation in the amplitude of summer radiation can cause a signi£cant change in surface ice temperature, which can therefore also strongly control summer melting. Note that most of the melting occurs within a few weeks during the summer. A change in the summer solar radiation can bring the ice surface temperature to above or below the melting temperature, while in the winter the temperature is too low for the Milankovitch variations to be able to bring the temperature to the melting point. This is why the Milankovitch summer radiation is what counts, and not the annual average nor the winter solar radiation.

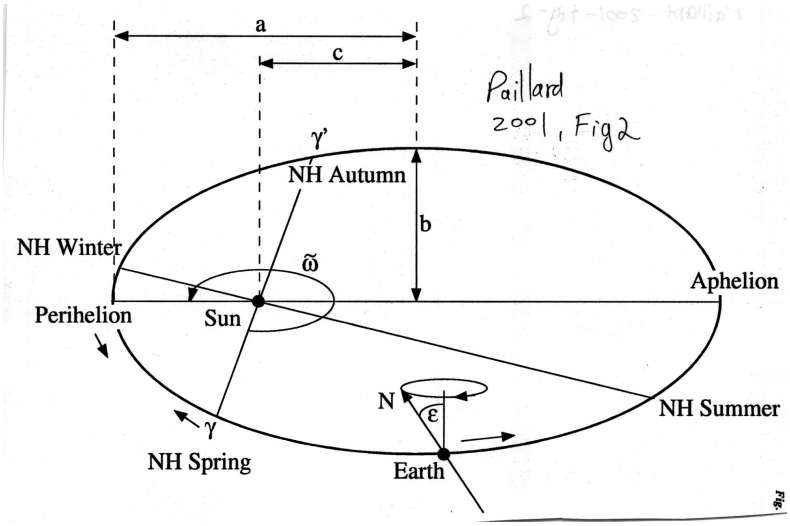

Figure 51: Orbital parameters (Paillard 2001, Fig. 2).

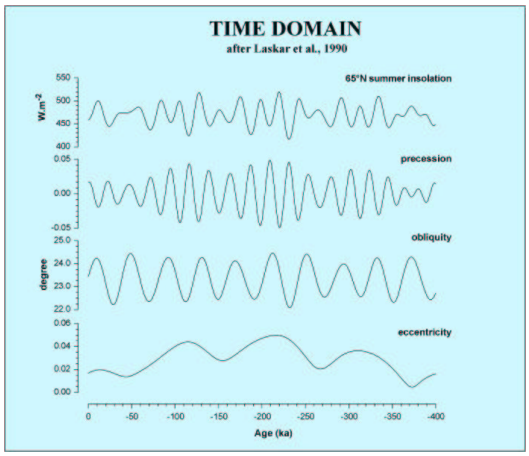

Figure 52: Milankovitch radiation in the time domain.

8.2.6 More feedbacks

The above list of climate feedbacks that may participate in glacial-interglacial dynamics is far from complete. In particular, we have concentrated only on feedbacks of the physical climate system, ignoring biogeochemical feedbacks that will be brie¤y mentioned below. There are certainly some additional physical feedbacks that have been neglected, such as the geothermal heating at the base of ice sheets, and numerous others... In any case, the above ingredients already allow us to describe some of the existing theories for the glacial cycles, which are the subject of the next lecture.

Lecture 9
Mechanisms and toy models of the glacial cycles

Eli Tziperman

Given the above climate feedbacks as our ingredients for making glacial theories, we now describe some of the physical mechanisms and models proposed for explaining the main features of the glacial cycles. As done throughout these lectures, we concentrate on conceptual (toy) models that attempt to explore the role of a limited number of feedbacks at a time.

9.1 Glacial mechanisms based on basic physical feedbacks

9.1.1 Temperature-precipitation feedback

(Ghil [14]) The ice albedo feedback, relating rate of change of the temperature (T) to the albedo and to the land ice volume (V_{ice}), may be written as

$$\frac{dT}{dt} \quad \propto \quad -\text{albedo} \propto -V_{ice}.$$

Together with the temperature-precipitation (p) feedback

$$\frac{dV_{ice}}{dT} \propto p \propto T$$

the two feedbacks may be combined into a single equation that has an oscillatory solution

$$\frac{d^2T}{dt^2} \propto -T.$$

However, it turns out the time scale of these linear oscillations is much too short (10,000 years). In addition, this linear mechanism cannot account for the saw-tooth structure of the oscillations, and some nonlinearity must be included.

9.1.2 Glacial oscillations based on isostatic adjustment: the Load-accumulation feedback

(Ghil [14]) Assume that higher elevation of the ice sheet surface results in colder ice-sheet surface temperature, therefore in less ablation, and therefore in *more* net accumulation (i.e. opposite of the elevation-desert effect). As the ice volume increases, the ice sheet sinks into the bedrock, moving more of the the glacier surface area into an elevation of less accumulation/ more ablation (or equivalently, moving the equilibrium line poleward). This results in a negative feedback between ice volume and net accumulation rate

$$\frac{dp}{dt} \propto -V_{ice}$$

which, together with the simple mass balance equation

$$\frac{dV_{ice}}{dT} \propto p$$

again results in an oscillatory equation. The oscillation time scale is too short again due to the too short time scale of the isostatic adjustment. Again, this linear mechanism cannot account for the saw-tooth structure of the oscillations, and some nonlinearity must be included. A more sophisticated version of this mechanism, including calving, Milankovitch, and a nonlinear isostatic adjustment parameterization will be presented below.

9.1.3 Milankovitch forcing

Orbital/ incoming solar variations seem natural candidates for a glacial theory given their time scale and potential climatic effects. Indeed, as reviewed by Paillard ([41], Fig. 53) such theories have been proposed as early as the nineteenth century. In fact, it turns out that Milankovitch forcing by itself is unlikely to be able to explain the observed characteristics of the glacial cycles, although it does seem to play a signi£cant, even if secondary, role in the cycles dynamics.

Milankovitch seems to have been the £rst to understand that the solar radiation during the summer season is the critical climatic factor, as cold summers allow the survival of new snow cover from winter season (section 8.2.5 above). He also accurately calculated the time variations of the different orbital parameters. However, the dominant effect of the precession and obliquity on the summer radiation leads to a prediction of glacial cycle frequency of 19, 23 and 41 kyr periods, not in agreement with the dominant 100 kyr climatic signal (Fig. 56).

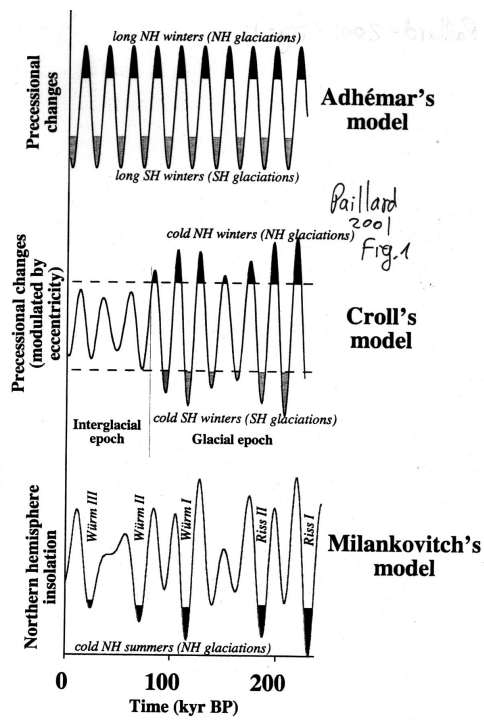

Figure 53: Three historical glacial theories based on orbital variations (Fig. 1 from Paillard [41])

The role of Milankovitch forcing is easily quanti£ed using some simple model equations, and various versions of such toy models have been proposed over the years (Calder, [6]; Imbrie and Imbrie [26]; Held [22]; see nice review by Paillard [41]). The simplest equation for the global ice volume in terms of Milankovitch forcing would be something like [6];

$$\frac{dV_{ice}}{dt} = -k(i - i_0) \tag{36}$$

where i is the insolation, i_o is the mean insolation, and where the proportionality constant k may have different values for melting ($i > i_0$) and for accumulation ($i < i_0$). While integrating this equation, one may also impose a condition that $V_{ice} > 0$. However, the £t to observations is rather poor... (Fig. 54, from Paillard [41], Fig. 9)

Next, Imbrie and Imbrie [26] use (nondimensional)

$$\frac{dV_{ice}}{dt} = (i - V_{ice})/\tau \tag{37}$$

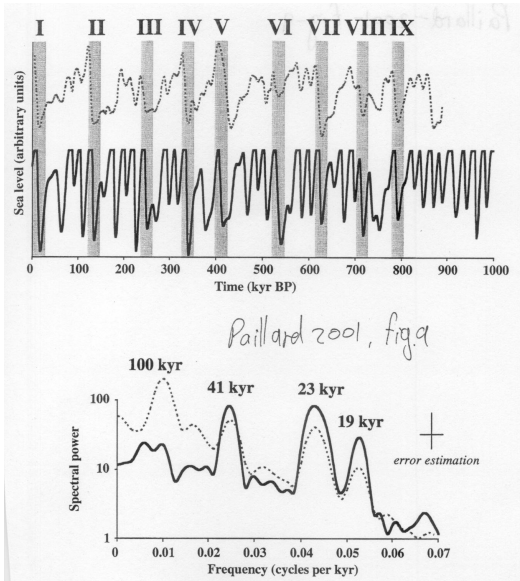

Figure 54: Results of the glacial cycle model of equation 36 (Paillard 2001, Fig. 9)

again with different τ for melting ($V_{ice} > i$) and accumulation. This model assumes a simple relaxation of the ice volume to the summer radiation, with the relaxation time scale given by τ. The results show a small peak at 100 kyr, and a larger one at 400 kyr, which is clearly still not a satisfactory result [41].

Analysis of the proxy records shows that the precession (19 & 23 kyr) and Obliquity (41 kyr) bands are likely to be linearly forced by Milankovitch forcing, but that the 100 kyr band is not likely to be directly and linearly forced by Milankovitch variations because Milankovitch forcing is much too weak at the 100 kyr period (Figs. 55, 56). Could the 100 kyr signal be a linear resonant response to the very weak Milankovitch forcing? Again not likely because there does not seem to be any linear time scale of the order of 100 kyr in the climate system that may be excited to produce the observed response. In order to obtain a time scale of 100 kyr, a different mechanism is clearly needed, most likely a nonlinear one. Various nonlinear feedbacks were indeed tried as will be discussed below.

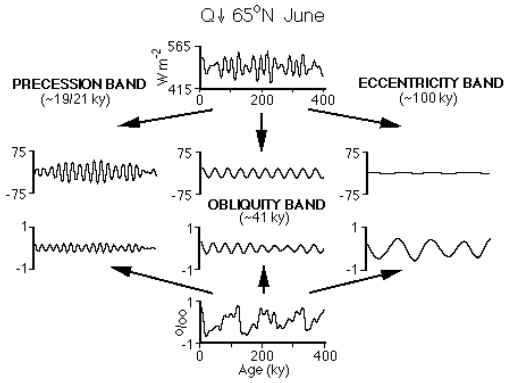

Figure 55: Imbrie et al; decomposition of climate record into Milankovitch spectral bands

Given the failure of the above simple linear models to explain the 100 kyr peak using Milankovitch forcing, Le-Treut and Ghil have tried to explain this peak as being due to nonlinear frequency transfer from Milankovitch

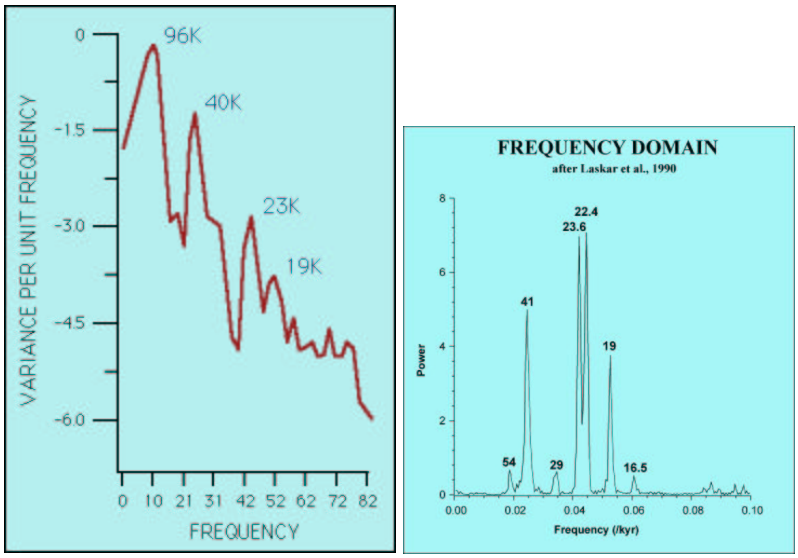

Figure 56: Spectra of Milankovitch (right) and proxy records (left), showing why Milankovitch is not the likely explanation for the 100 kyr time scale

frequencies to the 100 kyr period ([33], [14]). To do this, they combined the temperature-precipitation feedback and ice-albedo feedback which were shown above to produce glacial oscillations, using a few re£nements that produced nonlinear self-sustained oscillations with a time scale of some 7-10 kyr. The interaction of these nonlinear oscillations with the Milankovitch forcing results in a 100 kyr time scale. Let us begin the description of this mechanism by brie¤y describing the nonlinear oscillator model. Let the ratio of the ice sheet's accumulation area (a) and ablation area (a') be given by $\varepsilon(T) = a/a'$. This ratio varies nonlinearly as a function of the temperature (Fig. 57), and represents the effect of the temperature on the ablation/ accumulation according to the temperature precipitation feedback. In addition, the ocean albedo (α_{oc}) is also assumed to vary nonlinearly with the temperature (Fig. 57), while the land albedo is just linear in the land ice area.

The temperature equation (roughly equivalent to the over simpli£ed $dT/dt \propto -V_{ice}$ above) includes the effects of incoming solar radiation Q, land and ocean albedos and a linearized outgoing long wave radiation term

$$c_T \frac{dT}{dt} = Q\{1 - [\gamma\alpha_{land}(\ell) + (1-\gamma)\alpha_{oc}(T)]\} - \kappa(T - T_k).$$

The equation for the meridional extent of the land ice sheet, ℓ, is based on the temperature-precipitation feedback and has the form (roughly equivalent to the over simpli£ed $dV_{ice}/dt \propto T$ above)

$$c_L \frac{d\ell}{dt} = \ell^{\ 1/2}\{[1+\varepsilon(T)]\ell_T(T,\ell) - \ell\}$$

where c_L is some relaxation constant, and $\ell_T(T,\ell)$ represents the location of the boundary between the accumulation and ablation zones on the ice sheet.

As mentioned above, this model results in a self-sustained oscillation with a period that is quite robust around 6-7 kyr. Next, Milankovitch forcing is included by making the ratio of ablation to accumulation areas a function of temperatures $T_m(t), T_M(t)$ which are, in turn, a function of the Milankovitch radiation: $\varepsilon = \varepsilon(T, T_m(t), T_M(t))$, (see again Fig. 57 for an explanation of the physical role of $T_m(t), T_M(t)$). The Milankovitch forcing appears not as a free forcing term on the rhs, but as a parametric forcing term multiplying other terms in the equations. When the model is £rst forced with a single frequency f_j, one sees the response, instead of at the original (non-Milankovitch) frequency $f_0 \approx 7kyr^{\ 1}$, showing up at integer multiples of the forcing frequency f_j, so that the

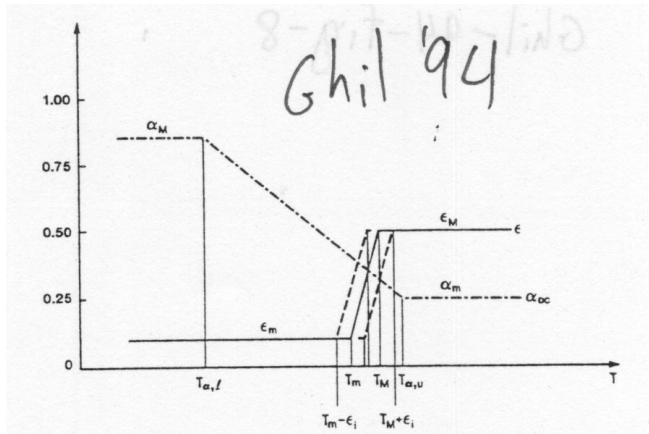

Fig. 8. The accumulation-to-ablation ratio $\varepsilon(T)$ (solid line) and the oceanic albedo $\alpha_{oc}(T)$ (dash-dotted line) as a function of globally-and-annually averaged temperature T (from [68]). The two parallel dashed lines are explained in Section 5.1, Eqs. (5.1a–c).

Figure 57: Sea ice albedo and accumulation factor as function of temperature (Fig. 8 from Ghil [14])

system oscillates at frequencies kf_j, with integer k, especially such that kf_j is close to the original unforced frequency f_0. This is again, as discussed in the case of El Nino, a nonlinear resonant response. When the model is forced with two Milankovitch frequencies the response is seen at "combination tones" of the form $k_1 f_1 + k_2 f_2$. This could be with a "sum tone" $k_1 k_2 > 0$ or a "difference tone" $k_1 k_2 < 0$. For suf£ciently strong Milankovitch forcing, one gets a chaotic response with many different combination tones. In particular, the dominant response tone turns out to be at a frequency

$$\frac{1}{109} kyr^{-1} = f_1 - f_2 = \frac{1}{19} kyr^{-1} - \frac{1}{23} kyr^{-1}$$

So that we obtain an explanation of the 100 kyr as a nonlinear response to the two major precession frequencies! While the spectrum of this response is quite satisfactory, with the 109 kyr frequency dominating the 41, 23 & 19 kyr frequencies (Fig. 58), the detailed characteristic features of the time series, are perhaps not completely satisfactory (Fig. 59) when compared to the proxy (in particular ice core) records.

However, additional efforts to use combination tones of Milankovitch frequency to explain the 100 kyr peak continue, and Rial [51], for example, recently suggested a 'simple' explanation for the glacial cycle time scale based on the following combination tones ...

$$\frac{1}{107} kyr^{-1} = \frac{1}{95} kyr^{-1} - \frac{1}{826} kyr^{-1}.$$

Given the need to use some nonlinear mechanism together with the Milankovitch signal to explain the 100 kyr period, Paillard [40] suggested that the mechanism might be jumps between steady states of the climate system, driven by Milankovitch forcing. Such jumps between different steady states imply an important nonlinearity in the climate system that allows the existence of such multiple steady states and the jumping between them (both could not exist in a linear system). Paillard argues for separating the ice volume and global temperature and allowing them to be independent (yet coupled) degrees of freedom. He also assumes the glacial cycles to be due to jumps of the climate system between three different modes: ***i*** (interglacial), ***g*** (mild glacial), and ***G*** (full Glacial). Rules are *speci£ed* for the transition between these modes

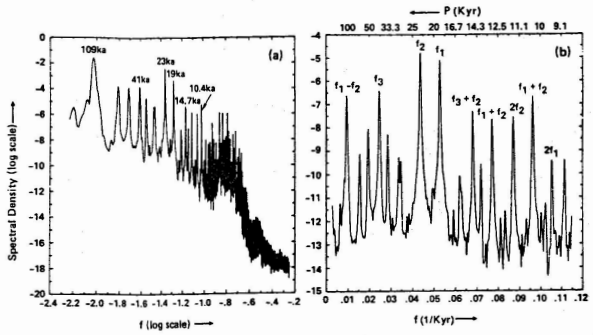

Fig. 10. Power spectrum of (a) simulated marine $\delta^{18}0$ and (b) ice-core $\delta^{18}0$ records. The periods associated with the labeled peaks in panel (b) are, from left to right, 109 kyr, 41 kyr, 23 kyr, 19 kyr, 14.7 kyr, 13 kyr, 11.5 kyr, 10.4 kyr and 9.5 kyr (from [90]).

Figure 58: Spectrum of chaotic model regime, showing a 100 kyr peak (Fig. 10 from Ghil [14])

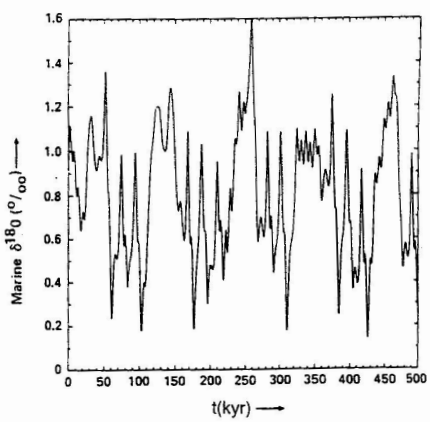

Fig. 11. Model-simulated marine $\delta^{18}0$ record; its power spectrum appears in Fig. 10a (from [90]).

Figure 59: Time series of the same model as in the previous £gure [Fig. 11, Ghil [14]]

- $\boldsymbol{i} \rightarrow \boldsymbol{g}$ (glaciation begins) occurs when the insolation decreases below a threshold i_0.
- $\boldsymbol{g} \rightarrow \boldsymbol{G}$ (glaciation approaching its maximum) occurs when the ice volume increases above some threshold value v_{max}.
- $\boldsymbol{G} \rightarrow \boldsymbol{i}$ (deglaciation) occurs when the insolation increases above some threshold i_1, where $i_1 > i_0$.

The equation determining the ice volume evolution at each "mode" or "regime" (indicated by the index R which can take the values $\boldsymbol{i}, \boldsymbol{g}, \boldsymbol{G}$) is

$$\frac{dV_{ice}}{dt} = -\frac{V_R - V}{\tau_R} - \frac{F}{\tau_F}$$

where the ice volume to which the system is restored at each mode is different

$$V_i = 0; \qquad V_g, V_G = 1$$

and where F is the Milankovitch summer radiation. This model may be seen as an extension of the Imbrie and Imbrie model to a multiple-regimes scenario. The results of this model £t the SPECMAP record very nicely (Fig. 60), although perhaps this is not completely surprising given the quite a few available tuning parameters ($V_R, \tau_R, R = \{i, g, G\}$).

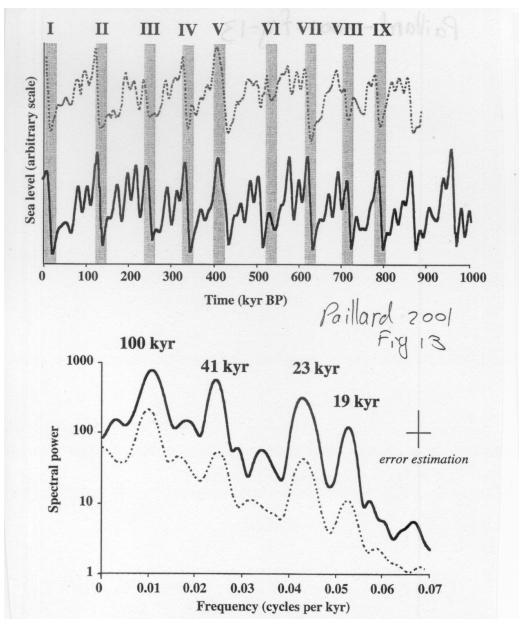

Figure 60: Fig. 13 from Paillard 2001

This model does not provide us with an explanation of what the actual physical mechanism is, what component of the climate system is responsible for the thresholds/ multiple modes, why are the relaxation times τ_R different for each regime and what determines them, etc.

This simple model does indicate that thresholds and rapid transition processes are important. It also demonstrates that one can get a good £t to observations due to a phase locking to Milankovitch forcing, as also shown by Saltzman's models and discussed next. This is the same phenomenon discussed in the context of El Nino and seen in Fig. 28: any nonlinear oscillator with a time scale of roughly 100 kyr that is constructed based on some internal variability mechanism yet is driven by Milankovitch radiation is likely to be phase locked to the

Milankovitch forcing. A phased locked glacial oscillation is shown for example in Fig. 61 from the work of Gildor and Tziperman [16] discussed below. Thus it seems that while the 100 kyr Milankovitch forcing plays no signi£cant role in glacial dynamics, the phase locking to 19, 23 and 41 kyr accounts for the observed phase of the oscillations; that is, for the observed timing of deglaciations. Note that because the Milankovitch forcing is not periodic but rather quasi-periodic and therefore somewhat irregular in time, the locking of the glacial cycle to the Milankovitch forcing also induce somewhat irregular glacial cycles. In particular, this explains the variability of the glacial period around 100 kyr between different glaciations. It seems, therefore, that the irregularity of the glacial cycles is likely due to the quasi-periodic nature of Milankovitch forcing, rather than an indication that the glacial dynamics themselves are chaotic.

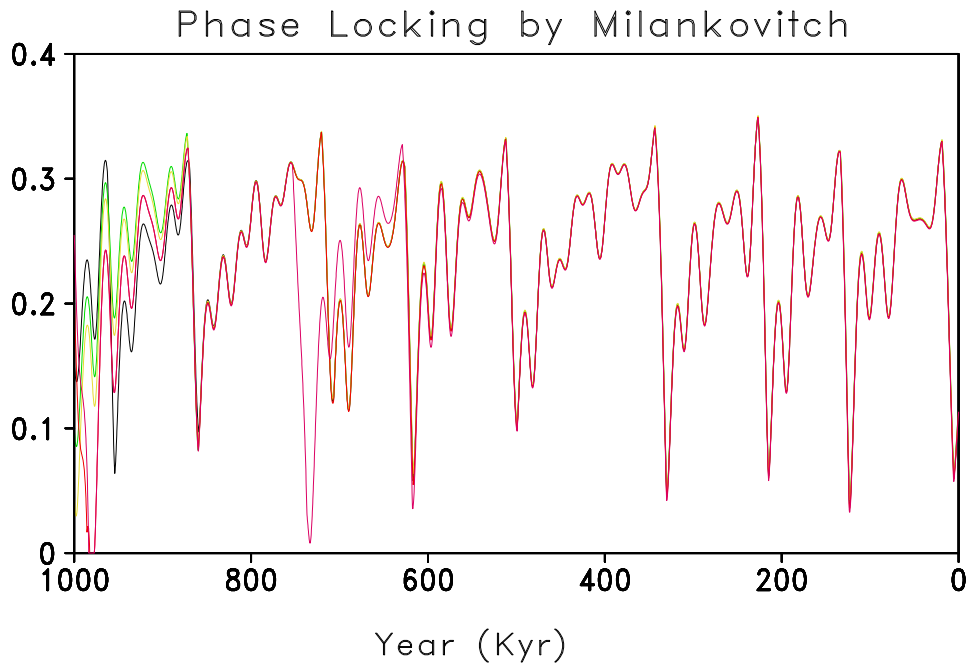

Figure 61: Phase locking to Milankovitch: land ice volume as function of time for six different model runs having different initial conditions. All runs converge fairly rapidly to a single time series as they are all locked to the phase imposed by speci£ed Milankovitch forcing (Gildor and Tziperman, [16]).

9.1.4 Glacial oscillations based on isostatic adjustment + Milankovitch + Calving

Another effort to obtain a 100 kyr glacial cycle from Milankovitch forcing is based on a nonlinear version of the load accumulation linear mechanism discussed in section 9.1.2 and based on the isostatic adjustment. To do that, the nonlinear dynamics of ice sheet ¤ow is added, as well as a calving parameterization (Pollard, [48, 49]). The Milankovitch forcing is speci£ed, similarly to [33], by making the equilibrium line location vary with the Milankovitch radiation at, say, 55N:

$$E(y,t) = E_0 + E_1 y + E_2 Q(55\ )$$

The results are shown in Fig. 62 and the £t to the observed global ice volume is not too bad (lowest panel of that Figure). It turns out, however, that when trying to formulate a model that uses isostatic adjustment to obtain the 100 kyr glacial cycles, one needs to use too long time scale for the isostatic adjustment (10 kyr instead of the more realistic 3 kyr) in order to obtain a good £t to observations. Furthermore, one needs to add quite a few additional feedbacks such as the topography of the crust (which enters the isostatic adjustment parameterization

discussed above, and affects the initial ground height, which is important for the source-sink function for the glacier mass balance), and a calving parameterization. Overall, it seems that too many different feedbacks are needed (Fig. 62) and that this mechanism is not as simple and clean as one would have hoped given the seemingly simple structure of the glacial signal.

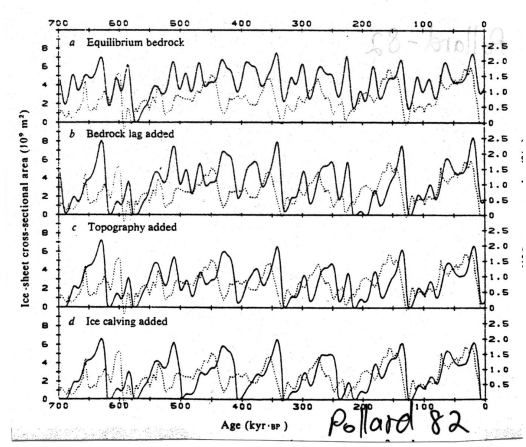

Figure 62: Fit of a glacial model results to observations. The complexity of the feedbacks used increases from the upper panel toward the lower one. See text for details. (Fig. 1 from Pollard [48]).

9.1.5 Stochastic resonance

An elegant mechanism that combines 100 kyr Milankovitch forcing with stochastic noise forcing has been suggested by Benzi, Parisi, Sutera and Vulpiani [3]. This mechanism is not likely to be a correct explanation for the glacial dynamics, yet the physical idea seems to have found many interesting applications outside the research area of climate dynamics, so it is worth examining. Consider a simple model of the climate system that is governed by a zero-dimensional global energy balance model equation such as

$$\frac{dT}{dt} = R_{in}(T) - R_{out}(T) + \sigma\eta(t) = F(T) + \sigma\eta(t) = -\frac{\partial\Phi}{\partial T} + \sigma\eta(t)$$

where $R_{in}(T)$ and $R_{out}(T)$ are the incoming and outgoing radiation terms and $\sigma\eta(t)$ is a white noise term due to internal noise of the climate system (e.g. weather). The potential function $\Phi(T)$ chosen such that it has two minima where $F = -\partial\Phi/\partial T = 0$ at the two temperatures T_1, T_2, which represent stable equilibria corresponding to glacial and interglacial conditions) separated by a maximum (an unstable equilibrium point). More explicitly, the potential Φ is given by

$$F(T) = -\frac{\partial\Phi}{\partial T} = \frac{\varepsilon(T)}{C} \times \frac{\mu(t)}{1+\beta(1-T/T_1)(1-T/T_2)(1-T/T_3)},$$

with

$$\mu(T) = 1 + 0.0005\cos(\omega t); \qquad \omega = 2\pi/10^5 years$$

representing the 100 kyr orbital forcing frequency. The system is therefore driven by both slow small amplitude oscillations in the potential due to Milankovitch forcing, $\mu(t)$, and by the white noise $\sigma\eta(t)$. To see the potential function, try in Matlab:

```
for i=1:40; f(i)=1.0/(1+ 0.1*(1.0-i/10.1)*(1.0-i/20.1)*(1.0-i/30.1));end; plot(f)
g(1)=0; for i=1:40; g(i+1)=g(i)+f(i)-1; end; plot(g)
```

The effect of $\mu(t)$ is to lower and raise the two minima of the potential with respect to the middle barrier, as shown in Fig. 63. In the absence of the white noise, the system undergoes small oscillations about one of the stable steady states due to the oscillations in $\mu(t)$. Similarly, in the absence of the periodic changes to the potential, the white noise term induces variability depending on its amplitude: if the white noise is not suf£ciently strong, there would be no transition in this case between the minima, but only small stochastic variability about one of the minima; if the stochastic forcing is strong enough, there is some probability of jumping between the stable equilibria, but with no preferred periodicity.

Now, suppose that both the stochastic white noise forcing and slow 100 kyr variations act together. Assume further that the white noise by itself is not suf£ciently strong to induce transitions between the equilibria. Such transitions may still be possible because of the slow variations in the potential induced by $\mu(t)$: when these slow variations lower the potential barrier as in panel A of Fig. 63, the white noise may be suf£ciently strong to cause a transition from the left to the right potential wells. The next transition will be possible when the potential barrier is reduced for the potential well on the right (panel C). As a result of this combination of white noise and slow modulations of the potential well, the system will produce a preferred periodicity at 10^5 years and a corresponding spectral peak at that frequency. This is termed "stochastic resonance" because a too weak noise wont induce transitions, and too strong noise will not show the preferred periodicity (it the stochastic forcing would then be able to induce transitions regardless of the slow oscillations in the potential). That an optimal noise level is needed, justi£es the use of the term "resonance".

Because this mechanism relies on the 100 kyr Milankovitch signal which is very weak climatically, and because the resulting time series does not have the saw tooth structure, the stochastic resonance is not a likely candidate for the 100 kyr glacial cycle mechanism. Furthermore, the mechanism is formulated in very general terms, avoiding the issues of what is the source of the white noise, which speci£c climate component is responsible for the double well potential (this needs to be some nonlinearly behaving component that allows for multiple minima), etc. This mechanism therefore does not make speci£c physical predictions that may be falsi£ed beyond the shape of the time series which, as mentioned above, is already inconsistent with the observed one.

9.1.6 "Earth-system" models (Saltzman et al.)

In a series of works, Saltzman and co-workers have used various models that are all based on a similar approach: write a set of three ordinary differential equations for three prognostic climate variables; include various linear and nonlinear feedbacks between the three variables; while allowing the physical assumptions and prognostic variables that vary somewhat from work to work, always assume that: (1) the system should have a free (self sustained) oscillation of roughly 100,000 year period; (2) Milankovitch forcing provides the precise phase of the oscillation via nonlinear phase locking. In many of these works CO_2 is assumed to be a key variable that maintains the 100 kyr oscillation which will not exist without it. The set of feedbacks used for example by Saltzman and Sutera [52] is shown in Fig. 64.

Let us consider two examples of feedback loops used in this approach and see how they are converted into a mathematical form. In the following, $\xrightarrow{\oplus}$ and $\xrightarrow{\ominus}$ correspond to a positive and negative feedbacks, correspondingly:

1. (#2 in Saltzman and Sutera [52], p 740): Increased marine-based ice volume $\xrightarrow{\oplus}$ increased marine ice area and albedo $\xrightarrow{\ominus}$ decreased temperature and therefore decreased source term for land glacier mass balance (via temperature-precipitation feedback) $\xrightarrow{\oplus}$ decreased land ice volume. Bottom line, it's a negative feedback, add a term to the equation for the land ice volume that depends on the marine ice

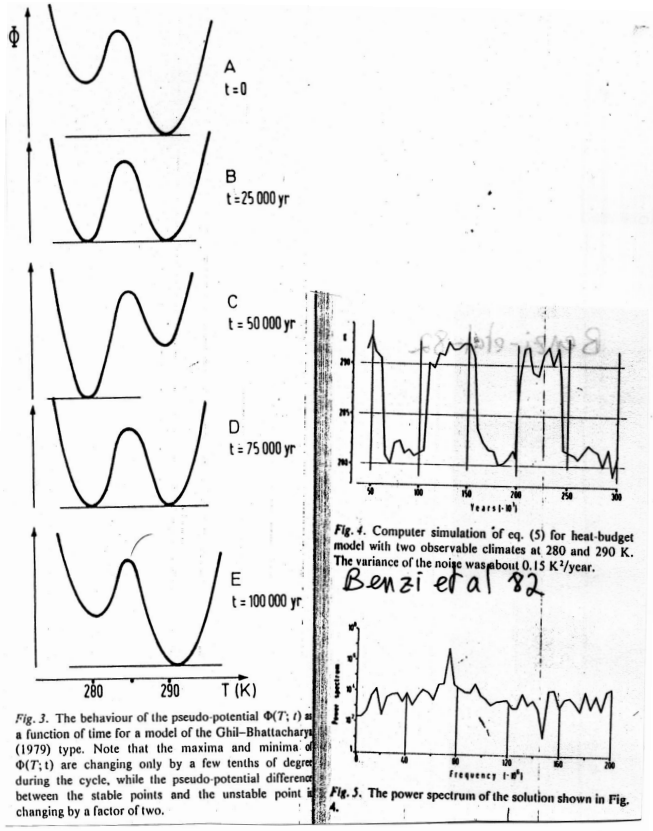

Figure 63: Figs. from Benzi et al showing potential function and time series of transitions

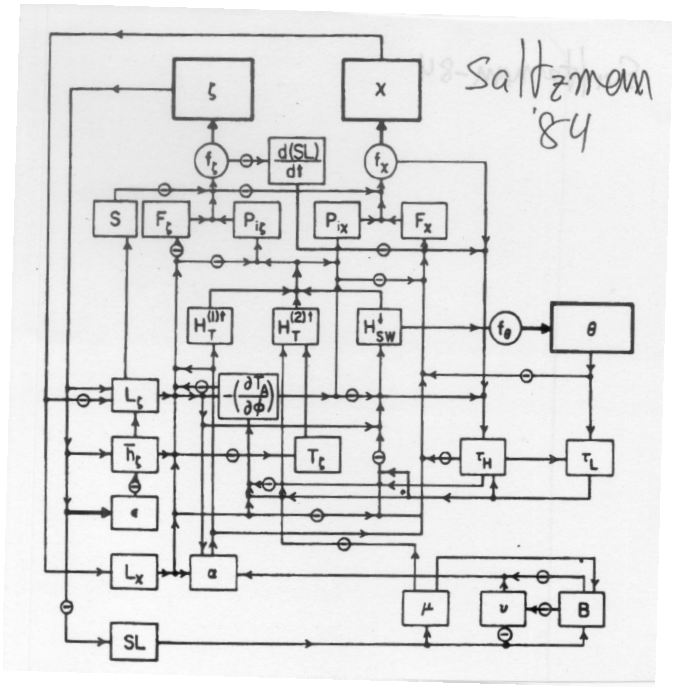

Figure 64: A set of feedbacks included in a simple climate model... (Fig. 3 from Saltzman and Sutera [52]).

volume

$$\frac{dV_{land\,ice}}{dt} = \ldots - C_1 \times [\text{marine based ice}]$$

2. CO_2 feedback (#11 in Saltzman and Sutera [52], p 741): increased land ice volume $\rightarrow\!\ominus\!\rightarrow$ reduced sea level $\rightarrow\!\oplus\!\rightarrow$ reduced atmospheric CO_2 (why...?) $\rightarrow\!\ominus\!\rightarrow$ increased outgoing long-wave radiation increased accumulation over land glaciers $\rightarrow\!\ominus\!\rightarrow$ increased land ice volume. Bottom line: a positive feedback

$$\frac{dV_{land\,ice}}{dt} = \ldots + C_2 \times V_{land\,ice}$$

The resulting set of nondimensional equations (from Saltzman [53]) is of the form

$$\begin{aligned}
\frac{dX}{dt} &= -\alpha_1 Y - \alpha_2 Z - \alpha_3 Y^2 \\
\frac{dY}{dt} &= -\beta_0 X + \beta_1 Y + \beta_2 Z - (X^2 + 0.004Y^2)Y + F_Y \\
\frac{dZ}{dt} &= X - \gamma_2 Z
\end{aligned}$$

where in this particular case X, Y and Z are the ice mass, deep ocean temperature and atmospheric carbon dioxide. The £t to the global ice volume proxy curves in these models is normally quite impressive (Fig. 65). This is not necessarily a surprise, as the quite a few coef£cients in the above three equations are chosen to optimize this £t.

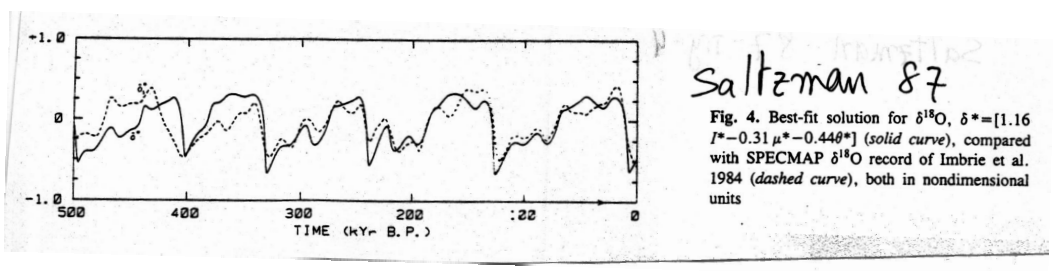

Figure 65: Fit of model to global ice volume proxy data. Fig. 4 from Saltzman [53]

Of course, one needs to be very careful in trying too hard to £t model results to proxy data, as shown by the excellent £t of the above model to a CO_2 curve deduced from some indirect proxy data (Fig. 66). This £t was obtained before the much more reliable paleo CO_2 ice core data became available, which does not seem at a;; close to the £tted proxy of Fig. 66.

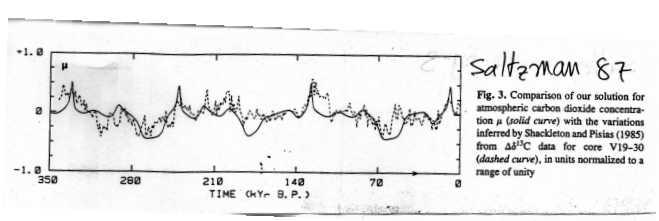

Figure 66: Fit of model results to CO_2 proxy. Fit is quite wonderful, but the proxy data turned out later not to be very accurate... (Fig. 3 from Saltzman [53]).

The parameterization of physical processes is quite vague in these models (e.g. “we are assuming that positive feedbacks due to ice albedo and ice baroclinicity effects, bedrock depression, and sea level changes can roughly

balance the dissipative tendencies"... or "the second order nonlinear term $-a_2\mu'^2$ is included to represent the weakening of the climate forcing of ice accumulation as increasing sea ice and cold ocean surface temperatures associated with decreasing μ reduce the sources for snowfall over the ice sheets"). This vagueness often does not allow the model to make speci£c predictions that may be falsi£ed by observations.

These models do teach us one important lesson: it seems likely that practically any model that has a free (self-sustained) nonlinear oscillation at about 100 kyr period and that is forced by Milankovitch forcing will result in a good £t to the global ice volume proxy curves, so that these two elements seem a robust part of the glacial puzzle. Saltzman's philosophy was to consider numerous climate feedbacks such that "... a qualitative judgment must be made concerning the dominance of one [feedback] over the other. The ultimate test of the validity of the judgment is the agreement of the output with the observational evidence". This approach and the good £t to observations it yields might have been useful initially, but the next step in understanding the glacial oscillations must be based on a more detailed and speci£c model that makes speci£c ***falsi£able*** predictions that may be tested using the paleo record.

9.1.7 Some additional glacial mechanisms and models

There are quite a few more glacial theories that we shall not describe here, some of which are worth mentioning at least brie¤y:

1. Thermohaline circulation (as an explanation for ice ages, and/ or for the global scale of the glacial signal). This mechanism is based on the following feedback loop. A stronger THC results in more poleward heat transport, therefore in more melting of land ice. This results in a fresh water input into the oceans which weakens the THC, and so on, leading to an oscillation. Note that the THC is often also mentioned as the source of multiple steady states in the climate system (e.g. [40]); these ideas are more often than not formulated descriptively (Fig. 67) and sometime a bit vaguely rather than using a speci£c mathematical model for the thermohaline circulation.

2. Some older and/ or just likely wrong ideas for the source of the glacial cycles: Volcanic eruptions, the earth passing through interplanetary dust clouds every 10^5 years; The lost continent of Atlantis ...

3. DMS feedbacks (Charlson, Lovelock et al [7]). Here the feedback loop is as follows: increased temperature $\rightarrow$ more biological productivity $\rightarrow$ more Dimethylsulphide (CCN) $\rightarrow$ more clouds $\rightarrow$ higher albedo $\rightarrow$ lower temperature. etc, again leading to an oscillation. On the other hand DMS feedbacks may act in a different way (Watson and Liss [64]): ice cores seem to show that colder periods have more DMS $\rightarrow$ biology caused additional cooling and therefore helped amplifying the glacial signal.

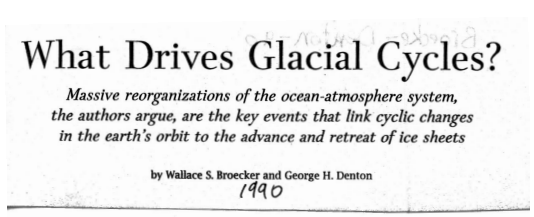
What Drives Glacial Cycles?

Massive reorganizations of the ocean-atmosphere system, the authors argue, are the key events that link cyclic changes in the earth's orbit to the advance and retreat of ice sheets

by Wallace S. Broecker and George H. Denton

1990

Figure 67: A thermohaline theory for the glacial cycles

9.2 Sea-ice switch mechanism

Gildor and Tziperman [16, 18, 17] proposed that there are three major components that determine the glacial cycle dynamics: land ice, global temperature, and sea ice extent. Their mechanism is based on the temperature-precipitation feedback, modi£ed by the effects of sea ice which acts as a "switch" of the climate system, switching it from glaciation to deglaciation modes. The model used to demonstrate the sea ice switch mechanism was a detailed box model with prognostic sea ice, an 8-box ocean model for the THC temperature and salinity, a prognostic land ice model, and an atmospheric 4-box energy balance model. However, the essence of the mechanism may be described using a far simpler toy model used by [60]. We start by assuming, based on the results of the more detailed model, that the sea ice area is very sensitive to the climate temperature, and jumps from very small area to large area as the temperature decreases below some critical freezing temperature. In the detailed box model mentioned above, the sea ice growth occurs within some 50 years and is accelerated by the sea ice albedo feedback. Note that a similar assumption regarding the dependence of sea ice albedo on the temperature was used for example by [33] as shown in Fig. 57. This assumption allows us to parameterize the sea ice area as function of atmospheric temperature

$$a_{sea\ \ ice} = \begin{cases} \delta I^0_{sea\ \ ice} & T > T_f \\ I^0_{sea\ \ ice} & T < T_f \end{cases} \tag{38}$$

where $I^0_{sea\ \ ice}$ is the maximal sea ice area during a cold period, and $\delta I^0_{sea\ \ ice}$ represents the much smaller sea ice area during warm periods. Snow accumulation over the land glaciers is assumed to depend on both the temperature (temperature-precipitation feedback) and the extent of sea ice (due to its effects on the precipitation over land ice via limiting evaporation from the polar ocean and via the diversion of the storm track, see previous lecture),

$$P(T, a_{sea\ \ ice}) = (P_0 + P_1\, q(T)) \times \left(1 - \frac{a_{sea\ \ ice}}{a_{ocn}}\right)$$

where a_{ocn} is the ocean area. The humidity $q(T)$ appearing in the last equation is determined by the approximate Clausius-Clapeyron equation

$$q(T) = q_r\, \varepsilon_q A \exp(-B/T)/P_s.$$

The ablation is function of the temperature and of the 41 kyr component of the Milankovitch summer radiation,

$$S_{abl}(T,t) = S_0 + S_M \sin(2\pi t/41kyr) + S_T T.$$

The two prognostic model equations may now be written for the land ice mass balance

$$\frac{dV_{land\ \ ice}}{dt} = P(T, a_{sea\ \ ice}) - S_{abl}(T,t)$$

and for the global temperature

$$\frac{dT}{dt} = -\varepsilon\sigma T^4 + H_s(1 - \alpha_s \frac{a_{sea\ \ ice}}{a_{ocn}})(1 - \alpha_L \frac{a_{land\ \ ice}}{a_{land}})(1 - \alpha_C)$$

where the albedos of sea ice, land and clouds are represented by $\alpha_s, \alpha_L, \alpha_C$ respectively. These equations result in a self-sustained 100 kyr oscillations even without the Milankovitch forcing, which are basically the same as the oscillations of the more elaborated box model. Fig. 68 shows the results of the detailed box model with no Milankovitch forcing, which we now use to explain the different stages in the sea ice switch mechanism for the glacial cycles.

- start at $t = 200$ kyr; An interglacial period, warm ocean and atmosphere, no glaciers over land and no sea ice (sea ice switch is "off")

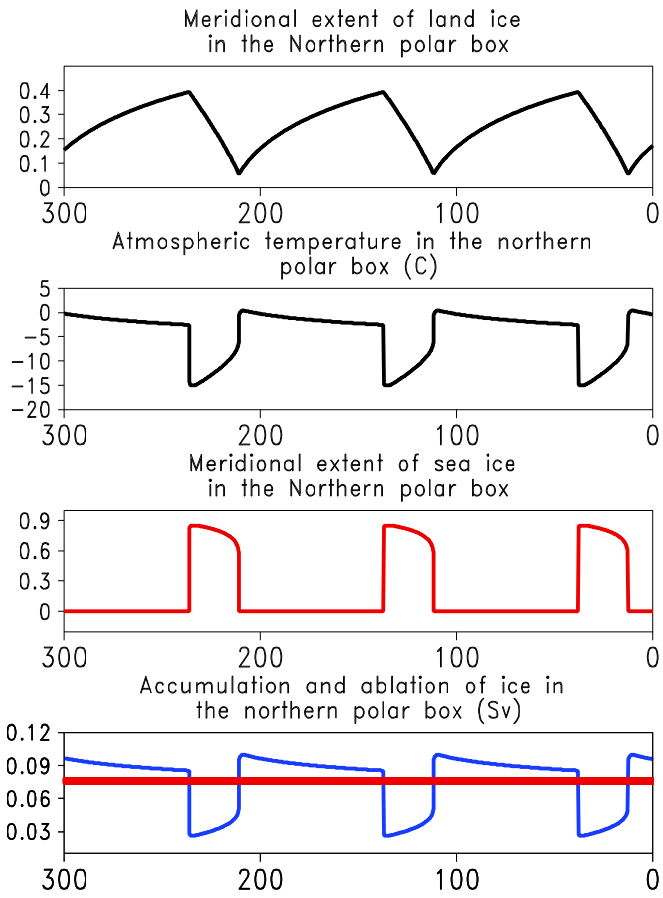

Figure 68: The sea ice switch glacial cycle mechanism. Shown are the results of the box model of [18] as function of time; time is plotted "backward", in units of 10^3 years before "present".

- The warm and therefore moist atmosphere results in a large snow accumulation rate, and the glaciers grow slowly (panel a). Land albedo therefore increases and this results in a slow cooling (panel b). This stage lasts some 70-90 kyr.

- $t = 130$ kyr; The general slow cooling £nally causes the upper ocean to cool to the freezing temperature. At this stage a large sea ice cover forms within a few decades, growth being accelerated by the sea ice albedo feedback: once some sea ice is formed, its albedo effect cools the atmosphere, which in turns cools the ocean, leading to the formation of more sea ice. The sea ice growth is also self-limiting: a large sea ice cover insulates the ocean from the cold atmosphere, eventually preventing more cooling of the ocean and more sea ice growth. Sea ice tends to grow at a uniform thickness of some 2-4 meters, rather than grow in thickness. At this time the sea ice switch is "on", panel c; this is the glacial maximum: large glaciers, extensive sea ice, cold atmosphere and ocean.

- The large sea ice area cover results in a cold and therefore dry atmosphere. This implies a low rate of precipitation, so that ablation (melting) of glaciers is larger than accumulation (panel d), and the start of deglaciation.

- $t = 110$ kyr; land glaciers withdraw and land albedo gets smaller. The atmospheric and oceanic temperature therefore increases, until the ocean warms suf£ciently and sea ice melts within decades again (switch is "off"). The climate system is back to the initial state, and the cycle starts over.

Bottom line: land glaciers grow during warm periods when there is no sea ice cover, and withdraw during cold period when there is an extensive sea ice cover. Note the hysteresis effect which may be seen by plotting the sea ice extent vs land ice volume throughout the cycle.

9.2.1 Mid-Pleistocene transition from 41 kyr to 100 kyr glacial cycles

Earth's climate has been gradually cooling over the past few millions of years due to gradual CO_2 drop induced by tectonic weathering processes (Fig. 2). This cooling was suggested as a possible source of the change in the character of the glacial oscillations during the Mid-Pleistocene, some 1 Myr ago (Fig. 3), from a 41 kyr oscillation to a 100 kyr oscillation (Maach and Saltzman [34]). An alternative/ complementary explanation has been a hypothesized gradual increase of land ice sheets (Ghil and Childress [15]).

A theory for the glacial cycles should certainly also explain the mid-Pleistocene change in the characteristics of these cycles. Let us consider here a speci£c mechanisms for the Mid-Pleistocene transition, based on the sea ice switch mechanism. Begin by considering the accumulation of snow over land ice as function of some averaged global atmospheric temperature (Fig. 69).

Note £rst that due to the temperature-precipitation feedback, a warmer temperature implies a larger precipitation rate, and therefore a larger rate of snow accumulation over land glaciers. This regime is seen to the right of the vertical dash line in the £gure. If the temperature is yet warmer (beyond point (a) in Fig. 69), precipitation falls as rain instead of snow, and the rate of accumulation drops. Now, at colder temperatures, extensive sea ice forms at at some critical temperature as the ocean reaches the freezing point, and this reduces the accumulation rate because of the effects of sea ice on the atmospheric temperature, on the storm track, and on limiting evaporation from the polar ocean as discussed above. We have seen that the growth of an extensive sea ice cover occurs at some critical temperature, so it in fact induces a jump in the accumulation rate at that temperature, as seen in the vertical dash line in the £gure. Below the temperature at which sea ice forms, the accumulation rate is small and is less sensitive to the temperature changes.

The ablation of land ice is expected to increase with increasing temperature which enhances melting (red dotted line in £gure), and we also note again that ablation is also strongly controlled by summer solar radiation (Held [22]).

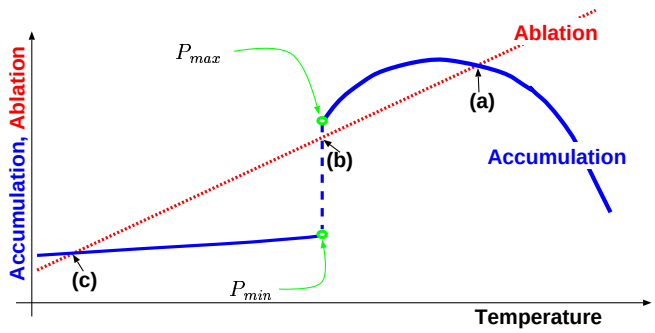

Figure 69: Schematic plot of ablation and accumulation as function of temperature.

Proxy observations indicate a very warm deep ocean a few Myr ago, of the order of 15 degree C. Let us consider, therefore, the effect of the deep ocean temperature on the accumulation - temperature relation (Fig. 70).

A warm deep ocean leads to weaker vertical strati£cation, and therefore stronger mixing between deep and surface ocean. As a result, the entire ocean, not only the upper ocean, needs to be cooled to create sea ice. Stronger vertical mixing also leads to stronger THC (Bryan, [5]), and therefore to higher polar temperatures. These effects mean that, when deep ocean is warmer, atmospheric temperature needs to be colder before sea ice can form. This amounts to a change in the value of T_f of equation (38). This all means that when the deep ocean is warmer, the vertical dash line representing the jump in accumulation due to the formation of sea ice is further to the left as seen in the upper panel of Fig. 70. This £gure is the base for our speculations regarding the Mid-Pleistocene transition.

Consider the climate steady states and their stability based on Fig. 70.

- At points (a,b,c) in the upper panel of Fig. 70, ablation equals accumulation, so that the land glaciers and therefore the climate system is in steady states at these temperatures.

- By considering the effects of small temperature changes on the accumulation and ablation rates, it is easy to see that points (a) and (c) are unstable steady states, leading in the direction of runaway greenhouse and snowball earth scenarios. Suppose, for example, that the climate system is at point (a) and consider a small warm temperature perturbation. The small warming leads according to the £gure to a regime in which the ablation is larger than the accumulation, so the glaciers would withdraw. The albedo effect of the withdrawing glaciers leads to further warming, hence a positive feedback that results in an instability that causes the climate to get away from point (a). Similar considerations show that point (c) is also unstable.

- For warm deep ocean (upper panel of Fig. 70), point (b) is a stable steady state. Adding the effect of Milankovitch variations on ablation, results in small, linear, symmetric oscillations around this steady state. This is the proposed mechanism of the 41 kyr glacial variability prior to the Mid-Pleistocene. Admittedly this does not explain why the oscillations prior to the bifurcation point are of a period of 41 kyr and not 19 or 23 kyr, and this would have to wait for further work.

- For cold deep ocean, point (b) is no longer on the accumulation curve in the lower panel of Fig. 70, because it lies on the sea-ice induced jump in accumulation. This is the regime in which the sea ice switch 100 kyr glacial oscillations occur, as described in the following section.

So, a deep ocean cooling induces a transition from symmetric 41 kyr oscillation to asymmetric nonlinear 100 kyr oscillation. This is due to a bifurcation of the climate system due to the change in the accumulation temperature relation as described above. That this is a bifurcation means that there is a threshold that the deep ocean cooling

crosses in order to have the system cross the bifurcation point (that is, make point (b) lie on the vertical dash line). This is the proposed mechanism for the observed climate shift of 1 Myr ago [60]. Note that since the deep water cooling needs to cross a certain threshold to activate the sea ice switch oscillations, it does not matter when most of the deep ocean cooling has occurred (presumably more than a few million years ago), but only when the threshold was crossed by T_f in equation (38) (which we speculate has happened one Myr ago).

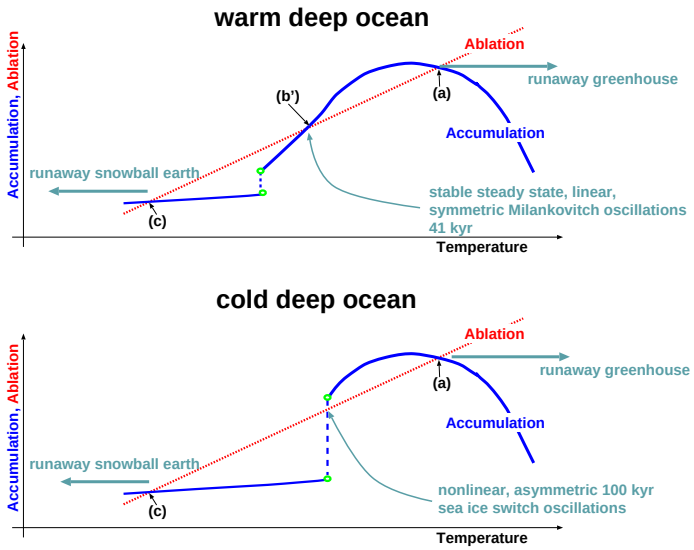

Figure 70: Ablation and accumulation as function of temperature, for warm and for cold deep ocean states.

Making T_f in (38) a slowly varying function, decreasing with time, and integrating the above simple model of the sea ice switch mechanism, we obtain the results in Fig. 71, showing a Mid-Pleistocene like transition from small amplitude 41 kyr oscillations to larger amplitude 100 kyr glacial oscillations. It would certainly be interesting to perform a more careful bifurcation analysis to £nd out precisely what kind of a bifurcation the Mid-Pleistocene transition corresponds to in this model. . .

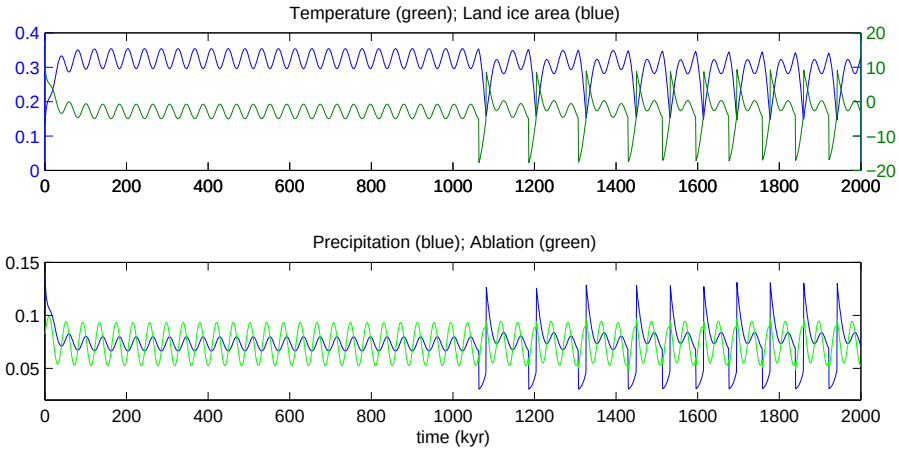

Figure 71: A simulation of the mid-Pleistocene transition from [60].

9.3 Biogeochemical toy models for glacial CO2 variability

Given the clear signal of glacial-interglacial CO_2 changes (Fig. 37), it is natural to wonder if CO_2 variations cause the glacial cycles via their greenhouse effect. Alternatively, could the CO_2 variations have been caused by the glacial cycle in the physical climate system so that they only served to amplify the glacial variability? We only discuss here the possibility that CO_2 variations are driven by the glacial cycles rather than being an essential element for the existence of these cycles. We therefore need to explain how the CO_2 variations are caused. As a background material, the reader is referred to the various geochemical textbooks for a review of some of the relevant feedbacks and issues [63], including the following terms.

1. Soft tissue pump (reduces atmospheric CO_2).
2. Hard tissue pump (increases atmospheric CO_2 due to Alkalinity effects).
3. Solubility pump: increased atmospheric CO_2 when the ocean warms.
4. Red£eld ratio: **106 C : 16 N : 1 P**.
5. Productivity (and its dependence on light and nutrients), export production.
6. Iron fertilization (possible increase in biological productivity in high latitudes during the last glacial maximum; effects of increased dust levels etc.
7. CO_2 gas exchange between ocean and atmosphere; dominance of oceanic carbon reservoir, and especially of the deep ocean reservoir.

9.3.1 Atmospheric CO_2 and vertical ocean mixing

Toggweiler [57] has used a variety of box models, starting with the simplest 3 box model (Fig. 72) to propose a geochemical mechanism for the glacial changes in atmospheric CO_2.

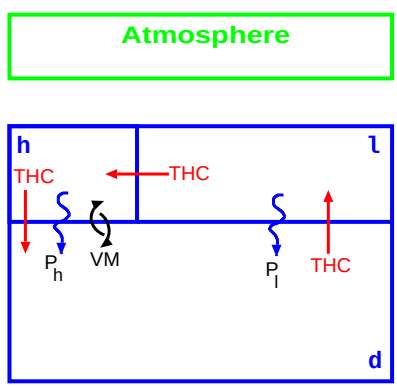

Figure 72: A box model for glacial-interglacial CO_2 variations. The boxes represent the upper mid-latitude ocean (l), the surface polar ocean (h) and the deep ocean (d), as well as the atmosphere.

In the box model of Fig. 72, one may write the (total) carbon ΣCO_2 balance for the deep box under steady-state conditions as a balance of advection (by the thermocline circulation THC) and mixing (by VM, via some internal wave mechanism), plus a term that represents the sinking of carbon from the surface boxes to the deep box as part of the export production from the low and high latitude surface boxes $P_l + P_h$:

$$0 = (VM_{hd} + THC) * (\sum CO_{2h} - \sum CO_{2d}) + Red_{C:P}(P_l + P_h),$$

where $Red_{C:P}$ is the Red£eld Ratio. Assume $P_l = THC * PO_{4d}$, which means that we assume all the surface nutrients in the mid-latitude box to be utilized by the biological activity and be converted to export production. Further assume $P_l \gg P_h$ meaning again that the mid-latitude biological activity is very ef£cient, acts over a larger area relative to that of the high latitudes, and therefore utilizes all the available nutrients. Using these assumptions we have

$$\sum CO_{2d} - \sum CO_{2h} = Red_{C:P} \frac{THC * PO_{4d}}{VM_{hd} + THC}.$$

For a suf£ciently fast gas exchange with the atmosphere, upper ocean $\sum CO_2$ in lower and higher latitudes are equal, so that

$$\sum CO_{2d} - \sum CO_{2l} \sim Red_{C:P} \frac{THC * PO_{4d}}{VM_{hd} + THC}, \tag{39}$$

which is the result we were after: the $\sum CO_2$ difference between the upper and deep ocean is controlled by vertical mixing and by the amplitude of the THC. A reduction in vertical mixing in the high latitude Southern Ocean should result according to (39) in an increase of the concentration of (total) carbon difference between the upper and deep ocean. Taking the deep ocean concentration to be constant due to its large reservoir, this implies a reduction of the surface total carbon and CO_2 concentration. Since the atmospheric CO_2 concentration is determined by that of the upper ocean, we can expect that a reduction of the vertical mixing in the Southern Ocean would lead to a reduction in atmospheric CO_2 [57]. However, this mechanism is not capable of explaining why the vertical mixing in the ocean should change, and this is what we do in the following section based on the sea ice switch mechanism again.

9.3.2 Sea ice switch and mechanism of vertical mixing change in the Southern Ocean

The biochemistry mechanism of Toggweiler [57] described in the above section speci£es a change in the vertical mixing between the deep and the surface Southern Ocean. However, no physical mechanism is provided for this change in the physical climate system. A physical mechanism for the vertical mixing changes that may result in the glacial-interglacial CO_2 variations was proposed by Gildor and Tziperman [17], based on the sea ice switch mechanism, as follows. The strati£cation in the Southern Ocean (SO) is composed of cold, fresh and therefore light water above warm, salty and therefore dense water. Glacial conditions in the northern hemisphere cool the North Atlantic Deep Water (NADW), and consequently, via the southward ¤ow of NADW, cool the deep temperature in the SO. Because of the permanent ice cover over Antarctica, the surface ocean temperature in the SO near Antarctica is close to the freezing point during the entire glacial cycle, so that it cannot cool very much even during glacial conditions in the northern hemisphere. Glacial conditions therefore increase the density of deep SO water but not of the surface SO water. This strengthens the vertical strati£cation in the SO. As a result, vertical mixing in the SO is expected to be reduced, based on a simple internal wave parameterization for the vertical mixing coef£cient such as $\kappa_v \propto \left(\frac{\partial \rho}{\partial z}\right)^{\alpha}$ (Gargett [13]). Thus we have explained the vertical mixing change in the Southern ocean as being a result of the northern hemisphere glaciation, and hence provided the missing link between the atmospheric CO_2 variations induced by the biogeochemistry and between the physical climate system.

Note that this mechanism implies that the northern hemisphere leads the southern hemisphere during the glacial cycles, and that temperature changes in the northern hemisphere lead CO_2 changes in the southern hemisphere. The time lag between the two hemispheres, and in particular between temperature northern hemisphere temperature and atmospheric CO_2, is expected to be the time it takes the cooling signal to propagate from the northern hemisphere to the southern hemisphere, via the advection of the NADW. This is roughly a time scale of 500-1500 years. The phase relation between the two hemisphere seems to still be under debate in the paleo literature.

References

[1] P. Bak, T. Bohr, and M. H. Jensen. Mode-locking and the transition to chaos in dissipative systems. *Physica Scripta*, T9:50–58, 1985.

[2] D. S. Battisti. The dynamics and thermodynamics of a warming event in a coupled tropical atmosphere/ocean model. *J. Atmos. Sci.*, 45:2889–2919, 1988.

[3] R. Benzi, G. Parisi, A. Sutera, and A. Vulpiani. Stochastic resonance in climatic change. *Tellus*, 34:10–16, 1982.

[4] W. S. Broecker. *The glacial world according to Wally*. Eldigio Press, 1995.

[5] F. Bryan. Parameter sensitivity of primitive equation ocean general circulation models. *J. Phys. Oceanogr.*, 17:970–985, 1987.

[6] N. Calder. Arithmetic of ice ages,. *Nature,*, 252:216–218, 1974.

[7] R. J. Charlson, J. E. Lovelock, M. O. Andreae, and S. G. Warren. Oceanic phytoplankton, atmopsheric sulphur, cloud albedo and climate. *Nature*, 326:655–661, 1987.

[8] K.M. Cuffy and G.D. Clow. Temperature, accumulation, and ice sheet elevation in central greenland through the last deglacial transition. *J. Geophys. Res.*, 102:26,383–26,396, 1997.

[9] H. A. Dijkstra. *Nonlinear physical oceanography*. Kluwer Academic Publishers, 2000.

[10] B. F. Farrell and P. J. Ioannou. Generalized stability theory part i: autonomous operators. *JAS*, 53:2025–2040, 1996.

[11] Brian Farrell. Optimal excitation of neutral Rossby waves. *J. Atm. Sci.*, 45:163–172, 1988.

[12] E. Galanti and E. Tziperman. On enso's phase locking to the seasonal cycle in the fast sst, fast wave, and mixed mode regimes. *Journal of the Atmospheric Sciences*, in press, 2000.

[13] A.E. Gargett. Vertical eddy diffusivity in the ocean interior. *J. Mar. Res.*, 42:359–393, 1984.

[14] M. Ghil. Cryothermodynamics: the chaotic dynamics of paleoclimate. *Physica D*, 77:130–159, 1994.

[15] M. Ghil and S. Childress. *Topics in Geophysical Fluid Dynamics: Atmospheric Dynamics, Dynamo Theory and Climate Dynamics*. Springer-Verlag, New York, 1987.

[16] H. Gildor and E. Tziperman. Sea ice as the glacial cycles climate switch: role of seasonal and milankovitch solar forcing. *Paleoceanography*, 15:605–615, 2000.

[17] H. Gildor and E. Tziperman. Physical mechanisms behind biogeochemical glacial-interglacial co_2 variations. *Geophys. Res. Letters*, 28:2421–2424, 2001.

[18] H. Gildor and E. Tziperman. A sea-ice climate-switch mechanism for the 100 kyr glacial cycles. *J. Geophys. Res.*, 106(C5):9117–9133, 2001.

[19] A. E Gill. Some simple solutions for heat-induced tropical circulation. *Quart. J. Roy. Meteor. Soc.*, 106:447–462, 1980.

[20] A. E Gill. *Atmosphere–ocean dynamics*. Academic Press, London, 1982.

[21] Z. Hao, J. D. Neelin, and F.F. Jin. Nonlinear air-sea interaction in the fast-wave limit. *J. Climate*, 6:1523–1544, 1993.

[22] I.M. Held. Climate models and the astoromical theory of ice age. *Icarus*, 50:449–461, 1982.

[23] A. C. Hirst. Unstable and damped equatorial modes in simple coupled ocean-atmosphere models. *J. Atmos. Sci.*, 43:606–630, 1986.

[24] T. J. Hughes. *Ice sheets*. Oxford University Press, 1998.

[25] P. Huybrechts and J. Oerlemans. Response of the antarctic ice sheet to future greenhouse warming. *Clim. Dyn.*, 5:93–102, 1990.

[26] J. Imbrie and J. Z. Imbrie. modelling the climatic response to orbital variations. *Science*, 207:943–953, 1980.

[27] F.-F. Jin. An equatorial ocean recharge paradigm for enso. part i: conceptual model. *J. Atmos. Sci.*, 54:811–829, 1997.

[28] F.-F. Jin. An equatorial ocean recharge paradigm for enso. part ii: a stripped-down coupled model. *J. Atmos. Sci.*, 54:830–847, 1997.

[29] F.-F. Jin and D. Neelin. Models of interannual tropical ocean-atmosphere interaction - a uni£ed view. part i: numerical results. *J. Atmos. Sci.*, 50:3477–3503, 1993.

[30] F.-F. Jin and D. Neelin. Models of interannual tropical ocean-atmosphere interaction - a uni£ed view. part iii: analytical results in fully coupled cases. *J. Atmos. Sci.*, 50:3523–3540, 1993.

[31] F-F Jin, D. Neelin, and M. Ghil. Enso on the devil's staircase. *Science*, 264:70–72, 1994.

[32] R. Kleeman and A. M. Moore. A theory for the limitation of enso predictability due to stochastic atmospheric transients. *JAS*, 54:753–767, 1997.

[33] H. Le-Treut and M. Ghil. Orbital forcing, climatic interactions, and glaciations cycles. *J. Geophys. Res.*, 88:5167–5190, 1983.

[34] K.A. Maasch and B. Saltzman. A low-order dynamical model of global climatic variability over the full pleistocene. *J. Geophys. Res.*, 95:1955–1963, 1990.

[35] G.H. Miller and A. de Vernal. Will greenhouse warming lead to northern hemisphere ice-sheet growth? *Nature*, 355:244–246, 1992.

[36] M. Munnich, M. A. Cane, and S. E. Zebiak. A study of self-excited oscillations of the tropical ocean-atmosphere system. *J. Atmos. Sci.*, 48:1238–1248, 1991.

[37] J. D. Neelin. The slow sea surface temperature mode and the fast-wave limit: analytic theory for tropical interannual oscillations and and experiments in a hybrid coupled model. *J. Atmos. Sci.*, 48:584–605, 1991.

[38] J. D. Neelin and F.-F. Jin. Models of interannual tropical ocean-atmosphere interaction - a uni£ed view. part ii: analytical results in the weak-coupling limit. *J. Atmos. Sci.*, 50:3504–3522, 1993.

[39] J. Oerlemans. Some basic experiments with a vertically integrated ice sheet model. *Tellus*, 33:1–11, 1981.

[40] D Paillard. The timing of pleistocene glaciations from a simple multiple-state climate model. *Nature*, 391:378–381, 1998.

[41] D. Paillard. Glacial cycles: toward a new paradigm. *reviews of geophysics*, 39:325–346, 2001.

[42] W. S. B. Paterson. *The physics of glaciers*. Pergamon, 3rd edition, 1994.

[43] J. Pedlosky. *Geophysical Fluid Dynamics.* Springer-Verlag, Berlin-Heidelberg-New York., 1979.

[44] W.R. Peltier and S. Marshall. Coupled energy-balance/ice-sheet model simulations of the glacial cycles: a possible connection between terminations and terrigenous dust. *J. Geophys. Res.*, 100:14,269–14,289, 1995.

[45] C. Penland and P. D. Sardeshmukh. The optimal-growth of tropical sea-surface temperature anomalies. *Journal of Climate*, 8(8):1999–2024, August 1995.

[46] S. G. Philander. El Niño southern oscillation phenomena. *Nature*, 302:295–301, 1983.

[47] S. G. H. Philander. *El Niño, La Niña, and the Southern Oscillation.* Academic Press, San Diego, 1990.

[48] D. Pollard. A simple ice sheet model yields realistic 100 kyr glacial cycles. *Nature*, 296:334–338, 1982.

[49] D Pollard. A coupled climate-ice sheet model applied to the quaternary ice ages. *Journal of Geophysical Research-Oceans and Atmospheres*, 88:7705–7718, 1983.

[50] D. Pollard. Ice-age simulations with a calving ice-sheet model. *Quat. Res.*, 20:30–48, 1983.

[51] J. A. Rial. Pacemaking the ice ages by frequency modulation of earth's orbital eccentricity. *Science*, 285:564–568, 1999.

[52] B. Saltzman and A. Sutera. A model of the internal feedback system involved in late quaternary climatic variations. *J. Atmos. Sci.*, 41:736–745, 1984.

[53] Barry Saltzman. Carbon dioxide and the $\delta^{18}O$ record of late-quaternary climatic change: a global model. *Climate Dyn.*, 1:77–85, 1987.

[54] H. G. Schuster. *Deterministic Chaos*. VCH, 2nd edition, 1989.

[55] H. Stommel. Thermohaline convection with two stable regimes of ¤ow. *Tellus*, 13:224–230, 1961.

[56] M. J. Suarez and P. S. Schopf. A delayed action oscillator for ENSO. *J. Atmos. Sci.*, 45:3283–7, 1988.

[57] J. R. Toggweiler. Variation of atmospheric CO_2 by ventilation of the ocean's deepest water. *Paleoceanography*, 14:572–588, 1999.

[58] E. Tziperman, M. A. Cane, and S. E. Zebiak. Irregularity and locking to the seasonal cycle in an enso prediction model as explained by the quasi-periodicity route to chaos. *Journal of the Atmospheric Sciences*, 52(3):293–306, feb 1 1995.

[59] E. Tziperman, M. A. Cane, S. E. Zebiak, Y. Xue, and B. Blumenthal. Locking of el nino's peak time to the end of the calendar year in the delayed oscillator picture of enso. *Journal of Climate*, 11(9):2191–2199, September 1998.

[60] E. Tziperman and H. Gildor. The mid-pleistocene climate transition and the source of asymmetry between glaciation and deglaciation times. *submitted*, 2001.

[61] E. Tziperman, L. Stone, M. A. Cane, and H. Jarosh. El-nino chaos: Overlapping of resonances between the seasonal cycle and the paci£c ocean-atmosphere oscillator. *Science*, 264(5155):72–74, apr 1 1994.

[62] E. Tziperman, S. E. Zebiak, and M. A. Cane. Mechanisms of seasonal: Enso interaction. *Journal of the Atmospheric Sciences*, 54(1):61–71, jan 1 1997.

[63] T. Volk and M.I. Hoffert. Ocean carbon pumps: analysis of relative strengths and ef£ciencies in ocean-driven atmospheric CO_2 changes. In E. T. Sundquist and W. S. Broecker, editors, *The carbon cycle and atmospheric CO_2: natural variations Archean to present*, volume 32 of *Geophysical monograph*, pages 99–110. American Geophysical Union, 1985.

[64] A. J. Watson and P. S. Liss. Marine biological controls on climate via the carbon and sulphur geochemical cycles. *Phil. Trans. R. Soc. Lond. B*, 353:41–51, 1998.

[65] R.G. Watts and E. Hayder. A two-dimensional, seasonal, energy balance climate model with continents and ice sheets: testing the milankovitch theory. *Tellus*, 36:120–131, 1984.

[66] S. E. Zebiak and M. A. Cane. A model El Niño-Southern Oscillation. *Mon. Wea. Rev.*, 115:2262–2278, 1987.

Lecture 10

Paleoclimates and Mars

Raymond T. Pierrehumbert

Much of the motivation for climate theory stems from the need to understand the current-day climate and the possibility that we are irrevocably changing it by burning fossil fuels, pumping pollutants into the atmosphere and cutting down rainforests. Unfortunately, our pursuit of the problem is hampered by the fact that the record of our quantitative observations of key quantities like sea surface temperature, CO_2 concentration and humidity is far shorter than most of the timescales on which the climate seems to vary intrinsically. Instead we need to rely on, for example, geology and geochemistry to construct proxy signals for the important climate variables that can be traced much further back in time. The reconstruction can then be used to further test and improve our understanding and models of the climate. Somewhat similarly, we need not only focus on our own terrestrial climatological experiment: the atmospheres of Mars and Venus, whilst very different in detail from our own, might also operate with analogous dynamical controls. Thus, one is tempted to assess our understanding by exploring past and extra-terrestrial climates. Unfortunately, this also highlights many other thorny issues which expose our basic lack of understanding and the shortcomings of our models. This lecture mentions some of the open and partiall answered questions that are raised by consideration of climate history and other planets.

1 The Eocene

About two million years ago, glacial cycles were initiated. Before that relatively late epoch of Earth's history, the climate appears to have been in a state of gradual cooling, lasting for some 65 million years. One possible explanation for this trend is based on the gradual reduction of atmospheric CO_2, and therefore the greenhouse effect (the precise cause of this reduction is not clear – the weathering of the uplifting Himalayas, which converts atmospheric CO_2 to carbonate minerals, could be responsible). Whatever the precise cause, this sets the stage for the "Eocene", a period about 55 million years ago when the climate was apparently relatively warm.

The evidence for a warm Eocene climate rests partly on paleoclimate data for oxygen isotopes in marine sediments which suggests that the deep ocean temperature was approximately 10° C (substantially warmer than present-day temperatures). This also suggests that there was no permanent polar ice cover because the melting of any polar ice would immediately flood the deep ocean with water of much lower temperatures. Further evidence

is provided by fossil records from the Eocene period which reveal the presence of animal species in geographical regions that would be inhospitable for them today (for example, crocodiles inhabited the Hudson Bay and lemurs lived in Spitzbergen in Scandinavia). The overall conclusion is that the midlatitudes and poles were warmer during the Eocene, a conclusion that is generally accepted by climatologists.

By contrast, foraminifera (plankton) data suggests that the tropical temperature during this time was about 305 K or less, which is more comparable with temperatures experienced today. This highlights a curious puzzle: how can the climate maintain a relatively cool tropical region whilst raising the polar temperatures sufficiently to melt the ice caps? No compelling explanation currently exists. Certainly it is possible to explain elevated temperatures if the CO_2 concentration (and greenhouse effect) was higher. However, one then must increase the latitudinal heat transport significantly over present-day values in order to lower the surface temperature gradient to that required to keep the tropics cool. Unfortunately, detailed, state-of-the-art, coupled atmosphere-ocean models are unable to explain such enhanced heat transports (if anything, in the warmer Eocene temperatures, these models predict lower latitudinal heat transport). One possibility is that the ocean heat transport was enhanced in the Eocene, perhaps as a result of pronounced tidal dissipation or some other physical effect not incorporated into the coupled models. Another is that stratospheric clouds shrouded the tropics and reduced the incoming radiation sufficiently to render the tropics more temperate. Either way, we need some important revision of the climate models in order to solve the puzzle. Alternatively, it is conceivable that the estimated equatorial temperature is simply in error, in which case the interesting puzzle vanishes altogether.

2 The Neoprotozoic Snowball

Even further back in Earth history, about 600 million years, we arrive at another climate conundrum, the possibility that, on two or three occasions, the planet was completely frozen over – the Neoprotozoic "snowball Earth".

There are, in fact, some compelling reasons to believe the Earth was a snowball in the past. First, the C^{12} to C^{13} ratio in ocean sediments implies the ocean was relatively abiotic (devoid of organisms) in the past (the two isotopes of carbon are used differently by marine organisms), and one of the best explanations for an abiotic ocean is that it was frozen over. Second, there is geological evidence that the atmosphere contained high levels of CO_2. Under normal conditions, CO_2 is precipitated out of the atmosphere and removed by the weathering of rock. High CO_2 levels, however, can be built up and maintained by volcanic activity in a snowball Earth in which weatherable rocks are covered by ice. Finally, there is even geomorphological evidence for glaciation at low latitudes.

There are three main questions regarding the snowball Earth during this period. First, what are the conditions necessary for the Earth to become a snowball? Second, how would the Earth get out of a snowball climate as models suggest that, if it exists, the snowball is a stable state? Third, if the snowball Earth is commensurate with large quantities of atmospheric CO_2, what happened to all this CO_2, and could the high CO_2 level allow one to discriminate against models that then predict a runaway greenhouse climate? It is often impractical to address such issues with GCMs, so we attempt to offer some answers to these

questions using a one-dimensional energy balance model.

As in lecture 7, the main ingredient to the model is the balance between the solar heat input and the outgoing long-wave radiation (OLR). The solar heating is determined by the total incoming radiation (S), which was 6% less during the neoprotozoic than today, and the albedo (α), which is in turn a function of land fraction and cloud parameterization. The OLR is a function of the Earth's surface temperature (T), the atmospheric CO_2 (about 20% for the neoprotozoic) and the (constant) relative humidity. Unlike in lecture 7, we simplify the model somewhat by fixing the latitudinal structure of the temperature to be uniform over the tropics and parabolic in $y = \sin\phi$ (with ϕ latitude) elsewhere; see figure 1. The equator-to-pole temperature gradient (DT) and the latitude of the ice margin are then variables of the model. However, as in lecture 7, we treat the latitude of the ice margin as a free parameter, compute the thermal structure of the model and search for the special location of the ice margin that gives the corresponding temperature to be 273 degrees Kelvin. The pole-equation temperature difference DT is thereby determined by the global energy balance.

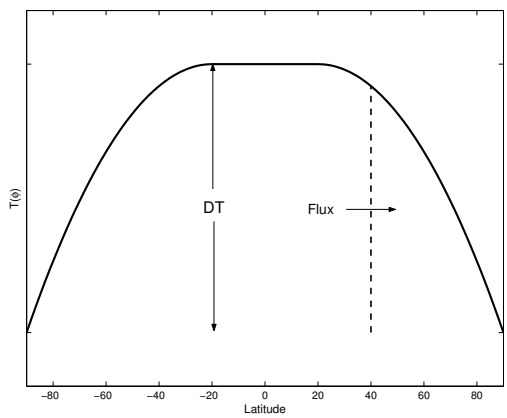

Figure 1: Temperature profile used in the one dimensional energy balance model for the snowball Earth.

Figure ??? shows the temperature at the ice margin for computations with different levels of atmospheric CO_2 and different cloud parameterizations. *This figure is not yet available.* As in lecture 7, for several cases there are multiple equilibria consisting of solutions with polar ice caps (with a finite ice margin latitude whose temperature is $273K$), and a completely ice-covered snowball (for which the ice margin is at zero latitude and the temperature is less than $273K$). Other computations reveal no equilibria other than the snowball; a frozen planet would inevitably result under the corresponding conditions. Unfortunately, as with all climate models, the parameterization of clouds represents the largest source of error and uncertainty. However, the model suggests that a snowball Earth is possible. The main physical ingredient needed seems to be a significant contribution to the albedo from the clouds.

If the Earth does becomes a snowball, how does it escape this snowball climate? In order to deglaciate, the ambient conditions must change so that the system is kicked away from the snowball solution and proceeds to another solution such as a stable ice-cap solution or

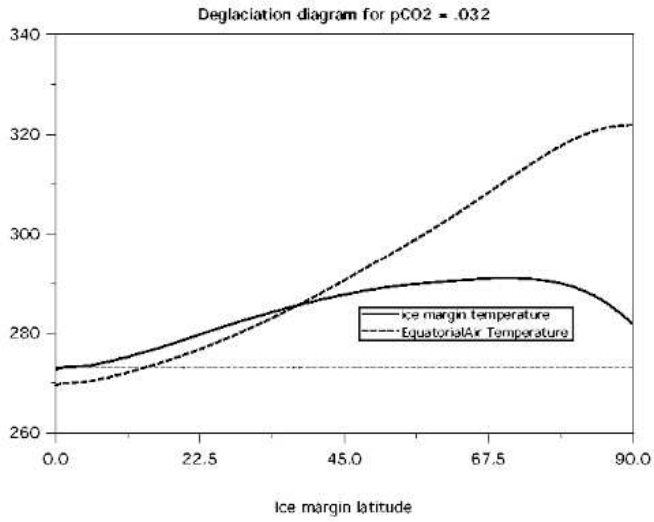

Figure 2: The possibility of deglaciation: A completely snowball Earth subject to large levels of CO_2.

an ice-free one. For example, as shown in figure 2, by building up the atmospheric CO_2, we can induce the disappearance of the snowball solution and a runaway deglaciation. The computation shown is on the brink of deglaciation – the slightest perturbation or further increase in CO_2 would open up an ice-free equatorial region that would permit more heating and deglaciate the planet completely. The equatorial temperature would eventually settle down to a warm $320K$.

Thus with different settings for the cloud physics and CO_2, it certainly seems plausible to evolve the Earth into a snowball state, and then deglaciate it. One unappealing feature of the model is that the settings required for each event are incompatible. The main conclusion from the toy model is therefore that the neoprotozoic snowball scenario is conceivable, if critically dependent on the cloud parameterization. Such a sensitivity does not bode well for the robustness of results from GCMs, which use a variety of such parameterizations.

3 Early Mars

Now we turn to the climates of other planets, and focus on Mars for which recent space missions have provided a wealth of new information. One of the most significant results is that there is now fairly conclusive evidence that there was once a flowing liquid on the surface of this planet. For example, Figs. 3 and 4 show photographs of features reminiscent of river valleys and catastrophic flood plains, and Fig. 5 outlines the large, flat polar area that resembles an ocean floor. Also notable are apparently glacial landforms.

The flood features can be dated to be about 4 billion years old. But Mars today is too cold to have running water, so could it have been warm enough in the past, particularly given that the sun's output then was approximately 70% of its current value? The answer might

Figure 3: Figure showing possible water features on Mars.

Figure 4: Figure showing the Martian surface (complete with principal lecturer and family).

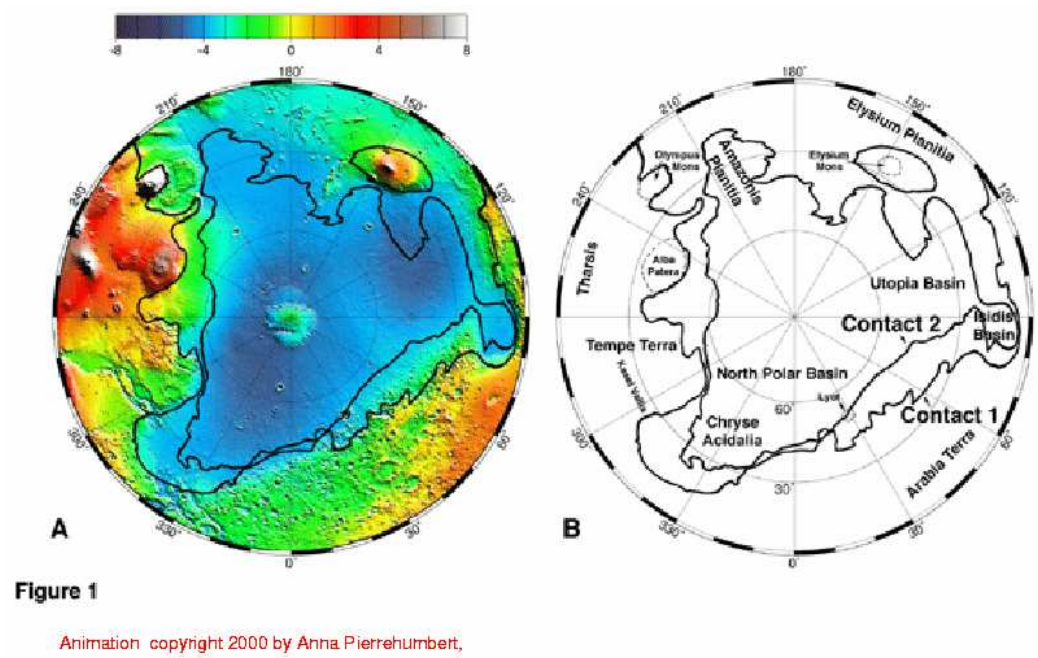

Figure 5: Laser altimetry data showing a possible polar ocean.

lie in CO_2: It is thought that early Mars may have had an almost pure CO_2 atmosphere, which may have been instrumental in raising the temperature sufficiently to allow water to flow on the surface. Somewhat later, Mars must have lost this atmosphere, leaving the planet as it is today.

To decide how tenable such an explanation is, we need to think more carefully about the structure of the early Martian atmosphere and the possible climate dynamics associated with it. One important ingredient is that CO_2 condenses (to solid dry ice) within the temperature range of the Martian atmosphere. By analogy with the atmospheric structure of the Earth's tropics, we might then expect that the thermal stratification would follow some analogue of the moist adiabat in the layers where CO_2 can condense. More specifically, the Clausius-Clapeyron relationship for CO_2 between the condensation temperature, T_c, and the pressure, p, can be written in the form,

$$T_c(p) = \frac{3148}{23.02 - \ln p} \tag{1}$$

(p in mbar), which plays the role of the moist adiabat for early Mars.

By suitably modifying the radiative energy balance models described in earlier chapters to incorporate this and other physics of the Martian atmosphere, we can proceed to explore whether the surface was ever warm enough to support liquid water. The results suggest that no matter how much CO_2 is put into the Martian atmosphere, the temperature never rises above the freezing point of CO_2 on the surface; the highest attainable temperature is 220K with 2 bars of surface pressure. However, these computations ignore the Martian analogue of clouds.

The condensation of CO_2 could in principle also generate clouds of dry ice. Such clouds scatter large amounts of infrared radiation, and might significantly warm the surface. Indeed, the incorporation of parameterizations of dry-ice clouds in the radiative balance models suggests that for a surface pressure of 2 bar it is possible to warm the Martian surface temperature to 300K. (It is not necessary to include water vapor and nitrogen in such a model, however, the increase in temperature is more dramatic if they are included.) Thus, with dry-ice clouds, we might be able to achieve our goal of warming the surface above freezing so that water flow can shape the early Martian landscape.

The next step is to explain how early Mars evolved. The cloudy model requires a surface pressure of at least 2 bars to achieve sufficiently high surface temperatures. But Mars today has only 6 mb of surface pressure, so where did it all go? One explanation resides in the dynamics of immense CO_2 glaciers that may have existed at the Martian poles.

Given current Martian surface temperatures, one expects that CO_2 only condenses well above the surface near the equator. However, surface temperatures decrease with latitude, and eventually fall beneath the condensation temperature. Poleward of this margin, CO_2 snow falls from the atmosphere, and the planet surface could become covered by dry ice. In principle, large quantities of CO_2 could be stored in such ice caps (in fact, the whole atmosphere, if condensed, could be contained in a 1km high glacier), leading to a delicate mass balance between the atmosphere and the glaciers. This delicate balance could easily be upset by greenhouse and albedo feedback effects, the result of which could be the runaway to the current Martian climate (in which neither ice cap is pure CO_2, and the north polar ice cap is, in fact, predominantly H_2O).

The glaciers are, however, restricted in thickness: At typical subglacial temperatures, and for pressures greater than about 5 bars, instead of solidifying to dry ice, CO_2 is forced into its liquid form. Such pressures first occur at the base of a glacier with a depth of about 100m due to the weight of the overlying dry ice. This liquid CO_2 flows toward the ice-margin until the pressure decreases sufficiently for it to re-freeze. However, the liquid layer lubricates the base of the glacier, and should the ice become any thicker, the glacier may well slide freely (surge) to lower latitudes. This action redistributes the mass of the glacier, causing the shape to become more rectangular, and provides a dynamical control on the glacier thickness. It is also notable that, unlike water and ice, the density of solid CO_2 is greater than that of liquid CO_2. Thus glacier fragments sink into the liquid and perhaps melt rather than float like terrestrial icebergs. All this suggests the intriguing possibility that an entirely different kind of glaciology existed in the early Martian Chronicles.

Given these rough ideas, we can also build a simple energy balance model for Mars including the CO_2 ice caps. The methodology is somewhat similar to the models of the neoprotozoic snowball Earth, but with the additional novelties that a change in the location of the ice margins also changes the amount of atmospheric CO_2 (and therefore the OLR), and that the temperature of the ice margin should be given by the condensation temperature appropriate to the specific surface pressure, $T_c(p)$, as in (1).

Results from such a model are shown in Figs. 6 and 7. A twist in the solution of the current model is that the ice margin is specified by assuming the toe of the glacier to be at the freezing temperature. Then the energy budget is calculated - the albedo and greenhouse effect being affected by the ice margin's location. Fig.6 shows the global surface pressure plotted against ice-margin position. This plot confirms the expected mass balance - when

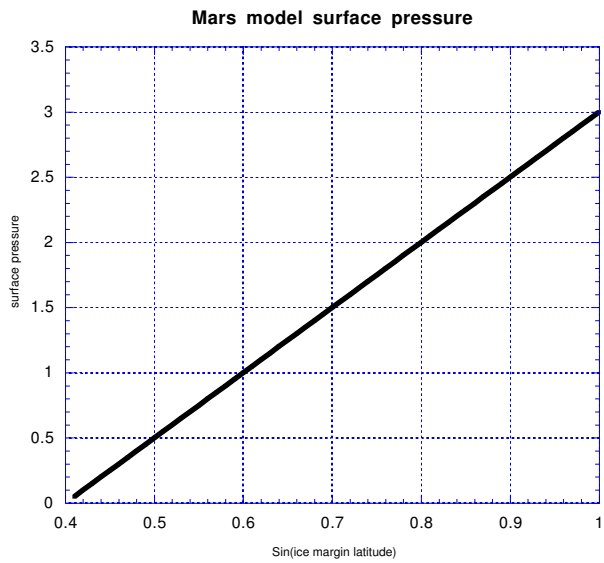

Figure 6: Plot of surface pressure against sine of the latitude of the ice margin.

the ice margin is at the equator, practically all the CO_2 is captured in the ice sheet and thus the pressure of the atmosphere approaches zero. As the ice-sheet recedes back to the pole, CO_2 is reinjected into the atmosphere and the pressure increases accordingly.

Fig.7 shows the global net heat flux (incoming minus outgoing radiation) against the position of the ice margin. The fixed points of the system are where the plot crosses the line of zero net flux. There are two such equilibria; the right-hand fixed point is unstable, whereas the left-hand one, a low-latitude glacier, is stable. These stability characteristics follow because a positive flux perturbation at the high-latitude glacial state corresponds to an increase in the latitude of the glacier margin. But such a flux perturbation also leads to a warming of the climate which provokes further recession of the glacier to the pole. Conversely, for the low-latitude equilibrium glacier, the introduction of a similar flux excess increases the glacier margin, and the subsequent heating of the climate melts the margin back to its original position.

To summarize, it is possible that early Mars was warmer and wetter in the past. With less CO_2 stored in the glaciers, the combined effect of greenhouse gases, reduced albedo and cloud dynamics can produce a ground temperature high enough to allow liquid to flow over the surface to shape the land. Subsequently, the dynamics of the CO_2 glaciers could have played an important role in the evolution of the Martian climate to its current state.

Notes by Matt Spydell, Fiona Eccles, and Helén Andersson

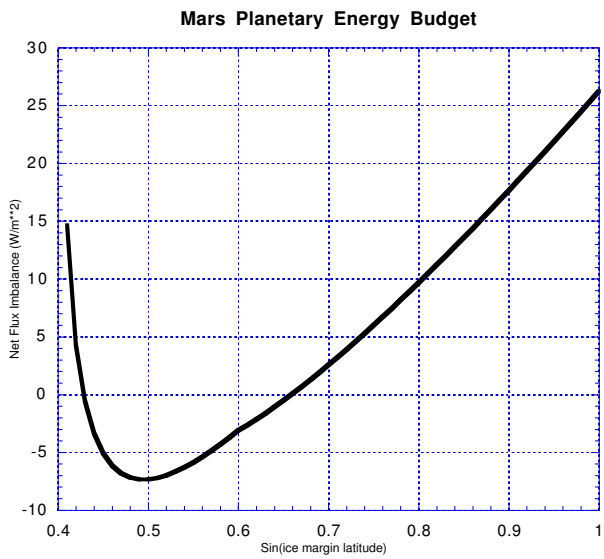

Figure 7: Plot of net heat flux (incoming-outgoing radiation) against sine of the latitude of the ice margin.

Slipping instability in a system of two superposed fluid layers

Chiara Toniolo

1 Introduction

The stability of the interface between two layers of immiscible, incompressible fluids is studied. Since the fluids may have distinct physical properties, the interface is susceptible to instabilities due to density stratification, shear-flow instabilities or interfacial ones, arising from discontinuities in longitudinal stresses at the boundary between the two media ([14], [15], [4], [13]).

The motivation of this analysis is the study of a particular kind of fast flowing glacier, found in the Antartica and in Greenland and known with the name of *ice stream*. An ice stream can be generically identified, as a part of an inland ice sheet that flows rapidly through the surrounding ice ([10]). Ice streams appear as long, shallow tongues, extended in the two horizontal directions and may end as outlet glaciers, bordered by rocks, or as ice shelves, floating over water. Altough they represent only a low percentage of the Antarctic coastline, they may drain out of the polar regions a substancial part of the accumulation in the interior.

Since ice stream motion provides a process for rapid dispersal and disintegration of ice sheets, an understanding of the underlying physical mechanism of ice streaming flow is, other than intriguing by itself, relevant in attempting to evaluate the dynamics of continental expanses.

In order to explain the basic mechanisms of the instability is necessary to explore the physical properties of the till, the layer at the bottom of these fast moving streams. The till is a complex material consisting of a liquid, deformable, inhomogeneous, anisotropic mixture of water and unconsolidated sediments ([5]). As a consequence of the high pressures, the base of the stream is often melted rather than frozen.

All the existing quantitative models of ice stream dynamic thus relate the characteristics of the flow to the complex nature of the basal layer and to the interactions between the latter and the thick overlying frozen one.

In general, four different kind of explanations of ice-stream behaviour are usually found in literature:

- sliding of the thick ice layer over the thin till, acting as a lubricant ([8], [9]);
- shear deformation of the water-saturated till underlying the ice ([1]);

- thermomechanical feedback, arising from the dependence of viscosity on temperature of ice ([11], [12]);
- superplasticity of the till ([7]).

What follows will be concerned with the first two mechanical interpretations of ice stream dynamic. The aim of this work is the investigation of the peculiar properties of such a kind of flow, considered as a mechanism resulting from the combination of glacier-like sliding and ice-shelf slipping.

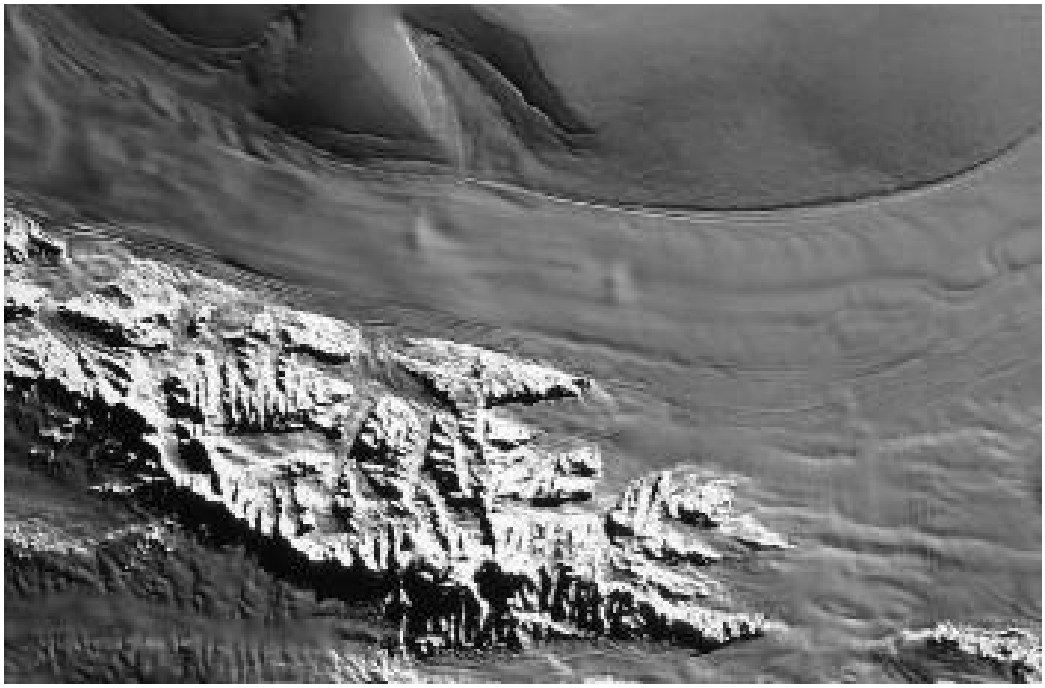

Figure 1: Landsat image of Rutford Ice Stream B, West Antartica, flowing from left to right between the solid rock wall on one side and low lying ice-covered promontory on the other. Image courtesy of D. D. Blankenship et al., Geophysical and Polar research Center, University of Wisconsin-Madison.

In the past, several models of fast sliding glaciers have been applied to ice-streams, most of them having included semiempirical laws to express the stress at the bottom of the mass of ice. This trick allows to simplify the mathematics, since an explicit formulation of the basal dynamic is not required, but in some way it introduces arbitrary assumptions in the formulations.

In the commonly accepted interpretation, the glacier is sliding on a deforming bed, usually a frozen one, absorbing most or all of the differential motion between the ice and the bedrock. On the other hand an ice-shelf spreading is due to longitudinal, rather than

shear stresses, which its floating base cannot support. Given these, there is a deep dynamic difference between a fast moving glacier and an ice-shelf.

To the discussion about the governing equations, the derivations of the glacier and ice-shelf models and a preliminary stability analysis will follow. Finally, a one-dimensional ice-stream model will be introduced.

2 Mathematical Formulation

Since the key ingredient in the fast stream dynamic is the interaction between the till and the ice over it, in order to limit as much as possible the amount of assumptions on the structure of the stresses regarding the till, all the models presented hereafter will be two layer ones.

2.1 Basic equations

The evolution of a flow with longitudinal and transversal structure is described by a set of three dimensional, non steady, isothermal equations.

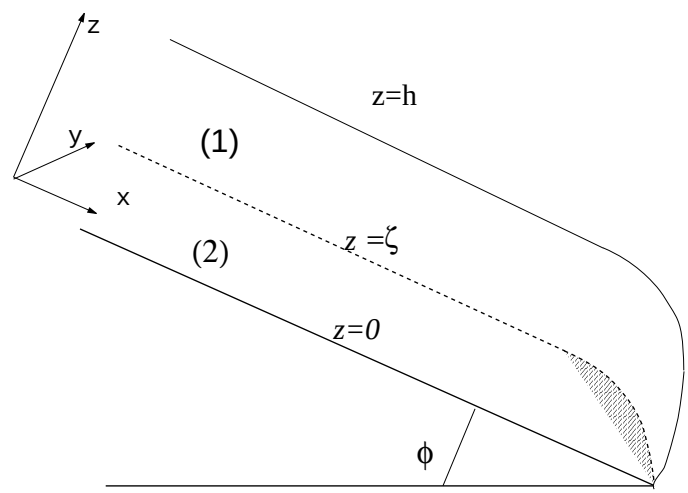

Figure 2: The coordinate system and the configuration for the two fluids

In the continuum hypothesis, having decoupled the dynamic problem from the thermodynamic one, the governing equations for the two fluids reduce to the incompressible continuity equation and to the conservation of momentum. Defined an orthogonal coordinate system as in figure (2), z being the vertical coordinate and $S = tan(\phi)$ the slope of the fixed bottom, the equations representing the two layers are:

$$\begin{aligned} u_{1x} + v_{1y} + w_{1z} &= 0 \\ u_{1t} + uu_{1x} + vu_{1y} + wu_{1z} &= -\frac{1}{\rho_1}p_{1x} + \frac{1}{\rho_1}(\partial_x\tau_{xx} + \partial_y\tau_{xy} + \partial\tau_{xz}) + gsin(\phi) \end{aligned}$$

$$
\begin{aligned}
v_{1t} + uv_{1x} + vv_{1y} + wv_{1z} &= -\frac{1}{\rho_1}p_{1y} + \frac{1}{\rho_1}(\partial_x\tau_{xy} + \partial_y\tau_{yy} + \partial_z\tau_{yz}) \\
w_{1t} + uw_{1x} + vw_{1y} + ww_{1z} &= -\frac{1}{\rho_1}p_{1z} + \frac{1}{\rho_1}(\partial_x\tau_{xz} + \partial_y\tau_{yz} + \partial_z\tau_{zz}) - gcos(\phi) \qquad (1)
\end{aligned}
$$

and:

$$
\begin{aligned}
u_{2x} + v_{2y} + w_{2z} &= 0 \\
u_{2t} + uu_{2x} + vu_{2y} + wu_{2z} &= -\frac{1}{\rho_2}p_{2x} + \frac{1}{\rho_2}(\partial_x\sigma_{xx} + \partial_y\sigma_{xy} + \partial\sigma_{xz}) + gsin(\phi) \\
v_{2t} + uv_{2x} + vv_{2y} + wv_{2z} &= -\frac{1}{\rho_2}p_{2y} + \frac{1}{\rho_2}(\partial_x\sigma_{xy} + \partial_y\sigma_{yy} + \partial_z\sigma_{yz}) \\
w_{2t} + uw_{2x} + vw_{2y} + ww_{2z} &= -\frac{1}{\rho_2}p_{2z} + \frac{1}{\rho_2}(\partial_x\sigma_{xz} + \partial_y\sigma_{yz} + \partial_z\sigma_{zz}) - gcos(\phi) \qquad (2)
\end{aligned}
$$

where the subscripts (x,y,z) denote partial derivatives, (1) and (2) refer to the upper and lower fluid, $\mathbf{u} = (u, v, w)$ is the velocity field, $\mathbf{g} = (gsin(\phi), 0, -gcos(\phi))$ is the gravity force, τ_{ij} and σ_{ij} the anisotropic parts of the stress tensors, the total deviatoric tensors being respectively:

$$
\begin{aligned}
\mathbb{T} &= \tau - p_1\mathbb{I} \\
\mathbb{S} &= \sigma - p_2\mathbb{I} \qquad (3)
\end{aligned}
$$

2.2 Boundary conditions

The problem needs, to be defined, the specification of the associated boundary conditions.

At the base of the stream a no-slip condition is required. Since the base is kept fixed, this imposes on z=0:

$$u_2 = v_2 = w_2 = 0 \qquad (4)$$

At the interface $z = \zeta$ between the two media the physical request of matching of the stresses has to be satisfied:

$$\mathbb{T} \cdot \mathbf{n}_\zeta = \mathbb{S} \cdot \mathbf{n}_\zeta \qquad (5)$$

having defined $\mathbf{n}_\zeta = (-n_x, -n_y, 1)/(n_x^2 + n_y^2 + 1)$ as the unit normal pointing out of the surface $z = \zeta$.

The last one at the free surface imposes a zero stress at the elevation $z = h$:

$$\mathbb{T} \cdot \mathbf{n}_h = \mathbf{0} \qquad (6)$$

and expresses the continuity of stresses between the upper layer and a medium (air) much less dense overlying it.

2.3 Rheology of the problem

The system is then closed specifying the functional relation between the stress tensors $\mathbb{T}$ and $\mathbb{S}$ and the properties of the two fluids. This defines the analogous of the Newtonian constant viscosity in the case of a nonlinear relationship between strain rate and stress.

A fairly general model is a power law contitutive relation of the kind:

$$\tau_{ij} = K\dot{\gamma}^{n-1} \cdot \dot{\gamma}_{ij} \tag{7}$$

where K is the consistency, dependent on temperature, pressure, composition of the material, $n > 0$ a fixed real exponent ($n = 1$ for a Newtonian fluid) and $\dot{\gamma}$ the second invariant of the strain rate, expressed by:

$$\dot{\gamma} = \sqrt{\frac{1}{2}\dot{\gamma}_{jk} \cdot \dot{\gamma}_{jk}} \tag{8}$$

According to the previous notation, the strain rate tensor becomes:

$$\dot{\gamma}_{ij} = \begin{pmatrix} 2u_x & u_y + v_x & u_z + w_x \\ u_y + v_x & 2v_y & v_z + w_y \\ u_z + w_x & v_z + w_y & 2w_z \end{pmatrix} \tag{9}$$

In the till-ice system, none of the two components has a simple behaviour. Nonetheless, a proper discussion of the rheological properties of the till goes beyond the aim of this work and could eventually follow to a first understanding of the primary instability mechanism.

In the model presented further on, the till will be considered like a Newtonian fluid, with constant viscosity, while for ice the constitutive relation will be a power law one of the kind discussed above (7). Ice is a shear thinning fluid, in the sense that an increased strain rate produces a decrease in the effective viscosity. In fact, for ice:

$$n \sim \frac{1}{3} \tag{10}$$

The equation (7) is in this case (and for all values of $n < 1$), not well behaved for some particular flow configuration, predicting in fact an infinite effective viscosity for values of the strain rate approaching zero.

3 The Glacier Theory

In a glacier the slab deformation at a generic depth is moslty due to shear stress, the bottom attached to the rock being commonly frozen.

Thus the minimum model for such a kind of system is represented by the superposition of two Newtonian fluids with different densities and viscosities, described at leading order by an hydrostatic balance in the vertical and by a balance between pressure gradient force and shear stress in the horizontal direction x.

3.1 Non-dimensional equations

Focusing the attention on the one-dimensional case, the relevant balance in the x-momentum equation is expressed for both fluids by:

$$p_{1x} \sim \partial_z \tau_{xz} \tag{11}$$

$$p_{2x} \sim \partial_z \sigma_{xz} \tag{12}$$

Continuity and momentum conservation equation reduce, in a one-dimensional framework, to:

$$\begin{aligned} u_{1x} + w_{1z} &= 0 \\ u_{1t} + u_1 u_{1x} + w u_{1z} &= -\frac{1}{\rho_1}\partial_x p_1 - \frac{1}{\rho_1}(\partial_x \tau_{xx} + \partial_z \tau_{xz}) + g sin\phi \\ w_{1t} + u_1 w_{1x} + w w_{1z} &= -\frac{1}{\rho_1}\partial_z p_1 - \frac{1}{\rho_1}(\partial_x \tau_{xz} + \partial_z \tau_{zz}) - g cos\phi \end{aligned} \tag{13}$$

$$\begin{aligned} u_{2x} + w_{2z} &= 0 \\ u_{2t} + u_2 u_{2x} + w u_{2z} &= -\frac{1}{\rho_2}\partial_x p_2 - \frac{1}{\rho_2}(\partial_x \sigma_{xx} + \partial_z \sigma_{xz}) + g sin\phi \\ w_{2t} + u_2 w_{2x} + w w_{2z} &= -\frac{1}{\rho_2}\partial_z p_2 - \frac{1}{\rho_2}(\partial_x \sigma_{xz} + \partial_z \sigma_{zz}) - g cos\phi \end{aligned} \tag{14}$$

where the subscripts 1 and 2 refer to the upper and lower fluid respectively.

The set of equations above is then non dimensionalized by choosing the following scales:

$$x = L\tilde{x},\ z = H\tilde{z},\ u = U\tilde{u},\ w = \frac{UH}{L}\tilde{w},\ t = \frac{L}{U}\tilde{t} \tag{15}$$

For pressure:

$$p = \rho_1 g H \tilde{p} \tag{16}$$

and strain rate:

$$\dot{\gamma}_{ij} = \frac{U}{H}\tilde{\dot{\gamma}}_{ij} \tag{17}$$

The leading order balance defines then the scale for horizontal velocity $U = \frac{\rho_1 g H^3}{\nu_1 L}$. With this restriction, defining as $\epsilon = \frac{H}{L}$ the aspect ratio for the two thin layers and indicating with $Re = \frac{\rho_1 U L}{\nu_1}$ the small Reynolds number of the flow, the inertial terms in the governing equations become negligible at leading orders, being proportional to $\epsilon^2 Re$.

The simplified non dimensional form of the governing equations, dropping the tilde superscript, is then:

$$\begin{aligned} 0 &= u_{1x} + w_{1z} \\ 0 &= -p_{1x} + \epsilon \partial_x \tau_{xx} + \partial_z \tau_{xz} + S \\ 0 &= -p_{1z} + \epsilon^2 \partial_x \tau_{xz} + \epsilon \partial_z \tau_{zz} - 1 \end{aligned} \tag{18}$$

$$\begin{aligned} 0 &= u_{2x} + w_{2z} \\ 0 &= -p_{2x} + \epsilon \partial_x \sigma_{xx} + \partial_z \sigma_{xz} + SD \\ 0 &= -p_{2z} + \epsilon^2 \partial_x \sigma_{xz} + \epsilon \partial_z \sigma_{zz} - D \end{aligned} \tag{19}$$

where $S = \frac{tan\phi L}{H}$ is the non dimensional slope and $D = \frac{\rho_2}{\rho_1}$ is the density ratio. The components of the strain rate tensor, in the new rescaled variables are:

$$\dot{\gamma}^{(i)}_{xx} = 2\epsilon u_{ix} \qquad \dot{\gamma}^{(i)}_{xz} = u_{iz} + \epsilon^2 w_{ix} \qquad \dot{\gamma}^{(i)}_{zz} = 2\epsilon w_{iz} \tag{20}$$

where i=1,2.

The system is finally defined by the boundary conditions at the rigid bottom boundary $z = 0$:

$$u_2 = w_2 = 0 \tag{21}$$

at the interface $z = \zeta$ between the two fluids:

$$\begin{aligned} -\epsilon(\tau_{xx} - p_1)\zeta_x + \tau_{xz} &= -\epsilon(\sigma_{xx} - p_2)\zeta_x + \sigma_{xz} && (22)\\ -\epsilon\tau_{xz}\zeta_x + (\tau_{zz} - p_1) &= -\epsilon\sigma_{xz}\zeta_x + (\sigma_{zz} - p_2) && (23)\\ & && (24) \end{aligned}$$

and at the free surface $z = h$:

$$\begin{aligned} -\epsilon(\tau_{xx} - p_1)\zeta_x + \tau_{xz} &= 0 && (25)\\ -\epsilon\tau_{xz}\zeta_x + (\tau_{zz} - p_1) &= 0 && (26) \end{aligned}$$

3.2 The 1-D thin glacier theory

The derivation of a thin layer model ([2], [3]) describing the evolution of the system at the boundaries, follows directly from the assumption of a shallow layer for both ice and till.

The smallness of the aspect ratio ϵ allows to perform an asymptotic expansion of the governing equations, reducing the complexity of the initial formulation to a simplified set of equations that incorporate the basic physical aspects of the phenomenon.

This is done by expanding all the variables in power series of ϵ:

$$u_i = u_i^{(0)} + \epsilon u_i^{(1)} + O(\epsilon^2), w_i = w_i^{(0)} + \epsilon w_i^{(1)} + O(\epsilon^2), p_i = p_i^{(0)} + \epsilon p_i^{(1)} + O(\epsilon^2) \quad \cdots \tag{27}$$

and so on. Collecting terms of the same order in ϵ one obtain a set of governing equations that solves the problem at the different orders.

At leading order, according to the previous definition (20) of the strain rate tensor:

$$\tau_{zz}^{(0)} = -\tau_{xx}^{(0)} = 0 \tag{28}$$

and seemingly:

$$\sigma_{zz}^{(0)} = -\sigma_{xx}^{(0)} = 0 \tag{29}$$

indicating a basic flow independent on z in the upper layer.

The interior flow is thus completely determined specifying the velocity field (u, w) at the boudaries and solving the two evolution equations for ζ and h:

$$\begin{aligned} \zeta_t + u(\zeta)\zeta_x &= w(\zeta) && (30)\\ h_t + u(h)h_x &= w(h) && (31) \end{aligned}$$

The pressure field, hydrostatic at leading order, is given by:

$$p_1^{(0)} = h - z \tag{32}$$

and

$$p_2^{(0)} = h - \zeta + D(\zeta - z) \tag{33}$$

(the (0) superscript at the right end side of the equations have been dropped for convenience).

Then, integrating the second of (18) along the vertical and given the upper boundary condition $\tau_{xz}^{(0)}(h) = 0$:

$$\sigma_{xz}(\zeta) = (S - h_x)(h - \zeta) \tag{34}$$

Here, the stress component σ_{xz} is evaluated from an integration in the lower layer:

$$\sigma_{xz}^{(0)}(\zeta) = (\zeta - z)(h_x - \zeta_x + D\zeta_x - SD) + \sigma_{xz}(z) \tag{35}$$

The velocity at the boundary $z = \zeta$, equating (34) and (35) is:

$$u = \frac{1}{\nu_2}[(S - h_x)(h - \zeta)\zeta - (h_x - \zeta_x + D\zeta_x - SD)\frac{\zeta^2}{2}] \tag{36}$$

Since at leading order the flow is independent on z:

$$u(h) = u(\zeta) \tag{37}$$

while for the vertical component of velocity (integration of continuity equation):

$$w(h) = w(\zeta) - \int_{\zeta}^{h} u_x dz = w(\zeta) - u_x(\zeta)(h - \zeta) \tag{38}$$

The final set of equations, defining $\theta = h - \zeta$ to be the thickness of the upper layer is then:

$$\zeta_t + \partial_x[(S - h_x)\frac{\theta\zeta^2}{2} + (\theta_x + D\zeta_x - DS)\frac{\zeta^3}{3}] = 0 \tag{39}$$

$$R\theta_t + \partial_x[(S - h_x)\frac{\theta^3}{3} + \theta u] = 0 \tag{40}$$

$$u = R[\frac{\zeta^2}{2}(DS - D\zeta_x - \theta_x) + (S - h_x)\theta\zeta] \tag{41}$$

where the new relevant parameter R is a viscosity ratio of the form $\frac{\nu_1}{\nu_2}$.

3.3 The 2-D extension

It's straightforward the generalization in presence of a bidimensional horizontal structure:

$$\begin{aligned} u - R[(S - h_x)\theta\zeta + \frac{\zeta^2}{2}(DS - D\zeta_x - \theta_x)] &= 0 \\ v + R[h_y\theta\zeta + \frac{\zeta^2}{2}(D\zeta_y + \theta_y)] &= 0 \\ R\theta_t + \partial_x[(S - h_x)\frac{\theta^3}{3} + \theta u] + \partial_y[-h_y\frac{\theta^3}{3} + \theta v] &= 0 \\ \zeta_t + \partial_x(S - h_x)\frac{\theta\zeta^2}{2} - (\theta_x + D\zeta_x - DS)\frac{\zeta^3}{3}] - \partial_y[h_y\frac{\theta\zeta^2}{2} + (\theta_y + D\zeta_y)\frac{\zeta^3}{3}] &= 0 \end{aligned} \tag{42}$$

here (u,v) indicate the velocity components in the directions (x,y).

4 The Ice-Shelf Theory

In a ice-shelf, floating on the sea, the lower layer is liquid water, much less viscous than the ice moving on it. In this case, considering pretty uniform the thickness of the shallow layer of ice, the vertical shear is zero and the big mass of ice behaves like a uniform slab, subject to zero fricton at its upper and lower surfaces.

4.1 Non-dimensional equations

In the 1-D model, the essential balances for the two fluids are expressed by:

$$p_{1x} \sim \partial_x \tau_{xx} \tag{43}$$

$$p_{2x} \sim \partial_x \tau_{xz} \tag{44}$$

From equation (43) it's clear the relevance of the longitudinal stresses in the ice layer.

The set of equations (13), (14) is again non-dimensionalized using the same scales as for the glacier case, getting:

$$\begin{aligned} 0 &= u_{1x} + w_{1z} \\ 0 &= -\epsilon p_{1x} + \epsilon \partial_x \tau_{xx} + \partial_z \tau_{xz} + S \\ 0 &= -p_{1z} + \epsilon \partial_x \tau_{xz} + \partial_z \tau_{zz} - 1 \end{aligned} \tag{45}$$

and:

$$\begin{aligned} 0 &= u_{2x} + w_{2z} \\ 0 &= -p_{2x} + \epsilon \partial_x \sigma_{xx} + \partial_z \sigma_{xz} + SD \\ 0 &= -p_{2z} + \epsilon^2 \partial_x \sigma_{xz} + \epsilon \partial_z \sigma_{zz} - D \end{aligned} \tag{46}$$

where the components of the strain rate tensors are respectively:

$$\dot{\gamma}^{(1)}_{xx} = 2u_{1x} \qquad \dot{\gamma}^{(1)}_{xz} = \frac{1}{\epsilon} u_{1z} + \epsilon w_{1x} \qquad \dot{\gamma}^{(1)}_{zz} = 2w_{1z} \tag{47}$$

and:

$$\dot{\gamma}^{(2)}_{xx} = 2\epsilon u_{2x} \qquad \dot{\gamma}^{(2)}_{xz} = u_{2z} + \epsilon^2 w_{2x} \qquad \dot{\gamma}^{(2)}_{zz} = 2\epsilon w_{2z} \tag{48}$$

It's worth noting how the stress components are defined and scaled differently in the two layers. In fact, for the upper fluid:

$$[p_1] = [p] = [\tau_{ij}] \tag{49}$$

while for the lower one:

$$[p_2] = [p] = \frac{1}{\epsilon}[\sigma_{ij}] \tag{50}$$

and from the continuity of pressures at the boundary $z = \zeta$ between the two media:

$$[\sigma_{ij}] = \epsilon[\tau_{ij}] \tag{51}$$

In the case of two Newtonian fluids, remembering the definitions given above for the components of the strain rate:

$$\frac{[\tau_{ij}]}{[\sigma_{ij}]} = \frac{\nu_1}{\nu_2} = R = \epsilon^{-2} \tag{52}$$

The boundary conditions at the rigid bottom z=0:

$$u_2 = w_2 = 0 \tag{53}$$

at level $z = \zeta$:

$$\begin{aligned} -\epsilon\zeta_x(\tau_{xx} - p_1) + \tau_{xz} &= -\epsilon\zeta_x(\epsilon\sigma_{xx} - p_2) + \epsilon\sigma_{xz} && (54)\\ -\epsilon\zeta_x\tau_{xz} + \tau_{zz} - p_1 &= -\epsilon\zeta_x\epsilon\sigma_{xz} + \epsilon\sigma_{zz} - p_2 && (55) \end{aligned}$$

and at the free surface $z = h$:

$$\begin{aligned} -\epsilon h_x(\tau_{xx} - p_1) + \tau_{xz} &= 0 && (56)\\ -\epsilon h_x\tau_{xz} + \tau_{zz} - p_1 &= 0 && (57) \end{aligned}$$

finally close the problem.

4.2 The thin ice-shelf theory

With a procedure completely similar to the one followed in section (3.2) one can obtain the evolution equations for the two boundaries $z = \zeta$, $\theta = h - \zeta$ and for the velocity u in a 1-dimensional framework:

$$\begin{aligned} R[\theta(2\tau_{xx})]_x - (\theta_x + \zeta_x - S)\theta - \frac{u}{\zeta} - \frac{\zeta}{2}(\theta_x + D\zeta_x - DS) &= 0\\ \theta_t + (u\theta)_x &= 0\\ \zeta_t + (\frac{u\zeta}{2})_x - \frac{1}{12}[\zeta^3(\theta_x + D\zeta_x - DS)]_x &= 0 && (58) \end{aligned}$$

and in the 2-dimensional one:

$$\begin{aligned} R([\theta(2\tau_{xx} + \tau_{yy})]_x + [\theta\tau_{xy}]_y) - (\theta_x + \zeta_x - S)\theta - \frac{u}{\zeta} - \frac{\zeta}{2}(\theta_x + D\zeta_x - DS) &= 0\\ R([\theta(\tau_{xx} + 2\tau_{yy})]_y + [\theta\tau_{xy}]_x) - (\theta_y + \zeta_y)\theta - \frac{v}{\zeta} - \frac{\zeta}{2}(\theta_y + D\zeta_y) &= 0\\ \theta_t + (u\theta)_x + (v\theta)_y &= 0\\ \zeta_t + (\frac{u\zeta}{2})_x + (\frac{v\zeta}{2})_y - \frac{1}{12}[\zeta^3(\theta_x + D\zeta_x - DS)]_x - \frac{1}{12}[\zeta^3(\theta_y + D\zeta_y)]_y &= 0 && (59) \end{aligned}$$

with the usual meaning of the parameters R, D and S involved.

5 Stability analysis

5.1 Linear stability

The first step in the understanding of the instability mechanism is to perform a linear stability analysis of the two systems presented, in a drastically simplified configuration of two Newtonian superposed fluids, perturbing around a basic state independent on the transversal coordinate y and uniform along the longitudinal x-direction.

One of the aims of this kind of study is to look for the occurrence of fingering instabilities in the horizontal plane.

The parameters determining the stability properties are:

- the non-dimensional slope S;
- the density ratio D ($=\rho_2/\rho_1$);
- the viscosity ratio R ($=\nu_1/\nu_2$);
- the scale of the upper layer thickness Θ.

It's not a restrictive choice to fix the slope (S=1) and to analyse the behaviour of the two bidimensional models already described in presence of a stable density stratification (D=1.1). This is in fact the configuration relevant in practise when dealing with ice flowing on a lower denser layer, represented by frozen compressed till or by liquid water.

The definition of the two basic states follows directly from the sets of equations (42) and (59) previously derived, being for both models:

$$\theta(x,y,t) = \Theta, \qquad \zeta(x,y,t) = Z = 1 - \Theta, \qquad h(x,y,t) = \Theta + Z = 1 \tag{60}$$

and:

$$v(x,y,t) = 0 \tag{61}$$

The longitudinal velocity component is then expressed for the glacier case by:

$$u(x,y,t) = U = R\Theta(Z + D\frac{Z}{2}) \tag{62}$$

while for the ice-shelf one:

$$u(x,y,t) = U = \Theta(Z + D\frac{Z}{2}) \tag{63}$$

Now, since the geometry is unbounded in the y direction and supposed periodic along x, is possible to expand the perturbations from the uniform state for all the variables concerned in the following form:

$$a = A + \tilde{a}(z)exp(ikx + ily + \sigma t) \tag{64}$$

indicating with k and l the longitudinal and trasversal wave numbers of the disturbances and with σ the associated complex eigenvalue. In particular, $Re(\sigma)$ being the growth rate and $Im(\sigma)$ the celerity of the correspondent waves.

Stability conditions are found solving analitically a quadratic algebraic expression in σ and are simply determined by the sign of the real part of the eigenvalue.

The range of unstable wave numbers depends obviously on the choice of the parameters. By fixing $\Theta = 0.5$ (S=1 and D=1.1), it's interesting to note Fig (3) that the sensitivity of the interval of unstable wave numbers on the variations of R appears evident for the glacier model and not for the ice-shelf one.

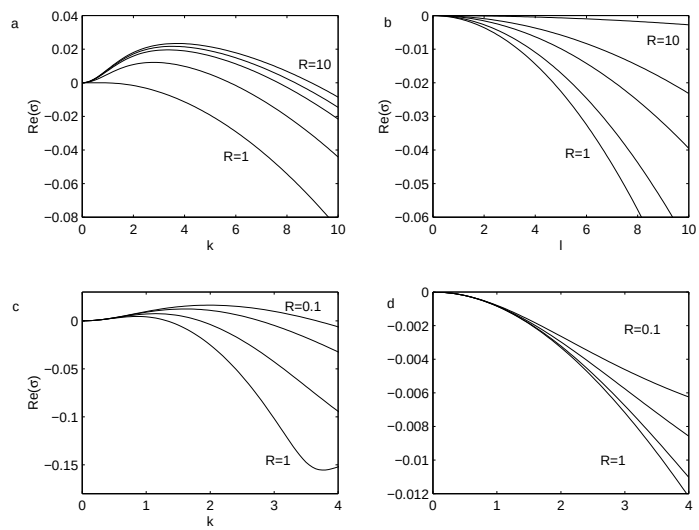

Figure 3: Growth rates as a function of k and l wave numbers, evaluated for increasing values of the parameter R. Curves (a) and (b) show the growth rates for R=1, 2, 5, 10, 100 for the glacier model, while (c) and (d) correspond to R=0.1, 0.2, 0.5, 1 for the ice-shelf approximation.

Two representative solutions of the linear problem are then plotted in Figures (4) and (5).

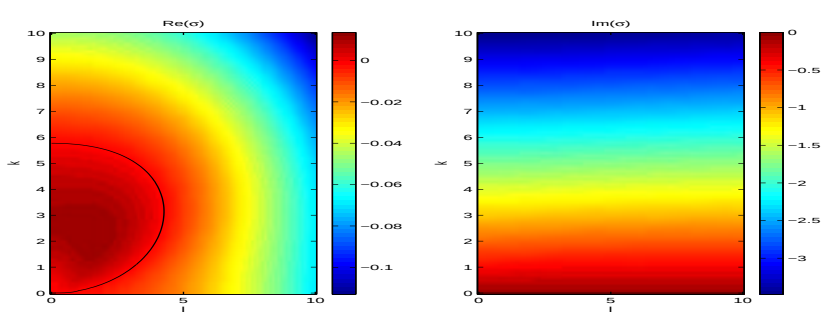

Figure 4: Growth rate $Re(\sigma)$ and phase speed $Im(\sigma)$ in the wave number plane [k,l] for the glacier case, choosen $R = 2$, $\Theta = 0.5$ and $D = 1.1$. The black line in the first plot is the marginal stability curve.

In both cases one can observe the appearance of an instability region in a limited part of the [k,l] plane. The celerities ($c = Im\sigma$) are almost constant along l and show a quite clear linear dependence on k, indicating that all the waves in the plane are moving with the same phase speed ω ($\omega = c/k$).

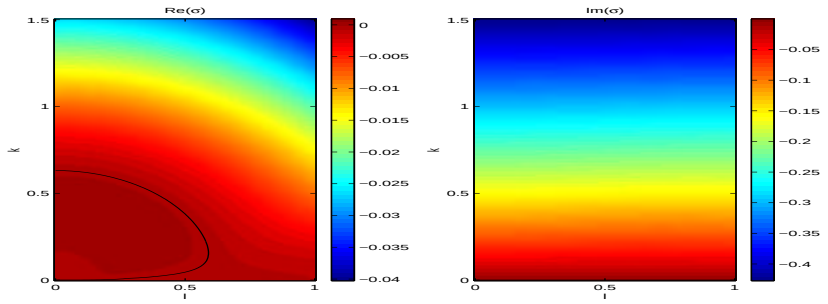

Figure 5: Growth rate $Re(\sigma)$ and phase speed $Im(\sigma)$ in the wave number plane [k,l] in the ice-shelf model with $R = 5$, $\Theta = 0.5$, $D = 1.1$.

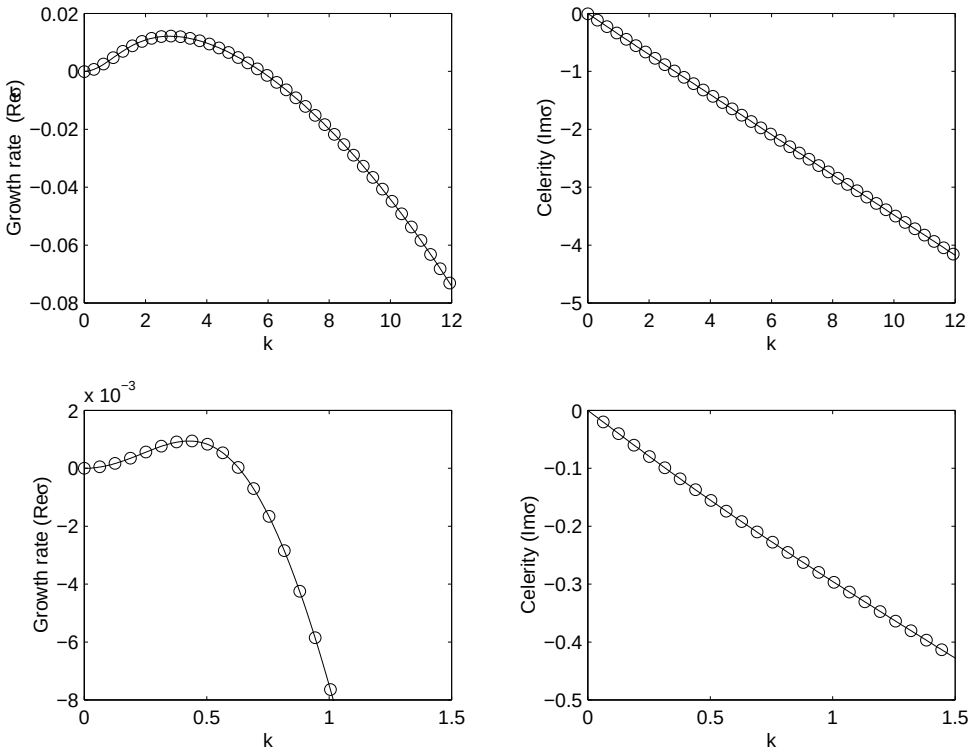

Figure 6: Growth rates and Celerities for a glacier configuration (the upper one, R=2, D=1.1, $\Theta = 0.5$) and for an ice-shelf one (the lower one, R=5, D=1.1, $\Theta = 0.5$) evaluated by the linear theory (solid lines) and by a numerical experiment (circles), running a spectral code with respectively N=128 (Time=500, dt=0.01, Computational domain=20) and N=64 (Time=500, dt=0.002, Computational domain=100) modes.

Figure (6) shows a comparison between the linear theory predictions and numerical experiments performed with the use of a spectral code, displaying a pretty good agreement among theory and simulations.

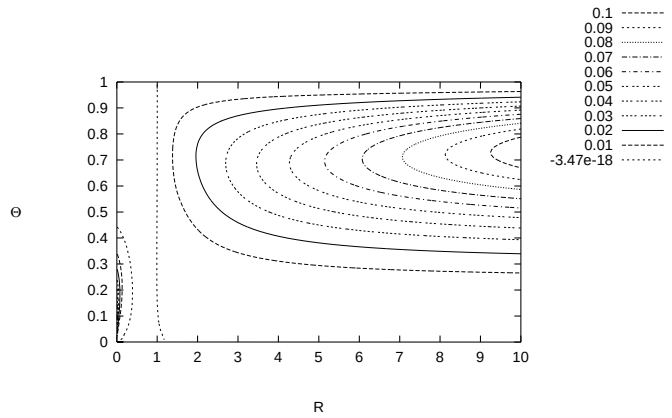

Figure 7: Stability region in the parameter plane $[R, \Theta]$ for S=1, D=1.1 in the glacier case.

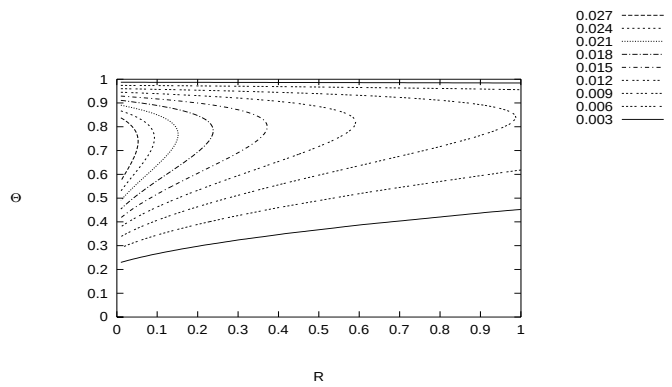

Figure 8: Stability region in the parameter plane $[R, \Theta]$ for S=1, D=1.1 in the ice-shelf case.

Plotting the maximum growth rate in the plane of the parameters R and Θ, is then evident the existence, for the glacier model, of two distinct instability regions (Fig. 7). The first comes out for $R > 1$, no matter the value of Θ, and it's enhanced for increased value of R. The second corresponds to a pretty curious situation with $R \ll 1$ and $\Theta \ll 1$.

In the other model the instability region (Fig.8) covers the whole parameter plane $[\Theta, R]$ and this is in accordance with the interpretation of the ice-shelf approximation as a limit situation for $R = O(\epsilon^{-2}) \gg 1$.

Figure (9) reports then the purely two dimensional instability occurring for values of $R = 0.1, \Theta = 0.2$ in the shear dominated, glacier-like model. A clear explanation of this unespected (at least to the author knowledge) unstable configuration is not available.

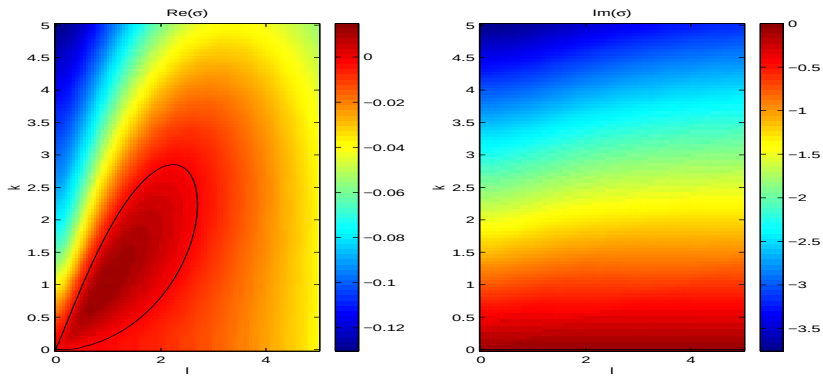

Figure 9: Growth rate $Re(\sigma)$ and phase speed $Im(\sigma)$ in the wave number plane [k,l] for the glacier case, choosen $R = 0.2$, $\Theta = 0.1$ and $D = 1.1$. The black line in the first plot is the marginal stability curve.

The results of such a kind of investigation are interesting, but discouraging to some extent, showing no possibility for fingering to occur.

5.2 Nonlinear dynamic

The governing equations of the two models contain up to fourth order nonlinearities. As a consequence, the evolution of the two interfaces $z = \zeta$ and $z = h$ far away in the future is completely dominated by the nonlinear terms.

The integration in time of the one-dimensional glacier-equations, in a fixed system of reference, is shown in figures (10) and (11).

The initial bump entering the domain at time t=0 moves downstream, growing and evolving as time passes. It's interesting to note the tendence of the system, as time goes on, to sharpen an initially smooth disturbance developing sharp shocks.

The two thicknesses ζ and θ are strongly coupled, oscillating out of phase in time with almost the same amplitude. This means, remembering the physical interpretations of the two, that in a realistic setting one should observe no evolution in time of the free surface.

The same result comes out computing the equilibrium shapes for wave-like solutions of the kind $\theta = \theta(x - ct), \zeta = \zeta(x - ct)$ starting from an initial condition periodic in the spatial domain. Figure (12) displays two equilibrium configurations and a regime diagram indicating the supercritical nature of the bifurcation.

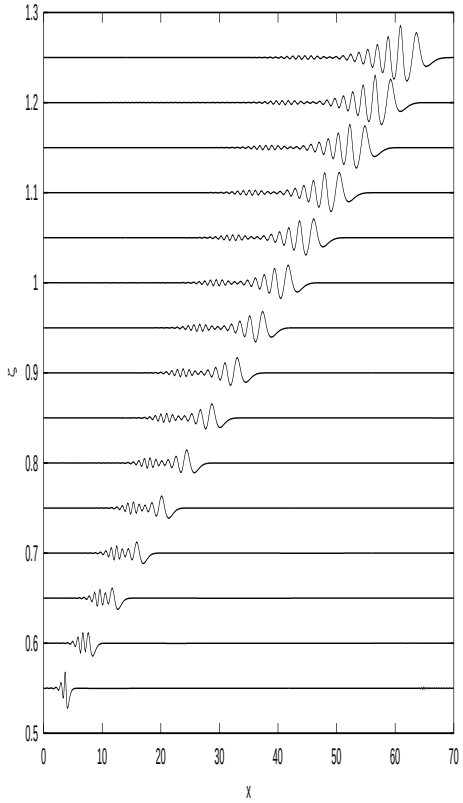

Figure 10: Time evolution of the interface $z = \zeta$ for the glacier case, having fixed $S = 1, D = 1.1, \Theta = 0.5, R = 2$. The system was integrated to time T=500, with time step dt=0.01

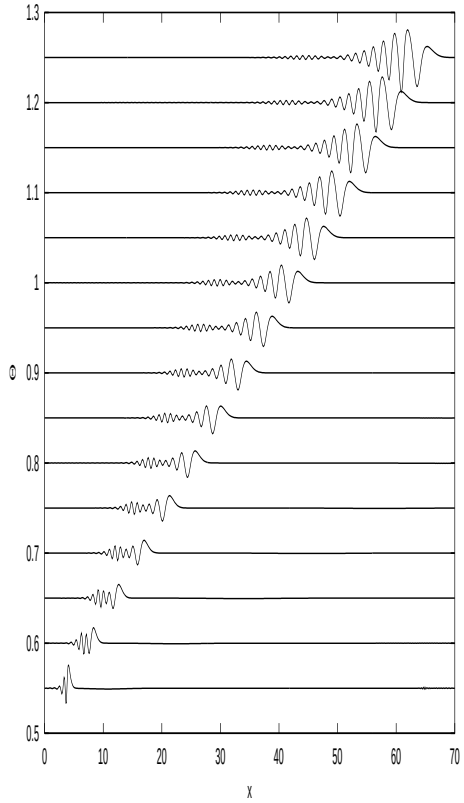

Figure 11: Evolution of $z = \theta$ for the same system. The bump entering the domain from the left is expressed by an exponential law of the form: $F(t) = A * t/t_0 * exp(-t/t_0)$.

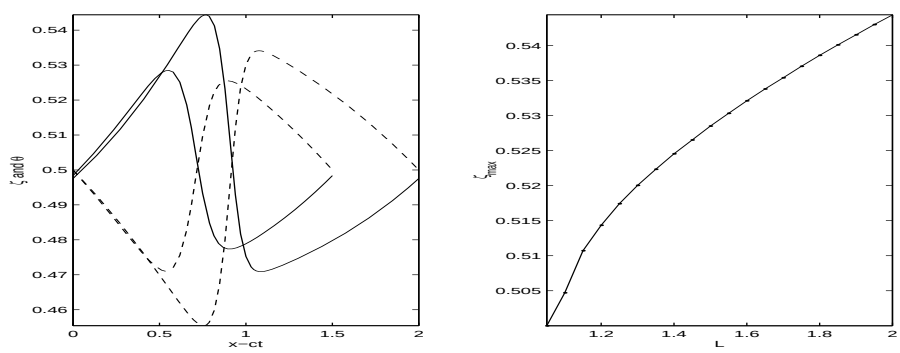

Figure 12: Equilibrium shapes and bifurcation diagram for the glacier model with $S = 1, D = 1.1, R = 2$ and $\Theta = 0.5$. In the plot to the right the solid lines represents the equilibrium shapes of ζ, while the dashed ones describe θ. The couple of solutions correspond to two different choices of the domain lenght, being respectively L=2 and L=1.5

6 The Ice-Stream Model

The models described so far have to do with two furthermost and completely uncorrelated situations, that solely take into account the effects or of the shear stresses (glacier approximation) or of the longitudinal ones (ice-shelf model).

But, to some extent, the behaviour of ice-streams is something in between that ones of glaciers or of ice-shelves. In fact, it becomes rather hazy also in practice to locate the geometric limits of a fast moving ice-stream bounded by an outlet glacier or entering an ice-shelf.

An intermediate model is thus built taking the 1-D non-dimensional set of equations (18) and (19) of the glacier, but without discarding the adjustment produced by the longitudinal stresses on the velocity profile.

The starting point are the followings, describing the system at leading order:

$$\begin{aligned} 0 &= u_{1x} + w_{1z} \\ 0 &= -p_{1x} + \epsilon \partial_x \tau_{xx} + \partial_z \tau_{xz} + S \\ 0 &= -p_{1z} - 1 \end{aligned} \tag{65}$$

$$\begin{aligned} 0 &= u_{2x} + w_{2z} \\ 0 &= -p_{2x} + \partial_z \sigma_{xz} + SD \\ 0 &= -p_{2z} - D \end{aligned} \tag{66}$$

With the usual meaning for the parameters involved, these equations are closed by the set of conditions at the boundaries previously stated.

The longitudinal stresses are expressed by the term $\epsilon \partial_x \tau_{xx}$ in the second of equations (65). It's clear, modeling again the upper fluid as a Newtonian one (and in this case $\tau_{xx} = 2\epsilon\nu_1 u_x$), that this term becomes relevant whenever:

$$\epsilon^2 \nu_1 \sim O(1) \tag{67}$$

This condition is satisfied if $R = \frac{\nu_1}{\nu_2} \gg 1$ and describes a situation in which a much more viscous fluid, characterized by a nearly uniform velocity profile, slides over a less viscous one, with a velocity profile that is parabolic at leading order.

This model is valid for ice-streams since it incorporates the corrections due to longitudinal stresses to a velocity that is not yet completely independent on x.

The next step is the derivation of a consistent and more general thin layer theory, following a procedure analogous to that one described for the glacier. The ice-stream thin layer theory is then expressed by:

$$\begin{aligned} \zeta_t + \partial_x[\frac{1}{2}u\zeta - \frac{1}{12}(DS - \theta_x - D\zeta_x)\zeta^3] &= 0 \\ \theta_t + \partial_x[\theta u + (S - h_x)\frac{\theta^3}{3R}] &= 0 \\ \frac{\zeta^2}{2}(DS - D\zeta_x - \theta_x) + (S - h_x)\theta\zeta + 2\epsilon^2 R\zeta\partial_x(\theta\tau_{xx}) &= u \end{aligned} \tag{68}$$

These equations incorporate two different approximations, reducing to:

- the glacier ones for $R \sim O(1)$;
- the ice-shelf ones for $R \sim O(\epsilon^{-2})$.

7 Conclusions

The purpose of this work was the investigation of two of the mechanisms considered relevant in ice-stream dynamics.

In particular, the extremely simplified models described, were formulated in order to understand the effects on the flow of the different stresses conditions found at the boundary between the flowing ice and its bottom. The explicit treatment of the basal layer, altough complicating the formulation, had the advantage of avoiding strong unphysically grounded assumptions about the structure of the stresses. A second task was, possibly, to relate the action of the stresses to the instability patterns effectively observed in nature.

In this context the glacier and the ice-shelf approximations (the first dominated by shear and the second by longitudinal stresses) were derived and studied. The linear stability analysis revealed the presence of instabilities at the boundaries between the two fluids in both of the models, but showed also the lack of an effective mechanism generating fingers.

Combining the sliding and the slipping properties of the glacier and of the ice-shelf motion, a one-dimensional ice-stream model was then formulated.

These results are far from being relevant for ice, but the analysis can in principle be extended to the consideration of a non Newtonian fluid in motion over a bottom layer, including in the governing equations a different constitutive law.

It could finally be intriguing, for the future, to analyse in more detail the non-linear properties of the models presented, in order to better define their effective capability (or inability) in explaining ice-stream dynamic.

Acknowledgments

I am really greateful to Neil for the long stimulating discussions and for the contagious enthusiasm he was showing when, with the sole help of the chalk, we were fighting on the blackboard against potentially discouraging issues.

I wish then to express my solidariety and admiration to Helen, Fiona, Lianke, Ed, Matt and Taka, that succeeded in bearing me for ten tormented weeks. Thanks for the laughs, the colors, the help and the nice talks.

A lot of people that passed through Walsh Cottage contributed to make it an enjoyable and not conventional environment.

A special mention deserves Shre, that shared my office for all the summer (demonstrating to be extremely patient) and who assisted with me to an impressive number of sunrises, while getting out from the cottage after interminable study sessions.

References

[1] R. B. Alley et al., "Till beneath ice stream B, 3, Till deformation: evidence and implications", J. Geophys. Res., Vol.92 (B9), pp. 8921–8929, 1987

[2] N. J. Balmforth et al., "A consistent thin-layer theory for Bingham plastics", J. Non-Newtonian Fluid Mech., Vol. 84, pp. 65–81, 1999

[3] N. J. Balmforth et al., "Visco-plastic models of isothermal lava domes", J. Fluid Mech., Vol. 403, pp. 37–65, 2000

[4] K. P. Chen, "Wave formation in the gravity-driven low-Reynolds number flow of two liquid films down an inclined plane", Phys. Fluids A, Vol. 5 (12), 3038–3048, 1993

[5] H. Engelhardt et al., "Physical conditions at the base of a fast moving Antartic ice stream", Science, Vol. 248 (4985), pp. 57–59, 1990

[6] A. C. Fowler, "Ice-sheet surging and ice-stream formation", Ann. Glac., Vol. 23, pp 68–73, 1996

[7] T. J. Hughes, Rev. Geophys. Space Phys., Vol. 15, 1977

[8] D. R. MacAyeal, "Large-Scale Ice Flow Over a Viscous Basal Sediment: Theory and Applications to Ice Stream B, Antarctica", J. Geophys. Res., Vol. 94, No. B4, pp. 4071–4087, 1987

[9] D. R. MacAyeal, "The basal stress distribution of Ice Stream E, Antarctica, inferred by control methods", J. Geophys. Res., Vol. 97 (B1), pp. 595–603, 1992

[10] W. S. B. Paterson, *The Physics of Glaciers*, Butterworth-Heinemann, 1998

[11] A. J. Payne, "A Thermomechanical Model of Ice-Flow in West-Antartica", Climate Dynamics, Vol. 15, pp. 115–125, 1999

[12] A. J. Payne, "Dynamics of the siple coast ice stream, West Antartica: results from a thermomechanical ice sheet model", Geophys. Res. Lett., Vol. 25 (16), pp. 3173–3176, 1998

[13] C. Pozrikidis, "Gravity-driven creeping flow of two adjacent layers through a channel and down a plane wall", J. Fluid Mech., Vol. 371, pp. 345–376, 1998

[14] B. S. Tilley et al., "Linear stability theory of two-layer fluid flow in an inclined channel", Phys. Fluids, Vol. 6 (12), pp.3906–3922, 1994

[15] S. J. Weinstein, "Large growth instabilities in three-layer flow down an incline in the limit of zero wave Reynolds wave number", Phys. Fluids, Vol. 11 (11), 3270–3282, 1999

The Time Evolution of Water Vapor "Black Holes" in the Upper Troposphere

Edwin P. Gerber*

1 Introduction

The water vapor channels on the United States' GOES 10 and GOES 8, the European METEOSAT, and the Japanese GMS geostationary satellites measure long-wave radiation of wavelength 5.7–7.1 μm. Images at these wavelengths do not show any surface features of the Earth, since the radiation emitted by the surface at 5.7–7.1 μm is entirely absorbed by low-level atmospheric water vapor. Rather, they reveal planetary and synoptic scale variations of water vapor in the middle and upper troposphere.

In regions of subsidence, where the large-scale vertical motion is downward, the troposphere becomes filled with dry air from the upper troposphere, and the 5.7–7.1 μm radiation received by the satellite comes primarily from the relatively warm lower troposphere. When the large-scale vertical motion is upward, the cold upper troposphere becomes saturated (or nearly so) with humid air from the surface, and the 5.7–7.1 μm radiation seen by the satellites is the cold water vapor in the upper troposphere. In this way the "equivalent black body temperature" of the 5.7–7.1 μm radiation is a proxy for the vertical motion field. An empirical connection between water vapor and vertical motion is confirmed in [9] and [11], in which a correlation is found between convergence of the mean circulation of the upper troposphere (implying subsidence, by continuity) and dry regions in the satellite images.

In the absence of tropical storms, water vapor images of the low latitude East Pacific are often dominated by two features, the moisture rich Intertropical Convergence Zone (ITCZ) and "black holes," vast regions of low humidity. As shown in Figures 1-3, images taken during the northern hemisphere summer, the ITCZ forms a band of convection across the thermal equator in the East Pacific, centered at approximately 8^0 N. North and south of the ITCZ are the arid regions, centered, in Figure 1, at 145^0 W, 16^0 N and 130^0 W, 8^0 S. The black hole in the southern (winter) hemisphere is comparable in size to the continental United States. In the far west we see a second region of deep convection over Indonesia, associated with the warm La Nina West Pacific.

We seek to explain the shape, particularly the north-south and east-west asymmetries, the intensity, and the time evolution of these East Pacific water vapor black holes as a product of the circulation driven by deep convection in the ITCZ. In the spirit of this

*with Takamitsu Ito and Wayne Schubert

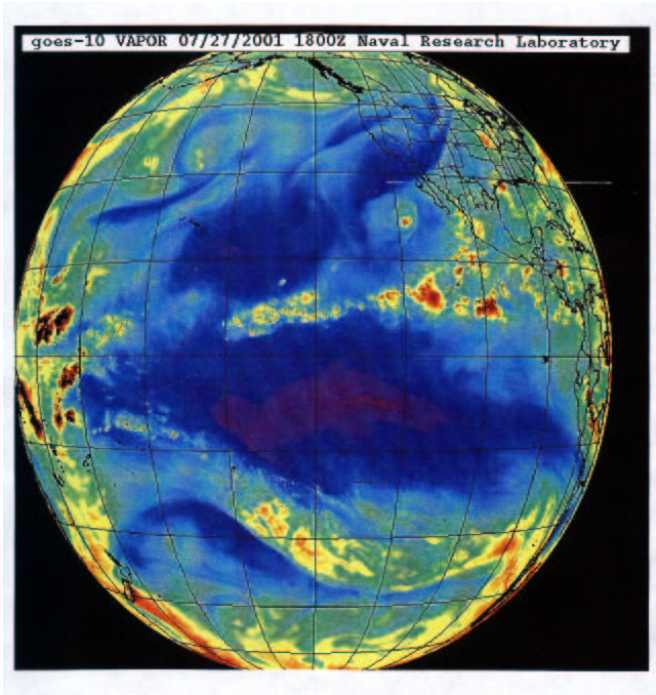

Figure 1: GOES 10 Water Vapor Image, July 27, 2001 1800z. The longitude and latitude interval is 15^0. The center meridian is 135^0 W, and crosses the equator at the center of the image. Green, yellow, and red indicate areas where the upper troposphere is rich in moisture (increasing from green to red). Blue, purple, and black colors indicate an increasingly dry upper troposphere.

summer's GFD program, we have built a conceptual model of the tropical atmosphere to aid us.

1.1 The Basic Model

We begin with stratified β-plane atmosphere extending to infinity in both x and y. We next linearize about a basic state at rest and perform a vertical mode transformation, as in [1]. This separates the motion of the atmosphere into baroclinic modes, each obeying an independent set of equations equivalent to the linearized shallow water system.

We next assume that the latent heat release excites only the first baroclinic mode. The vertical profile of the first mode takes a form similar to a cosine wave from 0 to π. Fluid on the bottom flows opposite that on top, connected by a smooth profile with no motion at a node near the midpoint of the atmosphere. We can view the shallow water equations as prescribing flow at the base of the atmosphere, and then use the sinusoidal vertical profile to complete the picture. Deep convection in this simple system has the effect of transferring mass from the lower layer to the upper layer. We thus prescribe a mass sink in our lower layer to model the effect of the ITCZ, or any other regions of deep convection. Given our forcing, we solve for the resulting subsidence field, and hence the water vapor field, to find the black holes.

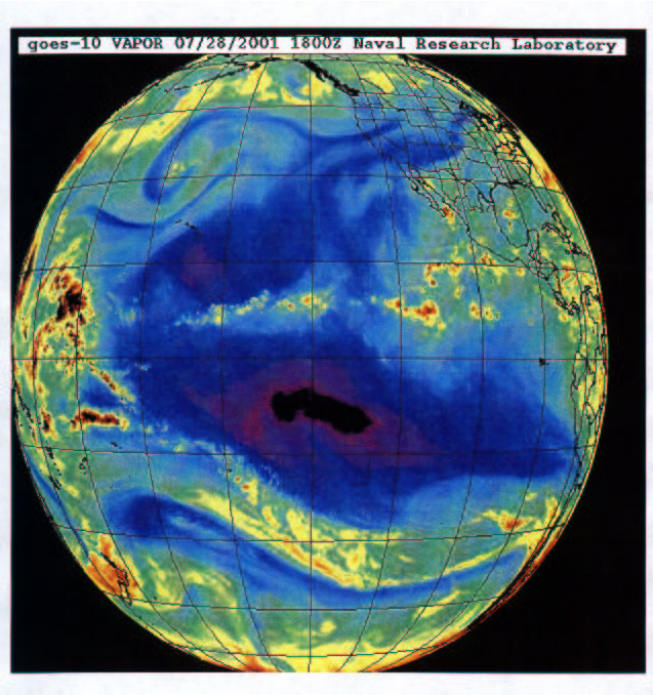

Figure 2: GOES 10 Water Vapor Image, July 28, 2001 1800z

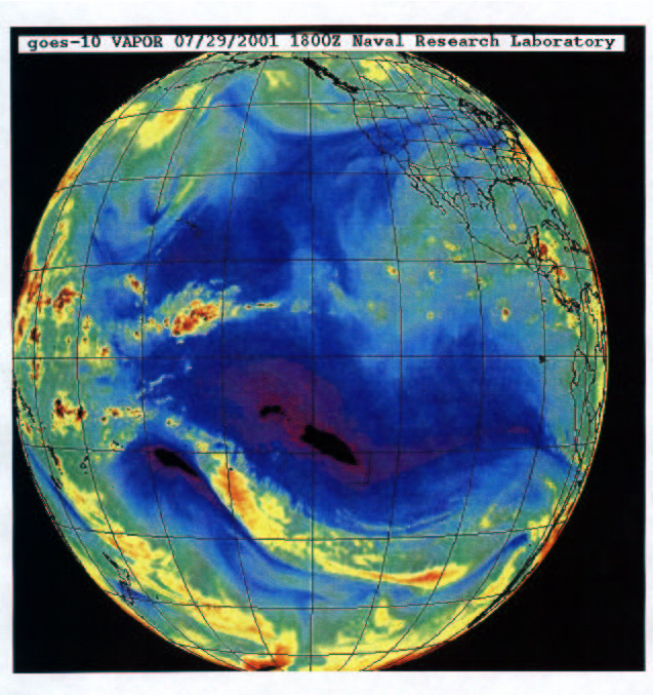

Figure 3: GOES 10 Water Vapor Image, July 29, 2001 1800z

We are following in the footsteps of A. E. Gill, who with others studied this model extensively in the 1980's in [2], [5], and [8]. We do not, however, make the long wave approximation, following rather the original eigenvalue formulation of Matsuno [7] in 1966, later developed in [12], where the time dependent evolution of tropical circulation around the amazon basin was studied. In contrast to [12], however, we attempt to include dissipation and Newtonian cooling in our model. We are thus applying a tried and true theory, seeking to focus a new application; the formation of water vapor black holes.

2 Theory

2.1 The Linearized Equatorial β-Plane

Consider the motions of an incompressible, forced, shallow water fluid on the equatorial β-plane. In our model, this shallow water layer corresponds to the lower layer in the first baroclinic mode. The governing equations, linearized about a resting basic state, are

$$\frac{\partial u}{\partial t} - \beta y v + g\frac{\partial h}{\partial x} = -\epsilon u, \tag{1}$$

$$\frac{\partial v}{\partial t} + \beta y u + g\frac{\partial h}{\partial y} = -\epsilon v, \tag{2}$$

$$\frac{\partial h}{\partial t} + \bar{h}\left(\frac{\partial u}{\partial x} + \frac{\partial v}{\partial y}\right) = -\epsilon h - S, \tag{3}$$

where u and v are velocity components in the x- and y-directions, respectively, h is the deviation of the fluid depth from the constant mean depth $\bar{h}$, βy is the Coriolis parameter, ϵ is the constant Rayleigh friction and Newtonian damping coefficient, and $S(x, y, t)$ is the lower layer mass sink. Before solving (1)–(3) it is convenient to put the problem in nondimensional form. We define $c = (g\bar{h})^{\frac{1}{2}}$ as the constant gravity wave speed based on the mean depth $\bar{h}$. As a horizontal length scale let us choose $L = (c/\beta)^{\frac{1}{2}}$. Similarly, let us choose as a unit of time $T = (\beta c)^{-\frac{1}{2}}$. Data from the ITCZ in the Pacific (specifically the Marshall Islands) and in the Atlantic [1] suggests that, for the first baroclinic mode, $c \approx 7.5 \times 10^1\, m/s$ and $\bar{h} \approx 5.7 \times 10^2\, m$, so that $L \approx 1.8 \times 10^3 km$ and $T \approx 0.28\, day$. For now, we choose c as the unit of speed and $\bar{h}$ as the unit of depth, so that (1)–(3) reduce to the nondimensional form

$$\frac{\partial u}{\partial t} - y v + \frac{\partial h}{\partial x} = -\epsilon u, \tag{4}$$

$$\frac{\partial v}{\partial t} + y u + \frac{\partial h}{\partial y} = -\epsilon v, \tag{5}$$

$$\frac{\partial h}{\partial t} + \frac{\partial u}{\partial x} + \frac{\partial v}{\partial y} = -\epsilon h - S, \tag{6}$$

where all the independent variables x, y, t, all the dependent variables u, v, h, the parameter ϵ and the function $S(x, y, t)$ are now nondimensional. The system (4)–(5) can also be written in the more compact form

$$\frac{\partial \mathbf{w}}{\partial t} + \mathcal{L}\mathbf{w} = -\epsilon \mathbf{w} - \mathbf{S}, \tag{7}$$

where

$$\mathbf{w}(x,y,t) = \begin{pmatrix} u(x,y,t) \\ v(x,y,t) \\ h(x,y,t) \end{pmatrix}, \quad \mathbf{S}(x,y,t) = \begin{pmatrix} 0 \\ 0 \\ S(x,y,t) \end{pmatrix}, \quad \mathcal{L} = \begin{pmatrix} 0 & -y & \partial/\partial x \\ y & 0 & \partial/\partial y \\ \partial/\partial x & \partial/\partial y & 0 \end{pmatrix}. \tag{8}$$

The potential vorticity (PV) principle associated with (4)–(6) is

$$\frac{\partial q}{\partial t} + v = -\epsilon q + yS, \tag{9}$$

where

$$q = \frac{\partial v}{\partial x} - \frac{\partial u}{\partial y} - yh \tag{10}$$

is the potential vorticity anomaly. The total energy principle associated with (4)–(6) is

$$\frac{\partial}{\partial t}\left[\tfrac{1}{2}\left(u^2+v^2+h^2\right)\right] + \frac{\partial(uh)}{\partial x} + \frac{\partial(vh)}{\partial y} = -2\epsilon\left[\tfrac{1}{2}\left(u^2+v^2+h^2\right)\right] - hS, \tag{11}$$

or, in integral form

$$\frac{\partial}{\partial t}\int_{-\infty}^{\infty}\int_{-\infty}^{\infty} \tfrac{1}{2}\left(u^2+v^2+h^2\right) dxdy = -2\epsilon\int_{-\infty}^{\infty}\int_{-\infty}^{\infty} \tfrac{1}{2}\left(u^2+v^2+h^2\right) dxdy - \int_{-\infty}^{\infty}\int_{-\infty}^{\infty} hSdxdy. \tag{12}$$

The energy principle suggests an inner product,

$$(\mathbf{f},\mathbf{g}) = \int_{-\infty}^{\infty} (f_1 g_1^* + f_2 g_2^* + f_3 g_3^*) dy, \tag{13}$$

given

$$\mathbf{f} = \begin{pmatrix} f_1 \\ f_2 \\ f_3 \end{pmatrix}, \qquad \mathbf{g} = \begin{pmatrix} g_1 \\ g_2 \\ g_3 \end{pmatrix}, \tag{14}$$

where we use the * symbol to denote the complex conjugate, anticipating work with complex numbers. We have defined our inner product with respect to y in preparation for a Fourier transform of our equations in x. We may now write our energy principle in more compact form,

$$\int_{-\infty}^{\infty} \frac{1}{2}(\mathbf{w},\mathbf{w}) dx = -2\epsilon\int_{-\infty}^{\infty} \frac{1}{2}(\mathbf{w},\mathbf{w}) dx - \int_{-\infty}^{\infty}\int_{-\infty}^{\infty} hSdxdy. \tag{15}$$

2.2 The Matsuno Eigenvalue Problem

Our goal is to solve (7) for $\mathbf{w}(x,y,t)$ subject to a specified initial condition $\mathbf{w}(x,y,0)$ and mass sink $\mathbf{S}(x,y,t)$. By first solving the inviscid, unforced system,

$$\frac{\partial \mathbf{w}}{\partial t} + \mathcal{L}\mathbf{w} = 0, \tag{16}$$

our goal becomes easier. Let us search for solutions of the form $u(x,y,t) = \mathcal{U}(k,y)e^{i(kx-\omega t)}$, $v(x,y,t) = \mathcal{V}(k,y)e^{i(kx-\omega t)}$, and $h(x,y,t) = \mathcal{H}(k,y)e^{i(kx-\omega t)}$, where k is the zonal wave number and ω the frequency. Hence in our vector notation, we make the substitution

$$\mathbf{w}(x,y,t) = \mathbf{K}(k,y)e^{i(kx-\omega t)}, \tag{17}$$

where

$$\mathbf{K}(k,y) = \begin{pmatrix} \mathcal{U}(k,y) \\ \mathcal{V}(k,y) \\ \mathcal{H}(k,y) \end{pmatrix}, \tag{18}$$

into (16). The substitution results in the eigenvalue problem,

$$-i\omega\mathbf{K} + \hat{\mathcal{L}}\mathbf{K} = 0, \tag{19}$$

where

$$\hat{\mathcal{L}} = \begin{pmatrix} 0 & -y & ik \\ y & 0 & d/dy \\ ik & d/dy & 0 \end{pmatrix}. \tag{20}$$

The adjoint of $\hat{\mathcal{L}}$ with respect to the inner product (13) is the operator $\hat{\mathcal{L}}^\dagger$ which satisfies

$$(\hat{\mathcal{L}}\mathbf{f}, \mathbf{g}) = (\mathbf{f}, \hat{\mathcal{L}}^\dagger\mathbf{g}) \tag{21}$$

for all $\mathbf{f}(y)$ and $\mathbf{g}(y)$ satisfying the boundary conditions, that is $(f,g) < \infty$. Our operator $\hat{\mathcal{L}}$ is skew-Hermitian, as $\hat{\mathcal{L}}^\dagger = -\hat{\mathcal{L}}$, so that (21) becomes

$$(\hat{\mathcal{L}}\mathbf{f}, \mathbf{g}) = -(\mathbf{f}, \hat{\mathcal{L}}\mathbf{g}). \tag{22}$$

The skew-Hermitian property dictates that the eigenvalues of $\hat{\mathcal{L}}$ are purely imaginary, so that we have a mathematical basis for looking for wave-like solutions (solutions where ω is purely real). In addition, the eigenfunctions form a complete orthogonal set. Hence there exist a set of eigenfunctions $\mathbf{K_i}$ that span all functions f satisfying $(f,f) < \infty$ with

$$(\mathbf{K_i}, \mathbf{K_j}) = 0 \tag{23}$$

if $i \neq j$.

The eigenvalue problem was solved in [7], which revealed that (19) has bounded solutions as $y \to \pm\infty$, only if $\omega^2 - k^2 - k/\omega$ is an odd integer, that is, only if

$$\omega^2 - k^2 - k/\omega = 2n + 1, \tag{24}$$

with $n = 0, 1, 2, \ldots$ We shall denote the solutions of this cubic equation by $\omega_{n,r}$, since the frequency will depend on the particular odd integer $2n+1$ chosen, and where the subscript $r = 0, 1, 2$ indicates which of the three roots of the frequency equation we are discussing.

For $n > 0$ our dispersion relation (24) separates nicely into three modes: low frequency Rossby waves which always propagate to the west (ω has the opposite sign of k) and high frequency westward and eastward propagating inertial gravity waves. We have given the

modes the subscripts 0, 1, and 2, respectively. Approximate values for the frequencies are given below. They are more accurate for large n.

$$\omega_{n,0} \approx \frac{-k}{k^2+2n+1} \tag{25}$$

$$\omega_{n,1} \approx -(k^2+2n+1)^{\frac{1}{2}} \tag{26}$$

$$\omega_{n,2} \approx (k^2+2n+1)^{\frac{1}{2}} \tag{27}$$

For $n=0$, (24) factors to $(\omega_{0,r}+k)(\omega_{0,r}^2-k\omega_{0,r}-1)=0$, yielding two mixed modes and one forbidden mode $\omega_{0,1}=-k$ that cannot be normalized. The allowable waves have Rossby and gravity wave character.

$$\omega_{0,0} = \frac{k-(k^2+4)}{2} \tag{28}$$

$$\omega_{0,2} = \frac{k+(k^2+4)}{2} \tag{29}$$

Let $\mathbf{K_{n,r}}$ denote the eigenfunction corresponding to rth root of (24) given n.

$$\mathbf{K_{n,r}} = A_{n,r}e^{-\frac{1}{2}y^2}\begin{pmatrix} -\frac{1}{2}(\omega_{n,r}+k)H_{n+1}(y)-n(\omega_{n,r}-k)H_{n-1}(y) \\ i(\omega_{n,r}^2-k^2)H_n(y) \\ -\frac{1}{2}(\omega_{n,r}+k)H_{n+1}(y)+n(\omega_{n,r}-k)H_{n-1}(y)\end{pmatrix}, \tag{30}$$

where

$$A_{n,r} = \pi^{-\frac{1}{4}}\{2^n n![(n+1)(\omega_{n,r}+k)^2+n(\omega_{n,r}-k)^2+(\omega_{n,r}^2-k^2)^2]\}^{-\frac{1}{2}} \tag{31}$$

is a normalization constant which assures that

$$(\mathbf{K_{n,r}},\mathbf{K_{n,r}}) = 1 \tag{32}$$

The Hermite polynomials $H_n(y)$ are given by $H_0(y)=1$, $H_1(y)=2y$, $H_2(y)=4y^2-2$, $H_3(y)=8y^3-12y$, $\cdots$, with recurrence relation $H_{n+1}(y)=2yH_n(y)-2nH_{n-1}(y)$.

We have not quite found all the solutions of (19), because it is possible to have the trivial solution $\mathcal{V}=0$, but nontrivial $\mathcal{U}$ and $\mathcal{H}$. If we expand (19) with $\mathcal{V}=0$ we find that

$$-\omega\mathcal{U}+k\mathcal{H}=0 \tag{33}$$

$$y\mathcal{U}+\frac{d\mathcal{H}}{dy}=0 \tag{34}$$

$$-\omega\mathcal{H}+k\mathcal{U}=0. \tag{35}$$

The first and third of these can be considered as two linear, homogeneous algebraic equations for $\mathcal{U}$ and $\mathcal{H}$. Requiring the determinant of the coefficients to vanish gives $\omega^2=k^2$, with solutions $\omega=\pm k$. When $\omega=-k$, $\mathcal{H}=-\mathcal{U}$ and (34) becomes $d\mathcal{U}/dy=y\mathcal{U}$, with solution $\mathcal{U}\sim e^{\frac{1}{2}y^2}$. This solution must be discarded since it is not bounded as $y\to\pm\infty$. When $\omega=k$, $\mathcal{H}=\mathcal{U}$ and (34) becomes $d\mathcal{U}/dy=-y\mathcal{U}$, with solution $\mathcal{U}\sim e^{-\frac{1}{2}y^2}$. This solution is acceptable. Thus, we have found the additional (Kelvin wave) eigenfunction

$$\mathbf{K_{-1}} = A_{-1}e^{-\frac{1}{2}y^2}\begin{pmatrix}1\\0\\1\end{pmatrix}, \tag{36}$$

with corresponding eigenvalue (dispersion relation) $\omega_{-1}=k$. The subscript -1 is chosen because the dispersion relation $\omega=k$ is a solution of $\omega^2-k^2-k/\omega=2n+1$ when $n=-1$.

2.3 The Normal Mode Transformation

We may now use our eigenfunctions to decompose the forced, damped problem into normal modes. First, we introduce the Fourier transform pair in x,

$$u(x,y,t) = (2\pi)^{-\frac{1}{2}} \int_{-\infty}^{\infty} \hat{u}(k,y,t) e^{ikx} dk, \tag{37}$$

$$\hat{u}(k,y,t) = (2\pi)^{-\frac{1}{2}} \int_{-\infty}^{\infty} u(x,y,t) e^{-ikx} dx, \tag{38}$$

where k is the zonal wavenumber. Similar transform pairs exist for $v(x,y,t)$ and $\hat{v}(k,y,t)$, for $h(x,y,t)$ and $\hat{h}(k,y,t)$, and for $S(x,y,t)$ and $\hat{S}(k,y,t)$. We can now write (7) as

$$\frac{\partial \hat{\mathbf{w}}}{\partial t} + \hat{\mathcal{L}}\hat{\mathbf{w}} = -\epsilon \hat{\mathbf{w}} - \hat{\mathbf{S}}, \tag{39}$$

where

$$\hat{\mathbf{w}}(k,y,t) = \begin{pmatrix} \hat{u}(k,y,t) \\ \hat{v}(k,y,t) \\ \hat{h}(k,y,t) \end{pmatrix}, \qquad \hat{\mathbf{S}}(k,y,t) = \begin{pmatrix} 0 \\ 0 \\ \hat{S}(k,y,t) \end{pmatrix}, \tag{40}$$

and $\hat{\mathcal{L}}$ is defined as in (20).

Our second task is to transform (39) in y. As our eigenfunctions $\mathbf{K}_{n,r}(k,y)$ satisfy the orthonormality condition

$$\left(\mathbf{K}_{n,r}(k,y), \mathbf{K}_{n',r'}(k,y)\right) = \begin{cases} 1 & (n',r') = (n,r) \\ 0 & (n',r') \neq (n,r) \end{cases}, \tag{41}$$

we can set up a transform pair

$$\hat{w}_{n,r}(k,t) = \left(\hat{\mathbf{w}}(k,y,t), \mathbf{K}_{n,r}(k,y)\right), \tag{42}$$

$$\hat{\mathbf{w}}(k,y,t) = \sum_{n,r} \hat{w}_{n,r}(k,t) \mathbf{K}_{n,r}(k,y). \tag{43}$$

Taking the inner product of (39) with $\mathbf{K}_{n,r}(k,y)$, we obtain

$$\begin{aligned}
\left(\frac{\partial \hat{\mathbf{w}}(k,y,t)}{\partial t}, \mathbf{K}_{n,r}(k,y)\right) + \left(\hat{\mathcal{L}}\hat{\mathbf{w}}(k,y,t), \mathbf{K}_{n,r}(k,y)\right) &= \\
-\epsilon \left(\hat{\mathbf{w}}(k,y,t), \mathbf{K}_{n,r}(k,y)\right) &- \left(\hat{\mathbf{S}}(k,y,t), \mathbf{K}_{n,r}(k,y)\right) \\
\frac{\partial}{\partial t}\left(\hat{\mathbf{w}}(k,y,t), \mathbf{K}_{n,r}(k,y)\right) - \left(\hat{\mathbf{w}}(k,y,t), \hat{\mathcal{L}}\mathbf{K}_{n,r}(k,y)\right) &= -\epsilon \hat{w}_{n,r}(k,t) - \hat{S}_{n,r}(k,t) \\
\frac{d\hat{w}_{n,r}(k,t)}{dt} - \left(\hat{\mathbf{w}}(k,y,t), i\omega_{n,r}\mathbf{K}_{n,r}(k,y)\right) &= -\epsilon \hat{w}_{n,r}(k,t) - \hat{S}_{n,r}(k,t) \\
\frac{d\hat{w}_{n,r}(k,t)}{dt} + i\omega_{n,r}\left(\hat{\mathbf{w}}(k,y,t), \mathbf{K}_{n,r}(k,y)\right) &= -\epsilon \hat{w}_{n,r}(k,t) - \hat{S}_{n,r}(k,t)
\end{aligned}$$

so that

$$\frac{d\hat{w}_{n,r}(k,t)}{dt} + (\epsilon + i\omega_{n,r})\hat{w}_{n,r}(k,t) = -\hat{S}_{n,r}(k,t). \tag{44}$$

Equation (44) is the transformation to spectral space of the original system (7) and has solution

$$\hat{w}_{n,r}(k,t) = \hat{w}_{n,r}(k,0)e^{-(\epsilon+i\omega_{n,r})t} - \int_0^t \hat{S}_{n,r}(k,t')e^{-(\epsilon+i\omega_{n,r})(t-t')}dt'. \tag{45}$$

When this spectral space solution is inserted into (43), we obtain the vector equation

$$\hat{\mathbf{w}}(k,y,t) = \sum_{n,r} \hat{w}_{n,r}(k)\mathbf{K}_{n,r}(k,y), \tag{46}$$

Taking the inverse Fourier transform of (46) and breaking back into component form, we obtain our final physical space solutions

$$u(x,y,t) = (2\pi)^{-\frac{1}{2}} \int_{-\infty}^{\infty} \sum_{n,r} \hat{w}_{n,r}(k)\mathcal{U}_{n,r}(k,y)e^{ikx}dk, \tag{47}$$

$$v(x,y,t) = (2\pi)^{-\frac{1}{2}} \int_{-\infty}^{\infty} \sum_{n,r} \hat{w}_{n,r}(k)\mathcal{V}_{n,r}(k,y)e^{ikx}dk, \tag{48}$$

$$h(x,y,t) = (2\pi)^{-\frac{1}{2}} \int_{-\infty}^{\infty} \sum_{n,r} \hat{w}_{n,r}(k)\mathcal{H}_{n,r}(k,y)e^{ikx}dk. \tag{49}$$

According to (47) – (49) the general solution of our initial value problem consists of a superposition of normal modes. The superposition involves all zonal wavenumbers (integral over k), all meridional wavenumbers (sum over n), and all wave types (sum over r).

It should be noted that typical superpositions of many normal modes result in spatial patterns which differ greatly from individual normal modes. We found that the $w_{n,r}$ decay exponentially with n for all choices of k. Thus, given a specified degree of accuracy, we can select an N so that the partial sum of all modes $n < N$ meets the requirement. In general, we found that $N = 200$ gave very good results.

It was also necessary to perform the Inverse Fourier Transform via a numeric approximation to the integral. A simple mid-point rule numeric integration was sufficient.

2.4 Forcing

We consider cases where the time evolution of the forcing is separable from its spatial dependence.

$$S(x,y,t) = (\pi ab)^{-1}e^{-x^2/a^2}e^{-(y-y_0)^2/b^2}\tilde{S}(t), \tag{50}$$

where y_0 is the center of the Gaussian shaped mass sink and a and b control the spatial extent in x and y. The factor $(\pi ab)^{-1}$ has been included so that

$$\int_{-\infty}^{\infty}\int_{-\infty}^{\infty} S(x,y,t)dxdy = \tilde{S}(t), \tag{51}$$

i.e., the rate of total mass removal is independent of the choices of a and b.

The Fourier transform of this forcing is

$$\hat{S}(k,y,t) = (\pi ab)^{-1}(2\pi)^{-\frac{1}{2}}e^{-(y-y_0)^2/b^2}\tilde{S}(t)\int_{-\infty}^{\infty} e^{-x^2/a^2}e^{-ikx}dx \tag{52}$$

$$= 2^{-\frac{1}{2}}(\pi b)^{-1}e^{-(y-y_0)^2/b^2}e^{-\frac{1}{4}k^2a^2}\tilde{S}(t). \tag{53}$$

Then, using (42), we obtain

$$\begin{aligned}\hat{S}_{n,r}(k,t) &= \left(\hat{\mathbf{S}}(k,y),\mathbf{K}_{n,r}(k,y)\right) = \int_{-\infty}^{\infty}\hat{S}(k,y,t)\mathcal{H}_{n,r}(k,y)dy \\ &= 2^{-\frac{1}{2}}(\pi b)^{-1}e^{-\frac{1}{4}k^2a^2}\tilde{S}(t)\int_{-\infty}^{\infty} e^{-(y-y_0)^2/b^2}\mathcal{H}_{n,r}(k,y)dy \\ &= 2^{-\frac{1}{2}}(\pi b)^{-1}e^{-\frac{1}{4}k^2a^2}A_{n,r}\tilde{S}(t) \\ &\quad\cdot\int_{-\infty}^{\infty} e^{-(y-y_0)^2/b^2}e^{-\frac{1}{2}y^2}\left[-\tfrac{1}{2}(\omega_{n,r}+k)H_{n+1}(y)+n(\omega_{n,r}-k)H_{n-1}(y)\right]dy.\end{aligned}$$

From [3] we have

$$\int_{-\infty}^{\infty} e^{-(y-y_0)^2/b^2}e^{-\frac{1}{2}y^2}H_n(y)dy = \left(\frac{2\pi b^2}{2+b^2}\right)^{\frac{1}{2}}\left(\frac{2-b^2}{2+b^2}\right)^{\frac{n}{2}}e^{-y_0^2/(2+b^2)}H_n\left(\frac{2y_0}{(4-b^4)^{\frac{1}{2}}}\right) \tag{54}$$

for $0 < b < 2^{\frac{1}{2}}$. (For $b > 2^{\frac{1}{2}}$, there exists a recursion formula to solve the integral, but the modulus of the forcing term will increase with n, making for poor convergence.) Utilizing (54), we finally obtain

$$\begin{aligned}\hat{S}_{n,r}(k,t) &= \pi^{-\frac{1}{2}}A_{n,r}(2+b^2)^{-\frac{1}{2}}e^{-\frac{1}{4}k^2a^2}e^{-y_0^2/(2+b^2)}\tilde{S}(t) \\ &\cdot\left\{-\tfrac{1}{2}(\omega_{n,r}+k)\left(\tfrac{2-b^2}{2+b^2}\right)^{\frac{n+1}{2}}H_{n+1}\left(\tfrac{2y_0}{(4-b^4)^{\frac{1}{2}}}\right)+n(\omega_{n,r}-k)\left(\tfrac{2-b^2}{2+b^2}\right)^{\frac{n-1}{2}}H_{n-1}\left(\tfrac{2y_0}{(4-b^4)^{\frac{1}{2}}}\right)\right\},\end{aligned} \tag{55}$$

for all modes with the exception of the Kelvin wave, which takes a similar (and simpler) form.

To focus on the time dependence, (55) can be viewed as a function $\breve{S}_{n,r}$ of n, r, k, a, and b multiplying the time dependent part,

$$\hat{S}_{n,r}(k,t) = \breve{S}_{n,r}(k)\tilde{S}(t). \tag{56}$$

If we separate $\hat{w}_{n,r}(k,t) = \breve{w}_{n,r}(k)\tilde{w}_{n,r}(t)$ also, (44) yields,

$$\breve{w}_{n,r}(k)\left(\frac{d\tilde{w}_{n,r}(t)}{dt}+(\epsilon+i\omega_{n,r})\tilde{w}_{n,r}(t)\right) = -\breve{S}_{n,r}(k)\tilde{S}(t) \tag{57}$$

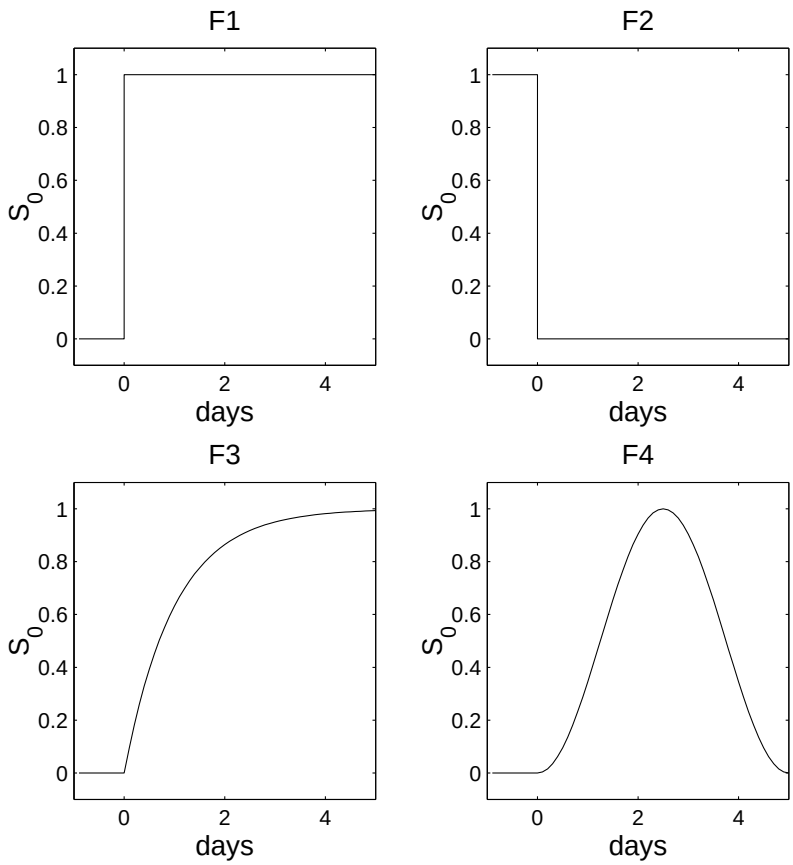

Figure 4: $\tilde{S}(t)$

We can now take $\breve{w}_{n,r}(k) = -\breve{S}_{n,r}(k)$, leaving

$$\frac{d\tilde{w}_{n,r}(t)}{dt} + (\epsilon + i\omega_{n,r})\tilde{w}_{n,r}(t) = \tilde{S}(t), \tag{58}$$

which has solution, following (45),

$$\tilde{w}_{n,r}(t) = e^{-(\epsilon+i\omega)t}\left(\int_0^t e^{(\epsilon+i\omega)t'}\tilde{S}(t')dt' + \tilde{w}_{n,r}(0)\right). \tag{59}$$

If $\tilde{S}(t)$ converges to a steady value, $\tilde{S}$, the solution will converge to the steady state solution, where

$$\tilde{w}_{n,r}(t) = \frac{\tilde{S}}{(\epsilon + i\omega)}. \tag{60}$$

We experimented with four different forcing functions, shown in Table 1 (and in Figure 4), hoping to model the onset and termination of convection. Forcing F1 is the Rossby adjustment problem, in which an atmosphere at rest adjust to a sudden, steady release of

Type	$\tilde{S}(t)$	$\tilde{w}_{n,r}(0)$	$\tilde{w}_{n,r}(t)$
F1	S_0	0	$S_0(1-e^{-(\epsilon+i\omega)t})\frac{1}{\epsilon+i\omega}$
F2	0	$\frac{S_0}{(\epsilon+i\omega)}$	$S_0 e^{-(\epsilon+i\omega)t}\frac{1}{\epsilon+i\omega}$
F3	$S_0(1-e^{-\gamma t})$	0	see (61)
F4	$\frac{S_0}{2}(1-cos(\gamma t))$	0	see (63)

Table 1: Forcing Functions

latent heat. Such forcing has been modeled before, but with the long wave approximation [5]. F2 is the adjustment problem in reverse, in which we shut off the heating in an atmosphere in equilibrium with a steady forcing. F3 was chosen as a simple, more realistic way to model the onset of convection. F4 attempts to capture the response to both the onset and termination of heating.

Forcing F3 yielded the following solution,

$$\tilde{w}_{n,r}(t) = S_0\left(\frac{1}{(\epsilon+i\omega_{n,r})} - \frac{e^{-\gamma t}}{(\epsilon-\gamma+i\omega_{n,r})} + \frac{\gamma e^{-(\epsilon+i\omega_{n,r})t}}{(\epsilon^2-\epsilon-\omega_{n,r}^2)+i\omega_{n,r}(2\epsilon-\gamma)}\right). \tag{61}$$

In the the limit $\gamma \gg \epsilon$, that is, when the rate at which the forcing turns on is fast relative to the rate of dissipation, (61) approaches the solution to forcing F1. In the other extreme, $\epsilon \gg \gamma$, (61) reduces to

$$\tilde{w}_{n,r}(t) = \frac{S_0}{(\epsilon+i\omega_{n,r})} - (1-e^{-\gamma t}). \tag{62}$$

in which the atmospheric response is always in equilibrium with the forcing. Forcing F4 results in

$$\tilde{w}_{n,r}(t) = \frac{S_0}{2}\left(\frac{1-e^{-(\epsilon+i\omega_{n,r})t}}{(\epsilon+i\omega_{n,r})} + \frac{(\epsilon+i\omega_{n,r})\left(e^{-(\epsilon+i\omega_{n,r})t}-cos(\gamma t)\right)-\gamma sin(\gamma t)}{(\epsilon+i\omega_{n,r})^2+\gamma^2}\right). \tag{63}$$

In the limit $\epsilon \gg \gamma$ (slow forcing) it reduces to a form similar to (62) in which the response is in equilibrium with the forcing at all times. In the opposite extreme, $\gamma \gg \epsilon$, we find

$$\tilde{w}_{n,r}(t) = S_0\left(\frac{1-e^{-(\epsilon+i\omega_{n,r})t}}{2(\epsilon+i\omega_{n,r})} - \frac{sin(\gamma t)}{2\gamma}\right). \tag{64}$$

The first term on the left hand side corresponds to a system adjusting as in forcing function F1 to the average value of the forcing, $S_0/2$, while the second term corresponds to a small out of phase response to the forcing.

2.5 Subsidence

w_{nd}, the nondimensional upward velocity, can be calculated directly from our shallow water solutions. Shallow water continuity implies that

$$w_{nd} = \frac{\partial h}{\partial t} = -\left(\frac{\partial u}{\partial x} + \frac{\partial v}{\partial y}\right). \tag{65}$$

For the first baroclinic mode, w is zero at the top and bottom of the atmosphere, reaching a maximum near the center. The complete vertical velocity profile takes on a form similar to a sine wave from 0 to π. w_{nd}, once properly dimensionalized, tells us the amplitude of the z-velocity in the first baroclinic mode, and hence corresponds to the maximum velocity found at the center of the vertical profile.

In spectral space,

$$\begin{aligned} \mathcal{W} &= \frac{\partial \mathcal{H}}{\partial t} \\ &= -i\omega\mathcal{H} \end{aligned} \tag{66}$$

for each mode. This enables us to calculate w analytically, the only error coming from the fact that we truncate our sum at the Nth mode.

2.6 Comparison with Gill

The long wave approximation is made in the linearized equatorial β-plane model first proposed by Gill in 1980 [2], and later developed further in [5, 8]. The only difference from our model is that the $\frac{\partial v}{\partial t}$ and $-\epsilon v$ terms are dropped from (2), based on scaling analysis, leaving the modified y-momentum equation

$$\beta y u + g\frac{\partial h}{\partial y} = 0. \tag{67}$$

The y-momentum equation hence reduces to simple geostrophic balance, and adjustment in v becomes instantaneous. (1) and (3) remain the same. While Gill concisely solves this system with the use of parabolic cylinder functions, analysis with Matsuno's eigenfunctions provides insight into the coupling between the inertial gravity and Rossby waves resulting from the long wave approximation. (Note that, as $v = 0$ in the Kelvin wave, it is unaffected by the long wave approximation.)

We proceed with the same analysis as before, applying a Fourier transform in x to reach the Gill equivalent of (39)

$$\frac{\partial}{\partial t}\begin{pmatrix} \hat{u}(k,y,t) \\ 0 \\ \hat{h}(k,y,t) \end{pmatrix} + \hat{\mathcal{L}}\hat{\mathbf{w}} = -\epsilon\begin{pmatrix} \hat{u}(k,y,t) \\ 0 \\ \hat{h}(k,y,t) \end{pmatrix} - \hat{\mathbf{S}}, \tag{68}$$

where $\mathbf{w}$, $\hat{\mathcal{L}}$ and $\mathbf{S}$ are defined as before in (20) and (40). We introduce the matrix

$$\mathbf{F} = \begin{pmatrix} 0 & 0 & 0 \\ 0 & 1 & 0 \\ 0 & 0 & 0 \end{pmatrix} \tag{69}$$

so that we may write (68) in a form more similar to (39), having now just two corrections to account for the long wave approximation

$$\frac{\partial \hat{\mathbf{w}}}{\partial t} - \frac{\partial \mathbf{F}\hat{\mathbf{w}}}{\partial t} + \hat{\mathcal{L}}\hat{\mathbf{w}} = -\epsilon\hat{\mathbf{w}} + \epsilon\mathbf{F}\hat{\mathbf{w}} - \hat{\mathbf{S}}. \tag{70}$$

We now express $\mathbf{w}$ a sum of the $\mathbf{K}_{n,r}$ as in (43) and take the inner product of (70) with a particular $\mathbf{K}_{n',r'}$,

$$\left(\frac{\partial}{\partial t}\sum_{n,r}\hat{w}_{n,r}\mathbf{K}_{n,r},\mathbf{K}_{n',r'}\right)-\left(\frac{\partial}{\partial t}\mathbf{F}\sum_{n,r}\hat{w}_{n,r}\mathbf{K}_{n,r},\mathbf{K}_{n',r'}\right)+\left(\hat{\mathcal{L}}\sum_{n,r}\hat{w}_{n,r}\mathbf{K}_{n,r},\mathbf{K}_{n',r'}\right)=$$

$$-\epsilon\left(\sum_{n,r}\hat{w}_{n,r}\mathbf{K}_{n,r},\mathbf{K}_{n',r'}\right)+\epsilon\left(\mathbf{F}\sum_{n,r}\hat{w}_{n,r}\mathbf{K}_{n,r},\mathbf{K}_{n',r'}\right)-\left(\hat{\mathbf{S}},\mathbf{K}_{n',r'}\right). \tag{71}$$

Applying the orthonormality condition of the $\mathbf{K}_{n,r}$ cleans up most of the terms, yielding a result comparable to (44), modulo our correction.

$$\frac{d\hat{w}_{n',r'}}{dt}+(\epsilon+i\omega_{n',r'})\hat{w}_{n',r'}=-\hat{S}_{n',r'}+\sum_{n,r}\left(\frac{d\hat{w_{n,r}}}{dt}+\epsilon w_{n,r}\right)\left(\mathbf{F}\mathbf{K}_{n,r},\mathbf{K}_{n',r'}\right). \tag{72}$$

Looking closer at our correction term, we have

$$\begin{aligned}\left(\mathbf{F}\mathbf{K}_{n,r},\mathbf{K}_{n',r'}\right) &= \int_{-\infty}^{\infty}\mathcal{V}_{n,r},\mathcal{V}_{n',r'}dy\\ &= A_{n,r}A_{n',r'}(\omega_{n,r}^2-k^2)(\omega_{n',r'}^2-k^2)\int_{-\infty}^{\infty}H_nH_{n'}e^{-y^2}dy.\end{aligned} \tag{73}$$

All is not lost, as the Hermite Polynomials have the property that

$$\int_{-\infty}^{\infty}H_nH_{n'}e^{-y^2}dy=\begin{cases}\pi^{\frac{1}{2}}n!2^n & n=n'\\ 0 & n\neq n'\end{cases}, \tag{74}$$

so that, and making use of the definition of $A_{n,r}$, (31),

$$\left(\mathbf{F}\mathbf{K}_{n,r},\mathbf{K}_{n',r'}\right)=\begin{cases}a_{n',r,r'} & n=n'\\ 0 & n\neq n'\end{cases} \tag{75}$$

with

$$a_{n,r,r'}=\prod_{q=r,r'}\frac{(\omega_{n,q}^2-k^2)}{\left((n+1)(\omega_{n,q}+k)^2+n(\omega_{n,q}-k)^2+(\omega_{n,q}^2-k^2)^2\right)^{\frac{1}{2}}}. \tag{76}$$

In light of these results the summation of n and r in (72) reduces to a sum over just r, yielding

$$\frac{d\hat{w}_{n',r'}}{dt}+(\epsilon+i\omega_{n',r'})\hat{w}_{n',r'}=-\hat{S}_{n',r'}+\sum_{r}a_{n',r,r'}\left(\frac{d\hat{w_{n,r}}}{dt}+\epsilon w_{n,r}\right). \tag{77}$$

The long wave approximation ties the evolution of the gravity and Rossby waves together by coupling $\hat{w}_{n,0}$, $\hat{w}_{n,1}$, and $\hat{w}_{n,0}$. For each n, (77) gives us three coupled ODE's, which can be combined into one matrix differential equation,

$$\mathbf{A}\frac{d\hat{\mathbf{w}}_\mathbf{n}}{dt}+\mathbf{B}\hat{\mathbf{w}}_\mathbf{n}=\hat{\mathbf{S}}_\mathbf{n} \tag{78}$$

where

$$\mathbf{A} = \begin{pmatrix} 1-a_{n,0,0} & -a_{n,0,1} & -a_{n,0,2} \\ -a_{n,0,1} & 1-a_{n,1,1} & -a_{n,1,2} \\ -a_{n,0,2} & -a_{n,1,2} & 1-a_{n,1,1} \end{pmatrix},$$

$$\mathbf{B} = \begin{pmatrix} \epsilon + i\omega_{n,0} - \epsilon a_{n,0,0} & -\epsilon a_{n,0,1} & -\epsilon a_{n,0,2} \\ -\epsilon a_{n,0,1} & \epsilon + i\omega_{n,1} - \epsilon a_{n,1,1} & -\epsilon a_{n,1,2} \\ -\epsilon a_{n,0,2} & -\epsilon a_{n,1,2} & \epsilon + i\omega_{n,2} - \epsilon a_{n,2,2} \end{pmatrix},$$

and

$$\hat{\mathbf{w}}_\mathbf{n} = \begin{pmatrix} \hat{w}_{n,0} \\ \hat{w}_{n,1} \\ \hat{w}_{n,2} \end{pmatrix}, \qquad \hat{\mathbf{S}}_\mathbf{n} = \begin{pmatrix} \hat{S}_{n,0} \\ \hat{S}_{n,1} \\ \hat{S}_{n,2} \end{pmatrix}. \tag{79}$$

We must make an exception when $n = 0$, for there is no $\mathbf{K_{0,1}}$ eigenfunction. In this case we have just two coupled ODE's, which can be represented by an otherwise similar two-dimensional matrix equation.

The steady state solution to (78) is simply

$$\hat{\mathbf{w}}_\mathbf{n} = \mathbf{B^{-1}}\hat{\mathbf{S}}_\mathbf{n}, \tag{80}$$

provided of course that $\mathbf{B}$ is invertible. This is a fair assumption, as the the $a_{n,r,r'}$ corrections are relatively small, so that $\mathbf{B}$ (and $\mathbf{A}$, for that matter) are diagonally dominant. This assumption is not necessarily accurate for the mixed modes corresponding to $n = 0$, and I am not sure we can solve this equation for all forcing functions.

We must make a few more assumptions on the properties of $\mathbf{A}$ and $\mathbf{B}$ to solve the time dependent version of (78). We first multiply by $\mathbf{A^{-1}}$ to obtain

$$\frac{d\hat{\mathbf{w}}_\mathbf{n}}{dt} + \mathbf{A^{-1}B}\hat{\mathbf{w}}_\mathbf{n} = \mathbf{A^{-1}}\hat{\mathbf{S}}_\mathbf{n}. \tag{81}$$

Next assume that $\mathbf{A^{-1}B}$ is diagonizable, so that there exist a constant, invertible matrix $\mathbf{P}$ such that,

$$\mathbf{PA^{-1}BP^{-1}} = \mathbf{D}, \tag{82}$$

with $\mathbf{D}$ diagonal. We then multiply (81) by $\mathbf{P}$, in preparation for defining a new time dependent vector $\mathbf{q_n}(t) = \mathbf{P}\hat{\mathbf{w}}_\mathbf{n}(t)$ so that

$$\frac{d\mathbf{P}\hat{\mathbf{w}}_\mathbf{n}}{dt} + \mathbf{PA^{-1}BP^{-1}P}\hat{\mathbf{w}}_\mathbf{n} = \mathbf{PA^{-1}}\hat{\mathbf{S}}_\mathbf{n} \tag{83}$$

$$\frac{d\mathbf{q_n}}{dt} + \mathbf{Dq_n} = \mathbf{PA^{-1}}\hat{\mathbf{S}}_\mathbf{n}. \tag{84}$$

In (84) we have decoupled the ODE's, so that each component of $\mathbf{q_n}$ may be solved individually with the same techniques used to solve (44), or, more elegantly, solved with a matrix exponential,

$$\mathbf{q_n} = \mathbf{e^{-Dt}q_n}(0) + \mathbf{e^{-Dt}}\int_0^t \mathbf{e^{Dt'}PA^{-1}}\hat{\mathbf{S}}_\mathbf{n}dt'. \tag{85}$$

Note that as $\mathbf{D}$ is diagonal,

$$\mathbf{e^{Dt}} = \begin{pmatrix} e^{d_1 t} & 0 & 0 \\ 0 & e^{d_2 t} & 0 \\ 0 & 0 & e^{d_3 t} \end{pmatrix}. \tag{86}$$

Lastly, we obtain our coefficients

$$\hat{\mathbf{w}}_\mathbf{n}(t) = \mathbf{P^{-1}}\mathbf{q_n}(t). \tag{87}$$

3 Results

3.1 The East Pacific, July 27-29, 2001

Figures 1, 2, and 3 reveal two large water vapor black holes evolving over the East Pacific. In the first image, taken on July 27 at 1800z, we see the East Pacific ITCZ spanning over 6000 km, from 150^0 W to Central America. The convection begins at 5^0 N in the west and rises to 15^0 N in the east, its meridional extent varying from 500 to 1000 km. This position of the ITCZ is typical during the northern hemisphere summer, as the ITCZ tends to follow the thermal equator. Another large region of deep convection is visible at the western edge of the image, centered over Papua New Guinea and Indonesia. Convection in this area is especially strong during La Nina years. To the east we see a bit of seasonal convection over the Amazon basin, and in the south, the South Pacific Convergence Zone (SPCZ) stretches northwest to southeast from 165^0 W, 15^0 S to 120^0 W, 40^0 S.

A large, arid black hole centered at 130^0 W, 7^0 S has already formed to south of the East Pacific ITCZ, spanning nearly 80 degrees of longitude. At is widest point it spans nearly 30^0 of latitude, over 3000 km. A smaller dry region has formed northwest of the the East Pacific ITCZ, centered near 145^0 W, 16^0 N.

The large black hole in the south reaches its apex 24 hours later on the 28th, Figure 2. The East Pacific ITCZ has extended further to the west, now stretching past 155^0 W. The broader convection in the east is still present. The southern black hole has intensified, especially in the center, where we now see a "black hole" in the image. The northern black hole has also increased in size, its eastern boundary now 500 km further west at 165^0 W.

The broad convection in the eastern half of the ITCZ, especially between 120 and 105^0 W, weakens by the 29th, as shown in Figure 3. Unfortunately for our linear theory, advection seems to be playing a large role now. Intense convection in the ITCZ is now only in the west, where it begins to merge into the West Pacific convection. The southern black hole has been contorted, and has shrunk slightly. The northern black hole is less affected, though it has been pushed slightly north by a new burst of convection.

3.2 Setting up the Model

We must model this complicated system with Gaussian regions of convection, as given by (50). To simulate the East Pacific ITCZ, we selected parameters a and b to create an elongated convection region with Gaussian folding distances in x and y of 2700 and 450 km, respectively. y_0 was selected so that the convection would be centered at 10.5^0 N.

The parameter ϵ determines both the momentum damping and Newtonian cooling rates in our model. Following Gill, we based our value on the momentum damping rate, taking $\epsilon = \frac{1}{3days}$ [2]. ($\epsilon = \frac{1}{10days}$ would be more appropriate for the Newtonian cooling rate. See the Fellow's report by Takamitsu Ito for a simulation in which this problem has been remedied.) S_0, the dimensional heating rate for the first baroclinic mode, is 57 m/day [1]. This value is based on measurements taken over the Marshall Islands in the Pacific and from the GATE survey of the Atlantic.

Note that we used a partial summation of normal modes truncated at $N = 200$ in all the data we present. We approximated the Inverse Fourier Transform, an integral over wavenumber k from $-\infty$ to ∞, as a numeric integral from -10 to 10 with 128 point resolution. The truncation of the integral is based on the fact that the Fourier transform decays as $e^{\frac{-a^2k^2}{4}}$. We projected our β-plane solutions, which span to infinity in all directions, onto maps by ignoring the sphericity of the globe in the tropics. The maps are included to provide a better sense of scale and positioning.

The steady state subsidence field for the East Pacific ITCZ (labeled region A) is shown in the top half of Figure 5. We show only contours of downward velocity, in units m/day. This is the velocity at the center of the atmospheric column, where it is largest for the first baroclinic mode. While the greatest subsidence rate is not even 2 m/day, the maximum upward motion exceeds 50 m/day. If we equate drier air with greater subsidence, we already see the basic features of Figures 1 - 3; two large subsidence regions with significant zonal and meridional asymmetries with respect to the ITCZ.

To better compare our simulation with observations, we also included a first approximation to the convection over the West Pacific. Convection in the region appears much more stable, in bulk, through our observational period. We thus included a steady state convection cell over Papua New Guinea as a backdrop for our time dependent simulation. (A linear theory allows one to paste solutions together!) We centered this convection region on the equator at 160^0 E, with Gaussian folding distance of 900 km in both x and y. The complete steady state subsidence field is shown in the lower half of Figure 5. Again, we show only contours of downward velocity. A comparison with the upper half of the figure reveals that the West Pacific Convection (labeled region B) increases the size and intensity of the southern black hole. This brings our model yet closer to the observations.

As is demonstrated in Takamitsu Ito's paper, the convection in the SPCZ does not affect the tropical black holes very much, serving mostly to trim off the southwest corner of the southern black hole. Convection in the South Pacific is generally less stable and more prone to advection. We found (and will describe later) that the response of the subsidence field to forcing becomes slower, smaller, and concentrated to the west as one moves poleward from the equator, so that the fluctuating SPCZ does not have much of an effect on the East Pacific subsidence fields.

As we observe a rather gentle evolution of the ITCZ convection in Figures 1 - 3, forcing function F4 is the most appropriate. γ was selected so that the period of forcing is 5 days. We are particularly interested in days 2-4, in which the convection reaches a maximum and then begins to decay. S_0 was set so that the average intensity of the forcing is consistent with the experiment measurements.

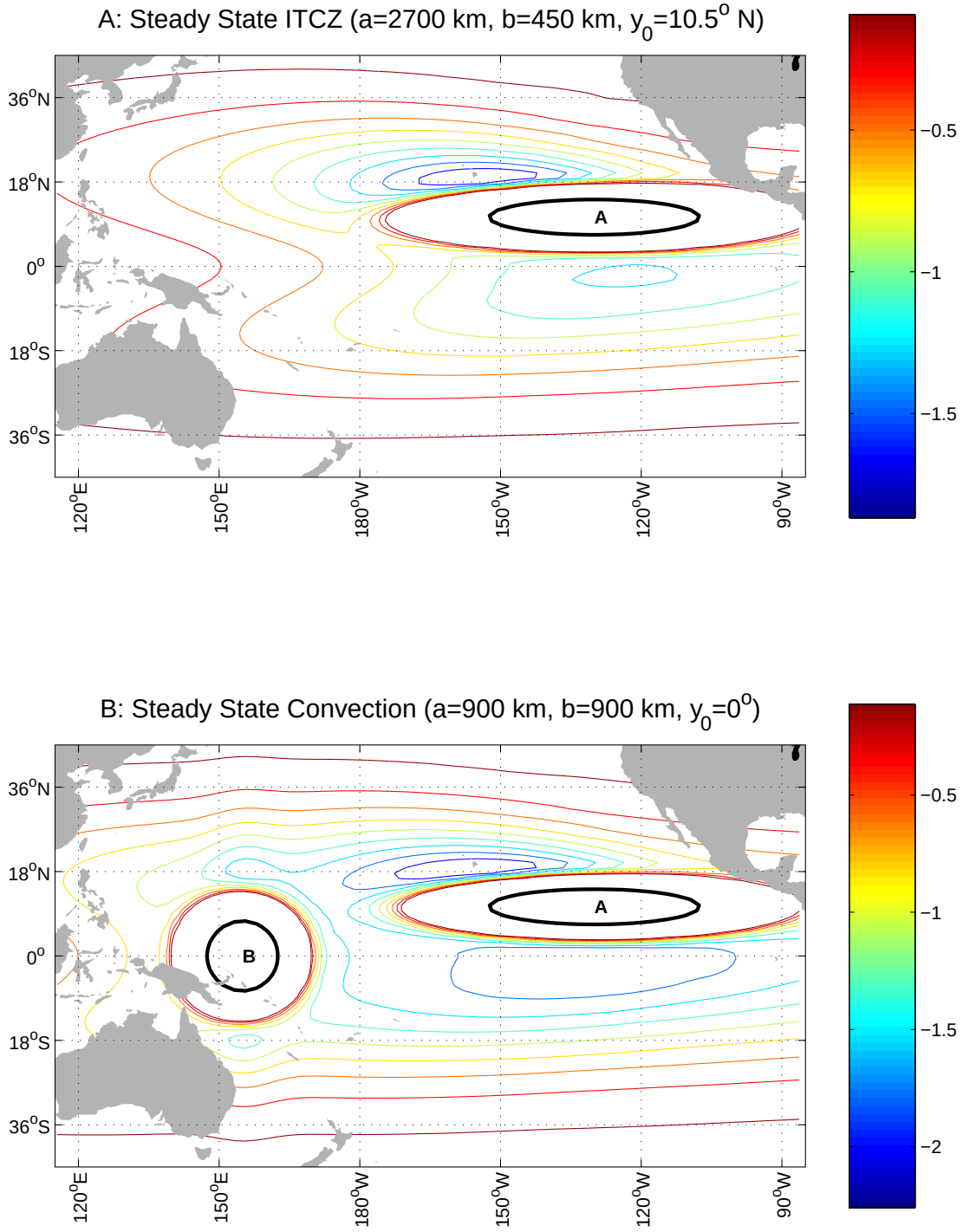

Figure 5: Subsidence (m/day) in Steady State Solutions

3.3 The Time Dependent Simulation

Figures 6 through 11 show the subsidence fields in increments of one day. The small cartoon in the bottom left hand corner of each figure illustrates the path of the forcing function, the marker showing the current intensity. Subsidence in each figure is given in m/day. It should be noted that our analytic technique gives us an exact solution for any time we choose, so that each field is equally accurate. For the discussion in this section, we will equate low humidity in the upper troposphere with subsidence.

We begin in Figure 6 with the steady state response of the West Pacific convection. When the East Pacific convection begins, there is initially very little east-west or north-south asymmetry in the subsidence field. (This will be further illustrated in the next section.) After one day, Figure 7, some asymmetry has developed, but the solution is more balanced than in the steady state. Note that the initial response is predominantly north and south of the ITCZ.

By day 2, Figure 8, the response has spread further east and west, and the characteristics of the steady state solution have developed. As we saw in Figures 1 and 2, the subsidence region to south of the ITCZ is much larger, and centered east of the small northern black hole.

When the convection begins to decline, as in Figure 9, we see the fastest response in the south east. The peak subsidence in the southern black hole has pushed from 120^0 to 145^0 W. A second peak region of subsidence has moved east over South America, and will propagate further east over the next few days of the simulation. This is a Kelvin wave packet! It may be difficult to observe this movement in the real atmosphere, as there is significant convection over the Amazon Basin.

By day 4, Figure 10, subsidence has ceased over much of the East Pacific, but held strong in the west. It is remarkably consistent with Figure 3, in which the eastern half of the southern black hole decays when the convection ceases. The northwestern subsidence regions slowly propagates further westward, as seen in Figure 11, again consistent with the movement of the actual northwestern black hole. Here we have a Rossby wave packet. We also note that the subsidence lingers in the north much longer than in the south; the asymmetry of the steady state has reversed.

3.4 Subsidence and Humidity?

In the steady state, the link between subsidence and humidity in the upper troposphere has been established empirically. In our time dependent simulation, we tread upon shakier ground in making comparisons. Our model only tells us the subsidence rate. In the future we must study the time dependence between subsidence and the drying of the upper troposphere. How long does it take the upper troposphere to dry out after subsidence begins, or moisten after it ceases? We may need to look at the full vertical motion field to obtain sound results.

3.5 Component Analysis

The Matsuno formulation of the equatorial β-plane response allows one to separate the atmospheric response into components, specifically the effect of Kelvin, Rossby, and westward

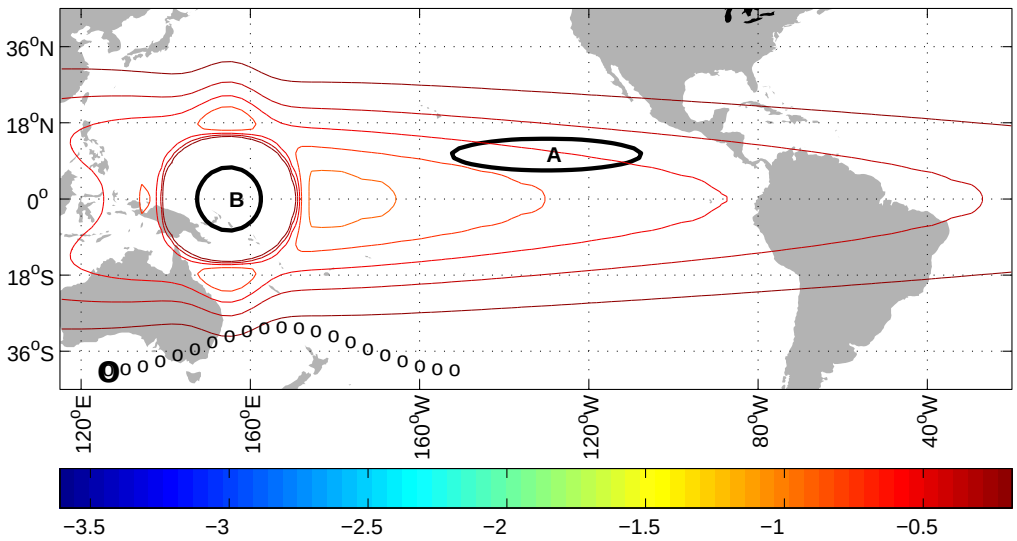

Figure 6: Full Solution, Time = 0

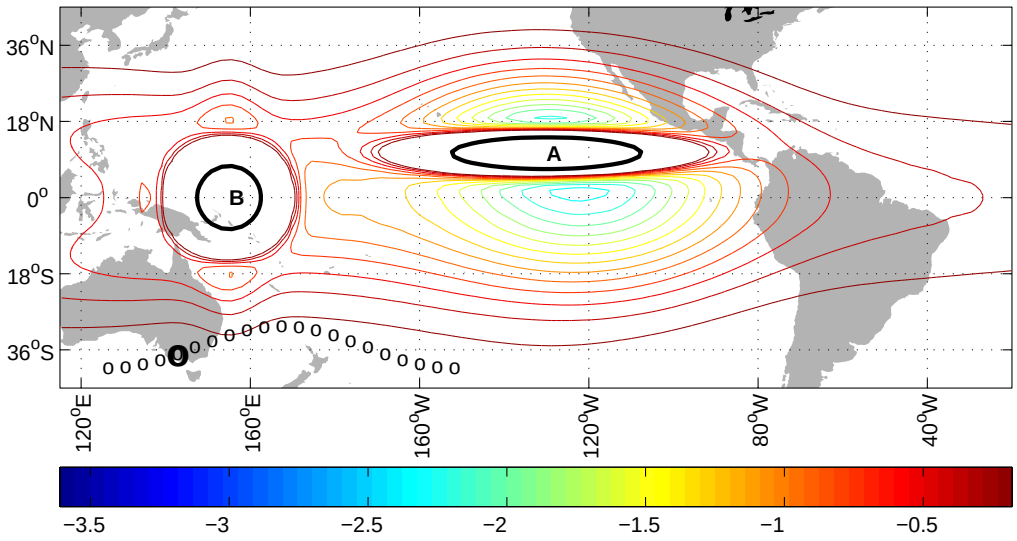

Figure 7: Full Solution, Time = 1 day

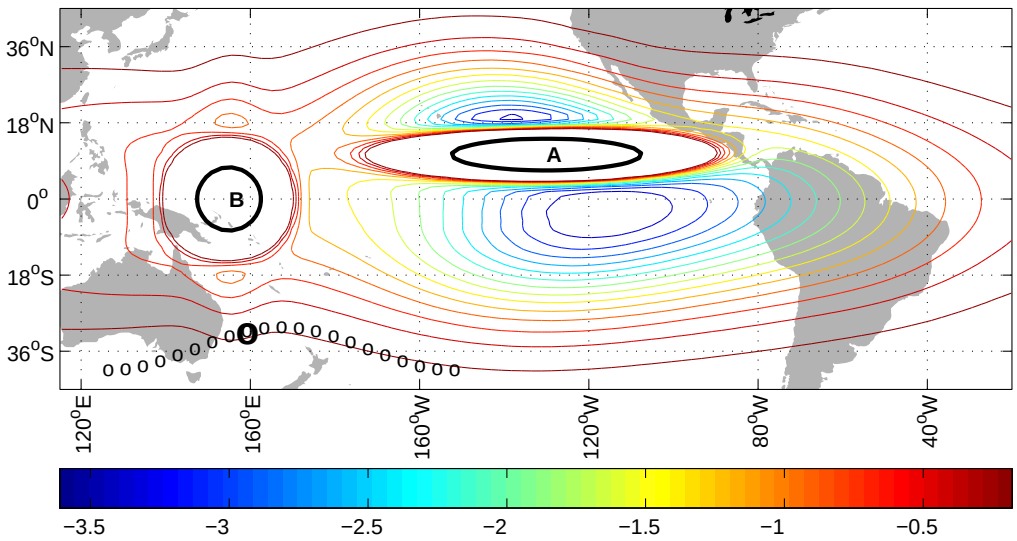

Figure 8: Full Solution, Time = 2 days

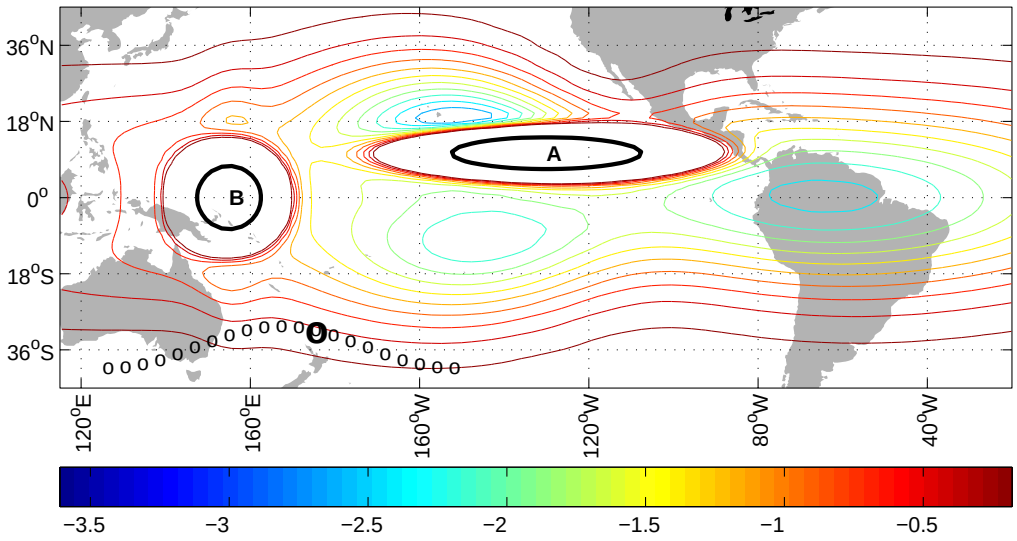

Figure 9: Full Solution, Time = 3 days

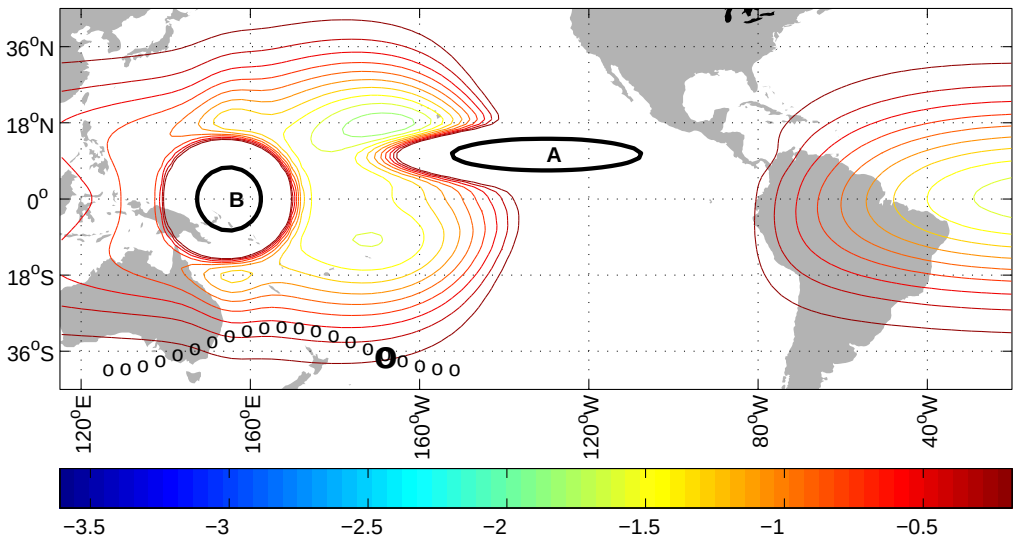

Figure 10: Full Solution, Time = 4 days

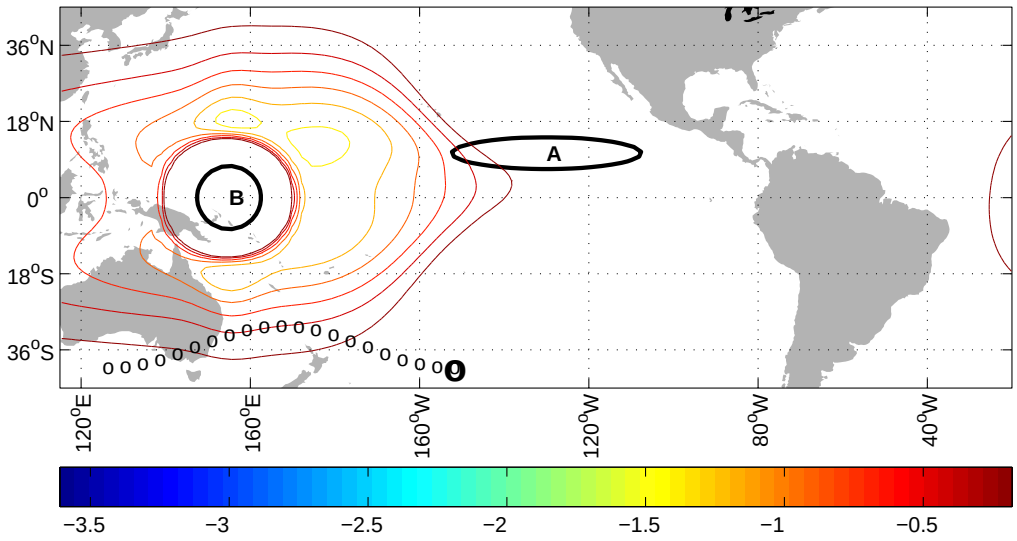

Figure 11: Full Solution, Time = 5 days

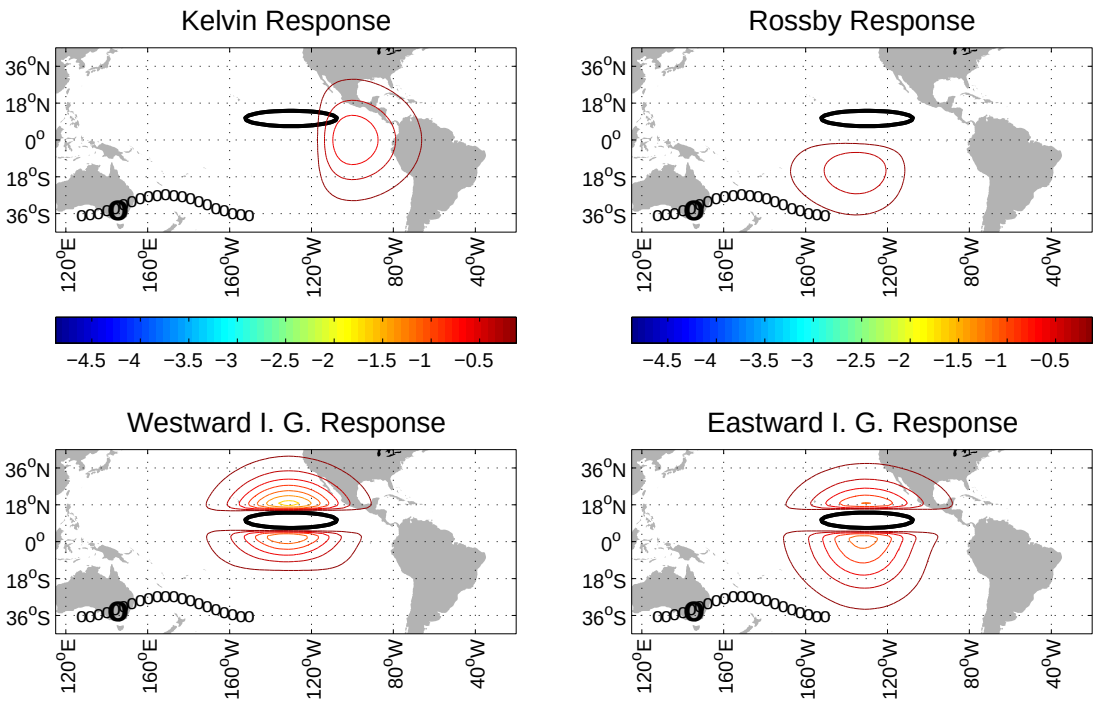

Figure 12: Components, Time = 1 day

and eastward propagating inertial gravity waves. In Figures 12 to 15 we present the total response to each type of wave. Note that the total subsidence fields is not necessarily the sum of these fields, as we have not shown the regions in which air is rising.

The east-west asymmetries in the response are the result of differences between Kelvin and Rossby waves. The Kelvin response grows much faster than the Rossby response, as one would expect based on the group velocities at which they propagate. The group velocity of nearly nondispersive long Rossby waves of order n is dwarfed by the Kelvin group velocity by a factor of $1/(2n+1)$ for $n > 0$. As the forcing decays, we see the Kelvin response propagating off to the east in a coherent packet.

The Rossby response focused south of the forcing is due to contribution from the $n = 0, r = 0$ mixed mode wave, and hence behaves in part like an inertial gravity wave. It dies faster than the other Rossby waves in the end when the forcing decays. The two pronged Rossby response west of the forcing, seen best in Figure 15, is due to the low frequency Rossby waves of order $n = 1$ and above. It becomes the dominant feature at the end of the simulations, explaining the enhanced stability of the western half of a black holes. The northern half of the Rossby packet is the slowest to grow and decay. Higher order Rossby waves, with their low group velocities, generate the response away from the equator.

The relative intensity at which the different wave types are excited is highly dependent on the spatial extent and latitude of the forcing. For instance, Kelvin waves are excited to a larger extent when the forcing is near the equator. Lower order waves are favored in general when the response is broad and near the equator.

As the forcing is moved further poleward, the black hole associated with it will decline

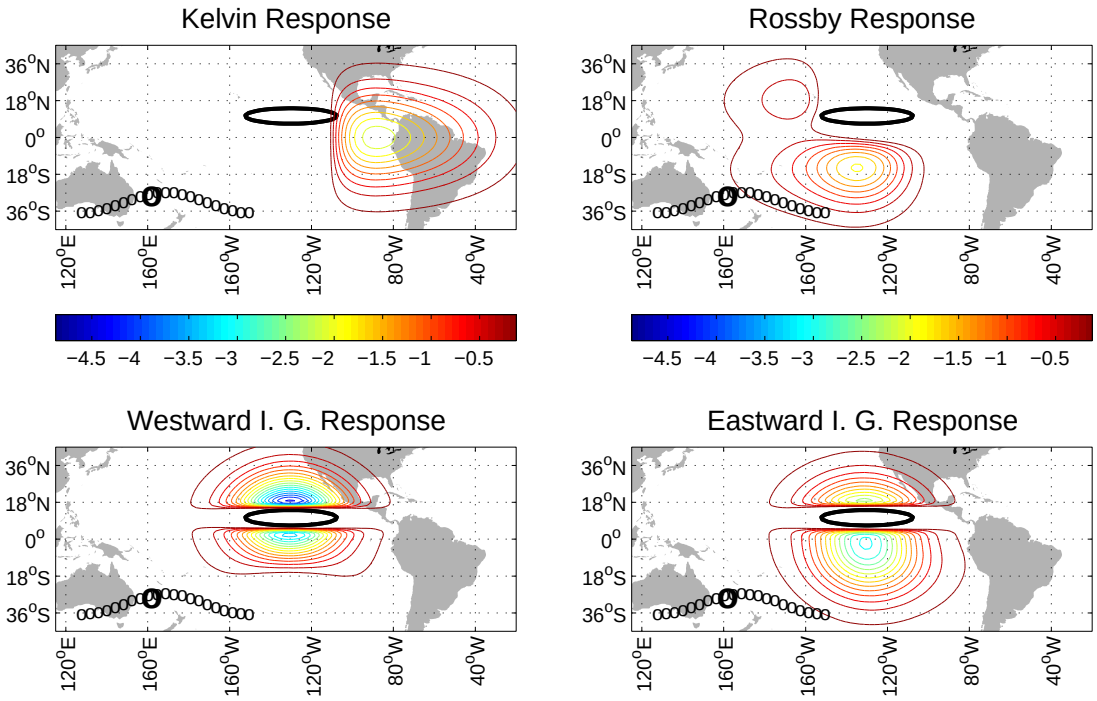

Figure 13: Components, Time = 2 days

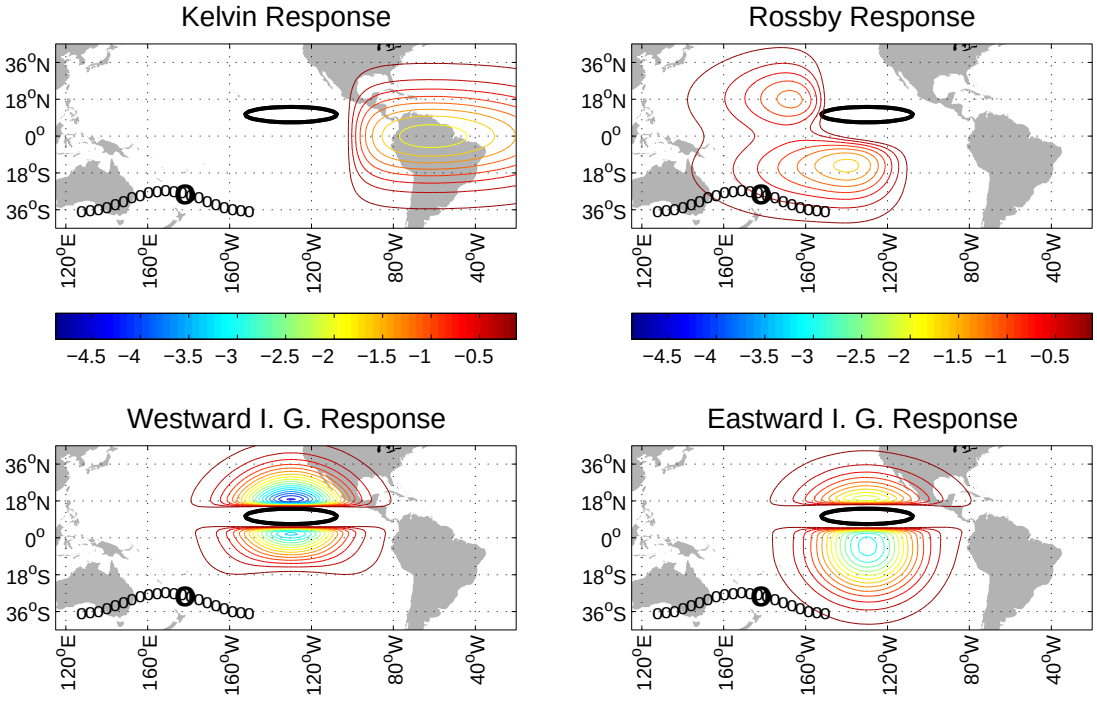

Figure 14: Components, Time = 3 day

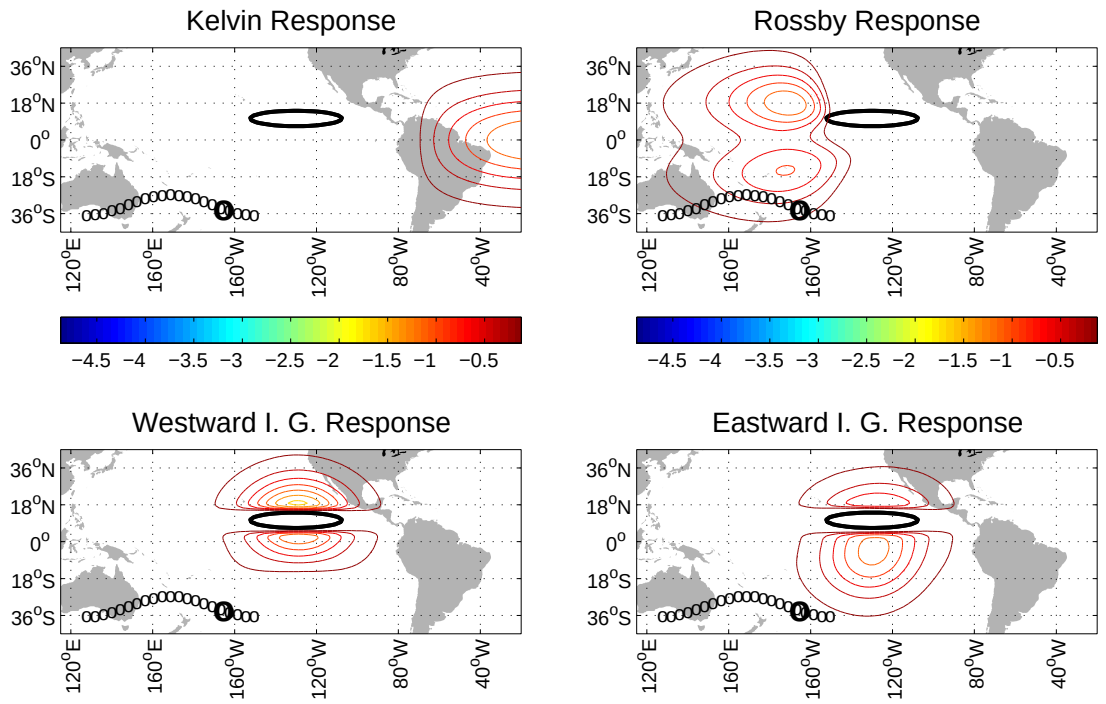

Figure 15: Components, Time = 4 days

in size, gain in local intensity, and move west of the forcing. The shift to the west comes from the fact that Kelvin waves can only be excited near the equator. The decline in spatial extent, which is coupled with an increase in intensity necessary to maintain continuity, can be attributed to the shrinking Rossby radius of deformation. Away from the equator the deformation radius is inversely proportional to the local Coriolis parameter, βy, on our β-plane. At high latitudes the Rossby waves tend to dominate over inertial gravity waves, too. The gravity wave response decreases with the Rossby number, which is also inversely proportional to the Coriolis parameter. Once the forcing is 1 or 2 Rossby radii poleward of the equator, the quasi-geostrophic equations become a good approximation to our system provided that our forcing is broad, and we can neglect inertial gravity waves all together.

3.6 The Time Dependence of the Hadley and Walker Circulations

Flow in the first baroclinic mode takes place in two layers. Air is sucked in from all directions toward the convection region in the lower half of the troposphere, and propelled upward by the convection. It then flows back in the upper half of the atmosphere, subsiding gently into the lower flow over broad regions to complete the cell. The Walker Circulation describes the east-west part of this flow (or perhaps I should say, the east-west flow "is" the Walker Circulation), and the Hadley Circulation is the north-south flow. We define the magnitude of the Walker circulation to be the maximum zonal mass transport toward the convection region in the lower layer, or equivalently, away from the convection in the upper layer. Similarly, we measure the Hadley circulation by the maximum meridional transport.

We can further divide the Walker circulation into western and eastern branches. The western branch is the maximum zonal transport to the convection coming from the west, and hence is due primarily to the Rossby response. The eastern branch tracks the flow from the east, and is generated by the Kelvin response. The Hadley circulation divides into northern (summer) and southern (winter) cells. These cells are established, to the most part, by the interaction of inertial gravity waves and the the mixed Rossby-inertial gravity modes.

As subsidence completes the Walker and Hadley circulations, the asymmetries of the meridional and zonal flows are the same as those we see in the formation of black holes. Calculating the flows thus gives a quantitative measure of the black hole asymmetries. For each forcing function we plotted the intensity of the four cells as a function of time relative to their steady state values. The total transports east-west and north-south at steady state are roughly equivalent so that the units in both diagrams are effectively the same.

For example, in the plots of the northern and southern branches of the meridional circulation, 1 unit on the y-axis corresponds to the total mass transport at steady state. The total is the sum of the absolute values of both cells, and hence corresponds to the total mass drawn into the convection region. The sign for transport in the northern cell is negative because mass is moving southward toward the convection region in the lower layer. The zonal mass transports are also plotted relative to the total steady state transport. The eastern branch is negative, as mass is moving to the west.

Forcing function F1 presents the unrealistic adjustment problem. As shown in Figure 16, the meridional transport is initially quite unstable. The inertial gravity waves slosh the circulation back and forth as they adjust to the sudden shock. While the meridional circulation reaches values comparable to the steady solution almost instantaneously, the zonal transport lags behind, and has not reached the steady state values after 2.5 days of simulation.

In the lower half of Figure 16, we compare the dissipation limited growth to the growth of the zonal mass transport. If the frequency ω is small relative to ϵ, our forcing function reduces to

$$\tilde{S}(t) = S_0 \frac{1 - e^{-(\epsilon + i\omega)t}}{\epsilon + i\omega} \rightarrow \frac{1 - e^{-\epsilon t}}{\epsilon}, \tag{88}$$

and growth is controlled by the friction. This will only hold for the full solution if it holds for all modes. Clearly it is not the case, for the friction dominated curve should match that of the total transport.

The response to forcing function F2, as pictured in Figure 17, is also quite unrealistic. The meridional response is not quite as instantaneous, but still sloshes back and forth. We compare both the meridional and zonal decay rates to the dissipation dominated spin down,

$$\tilde{S}(t) = S_0 e^{-(\epsilon + i\omega)t} \frac{1}{\epsilon + i\omega} \rightarrow \frac{e^{-\epsilon t}}{\epsilon}. \tag{89}$$

While the curve does not match for the Hadley circulations, it gives a pretty sound fit for the decay of the Walker cells. This indicates that the the bulk of the Rossby and Kelvin response at steady state is controlled by low frequency waves. As indicated by the poor fit in Figure 16, higher frequency modes were important at the onset of forcing.

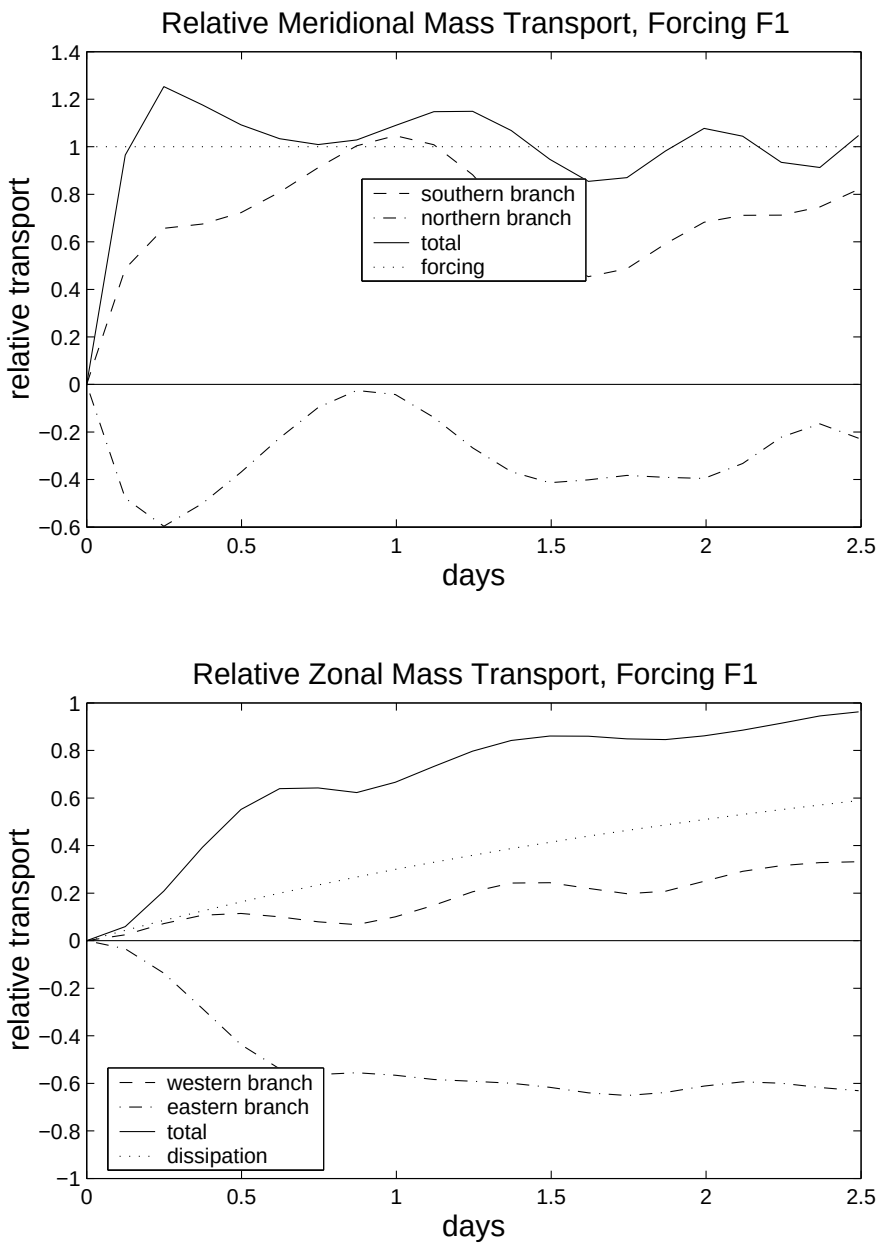

Figure 16: Hadley and Walker Circulations, Forcing Function F1

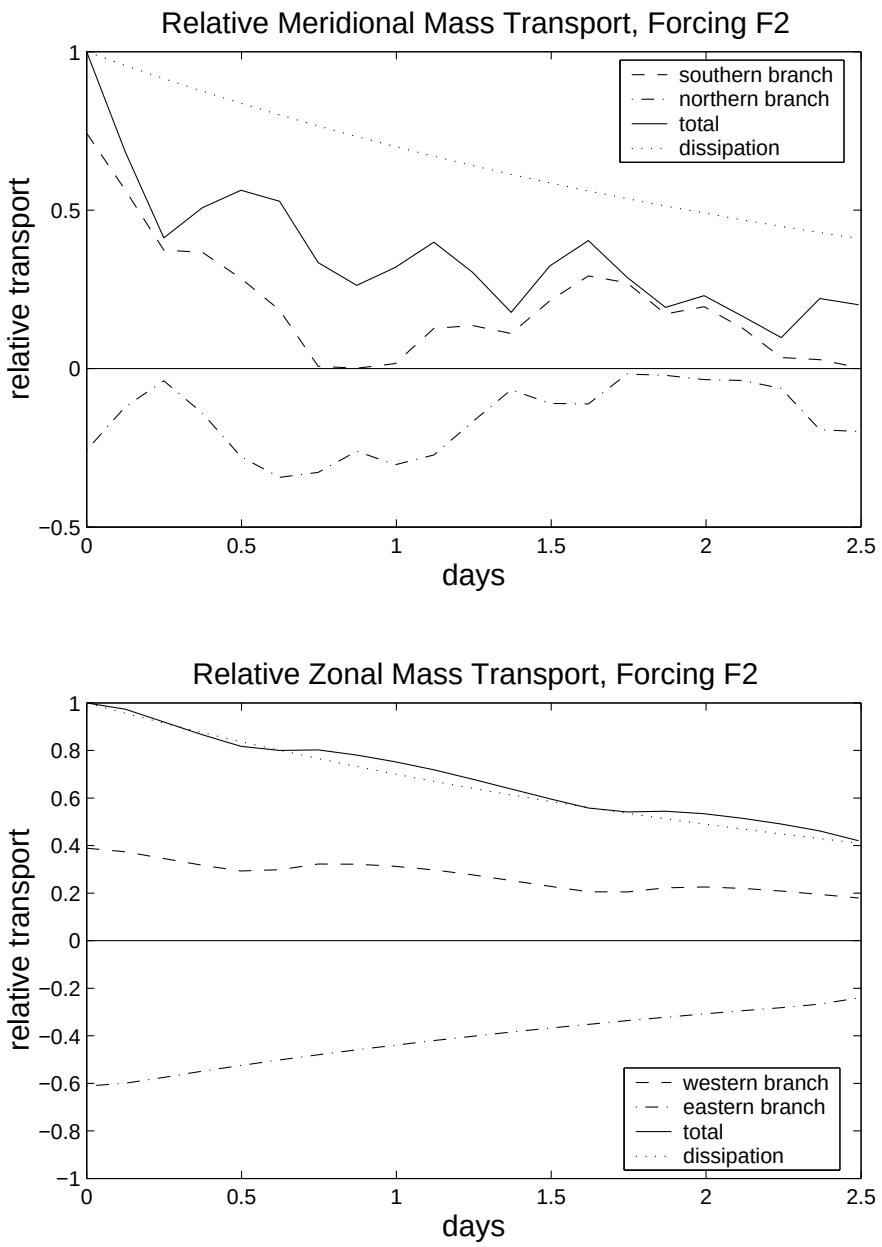

Figure 17: Hadley and Walker Circulations, Forcing Function F2

Forcing function F3 presents a more realistic rise to steady state convection. In the upper half of Figure 18 we find the meridional circulation nearly perfectly in step with the forcing. There are still some oscillations due to the abrupt start. These oscillations are absent with the smooth forcing F4, as shown in Figure 20. As shown in the bottom half of 18, the Walker circulation lags behind the forcing by 1-2 days.

A close look at Figure 19 reveals that northern and southern cells of the Hadley circulation are nearly symmetric at the onset of convection. Figure 19 better illustrates this phenomenon. We present the ratio between the two branches of the Hadley and Walker circulations as a function of time. The horizontal lines indicate the steady state ratios. For instance, at steady state, the southern branch of the Hadley circulation is nearly 3 times stronger than the northern half. In the beginning, however, the north and south cells are nearly equal. The $n = 0$ mixed mode response accounts for much of the steady state asymmetry, and takes longer to establish itself.

The west-east asymmetry also evolves with time. It begins close to its steady state value, and then drops to a point where the eastern cell is five times larger than its western counterpart. This can be attributed to the larger group velocity of Kelvin waves, which gives the eastern branch a quicker start. The initial surge by the Rossby wave is due to the mixed mode. It is slower than the other gravity waves, but faster than Rossby and Kelvin waves!

Lastly we look at response to the smooth forcing F4, shown in Figures 20 and 21. While the total meridional circulation is nearly in perfect step with the forcing, the zonal circulations lag, the Eastern cell by 1/2 a day, the western cell by over a day. In this trial in took 1.5 days to establish the north-south asymmetry - the acceleration of the forcing function seems to promote a symmetric response. Note that the drop in the north-south ratio at the left of Figure 21 is due to a problem in how we calculated the ratio, and is not at all physical. The west-east ratio curve appears similar to that in Figure 19.

4 Limits of our Theory

4.1 The Nonlinear Terms

We have neglected the advective terms in the shallow water equations throughout our analysis. We must ask what differences we should expect in a solution of the complete equations,

$$\frac{\partial u}{\partial t} - yv + \frac{\partial h}{\partial x} = -\epsilon u - (u\frac{\partial u}{\partial x} + v\frac{\partial u}{\partial y}) \tag{90}$$

$$\frac{\partial v}{\partial t} + yu + \frac{\partial h}{\partial y} = -\epsilon v - (u\frac{\partial v}{\partial x} + v\frac{\partial v}{\partial y}) \tag{91}$$

$$\frac{\partial h}{\partial t} + \frac{\partial u}{\partial x} + \frac{\partial v}{\partial y} = -\epsilon h - S - (u\frac{\partial h}{\partial x} + v\frac{\partial h}{\partial y}). \tag{92}$$

As a first line of inquiry, we calculate the magnitude of the nonlinear terms given our final solution. They must be much relatively small for our solutions to be at least self-consistent. Table 4.1 lists the worst case ratio of the magnitude of the nonlinear terms to

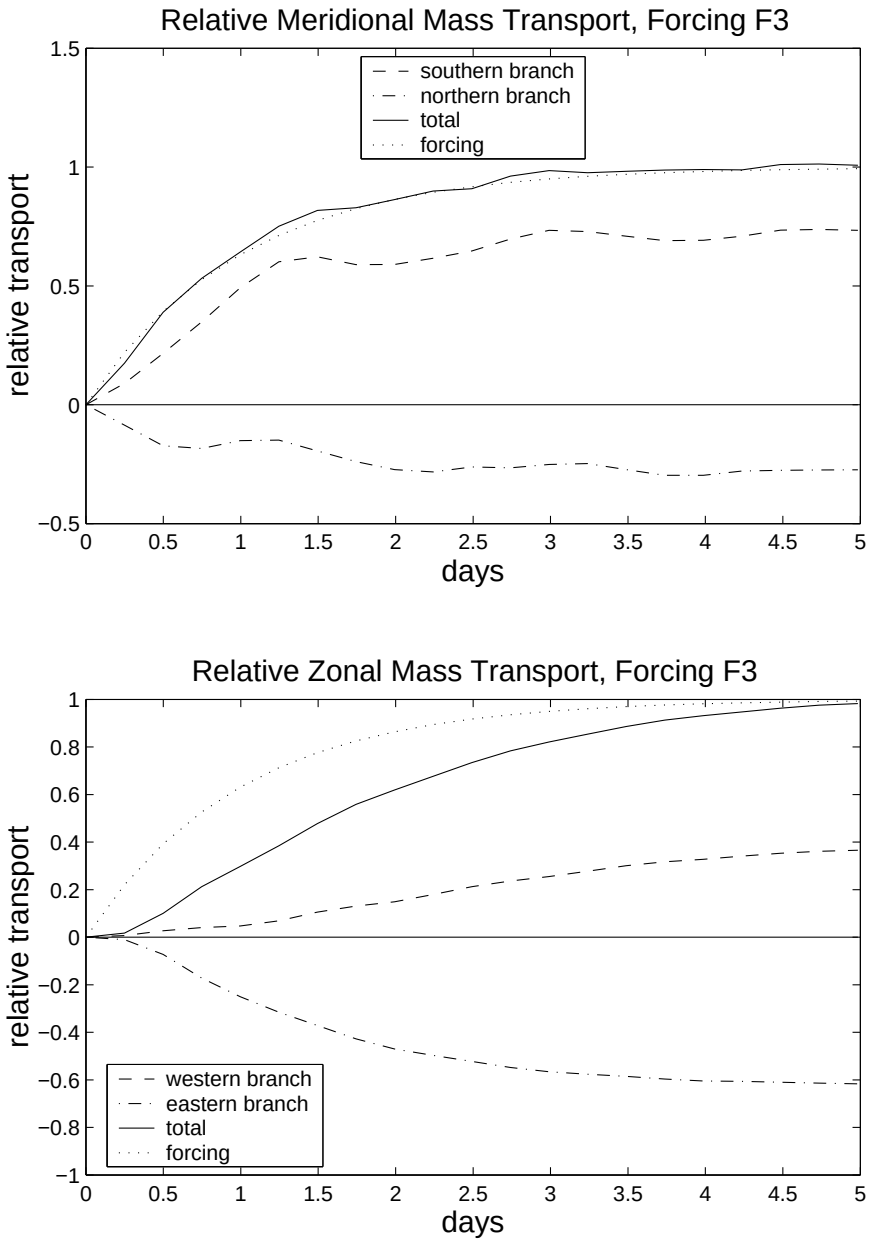

Figure 18: Hadley and Walker Circulations, Forcing Function F3

	Ratio $\frac{nonlinear}{linear}$
x-momentum	30%
y-momentum	7%
mass conservation	4%

Table 2: Relative Size of the Nonlinear Terms

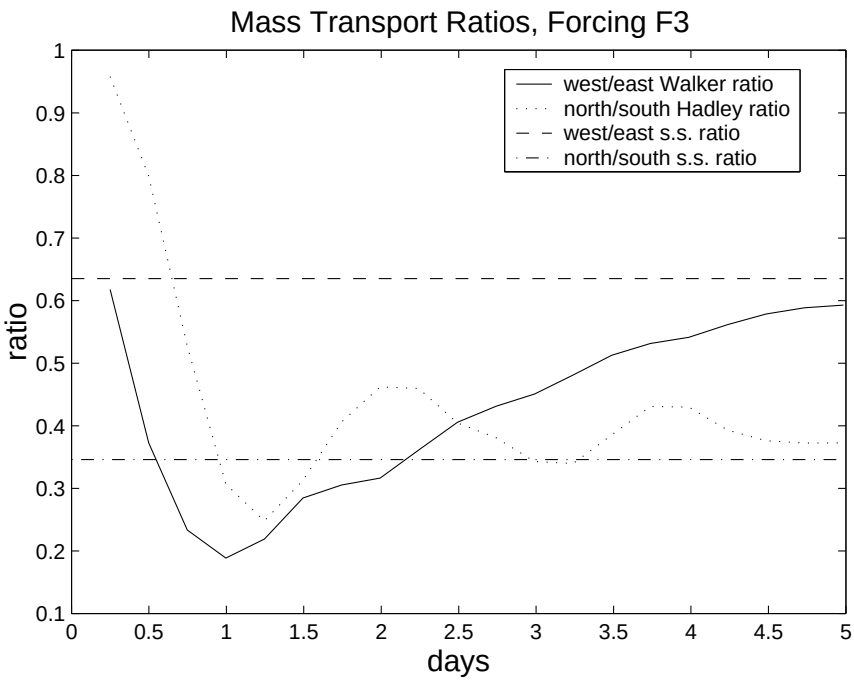

Figure 19: Asymmetries in the Circulation, Forcing Function F3

the combined magnitude of the linear terms for each of (90) - (92), as calculated by finite differencing the linear, steady state solutions.

With the exception of (90), the nonlinear terms are small enough to justify neglecting them. In (90), the nonlinear terms are the most problematic on the equator where subsidence is strongest in the southern black hole, as illustrated in Figure 22. The loss of the Coriolis force on the equator makes this region particularly susceptible to nonlinearities. In addition, the upward velocity, given by (65), is large in regions where partial derivatives u_x and v_y are strong. As such partials are present in the nonlinear terms, we should expect them to be strong in regions of subsidence.

4.2 Susceptibility to Barotropic Instability

As friction plays a small role in our system of equations, we can anaylze them in the inviscid limit. We then expect the flow to become susceptible to barotropic instability when there exists a reversal in the potential vorticity gradient. The linear (nondimensional) PV principle in our model was given in (9), with the PV anomaly q defined by (10). q can be calculated in spectral space, as PV is conserved by each unforced mode. (It is important the note that the forcing and dissipation terms serve only to tell us the magnitude of each mode, and do not effect the velocity fields, or the PV!) First, we have that

$$\frac{dq}{dt} + v = 0 \tag{93}$$

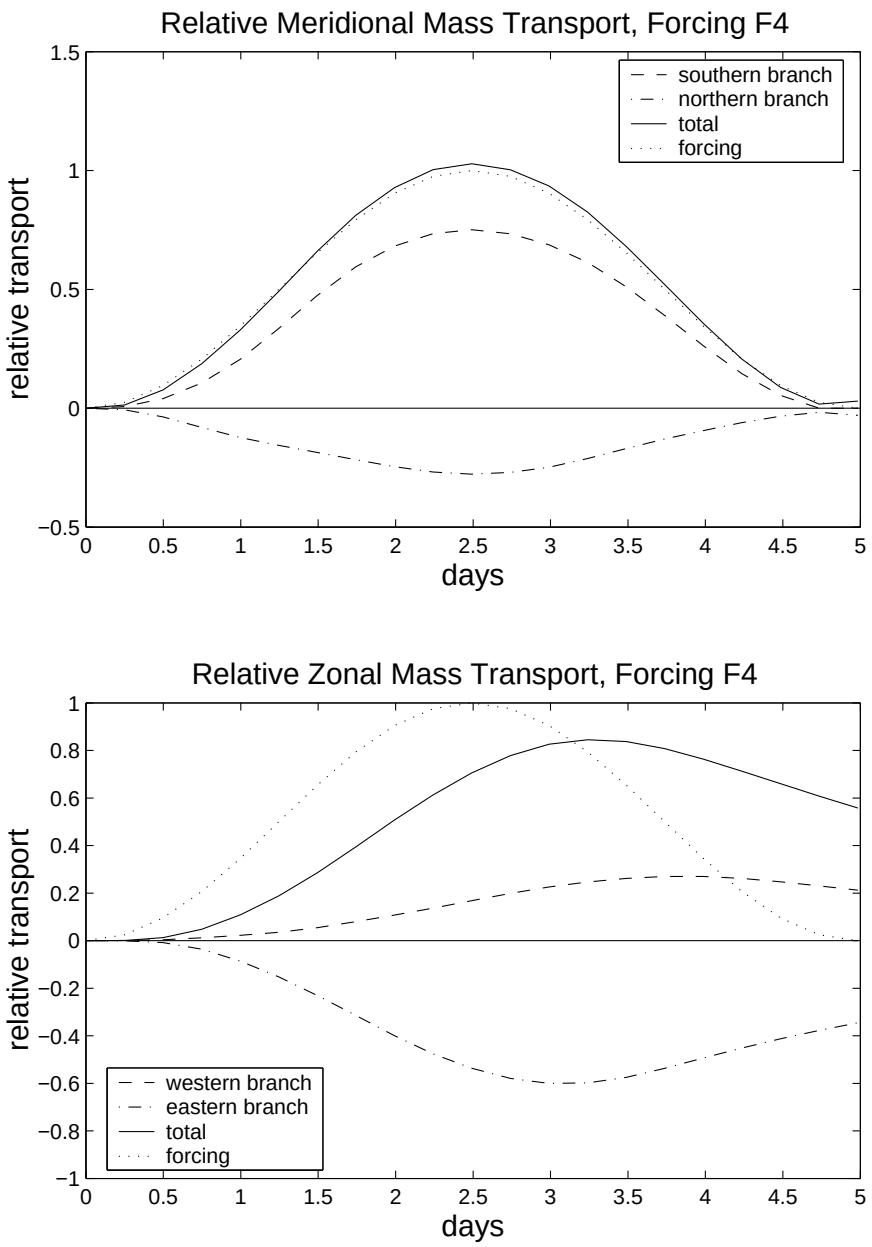

Figure 20: Hadley and Walker Circulations, Forcing Function F4

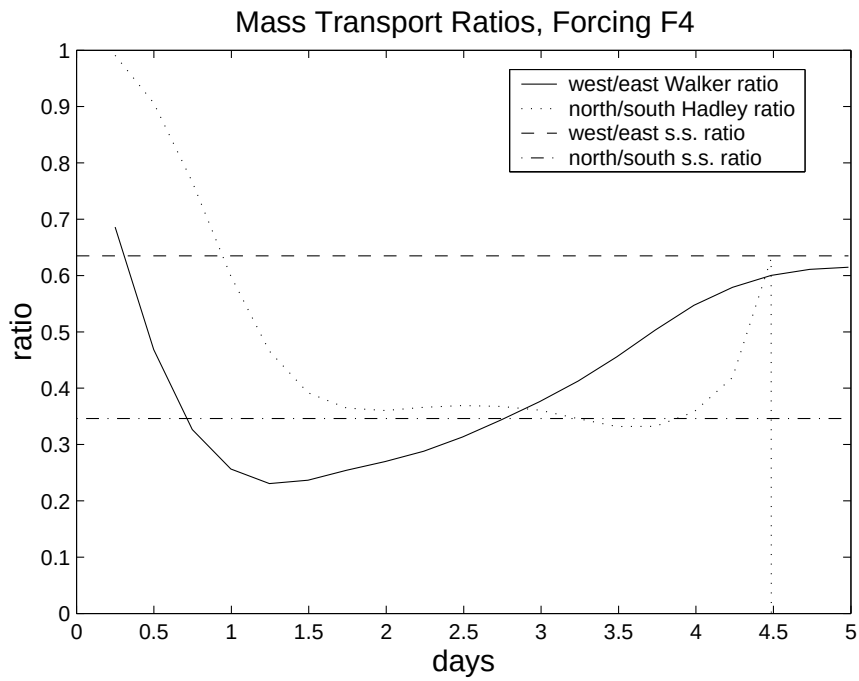

Figure 21: Asymmetries in the Circulation, Forcing Function F4

in the inviscid, unforced problem. Move to Fourier space and write $\hat{q}$ as a sum of the contributions from each normal mode,

$$\hat{q} = \sum_{n,r} \hat{w}_{n,r}(k,t)\mathcal{Q}_{n,r}, \tag{94}$$

to obtain the transform of (93),

$$-i\omega_{n,r}\mathcal{Q}_{n,r} + \mathcal{V}_{n,r} = 0. \tag{95}$$

$\mathcal{Q}_{n,r}$ is the PV contained in the nth, rth normal mode. A quick rearrangement yields

$$\mathcal{Q}_{n,r} = \frac{\mathcal{V}_{n,r}}{i\omega_{n,r}}. \tag{96}$$

Likewise,

$$\frac{d\mathcal{Q}_{n,r}}{dy} = \frac{\frac{d\mathcal{V}_{n,r}}{dy}}{i\omega_{n,r}}. \tag{97}$$

We can then calculate q and $\partial q/\partial y$ as u, v, h, and w before.

The nondimensional PV anomaly q has units $\frac{c}{L} = \left(\frac{\beta}{c}\right)^{\frac{1}{2}}$, while $\partial q/\partial y$ has units of β. Hence, the criterion for a reversal of the total PV gradient in y is that nondimensional $\partial q/\partial y < -1$.

The PV field and gradient in y are shown in Figure 23, which indicates that the first baroclinic mode is linearly stable. The top half of the diagram illustrates the PV field. Note

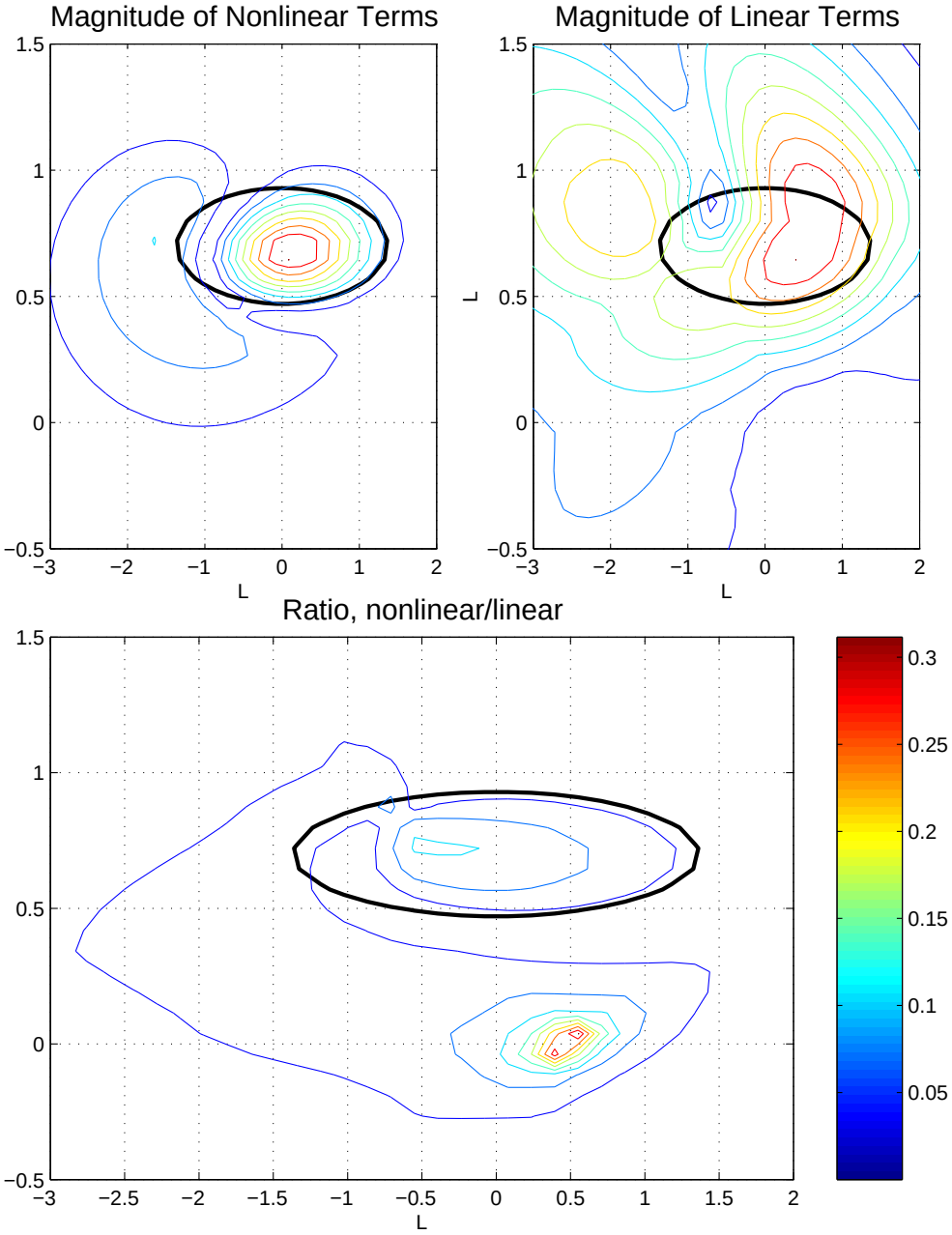

Figure 22: The Nonlinear Terms (Note that we have used nondimensional length units. 1 unit is appoximately 1800 km.)

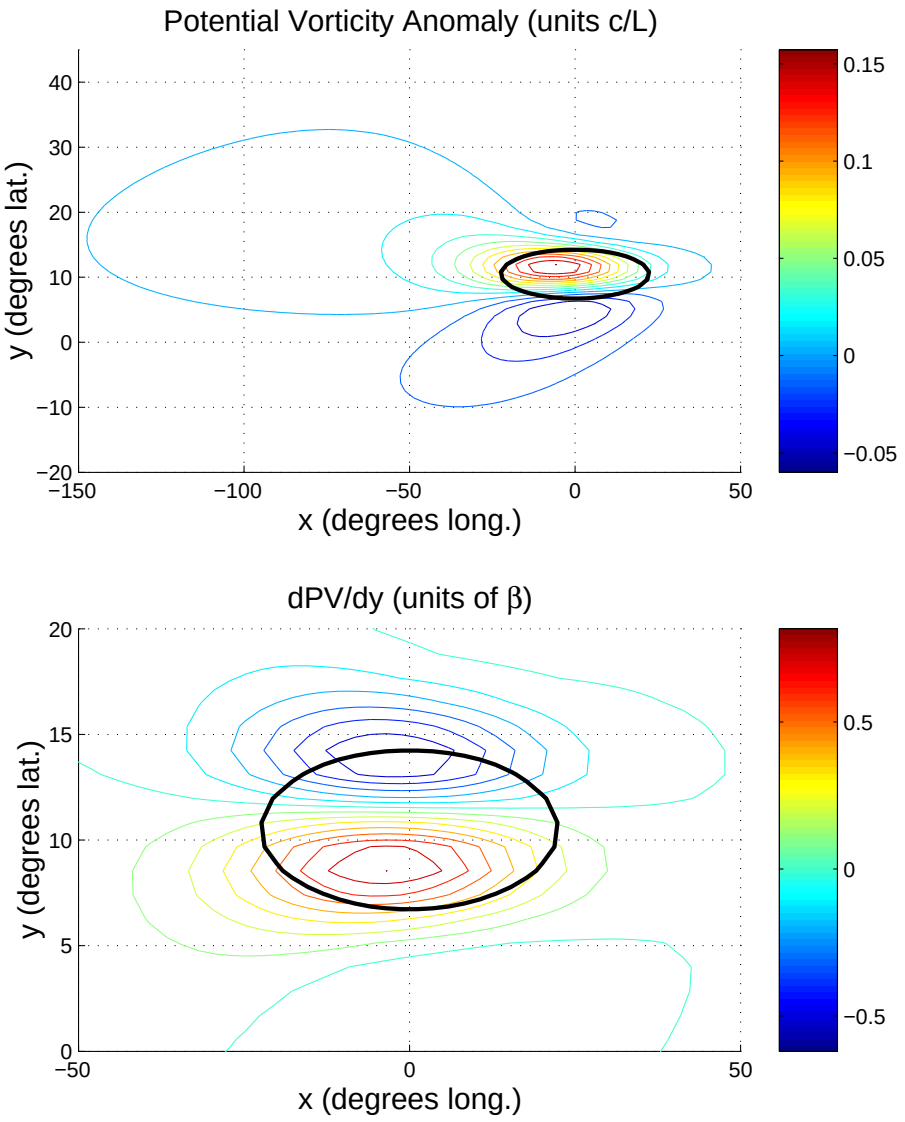

Figure 23: The Potential Vorticity Anomaly

mode	c (m/s)	$\bar{h}$ (m)	S_d (m/day)	S_{nd}
1	77	610	57	0.026
2	47	220	55	0.086
3	31	98	5.6	0.025
4	23	56	3.2	0.053

Table 3: Marshall Island Data

that it is biased heavily to the west and, to a lesser extent, to the north. The east-west asymmetry is more easily explained: Kelvin waves carry no PV, whereas Rossby waves do. The north-south asymmetry can be explained in view of PV stretching. The yS term in our PV principle, (9), corresponds to the stretching of the planetary potential vorticity. The effect becomes more pronounced as the Coriolis force grows with latitude.

4.3 Higher Baroclinic Modes

A study of the atmosphere over the the Marshall Islands gives us a measure of the intensity at which each baroclinic mode is excited by the release of latent heat [1]. The relevant data, shown in Table 4.3, indicates that the bulk of the latent heat release excites the first two baroclinic modes; S_d, the dimensional forcing, indicates the strength of the excitation for each mode.

Recall that the physical scales of the system are determined by c. As c becomes smaller, the length scales shrink and the time scales lengthen. The magnitude of the nonlinear terms and intensity of the PV gradient involve spatial derivatives, and thus are enhanced as the length scales shrink. They are proportional to the nondimensional forcing $S_{nd} = S_d\, g\beta^{-\frac{1}{2}} c^{-\frac{5}{2}}$. Hence for the second baroclinic mode the relative intensity of the nonlinear terms is 3.3 times larger than for the first mode, as is the PV gradient! We should then expect the second baroclinic mode to be nonlinear and potentially unstable, were it to exist by itself. Nonlinearities ruin our ability to paste modes atop each other, making it difficult to say whether the full solution (taking into account the nonlinear terms and all baroclinic modes) would be unstable. Note, however, that w is proportional to S_d, so that the subsidence field is determined by just the first two baroclinic modes.

5 Conclusions

Linear theory has performed remarkably well in revealing the gross features of the time evolution of water vapor black holes. The asymmetries in the growth and decay of the dry regions are readily seen as a ballet of Kelvin, Rossby, and inertial gravity waves.

A better fit to observations could be made by including more baroclinic modes. I am not sure, however, how much more such activity would teach us about the physics of the system. It may, however, prove very instructive to follow further in the footsteps of Gill and linearize about a mean zonal wind, as in [8]. It is difficult to tell if the movement of the real black holes in Figures 1-3 was due to the propagation of wave packets or advection by the easterly Trade Winds. Linearizing about a mean wind may help settle this question.

The response of the Hadley circulation to forcing is much faster than that of the Walker Circulation. In addition, the western branch of the Walker circulation responds slower to forcing that the Eastern branch. While these properties were known before, it is fruitful to extend these insights to the study of black hole formation. Black holes are often associated with the formation and movement of tropical storms [10], which can be viewed as massive centers of convection. The initial subsidence response is driven by inertial gravity waves, and appears north and south of the system, especially in the winter hemisphere. As the storm moves poleward, the effect of gravity waves and Kelvin waves decrease, and we see primarily a Rossby response to the west of the storm.

As a first attempt to apply these insights to a real storm, we tracked the response generated by Typhoon Pabuk over the west Pacific in August, 2001. When the storm formed over the tropics we observe a massive Black hole extending down over northern Australia. As the storm moved north, we then observed the formation of a intense black hole west of the storm, which appeared to be advected around the storm by anticyclonic winds in the upper troposphere. This interaction between tropical storms and black holes presents an exciting area for future study.

6 Acknowledgments

I would like to thank Wayne Schubert and Takamitsu Ito for all their guidance and insight, both in completing this project and in making my summer GFD experience so wonderful. I also would like to thank Joe Keller for invaluable advice and Janet Fields for all her support throughout the summer. Thanks also to Dargan Frierson for assistance in editing this paper. Lastly, I would like to acknowledge the Naval Research Laboratory, Marine Meteorology Division, 7 Grace Hopper Ave, Monterey, CA 93943 for providing the GOES satellite images, Figures 1 - 3.

References

[1] Fulton, S. R. and W. H. Schubert, 1985: Vertical Normal Mode Transforms: Theory and Application. *Mon. Wea. Rev.*, **113**, 647-658

[2] Gill, A. E., 1980: Some simple solutions for heat induced tropical circulation. *Quart. J. Roy. Meteor. Soc.*, **106**, 447-462

[3] Gradshteyn, I. S. and I. M. Ryzhik, 1965: *Table of Integrals, Series, and Products.* Academic Press, New York, p 1067

[4] Hack, J. J., W. H. Schubert, D. E. Stevens, and H. Kuo, 1989: Response of the Hadley Circulation to Convective Forcing in the ITCZ. *J. Atmos. Sci.*, **46**, 2957-2973

[5] Heckley, W. A. and A. E. Gill, 1984: Some simple analytic solutions to the problem of forced equatorial long waves. *Quart. J. Roy. Meteor. Soc.*, **110**, 203-217

[6] Martin, D. W. and B. B. Hinton, 1999: Annual Cycle of Rainfall of the Indo-Pacific Region. *J. Clim.*, **12**, 1240-1256

[7] Matsuno, T., 1966: Quasi-Geostrophic Motions in the Equatorial Area. *J. Met. Soc. Japan*, **44**, 25-43

[8] Phlips, P. J. and A. E. Gill, 1987: An analytic model of the heat-induced tropical circulation in the presence of a mean wind. *Quart. J. Roy. Meteor. Soc.*, **113**, 213-236

[9] Picon, L. and M. Desbois, 1990: Relation between METEOSAT Water Vapor Radiance Fields and Large Scale Tropical Circulation Features. *J. Clim.*, **3**, 865-876

[10] Rosendal, H., 1998: The Black Hole of Water Vapor and its Use as an Indicator of Tropical Cyclone Development and Intensity Changes. http://members.aol.com/Rosendalhe/black.htm, April 17

[11] Schmetz, J. et. al., 1995: Monthly Mean Large-Scale Analyses of Upper Tropospheric Humidity and Wind Field Divergence Derived from Three Geostationary Satellites. *Bull. Am. Met. Soc.*, **76**, 1578-1584

[12] Silva Dias, P. L.,W. H. Schubert, and M. DeMaria, 1983: Large-Scale Response of the Tropical Atmosphere to Transient Convection. *J. Atmos. Sci.*, **40**, 2689-2707

Nonlinear effects on ENSO's period

Fiona Eccles

1 Introduction

El Niño is roughly defined as the warming of the east equatorial water of the Pacific Ocean about every 3 to 6 years and is accompanied by a "Southern Oscillation" signal in the atmosphere, the events together being known as ENSO. In normal, non-El Niño conditions the trade winds blow towards the west across the tropical Pacific. The sea surface temperature (SST) is about 8 °C higher in the west (so there are relatively cool temperatures off South America) with a corresponding slope in the thermocline, it being deeper in the west. During El Niño the trade winds relax in the central and western Pacific leading to a depression of the thermocline in the eastern Pacific, and an elevation of the thermocline in the west.

Despite much study to understand this complex phenomenon the reason for the particular period of the ENSO event, every 3–6 years, is as yet poorly understood. In this study we examined different El Niño periods in a delayed oscillator model, in particular the behaviour of the wave dynamics and nonlinearity, to further advance our understanding of this issue (at least in the model!) We believe the nonlinearity plays a key role in setting the period in the model and it was specifically this role that we hoped to further comprehend.

However, the ENSO period in the model is dependent not only on this nonlinearity but is also a function of the model parameters. In order to separate out purely the effect of the nonlinearity we ran the model in a chaotic regime with *one* set of model parameters. The different periods present in this regime could then be extracted as unstable periodic orbits, using the method outlined below. Thus it was possible to examine various ENSO frequencies with the *same* model parameters and therefore study solely the effect of the nonlinearity on the wave dynamics. It is important to note that the use of the chaotic regime is merely a tool used here. The results regarding the effect of the nonlinearity on the period of ENSO should also be valid when ENSO is in a non-chaotic regime.

This report is structured as follows. In the next section we present the evidence for the four year El Niño cycle and the failure of a current GCM and of linear theory to fully reproduce or explain this. In section 3 there is a brief outline of the model used for this study, and the model's transition to chaos, the state used to examine the role of the nonlinearity, is shown in section 4. The method of finding unstable periodic orbits (UPOs), the cycles with different periods within the chaos, is described in section 5. Section 6 presents an observation of an amplitude-period relationship in the model, found using the UPOs, with a comparison with the Cane and Zebiak [1] model. The wave dynamics analysis of the results is presented in section 7 before concluding remarks (section 8) and acknowledgments.

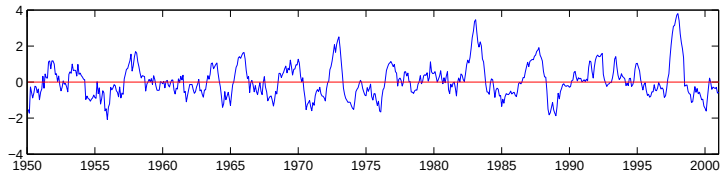

Figure 1: Niño3 record (average SST 5N-5S, 150W-90W) for 1950-2001, data from http://www.cpc.ncep.noaa.gov/data/indices/, figure courtesy of Eli Tziperman.

2 ENSO's period

2.1 The observations

The Niño3 record, figure 1, shows the average SST in an equatorial region of the east Pacific which corresponds to the region where El Niño warming is observed. This clearly shows the ENSO cycle over the last 50 years, with a period of 2–6 years, and indeed a power spectrum of such records yields a broad peak at around four years. However it would appear the El Niño cycle is not just a feature of the Holocene climate (see e.g. Hughen et al. [2]). Information about the temperature in the last interglacial period (120,000 years ago) can be inferred from the exoskeletons of coral. The amount of the heavy isotope ^{18}O absorbed depends on the SST and the quantity of the isotope in the surrounding water (which depends on precipitation and evaporation rates). Cooler SSTs and drought conditions caused during El Niño in Indonesia (from where the coral record was extracted) create large positive anomalies in the ^{18}O record. The evidence here too points to a broad peak around a similar timescale in the power spectrum.

2.2 Models

Simulating and/or explaining this cycle at around four years is proving to be a challenge to the climate community. GCMs often get the period wrong; usually it is too short. For example Timmerman et al. [3] performed runs with a GCM with an increasing greenhouse gas scenario to evaluate the impacts this might have on El Niño. They concluded that this scenario had little effect on the El Niño period (although the same was not true for the amplitude of the event.) However the El Niño period in their control runs is 2 years, i.e. too short by a factor of 2! It would be interesting to be able to explain the period in this model to verify that the result of no change in period didn't depend on the control run period.

2.3 Linear analysis

Münnich et al. [4] compare versions of their iterative map model of ENSO with linear and nonlinear ocean-atmosphere couplings. They find that a linear version of their model can only produce periods up to about two years but demonstrate that when nonlinearity is included periods more akin to the real world ENSO are produced. They postulate that the mechanism choosing the preferred period (of approximately 4 years) is in essence nonlinear.

For our study we used a similar, though simplified, delayed oscillator type model, which is described in the next section. As linearised analysis seems unable to fully explain the

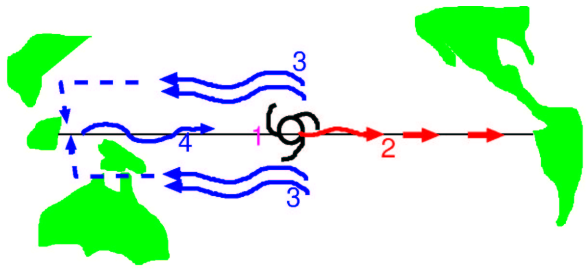

Figure 2: The delayed oscillator mechanism (see text for description), figure courtesy of Eli Tziperman.

source of ENSO's period it was the purpose of this project to explore nonlinear effects on the period in a delayed oscillator model. More specifically we asked the following two questions: what role could nonlinearity play in setting or affecting ENSO's period? Is there a relation between the period of ENSO and its amplitude?

3 The delayed oscillator

The delayed oscillator description of El Niño (Suarez and Schopf [5], Battisti [6]), can be described as follows (see figure 2). An easterly wind weakening (1) creates an equatorial warm (downwelling) Kelvin wave (2) that travels to the east Pacific arriving within 1–2 months, where a thermocline rise induces SST heating and starts an El Niño. The event is amplified by ocean-atmosphere instability: the SST heating causes further wind weakening therefore there is a positive feedback that strengthens the east Pacific warming. However the original wind weakening also creates off-equatorial (upwelling) Rossby waves (3) which propagate westward and are reflected from the western boundary as cold Kelvin waves (4) to arrive six months later at the eastern boundary and terminate the event. The equation which Suarez and Schopf [5] used to capture this behaviour in the SST ($T(t)$) is (in nondimensional form)

$$\frac{dT(t)}{dt} = T(t) - \alpha T(t - \delta_T) - T^3(t)\,. \tag{1}$$

The first term represents the positive feedback effects of the Kelvin wave (ignoring the short delay in the time for it to travel to the eastern basin), the second term is the Rossby wave and the third a nonlinear damping term to stabilise the system. δ_T is the nondimensional Rossby wave delay time and α measures the influence of the returning signal relative to that of the local feedback (i.e. relative to the Kelvin wave term.) This model produces oscillations, although whether or not the timescale of these oscillations is the required 3–6 years depends sensitively on the specific model parameters chosen so ENSO's period is not a robust feature of this model.

We now go on to consider the delayed oscillator used for the present study.

3.1 A brief derivation of the delayed oscillator used here

Models of ENSO when run in certain parameter regimes can generate SST behaviour which is self-sustained and periodic; the period obtained depends on the model parameters. However we wanted to extract the role of nonlinearity on the period separately from the role of parameters and for this it is necessary to run the model in a chaotic regime in a way which shall be outlined in section 4 onwards. First we shall describe briefly the model used though the reader is referred to [7] and the references therein for a full description. The model we used in this study was that of Galanti and Tziperman [7] (hereafter GT). It is based on that of Jin [8, 9] which is turn is simplified from the model of Zebiak and Cane [1], hereafter CZ.

3.2 Ocean dynamics

The ocean dynamics follow from a shallow water anomaly model on an equatorial β plane with linear friction using the long wave approximation, (i.e. no $\partial v/\partial t$ term). The meridional damping and meridional wind stress are also neglected. The resulting set of equations is

$$\begin{aligned} \frac{\partial u}{\partial t} - \beta y v + g' \frac{\partial h}{\partial x} &= \epsilon_m u + \frac{\tau_x}{\rho H}\,, \\ \beta y u + g' \frac{\partial h}{\partial y} &= \epsilon_m v + \frac{\tau_y}{\rho H}\,, \\ \frac{\partial h}{\partial t} + H(\frac{\partial u}{\partial x} + \frac{\partial v}{\partial y}) &= -\epsilon_m h\,, \end{aligned} \tag{2}$$

where u and v are the zonal and meridional anomaly velocities, h is the thermocline depth departure from its mean state, g' is the reduced gravity acceleration, ϵ_m is the oceanic damping coefficient, and H is the mean thermocline depth. Jin makes the "two strip approximation" which assumes that the ocean dynamics in the equatorial region is well represented by a combination of equatorial Kelvin waves and off-equatorial long Rossby waves. The ocean basin is also divided into two zonal boxes. GT instead of using the two box approach integrate along characteristics for Kelvin waves (along the equatorial strip) and Rossby waves (along the off-equatorial strip) to obtain a delay equation. The Kelvin delay time is retained in GT's analysis, and is neglected by Jin.

3.3 The ocean-atmosphere interaction

GT follow Jin in that they have a (truncated) Gill's atmosphere; CZ use a full Gill's atmosphere. The wind stress is assumed to affect the waves only in the central part of the basin and is assumed to be a linear function of SST on the eastern equator (Jin [8]),

$$\tau_x(t) = \mu(t) b_0 T(t) \exp(-\frac{y^2 \alpha}{2L_0^2})\,, \tag{3}$$

where $\sqrt{\alpha}/L_o$ is the atmospheric Rossby radius of deformation, b_0 is the annual mean coupling and $\mu(t)$ a seasonally varying coupling. Thus the analysis of GT yields an equation for the thermocline depth anomaly in the eastern equatorial Pacific, h,

Parameter	Description
h	thermocline depth anomaly on the Eastern equator
T	temperature anomaly on the Eastern equator
ϵ_m	oceanic damping coefficient
τ_2	Kelvin wave basin crossing time
τ_1	Rossby wave basin crossing time
r_W, r_E	the reflection coefficients at the western/eastern boundaries
$dt = 0.5$	the fraction of crossing time that wind stress affects waves
ρ	mean density of ocean
A^*	a constant relating wind stress anomalies to SST anomalies
b_0	annual mean coupling strength
μ	relative coupling coefficient which changes seasonally
$\bar{w}$	mean upwelling
ϵ_T	thermal damping coefficient
T_{sub}	temperature anomaly at depth H_1; a function of h
h	thermocline depth anomaly
γ	relates the temperature anomalies entrained into the surface layer to the deeper temperature variations due to $T_{sub}(h)$.

Table 1: Parameters in equations 4 and 7.

$$\begin{aligned} h(t) &= e^{-\epsilon_m \tau_2} r_W r_E h(t-\tau_1-\tau_2) e^{-\epsilon_m \tau_1} \\ &- e^{-\epsilon_m \tau_2} r_W \frac{1}{\beta\rho} A^* dt \tau_1 \mu(t-\tau_2-\frac{\tau_1}{2}) b_0 T(t-\tau_2-\frac{\tau_1}{2}) e^{\epsilon_m \tau_1/2} \\ &+ \frac{1}{\rho C_o} dt \tau_2 \mu(t-\frac{\tau_2}{2}) b_0 T(t-\frac{\tau_2}{2}) e^{\epsilon_m \tau_2/2}. \end{aligned} \tag{4}$$

where the model parameters are described in Table 1. Equation 4 can be physically interpreted as the thermocline depth anomaly due to signals propagated by slow moving Rossby waves and faster Kelvin waves. In the GT model the wind stress excites these waves which are responsible for the El Niño event. The seasonal coupling μ is given by

$$\mu = 1 + \delta \cos(w_a t - \phi). \tag{5}$$

$w_a = 2\pi/12$ is the annual frequency and $\phi = 5\pi/6$ is the phase; the coupling peaks in May. This represents the fact that the strength of the response of the wind stress anomalies to SST anomalies varies with season. It has several contributions (see Tziperman et al. [10] and GT), chief amongst them the variation of the mean wind convergence due to the movement of the ITCZ. Another important contribution is the seasonal variation of the mean SST.

All Rossby waves move westward across the basin damped by $e^{-\epsilon_m \tau_1}$, travelling along the off equatorial strip, whereas the Kelvin waves move eastward as damped equatorial waves ($e^{-\epsilon_m \tau_2}$). τ_1 and τ_2 are the basin crossing times for Rossby and Kelvin waves respectively and r_W (r_E) the reflection coefficient at the western (eastern) boundary.

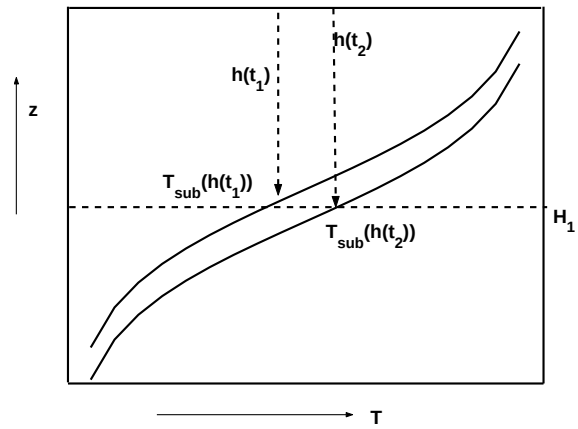

Figure 3: A schematic of the variation of T_{sub} with the movement of h. At t_1 the thermocline is nearer the surface and thus the temperature T_{sub} (measured at depth H_1) is less than when the thermocline is deeper at time t_2.

At each timestep equation 4 has three contributions. The first term on the RHS represents a "free" wave which left the eastern basin (after a reflection by the eastern boundary) at a time $t - \tau_1 - \tau_2$ and travelled as a Rossby wave, to the western boundary arriving at time $t - \tau_2$. It was then reflected by the western boundary and travelled back to the eastern boundary as a Kelvin wave, arriving at time t. The second term represents the Rossby waves excited at a time $t - \tau_2 - \tau_1/2$ in the central Pacific which travelled westward, again being reflected at $t - \tau_2$ and which travelled back as a Kelvin wave arriving again at t. The final term is a Kelvin wave, excited at a time $t - \tau_2/2$ in the centre of the basin which then travelled to the eastern basin. Note the negative sign for the Rossby wave term due to the fact it is proportional to the curl of the wind stress (the Kelvin wave term is proportional to the wind stress itself, hence a positive feedback). Thus a weakening of the westward winds results in an excitation of warm Kelvin waves and cold Rossby waves (and a strengthening of the winds leads to vice versa); hence the system oscillates.

3.4 The SST equation

The model solves equation 4 coupled with an equation for the evolution of SST. GT follow Jin and keep only the time rate of change, the advection by the mean upwelling $\overline{w}$ and the damping term (cooling) from a usual advection diffusion temperature equation.

$$\frac{\partial T}{\partial t} = -\epsilon_T T - w\frac{\partial T}{\partial z} \tag{6}$$

The second term on the RHS is parameterised, following CZ, as

$$\gamma\frac{\overline{w}}{H_1}(T - T_{sub}(h))\,,$$

where T_{sub} is the temperature anomaly at depth H_1 (the mean thermocline depth) and is approximated as a tanh function (Münnich et al. [4]). This is explained in figure 3.

Hence the SST in the east varies as

$$\partial_t T = -\epsilon_T T - \gamma \frac{\bar{w}}{H_1}(T - T_{sub}(h)) \,. \tag{7}$$

Note that the main nonlinearity in the model is due to T_{sub} and that the mechanism of oscillation in the GT model has an explicit delay for the time it takes SST to adjust to changes in h.

4 Transition to chaos

As we stated in section 3, in order to separate the role of nonlinearity from that of the parameters in setting the period of El Niño we have used the idea of running the model in a chaotic regime. This will become clear as we proceed below. We changed the parameters b_0 and μ, i.e. the mean coupling and the seasonal coupling in the search for chaos. To diagnose the chaos we examined the time series of temperature, the frequency spectrum and the reconstructed delayed coordinate phase space. The latter of these is found as follows. Take the data set of SST output every day and from this form a subset of the data subsampled every year, $T(t)$. Then plot $T(t)$ versus $T(t-\tau)$ where τ is one year.

The GT model follows the quasi-periodic route to chaos (Tziperman et al. [11]), as opposed to that of period doubling or intermittancy. As b_0 and μ (or equivalently δ) are changed the model exhibits different types of behaviour.

It should be noted that for oscillations to be sustained the coupling must be greater than a critical value otherwise the damping of the waves overcomes the positive feedback effect as described in section 3 and a constant temperature results.

4.1 The quasi-periodic regime

In this regime the ratio of the frequency of El Niño (ω_{el}) to the seasonal cycle (ω_a) cannot be written as a rational fraction i.e. it is not possible to write ω_{el}/ω_a as n/m where n and m are integers. An example with period of approximately 4.35 years can be seen in figure 4. The phase space Poincaré section is a closed loop and the time series is periodic. The spectrum demonstrates there are other frequencies present, due to the nonlinearity of the oscillation.

4.2 The mode locked regime

In this regime the signal is locked to some rational multiple of the seasonal cycle. For this type of chaos we need a damped nonlinear oscillator forced by a period forcing. This regime is seen in figure 5; the frequency for this particular choice of parameters is 1/4 the annual period.

4.3 The chaotic regime

In figure 6 the spectrum shows a very broad peak at around 3-4 years which together with the phase plot identifies this as a strongly chaotic regime and hence the one we shall use for our study.

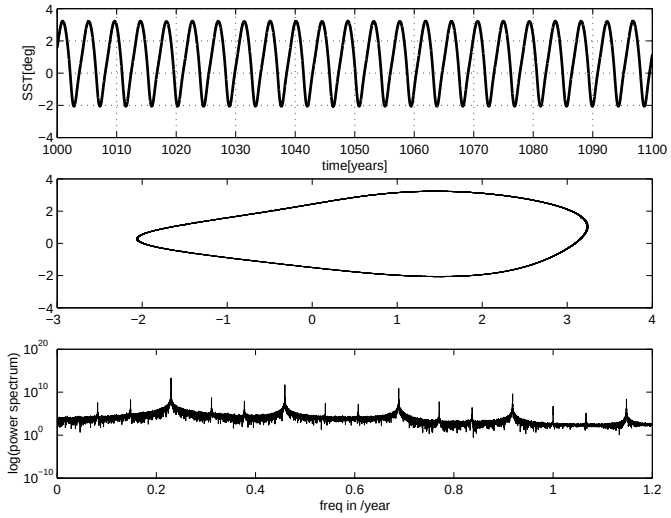

Figure 4: SST for a b_0=7.5×10^{10} kg month^{-2} m^{-1} °C^{-1} and δ=0.001

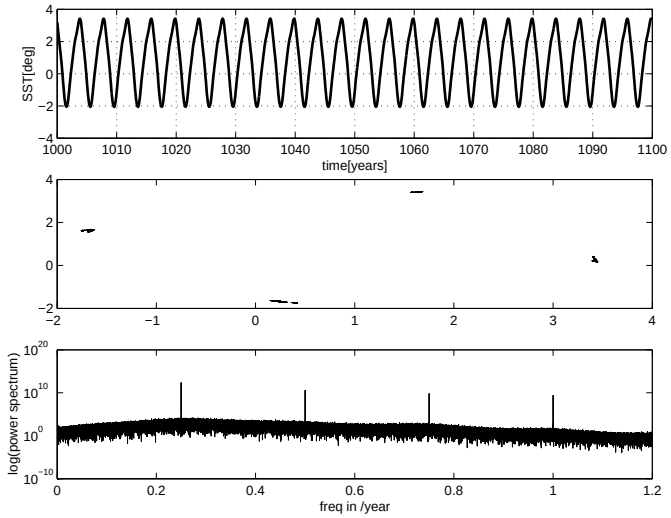

Figure 5: SST for a b_0=7.5×10^{10} kg month^{-2} m^{-1} °C^{-1} and δ=0.04

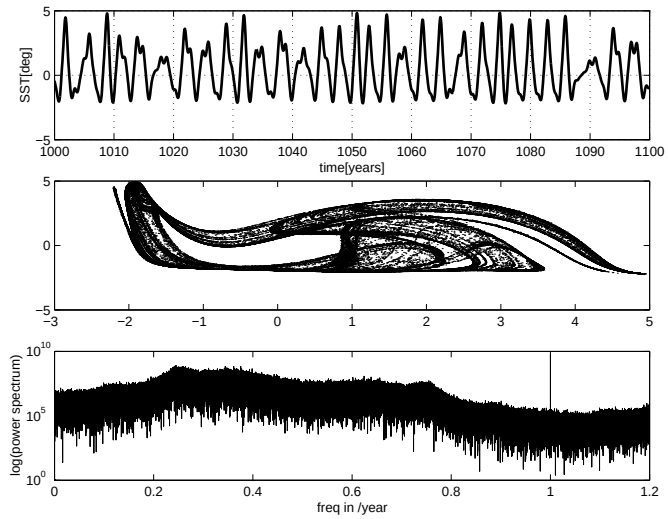

Figure 6: SST for a b_0=7.5×10^{10} kg month^{-2} m^{-1} °C^{-1} and δ=0.18.

4.4 Other periods

As an aside we mention as stated in section 2, that the model can support varying periods depending on the model parameters. Figure 7 for example shows an example of a longer period than figure 4 (the period is approximately 9.9 years in contrast to the 4.35 years of figure 4), while still being in the quasi-periodic regime.

5 Finding unstable periodic orbits

We wanted to compare the wave dynamics of several different periods of El Niño which the model supports. As the model is now in the chaotic regime, different periodical solutions exist as unstable periodic orbits; we have many different El Niño periods for the *same* values of the model parameters.

To enable us to study the unstable periodic orbits (UPOs) we ran the model in the chaotic regime for 100,000 years, with output every day to obtain a time series of the SST, T(t). Then following the method outlined in Tziperman et al. [12], we determined the UPOs in a 3 dimensional delay-coordinate phase-space reconstruction from the T(t). The delay coordinates are defined as $\mathbf{X}(t) = \{X_1, X_2, X_3\} = \{T(t-2\tau), T(t-\tau), T(t)\}$ where τ is one year. For a given period p we searched for phase space points $\mathbf{X}(t)$ that returned to the same neighbourhood after a period p, so that $||\mathbf{X}(t) - \mathbf{X}(t-p)|| < \epsilon$ for some small ϵ. When plotting the number of peaks which fall into this criterion against p, the UPOs show up as peaks (figure 8). The points $\mathbf{X}(t)$ which satisfy the above criterion for p= 3,4,5 and 6 years can be seen in figure 9. Note there are two separate three year UPOs and the six year one appears to be just a period doubling of that for three years. It is then necessary to extract one orbit for each of the UPOS, i.e. one "loop of the circuit". We can then also examine the corresponding segment of the time series and subsequently the wave dynamics for each of the segments. The single UPOs are shown in figure 10 with the corresponding

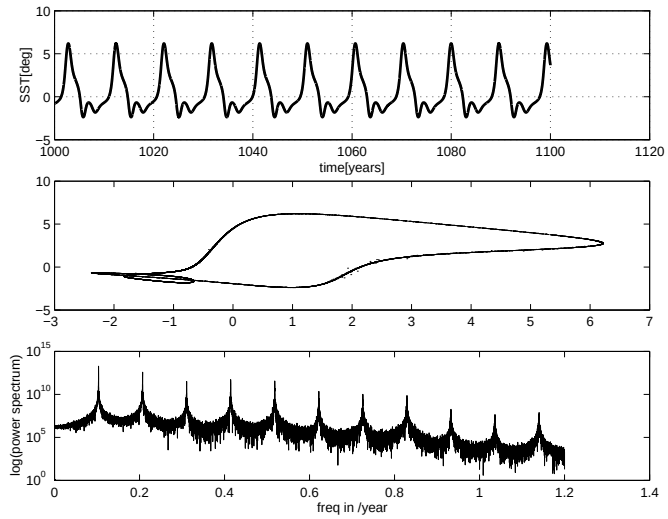

Figure 7: SST for a b_0=8.5×10^{10} kg month^{-2} m^{-1} $^{\circ}C^{-1}$ and δ=0

time series in figure 11.

For our study we wanted to examine the dynamics of "independent orbits". From figure 11 it is evident that the five and eight year orbits are composed of two other UPOs; the five year one being composed of a two year orbit and a three year orbit for instance. The two shorter period UPOs have merged in phase space to form the five and eight year UPOs. In order to build up the wave dynamics picture therefore we concentrated our attention on the three and four year UPOs.

The system jumps irregularly between the different UPOs (not just those pictured). With no seasonal cycle present the "natural" El Niño period is largely about 3–5 years. It would be no surprise therefore if the system spent most time near the three, four and five year UPOs, i.e. they were the least unstable.

6 Amplitude period relations in the delayed oscillator

From figure 12 it is feasible to postulate an amplitude period relationship; the shorter period has a larger amplitude. This seems to be true of even the merged orbit; at least the two year cycle visible in figure 11c (as part of the five year UPO) has a still larger amplitude than either the three or four year SST series. This relationship is not in general true of nonlinear oscillators. For example the unforced Duffing oscillator/spring equation

$$\ddot{x} + \omega^2 x + bx^3 = 0\,,$$

yields solutions for both a spring which increases in frequency ($b > 0$) with increasing amplitude and the converse[1] ($b < 0$). So how robust is our amplitude frequency relationship? Also, what might be the physical mechanism behind this relationship?

[1]The question may well be asked as to whether this is a good comparison to make, after all the spring is an undamped, unforced oscillator, however we mention it briefly as a first thought. A better comparison might be to look at something like the Lorenz equations.

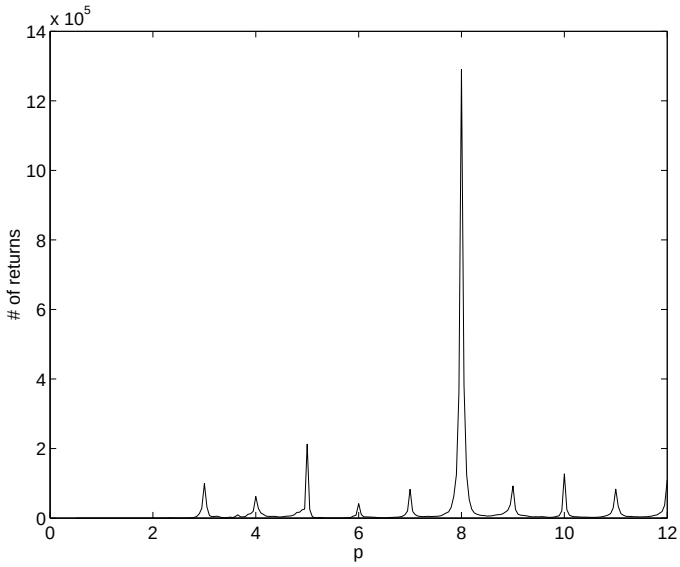

Figure 8: Number of returns for each value of p, ϵ=0.02.

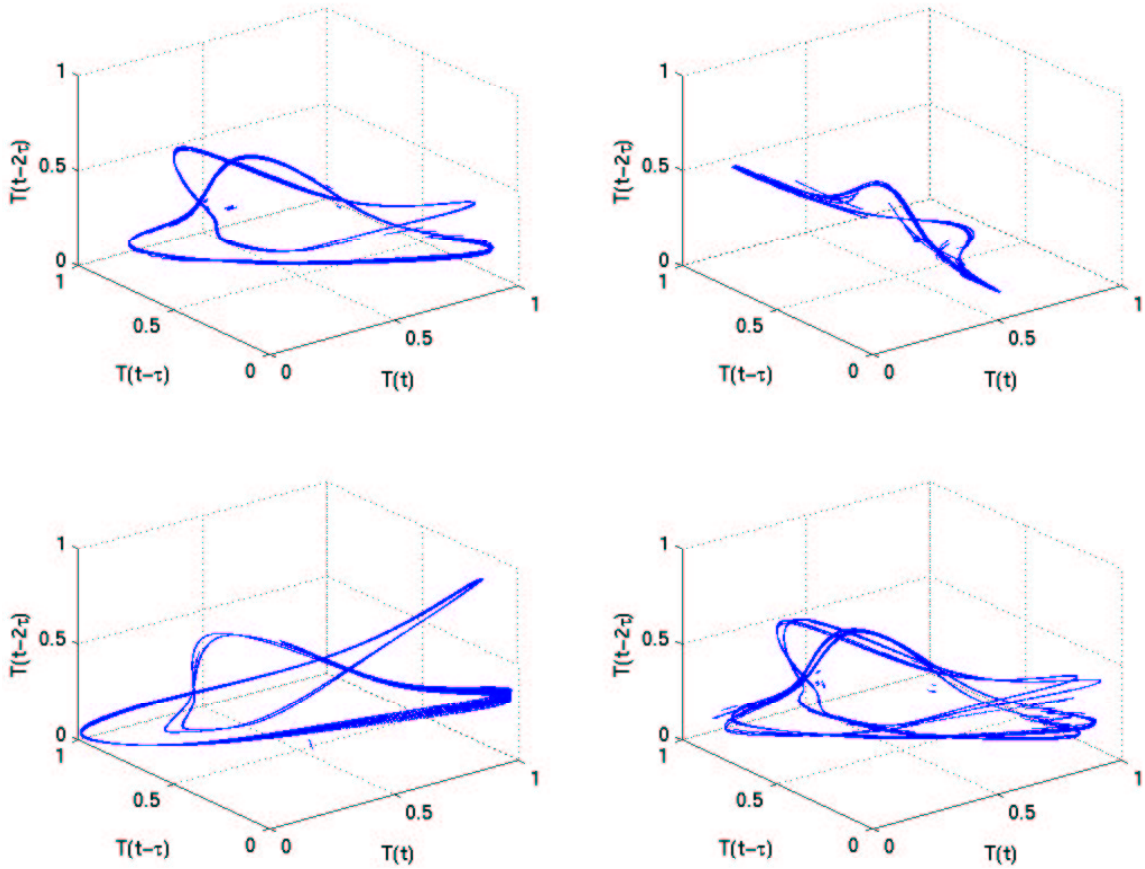

Figure 9: UPOs for a)p=3, b)p=4, c)p=5, d)p=6 years

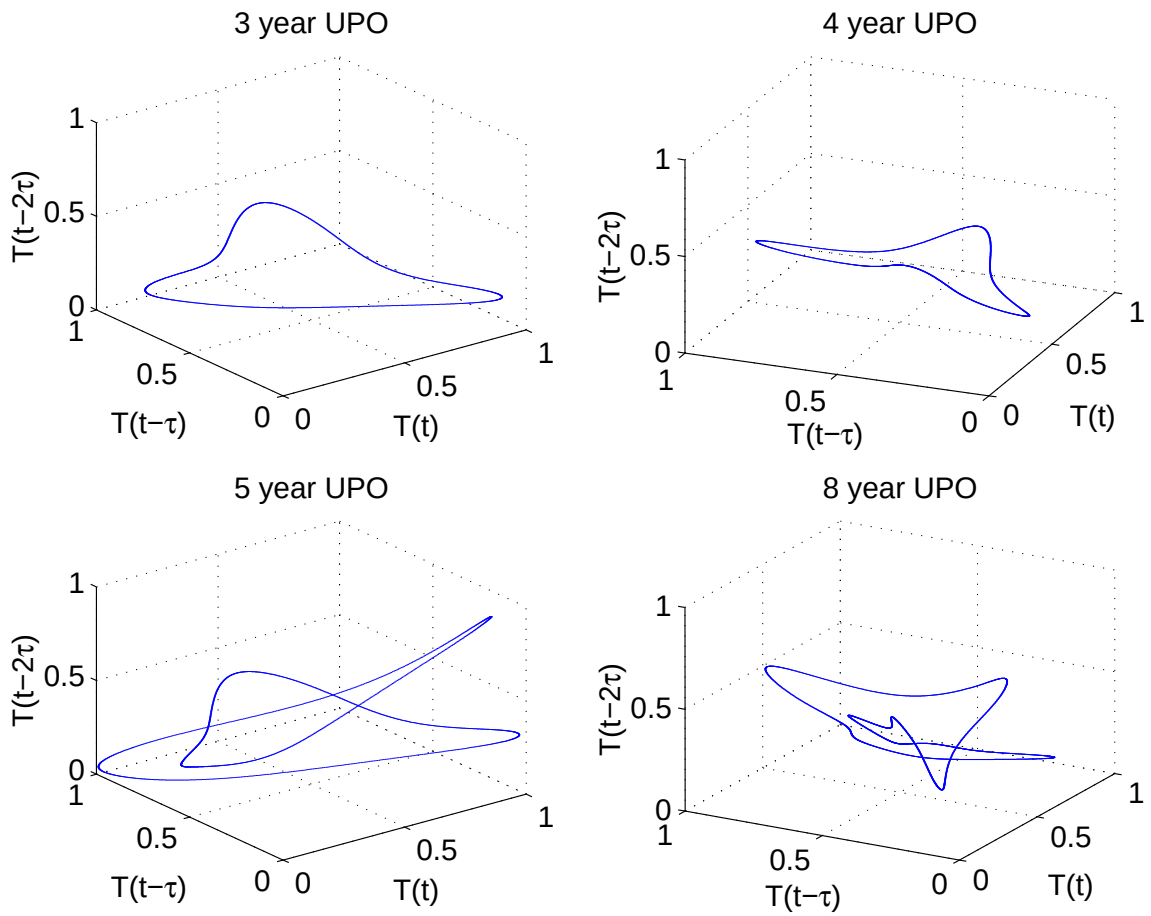

Figure 10: Single UPOs for a)3 years and b)4 years c)5 years and d)8 years

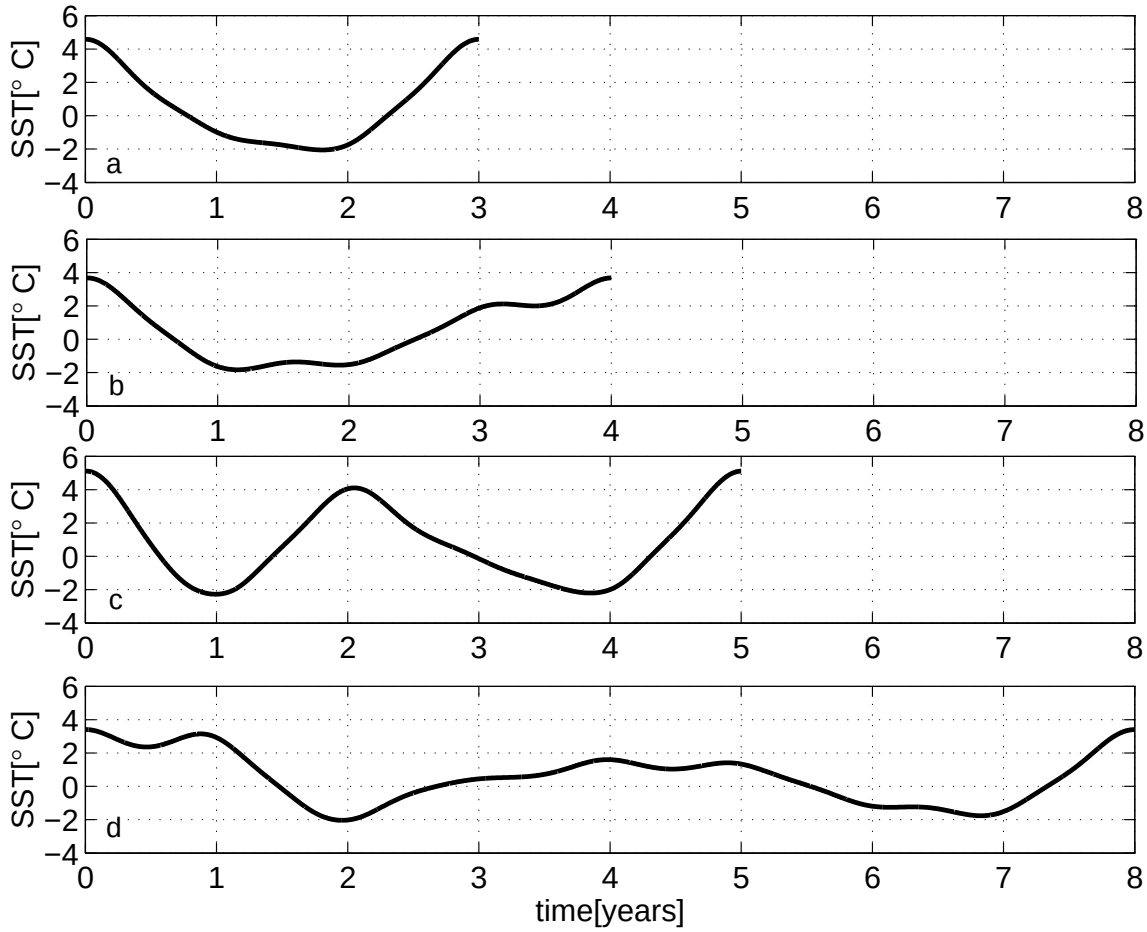

Figure 11: SST for a)3 years and b)4 years c)5 years and d)8 years

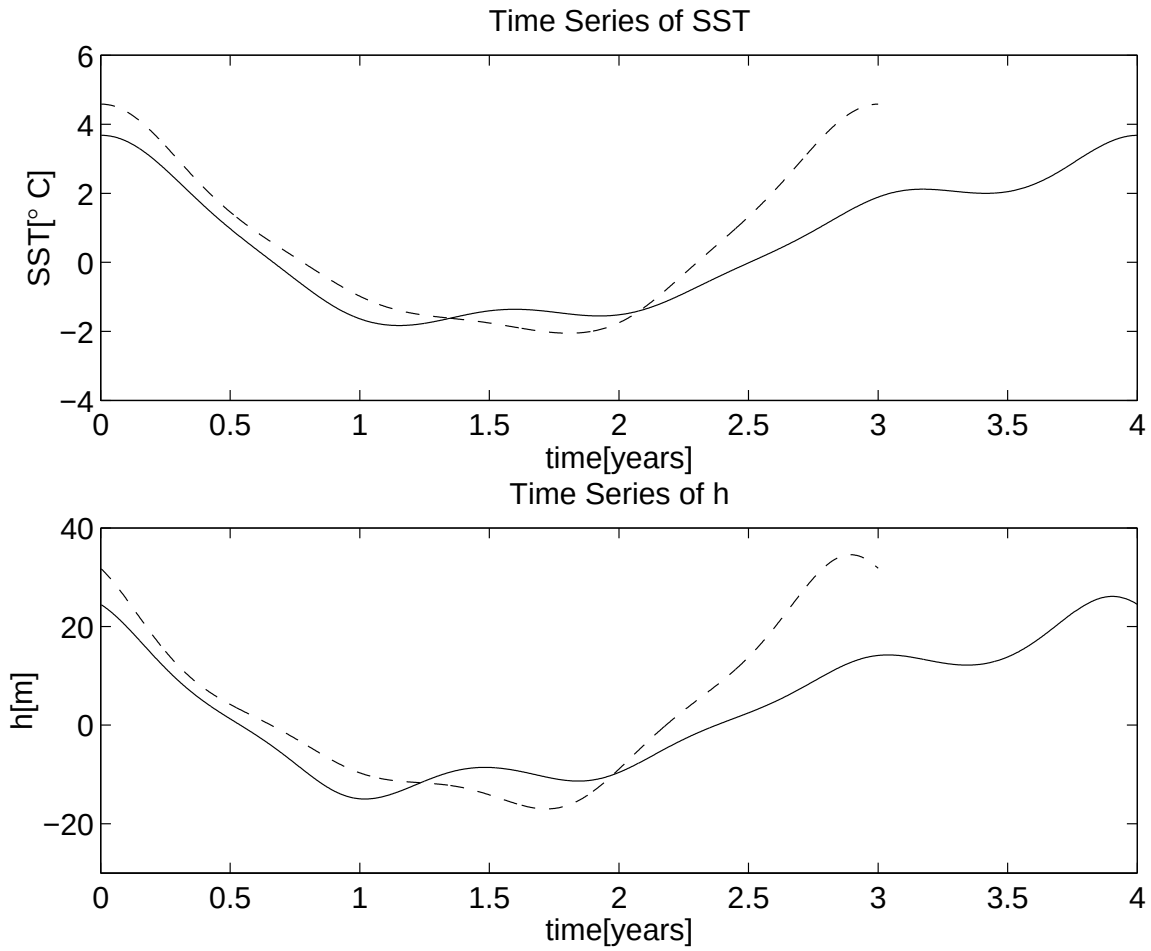

Figure 12: SST and h for the three $(- -)$ and four $(-)$ year UPOs

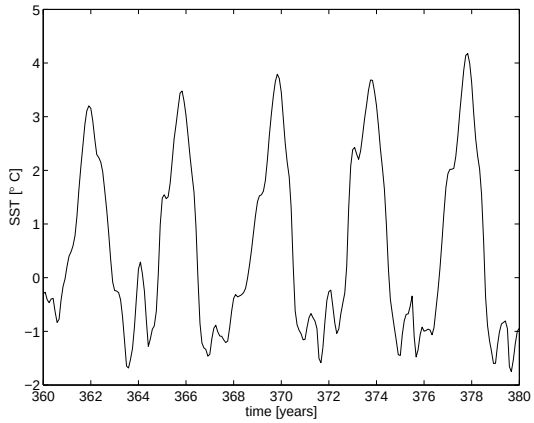

Figure 13: A section of a time series from the Cane-Zebiak [1] model showing events with an amplitude of just over 3°C.

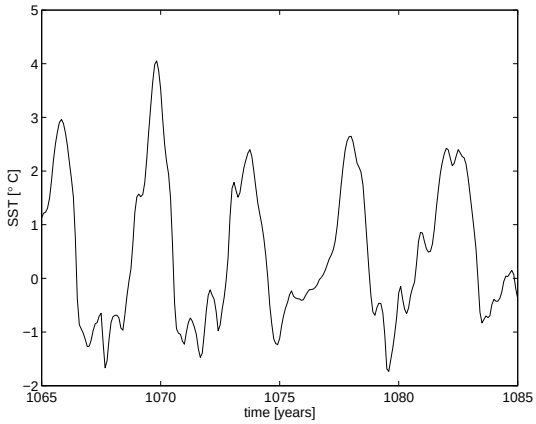

Figure 14: A section of a time series from the Cane-Zebiak [1] model showing events with an amplitude of just over 2 °C.

6.1 The Cane-Zebiak (1987) model

As a quick check on the amplitude frequency relationship we performed a preliminary comparison with the CZ model, mentioned in section 3.1. Looking at examples of El Niño events at just over 3°C (figure 13) and comparing them with those just over 2°C (figure 14) the periods appear to be about the same (4.1 years in the former case and 3.9 years in the latter case.) As a further example in figure 15 the smaller (just over 2°C) and larger events (just over 3°C) both have periods of exactly 4 years.

An examination of events smaller than 2 °C is problematic as it is depends very much then on the definition of an event. By how much does the SST have to warm before an El Niño is said to have taken place? Some of these small events/noise can be seen in figures 13 to 15. This preliminary investigation seems to suggest no clear period amplitude relation in the CZ data, however a fuller statistical analysis is clearly needed.

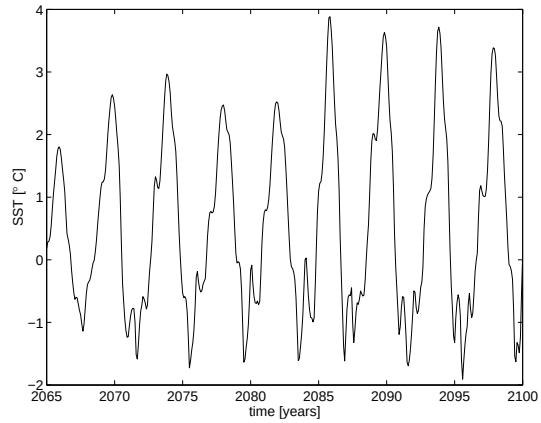

Figure 15: A section of a time series from the Cane-Zebiak [1] model showing consecutive events with amplitudes of just over 2 °C then just over .3 °C.

7 Wave dynamics analysis

Returning to look at figure 12 we can compare the features of the three and four year ENSO cycles. The four year cycle spends time between one and two years at an approximately constant temperature and the four year warming which begins around two years is longer and more gradual. To attempt to explain this behaviour in terms of the waves dynamics we examined the various terms in equation 4, and they are plotted for each UPO in figures 16 and 17. We use the following notation for the terms from equation 4. RK is the free Rossby-Kelvin wave, ER is the excited Rossby wave and EK is the excited Kelvin wave as described in section 3.3.

$$\begin{aligned} RK &\equiv e^{-\epsilon_m \tau_2} r_W r_E h_{eE}(t-\tau_1-\tau_2) e^{-\epsilon_m \tau_1} \\ ER &\equiv -e^{-\epsilon_m \tau_2} r_W \frac{1}{\beta\rho} A^* dt \tau_1 \mu(t-\tau_2-\frac{\tau_1}{2}) \times b_0 T_{eE}(t-\tau_2-\frac{\tau_1}{2}) e^{\epsilon_m \tau_1/2} \\ EK &\equiv +\frac{1}{\rho C_o} dt \tau_2 \mu(t-\frac{\tau_2}{2}) b_0 T_{eE}(t-\frac{\tau_2}{2}) e^{\epsilon_m \tau_2/2}\,. \end{aligned} \tag{8}$$

τ_1 is 8.5 months and τ_2 is 2.1 months. The effect on h at any point in time is therefore determined by the SST one month previously (via term EK) and by the SST about 6 months previously (via term ER). In figures 16 and 17 it can be seen that the Rossby wave term always lags the Kelvin wave term by about 6 months (and its amplitude is smaller and with an opposite sign.) The term RK is a slave to the other two as it only depends on h about 10.5 months before.

7.1 The three year event

Examine first figure 16. From approximately two years the Kelvin wave (EK) feedback produces higher and higher SSTs as we enter an El Niño event as described in section 3. The warmer SSTs however (via the weakening wind) also cause the generation of cold

Rossby waves which terminate the El Niño event at the end of year three. They then continue to bring a cooling signal such that the temperature begins to decrease and then the Kelvin wave feedback causes an increasing cooling of temperature until this is stopped again by the Rossby wave bringing a warming signal once more towards the end of the second year.

The balance between the Rossby and Kelvin waves required to terminate an event can only happen at the end of the year (see GT). Equation 3 for μ parameterises the coupling between atmosphere and ocean as being strongest in month five. i.e. the system is most unstable then. At the end of the year the coupling of the SST (which is generating the Kelvin term) is much weaker. However the Rossby wave signal felt by the east Pacific at the end of the year is due to the coupling 6 months previously, (when the coupling was strong). Thus a strong warming trend due to the Kelvin waves amplified by weak coupled instability balances the weak cooling trend due to Rossby waves amplified by a stronger coupled instability.

7.2 The four year event

For the first year the picture looks similar to the three year case, figure 18. However at about one year the Kelvin wave has a period of approximately constant amplitude; it seems to get "stuck". Hence six months later the Rossby wave has a similar constant period. At the end of year two the Rossby wave is, as in the three year case, strong enough to cause the warming to begin. The Kelvin wave feedback ensures continuing warming. However as the Rossby wave was constant for a year, by the end of year three it isn't "powerful enough" (i.e. it isn't cooling strongly enough) to cause a halt to the warming. The SST perturbation it was coupled to six months previously was around zero (see figure 12). Hence the Kelvin wave feedback continues to cause warming. As we progress in the third year the Rossby wave becomes stronger and hence limits the amount of warming caused by the Kelvin wave, thus the El Niño amplitude is smaller and finally at the end of year four the event is terminated.

The key then, to the four year cycle developing as opposed to a three year event is the halt of the cooling of the Kelvin wave at the end of the first year. The reason for this presumably involves the nonlinearity but a precise explanation is not immediately apparent. What we can say is that the four year event being weaker is consistent with the fact that the Kelvin and Rossby waves are weaker. This weakness makes the event develop more slowly, and in particular shift from phase to phase more slowly as described above. The stronger three year event sustains stronger Kelvin and Rossby terms which are able to shift the system from El Niño to La Niña faster. This wave dynamics perspective into the amplitude-period relation for the delayed oscillator model used here gives us some intuition regarding the physical processes responsible for this relation.

8 Concluding remarks

The mechanism causing ENSO's robust four year period is not yet fully understood and when simulated in models the explanation seems to rely on a nonlinear effect. In order to separate the nonlinear causes from those of the parameters we extracted UPOs from a

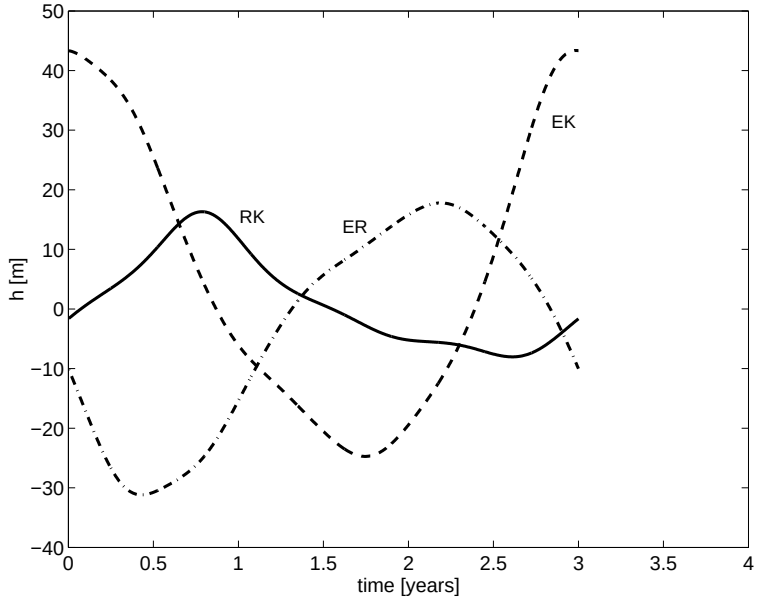

Figure 16: Terms in equation 4: RK(–), ER(–·), EK (– –)

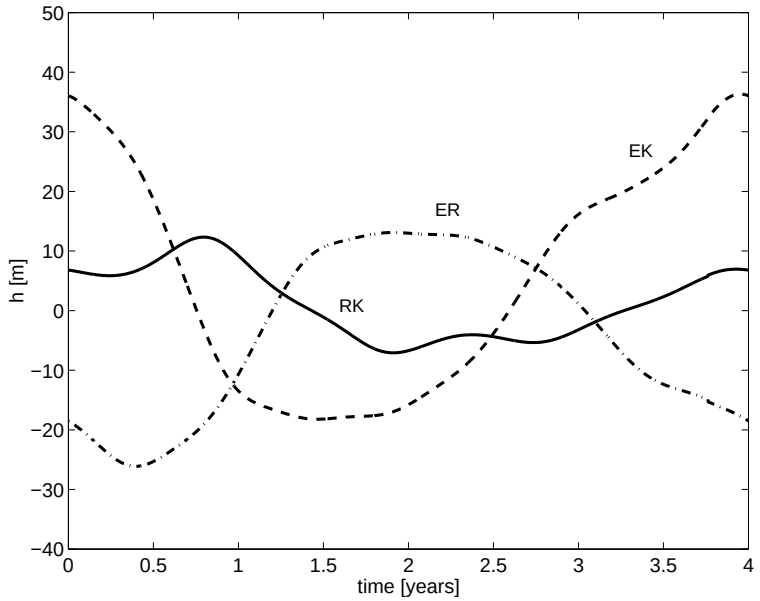

Figure 17: Terms in equation 4: RK(–), ER(–·), EK (– –)

simple delayed oscillator model. We found from these UPOs that a shorter period implied a larger amplitude of an El Niño event and whilst the precise nature of the nonlinearity was unclear it was possible to rationalise this amplitude period relation in terms of equatorial wave dynamics. Efforts to verify this relation with the CZ model were inconclusive at this stage. Further work is required to test its robustness in both fuller models and in the actual Pacific.

9 Acknowledgments

Many thanks indeed to my supervisor Eli Tziperman for suggesting the project and for his patience and guidance in teaching me so much in such a short space of time. Thanks too to Eli Galanti, for his code, his suggestions and his understanding when I used all the disk space! Thanks to Joe Keller, Bill Young and Lenny Smith for suggestions of ways to think and to my "fellow fellows", for going through it and being there with me. To everyone at Walsh cottage thanks for a great summer!

References

[1] S. E. Zebiak and M. A. Cane, "A model El Niño-Southern Oscillation," Mon. Wea. Rev. **115**, 2262 (1987).

[2] K. Hughen, D. Schrag, S. Jacobsen, and W. Hantoro, "El Niño during the last interglacial period recorded by a fossil coral from indonesia," Geophys. Res. Lett. **26**, 3129 (1999).

[3] A. Timmerman, J. Oberhuber, A. Bacher, M. Esch, M. Latif, and E. Roeckner, "Increased El Niño frequency in a climate model forced by future greenhouse warming," Nature **398**, 694 (1999).

[4] M. Munnich, M. Cane, and S. Zebiak, "A study of self-excited oscillations of the tropical ocean-atmosphere system. Part II: Nonlinear cases," J. Atmos. Sci. **48**, 1238 (1991).

[5] M. Suarez and P. Schopf, "A delayed action oscillator for ENSO," J. Atmos. Sci. **45**, 3283 (1988).

[6] D. Battisti, "The dynamics and thermodynamics of a warming event in a coupled tropical atmopshere-ocean model," J. Atmos. Sci. **45**, 2889 (1988).

[7] E. Galanti and E. Tziperman, "ENSO's phase locking to the seasonal cycle in the fast-SST, fast-wave, and mixed mode regimes," J. Atmos. Sci. **57**, 2936 (2000).

[8] F.-F. Jin, "An equatorial ocean recharge paradigm for ENSO. Part I: Conceptual model," J. Atmos. Sci. **54**, 811 (1997).

[9] F.-F. Jin, "An equatorial ocean recharge paradigm for ENSO. Part II: A stripped-down model," J. Atmos. Sci. **54**, 830 (1997).

[10] E. Tziperman, S. E. Zebiak, and M. A. Cane, "Mechanisms of seasonal-ENSO interaction," J. Atmos. Sci. **54**, 61 (1997).

[11] E. Tziperman, L. Stone, M. Cane, and H. Jarosh, "El Niño chaos: overlapping of resonances between the seasonal cycle and the Pacific ocean-atmosphere oscillator," Science **264**, 72 (1994).

[12] E. Tziperman, H. Scher, S. E. Zebiak, and M. A. Cane, "Controlling spatiotemporal chaos in a realistic El Niño prediction model," Phys. Rev. Lett. **79**, 1034 (1997).

Abyssal flow in a two-layer model with sloping boundaries and a mid-ocean ridge

Helén C. Andersson

1 Introduction

The vast abyssal ocean is comprised of layers of very cold and dense water. As this is true even for the deep water of the tropics, the source of this water must be of polar origin. The vertical circulation that enables ventilation of these layers is driven by surface processes resulting from air-sea interaction. Heat loss of the surface water in combination with increased salinity due to evaporation or ice formation produces a dense water that sinks toward the ocean bottom. During the descent its density gets reduced due to entrainment of lighter water, and the final depth of the water mass is a function of surface density and the extent of mixing during the descent. The water then flows in a deep, large-scale circulation that fills the ocean basins. Lighter water rises to the surface and flows in surface currents to the polar regions to replace the water that has sunk.

The abyssal ocean can be divided into three layers: an intermediate layer from the base of the thermocline to about 1500 m, a deep layer below this and finally a bottom layer that is in contact with the sea floor. The sources of new abyssal waters are few as there is only a small number of regions that can produce surface water dense enough to sink to the deeper layers of the ocean. Intermediate waters form mainly in the Labrador Sea and the sub polar areas from extensive cooling but also in the Mediterranean due to high evaporation rates. Deep water formation occurs in the Nordic seas where cooling, in combination with salt release on the shelves due to ice formation, creates a dense water mass that spills in to the North Atlantic, mainly through the Faeroe Bank Channel. In the Southern Hemisphere deep and bottom water are formed at the Antarctic continent with the main location in the Weddell Sea.

Obtaining long-term measurements of the circulation in the deep ocean is difficult and our understanding of these flows is hence somewhat limited. Tracer studies have lately increased the knowledge of the flow and information is also gained from models. Stommel [1] developed a model where the abyssal circulation is a result of the sinking of deep water in high latitudes which is replaced by upwelling of deep water through the thermocline. With geographically constricted sources of deep water at the poles, the return flow is specified to be equally distributed over the entire interface between the two layers. The resulting interior geostrophic Sverdrup flow is always poleward, the vertically uniform flow of the abyss being the result of its single layer representation. The Sverdrup interior is independent of the position of the sources (see section 2) and vanishes at the equator. Western boundary

currents are added to the solution in order to satisfy mass balance and these currents are also the only possibility for a flow across the equator.

Stommel's [1] model shows the characteristics of the mean abyssal flow. However, strong baroclinic motion evident from observations are not captured by the model. Topographic features in the basin will also affect the flow. In the present study, the objective is to find an analytical solution for a model of flow in a closed basin with bottom topography and stratification. We first explore the solution to a homogeneous flow with sloping northern and western boundaries and a mid ocean ridge, before turning to the two-layer model.

2 The homogeneous model

We will first consider the case in which the ocean is represented by a single active layer. The bottom topography of the basin is shown in Fig. 1. The 500 km wide western and northern boundaries slope linearly from the ocean surface to the flat ocean floor at a depth of 4000 m. The mid-ocean ridge has a height of 3000 m and is 1000 km wide. The southern boundary is located at the equator. The isobaths of the basin geometry are shown in Fig. 2, where the slope region on the northern boundary is added for analytical convenience.

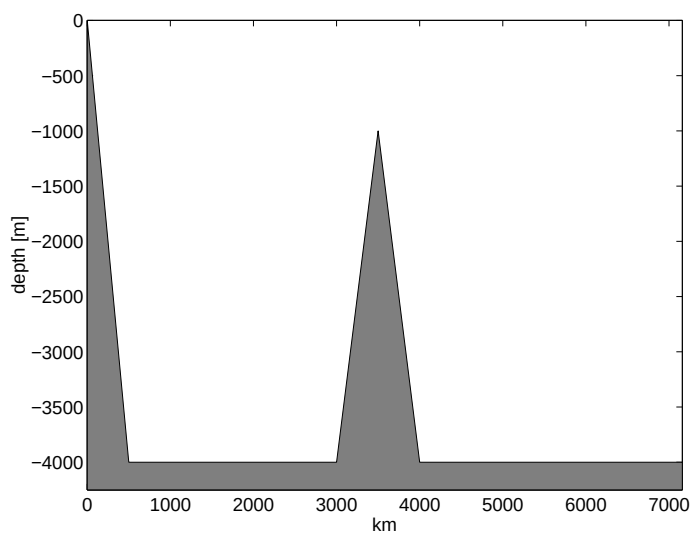

Figure 1: The bottom topography of the model basin.

The flow in the basin is driven by uniform upwelling, w_o, through the upper surface over the flat bottom (not over the boundaries). The layer gains water by sinking of upper layer water at the north-eastern corner. In the linear and steady state the interior flow is in geostrophic balance, hydrostatic and on a β-plane described by

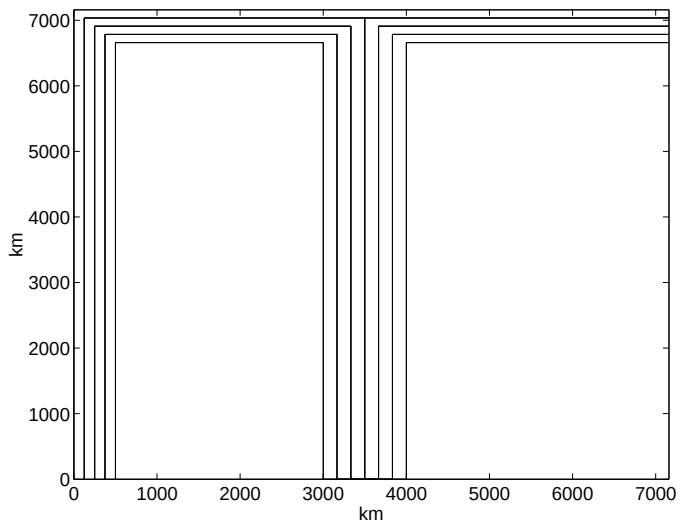

Figure 2: The isobaths of northern hemisphere model basin.

$$fv - g'\frac{\partial \eta}{\partial x} = 0 \tag{1}$$

$$fu + g'\frac{\partial \eta}{\partial y} = 0 \tag{2}$$

$$\frac{\partial u}{\partial x} + \frac{\partial v}{\partial y} + \frac{\partial w}{\partial z} = 0 \tag{3}$$

where u, v, w are velocities positive to the east (x), north (y) and upward (z), η the elevation of the interface, $f = \beta y$, $g' \equiv \frac{(\rho_2 - \rho_1)}{\rho_2}$ where ρ_1 and ρ_2 are the densities of the upper and lower layer respectively and g the gravitational acceleration. The upper layer is assumed to be passive.

For small amplitude disturbances $h + \eta \approx h$, where h is the average height of the layer. By specifying the vertical velocity w_0 as the upwelling velocity through the interface at $z = 0$ and taking u and v independent of z, we obtain after vertical integration of (3)

$$\frac{\partial u}{\partial x} + \frac{\partial v}{\partial y} = -\frac{1}{h}\left(u\frac{\partial h}{\partial x} + v\frac{\partial h}{\partial y}\right) - \frac{w_0}{h} \ . \tag{4}$$

Cross-differentiating (1) and (2) yields

$$\frac{\partial u}{\partial x} + \frac{\partial v}{\partial y} + \frac{\beta v}{f} = 0 \tag{5}$$

and in the flat interior of the basin where $u\frac{\partial h}{\partial x} = v\frac{\partial h}{\partial y} = 0$ we can now obtain the Sverdrup relation from (4) and (5)

$$v = \frac{w_0 f}{\beta h} \ . \tag{6}$$

The meridional velocity v is independent of the location of the sinks in the basin. With a positive vertical velocity w_0 it will always be positive and increase with increasing latitude.

From (5) and (6) we get

$$\frac{\partial u}{\partial x} + \frac{2w_0}{h} = 0 \tag{7}$$

from which we obtain the zonal velocity u

$$u = \frac{-2w_0}{h}(x - x_E) \tag{8}$$

where u vanishes at x_E, the eastern boundary.

As there is upwelling in the interior of the basin, there is no constant streamfunction on the lines of constant transport. We can however determine the path of the flow using the definitions

$$u = \frac{dx}{dt} \tag{9}$$

$$v = \frac{dy}{dt} \tag{10}$$

from which we get

$$\frac{u}{v} = \frac{dx}{dy} = -2y(x - x_E) \ . \tag{11}$$

Integrating from (x_W, y_W), the point at the foot of the slope from which the trajectory enters the interior, to (x, y) yields the following equation for the trajectory in the interior

$$x = (x_W - x_E)\frac{{y_W}^2}{y^2} + x_E \ . \tag{12}$$

Over the slopes where there is no upwelling the streamlines of the flow can be determined by considering conservation of linear potential vorticity (PV)

$$\frac{D}{Dt}\left(\frac{f}{h}\right) = 0 \ . \tag{13}$$

In a steady state (13) gives

$$u\frac{\partial\left(\frac{f}{h}\right)}{\partial x} + v\frac{\partial\left(\frac{f}{h}\right)}{\partial y} = 0 \ . \tag{14}$$

With the stream function ψ over the sloping boundaries, we have by definition

$$u = -\frac{\partial \psi}{\partial y} \tag{15}$$

$$v = \frac{\partial \psi}{\partial x} \tag{16}$$

which in (14) yields

$$\frac{\partial \psi}{\partial x}\frac{\partial\left(\frac{f}{h}\right)}{\partial y} - \frac{\partial \psi}{\partial y}\frac{\partial\left(\frac{f}{h}\right)}{\partial x} = J\left(\psi, \frac{f}{h}\right) = 0 \tag{17}$$

where $J(A, B)$ is the Jacobian. From this we deduce that the streamfunction is constant on lines of constant f/h, i.e

$$\psi = \psi_0\left(\frac{f}{h}\right) \tag{18}$$

where ψ_0 is the value of ψ at the foot of the slope. For the zero order picture we treat the flow as essentially inviscid.

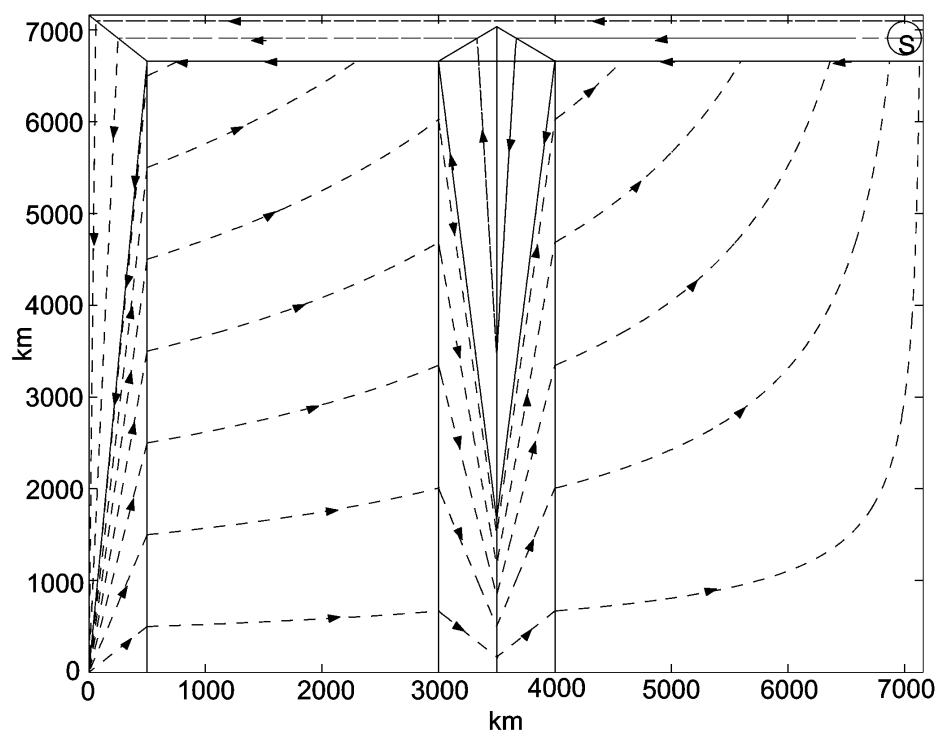

Figure 3: Trajectories of the flow

The resulting flow pattern is shown in Fig. 3. The flow enters the basin in the north-eastern corner. Shallower columns of fluid follow the northern slope on the isobath of entry. Deeper columns encounter the mid-ocean ridge and are diverted southwards and up-slope in order to conserve PV while crossing the eastern side of the ridge. In this nearly inviscid system friction will have to act along the top of the ridge in order to enable flow to cross lines of constant PV. On the western part of the ridge the PV-conserving flow will be northward and down-slope to rejoin the original isobath on the northern slope. The symmetric trajectories are a result of neglecting upwelling over the ridge. Because the

velocities over the narrow ridge are considerably stronger than the velocities induced by upwelling, the trajectory pattern is not significantly different from one which would include upwelling. When reaching the western boundary slope the flow over the north slope will again follow lines of constant PV. In a narrow region at the southwest corner, friction will again be needed to get flow across lines of constant PV so that the fluid can flow northwards to join on to the trajectories of the interior basin where the flow is determined by Sverdrup dynamics.

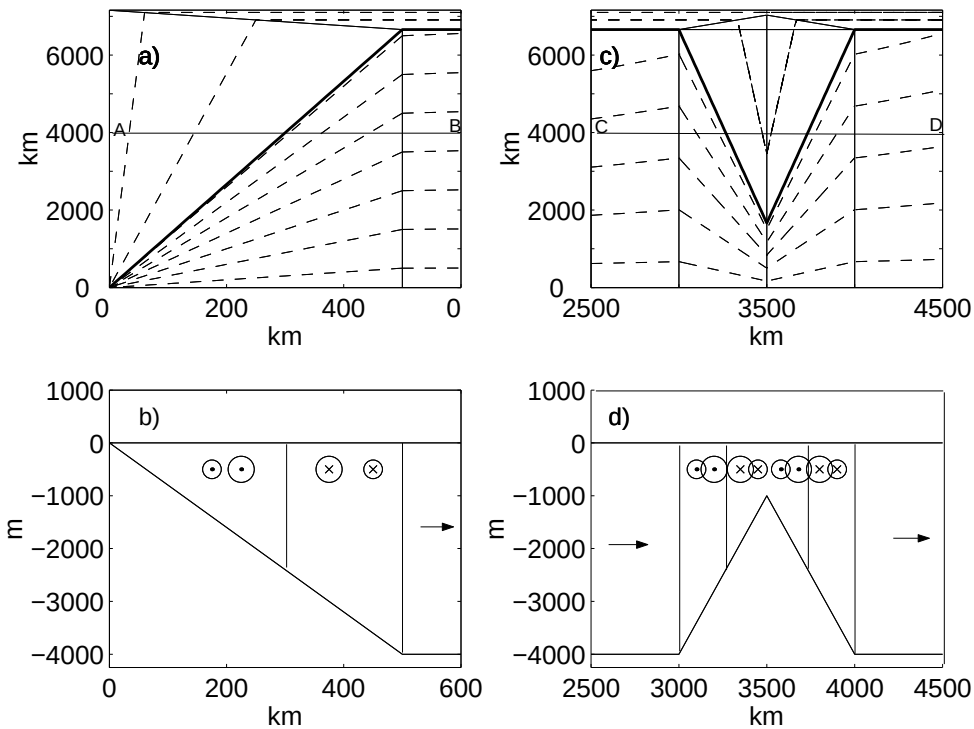

Figure 4: Close-ups and vertical cross-sections of the western boundary and the ridge area. a) The western boundary. b) Section along the line A-B in the western boundary. c) The mid-ocean ridge. d) Section along the line C-D across the ridge.

Fig. 4 shows cross-sections along the lines A-B in the western boundary and C-D across the ridge. The heavy solid line in Fig. 4 a), from $(0, 0)$ to $(500, 6660)$, is the region where all the interior fluid flows southward, coming in to the western boundary layer from the foot of the northern boundary slope. To the west of the heavy line, the transport is also southwards, bringing fluid from the sinking regions. To the east a northward flow supplies the interior with fluid. In the southward flowing region, the transport of fluid will increase eastwards, as shown by the size of the circles in Fig. 4 b), because the transport of sinking water on the northern boundary is proportional to the depth. Hence streamlines originating from a deeper depth contour in the northern boundary will transport more fluid than streamlines from a more shallow depth contour. As the meridional velocity in the interior increases with latitude (Eq. 6), the transport to the eastern side of the solid line decreases eastwards.

As a result of the high speeds on both sides of the intersection between flows in opposing directions, this will be a region of high shear where friction can be expected to be important.

In a similar manner regions of opposing flow at the mid-ocean ridge, as shown by the solid lines in Fig. 4 c) and Fig. 4 d) are regions of high shear. However, we are treating the inviscid limit and friction and diffusion are confined to infinitesimal regions compared to the ocean basin size, and it is assumed that these regions play a rather small part in the overall pattern of the circulation.

The flow pattern at the mid-ocean ridge resembles the picture of Defant's [2] stratospheric circulation in which he used the absolute topography of the 2000-decibar surface to compute the abyssal flow. The result is a Mid Atlantic southward flow, with a northward flow on its eastern side originating from about 5° north, producing a V-shaped mid-ocean flow pattern (corresponding to the dashed lines over the ridge in Fig. 3). Also numerical studies of abyssal flow over topography confirm the pattern seen in Fig. 3. Condie and Kawase [3] used a one and a half layer model to represent the abyssal flow over exponentially sloping side walls at all boundaries and a Gaussian shaped mid-ocean ridge. The eddy activity associated with the sinking region in the north-west corner of the basin in their study has an impact on the flow pattern in the boundary region. The general flow pattern is however confined to closed geostrophic contours, i.e the fluid follows lines of constant f/h and the same V-shaped structure of the flow is visible at the mid-ocean ridge.

3 The two-layer model

In section 2, a geometrical picture was obtained on how the influence of sloping topography will alter the boundary layer flow of a homogeneous fluid. Extending the theory to a baroclinic flow, we will study the simplest case, two layers of inviscid fluid with uniform densities ρ_1 and ρ_2. The flat bottom interior solution to a two-layered model of the abyssal flow on a spherical earth was studied by Veronis [4]. The outline of that paper is followed, but here with a β-plane approximation. The steady state of each layer in the interior is geostrophic, hydrostatic and described by the vertically integrated equations

$$fV_1 = gh\frac{\partial h_1}{\partial x} \tag{19}$$

$$fU_1 = -gh\frac{\partial h_1}{\partial y} \tag{20}$$

$$\frac{\partial U_1}{\partial x} + \frac{\partial V_1}{\partial y} = w_0 \tag{21}$$

$$fV_2 = gh_2\frac{\partial}{\partial x}\left(\frac{\rho_1}{\rho 2}h_1 + \frac{\Delta\rho}{\rho_2}\right) \tag{22}$$

$$fU_2 = -gh_2\frac{\partial}{\partial y}\left(\frac{\rho_1}{\rho 2}h_1 + \frac{\Delta\rho}{\rho_2}h_2\right) \tag{23}$$

$$\frac{\partial U_2}{\partial x} + \frac{\partial V_2}{\partial y} = -\frac{\rho_1}{\rho_2}w_0 \ . \tag{24}$$

Here U and V are the vertically integrated zonal and meridional velocities, h the thick-

ness of the upper layer and h_1 and h_2 the heights of the upper surface and interface respectively so that

$$h_1 = h + h_2 \ . \tag{25}$$

Cross-differentiating the momentum equations and making use of the continuity equations for each layer gives the relations

$$\beta V_1 = -f w_0 - g J(h, h_1) \tag{26}$$

$$\beta V_2 = \frac{\rho_1}{\rho_2} \left(f w_0 + g J(h, h_1) \right) \ . \tag{27}$$

From (26) and (27) we find that the total mass transport is equal and opposite at each point, i.e.,

$$\frac{\rho_1}{\rho_2} V_1 + V_2 = 0 \ . \tag{28}$$

Taking the sum of $\rho_1/\rho_2 \times$(19) and (22) we now have

$$\frac{\rho_1}{\rho_2} V_1 + V_2 = \frac{g}{2f} \frac{\partial}{\partial x} \left(\frac{\rho_1}{\rho_2} h_1^2 + \frac{\Delta\rho}{\rho_2} h_2^2 \right) = 0 \ . \tag{29}$$

From (29) we can obtain an expression for the variation of the upper layer height h_1 in the x-direction:

$$\frac{\rho_1}{\rho_2} h_1 \frac{\partial h_1}{\partial x} = -\frac{\Delta\rho}{\rho_2} h_2 \frac{\partial h_2}{\partial x} = -\frac{\Delta\rho}{\rho_2} (h_1 - h) \frac{\partial}{\partial x} (h_1 - h) \ . \tag{30}$$

Replacing h_1 with H, the mean basin depth, where h_1 appears as a coefficient and neglecting the term $\frac{\Delta\rho}{\rho_2} \frac{h}{H} \frac{\partial h_1}{\partial x}$ we have

$$\frac{\partial h_1}{\partial x} = \frac{\Delta\rho}{\rho_2} \left(1 - \frac{h}{H} \right) \frac{\partial h}{\partial x} \ . \tag{31}$$

Integrating (31) gives

$$h_1 = h_{1E} + \frac{\Delta\rho}{\rho_2} \left(h - \frac{h^2}{2H} - \left(h_E - \frac{h_E^2}{2H} \right) \right) \tag{32}$$

from which, with a constant h_{1E} and h_E at the eastern wall, we obtain

$$\frac{\partial h_1}{\partial y} = \frac{\Delta\rho}{\rho_2} \left(1 - \frac{h}{H} \right) \frac{\partial h}{\partial y} \ . \tag{33}$$

From (31) and (33) we see that $J(h, h_1) = 0$, so from (26) and (27) we can now obtain the vertically averaged meridional velocities in the upper and lower layer

$$V_1 = -\frac{fw_0}{\beta} \tag{34}$$

$$V_2 = \frac{\rho_1}{\rho_2}\frac{fw_0}{\beta} \ . \tag{35}$$

The zonal velocities can be derived using (34) and (35) in (21) and (24) respectively, which gives

$$U_1 = 2w_0(x - x_E) \tag{36}$$

$$U_2 = -\frac{\rho_1}{\rho_2}2w_0(x - x_E) \ . \tag{37}$$

Using (31) in (19) yields

$$fV_1 = g'\frac{\partial}{\partial x}\left(\frac{h^2}{2} - \frac{h^3}{3H}\right) \tag{38}$$

and using (34) for V_1, this can now be integrated from x to x_E and we can specify h by

$$\frac{h^2}{2} - \frac{h^3}{3H} = \frac{h_E^2}{2} - \frac{h_E^3}{3H} + \frac{f^2 w_0}{g'\beta}(x_E - x) \ . \tag{39}$$

As in the homogeneous case we can now get the trajectories of the flow from the zonal and meridional velocities.

Considering zonally integrated transport balances for the system, we have that the interior transport in the upper layer, T_1, across a zonal line y is given by integrating V_1 over the basin width. With T_1 taken positive northwards we get

$$T_1 = -w_0(x_E - x_W)y \ . \tag{40}$$

The upper layer gains water from the total upwelling, W, taking place north of y. This is given by integrating w_0 over the width and length of the basin

$$W = w_0(x_E - x_W)(y_N - y) \ . \tag{41}$$

As the sinking takes place in the northeastern corner, there is a net loss of upper layer fluid of amount S to the lower layer and

$$S = -w_0(x_E - x_W)y_N \ . \tag{42}$$

To obtain a mass balance for the basin, the transport T_W carried in the western boundary current is

$$T_W = S - W - T_1 = 2w_0(x_E - x_W)y \ . \tag{43}$$

From (43) it can be seen that across each zonal line, the western boundary current must carry twice the interior transport.

Having obtained a solution for the flat bottom interior, we will now seek a solution for a two-layer system with bottom topography. Salmon [5] considered the planetary geostrophic equations for a two-layer system over a sloping western boundary. In his notation the governing equations for a frictionless steady state read

$$\mathbf{f} \times \mathbf{u_1} = -\nabla \phi_s \tag{44}$$

$$\mathbf{f} \times \mathbf{u_2} = -\nabla \phi_s + g' \nabla h \tag{45}$$

$$\nabla \cdot (\mathbf{u_i} h_i) = 0, \quad i = 1, 2 \tag{46}$$

where $\mathbf{u_i} \equiv (u_i, v_i)$ are the horizontal velocities and ϕ_s is the pressure at the surface divided by a reference density.

Adding (46) for $i = 1$ and $i = 2$ yields

$$\nabla \cdot (h_1 \mathbf{u_1} + h_2 \mathbf{u_2}) = 0 \tag{47}$$

and thus

$$h_1 \mathbf{u_1} + h_2 \mathbf{u_2} = \mathbf{k} \times \nabla \Psi \tag{48}$$

where $\mathbf{k}$ is the vertical unit vector and Ψ the total transport streamfunction.

Eq. (44) and (45) gives

$$\mathbf{f} \times (\mathbf{u_1} - \mathbf{u_2}) = -g' \nabla h \ . \tag{49}$$

From (48) and (49)

$$\mathbf{u_1} = \frac{1}{H} \mathbf{k} \times \nabla \Psi + \frac{g' h_2}{f H} \mathbf{k} \times \nabla h \tag{50}$$

$$\mathbf{u_2} = \frac{1}{H} \mathbf{k} \times \nabla \Psi - \frac{g' h_1}{f H} \mathbf{k} \times \nabla h \tag{51}$$

and using (50) and (51) and taking the curl of the vertical average of (44) and (45) we can write the total streamfunction equation as

$$J\left(\frac{f}{H}, \Psi\right) + J\left(\frac{1}{2} g' h^2, \frac{1}{H}\right) = 0 \ . \tag{52}$$

From (46) and (50) we get an equation for the upper layer thickness

$$J\left(\Psi, \frac{h}{H}\right) + J\left(g' h, \frac{h}{f}\left(1 - \frac{h}{H}\right)\right) = 0 \ . \tag{53}$$

By defining

$$q_1 \equiv \frac{h}{f}, \quad q_2 \equiv \frac{H - h}{f} \tag{54}$$

it can be shown that (52) and (53) can be written in the forms

$$J(\Psi, q_1) + q_2 J(g'h, q_1) = 0 \tag{55}$$
$$J(\Psi, q_2) - q_1 J(g'h, q_2) = 0 \tag{56}$$

which describes the PV in the upper and lower layers.

Salmon [5] obtained general solutions to (55) and (56) for the two cases $J(q_1, q_2) \neq 0$ and $J(q_1, q_2) = 0$. In the latter case he showed that a solution is possible only if either q_1 or q_2 is constant in a particular region. That would appear to be simply a mathematical curiosity but he showed, in fact, that one can obtain realistic features in the vicinity of the Gulf Stream by making use of $q_1 = constant$ and $q_2 = constant$ in different regions near the Gulf Stream.

We have sought a solution with $q_1 = constant$ in the slope regions. In order for that to be a valid solution it is necessary that it match to the interior solution at the foot of the slope in the different regions. The latter comes from (39). In the special case with $h_E = 0$, we can obtain a solution with constant q_1 if we take the lowest order solution to (39) by neglecting the term with H in the denominator (neglecting that term involves a maximum error of about 5 % but a correction for that term can be taken into account iteratively). The resulting solution is

$$h^2 = \frac{2f^2}{g'}\frac{w_0}{\beta}(x_E - x) \ . \tag{57}$$

Evaluating (57) at the western edge of the interior, i.e. $x = x_W \approx 0$, we have

$$\frac{h}{f} = \left(\frac{2w_0}{g'\beta}x_E\right)^{\frac{1}{2}} \ . \tag{58}$$

So $h/f = constant$ is an exact solution over the western boundary slope and it also matches the interior at the eastern edge of the boundary. Therefore, h is constant on lines of constant y in the boundary layer and is given by the thickness of the interior upper layer at $x = x_W$.

From the planetary geostrophic equation for the lower layer, (45), we also have

$$\frac{f}{h_2}(\mathbf{u_2}h_2) = \mathbf{k} \times \left(\nabla\phi_s - g'\nabla h\right) \ . \tag{59}$$

As we neglect the upwelling in the boundary layer, we have $\nabla \cdot (\mathbf{u_2}h_2) = 0$ so the divergence of (59) yields

$$\mathbf{u_2}h_2 \cdot \nabla\frac{f}{h_2} = 0 \tag{60}$$

and with $\mathbf{u_2}h_2 = \mathbf{k} \times \nabla\psi_2$ we have

$$J\left(\psi_2, \frac{f}{h_2}\right) = 0 \ . \tag{61}$$

With h constant on lines of constant y, h_2 can be determined from $h_2 = H - h$ and with ψ_2 constant on lines of constant $\frac{h_2}{f}$ in the boundary layer, we can match the upper and lower

layer solutions to the interior solutions at the foot of the slope. With the same reasoning for the mid-ocean ridge area we get the lower layer flow pattern shown in Fig. 5. The dashed lines are the trajectories of the flow and the solid lines in the interior are contours of the lower layer height h_2. The upper layer thickness is set to zero at the eastern boundary and the mean basin depth is 4000 m. The upwelling velocity is specified to $2 \cdot 10^{-7}$ m/s and $\Delta\rho/\rho_2 = 0.0015$.

Given that $\frac{h}{f} = constant$ over the mid-ocean ridge, when crossing the ridge, the lower layer flow follows lines of constant $\frac{h_2}{f}$. The path is again symmetric about the center of the ridge.

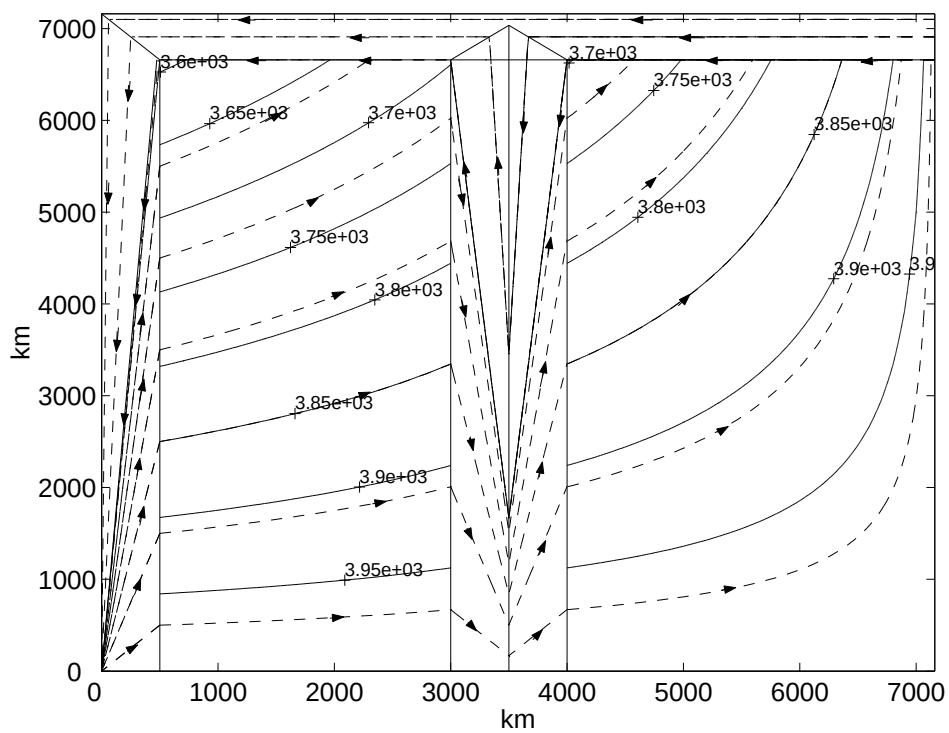

Figure 5: Flow pattern of the lower layer. The calculations were made for $w_0 = 2 \cdot 10^{-7}$ m/s, $h_E = 0$ m and $\Delta\rho/\rho_2 = 0.0015$

The westward jet along the foot of the northern slope turns southward at the northwest corner of the interior and continues as a jet toward the southwest corner. To the west of that jet, water that has sunk in the north will move southwards on lines of constant $\frac{h_2}{f}$ set by the lower layer depth on the northern boundary. On the eastern side of the $\frac{h_2}{f}$ line carrying the interior water southward, fluid flows northward along lines of constant $\frac{h_2}{f}$ to the interior. The vicinity of the region separating southward and northward flow must represent a region of intense shear. Therefore, friction is likely to be important here.

The upper layer flow pattern is shown in Fig. 6. In the interior the trajectories are the same as for the lower layer but in the opposite direction so the fluid moves in a south-

westward direction. Contours of upper layer thickness are parallel to the paths of the trajectories. Over the western boundary slope and over the mid-ocean ridge, the upper layer flow is zonal on lines of constant $\frac{h}{f}$.

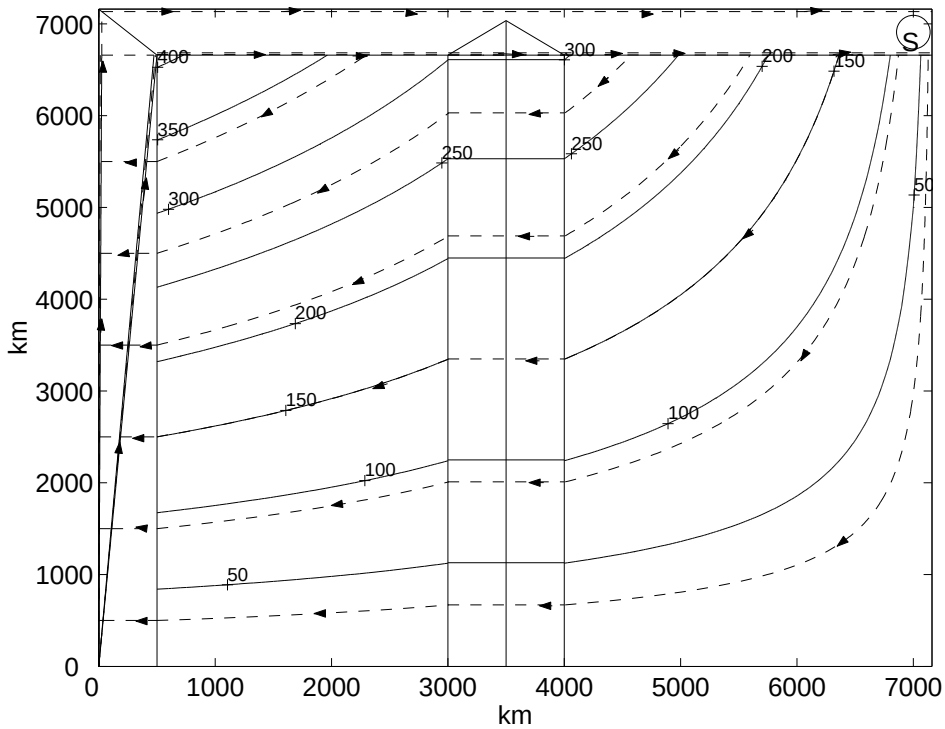

Figure 6: Flow pattern of the upper layer

Just south of the southern edge of the northern boundary, the upper layer western boundary transport is, due to conservation of mass

$$T_W = S + T_I \ . \tag{62}$$

Just north of that edge, the interior transport is zero, which gives

$$T_W = S \ . \tag{63}$$

Hence, there must be a jet that heads eastward along the foot of the slope from the northwestern corner of the interior. Just as the lower layer takes fluid from the westward jet along the foot of the north slope and transports it southward along the line of constant $\frac{h_2}{f}$ that goes from the northwestern corner of the interior to the southwestern corner on the western slope, the upper layer must deliver an equal amount of fluid northeastward to supply the eastward flow along the southern edge of the northern slope. So there will be a jet in the western boundary upper layer flow, also along this line of constant $\frac{h_2}{f}$. In that jet, to induce the northward transport in the upper layer, the sea surface will rise sharply toward the east. We must also have a compensating drop of the interface. The displacement

of the interface across the western boundary jet can be obtained from the equations for the upper and lower layer

$$\rho_1 f V_1 = \rho_1 g h \frac{\partial \eta_1}{\partial x} \tag{64}$$

$$\rho_2 f V_2 = g h_2 \frac{\partial}{\partial x} \left(\rho_1 \eta_1 + \Delta\rho \eta_2 \right) \tag{65}$$

where subscript 1 and 2 denotes the upper and lower layer respectively. As the transports in the upper and lower layer are equal and opposite, Eq.(28) is valid also in the jet, i.e. the total transport vanishes at each point in the jet. From (64) and (65) we then get

$$\frac{\partial \eta_2}{\partial x} = -\frac{\rho_1 H}{\Delta\rho h_2} \frac{\partial \eta_1}{\partial x} \ . \tag{66}$$

As $h = \eta_1 + \hbar - \eta_2$, where $\hbar$ is the mean upper layer depth, we have that

$$\frac{\partial \eta_2}{\partial x} = \frac{\partial \eta_1}{\partial x} - \frac{\partial h}{\partial x} \ . \tag{67}$$

Applying (67) to (66) we find that

$$\frac{\partial \eta_1}{\partial x} \approx \frac{\Delta\rho h_2}{\rho_1 H} \frac{\partial h}{\partial x} \tag{68}$$

and (64) becomes

$$f V_1 = \frac{g \Delta\rho h_2}{2\rho_1 H} \frac{\partial h^2}{\partial x} \ . \tag{69}$$

Since the assumption is of an infinitesimally thin jet, we can consider h_2/H to be constant. Eq. (69) can then be integrated in the x-direction and becomes

$$f T_1 = \frac{g \Delta\rho h_2}{2\rho_1 H} \left(h_R^2 - h_L^2 \right) \tag{70}$$

where subscript R and L denotes the right and left edge of the jet respectively.

As the upper layer thickness on the right edge of the jet is equal to the upper layer depth at the western boundary of the interior, we obtain the equation for the upper layer thickness at the western side of the jet

$$h_L^2 = h_W^2 - \frac{2 f T_1}{g} \frac{\rho_1}{\Delta\rho} \frac{H}{h_2} \ . \tag{71}$$

On the western side of the jet, the upper layer thickness is again constant and the transport is again purely zonal. Close to the western edge of the boundary layer, there will be a triangular wedge of only upper layer water, also with northward transport as the streamfunction must go to zero at the western edge of the boundary layer. So of the northward transport of upper layer water, the portion contributed by the jet feeds the northern boundary layer that supplies water to the interior and the portion contributed by the boundary current near the western edge of the basin supplies an equal amount of water to the sink.

A schematic of cross-sections of the western boundary, the ridge area and the northern boundary is shown in Fig. 7.

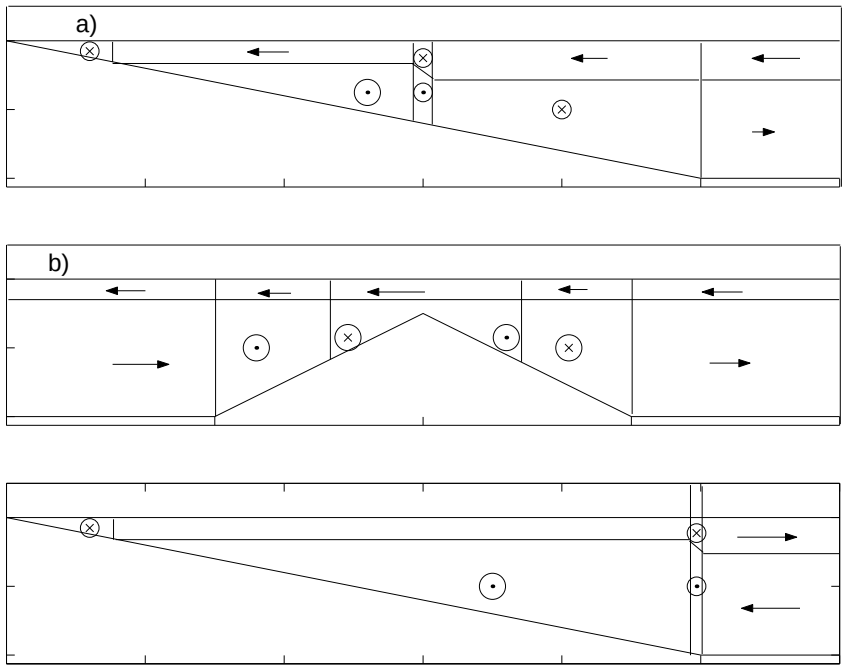

Figure 7: Schematic of zonal cross-sections of a) western boundary b) mid-ocean ridge area and c) meridional cross-section (looking eastward) of the northern boundary

In Fig. 7 a), the westward transport in the constant upper layer carries water to the northward jet. The upper layer thickness decreases across the jet and on the other side of the jet the upper layer thickness is again constant and carries water westward to the northward boundary current. In the lower layer, the region closest to the western edge of the boundary layer carries the sinking water southwards from the northern boundary. The southward moving jet in the lower layer carries water from the interior. On the eastern side of the jet, a northward flow supplies the interior with fluid.

Over the mid-ocean ridge (Fig. 7 b)) the upper layer thickness is constant and the flow purely westwards. In the lower layer, the inner region of the ridge is where the sinking water flows southward and then northward to cross the ridge. In the two outer regions of the ridge, fluid from the interior crosses the ridge. Along the lines joining the two regions the shear is intense and friction must be important.

On the northern slope (Fig. 7 c) the upper layer jet at the southern edge of the boundary supplies fluid to the interior while the current at the northern edge of the boundary layer provides water to the sink. The transport of water to the sinking regions must spread out across the upper layer, but the details of this flow have not been further considered. In the lower layer jet, water from the interior is carried westward and north of the jet the water that has sunk is carried to the western boundary layer.

4 Discussion

It has been shown that the presence of sloping boundaries considerably affects the flow pattern. In the presence of a mid-ocean ridge, dividing the ocean in two halves, the flow is diverted considerably to the south in order to continue to the other basin.

In the homogeneous case the flow will follow lines of constant f/h in order to conserve potential energy. The same holds when the fluid crosses the mid-ocean ridge and has to turn southward in order to decrease the depth of the water column.

In the two-layer model we have shown a simple solution consistent with an exact solution to the general equations (55) and (56) for the case when $J(q_1, q_2) = 0$. The solution keeps the upper layer thickness constant on lines of constant y in the western boundary layer and the ridge area. In the lower layer the transport streamfunction follows lines of constant $\frac{h_2}{f}$. The solution requires a northward jet in the upper layer of the western boundary layer and the jet will continue eastward along the foot of the north slope. Although friction must be clearly be important in parts of the slopes, we have confined the analysis to the inviscid limit using transport balance arguments. This led to the conclusion that half of the total northward transport in the western boundary layer will take place in the jet and half of the transport will occur in a triangular wedge occupied by only upper layer water along the western edge of the western slope. As the streamfunction must be zero at the western edge, the transport will have to turn northwards and the dynamics will be that of a single layer fluid. The exact dynamics of the northern boundary have not been analyzed, but the flow will more or less follow lines of constant H (total depth) in this region as $y \sim constant$ and $H - h \sim H$ except close to the northern edge where we again have dynamics of a single layer as the total depth goes to zero. Upper layer water sinks in the northeastern corner and flows westward in the lower layer of the northern boundary region and then southward along lines of constant f/h_2 to the southwest corner of the western boundary slope. The exact path can not be determined here, due to the absence of a complete picture of the northern boundary upper layer thickness.

The reasoning holds for slope regions that are very narrow compared to the basin size. The analytical solution was pieced together, treating the slope regions in the inviscid limits. As it turned out, friction must be important in isolated regions over the slopes. It allows the fluid to cross lines of constant PV where needed and it will also be required to smooth out the abrupt change in direction of flow over the slopes. A numerical model of this system should help to determine how much of this study is consistent with the full equations including friction. A next step analytically would be to try to include wind stress in addition to the upwelling.

5 Acknowledgments

I wish to express my sincere thanks to George Veronis, for the uncountable hours of discussion, his friendship and for the nice walks. The fellows provided many laughs and kept me sane during the last weeks of hectic work. Everyone that passed through Woods Hole and Walsh Cottage made the summer of 2001 a very memorable one.

References

[1] H. M. Stommel, "The abyssal circulation," Deep-Sea Res. **5**, 80 (1958).

[2] A. Defant, *Die absolute topographie des phys. meeresniveaus und der druckflächen, so wie die wasswer bewegungen im Atl. Ocean* (Meteor Werk. 6/2, 5, Lief. Berlin, 1941).

[3] S. A. Condie and M. Kawase, "Models of abyssal flow in basins separated by a mic-ocen ridge," J. Mar. Res. **50**, 199 (1992).

[4] G. Veronis, "Model of world ocean circulation: II. Thermally driven, two-layer," J. Mar. Res. **34**, 421 (1976).

[5] R. Salmon, "A two-layer Gulf Stream over a continental slope," J. Mar. Res. **50**, 341 (1992).

Convective oscillations in a laboratory model

Lianke te Raa

Abstract

A laboratory experiment has been conducted in which a small basin was heated from below. This basin was connected to a large reservoir that was filled with a layer of salt water at the bottom and fresh water above it, by tubes at the top, the middle and the bottom. It was shown that different flow regimes exist in this experiment. For low forcing temperatures, self-sustained oscillations occur, whereas the system reaches a steady state with deep convection for higher forcing temperatures. During an oscillation a shallow convecting layer of salty water at the bottom of the basin grows and entrains fresh water, until the water column becomes unstable and deep convection can occur. Inflow of salty water through the bottom tube stops the deep convection and the cycle starts again. In a configuration in which the top and middle tubes had smaller diameters, no oscillations were found. Instead, a regime with steady shallow convection states and a regime with steady deep convection states were found.

1 Introduction

An important part of the ocean's thermohaline circulation is the formation of deep water at high latitudes. Locations of deep convection are confined to certain specific areas in the North Atlantic Ocean and near Antarctica, including the Greenland-Norwegian Sea, the Labrador Sea, the Weddell Sea and the Ross Sea [1]. There are two types of deep convection in the ocean. One is convection near an ocean boundary, where dense water reaches the bottom of the ocean by descending a continental slope. The second process is called open-ocean convection and involves sinking of water in narrow area's far away from land. In both cases deep convection is a very complicated process, but general features of the polar oceans that are important are the intense surface cooling and the very fresh surface water [2]. In order to get deep convection an increase in salinity of the surface water is therefore needed, for instance due to brine rejection or mixing with a saltier water mass [3]. Due to these and other conditions, the areas in which deep-water formation occurs are not only small compared to the total area of the ocean, but the deep convection required for producing dense bottom water does also not occur every winter.

A good way to gain more understanding of complex processes as deep convection is the use of simple models. Recently, Whitehead [4] analyzed a simplified box model consisting of a small basin that is cooled from above and that is connected via three tubes to a large isothermal basin with a fresh surface layer. This is a very schematic model of the situation in the Arctic Ocean. For small cooling rates this model was shown to exhibit a steady state with shallow convection, whereas for strong cooling a state with deep convection occurred.

In the shallow state fresh and warm water enters the small basin via the upper tube, is cooled and convects downward and leaves through the middle tube. Or, if the cooling is stronger, water comes in through the upper tube and leaves via both the middle and the bottom tube. In the deep convection state the warm and fresh water enters the small basin through the upper tube, but there is also inflow of warm and salty water through the middle tube, whereas cold water leaves the small basin through the bottom tube.

If the cooling rate depends on temperature via a relaxation condition, this model was shown to exhibit multiple equilibria: both the shallow and the deep convection state could exist for the same forcing temperature [4]. In this case, sudden rapid transitions between both states can occur for only very slight changes in forcing temperature. Although obviously these results cannot be simply extended to the real ocean, these model results might still have important implications for the ocean. Periods of deep water formation might be followed by periods of shallow convection in which only intermediate water is formed if forcing conditions change slightly.

The original goal for this summer project was to investigate if the multiple equilibria predicted by the theoretical box model can also be found in the laboratory. However, the project evolved in a different direction, so that finally it turned out to be an exploration of the behavior of the flow in the laboratory version of this convective model. The laboratory model was turned upside-down with respect to the case of the Arctic Ocean (heating at the bottom and a layer of salty water at the bottom of the large basin) for practical reasons.

The theoretical model of Whitehead [4] is presented in section 2 of this report. This section closely follows his derivation, but describes the situation for the case with heating at the bottom instead of cooling at the top. The experimental apparatus and method are described in section 3.1 and the results follow in section 3.2 and 3.3. In section 4 the experimental results are compared to the box model theory and a discussion and the conclusions are given in section 5.

2 Theory

A small basin with two layers of water in a field of gravity is heated from below. This small basin is connected to a large basin, which is called the reservoir, with three tubes, one at the surface, one at mid-depth ($D/2$) and one at a depth D (Fig. 1). The reservoir contains a layer of salty water of salinity S_0 of constant thickness d with fresh water above it. Both layers have temperature T_0 (room temperature). The reservoir is taken to be so large and so well mixed that d, T_0 and S_0 remain fixed, irrespective of the flow into and out of the tubes.

In the small basin a convecting layer of thickness δ of water with temperature $T_0 + T$ and salinity S will develop, where δ, T and S still have to be determined. This layer is assumed to be well mixed, as it is heated from below, and its thickness will grow with increasing heating rate. Heat losses are neglected and it is assumed that there is no mixing of heat and salt across the interface between the warm and salty, convecting layer and the non-convecting layer of cold and fresh water above it.

The flow through the tubes is determined by the pressure difference between the two ends of the tubes and depends therefore on temperature and salinity in both the small basin and the reservoir. We assume that there is a steady-state relation between the flow through

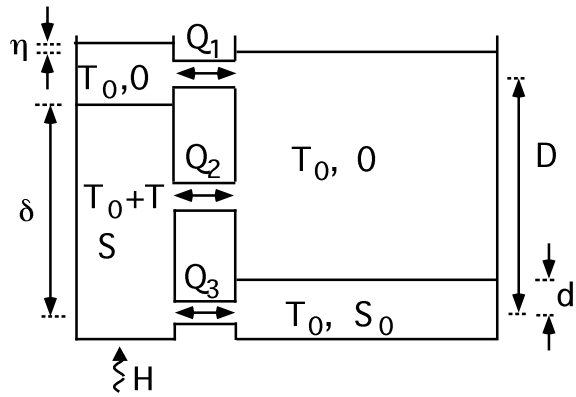

Figure 1: Sketch of the model configuration. The reservoir contains a layer of fresh water with temperature T_0 and zero salinity overlying a layer of salty water with the same temperature and salinity S_0. The temperatures and salinities in this basin remain constant. The temperature T and salinity S in the convecting layer in the small basin are determined by the flow rates Q_1, Q_2 and Q_3 and the heating rate H.

a tube and the pressure difference between the small basin and the reservoir at the height of that tube. The volume flux through tube i is denoted by Q_i, where $i = 1, 2, 3$ denotes top, middle and bottom tube, respectively and can then be expressed as

$$Q_i = C_i(p_{i,res} - p_i) \tag{1}$$

where p_i is the pressure in the small basin at the height of tube i, $p_{i,res}$ is the pressure in the reservoir at that height and C_i is the hydraulic resistance of tube i. Note that flow into the small basin is defined positive. The pressures in the small basin and the reservoir are assumed to be hydrostatic, and furthermore a linear equation of state is used

$$\rho = \rho_0(1 - \alpha(T - T_0) + \beta S) \tag{2}$$

where ρ_0 is the density of fresh water at room temperature. The pressures in the reservoir are then given by

$$p_{1,res} = 0 \tag{3a}$$
$$p_{2,res} = \rho_0 g D/2 \tag{3b}$$
$$p_{3,res} = \rho_0 g(D - d) + \rho_0 g(1 + \beta S_0)d \tag{3c}$$

Using the Boussinesq approximation by assuming that βS, βS_0 and $|\alpha T| \ll 1$ everywhere, the pressures p_1, p_2 and p_3 in the small basin are

$$p_1 = \rho_0 g\eta \tag{4a}$$
$$p_2 = \rho_0 g\eta + \rho_0 g D/2 + \rho_0 g(\delta - D/2)(\beta S - \alpha T) \tag{4b}$$
$$p_3 = \rho_0 g\eta + \rho_0 g D + \rho_0 g\delta(\beta S + \alpha T) \tag{4c}$$

where η is the surface elevation in the small basin with respect to the water surface in the reservoir and δ is the distance of the layer of convecting fluid in the small basin above the second tube. The volume fluxes are then given by

$$Q_1 = -C\rho_0 g \quad \eta \tag{5a}$$
$$Q_2 = C\rho_0 g \quad [-\eta + (\delta - D/2)(\alpha T - \beta S)] \tag{5b}$$
$$Q_3 = \gamma C\rho_0 g \quad [-\eta + \beta S_0 d + \delta(\alpha T - \beta S)] \tag{5c}$$

Following Whitehead [4], we assume that the hydraulic resistance of the upper two tubes is equal to C and that the resistance of the bottom tube is $C_3 = \gamma C$, with γ a positive number.

If the heating is so weak that the interface between the convecting and the non-convecting layer in the small basin is below the middle tube, steady state solutions are not possible, because mass cannot be conserved. For larger heating rates the interface will be between the middle and the upper tube, so that $\delta < D$. In this case steady state solutions can occur, but only if there is no flow through the upper tube, again because otherwise mass would not be conserved, so we have $Q_1 = 0$ and $\eta = 0$. The equation for steady state mass conservation reduces in this case to $Q_2 + Q_3 = 0$. Together with equation (5) this gives that the depth of the convecting layer is

$$\delta = \frac{1}{1+\gamma}\left[\frac{D}{2} - \frac{\gamma\beta S_0 d}{\alpha T - \beta S}\right] \tag{6}$$

yielding for the volume fluxes

$$Q_1 = 0 \tag{7a}$$
$$Q_2 = \frac{\gamma C\rho_0 g[(\beta S - \alpha T)D - 2\beta S_0 d]}{2\gamma + 2} \tag{7b}$$
$$Q_3 = -\frac{\gamma C\rho_0 g[(\beta S - \alpha T)D - 2\beta S_0 d]}{2\gamma + 2} \tag{7c}$$

It can easily be shown that the case in which $Q_2 > 0$ and $Q_3 < 0$ is inconsistent, so we have to have inflow through the bottom tube and outflow through the middle tube ($Q_2 < 0$ and $Q_3 > 0$) as long as the interface in the small basin is between the top and middle tube. In this case the steady state heat budget is

$$0 = H + \rho_0 C_p Q_2 (T + T_0) + \rho_0 C_p Q_3 T_0 \tag{8}$$

where H is the heat flux into the small basin due to the heating at the bottom and C_p is the specific heat capacity. The steady state salt budget is

$$0 = Q_2 S + Q_3 S_0 \tag{9}$$

Using mass conservation, the steady state heat and salt budgets can be rewritten as

$$H = \rho_0 C_p Q_3 T; \quad S = S_0 \tag{10}$$

As we are considering the case for which $Q_2 < 0$, this gives that the temperature in the small basin has to be higher than a certain critical value T_{nil} in order to have steady state solutions, with

$$T_{nil} = \frac{\beta S_0}{\alpha}\left(1 - \frac{2d}{D}\right) \tag{11}$$

If the heating rate H is increased, the temperature and the height of the convecting layer will also increase. For a certain heating rate, the interface between the convecting and the non-convecting water will reach the upper tube. The critical temperature T_c at which this happens follows from $\delta = D$ and is given by

$$T_c = \frac{\beta S_0}{\alpha}\left(1 - \frac{2\gamma d}{(1+2\gamma)D}\right) \tag{12}$$

For $T > T_c$ there is also flow in the upper layer and the equation for mass conservation becomes

$$Q_1 + Q_2 + Q_3 = 0 \tag{13}$$

The interface stays at height D for temperatures greater than T_c as we have used the Boussinesq approximation. The height of the interface follows therefore from equations (5) and (13) with $\delta = D$ as

$$\eta = \frac{2\gamma\beta S_0 d + (\alpha T - \beta S)D(2\gamma+1)}{2(2+\gamma)} \tag{14}$$

so that the volume fluxes become

$$Q_1 = \frac{C\rho_0 g}{2+\gamma}\left[-\frac{1+2\gamma}{2}(\alpha T - \beta S)D - \gamma\beta S_0 d\right] \tag{15a}$$

$$Q_2 = \frac{C\rho_0 g}{2+\gamma}\left[-\frac{\gamma-1}{2}(\alpha T - \beta S)D - \gamma\beta S_0 d\right] \tag{15b}$$

$$Q_3 = \frac{\gamma C\rho_0 g}{2+\gamma}\left[\frac{3}{2}(\alpha T - \beta S)D + 2\beta S_0 d\right] \tag{15c}$$

which is consistent with equation (5) for $T = T_c$ and $\delta = D$.

At the critical temperature T_c we have $S = S_0$ and thus $Q_1 = 0$, $Q_2 < 0$ and $Q_3 > 0$. The positive surface elevation in the small basin causes the pressure at the height of the upper tube in the small basin to be higher than that in the reservoir, giving flow out of the small basin. From equations (12) and (14) we can see that if $T > T_c$ we will always have $\eta > 0$, which says that in order to have flow in the upper tube, the surface elevation has to be positive. So the flow in the upper tube will either be zero if the interface is below the upper tube or positive if the interface is at the top of the small basin. At mid-depth, the effect of salinity on the density dominates over the effect of temperature, so that at mid-depth there is a higher pressure in the small basin than in the reservoir. At the bottom however, the pressure in the reservoir is higher than that in the small basin, because the water in the reservoir is much colder than that in the small basin.

From equation (15) we see that for $T > T_c$ Q_1 becomes negative starting from zero and Q_3, which is already positive, becomes more positive, also if $S \neq S_0$ (note that S can never

become greater than S_0). For $\gamma \geq 1$ Q_2, which is negative already, becomes more negative, so that no fresh water can enter the small basin and the small basin stays always filled with water of salinity S_0. If $\gamma < 1$ however, Q_2, which is negative, becomes less so and eventually will become zero. So if the resistance of the bottom tube is higher than those of the middle and upper tubes, there is a value of the heating rate for which the flow in the second tube reverses sign, so that fresh water can enter the small basin. Note though that there will always be inflow through the bottom tube and outflow through the top tube.

The point for which $Q_2 = 0$ defines a second critical temperature

$$T_{cc} = -\frac{\beta S_0}{\alpha}\left[\frac{2\gamma d}{(\gamma-1)D} - 1\right] \tag{16}$$

At this temperature the water is heated so much, that the effect of the temperature dominates over the effect of salinity and the pressure due to the surface elevation. The pressure in the small basin at mid-depth is now lower than the pressure in the reservoir at that height and there will be inflow of cold and fresh water into the small basin. For $T_c < T < T_{cc}$ the heat and salt balances are still given by equation (10). For $T > T_{cc}$ the steady state heat and salt balances are

$$0 = H + \rho_0 C_p Q_1 T \tag{17a}$$

$$0 = Q_1 S + Q_3 S_0 \tag{17b}$$

As the solutions of equations (15) and (17) are complicated polynomials, we calculate them numerically, using time-dependent heat and salt balances. The equations are made dimensionless using

$$\tilde{Q} = \frac{Q}{Q_s}, \quad Q_s = \frac{\gamma C \rho_0 g \beta S_0 D}{2+\gamma}, \quad \tilde{T} = \frac{\alpha T}{\beta S_0}, \quad \tilde{d} = \frac{d}{D}, \quad \tilde{S} = \frac{S}{S_0} \tag{18a}$$

$$\tilde{t} = \frac{t}{AD/Q_s}, \quad \tilde{H} = \frac{H}{\rho_0 c_p T_s Q_s}, \quad T_s = \frac{\beta S_0}{\alpha} \tag{18b}$$

where Q_s is the volume flux scale, t is time and A is the horizontal area of the small basin. The dimensionless form of equation (7) is

$$\tilde{Q}_2 = -\tilde{Q}_3 = \frac{2+\gamma}{2+2\gamma}\left(1 - \tilde{T} - 2\tilde{d}\right) \tag{19}$$

and equation (15) transforms to

$$\tilde{Q}_1 = -\tfrac{2+1/\gamma}{2}(\tilde{T} - \tilde{S}) - \tilde{d} \tag{20a}$$

$$\tilde{Q}_2 = -\tfrac{1-1/\gamma}{2}(\tilde{T} - \tilde{S}) - \tilde{d} \tag{20b}$$

$$\tilde{Q}_3 = \tfrac{3}{2}(\tilde{T} - \tilde{S}) + 2\tilde{d} \tag{20c}$$

The dimensionless time-dependent heat and salt balances are

$$\frac{d\tilde{T}}{dt} = \tilde{H} + \tilde{T}[\tilde{Q}_1\Gamma(-\tilde{Q}_1) + \tilde{Q}_2\Gamma(-\tilde{Q}_2) + \tilde{Q}_3\Gamma(-\tilde{Q}_3)] \tag{21}$$

$$\frac{d\tilde{S}}{dt} = \tilde{Q}_1\tilde{S}\Gamma(-\tilde{Q}_1) + \tilde{Q}_2\tilde{S}\Gamma(-\tilde{Q}_2) + \tilde{Q}_3[\tilde{S}\Gamma(-\tilde{Q}_3) + \Gamma(\tilde{Q}_3)] \tag{22}$$

Numerical solutions were calculated for a wide range of heating rates by integrating equations (21) and (22), using (19) and (20), until a steady state was reached. If the heating rate depends on the temperature in the small basin via

$$\tilde{H} = K(\tilde{T}^* - \tilde{T}) \tag{23}$$

with K a constant, then Whitehead [4] shows that in the equivalent system for the Arctic-Ocean case multiple equilibria can be found: both shallow and deep convection states can exist for the same forcing temperature. The range of forcing temperatures $\tilde{T}^*$ for which multiple equilibria occur, depends on the parameters $\tilde{d}$, γ and K. A typical plot of temperature and salinity in the small basin as a function of forcing temperature for our case (heating from below) is shown in Fig. 2. The shallow convection states have a relatively

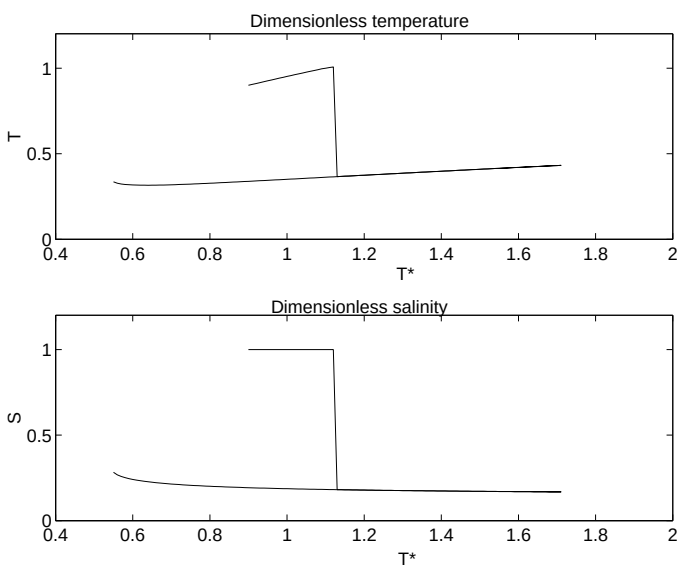

Figure 2: Dimensionless temperature and salinity as a function of (dimensionless) forcing temperature $\tilde{T}^*$ for the case with $\gamma = 0.05$, $d = 0.05$ and $K = 1$.

high temperature, and a dimensionless salinity $\tilde{S} = 1$, as only the salty water can enter the small basin. If T^* is increased above $\tilde{T}_{cc}$, deep convection states occur, with inflow of fresh and relatively cold water through the middle tube. In the deep convection states the temperature and the salinity are therefore much lower. If the forcing temperature is then decreased slowly, the system will remain in the deep convection state.

3 Experiments

3.1 Apparatus and method

The laboratory model consisted of a box of $20 \times 20 \times 20$ cm (the reservoir) that was connected via three tubes to a cylindrical small basin of 20 cm high with a diameter of about 5 cm (Fig.

3). The vertical distance between the centers of the top and bottom tubes was $D = 18\ cm$. The top, middle and bottom tubes had lengths of 99 mm, 98 mm and 9 mm, respectively.

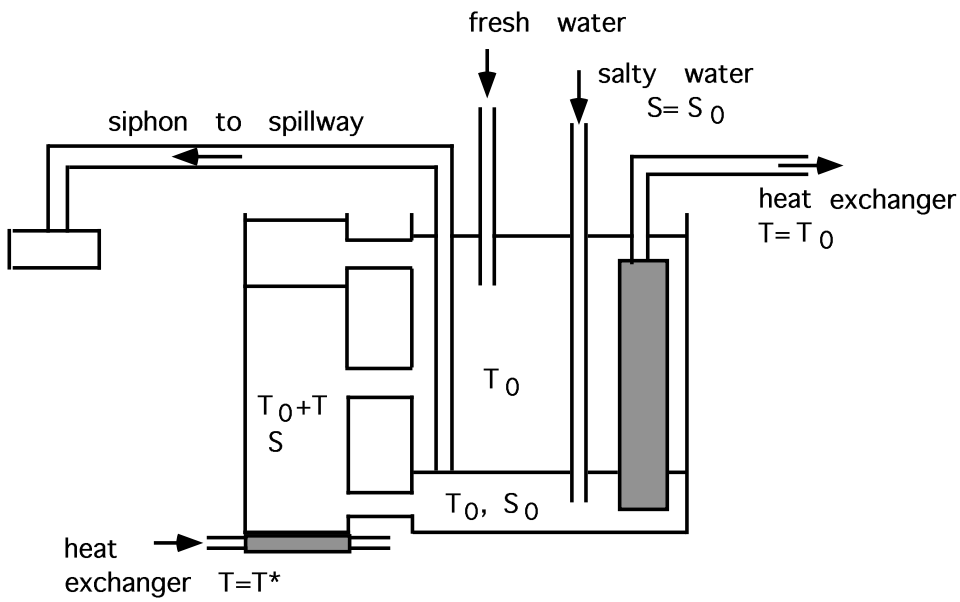

Figure 3: Sketch of the laboratory model (vertical section). The small basin is heated from below by a heat exchanger. Both fresh and salty water are pumped in at the top and bottom, respectively, and removed by a siphon at a fixed depth, thus maintaining a sharp interface between the salty and the fresh layer. A second heat exchanger keeps both layers in the reservoir at room temperature.

Fresh water at room temperature (about $21 \pm 2°C$) was pumped into the top of the reservoir at a rate of about 0.1 l/min, and salt water of the same temperature was pumped into the bottom of the reservoir at the same rate. The sum of these two fluxes was removed by a siphon that was placed at a certain distance above the center of the bottom tube. This maintained a sharp interface between the fresh and the salty water, at a level determined by the height of the siphon. The salty water was made by mixing fresh and salt water and adjusting this mixture to obtain a density of 1003.4 kgm^{-3} at room temperature, so that the density difference between the two layers in the reservoir was 5.2 kgm^{-3}. The salty water was dyed blue to see the difference between salty and fresh water. A heat exchanger flushed by water of $20°C$ was placed in the reservoir along the side opposite to the tubes. The reservoir was monitored routinely and both layers remained at $20°C$ within a range of $\pm 1.3°C$. The bottom of the small basin was heated by a second heat exchanger, which was flushed by water of a desired temperature.

Experiments have been done for two configurations. In the main experiments the radii of the top, middle and bottom tubes had their standard values $r_1 = r_2 = 9.5\ mm$ and $r_3 = 1.5\ mm$, respectively and the siphon was placed at $d = 0.6\ cm$ above the center of the bottom tube. In the second set of experiments the upper and the middle tube had radii $r_1 = 4.5\ mm$ and $r_2 = 3.1\ mm$, respectively (the radius of the bottom tube was still 1.5 mm), and the siphon was at 1.4 cm above the center of the bottom tube. The parameter

Set 1				Set 2			
d	=	0.6	cm	d	=	1.4	cm
r_1	=	9.5	mm	r_1	=	4.5	mm
r_2	=	9.5	mm	r_2	=	3.1	mm
r_3	=	1.5	mm	r_3	=	1.5	mm

Table 1: Values of parameters used in the two sets of experiments. The parameters of set 1 are the standard values.

values for the two sets of experiments are summarized in Table 1.

The temperature in the small basin was measured with three digital thermometers, with probes at 0.5 cm, 8.5 cm and 17.5 cm above the bottom. In some experiments, two additional temperature probes, which were connected to dataloggers, were placed at about 2 cm and 8 cm above the bottom. The dataloggers recorded the temperature once every 15 s. The experiments were also recorded on video tape. After a steady state had been reached, samples were taken near the bottom, in the middle and just below the top of the water column. With a densiometer the density of these samples could be measured. The salinity of the sample can then be determined from this density (which is measured at room temperature) and the density of fresh water at room temperature.

An experiment was started by filling both basins with fresh water, after which the salt water pump was switched on at a high flow rate. Within less than fifteen minutes the salty layer in the reservoir had formed. Then the fresh and salt water pumps were set at their normal rates and the temperature of the heat exchanger at the bottom of the small basin was set at the desired value. Then the system was left to come to equilibrium. This took typically two or three hours for the experiments of the first set, and six or more hours for the experiments of the second set.

Test measurements were done for different forcing temperatures. As water can contain less dissolved gases when it is heated, air bubbles will form on the bottom and the side walls of the small basin, and in particular around the opening of the bottom tube during an experiment. It turned out that, if the forcing temperature was about $35°C$ or higher, the flow through the bottom tube would get blocked by air bubbles in typically one or two hours. A situation in which this happened could be recognized visually by the fact that the water in the small basin became completely colorless. A sample taken from this water showed that the density was equal to that of fresh water. This is consistent with a blocked bottom tube, as salty water can then no longer enter the small basin.

The use of distilled fresh water in combination with de-aerated salt water did not solve the problem. Therefore we partly de-aerated the water of the salty mixture, by heating the water up to a temperature of about $45°C$ to $50°C$ and keeping it at this temperature for several hours. Then the water was left for one or two days to cool down to room temperature again. However, even with this procedure it remained necessary to remove the air bubbles regularly, by sticking a small metal wire into the bottom tube. This could be done with hardly any disturbance of the flow. Usually we removed air bubbles in this way about once every 30 minutes.

3.2 Convective oscillations

The forcing temperature T^* was varied between $35°C$ and $50°C$ for standard values of the parameters (Table 1). Two different flow regimes were found: for forcing temperatures $T^* = 42°$ and higher, the system reached a steady state within one or two hours, whereas self-sustained oscillations occurred for lower forcing temperatures. The temperature and the salinity contribution to the density in the small basin near the bottom and at mid-depth are plotted against the forcing temperature T^* in Fig. 4 for both steady states and oscillations.

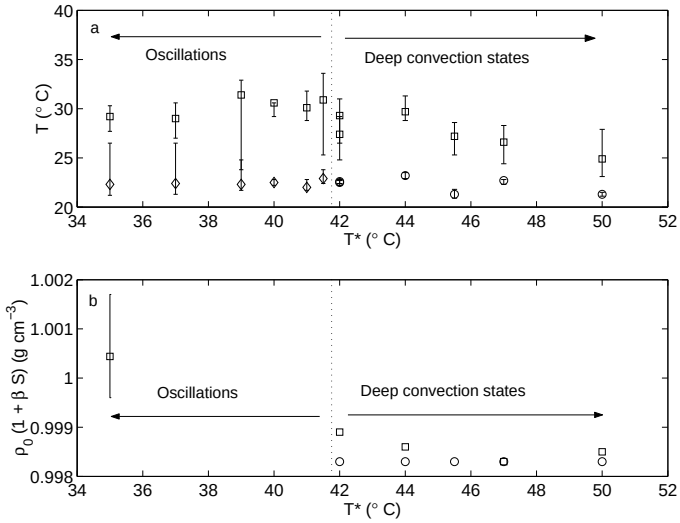

Figure 4: (a) Average temperature in the small basin as a function of the forcing temperature T^*. (b) Salinity contribution to the density (a measure for the salinity) in the small basin as a function of T^*. The squares are values at the bottom, the circles and diamonds are values at mid-depth. Temperature and salinity at the top are not plotted, as they were almost equal to the values at mid-depth. Average temperatures were calculated by averaging the temperature at 5 minute-intervals over one hour, or, in the case of oscillations with periods greater than one hour, by averaging temperatures at 15-minute intervals over one oscillation period. Vertical bars indicate the minimum and maximum values.

The average temperature at mid-depth lies around $22°C$ or $23°C$ for both the steady states and the oscillations, whereas the temperature at the bottom is several degrees higher. This is because the bottom temperature is measured within the thermal boundary layer that exists in a convecting fluid, heated from below [5], whereas the mid-depth temperature is measured in the well-mixed region. Temperatures at the top of the small basin are almost the same as at mid-depth and are therefore not shown. In all steady states there is flow into the small basin through the bottom and middle tube and outflow through the upper tube, which characterizes these states as deep convection states. In the steady states, the water in the small basin also has a very low salinity (Fig. 5b), due to the relatively strong inflow of fresh water through the middle tube (the diameter of the middle tube is much bigger than that of the bottom tube). The temperatures at mid-depth and near the bottom of the small basin as a function of time for a typical oscillation are shown in Fig. 5.

We start the description at the arbitrarily chosen time $t = 2.5\ hr$, when a layer of salty water has started to form at the bottom of the small basin. This could clearly be seen as a small layer of blue water at the bottom. The bottom temperature is at its maximum, whereas the temperature at mid-depth is low. As time progresses, the salty, convecting layer grows (during about one hour). The bottom temperature decreases only slightly, until the interface between the warm, salty water and the colder, fresher water breaks up rather rapidly and the whole water column mixes in typically several minutes (at $t = 3.2\ hr$ in Fig. 5). At this moment, the bottom temperature decreases rapidly, as the water at the bottom mixes with the colder water from the layer above. At the same time the temperature in the middle of the basin increases suddenly, due to the mixing with the much warmer water from the bottom layer. Then the whole water column is well mixed, which could be seen in the experiment because the whole water column was colored light blue. Within about ten minutes, during which the bottom temperature remains low, the water in the small basin becomes almost fresh (around $t = 3.4\ hr$). Then the cycle repeats itself. During the whole oscillation there was inflow through the middle tube and outflow through the top tube.

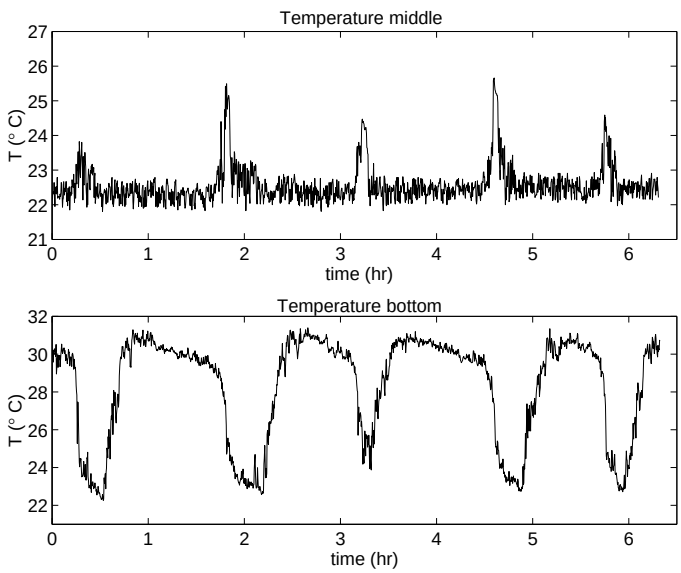

Figure 5: Temperature (a) at mid-depth and (b) at the bottom of the small basin as a function of time for the experiment with $T^* = 39°$.

During the experiment with $T^* = 35°C$, the salinity was measured at several times during an oscillation cycle (Fig. 6). While the convecting layer of salty water is growing and the temperature near the bottom is relatively high (Fig. 6a, between about 1 hr and 4.5 hr), the salinity decreases rapidly (Fig. 6b), due to entrainment of fresh water from the layer above. The salinity increases again when a new layer of salty water starts to form.

The oscillation mechanism can be understood by considering the vertical density profiles. At a certain point during the oscillation the whole water column is well mixed, so that the density is constant with depth. However, the inflow of salty water through the bottom tube creates a salty layer at the bottom of the small basin. Because the water is also heated from below, a well mixed salty layer will form at the bottom. This layer is heavier than the

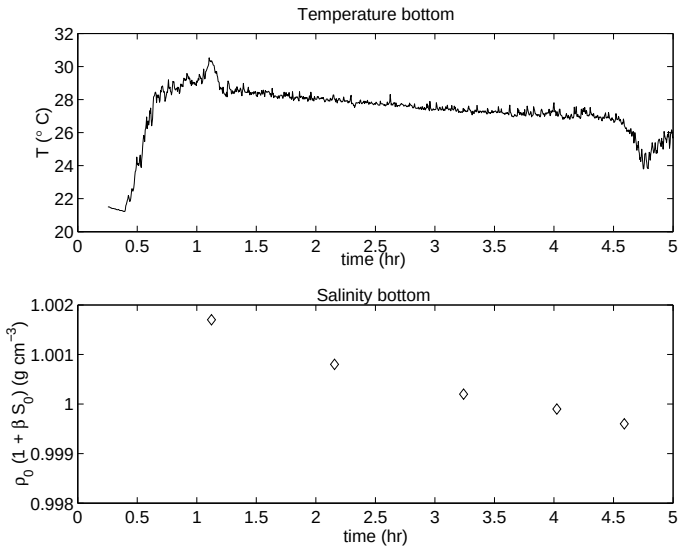

Figure 6: (a) Temperature at the bottom of the small basin as a function of time for the experiment with $T^* = 35°$. (b) Salinity contribution to the density at the bottom of the small basin as a function of time for the experiment with $T^* = 35°$.

fresher water above it due to its high salinity, so that the density profile will show a stable density step. The inflow of salty water and the entrainment of fresher water from the layer above make the salty layer grow in time, but the entrainment also decreases the salinity. As the temperature of this layer does not change very much, the density of the lower layer decreases. The temperature of the upper layer will increase slightly due to conduction of heat across the interface, but this is only a small effect. Finally, the effects of temperature and salinity on the density in the lower layer compensate so that both layers have equal density. On a slight decrease in salinity of the lower layer the water column now becomes unstable, causing the whole water column to overturn. The inflow of cold, fresh water through the middle tube and the outflow of well-mixed water through the top tube will lower the salinity and temperature and then the whole cycle starts again.

The period of the oscillation decreases with increasing forcing temperature (Fig. 7a), as stronger convection in the salty layer causes more entrainment and therefore a faster decrease of the density difference between the two layers, and correspondingly a shorter period. The maximum height of the salty layer during the oscillation also decreases with increasing forcing temperature (Fig. 7b). At higher forcing temperatures, the density difference decreases faster, so that the salty layer has not yet become very big when the water column overturns already.

3.3 Other flow regimes

In the second set of experiments, in which the upper and middle tubes had smaller diameters (Table 1), the forcing temperature was varied between $37°C$ and $46°C$ (Fig. 8). For all forcing temperatures within this range, the system eventually reached a steady state.

For forcing temperatures of $44°C$ and lower shallow convection states were found, with

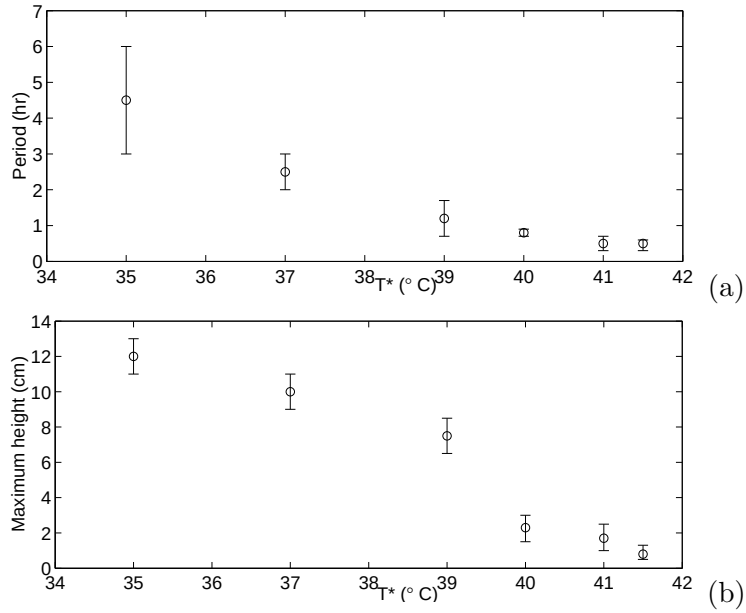

Figure 7: (a) Period of the oscillation as a function of forcing temperature T^*. (b) Maximum height of the salty layer during the oscillation as a function of T^*. The vertical bars indicate the range of maximum and minimum values of the period and the layer height, respectively.

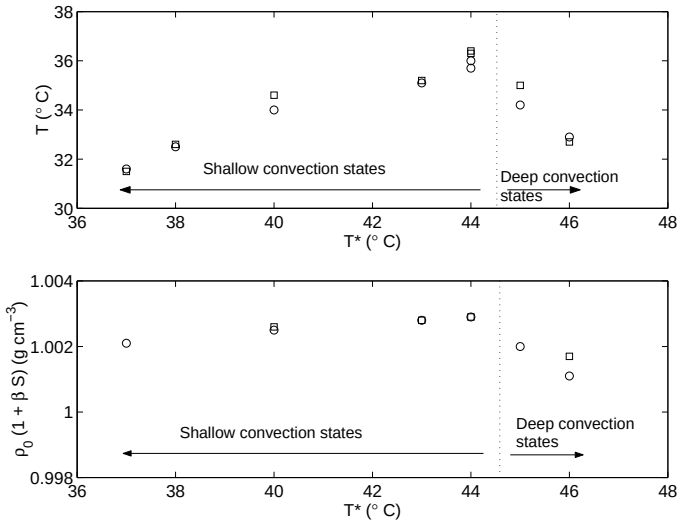

Figure 8: (a) Average temperature in the small basin as a function of the forcing temperature T^*. (b) Salinity contribution to the density in the small basin as a function of T^*. Squares indicate values at the bottom, circles values at mid-depth. Average temperatures were calculated by averaging the temperature at about 15 minute-intervals over one or two hours.

inflow through the bottom tube and outflow through the middle and top tubes. Deep convection states, with inflow through the bottom and middle tubes and outflow through the top tube, existed for forcing temperatures of $45°C$ and $46°C$. The temperatures at mid-depth and near the bottom of the small basin are almost the same (Fig. 8a), indicating that the thermal boundary layer is smaller than in the first set of experiments, so that bottom temperatures are now measured within the well-mixed layer. In the shallow convection states, the temperature in the small basin increases from about $31.5°C$ at $T^* = 37°C$ to about $36°C$ at $T^* = 44°C$. In the deep convection states, temperatures are lower again, due the inflow of relatively cold water through the middle tube. The salinity is relatively high in the shallow convection states (Fig. 8b) and is lower in the deep convection states, because the inflow through the middle tube is also fresh.

The two types of steady states could easily be distinguished, as in the shallow state the water in the small basin was blue (salty), whereas it was almost colorless (almost fresh) in the deep convection state. Also, the middle tube contained blue water in the shallow convection states (as there is outflow through that tube in a shallow convection state) and colorless water in a deep convection state (inflow through the middle tube). The flow in the middle and top tubes could also be visualized by injecting a little bit of red dye at one end of the tube.

Unfortunately, as the time needed to reach equilibrium was often more than six hours and as the air bubbles had to be removed regularly to prevent the bottom tube from being blocked, it was not possible to change the forcing temperature slightly after an equilibrium had been reached and let the system come to equilibrium again. Therefore, we could not investigate the possibility of multiple equilibria.

4 Comparison with theory

The experimental results can be compared to the box model theory, if the values of the model parameters γ, K and $\tilde{d}$ are known. These parameters have been determined for the first set of experiments (the standard configuration). The parameter $\tilde{d}$ is given by the distance between the height of the siphon inlet and the center of the bottom tube divided by the total height of the water column and was $\tilde{d} = 0.033$. The values of γ and K can be determined indirectly from measurements.

The ratio γ of the hydraulic resistances of the bottom and middle tube (the top and middle tubes are equal) depends on the characteristic flow timescales τ_b and τ_m of the bottom and middle tube, respectively. These two timescales can be determined as follows. Consider first the situation in which the small basin is filled with a layer of salty water of initial thickness h_0 (with $h_0 > d$) at the bottom and fresh water above it. Furthermore the middle tube is blocked, so that salty water will flow out of the small basin through the bottom tube (and fresh water will enter through the top tube). If the thickness of the salty layer in the small basin is denoted by $h(t)$, then the time evolution of h is given by

$$A\frac{dh}{dt} = Q_3 \tag{24}$$

where A is the horizontal area of the small basin. The flow rate Q_3 can be determined from

the pressure difference between both ends of the bottom tube and is given by

$$Q_3 = \gamma C \rho_0 g[-\eta + \beta S_0(d-h)] \tag{25}$$

If changes in surface elevation with time can be neglected, we can use $Q_1 + Q_3 = 0$, which gives

$$Q_3 = \frac{\gamma C \rho_0 g \beta S_0 (d-h)}{(1+\gamma)} \tag{26}$$

Then equation (24) turns into

$$\frac{dh}{dt} = -\frac{1}{\tau_b}(h-d) \tag{27}$$

with solution

$$h(t) = (h_0 - d)e^{-t/\tau_b} + d \tag{28}$$

where the constant τ_b is the characteristic timescale associated with flow in the bottom tube, given by

$$\tau_b = \frac{A(1+\gamma)}{C\rho_0 g \gamma \beta S_0} \tag{29}$$

An estimate of the time constant τ_m of the middle tube can be obtained when the same experiment is done, but now with the bottom tube instead of the middle tube blocked. The equation for the evolution of the layer thickness h', defined as the height of the layer of salty water above the center of the middle tube, is

$$\frac{dh'}{dt} = -\frac{h'}{\tau_m} \tag{30}$$

where

$$\tau_m = \frac{2A}{C\rho_0 g \beta S_0} \tag{31}$$

This has solution

$$h' = h'_0 e^{-t/\tau_m} \tag{32}$$

with h'_0 the initial layer thickness. From equations (29) and (31) it can easily be seen that

$$\gamma = \frac{\tau_m}{2\tau_b - \tau_m} \tag{33}$$

The constants τ_b and τ_m were determined by measuring h and h' as a function of time and fitting exponential curves to the data points. We found $\tau_b = 1080 \pm 10\ s$ and $\tau_m = 9 \pm 2\ s$, which gives $\gamma = 0.004 \pm 0.001$.

Another experiment was done to determine K. Consider the dimensional form of equation (23), which is

$$H = K^*(T^* - T) \tag{34}$$

where the dimensional heat exchange coefficient K^* is related to K via $K^* = \rho_0 C_p Q_s K$. If a layer of area A and thickness D is heated, then equation (34) can be written as

$$\frac{dT}{dt} = \frac{1}{\tau_T}(T^* - T) \tag{35}$$

where the thermal relaxation timescale τ_T is given by

$$\tau_T = AD/(Q_s K) \tag{36}$$

This has solution

$$T(t) = (T_0 - T^*)e^{-t/\tau_T} + T^* \tag{37}$$

The volume flux scale Q_s in (36) follows from (18a) and (29) and is

$$Q_s = \frac{AD}{\tau_b}\frac{1+\gamma}{2+\gamma} \tag{38}$$

Equations (36) and (38) can now be combined to yield

$$K = \frac{\tau_b}{\tau_T}\frac{2+\gamma}{1+\gamma} \tag{39}$$

The thermal time constant τ_T was measured by heating a layer of 19 cm of fresh water with $T^* = 41°C$. This gave $\tau_T = 2800 \pm 300$ s. When a layer of salty water of 9.5 cm (with fresh water above it) was heated with $T^* = 41°C$, a value $\tau_T = 1680 \pm 360$ s was obtained. These estimates of τ_T yielded values of K between $K = 0.6$ and $K = 1.7$. For our calculations we chose therefore $K = 1.2 \pm 0.5$.

The temperature and salinity data are non-dimensionalized using $\tilde{T} = \alpha T/\beta S_0$ and $\tilde{S} = S/S_0$ as in (18), with $\alpha = 3 \cdot 10^{-4}$ K^{-1} and $\beta S_0 = 5.2 \cdot 10^{-3}$, and compared to the theoretical curves for $\gamma = 0.004$, $K = 1.2$ and $\tilde{d} = 0.033$ (Fig. 9). The temperature and

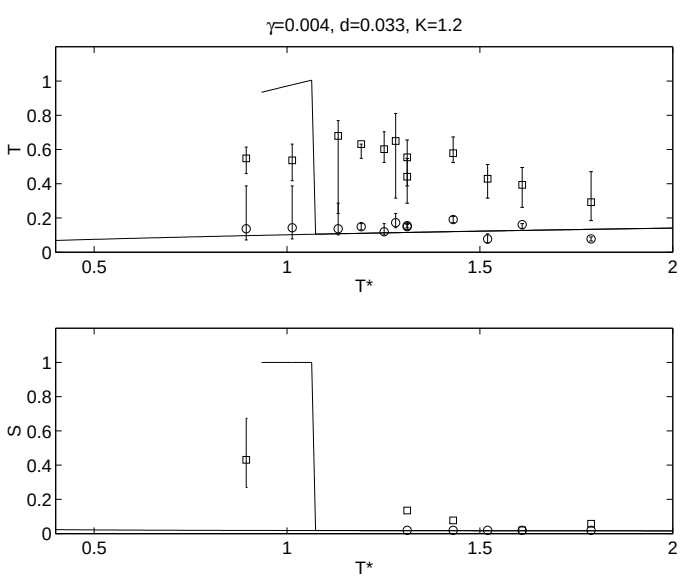

Figure 9: (a) Dimensionless temperature as a function of the dimensionless forcing temperature $\tilde{T}^*$. (b) Dimensionless salinity as a function of $\tilde{T}^*$. Solid lines are the theoretical curves, squares are measurements at the bottom and circles are measurements at mid-depth. Vertical bars indicate the maximum and minimum values of the measurements.

salinity at mid-depth for the deep convection states ($\tilde{T}^* \geq 1.3$) agree quite well with the

theoretical curve for the deep convection states. As was mentioned before, the bottom temperatures are much higher, as these are measured in the thermal boundary layer and do not represent the temperature of the well mixed layer, as the theoretical curves do. The average mid-depth temperatures for the oscillations ($\tilde{T}^* < 1.3$) agree also rather well with the theoretical curve for the deep convection steady states, but the reason for that is not yet clear.

5 Discussion and conclusions

A laboratory experiment has been conducted in which a small basin, that was connected to a large reservoir via three tubes, was heated from below. The reservoir had a shallow layer of salty water underneath a much bigger layer of fresh water, and both layers were kept at room temperature. It was shown that different flow regimes exist in this laboratory experiment.

An oscillatory regime exists for forcing temperatures below $42°C$, whereas there is a regime of steady deep convection states for higher forcing temperatures. The deep convection states are characterized by inflow of cold and salty water through the bottom tube into the small basin, inflow of cold and fresh water through the middle tube and outflow through the top tube. These deep convection states are in good agreement, both qualitatively and quantitatively, with the box model theory developed by Whitehead [4].

During an oscillation a convecting layer of salty water grows and entrains fresh water, thereby decreasing its density, until the water column becomes unstable and convection extends through the whole water column. The oscillation period decreases with increasing forcing temperature, as for a higher forcing temperature an unstable stratification is reached quicker, because there is more entrainment of fresh water. The box model theory presented in section 2 cannot explain this oscillation, even if time-dependent heat and salt balances are considered as in equation (21) and (22), because this theory does not take into account processes like entrainment and mixing of the two layers, which are crucial for the oscillation mechanism. A more quantitative theory for these oscillations still has to be developed.

It is helpful to return to the oceanic case for a moment and consider what this oscillation might look like in a situation where the small basin is cooled from above and connected to a reservoir with a shallow layer of fresh water overlying salty water. The inflow of fresh water through the upper tube will then create a surface layer of fresh water, that is convecting and extending downward as it is cooled from above. This layer will entrain salty water from below until it is dense enough to cause the whole water column to overturn. If the inflow of fresh water at the top is strong enough, deep convection stops and the cycle starts again. It is interesting to note that in this oscillation the fresh surface layer has to become saltier before deep convection can occur, similar to the fact that surface waters in the polar ocean are very fresh and have to become locally saltier before a deep convection event can happen. Although it is not straightforward to apply the results from such a laboratory model to the real ocean, these results suggest that deep convection in the ocean might be related to an internal oscillation, with deep convection occurring only during relatively short intervals.

It is not yet clear what role double diffusive processes play in this experiment. During the slow phase of the oscillation there is cold, fresh water overlying warm and salty water, which corresponds to the 'diffusive' regime in double diffusive problems. However, the

oscillation we find is different from the oscillatory instability in this diffusive regime [5], as we are certainly in the turbulent regime.

In a configuration in which the upper and middle tubes have smaller diameters (but still larger than that of the bottom tube), no oscillations were found. Instead, a regime of shallow convection states exists for forcing temperatures below $45°C$, in which there is inflow through the bottom tube and outflow through the middle and top tubes. For high forcing temperatures (above $45°C$), deep convection states were found.

It is still unclear why oscillations do not occur in this second set of experiments. This must have to do with the different flow rates and therefore also the different temperatures and salinities in the small basin, due to the different tube diameters. Unfortunately, τ_m has not been measured for the second set of experiments, so that the results from Fig. 8 cannot be compared with the theory. Another unanswered question is why steady shallow convection states were not found in the standard configuration, although the box model theory (that seems to work very well for higher forcing temperatures) predicts their existence between $\tilde{T}^* = 0.9$ and $\tilde{T}^* = 1.1$. Either shallow convection states cannot occur here, because oscillations prevent the establishment of a steady state, or steady shallow convection states do exist, but for much lower forcing temperatures. Further study is required to understand under what conditions the different flow regimes occur.

In future work also a new apparatus might be devised, to make the experiments faster. The flow through the bottom tube should also no longer get blocked by air bubbles. Then the question whether or not this laboratory experiment can also exhibit multiple equilibria can be investigated.

Acknowledgments

I would like to thank Jack Whitehead for his very enthusiastic support and supervision of this project. Special thanks also to Keith Bradley, who had many practical suggestions and also created a real nice atmosphere in the lab. Discussions with Joe Keller and George Veronis were both very pleasant and very useful. Finally, I would like to thank all the fellows for their friendship and support during this enjoyable summer.

References

[1] P. D. Killworth, "Deep convection in the world ocean," Rev. Geophys. Space Phys. **21**, 1 (1983).

[2] H. U. Sverdrup, M. W. Johnson, and R. H. Fleming, *The Oceans. Their physics, chemistry and general biology* (Prentice-Hall, New York, 1942).

[3] M. Tomczak and J. S. Godfrey, *Regional Oceanography: an introduction* (Pergamon, New York, 1994).

[4] J. A. Whitehead, "Stratified convection with multiple states," Ocean Modelling **2**, 109 (2000).

[5] J. S. Turner, *Buoyancy effects in fluids* (University press, Cambridge, 1973).

Diagnosing El Niño - La Niña Transitions

Matthew S. Spydell

1 Introduction

Climate variability on interannual time scales is exemplified by the El Niño -Southern Oscillation (ENSO). An El Niño event is marked by anomalously warm SST's in the eastern portion of the equatorial Pacific and the weakening of the trade winds over much of the equatorial Pacific, the opposite event is called La Niña. In addition to locally affecting the climate near the equator, El Niño and La Niña significantly affect the weather throughout the Americas. A standard ENSO index is the anomalous surface atmospheric pressure difference between Tahiti and Darwin, Australia. As a time series, this index shows significant variability around the 1/4 yr^{-1} frequency. Although much research has been devoted to the study of ENSO, there are still some open issues regarding: what starts El Niño, what sustains its quasi-periodic behavior, etc. Two complementary conceptual models of ENSO have been successful in exposing some of the main dynamics of ENSO.

Prior to the development of these conceptual models an intermediate model of ENSO was developed by Zebiac and Cane [1]. This model (henceforth ZCM) is a coupled ocean-atmosphere model that uses a steady state linearized atmosphere, and long-wave linear momentum equations for the ocean. The atmospheric model is essentially a Gill type equatorial model [2]. The ocean and atmosphere are coupled through the atmosphere being forced by anomalous SST's, and the ocean being forced by anomalous wind stresses. This model was shown to have variability similar to ENSO. However, it was difficult to show exactly what mechanisms resulted in ENSO variability because of the model's complexity.

In an effort to understand the basic mechanisms that result in ENSO variability, Battisti (1988) and Schopf & Suarez (1988) showed that the ZCM can be reduced to a delayed oscillator model that contains ENSO-like variability ([3] and [4]). The delayed oscillator model of ENSO emphasizes the role of equatorially trapped waves and the different crossing times of Kelvin and Rossby waves as the source of ENSO-like variability. Specifically, by integrating along characteristics of Kelvin and Rossby waves, and after making some simplifying assumptions, the delayed oscillator equation, $dT/dt = aT - bT(t-\tau) + \mathcal{N}$, was derived. The aT term represents the positive El Niño feedback and the $-bT(t-\tau)$ term represents the delay effect of the Rossby waves which effectively carry temperature of the opposite sign to the eastern equatorial region at a time τ later. It is this delay that is crucial to ENSO variability.

In 1997 a different conceptual model of ENSO was developed by Jin ([5] and [6]). This model is a recharge oscillator model and it deemphasizes the role of waves as the mechanism

of variability and emphasizes the role of mass transport as the mechanism responsible for ENSO variability. Specifically, this model shows that it is the different adjustment times that is responsible for ENSO variability: the thermocline slope adjusts almost instantly to wind stress changes, and the mass (volume) of the equatorial strip takes more time to adjust to wind stress changes. In this model it is crucial for the equatorial strips volume to oscillate in time; anomalous mass must be transported into the equatorial strip in order for an El Niño event to occur.

The purpose of this work is to see if the conceptual models are in agreement with idealize El Niño to La Niña transitions as produced by a shallow water model forced by periodic El Niño - La Niña wind stresses. Specifically, the following questions were addressed. One, are the delayed oscillator and the recharge oscillator complementary views of ENSO variability? Two, from the recharge oscillator perspective what are the specific mechanisms in space and time that charge and discharge the equatorial strip? To answer these questions, numerical simulations of the ocean adjustment process to periodic El Niño to La Niña wind stresses were performed. Additionally, a passive tracer was used to help diagnose the mass exchange process that occurs in El Niño - La Niña transitions.

2 The Equatorial β-Plane

The governing equations used to study El Niño are the reduced-gravity shallow-water β-plane equations. The scales of interest in this particular problem are such that the linearized version of these equations is adequate. The familiar equations are

$$\begin{aligned} u_t - v\beta y &= -g' h_x + \mathbb{D}_u + \mathbb{X} \\ v_t + u\beta y &= -g' h_y + \mathbb{D}_v + \mathbb{Y} \\ h_t + H_0(u_x + v_y) &= 0\,. \end{aligned} \tag{1}$$

These equations have been studied extensively and a review can be found in [7]. These particular equations represent a one and a half layer model; a dynamic upper-layer and a denser static lower layer. The reduced gravity, g', is defined as $g' = g(1 - \rho_1/\rho_2)$, and dissipation and forcing are symbolically represented. The appropriate scalings for this set of equations are

$$(x, y) = a_e(\hat{x}, \hat{y})\,, \quad (u, v) = c(\hat{u}, \hat{v})\,, \quad h = H_0\hat{h}\,, \quad \text{and} \quad t = t_0\hat{t} \tag{2}$$

where the length scale a_e is the equatorial Rossby deformation radius, c is the shallow water wave speed, H_0 is the mean thermocline depth around which the equations have been linearized, and t_0 is the time it takes a shallow gravity water wave to cross a deformation radius. For this particular problem we used

$$\begin{aligned} c = \sqrt{g' H_0} \quad &\rightarrow \quad 2.89\,\mathrm{m/s} \\ a_e = \sqrt{c/\beta} \quad &\rightarrow \quad 380\,\mathrm{km} \\ H_0 \quad &\rightarrow \quad 150\,\mathrm{m} \\ t_0 = a_e/c \quad &\rightarrow \quad 1.52\,\mathrm{days}\,, \end{aligned}$$

consistent with the previous models of ENSO. For ENSO, the x scale of interest is much larger than 380 km, and time scales of interest are much larger than 1.52 days. If we instead scale by

$$\begin{aligned}
(u,v) &\rightarrow (1, a_e/L_x)\,c && (1, 0.022)c \\
(x,y) &\rightarrow (L_x, a_e) && (17\,\mathrm{Mm}, 380\,\mathrm{km}) \\
t &\rightarrow t_0 = L_x/c && (70\,\mathrm{days}) \\
h &\rightarrow H_0 && (150\,\mathrm{m})
\end{aligned}$$

we arrive at the long-wave equations which are the same as (1) except the terms v_t and $\mathbb{Y}$ both go to zero. Without the *long-wave* approximation, (1) represent equatorially trapped wave modes. To obtain the modes, first (1) is nondimensionalized by (2) to obtain

$$\begin{aligned}
u_t - vy &= -h_x + \mathbb{D}_u + \mathbb{X} \\
v_t + uy &= -h_y + \mathbb{D}_v + \mathbb{Y} \\
h_t + u_x + v_y &= 0
\end{aligned} \tag{3}$$

where all variables are now nondimensional and the terms representing dissipation and forcing are scaled appropriately. The modes of this system are found by first making the change of variables

$$q = h + u \quad \text{and} \quad r = h - u\,. \tag{4}$$

The equations given by (3) in terms of q, r and v are

$$\begin{aligned}
q_t + q_x + v_y - vy &= \mathbb{X} \\
r_t - r_x + v_y + vy &= -\mathbb{X} \\
2v_t + q_y + qy + r_y - ry &= \mathbb{Y}\,,
\end{aligned} \tag{5}$$

where dissipation has been neglected. The normal modes of the unforced non-dissipative equations are found by assuming

$$\begin{pmatrix} q(x,y,t) \\ r(x,y,t) \\ v(x,y,t) \end{pmatrix} = \sum_{n=0}^{\infty} \begin{pmatrix} q(y) \\ r(y) \\ v(y) \end{pmatrix} \exp[i(kx - \sigma t)]\,. \tag{6}$$

The resulting equations are reduced to a single parabolic cylinder equation for v

$$v_{yy} + \left(\sigma^2 - k^2 - \frac{k}{\sigma} - y^2\right) v = 0\,. \tag{7}$$

The physically relevant boundary condition is that $\lim_{|y|\to\infty} |v| = 0$. With this boundary condition σ must satisfy

$$\sigma^2 - k^2 - \frac{k}{\sigma} = 2n + 1\,, \tag{8}$$

where $n \in \{0, 1, \ldots\}$. Additionally, there is a mode for $n = -1$ and it is called the Kelvin mode. This mode is derived from the momentum equations assuming $v = 0$. The mode for $n = 0$ is called the mixed-mode, and there are two modes for $n \geq 1$, inertia-gravity modes (high frequency) and Rossby modes (low frequency). The Kelvin and Rossby modes are

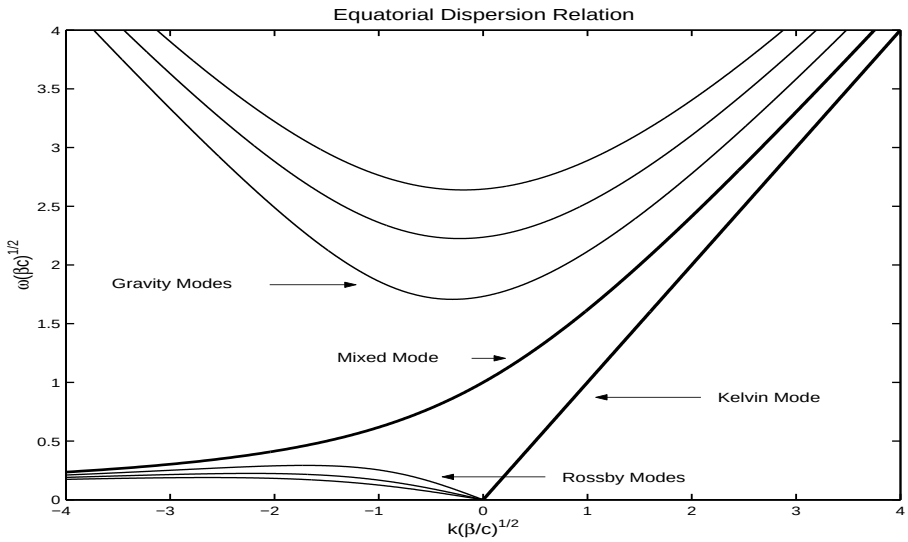

Figure 1: The dispersion relation for equatorial waves. The first three Rossby and gravity wave modes are included. The frequency of Rossby modes decrease with mode number and the frequency of gravity wave modes increase with mode number.

crucial to ENSO as we shall see later. The familiar dispersion relationship is plotted in Fig 1.

The ENSO adjustment process was our primary concern. In order to understand the role of equatorial waves in this adjustment process it is necessary to project the evolution of the system on to the systems modes. Following [2] and subsequently [3], but *not* making the long-wave approximation, we can arrive at amplitude equations for the modes of the system. Instead of assuming oscillatory solutions in x and t, we solve (5) by expanding the y component of these equations in "normalized" parabolic cylinder functions

$$\begin{pmatrix} q(x,y,t) \\ r(x,y,t) \\ v(x,y,t) \end{pmatrix} = \sum_{n=0}^{\infty} \begin{pmatrix} q_n(x,t) \\ r_n(x,t) \\ v_n(x,t) \end{pmatrix} D_n(y)\,, \tag{9}$$

where

$$D_n(y) = \frac{(-1)^n}{\sqrt{2^n n! \sqrt{\pi}}} \exp(y^2/2) \frac{d^n}{dy^n} \exp(-y^2)\,. \tag{10}$$

D_n is considered normalized because

$$\int_{-\infty}^{\infty} D_m D_n \, dy = \delta_{mn}$$

where n is the set of whole numbers. This results in equations for the mode amplitudes

$$\begin{aligned} 2v_{nt} + \sqrt{2(n+1)}q_{n+1} - \sqrt{2n}r_{n-1} &= 2\mathbb{Y}_n \\ q_{nt} + q_{nx} - \sqrt{2n}v_{n-1} &= \mathbb{X}_n \\ r_{nt} - r_{nx} + \sqrt{2(n+1)}v_{n+1} &= -\mathbb{X}_n\,, \end{aligned} \tag{11}$$

with $\mathbb{X}_n$ denoting the x forcing projected on the nth parabolic cylindric function

$$\mathbb{X}_n = \int_{-\infty}^{\infty} \mathbb{X}(y) D_n(y)\, dy\,,$$

similarly for $\mathbb{Y}_n$. This may appear complicated but the evolution equation for the equatorial waves can be found all in terms of q_n, the first two are

$$q_{0t} + q_{0x} = \mathbb{X}_0 \tag{12}$$

$$\sqrt{2} q_{1t} = 2\mathbb{Y}_0 - v_{0t} \tag{13}$$

and for $n \geq 1$

$$(2n+1) q_{(n+1)t} - q_{(n+1)x} = n\mathbb{X}_{n+1} - \sqrt{2(n+1)}\mathbb{X}_{n-1} + \sqrt{2(n+1)}[\frac{\partial}{\partial t} - \frac{\partial}{\partial x}](\mathbb{Y}_n - v_{nt})$$

where

$$v_{nt} = \frac{\partial}{\partial t}(q_{(n+1)t} + q_{(n+1)x} - \mathbb{X}_{n+1})$$

for all $n \geq 0$. The advantage of this notation is that the different wave modes have different y dependence. The amplitude of the Kelvin wave is given by q_0, the mixed wave by q_1, and the Rossby and inertia-gravity waves by q_m, $m \geq 2$. Note that the equation for v_{nt} is displayed separately to emphasize that if the long wave approximation had been made this term would be zero because the terms $v_{nt} = 0$, and $\mathbb{Y}_n = 0$. With this approximation the mixed mode and the gravity modes are not present, hence, the only modes that would survive are the Kelvin (q_0) and the Rossby modes (q_n's). If the long-wave approximation is not made, the Rossby modes and gravity modes have the same y dependence, therefore the modal amplitude $q_2(x,t)$ corresponds to the amplitude of the gravest gravity mode in addition to the the amplitude of the gravest Rossby mode. Thankfully, the scales of interest in this problem are such that the long-wave approximation is certainly valid and the amplitude of q_n with $n \geq 1$ corresponds to the amplitude of the $n \geq 1$ Rossby mode.

3 The Model Setup

The transition between La Niña and El Niño was diagnosed numerically by spinning up the shallow water model to a periodic El Niño to La Niña forcing. Specifically, (1) was solved numerically (see Appendix for details) using a standard shallow water model forced by wind stress fields obtained from a run of the ZCM. These fields can be seen in Figure 2.

The time dependence of the wind stress forcing was given by the function

$$\begin{aligned}\vec{\tau}(t) = &\frac{1}{2}\Big[\vec{\tau}_{El} + \vec{\tau}_{La} + \tanh\big[\alpha(t-1)\big]\big(\vec{\tau}_{El} - \vec{\tau}_{La}\big)\Big] \\ &\times H\big(2 - 4\,\mathrm{mod}(t/4)\big) \\ &+ \frac{1}{2}\Big[\vec{\tau}_{EL} + \vec{\tau}_{La} + \tanh\big[\alpha(t-3)\big]\big(\vec{\tau}_{La} - \vec{\tau}_{El}\big)\Big] \\ &\times H\big(4\,\mathrm{mod}(t/4) - 2\big)\,,\end{aligned} \tag{14}$$

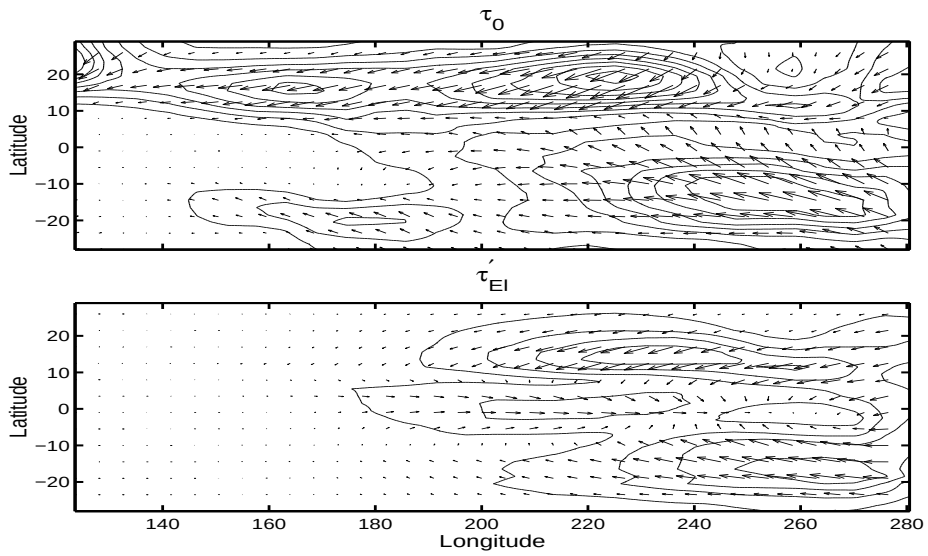

Figure 2: The mean wind stress and the El Niño anomaly. The La Niña anomaly is omitted since it is just the opposite of the El Niño anomaly because the time dependence of the winds is a linear combination of two fields. The total El Niño and La Niña wind stresses are used to force the shallow water model. Contour lines are magnitudes of wind stress in 0.25 dynes/cm^2.

where H is the heavy-side step function and t is measured in years. Figure 3 shows one period (4 years) of the oscillating wind stress. The parameter α is used to adjust how quickly the winds transition from La Niña to El Niño and we set $\alpha = 3$ for all results reported. It is acknowledged that this simple linear interpolation between two wind stress states is a simplification of the true transition process, which includes spatial propagation signals, however, this interpolation is used because it is simple yet physically revealing.

After the model spins up under periodic wind stress forcing, four years of data representing the transition from maximum La Niña winds to maximum El Niño winds and back to La Niña was saved and analyzed. In order to diagnose these idealized La Niña to El Niño

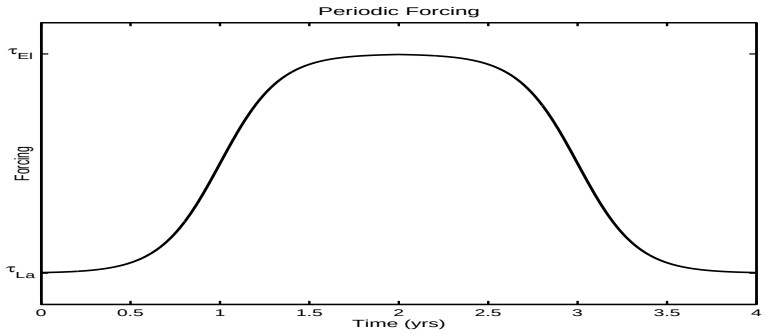

Figure 3: The time dependence of the periodic forcing used in the linear shallow water model used to diagnose the transitions between El Niño and La Niña .

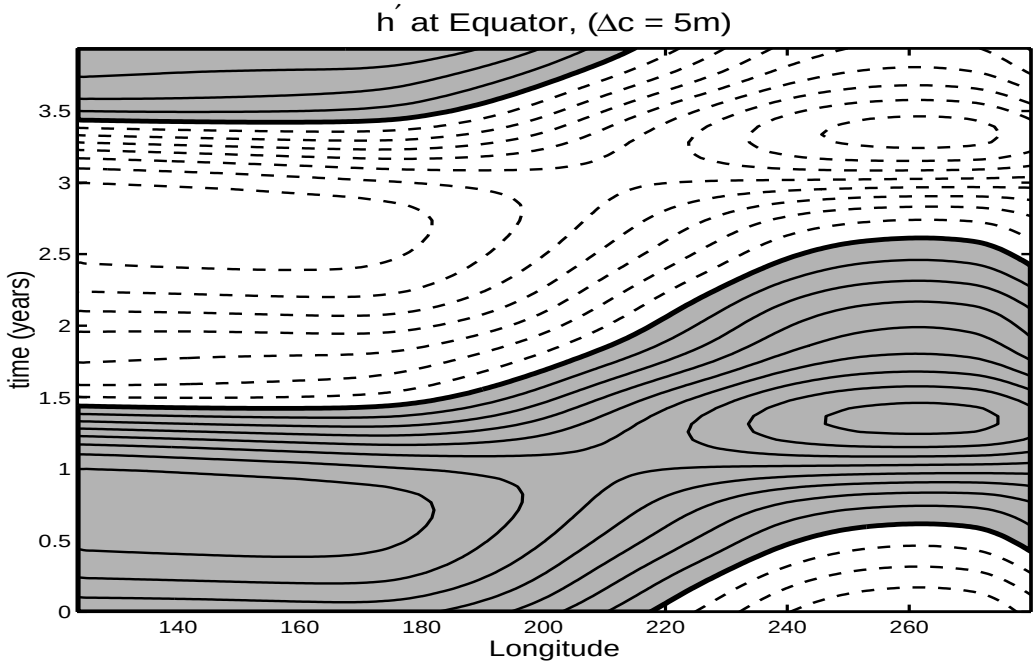

Figure 4: A time-longitude plot of the anomalous height at the equator. The shaded area is positive and the contour level is 5 m.

transitions the fields are split into climatologies and anomalies

$$\begin{aligned} h(x,y,t) &= h_0(x,y) + h'(x,y,t) \\ u(x,y,t) &= u_0(x,y) + u'(x,y,t) \\ v(x,y,t) &= v_0(x,y) + v'(x,y,t)\,. \end{aligned} \tag{15}$$

4 The Role of Waves

The first question to answer is whether these idealized El Niño - La Niña transitions exhibit characteristics implied by the idea of the delayed oscillator. Namely, to what extent are wave dynamics responsible for the time evolution of the anomalous fields? A Hovmöller diagram of h' at the equator is an appropriate place to start, see Figure 4.

From Figure 4 is it possible to see the role of waves in El Niño to La Niña transitions. Between time zero and one we can see a positive depth anomaly encountering the western boundary, this depth anomaly is then reflected and rapidly moves east across the equator between time 0.75 and 1.5. From Figure 4 it is not clear what occurs when this anomaly reaches the eastern boundary at time 1.5. Due to the symmetry of the forcing the negative depth anomaly evolves in the same manner starting at about time 2.5.

However, projecting $q = h' + u'$ on the normal modes of the system can clarify the role of waves in the transition process by explicitly indicating which equatorial waves are excited in the transition process. The evolution of q projected on the Kelvin and first Rossby mode can be seen in Figure 5.

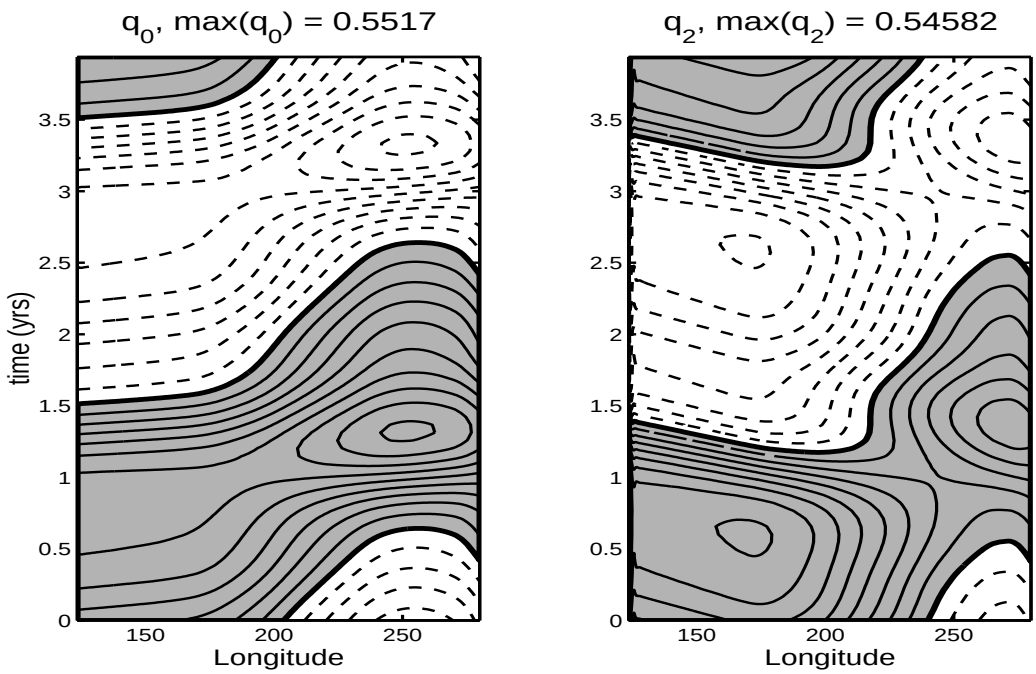

Figure 5: A time-longitude plot of the projection of $q(x, y, t)$ on to the Kelvin mode and the first Rossby mode. The shaded area is positive and the maximum value of the nondimensional projection is displayed.

From Figure 5 the role of the Kelvin and Rossby wave in the transition process is evident. We shall now analyze the positive depth anomaly or warm anomaly in some detail. At $t = 0.5$ the first mode Rossby wave has maximum amplitude near 200° East. This mode propagates along the equator at 1/3 the Kelvin wave speed and then encounters the eastern boundary at $t = .9$.[1] The Rossby wave is then reflected as a Kelvin wave but initially, for $t < 1$, the Kelvin wave loses intensity because the stress anomaly is negative. This is clear from the Kelvin modal amplitude equation (12) where $\mathbb{X}$ is the stress anomaly which is negative at the equator for $-1 < t < 1$. It is negative because during this time there are La Niña winds, hence the Kelvin wave amplitude q_0 decreases. At $t = 1$ the stress anomaly changes sign and the Kelvin wave intensifies. It is this intensification which brings El Niño to its maturity. The idea that an equatorial Rossby wave reflects from the western boundary as a Kelvin wave that is later intensified is the principle of the delayed oscillator. In the delayed oscillator model the equatorial Rossby wave is assumed to be excited by the anomalous wind stress in the central part of the basin from the previous El Niño. Is this the case here? See Figure 6 for the projection of q on the third and fifth Rossby modes. From this figure we see that the projection on the slower equatorial Rossby waves is weaker and occurs at the same time and place, $t = 0$ and x =200° East. We ask, what is responsible for the excitation of these modes?

Figure 7 shows the evolution of $h'(x, y, t)$ through the maximum La Niña wind stress

[1]These times denote the approximate time when the maximum amplitude encounters the eastern boundary, etc.

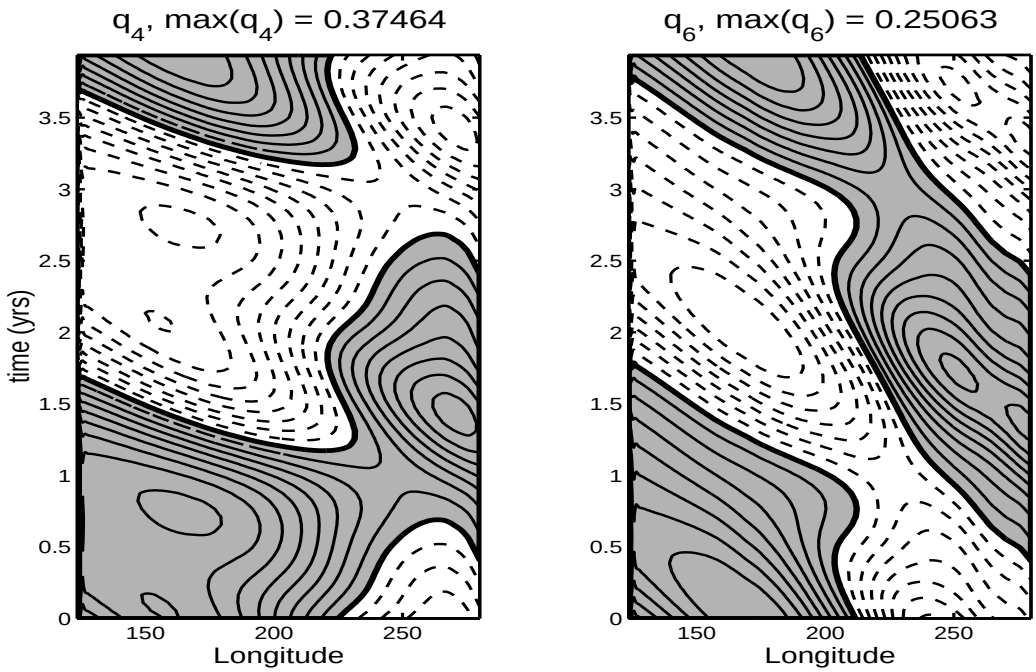

Figure 6: A time-longitude plot of the projection of $q(x, y, t)$ on to the third and fifth Rossby mode. The shaded area is positive and the maximum value of the nondimensional projection is displayed.

anomaly, notice especially the off-equatorial wave near 15° North. It is possible to show that this is a long-QG-Rossby wave at 15° North, i.e. $-a^{-2}\psi_t + \beta\psi_x = 0$, with a speed of about $\beta a^2 \approx 38°/\text{yr}$.

Beginning in panel 2 of Figure 7 this off equatorial long Rossby wave "leaks" into the equatorial region west of 200° E. This is rather unexpected because the delayed oscillator model of El Niño does not address off equatorial dynamics as part of the ENSO mechanism. However, this off equatorial Rossby does eventually "leak" into the equatorial region and excites equatorial Rossby waves that are crucial to ENSO mechanism according to the delayed oscillator mechanism. We will now show that it is the background potential vorticity that allows the off equatorial Rossby wave to leak into the equatorial region. Rossby waves propagate along lines of constant background potential vorticity

$$\zeta = f/H_0 \,. \tag{16}$$

Figure 8 shows lines of constant background potential vorticity superimposed on fourth panel of Figure 7.

We see a ridge of high potential vorticity that forces the off equatorial Rossby wave to travel north of 10°. This Rossby wave then "leaks" through the gap in the ridge of potential vorticity at about 170 E Longitude. Again, it is interesting to see off equatorial dynamics playing a role in ENSO transitions, not something usually associated with ENSO, nor is off equatorial dynamics apart of conceptual ENSO models. However, off equatorial dynamics is discussed in the context of El Niño in Philander (1997), where it is discussed in the context of decadal modulations of ENSO variability.

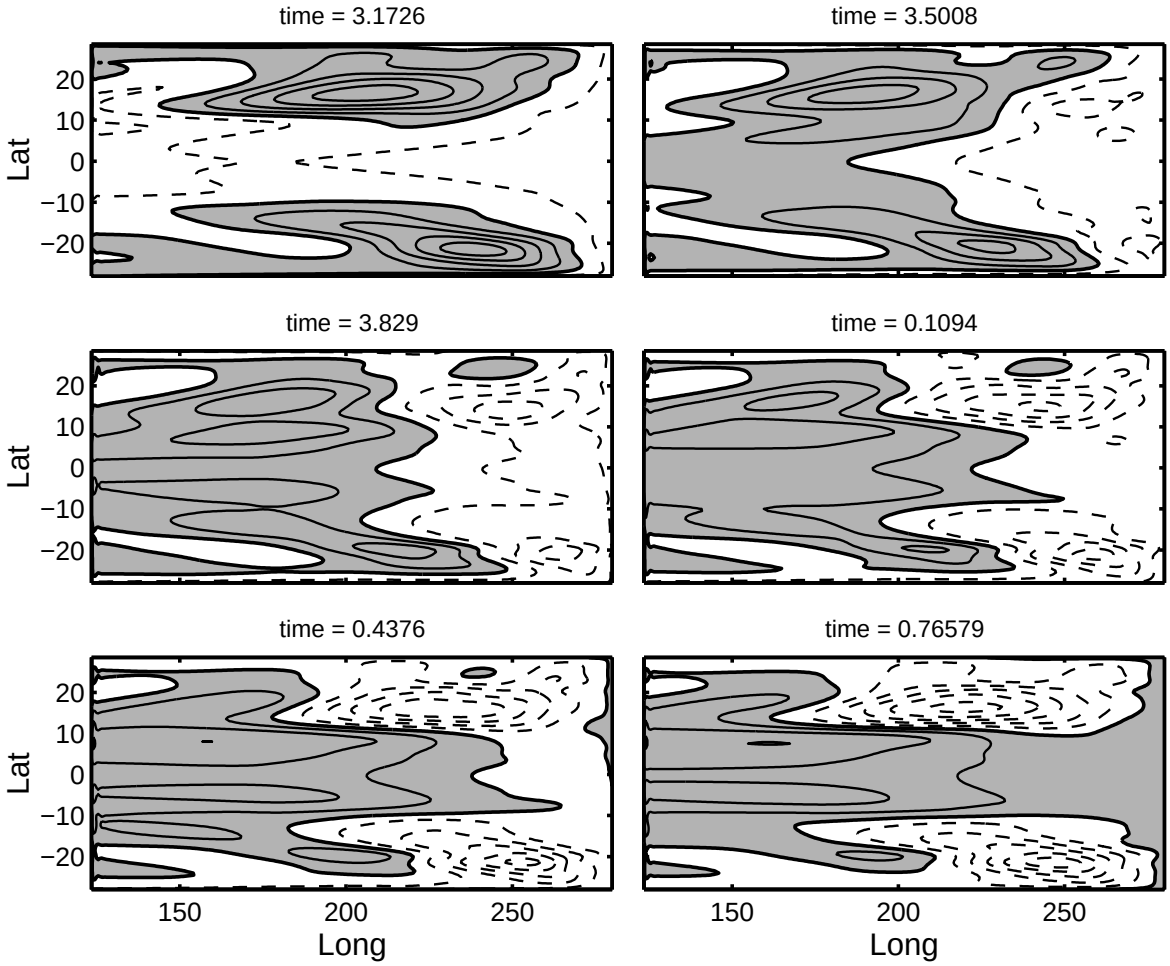

Figure 7: Six frames in the transition through the La Niña wind stress. Maximum La Niña stress anomalies occur at $t = 0$. An off equatorial positive anomaly Rossby wave is clearly seen moving west at around 15° N. Additionally, this Rossby wave can be seen to "leak" into the equatorial region beginning in the second panel. The contour interval is 20 m.

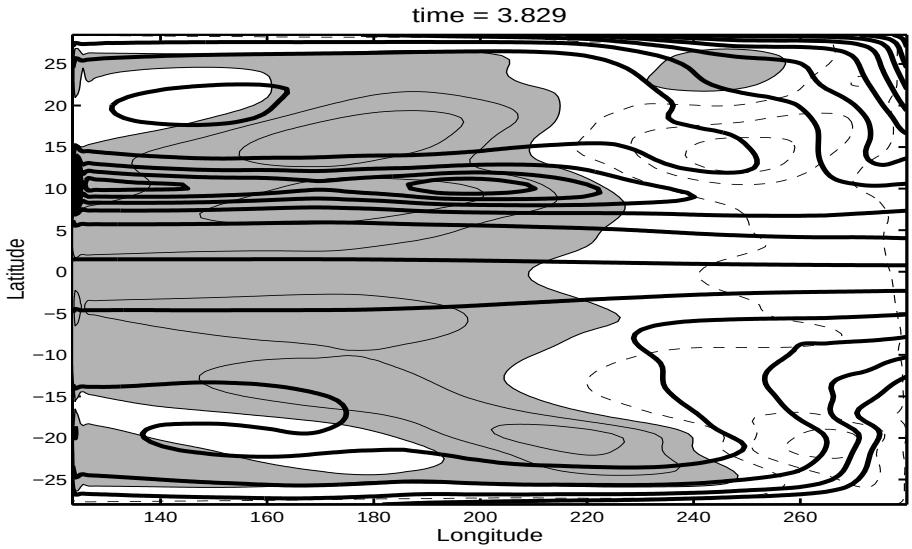

Figure 8: One frame in the transition through the La Niña wind stress with the background potential vorticity contours at a time when the off equatorial Rossby wave is "leaking" into the equator. The contour level for the anomalous height field is 20 m and the potential vorticity field is in bold contours.

5 Recharging and Sverdrup Flow

In the Section 4 it was demonstrated that the wave dynamics view of ENSO is indeed captured in the idealized ENSO transitions we simulated. Can we also see the recharge oscillator perspective in these simulations? If ENSO can be described as a recharge oscillator the total mass (volume) of the equatorial region must oscillate, i.e. the equatorial strip must charge and discharge. According to [5], the recharging takes place prior to an El Niño event, and in the case of our model ENSO transitions this recharging occurs during La Niña wind stresses. Figure 9 shows the zonal mean thermocline depth anomalies and from this Figure we see that the equatorial region has maximum volume prior to the onset of the El Niño, in other words prior to the El Niño wind stress anomaly.

It is obvious from Figure 9 that the equatorial region, between -10° S and 10°, exchanges mass periodically with the off equatorial region, thus these ENSO transitions can be viewed in terms of a recharge oscillator. Can we be more specific about the recharging of the equatorial region? Specifically, what is the mechanism that allows the equatorial region to recharge, and where is the mass responsible for the recharging coming from? It is possible to answer these questions from our idealized El Niño - La Niña transitions. To do so, we will start with the anomalous continuity equation

$$h'_t + H_0(u'_x + v'_y) = -rh' \,. \tag{17}$$

We can now integrate the anomalous continuity equation to obtain the anomalous transport

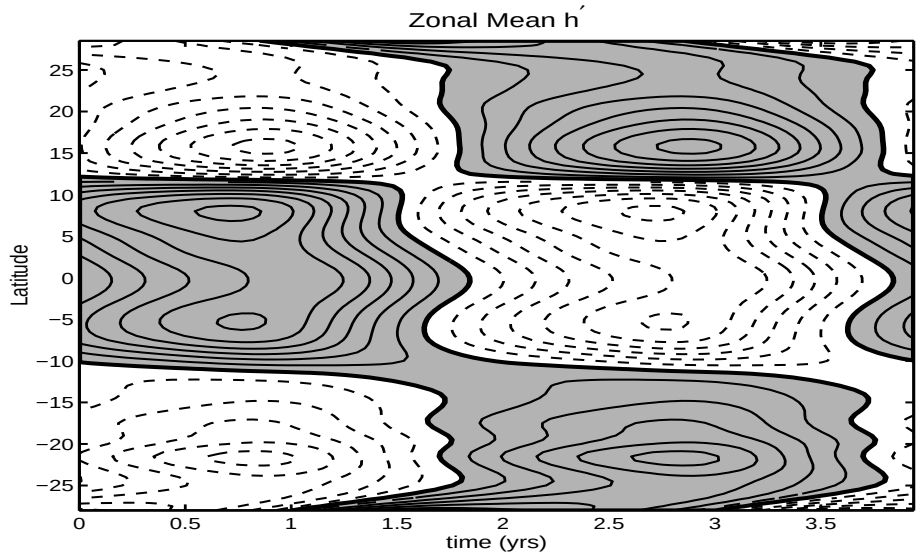

Figure 9: The zonal mean of the thermocline depth anomaly. Notice the recharging and discharging of the equatorial region. The contour interval is 5 m.

into the region east of x,

$$\begin{aligned}\frac{dV}{dt}(x,t) \equiv \int_{-10^\circ}^{10^\circ}\int_{x}^{X_e} \frac{dh'}{dt}(\tilde{x},y,t)\,dy\,d\tilde{x} = \\ - r\int_{-10^\circ}^{10^\circ}\int_{x}^{X_e} h'(\tilde{x},y,t)\,dy\,d\tilde{x} \\ - H_0\int_{x}^{X_e}[v'(\tilde{x},10^\circ,t) - v'(\tilde{x},-10^\circ,t)\,d\tilde{x} \\ + H_0\int_{-10^\circ}^{10^\circ} u'(x,y,t)\,dy\,.\end{aligned} \tag{18}$$

The total transport into this region, $\frac{dV}{dt}$, has contributions from the relaxation term, $-rh$, meridional velocity at $\pm 10^\circ$, v, and from the zonal velocity u at longitude x. A schematic of this idea is seen in Figure 10. If we let $x = X_w$ in (18) we get the total transport into the equatorial region. This is displayed in Figure 11. This figure clearly shows that the equatorial region is charging during the La Niña phase, $t < 1$ and $t > 3$, and discharging during the El Niño phase, $1 < t < 3$.

From (18) we can deduce where the anomalous transport is taking place such that the equatorial region charges and discharges. Figure 12 is a plot of dV/dt as a function of x for certain times during the recharging phase. This Figure shows where the anomalous velocities, more importantly the anomalous meridional velocities, are transporting anomalous mass into the equatorial region during this phase. In the first panel it is a negative $v'(10^\circ)$ east of 200 E is transporting anomalous mass into the equatorial region. West of 200 E v' is positive but small and is *not* helping to recharge the equatorial region. We can also see that u' is transporting anomalous mass west in the region where v' is transporting anomalous

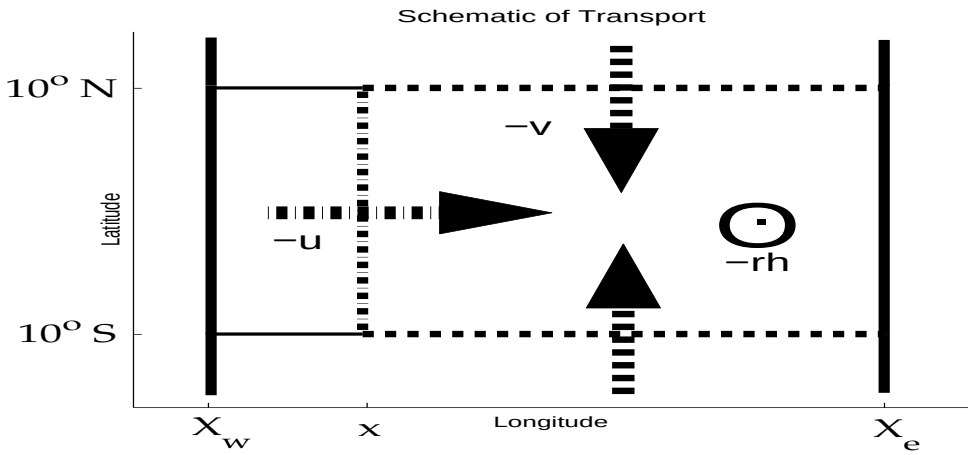

Figure 10: A schematic diagram of the contributions to the transport into the equatorial region east of x.

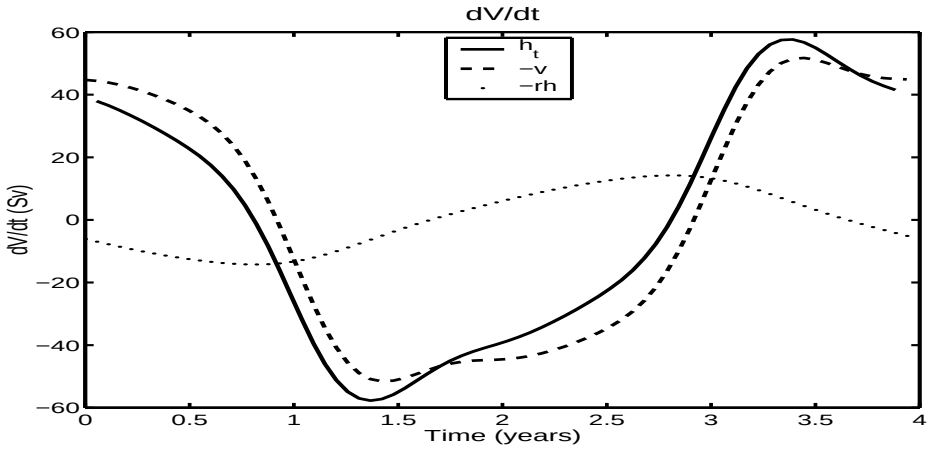

Figure 11: The transport into the entire equatorial region as a function of time. The net transport is depicted by the h_t curve and the contributions to this from the anomalous meridional velocity and the anomalous relaxation are displayed.

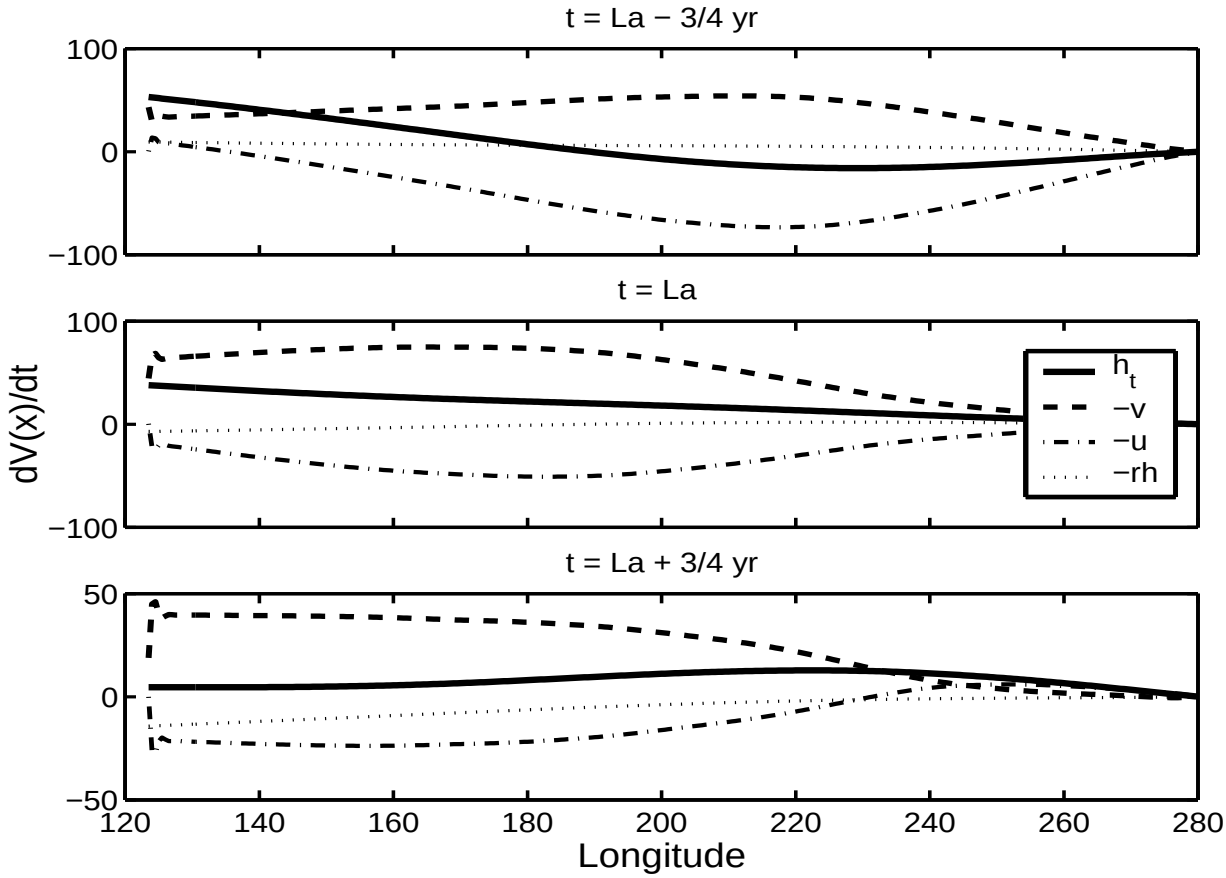

Figure 12: The transport dV/dt into the equatorial region east of x at different times during the recharging phase. The overall transport into the region and the contributions from the anomalous velocities and anomalous relaxation is displayed.

mass into the equator. Note that the anomalous transport due to the boundary current is contributing a small amount to the recharging at this time. In the second panel a negative v' is evident everywhere east of 180 E. This anomalous velocity is responsible for all of the anomalous mass transport into the equatorial region. A negative u' in this same region transports this anomalous mass west. Note that the boundary current is actually helping to expel mass from the equator at this time. Also, the rate at which the equatorial region is filling with mass is approximately constant for all x, i.e. the entire thermocline is filling with water at the same rate. We see this from the constant slope on the h_t curve of this panel. The third panel is at a time close to when the equatorial region begins to discharge. It is possible to see in this panel that the Kelvin wave is helping to transport mass into the eastern equatorial region. Because of the periodic nature of our linear problem and the wind stresses being a linear combination of two states, the discharging process is just the opposite of the charging process.

It was shown that anomalous meridional velocities at $\pm 10°$ mainly in the eastern portion are responsible for the anomalous mass transport that charges and discharges the equatorial

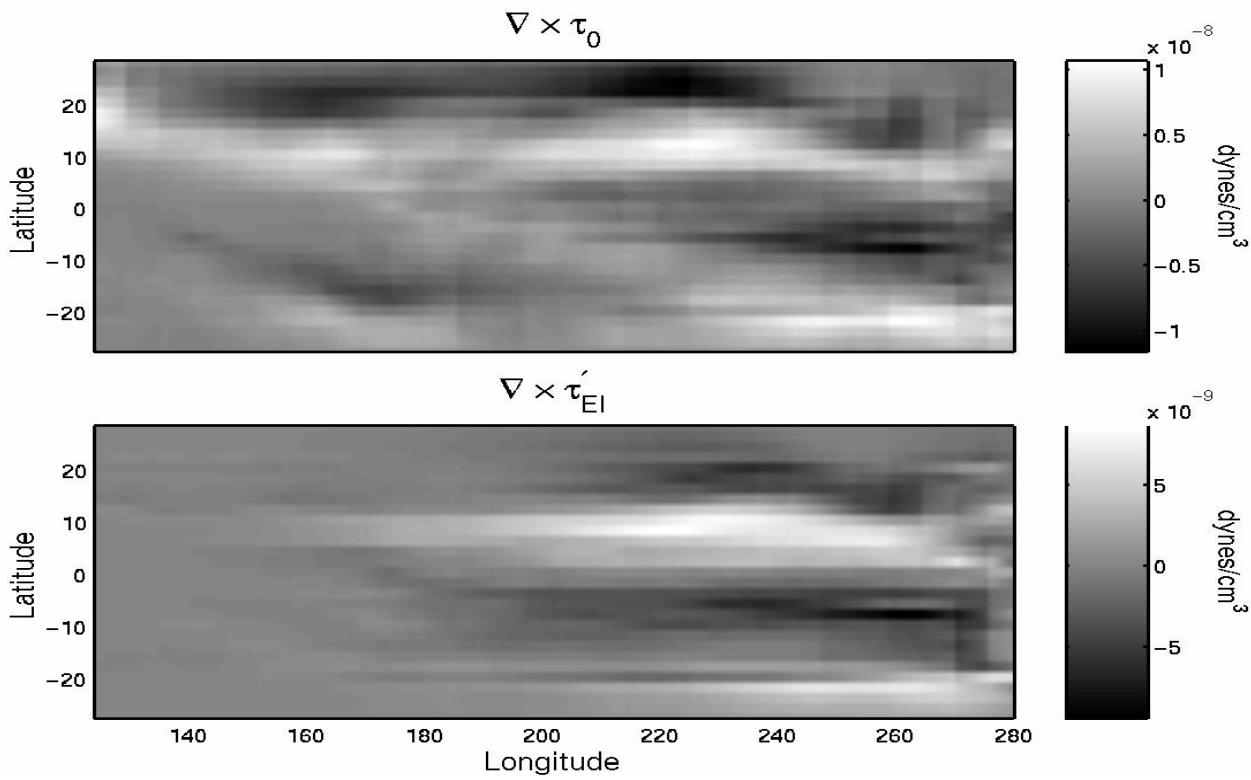

Figure 13: The curl of the mean wind stress field and the curl of the El Niño anomaly wind stress field.

region. From the scales of the problem we would expect the velocities to be in quasi-Sverdrup balance. We can then obtain the anomalous meridional velocities from the anomalous wind stress via the Sverdrup balance

$$\beta v' = \frac{\boldsymbol{\nabla} \times \boldsymbol{\tau}'}{\rho_0 H_0} \cdot \mathbf{k}\,. \tag{19}$$

Figure 13 shows that for El Niño there is a positive wind stress curl anomaly in the eastern equatorial region at 10 N and a negative curl anomaly at 10 S. These anomalous curls are responsible for the discharging of the equatorial region. The curl anomaly for La Niña has the opposite sign as the curl anomaly for El Niño and is hence responsible for the charging of the equatorial region.

Experiments were performed where tracers were injected into the flow at time $t = 0$ with constant gradients in y. These tracers were then advected by the *anomalous* velocities. These experiments were performed to see where the anomalous velocities were present and to show where *anomalous* mass was being transported. These experiments confirmed that anomalous equatorward meridional velocities were indeed responsible for the anomalous mass transport. This anomalous mass enters the eastern equatorial region and is then transported west by anomalous zonal velocities at the equator. Again, because of the symmetrical nature of the forcing the opposite is true for the expulsion of mass during the El Niño phase.

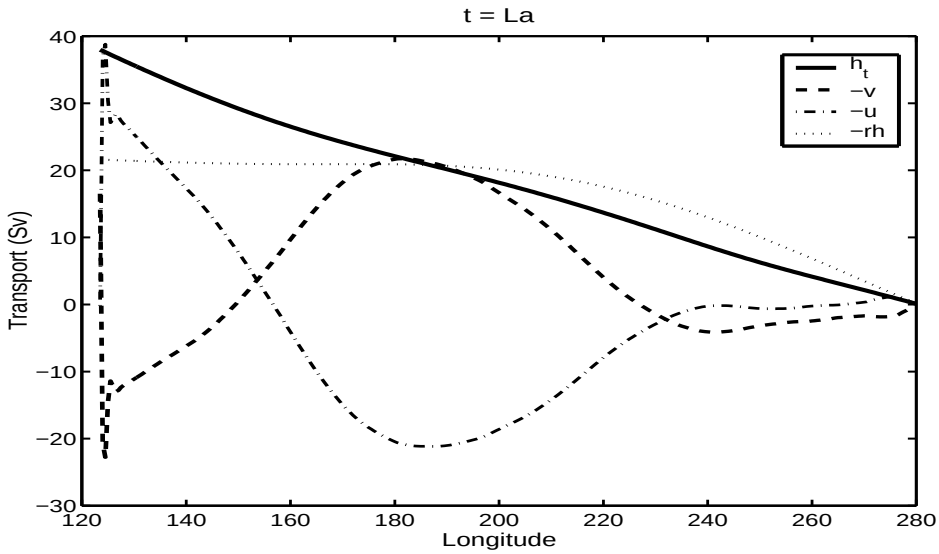

Figure 14: The transport into the equatorial region east of x and the contributions from the full velocity fields and the full relaxation.

6 Total Mass Transport & No Relaxation

The previous sections on transports have emphasized the role of anomalous velocities transporting anomalous mass. In these sections we have isolated what causes the recharging of the equatorial region. However, by using anomalous velocities we do not have a true Lagrangian perspective on the recharging of the equatorial region. In order to determine the origins of the water that actually recharges the equatorial region we must add in the climatological transport to the analysis performed in Section 5. Doing this equation (18) is now an equation that involves the total velocities and Figure 14 displays the total transport into the equatorial region during the recharging phase.

Figure 14 clearly shows that the meridional velocities east of 240 E are transporting mass out of the the equatorial region, between 180 E and 240 E v is transporting mass into the region, and west of 180 E mass is being transported out of the equatorial region. This figure also shows that if it were not for the Western Boundary Current the equatorial region would be losing mass from v transport. We can conclude that it is anomalously weak meridional velocities in the eastern portion of the equatorial region that allows the western boundary current to fill the region. From this figure we see that the relaxation term $(-rh)$ in the continuity equation is actually doing more work than v to recharge the equatorial region. Knowing that this term is a slightly nonphysical parameterization of upwelling and mixing, we should ask whether the recharging of the equatorial region should rely this heavily upon this term? Additionally, is this term necessary for the recharging of the equatorial region?

These questions were answered by running the same experiment but without the relaxation term in the continuity equation. From Figure 15 we see that the equatorial region still charges and discharges, hence the $-rh$ term is not mandatory for the recharging of the equatorial region. Additionally, the the transport analysis was performed on this ex-

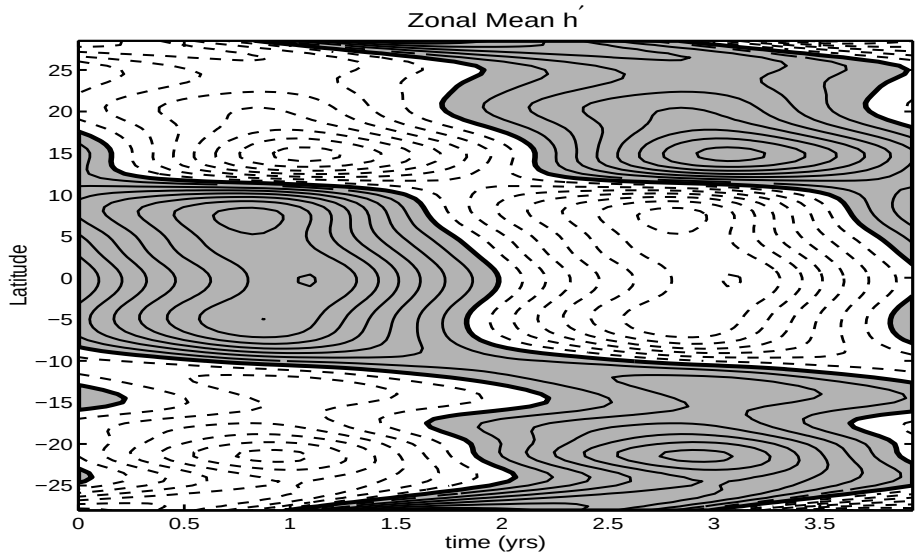

Figure 15: Zonal mean anomalous thermocline depth with no relaxation in the continuity equation.

periment and it was found that in this case the meridional transport is solely responsible for the recharging of the equatorial region. Specifically, it is the weakening of the meridional transport in the out of the basin that allows the western boundary current to fill the equatorial region with anomalous mass, as Figure 16 clearly shows. It is interesting that in Figure the contributions to this charging by u and v are such that the equatorial region is uniformly charging as seen in the constant slope of dh/dt.

7 Conclusions

The purpose of this project was to see if both the wave perspective of ENSO, as exemplified by the delayed oscillator model (Suarex & Schopt 98, Battisti 98), and the mass transport perspective of El Niño , as exemplified by the recharge oscillator model (Jin 97), may be diagnosed in a model simulation of ENSO transitions using a numerical model that is capable of capturing both mechanisms. Both perspectives of ENSO were clearly evident in the idealized ENSO transitions that we modeled. However, as regards to the wave dynamics perspective of ENSO our model shows that it is off equatorial Rossby waves that propagate anomalous thermocline depths from the eastern equatorial region to the west in contrast to equatorially trapped Rossby waves that are emphasized in the delayed oscillator picture of ENSO. The off equatorial Rossby wave does excite equatorial Rossby waves but not until it encounters a gap in the ridge of background potential vorticity in the western portion of the basin where it is able to "leak" into the equatorial region. Thus, this model indicates an interesting interaction between off equatorial dynamics and equatorial dynamics in ENSO transitions (Galanti & Tziperman have also noted this phenomena, personal communication 2001). It is this particular interaction that is worthy of future research.

The mass transport perspective of ENSO was also evident in these idealized ENSO transitions. Using this model we were able to specifically diagnose the mechanisms respon-

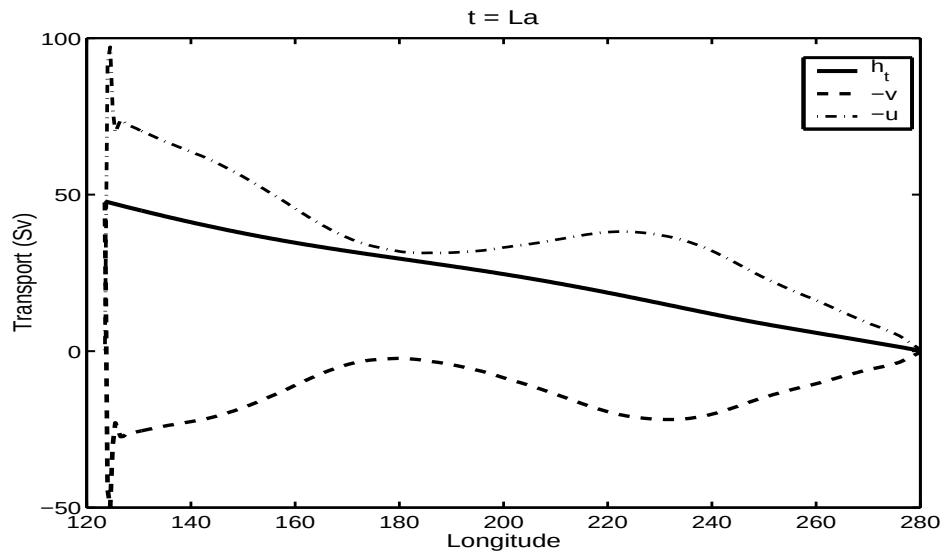

Figure 16: The x dependence of the total transport and the contributions from the full velocity fields with no relaxation in the continuity equation during the recharging phase.

sible for the recharging and discharging of the equatorial region. We found that anomalous wind stress curls in quasi-Sverdrup balance with meridional velocities are responsible for the charging and discharging of the equatorial region. These anomalous wind stress curls are present in the eastern portion of the equatorial region at $\pm 10°$. These anomalous meridional velocities allow the western boundary current to fill the equatorial region with mass. We also found that the $-rh$ term included in most models of ENSO for numerical purposes, is not necessary for the recharging of the equatorial region, nor does it distort the qualitative picture.

8 Thanks

Thanks to the two advisors who helped me with this project, Eli Tziperman for helping me to understand the results herein, and Eric Chassignet for helping to get the results; it was a pleasure working with both of you. Thanks to Paola Cessi for some remarks that forced me to understand and present this work more clearly. Thanks also to the fellows and their support, it was greatly appreciated.

9 Appendix

9.1 Numerical Methods

The numerical model used was a modification of the Bleck and Boudra isopycnic coordinate general circulation model. This code was modified to solve the linear shallow water equations. The model uses a standard "c" grid and a leap frog time stepping scheme. The

model solved the equations

$$
\begin{aligned}
u_t - v\beta y &= -g' h_x - ru + \nu \nabla^2 u + \frac{\tau^{(x)}}{\rho_0 H_0} \\
v_t + u\beta y &= -g' h_y - rv + \nu \nabla^2 v + \frac{\tau^{(y)}}{\rho_0 H_0} \\
h_t + H_0(u_x + v_y) &= -rh\,.
\end{aligned}
\tag{20}
$$

The resolution of the model was 0.5°, as measured at the equator, in both the x and y directions. The values of most of the constants were given in Section 2. The additional values used were:

$$
r = 1/30\,\mathrm{mo}^{-1} \quad \text{and} \quad \nu = 1100\,\mathrm{m}^2\mathrm{s}^{-1}\,. \tag{21}
$$

9.2 The Long-wave Approximation

In order to better understand the long wave approximation and why it is relevant to the equatorial basin and ENSO, we examined the reflection of equatorial Kelvin waves by the eastern boundary of a basin. Additionally, this problem was examined to better understand why in the delayed-oscillator model of ENSO eastern boundary reflection is sometimes ignored. The set up is simple, if a Kelvin wave is excited along the equator, perhaps by an anomalous wind stress, it will propagate along the equator until it reaches the eastern boundary of the basin at which point it must be reflected[2]. What is the outcome of this reflection? It can not reflect as a Kelvin wave or a mixed wave; they only propagate energy eastward. It must transmit its energy to coastally-trapped Kelvin waves (or some deviant of a coastally-trapped Kelvin wave[3], equatorially trapped Rossby waves or gravity waves. The structure of the disturbance in k space determines the outcome of this reflection. Consider an initial value problem of the linear shallow water equations. The initial disturbance is

$$
\begin{pmatrix} u(x,y,0) \\ v(x,y,0) \\ h(x,y,0) \end{pmatrix} = \begin{pmatrix} \alpha c \\ 0 \\ \alpha H_0 \end{pmatrix} \exp\left(-\frac{\beta}{2c} y^2\right) G(x/L)\,. \tag{22}
$$

This initial disturbance is designed to excite an equatorial Kelvin wave response that will propagate to the east with speed c and amplitude α. This disturbance will not disperse because Kelvin waves are not dispersive. We shall choose the specific x dependence to be

$$
G(x/L) = \exp[-(x/L)^2]\,. \tag{23}
$$

Assuming that the scale of this disturbance is small compared to the size of the basin we can assume that the disturbance is not affected by the presence of the boundaries, and we can analyze this initial disturbance as if x were unbounded. This disturbance excites

[2]Reflected is perhaps not the best word here, the energy fluxed into the eastern boundary of the basin must be fluxed out, and this is what is meant by reflection in this particular usage.

[3]A true coastally-trapped Kelvin wave only exist on an f-plane, therefore true coastally-trapped Kelvin waves can not exist at the equator since f goes to zero there [8].

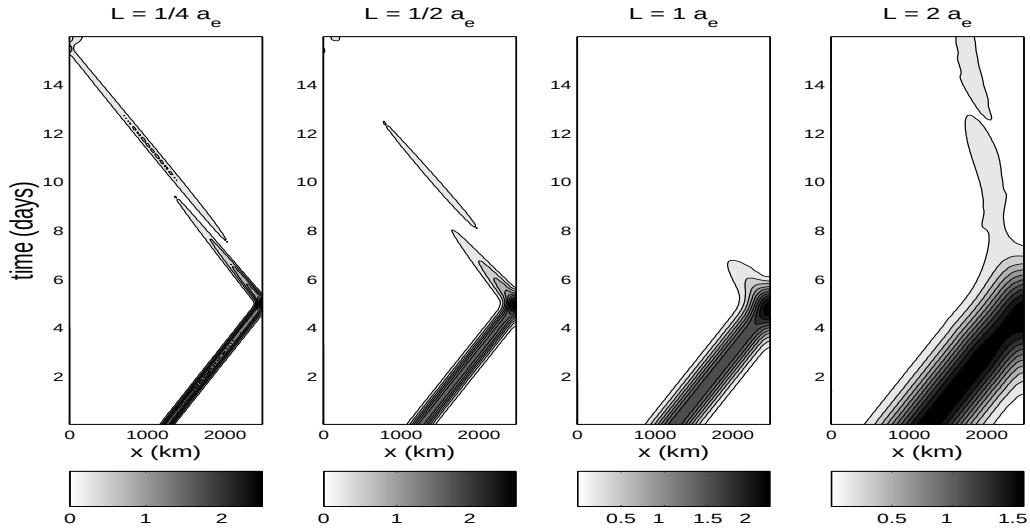

Figure 17: The energy density at the equator, in ergs/cm^2, of an equatorial Kelvin wave as it strikes the eastern boundary of the basin for four different zonal length scales of the disturbance. As the zonal length scale of the disturbance increases, is transmitted to equatorially-trapped gravity waves and more energy is transmitted to equatorial Rossby waves. There are ten equally spaced contours in each panel.

many plane wave Kelvin modes where the amplitude of these excited modes is given by the Fourier transform of (23)

$$\mathcal{G}(k) = \frac{L}{2\sqrt{\pi}} \exp[-(kL/2)^2] \tag{24}$$

assuming that $G(x) = \int_{-\infty}^{\infty} \mathcal{G}(k) \exp(ikx)\, dk$. We see that small initial disturbances (small L) project into high wave number plane waves - obviously the width of Gaussian in k space is inversely proportional to the width of the Gaussian in x space. Since these are Kelvin waves, the frequency is proportional to k ($\omega = ck$) and therefore a small disturbance projects into many high frequency Kelvin modes. When this disturbance encounters the eastern boundary the energy fluxed in must be radiated away by other waves. Some of this energy goes into coastally trapped Kelvin (like) waves that propagate away from the equator and some may be reflected back as either equatorial trapped gravity waves or Rossby waves depending on the frequency of the incident waves. If the disturbance is small, the frequencies may be large enough to reflect as gravity waves. Notice on the dispersion relation, Figure 1, that Kelvin waves with large positive k will have frequencies in the frequency range of the gravity waves.

Typically, simple models of ENSO ignore eastern boundary reflection because the long wave approximation has been assumed and Kelvin waves excited by anomalous wind stresses are assumed to have spatial scales large enough such that these disturbances do not project into high wave number Kelvin modes. When these large disturbances encounter the eastern boundary they will propagate away as coastally trapped Kelvin waves and equatorially trapped Rossby waves. The above analysis showed that Kelvin waves can reflect as fast gravity waves - how large do disturbances need to be such that they will not reflect some of

their energy as gravity waves? For any disturbance the majority of the energy must be in wave numbers less than some critical wave number k_c, where $k_c \sim (3/2)a_e$ according to the dispersion relation. To find the smallest length scale of the disturbance, L, such that the majority of the energy will be in wave numbers less than k_c it is possible to show that the percentage of energy in wave numbers less than k_c, for the Gaussian disturbance (23), is

$$\mathcal{E} = \frac{E(k \leq k_c)}{E_0} = \operatorname{erf}\left(\frac{k_c L}{\sqrt{2}}\right) . \tag{25}$$

The percentage of energy in wave numbers less than k_c must be greater than some threshold denoted by $\mathcal{T}$. This results in a bound for L,

$$L \geq \frac{\sqrt{2}}{k_c} \operatorname{erf}^{-1}(\mathcal{T}) . \tag{26}$$

For simplicity let's assume $\mathcal{T} = \operatorname{erf}(1) \approx 0.8427$ so that $L \geq \sqrt{2}/k_c$. As mentioned previously $k_c \sim 3/2a_e$ giving an approximate bound for L,

$$L \geq \frac{2\sqrt{2}}{3} a_e \approx a_e . \tag{27}$$

Thus the zonal length scale of disturbances must be larger than the equatorial deformation radius such that little energy is reflected as gravity waves. This was verified using our shallow water equatorial β-plane model. Four separate cases were considered in which the zonal length scale of the initial disturbance was set to $L = [1/4\ 1/2\ 1\ 2]\, a_e$, respectively. We can clearly see in Figure 17 that as the zonal length scale of the disturbance increases less energy is reflected as equatorially trapped gravity waves. Note that most of the energy fluxed into the boundary leaves as coastally trapped Kelvin waves which can not be seen in Figure 17 because Figure 17 only shows the energy density at the equator. In the fourth panel of Figure 17 notice that some of the incident energy is reflected as an equatorially trapped Rossby wave(s), which is inferred from the speed of this disturbance.

The reflection of the Kelvin wave was also studied by projecting the solution, $u = u(x, y, t)$, $v = v(x, y, t)$, and $h = h(x, y, t)$, on the normal equatorial modes as outlined in Section 2. The projection of the solution on the first five modes of q is given in Figure 18 and Figure 19 for length scales of the disturbance given by $L = [1/4\ 2]\, a_e$, respectively. In these figures the magnitude of the projection is squared and normalized by the magnitude of the Kelvin wave projection. We can see that before the reflection the projection of q is entirely in the equatorial Kelvin mode. For all times the projection of q on to odd numbered modes is very small because the odd numbered modes represent odd structure in y which should not exist because of the symmetric y structure of the initial disturbance. The small projection on these modes is due to numerical inaccuracies. For the small disturbance there is some projection on q_2 after the disturbance has reflected. The speed of this mode is consistent with the speed of the first equatorial gravity wave mode, however this mode is dispersive and the magnitude of the projection can not remain localized in space. Also notice that the maximum magnitude of the projection on this mode is only 6% of the projection on the Kelvin mode. Again this is evidence that most the energy that is in the original Kelvin wave is transferred to coastally trapped Kelvin (like) waves.

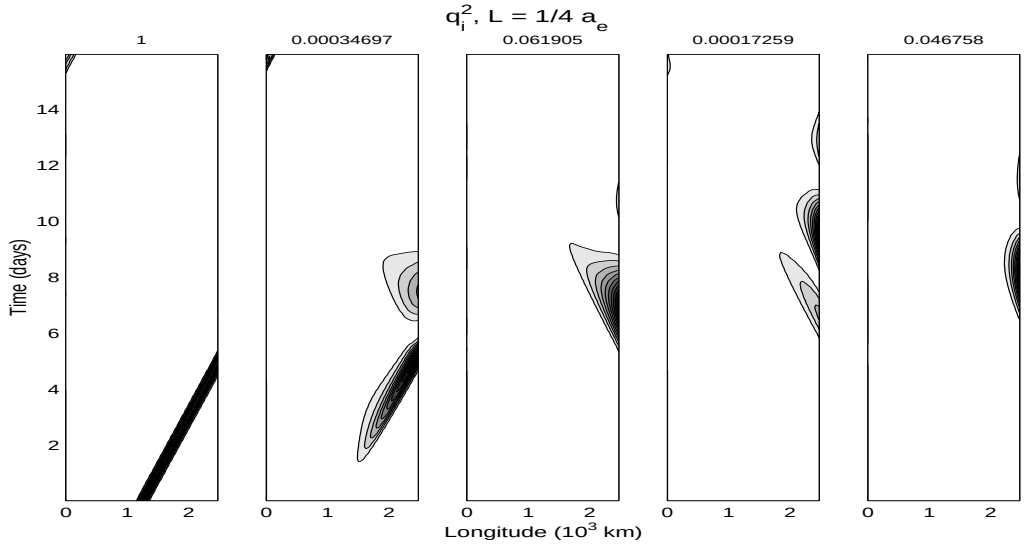

Figure 18: The magnitude squared of the projection of the Kelvin wave disturbance on the first five modes of the equatorial region for an initial disturbance with $L = 1/4\, a_e$. The number at the top of each panel represents $\max(q_i^2)/(\max q_0^2)$. The mode number, i, counts from zero to four, left to right. For all panels there are ten equally spaced contours.

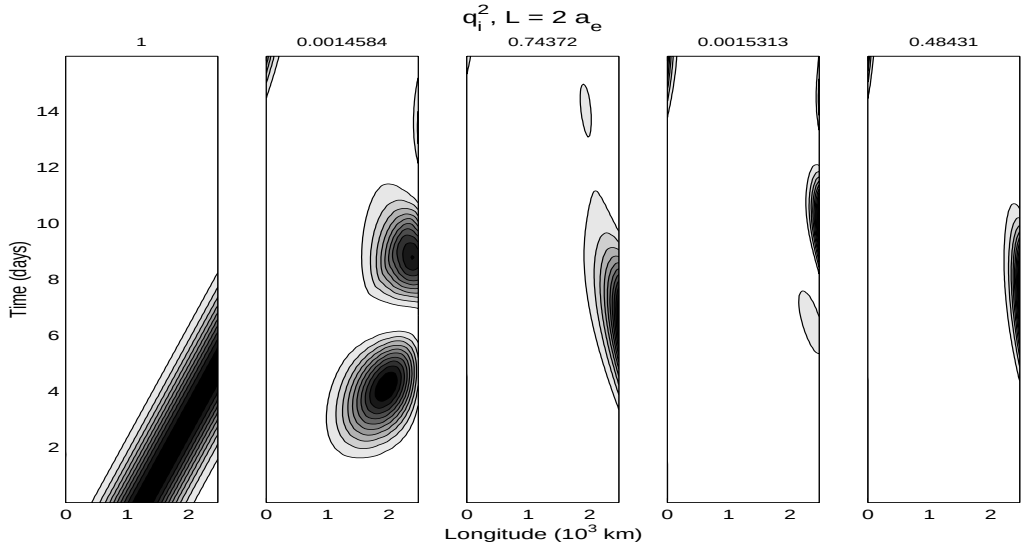

Figure 19: The magnitude squared of the projection of the Kelvin wave disturbance on the first five modes of the equatorial region for an initial disturbance with $L = 2\, a_e$. The number at the top of each panel represents $\max(q_i^2)/\max(q_0^2)$. The mode number counts from zero to four to the right. Notice the strong projection into Rossby mode one as the disturbance encounters the boundary. There are ten equally spaced contours for each panel.

The same procedure was performed with the initial disturbance with a length scale of $L = 2\,a_e$, and the results are in Figure 19. Again we can see that the initial disturbance is a pure equatorial Kelvin mode prior to reflection. However, after reflection the solution projects into the first and third Rossby modes, and these projections have speeds consistent with the appropriate Rossby mode wave speeds. Again the odd numbered modes corresponding to odd y structure are only excited because of numerical inaccuracies.

A discussion of incident waves on the eastern boundary of an equatorial basin is found in [8]. Philander shows that waves of frequency close to $\sqrt{c\beta}$ (the Kelvin and mixed modes) transmit their energy to coastally trapped disturbances of the form

$$v = A\sqrt{y}\exp\left[i\left(\sigma t - \frac{\sigma y}{c} + \frac{\beta x}{2\sigma}\right) - \beta y\frac{L_x - x}{c}\right].$$

We see that eastward-propagating equatorially-trapped waves do not transfer their energy to a coastally-trapped Kelvin waves, but rather a coastally-trapped Kelvin-like wave. Philander also shows that as the frequency of the incident Kelvin wave decreases more energy is reflected as Rossby waves, but there is always a finite amount of energy that is reflected as coastally trapped waves. This is shown by fixing σ in the dispersion relation, (8), and solving for all the possible k's by letting n vary. We find that there is always an infinite number of coastally trapped waves, imaginary k's, for a given σ.

References

[1] S. E. Zebiak and M. A. Cane, "A model el nino-southern oscillation," Mon. Wea. Rev. **115**, 2262 (1987).

[2] A. E. Gill, "Some simple solutions for heat-induced tropical circulation," Quart. J. Roy. Meteorol. Soc. **106**, 447 (1980).

[3] D. S. Battisti, "Dynamics and thermodynamics of a warming event in a coupled tropical atmoshpere-ocean model," jas **45**, 2889 (1988).

[4] M. J. Suarez and P. S. Schopf, "A delayed oscillator for enso," J. Atmos. Sci. **45**, 3283 (1988).

[5] F. Jin, "An equatorial ocean recharge paradigm for enso. part i: Conceptual model," J. Atmos. Sci. **54**, 811 (1997).

[6] F. Jin, "An equatorial recharge paradigm for enso. part ii: A stripped-down coupled model," J. Atmos. Sci. **54**, 830 (1997).

[7] A. E. Gill, *Atmoshpere-Ocean Dynamics* (Academic Press, San Diego, 1982).

[8] S. G. Philander, *El Nino, La Nina, and the Southern Oscillation* (Academic Press, San Diego, 1990).

Effect of bottom topography on roll wave instabilities.

Shreyas Mandre

1 Introduction

Turbulent flow over a sloping bottom becomes unstable if the Froude number becomes greater than a critical value. The basic mechanism of the instability was discovered by Jeffreys [1]. The instability arises when the velocity of the friction dominated flow becomes greater than twice the propagation velocity of the shallow water waves. The unstable uniform flow breaks down in a series of breaking waves or bores. Under favorable conditions these waves are more or less periodic and are called roll-waves. Dressler [2] constructed nonlinear, periodic solutions using shallow water equations with a turbulent bottom drag term. This solution consist of piecewise smooth profiles separated by discontinuities representing the bores. Novik [3] proposed a Burger's equation with a linear amplification term added to it to describe the roll-waves. Needham and Merkin [4] added a diffusive term to the momentum equation and were able to show that continuous roll-wave solutions exist for when the uniform flow is unstable. Kranenburg [5] showed that the modified Burger's equation proposed by Novik can be obtained using a short wave expansion of the shallow water equations with turbulent drag. Yu et. al. [6] used multiple scales to do a weakly nonlinear analysis of the problem and arrived at a generalised Kuramoto-Sivashinsky (GKS) equation to describe the amplitude evolution.

However, in reality the bottom topography is rarely flat. This project attempts to understand the phenomenon in the presence of a periodic bottom topography superposed on a constant slope. There is also an important limitation about Kranenburg's model for roll waves, i.e. the modified Burger's equation is valid only for short waves. Yu et. al. did a multiple scale expansion for long waves, however they had to mix orders to arrive at the GKS equation. We try to derive a more general nonlinear evolution equation for the amplitude of the roll wave instability to address these problems and to include the effect of a periodically varying bottom topography.

2 Formulation

The governing equations for this problem are the Navier-Stokes equations for fluid flow. However, the problem can be simplified by making a shallow water asuumption. The

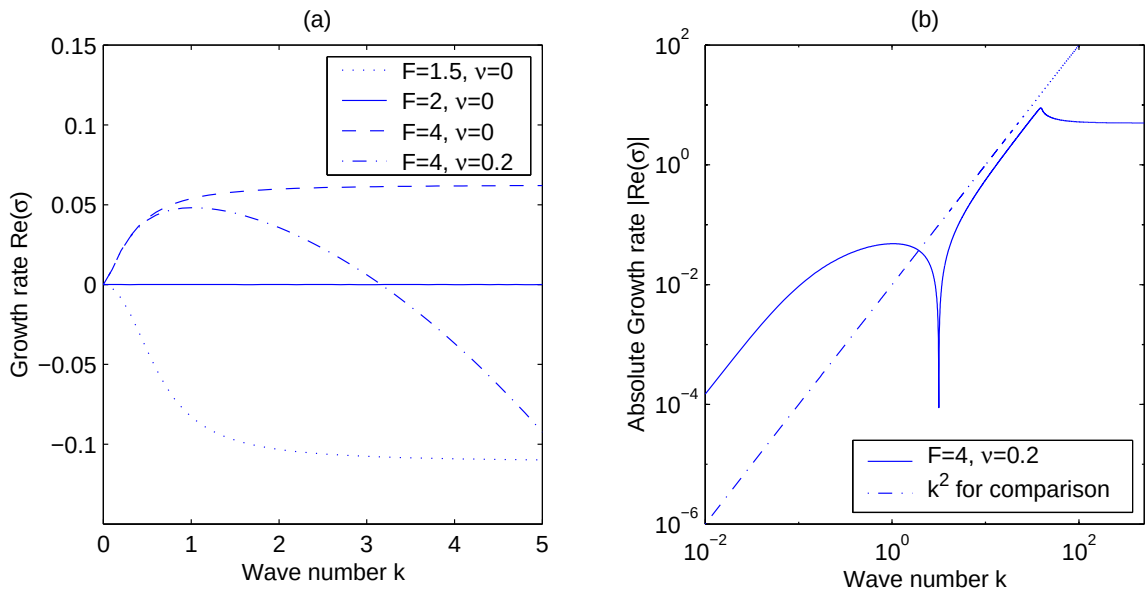

Figure 1: Growth rate against wave number (a) Linear scale (b) Logarithmic scale.

equations thus simplify to

$$u^*_{t^*} + u^* u^*_{x^*} + g h^*_{x^*} \cos\theta + g \zeta^*_{x^*} \cos\theta = g \sin\theta + D^* + \frac{\nu^*}{h^*}(u^*_{x^*} h^*)_{x^*}, \tag{1}$$

$$h^*_{t^*} + (u^* h^*)_{x^*} = 0, \tag{2}$$

where u^* is the fluid velocity, h^* is the fluid layer height, x^* is the coordinate down the slope, ζ^* is the periodic superposed bottom undulation, ν^* is the viscosity, g is acceleration due to gravity and θ is the angle the slope makes with the horizontal. We use an empirical form for the turbulent bottom drag D^* given by

$$D^* = C_f \frac{u^*|u^*|}{h^*}, \tag{3}$$

where C_f is the friction factor. The equations are non-dimensionalized using

$$x^* = xH \cot\theta, \tag{4}$$

$$u^* = uU, \tag{5}$$

$$h^* = hH, \tag{6}$$

$$\zeta^* = \zeta H, \tag{7}$$

$$t^* = \frac{H \cot\theta}{U} t, \tag{8}$$

where H is the height of the fully developed water stream and U is it's speed given by

$$U = \left(\frac{gH \sin\theta}{C_f} \right)^{1/2}. \tag{9}$$

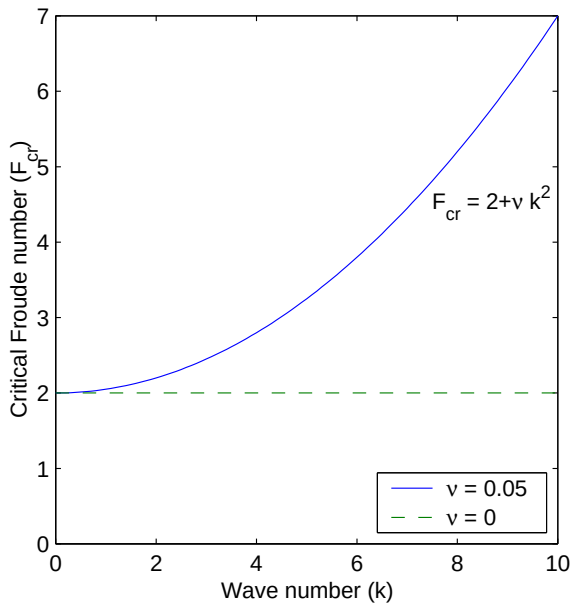

Figure 2: Critical Froude number as a function of wave number for the inviscid and viscous case.

The non-dimensional form of the governing equations are

$$F^2\left(u_t + uu_x\right) + h_x + \zeta_x = 1 - \frac{u|u|}{h} + \nu u_{xx}, \tag{10}$$

$$h_t + (uh)_x = 0. \tag{11}$$

Here F is the Froude number, which is the ratio of the steady state speed of the stream to the speed of gravity waves and ν is the inverse Reynolds number, which is the ratio of the viscous terms to the inertial terms.

$$F = \frac{\tan\theta}{C_f} = \left(\frac{U^2}{gH\cos\theta}\right)^{1/2}, \tag{12}$$

$$\nu = \frac{\nu^*}{UL} = \nu^*\left(\frac{\sin^3\theta}{C_f H^3 g\cos^2\theta}\right)^{1/2}. \tag{13}$$

3 Case $\zeta = 0$ revisited

3.1 Linear stability

The first natural thing to do is a linear stability analysis for the system above for a plane sloping bottom about the basic state $u = h = 1$ [1]. Representing the perturbed variables by

$$u = 1 + u' e^{\sigma t + \iota k x}, \tag{14}$$

$$h = 1 + h' e^{\sigma t + \iota k x}, \tag{15}$$

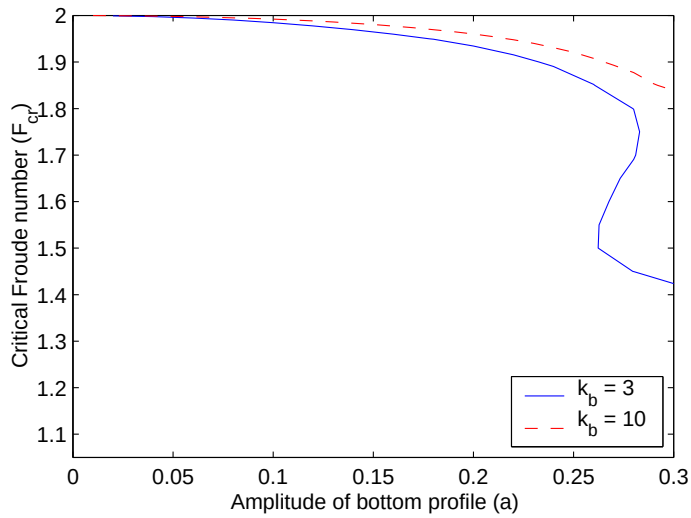

Figure 3: Neutral curve for two different wave number of bottom topography (k_b) for the case $\nu = 0.1$ and $K = 10^{-3}$

where σ is the complex growth rate of the disturbance and k is its wave number. The (linearised) governing equations now become

$$F^2(\sigma + \iota k + 2 + \nu k^2)u' + (\iota k - 1)h' = 0, \tag{16}$$

$$\iota k u' + (\sigma + \iota k)h' = 0. \tag{17}$$

Thus for solutions to exist the following condition must be satisfied:

$$F^2(\sigma + \iota k)^2 + (2 + \nu k^2)(\sigma + \iota k) + \iota k + k^2 = 0 \tag{18}$$

This is quadratic in $(\sigma + \iota k)$ and gives the solutions

$$\sigma = -\iota k - \frac{2 + \nu k^2}{2F^2} \pm \sqrt{\frac{(2 + \nu k^2)^2}{4F^4} - \frac{k^2 + \iota k}{F^2}}. \tag{19}$$

For the critical case, we put $\sigma = \iota \omega_{cr}$ and decomposing into real and imaginary parts gives

$$\omega_{cr} = -k - \frac{k}{2 + \nu k^2}, \tag{20}$$

$$F_{cr} = 2 + \nu k^2, \tag{21}$$

where F_{cr} is the critical Froude number. Fig. 1 illustrates the growth rate ($Re(\sigma)$) as a function of the wave number. It can be seen that for the inviscid case ($\nu = 0$) all the wave numbers become unstable at $F = 2$. The neutral curve is shown in Fig. 2. Everything above the curve is unstable while everything below is stable. For the inviscid case, there is no preferred wave number selection as can be seen from the neutral curve. If we expand the growth rate σ for small k (i.e. for long waves), we get

$$\begin{aligned} \sigma &\sim \iota k \left[-\frac{3}{2} + k^2 \left(\frac{F^2(F^2 - 4)}{16} + \frac{\nu}{4} \right) \right] \\ &+ \left[\frac{F^2 - 4}{8} k^2 - \left(\frac{F^2(F^2 - 4)(5F^2 - 4)}{128} + \frac{3F^2 - 4}{16} \nu \right) k^4 \right] + O(k^5) \end{aligned} \tag{22}$$

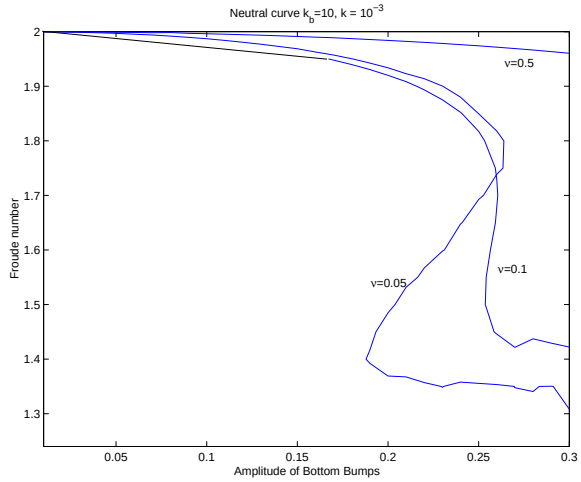

Figure 4: Neutral curve for different viscosities for the case k_b=10, K=10^{-3}

which for near critical cases ($F = 2 + \epsilon F_1$, $\epsilon \ll 1$) become

$$\sigma \sim \iota k \left[-\frac{3}{2} + k^2 \left(F_1 \epsilon + \frac{\nu}{4} \right) \right] + \left[\frac{\epsilon F_1 k^2}{2} - k^4 \left(2\epsilon F_1 + \frac{\nu}{2} \right) \right] \tag{23}$$

For large k it gives

$$\sigma \sim -\frac{1}{\nu} \tag{24}$$

However, it can be seen from Fig. 1 (b) that for not so large values of k, viscosity damps the system and the growth rate falls like k^2. If ν is small, this k^2 damping is dominantly visible.

3.2 Nonlinear analysis

Now that it is known that the uniform flow is unstable if the Froude number is greater than 2, there have been efforts to model the evolution of the roll waves. Dressler [2] proved in the inviscid case, no steadily propagating continuous solutions exist for this problem. He constructed periodic, piecewise smooth profiles connected by shocks as solutions to the nonlinear equations. However, he did not consider the evolution of the steady flow to these roll waves. Which of the Dressler's uncountably many profiles does a initial condition evolve to is still an unsolved problem. Kranenburg [5] derived a modified Burgers equation to describe the time evolution of roll waves on a flat sloping bottom. His idea was to use multiple scales in time

$$\chi = \frac{x - ct}{\epsilon} \qquad \text{where } c = 1 + \frac{1}{F} \tag{25}$$

$$\tag{26}$$

and expand the variables as

$$u = 1 + \epsilon U(\chi, t,) \tag{27}$$
$$h = 1 + \epsilon H(\chi, t) \tag{28}$$
$$\nu = \epsilon \nu_1 \tag{29}$$

to get an nonlinear evolution equation for U and H as

$$H = FU \tag{30}$$
$$2U_t + 3UU_\chi + \frac{2-F}{F^2}U = \frac{\nu_1}{F^2}U_{\chi\chi} \tag{31}$$

If we do a linear stability analysis of it, we get the dependence of growth rate on wave number as

$$Re(\sigma) = \frac{(F-2)}{2F^2} - \frac{\nu_1 k^2}{2F^2} \tag{32}$$

We know from the linear stability analysis of the exact problem that for small wave numbers, the dependence of growth rate on wave number is quadratic (Eqn. 22). However, this evolution equation concentrates only on the short waves and thus is inadequate in representing the long waves. The discrepancy can be solved if we make a multiple scale analysis in space as well as time as shown in the later sections.

Kranenburg [5] solved this equation with periodic boundary condition to observe the nonlinear effects. The equation is unconditionally ill-posed for non-zero periodic initial conditions on U, as proved by him. He showed that continuous periodic initial conditions lead to formation of a shock that propagates with a constant speed proportional to the average value of U across the shock. Thus shocks with greater averages propagate faster and combine with smaller shocks ahead of them which further increases the amplitude of the shock and consequently its speed. This phenomenon was termed as wave coarsening because due to merging of shocks, after a long enough time, the solution develops into a single discontinuity periodic with the largest harmonic wave present in the initial condition.

Recently Yu et.al. [6] used multiple scales in space and time and came up with a GKS equation given by

$$F^2(2u_t + 3uu_x) + 2F(F-2)u_{xx} + 2\nu u_{xxx} + 4\nu u_{xxxx} = 0 \tag{33}$$

which is valid only for near critical cases. A linear stability analysis around $u = 1$ gives for growth rate gives

$$\sigma = \frac{F-2}{F}k^2 - \frac{2\nu}{F^2}k^4 + \iota k\left(-\frac{3}{2} + \frac{\nu k^2}{F^2}\right) \tag{34}$$

This compares well with the linear stability results of the full problem. However, it has a very limited range of validity. We know that the descent of growth rate with wave number due to viscosity is like k^2 and not k^4 as proposed by Yu et. al. Also in the limiting case of no viscosity, the growth rate saturates for large values of k, whereas for the GKS it grows indefinitely. All this adds up to concluding that though the GKS has features that agree with the linear stability, it does so only for a very restricted range of wave numbers very

close to zero. Also, Yu et. al. had to use the technique of mixing orders to arrive at this equation.

In this article, we try to address this problem of deriving a nonlinear evolution equation for near critical roll waves. A general case with a sinusoidal bottom topography superposed over an incline is considered. A nonlinear long wave equation for the case of small but fast varying bottom profile, small viscosity and small amplitude of the disturbance is considered. The results of the linear stability of the equation and the original shallow water equations are compared. A linear stability of the shallow water equations is done using numerical techniques. We try to construct the neutral stability curves in the Froude number and amplitude of bottom topography plane for various values of the other parameters and the effect of each of these parameters is studied. The results given by the linear analysis of the long wave equation are compared with the numerical analysis of the full equations and good agreement is obtained.

4 Case $\zeta \neq 0$: Numerical study

Although it is easiest to study the roll wave instability on flat sloping bottom, in real world, the bottom is hardly flat. Rivers, gorges, flumes all have a slightly sloping bottom superposed with a profile that varies on all length scales, from ripples to dunes and anti-dunes. In efforts to analyse such systems it is essential to first study how the flow is modified due to these bottom profiles. Intuitively, if the bottom is a periodic superposition over a flat incline, the solution is also expected to be periodic with the bottom. However, this periodic flow can become unstable in some cases and the solution may evolve into a different kind of flow.

We start with a numerical linear stability analysis of this system in which our aim will be to find the stability boundary of the system. It is known from the flat incline case that the flow becomes unstable for Froude number exceeding 2. For small perturbations of the bottom from being a flat incline, this condition will be slightly modified. However the case of superposition of a finite amplitude bottom profile on the incline still remains to be studied. Section 4.1 does this. After identifying the unstable region in the parameter space, in section 4.5, we do a numerical time integration of the shallow water equations to see where the system evolves to in case of an instability. Then we present the derivation and the comparison with linear theory of the long wave equation in section 5. Finally, we close with a discussion and conclusions in 6.

4.1 Linear stability

We attempt to do a linear stability analysis in the case with periodically superposed bottom topography. The basic stages in this analysis are:

- Solve for the basic state. This is done by assuming that the basic state is also periodic with the same period as the bottom topography. Thus we can use a truncated Fourier series to approximate the steady state solution.
- Performing a linear stability analysis of this system about the basic state so found, we try to evaluate the growth rates and the corresponding disturbances.

4.1.1 Basic state

The basic state $\overline{u}$ and $\overline{h}$ satisfies the equations (assuming $u > 0$)

$$F^2\overline{u}\overline{u}_x + \overline{h}_x + \zeta_x = 1 - \frac{\overline{u}^2}{\overline{h}} + \nu\frac{(\overline{u}_x\overline{h})_x}{\overline{h}}, \tag{35}$$

$$\overline{u}\overline{h} = 1, \tag{36}$$

from which $\overline{h}$ can be eliminated to give

$$\left(F^2\overline{u} - \frac{1}{\overline{u}^2}\right)\overline{u}_x + \zeta_x + \overline{u}^3 - 1 = \nu\overline{u}\left(\frac{\overline{u}_x}{\overline{u}}\right)_x. \tag{37}$$

We use the following form of bottom topography.

$$\zeta(x) = a\cos k_b x, \tag{38}$$

where k_b is the wavenumber of the bottom topography and expand the basic state as

$$\overline{u} = \sum_{j=-N+1}^{N} \tilde{u}_k e^{\iota k_b j x}. \tag{39}$$

We can easily solve for $\tilde{u}_k$ substituting Eqn. 39 in Eqn. 37 using Newton's iterations.

4.1.2 Perturbation analysis

Let us represent the perturbations by $u'e^{\sigma t}$ and $h'e^{\sigma t}$. The perturbed equation now becomes

$$\left(\overline{u}u'\right)_x + F^{-2}\left(h'_x + 2\overline{u}^2u' - \overline{u}^4h' - \frac{\nu}{\overline{h}}\left(\overline{u}_xh' + \overline{h}u'_x\right)_x + \frac{\nu h}{\overline{h}^2}\left(\overline{h}\overline{u}_x\right)_x\right) = -\sigma u', \tag{40}$$

$$\left(\overline{u}h' + \overline{h}u'\right)_x = -\sigma h'. \tag{41}$$

Representing the perturbed variables in a truncated Fourier series with a block wave number K

$$u' = \sum_{j=-N+1}^{N} u_j e^{\iota j k_b x + \iota K x}, \tag{42}$$

$$h' = \sum_{j=-N+1}^{N} h_j e^{\iota j k_b x + \iota K x}, \tag{43}$$

and converting the operators to Fourier space as well, we get an algebraic eigenvalue equation for σ. The real part of σ gives the growth rate and the system is unstable if it is positive. We have the following parameters in our problem:

1. Froude number (F),
2. Wave number of bottom topography (k_b),
3. Amplitude of bottom topography (a),
4. Block wave number (K) and
5. Viscosity (ν).

4.2 Effect of block wave number (K)

The block wave number is just a means of analysing the wavenumbers which are not integer multiples of wave number of topography. We only need to consider

$$-\frac{k_b}{2} < K \leq \frac{k_b}{2} \tag{44}$$

Values of K outside this range do not give any additional information. It is seen that the case for $K = 0$ always gives an eigenvector with a zero growth rate. The spectrum of this eigenvector has a peak at $k = 0$. The existence of this eigenvector reflects invariance in the system with respect to some parameter. In this case, the invariance is that of the flow rate. The dependence is shown in Fig. 8 for a stable case and 9 for an unstable case. Both the figures are for near critical cases and small bottom profile, though the qualitative behaviour is similar for far from critical cases and O(1) bottom topography as well.

4.3 Effect of wave number of bottom topography

Fig. 3 shows the effect of the wave number of bottom topography on the neutral curve in the F-a plane. It is seen that the system becomes unstable for $F < 2$ because of the presence of the bottom topography. Also, the case with $k_b = 10$ becomes unstable for F much less than 2 for relatively large amplitudes. In general, the case with large k_b has a more severe effect on destabilizing the system.

4.4 Effect of viscosity

The neutral curve for different viscosities is plotted in Fig. 4. It can be seen that the effect of viscosity on the stability for small amplitudes of the bottom topography is not monotonous. The system is most unstable for a finite value of the viscosity. For large amplitudes, however, the system is always more unstable for smaller values of viscosity. It can also be seen that for certain relatively larger amplitudes of the bottom topography, there is a window in the Froude numbers much before $F = 2$ where the system is unstable. The range of amplitudes for which this happens grows as the viscosity is decreased.

4.5 Integration in time of the governing equations

A RK4 time integration scheme is used to integrate Eqns. 10 and 11 in time on a domain of unit length and with a bottom topography of the form given by Eqn. 38. Periodic conditions were imposed on the boundaries and the initial conditions used were of the form

$$u(x, t = 0) = 1 + A_1 \sin(2\pi x) + B_1 \sin(2\pi k_b x) \tag{45}$$

$$h(x, t = 0) = 1 + A_2 \sin(2\pi x) + B_2 \sin(2\pi k_b x) \tag{46}$$

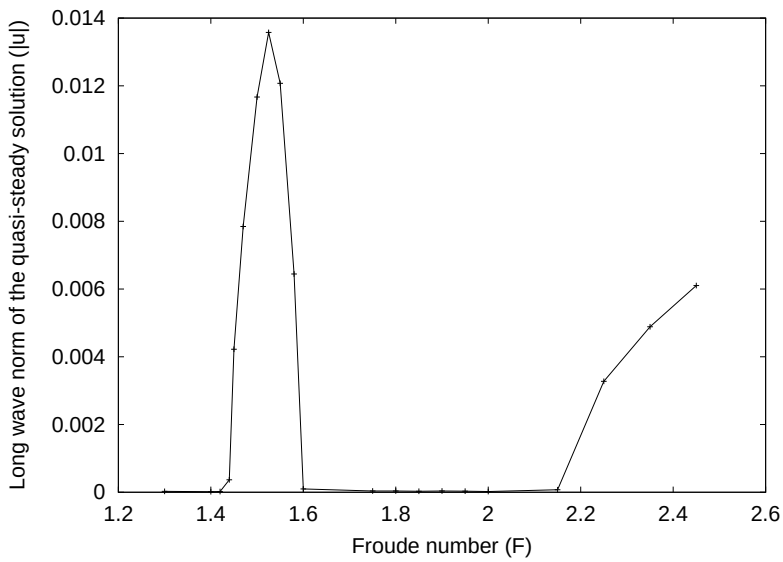

Figure 5: Bifurcation diagram for the case a=0.27, $k_b = 10$, $\nu = 0.005$

where A_1, A_2, B_1 and B_2 are appropropriately chosen numbers. A long wave norm was defined as follows:

$$u^j_{avg} = \int_{\frac{2\pi j}{k_b}}^{\frac{2\pi(j+1)}{k_b}} u(x)dx \qquad j = 0, 1, 2, \ldots, N-1 \tag{47}$$

$$\overline{u}_{avg} = \frac{1}{N}\sum_{j=0}^{N-1} u^j_{avg} \tag{48}$$

$$||u||_{Longwave} = \left[\frac{1}{N}\sum_{m=0}^{N-1}(u^m_{avg} - \overline{u}_{avg})\right]^{1/2} \tag{49}$$

Fig. 5 shows the saturated long wave norm for the case $a = 0.27$, $k_b = 10$ as a function of the Froude number. A window of Froude numbers much less than 2 can be clearly seen to have a non-zero saturated amplitude. The value of ν is 0.005.

5 Long Wave Analysis

The case of $O(1)$ bottom topography varying on a $O(1)$ length scale renders itself difficult to analysis. The case of a small but fast varying bottom topography will be considered. i.e.

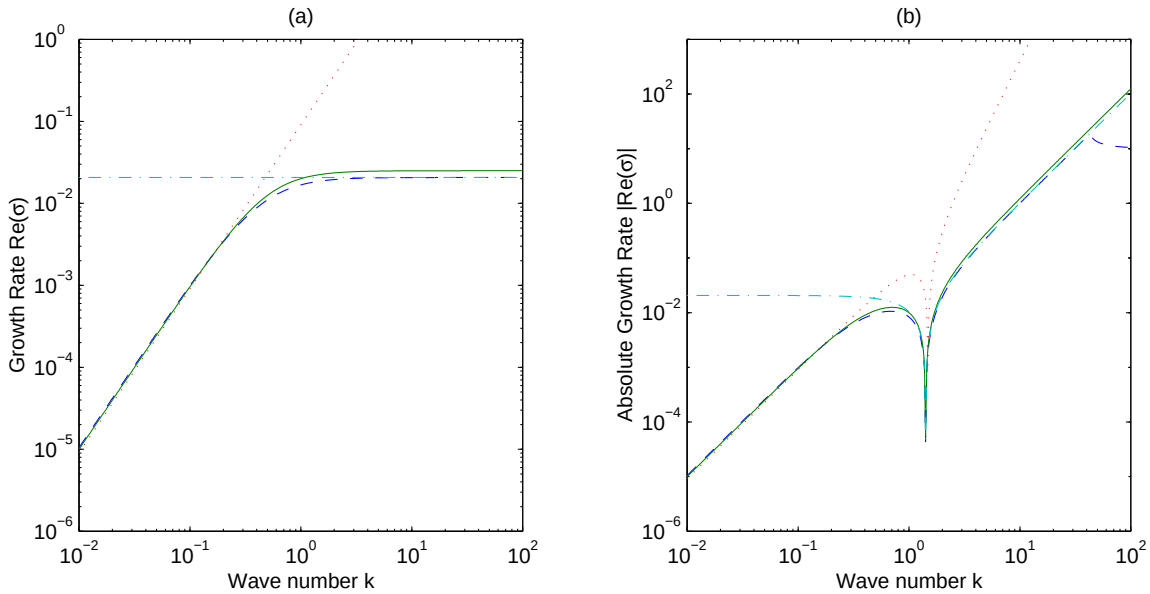

Figure 6: Linear Stability growth rates for (a) Inviscid case, $F = 2.1$, (b) Viscous case, $F = 2.1$, $\nu = 0.1$. Dashed line is using the exact shallow water equations, solid line using the long wave equation, dash-dots using Kranenburg's modified Burgers equation and dotted line using Yu et. al.'s GKS equation.

ζ is a function of $k_b x$ only. Assuming

$$k_b \gg 1 \tag{50}$$

$$\nu = \frac{\nu_1}{k_b} \tag{51}$$

$$\tau = \frac{t}{k_b} \tag{52}$$

$$\eta = k_b x \tag{53}$$

$$\zeta = \frac{\zeta_1}{k_b} = a_1 \cos(\eta) \tag{54}$$

$$\tag{55}$$

and expanding the variables as

$$F = F_0 + \frac{F_1}{k_b} + \dots \tag{56}$$

$$u = 1 + \frac{u_0(\eta) + U_0(x,t,\tau)}{k_b} + \frac{u_1(\eta) + U_1(x,t,\tau)}{k_b^2} + \dots \tag{57}$$

$$h = 1 + \frac{h_0(\eta) + H_0(x,t,\tau)}{k_b} + \frac{h_1(\eta) + H_1(x,t,\tau)}{k_b^2} + \dots \tag{58}$$

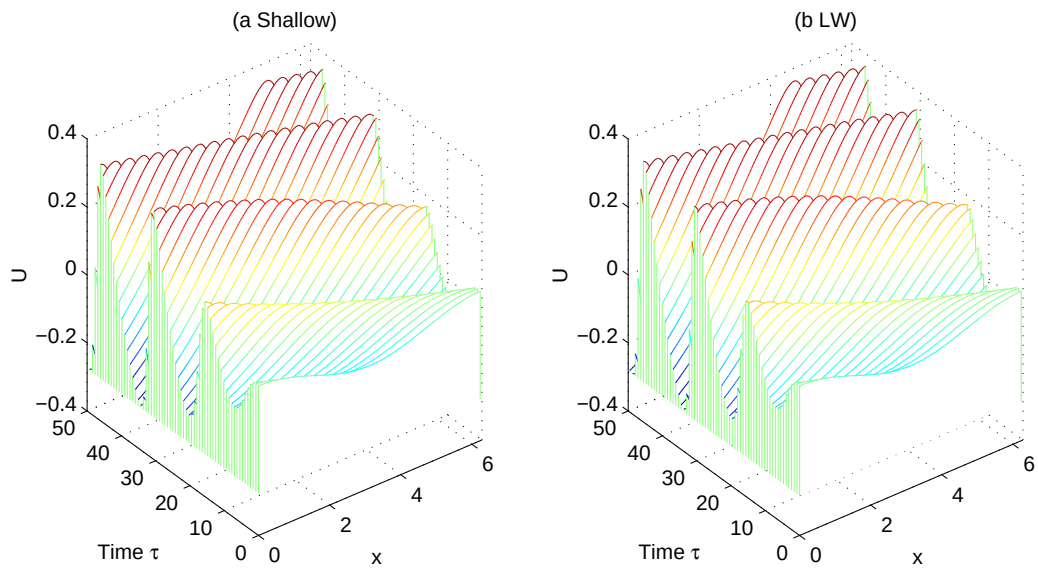

Figure 7: Comparison of numerical solutions for (a) Shallow water equations and (b) Long wave equation for the parameters $F_1 = 1$, $\nu_1 = 1$, $k_b = 64$ and $a_1 = 0$.

we get to various orders ($\epsilon = 1/k_b$)

$$\mathrm{O}(\epsilon) \quad : \quad F_0^2 u_{0\eta} + h_{0\eta} + \zeta_{1\eta} = \nu u_{0\eta\eta} \tag{59}$$

$$u_{0\eta} + h_{0\eta} = 0 \tag{60}$$

$$\tag{61}$$

which gives

$$u_0 = R_0 \cos(\eta + \phi_0) \tag{62}$$

$$h_0 = -R_0 \cos(\eta + \phi_0). \tag{63}$$

where

$$R_0 = \left(\frac{a_1^2}{(F_0^2 - 1)^2 + \nu_1^2} \right)^{1/2} \tag{64}$$

$$\phi_0 = tan^{-1} \left(\frac{\nu_1}{F_0^2 - 1} \right) \tag{65}$$

$$\begin{aligned} \mathrm{O}(\epsilon^2) \quad : \quad F_0^2 u_{1\eta} + h_{1\eta} - \nu_1 u_{1\eta\eta} = & - \left[F_0^2 (U_{0t} + U_{0x}) + H_{0x} + 2U_0 - H_0 \right] \\ & + \frac{F_0^2 R_0^2}{2} \sin(2\eta + 2\phi_0) + F_0^2 R_0 U_0 \sin(\eta + \phi_0) \\ & + 2F_0 F_1 R_0 \sin(\eta + \phi_0) - \nu_1 R_0^2 \sin^2(\eta + \phi_0) \end{aligned} \tag{66}$$

$$\begin{aligned} u_{1\eta} + h_{1\eta} = & - \left[H_{0t} + H_{0x} + U_{0x} \right] \\ & - [R_0^2 \sin(2\eta + 2\phi_0) + (U_0 - H_0) R_0 \sin(\eta + \phi_0)] \end{aligned} \tag{67}$$

Taking the average of these equations:

$$F_0^2(U_{0t} + U_{0x}) + H_{0x} + 2U_0 - H_0 = -\frac{\nu_1 R_0^2}{2} \tag{68}$$

$$H_{0t} + H_{0x} + U_{0x} = 0 \tag{69}$$

This gives the neutral stability condition

$$F_0 = 2 \tag{70}$$

$$H_0(\xi) = 2U_0(\xi) + \frac{\nu_1 R_0^2}{2} \tag{71}$$

where ξ is the coordinate moving with the wave given by

$$\xi = x - \frac{3}{2}t \tag{72}$$

Here we have ignored the slower wave as it decays on a time scale of $\mathrm{O}(t/\epsilon)$. For the periodic variation, the solution can be expressed as

$$u_1 = A_1 \cos(\eta + \phi_{11}) + A_2 \cos(2\eta + \theta_{11}) \tag{73}$$

$$h_1 = B_1 \cos(\eta + \phi_{12}) + B_2 \cos(2\eta + \theta_{12}) \tag{74}$$

where A_1, A_2, B_1 and B_2 need not be evaluated for further progress. Going one more order higher

$$\begin{aligned}
\mathrm{O}(\epsilon^3): \quad & F_0^2 u_{2\eta} + h_{2\eta} - \nu_1 u_{2\eta\eta} = -4\left[u_{1t} + U_{0\tau} + U_{0\xi} + (u_0 u_1 + U_0 u_1)_\eta + U_0 U_{0\xi} + u_0 U_{0\xi}\right] \\
& -4F_1\left[-\frac{1}{2}U_{0\xi} + u_{1\eta} + (u_0 + U_0)u_{0x}\right] - H_{1\xi} - 2(u_1 + U_1) + h_1 + H_1 \\
& -(u_0 + U_0 - h_0 - H_0)^2 + \nu_1\left[-(h_0 + H_0)(u_1 + U_1)_{\eta\eta} - (h_0 + H_0)h_{0\eta}u_{0\eta} + U_{0\xi\xi}\right] \\
& +\nu_1\left[H_{0\xi}u_{0\eta} + (h_0 u_{1\eta} + h_1 u_{0\eta})_x + h_{0\eta}U_{0\xi}\right] \qquad (75) \\
\text{and:} \quad & H_{0\tau} + H_{1t} + u_{2\eta} + h_{2\eta} + U_{1x} + H_{1x} + (U_0 H_0)_\xi \\
& +(u_0 h_1 + U_0 h_1 + u_0 H_1 + h_0 u_1 + H_0 u_1 + h_0 U_1)_\eta = 0 \qquad (76)
\end{aligned}$$

We are only interested in the average of this equation over η which after simplification is

$$\begin{aligned}
4U_{1t} + 4U_{1x} + H_{1x} + 2U_1 - H_1 = & - 4(U_{0\tau} + U_0 U_{0\xi}) + 2F_1 U_{0\xi} - (U_0 + \frac{\nu_1 R_0^2}{2})^2 \\
& - \frac{\nu_1}{2}R_0 A_1 \cos(\theta_{11} + \phi_0) + \frac{\nu_1}{2}R_0^2 H_0 + \nu_1 U_{0\xi\xi} \qquad (77) \\
\text{and } H_{1t} + U_{1x} + H_{1x} = & - [H_{0\tau} + (U_0 H_0)_\xi] \qquad (78)
\end{aligned}$$

U_1 and H_1 can be eliminated from these equations to give the evolution equation for U_0 as

$$4U_{0\tau} + 6U_0 U_{0\xi} - 8U_{0\tau\xi} = 6(U_0^2)_{\xi\xi} + (\nu_1 R_0^2 - 2F_1)U_{0\xi\xi} - \nu_1 R_0^2 U_{0\xi} - \nu_1 U_{0\xi\xi\xi} \tag{79}$$

5.1 Case with flat bottom: $\zeta = 0$

We put $R_0 = 0$ to get the following equation for the evolution of roll waves.

$$4U_{0\tau} + 6U_0U_{0\xi} = 8U_{0\tau\xi} + 6(U_0^2)_{\xi\xi} - 2F_1U_{0\xi\xi} - \nu_1U_{0\xi\xi\xi} \tag{80}$$

Doing a linear stability analysis of Eqn. 80, i.e. replacing the $\partial_\tau \to \sigma_1$ and $\partial_\xi \to k$ gives for the complex growth rate

$$\sigma_1 = \frac{2F_1k^2 + \iota\nu_(k^3}{4 - 8\iota k} \tag{81}$$

$$Re(\sigma_1) = \frac{F_1k^2 - \nu_1k^4}{2 + 8k^2} \tag{82}$$

Thus

$$Re(\sigma_1) \sim \frac{F_1k^2}{2} + \left(2F_1 + \frac{\nu_1}{2}\right)k^4 + \ldots \qquad \text{for } k \ll 1 \tag{83}$$

which agrees with Eqn. 22. Similarly, for short waves, this expression reduces to

$$Re(\sigma_1) \sim -\frac{\nu_1k^2}{8} \qquad \text{for } k \gg 1 \tag{84}$$

which agrees with Kranenburg's results (Eqn. 32).

For the inviscid case, the growth rate saturates to

$$\lim_{k\to\infty} Re(\sigma_1) = \frac{F_1}{8} \tag{85}$$

which agrees with the linear stability results of the shallow water equations. Fig. 6 shows the linear stability growth rates for the four equations, viz. shallow water equations, long wave equation, Kranenburg's modified Burgers equation and Yu et. al's GKS equation. From these results, it is suggestive that the long wave equation is a more general form of the modified Burger's equation and the GKS equation. It has properties that agree extremely well on short and long length scales. One can rescale

$$T = F_1\tau \tag{86}$$

$$V = \frac{U_0}{F_1} \tag{87}$$

to get a one parameter partial differential equation

$$4V_T + 3(V^2)_\xi = 8V_{T\xi} + 6(V^2)_{\xi\xi} - 2V_{\xi\xi} - \frac{\nu_1}{F_1}V_{\xi\xi\xi} \tag{88}$$

5.2 Comparison with numerical calculations

Fig. 7 compares the results of numerical solutions of the shallow water equations with the long wave equations. The parameters are chosen to be very close to the instability and the agreement with the shallow water equations is good. Fig. 8 and 9 show the comparison of the real and imaginary part of the complex growth rate for two cases with a periodic bottom

topography, one stable and other unstable. The agreement is close. For the imaginary part, the leading order term obtained from the phase speed of the wave ($\frac{3k}{2}$) has to be subtracted from the numerically calculated results. This introduces some numerical round off error and the effect is visible for the cases of small wave numbers. It is seen that the error decreases as the allowable numerical tolerance is reduced.

6 Results and Conclusion

We studied the effect of bottom topography on the roll wave instability. It is seen that the flow becomes unstable even for a Froude number less than 2. At small viscosities, there is a range of amplitudes of bottom topography for which the periodic flow becomes unstable for an interval of Froude numbers below 2. We tried to explain this phenomenon for small amplitudes and derived a nonlinear evolution equation for near critical roll waves. The results agree very well with the numerical calculations and the long wave discrepancy in Kranenburg's nonlinear equation is also resolved. The appropriate nonlinear equation for the roll wave instability seems to be Eqn. 79.

7 Acknowledgements

At every step, I was guided by Neil, Bill and Eli and I would like to express me sincere gratitude to them. Their unfaltering faith in me was most important to me. I also thank Paola, Joe (Keller) and Lou for their very instructive discussions. The fellows were an absolute pleasure to be with for the summer. It was because of there constant support and encouragement that kept me going. Ed (Gerber) and Dargan were wonderful house-partners and Chiara was a great office-mate (thanks to her for her random guesses for initial conditions.) I also thank everyone else who was a part of GFD to make it such a wonderful environment for research. Finally, I would like to thank the person at Smith Lab for helping me carry my luggage from Smith lab to Challenger house.

References

[1] H. Jeffreys, "The flow of water in an inclined channel of rectangular bottom," Phil. mag. **49**, 793 (1925).

[2] R. F. Dressler, "Mathematical solution of the problem of roll-waves in inclined open channels," Commun. Pure. Appl. Maths **2**, 149 (1949).

[3] O. B. Novik, "Model description of roll-waves," J. Appl. Math. Mech. **35**, 938 (1971).

[4] D. J. Needham & J. H. Merkin, "On roll waves down an inclined channel," Proc. R. Soc. Lond A **394**, 259 (1984).

[5] C. Kranenburg, "On the evolution of roll waves," J. Fluid Mech. **245**, 249 (1992).

[6] J. Yu, J. Kevorkian & R. Haberman, "Weak nonlinear long waves in chanel flow with internal dissipation," Stud. in Appl. Math. **105**, 143 (2000).

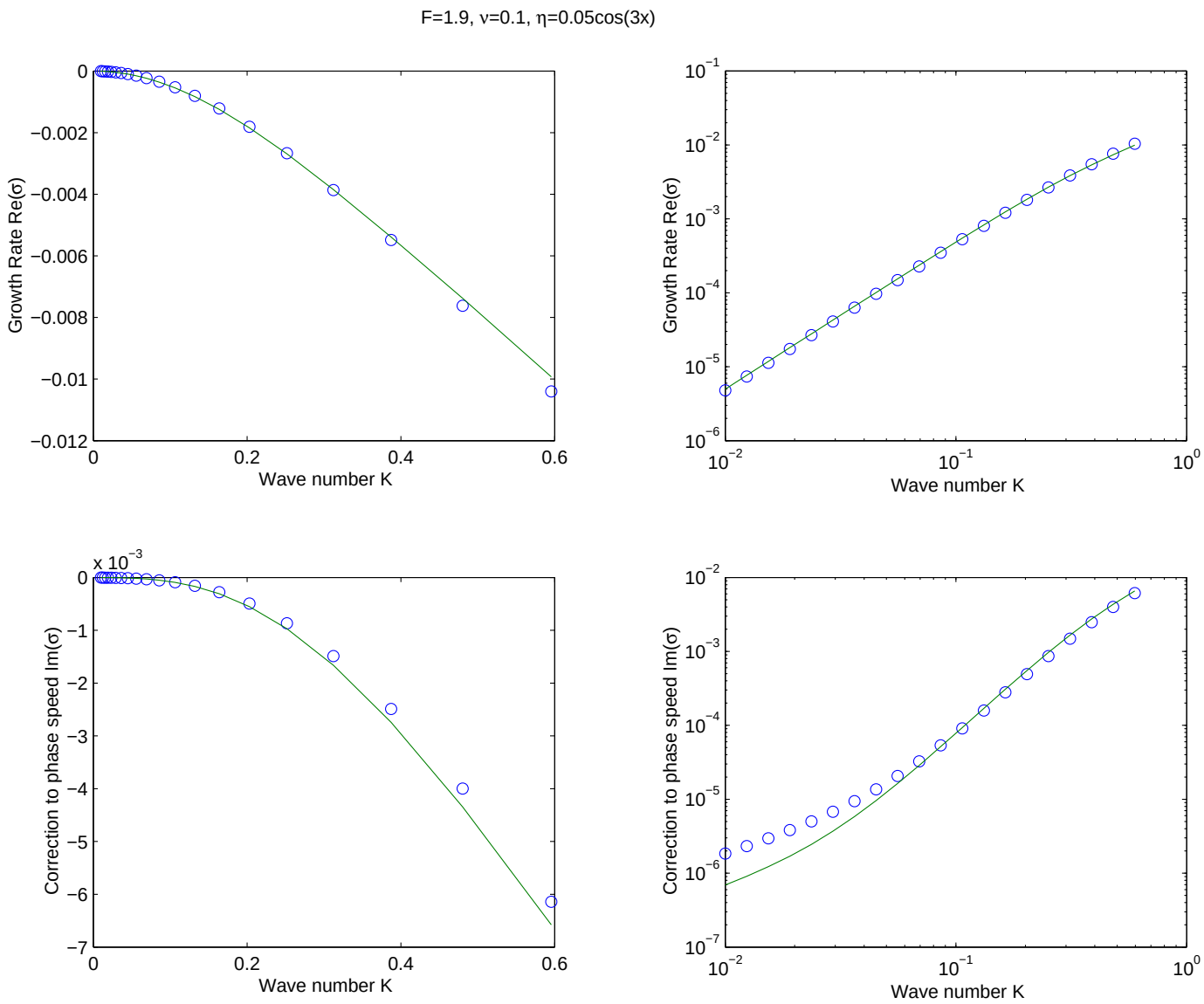

Figure 8: Complex growth rates obtained from numerical stability analysis and long wave asymptotics. Case F =1.9, $\nu = 0.1$, $k_b = 3$, $a = 0.05$. Circles denote numerical calculations and the solid line represents long wave theory.

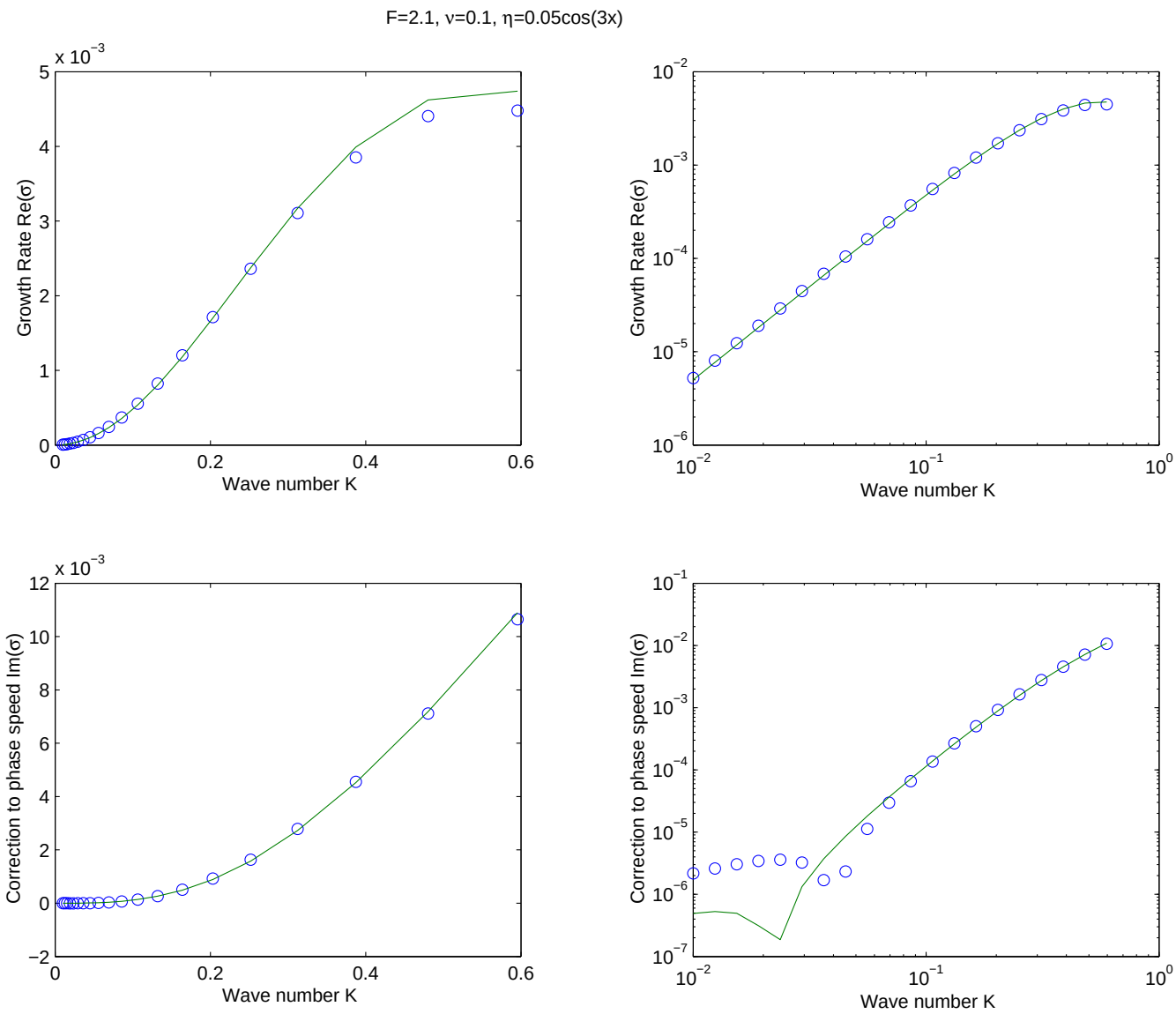

Figure 9: Complex growth rates obtained from numerical stability analysis and long wave asymptotics. Case F =2.1, $\nu = 0.1$, $k_b = 3$, $a = 0.05$. Circles denote numerical calculations and the solid line represents long wave theory.

The Black Hole of Water Vapor and the Asymmetries in the Tropical Circulation

Takamitsu Ito*

1 Introduction

The water vapor (hereafter, WV) satellite images comes from the long wave channel of wavelength 5.7–7.1 [μm]. Images of the earth at these wavelengths do not show any surface features of the earth, since the radiation emitted by the earth's surface at that wave length is entirely absorbed by low-level atmospheric WV. The features that these images reveal are related to planetary scale and synoptic scale variations of WV in the middle and upper troposphere.

Figure 1 is an upper tropospheric WV image taken during the northern hemisphere summer *(obtained from http://kauai.nrlmry.navy.mil/sat-bin/global.cgi)*. Intertropical Convergence Zone (ITCZ) is rich in moisture and is located at approximately 8 degrees latitude. Outside of the narrow band of ITCZ, the air is relatively dry, especially in the winter hemisphere. In Figure 1, there is a region of very low humidity in the tropical Eastern Pacific. It is the "Black Hole" of water vapor in the south of the equator about the same latitude as ITCZ.

Observational studies *[Picon and Desbios [7]; Schmez et al. [9]]* have shown the statistical correlation between the divergence of the large scale circulation and the satellite WV observations. In subsidence conditions, the upper troposphere become dry and the 5.7–7.1 [μm] radiation received by the satellite comes primarily from the relatively warm mid-troposphere. When the large-scale vertical motion is upward, the upper troposphere could become nearly saturated, and the 5.7–7.1 [μm] radiation comes from the relatively cold upper troposphere. In this way the "equivalent blackbody temperature" of the 5.7–7.1 [μm] radiation is a proxy for the vertical motion field. Since the vertical motion field is not directly measurable by any meteorological instrument, WV images can be an useful tool to diagnose the vertical velocity.

The size and the location of the Black Hole is not homogeneous in time and space. The extent and the intensity of the dry region is much greater in the winter hemisphere. The Black Hole tends to appear in the winter hemisphere of approximately the same latitude as the location of the deep convection in ITCZ. These features appears and disappears on the time scale of a few days to a few weeks. Figure 1 is the WV image over the Eastern Pacific from GOES-10. The Black Hole is formed over the Tropical Pacific in the late July,

*with Edwin P. Gerber and Wayne H. Schubert

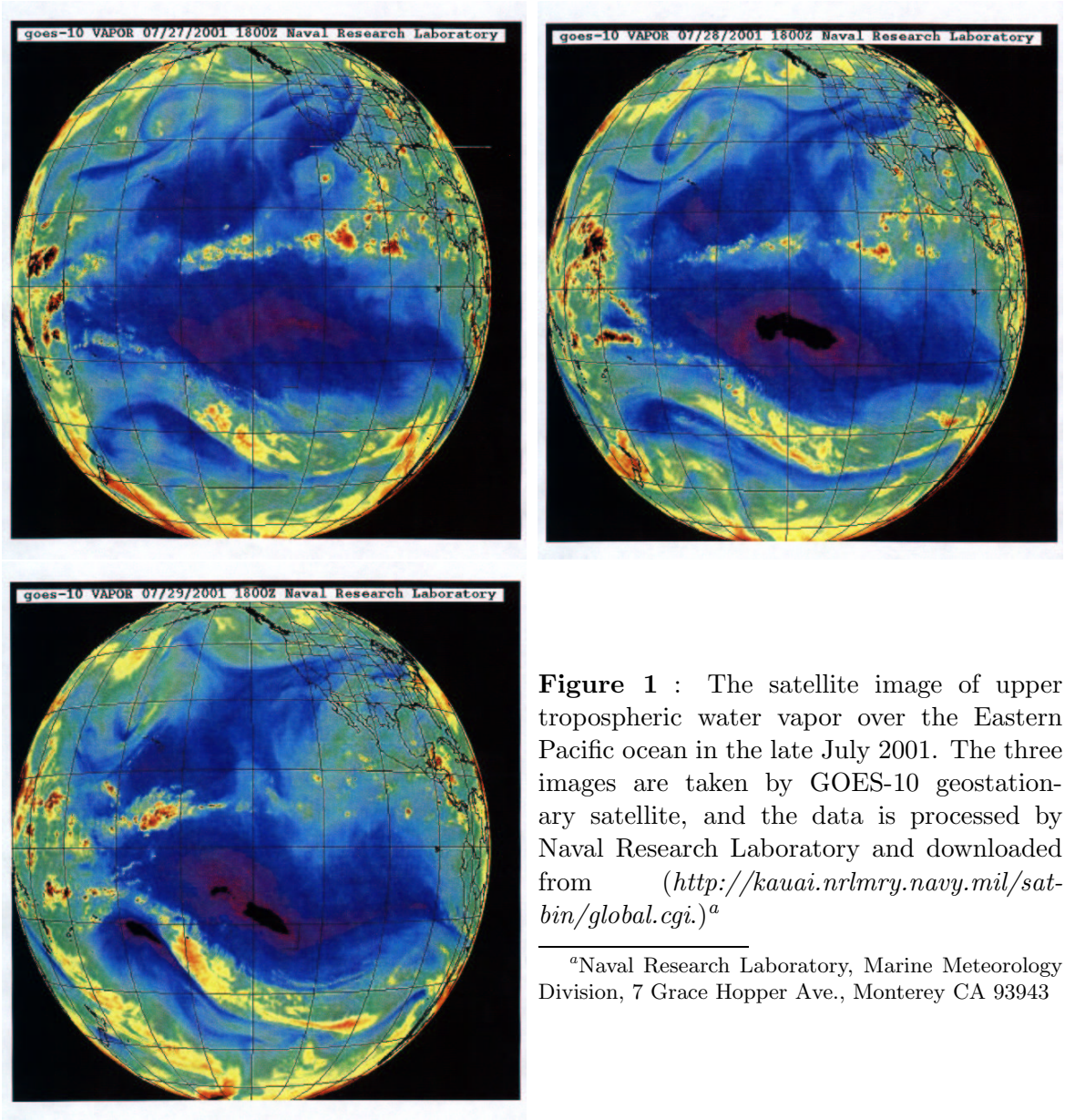

Figure 1 : The satellite image of upper tropospheric water vapor over the Eastern Pacific ocean in the late July 2001. The three images are taken by GOES-10 geostationary satellite, and the data is processed by Naval Research Laboratory and downloaded from (*http://kauai.nrlmry.navy.mil/sat-bin/global.cgi.*)[a]

[a]Naval Research Laboratory, Marine Meteorology Division, 7 Grace Hopper Ave., Monterey CA 93943

2001. What controls the spatial structure and intensity of the Black Hole ? Could we use a simple theory to explain these phenomena ?

This study is an attempt to understand the mechanisms which determines the structure of the Black Hole in the tropical atmosphere. We are particularly interested in the asymmetric structure of the vertical velocity field, assuming that the vertical velocity mainly determines the upper tropospheric WV in tropics. We use the linear shallow water equation on the equatorial $\beta-$plane as a conceptual tool to elucidate the dynamics which give rise to the Black Holes of upper tropospheric WV. We describe the asymmetries in the Hadley circulation and the Walker circulation. Then, we apply the linear theory with somewhat realistic heating and dissipation rates to the tropical circulation forced by ITCZ-type heating.

2 Method

2.1 The Linearized Equatorial β-Plane

Eigenvalue problem of the equatorial β-plane is first formulated and solved by *Matsuno* [5]. Heat-induced, frictionally controlled tropical circulation is studied by *Gill* [4] and others. Similar problem is solved by *Dias et al* [1] in the framework of stratified linear equatorial β-plane.

In this study, we use the equatorial β-plane, linear shallow water model similar to the model of *Gill* [4] as a conceptual tool to understand the governing dynamics. We calculate steady state solutions for the linear primitive equations forced by localized convection and dissipated by linear friction and radiative cooling.

The shallow water system can be considered as the representation of a vertical normal-mode in the stratified primitive equation [*Fulton [2]*]. For simplicity, we assume that the convective heating projects onto the first baroclinic mode only. Furthermore, we linearize the governing equation around the resting basic state. The model is now a single set of linear shallow water equations on the equatorial β-plane.

$$\frac{\partial u}{\partial t} - \beta y v + g\frac{\partial h}{\partial x} = -\epsilon_u u \tag{1}$$

$$\frac{\partial v}{\partial t} + \beta y u + g\frac{\partial h}{\partial y} = -\epsilon_v v \tag{2}$$

$$\frac{\partial h}{\partial t} + \bar{h}\left(\frac{\partial u}{\partial x} + \frac{\partial v}{\partial y}\right) = -\epsilon_h h - S, \tag{3}$$

where u and v are velocity components in the x- and y-directions, respectively, h is the deviation of the fluid depth from the constant mean depth $\bar{h}$. Considering the vertical transform [*Fulton [2]*], the mean depth is given as the equivalent depth for the first baroclinic mode which is $570[m]$. βy is the Coriolis parameter, ϵ_u is the constant for Rayleigh friction, and ϵ_h is the coefficient for Newtonian cooling. We parameterize the deep convection as a mass sink, $S(x, y, t)$.

Before solving (1)–(3) it is convenient to put the problem in nondimensional form. We define $c = (g\bar{h})^{\frac{1}{2}}$ as the constant gravity wave speed based on the mean depth $\bar{h}$. As

a horizontal length scale, let us choose the equatorial deformation radius, $L = (c/\beta)^{\frac{1}{2}}$. Similarly, a unit of time is determined as the time it takes for surface gravity wave to travel a unit of deformation radius, $T = (\beta c)^{-\frac{1}{2}}$. Data from the ITCZ in the Pacific (over the Marshall Islands) and in the Atlantic suggest that, for the first baroclinic mode, $c \approx 7.5 \times 10^1\, m/s$ and $\bar{h} \approx 5.7 \times 10^2\, m$, so that $L \approx 1.8 \times 10^3 km$ and $T \approx 0.28\, day$ [2]. We choose $\bar{h}$ as the unit of depth, so that (1)–(3) reduce to the nondimensional form

$$\frac{\partial u}{\partial t} - yv + \frac{\partial h}{\partial x} = -\epsilon_u u \tag{4}$$

$$\frac{\partial v}{\partial t} + yu + \frac{\partial h}{\partial y} = -\epsilon_v v \tag{5}$$

$$\frac{\partial h}{\partial t} + \frac{\partial u}{\partial x} + \frac{\partial v}{\partial y} = -\epsilon_h h - S \tag{6}$$

where all the independent variables x, y, t, all the dependent variables u, v, h, the parameter ϵ and the function $S(x, y, t)$ are now nondimensional. In the simple case where $\epsilon_u = \epsilon_h = \epsilon$, the system (4)–(6) can also be written in the more compact form

$$\frac{\partial \mathbf{w}}{\partial t} + \mathcal{L}\mathbf{w} = -\epsilon \mathbf{w} - \mathbf{S}, \tag{7}$$

where

$$\mathbf{w}(x,y,t) = \begin{pmatrix} u(x,y,t) \\ v(x,y,t) \\ h(x,y,t) \end{pmatrix}, \quad \mathbf{S}(x,y,t) = \begin{pmatrix} 0 \\ 0 \\ S(x,y,t) \end{pmatrix}, \quad \mathcal{L} = \begin{pmatrix} 0 & -y & \partial/\partial x \\ y & 0 & \partial/\partial y \\ \partial/\partial x & \partial/\partial y & 0 \end{pmatrix}. \tag{8}$$

2.2 Normal Mode Transformation

We solve the model equation (7) using the method of normal mode decomposition. We transform the model in spectral space in x. Defining $\hat{\mathbf{w}}(k, y, t)$ as the Fourier Transform of $\mathbf{w}(x, y, t)$, we can write the Fourier transform pair as

$$\hat{\mathbf{w}}(k,y,t) = \frac{1}{\sqrt{2\pi}} \int_{-\infty}^{\infty} \mathbf{w}(x,y,t) e^{-ikx}\, dx \tag{9}$$

$$\mathbf{w}(x,y,t) = \frac{1}{\sqrt{2\pi}} \int_{-\infty}^{\infty} \hat{\mathbf{w}}(k,y,t) e^{ikx}\, dk \tag{10}$$

We define the linear operator $\hat{\mathcal{L}}$ identical to $\mathcal{L}$ but with $\frac{\partial}{\partial x}$ replaced by ik.

$$\hat{\mathcal{L}} = \begin{pmatrix} 0 & -y & ik \\ y & 0 & d/dy \\ ik & d/dy & 0 \end{pmatrix}. \tag{11}$$

We also define the inner product,

$$(\mathbf{f},\mathbf{g}) = \int_{-\infty}^{\infty} (f_1 g_1^* + f_2 g_2^* + f_3 g_3^*) dy, \tag{12}$$

given

$$\mathbf{f} = \begin{pmatrix} f_1 \\ f_2 \\ f_3 \end{pmatrix}, \qquad \mathbf{g} = \begin{pmatrix} g_1 \\ g_2 \\ g_3 \end{pmatrix}, \tag{13}$$

where we use the * symbol to denote the complex conjugate.

The adjoint of $\hat{\mathcal{L}}$ with respect to the inner product (12) is an operator $\hat{\mathcal{L}}^\dagger$ which satisfies

$$(\hat{\mathcal{L}}\mathbf{f},\mathbf{g}) = (\mathbf{f},\hat{\mathcal{L}}^\dagger\mathbf{g}) \tag{14}$$

for all $\mathbf{f}(y)$ and $\mathbf{g}(y)$ satisfying the boundary conditions. Dias et al. [1] shows that the operator $\hat{\mathcal{L}}$ is skew-Hermitian (i.e., $\hat{\mathcal{L}}^\dagger = -\hat{\mathcal{L}}$) so that (14) becomes

$$(\hat{\mathcal{L}}\mathbf{f},\mathbf{g}) = -(\mathbf{f},\hat{\mathcal{L}}\mathbf{g}). \tag{15}$$

The eigenvalues of $\hat{\mathcal{L}}$ are purely imaginary, and the eigenfunction form an orthogonal set. Let us define the eigenvalue $i\omega$ and the eigenfunction $\mathbf{K}$. They satisfies following relationship.

$$\hat{\mathcal{L}}\hat{\mathbf{K}} = i\omega\hat{\mathbf{K}}, \tag{16}$$

The solutions to (16) are discussed in detail by *Matsuno* [5]. We summarize the relevant results here.

Equation (16) has bounded solutions, as $y \to \pm\infty$, only if $\omega^2 - k^2 - k/\omega$ is an odd integer. It results in the cubic dispersion relationship.

$$\omega^2 - k^2 - \frac{k}{\omega} = 2n + 1 \tag{17}$$

with $n = 0, 1, 2, \ldots$ for ω has three roots for given k and n. We denote the solutions of this cubic equation by $\omega_{n,r}(k)$ to indicate which of the three roots of the frequency equation we are discussing. The subscript r ($r = 0, 1, 2$) is related to Rossby modes ($r = 0$), Westward-propagating Inertial Gravity modes ($r = 1$), and Eastward-propagating Inertial Gravity modes ($r = 2$). Let $\mathbf{K_{n,r}}$ denote the eigenfunction corresponding to rth root of (17) given n.

$$\mathbf{K}(k,y) = \begin{pmatrix} \mathcal{U}(k,y) \\ \mathcal{V}(k,y) \\ \mathcal{H}(k,y) \end{pmatrix} \tag{18}$$

$$= A_{n,r} e^{-\frac{1}{2}y^2} \begin{pmatrix} -\frac{1}{2}(\omega_{n,r}+k)H_{n+1}(y) - n(\omega_{n,r}-k)H_{n-1}(y) \\ i(\omega_{n,r}^2 - k^2)H_n(y) \\ -\frac{1}{2}(\omega_{n,r}+k)H_{n+1}(y) + n(\omega_{n,r}-k)H_{n-1}(y) \end{pmatrix} \tag{19}$$

where

$$A_{n,r} = \pi^{-\frac{1}{4}}\{2^n n![(n+1)(\omega_{n,r}+k)^2 + n(\omega_{n,r}-k)^2 + (\omega_{n,r}^2 - k^2)^2]\}^{-\frac{1}{2}} \tag{20}$$

is a normalization constant which assures that

$$(\mathbf{K_{n,r}}, \mathbf{K_{n,r}}) = 1 \tag{21}$$

The Hermite polynomials $H_n(y)$ are given by $H_0(y) = 1$, $H_1(y) = 2y$, $H_2(y) = 4y^2 - 2$, $H_3(y) = 8y^3 - 12y$, $\cdots$, with recurrence relation $H_{n+1}(y) = 2yH_n(y) - 2nH_{n-1}(y)$.

Special care must be taken when $n = 0$, in which case the dispersion relation factors to $(\omega_{0,r} + k)(\omega_{0,r}^2 - k\omega_{0,r} - 1) = 0$. The root $\omega_{0,r} = -k$ must be discarded because the corresponding eigenfunction cannot be determined. Thus, for $n = 0$, only the two roots of $\omega_{0,r}^2 - k\omega_{0,r} - 1 = 0$ are allowed.

In addition, we obtain Kelvin mode by setting $\hat{v} = 0$. The eigenvalue for Kelvin mode is $\omega_{-1} = \pm k$. The subscript -1 is chosen because the dispersion relation $\omega = k$ is a solution of $\omega^2 - k^2 - k/\omega = 2n + 1$ when $n = -1$. The eigenfunction is

$$\mathbf{K_{-1}} = A_{-1}e^{-\frac{1}{2}y^2}\begin{pmatrix}1\\0\\1\end{pmatrix}, \tag{22}$$

with corresponding eigenvalue $\omega_{-1} = k$.

Since $\hat{\mathbf{K}}_{n,r}$ is orthogonal and complete, and we can introduce the meridional transform pair using the normal modes.

$$\hat{w}_{n,r}(k,t) = (\hat{\mathbf{w}}(k,y,t), \mathbf{K}_{n,r}(k,y)) \tag{23}$$

$$\hat{\mathbf{w}}(k,y,t) = \sum_{r=0}^{2}\sum_{n}^{\infty}\hat{w}_{n,r}(k,t)\mathbf{K}_{n,r}(k,y) \tag{24}$$

We may now use our eigenfunction to decompose the time dependent problem into normal modes.

Taking the inner product of the Fourier transform of (7) with $\mathbf{K}_{n,r}(k,y)$, we obtain

$$\left(\frac{\partial\hat{\mathbf{w}}(k,y,t)}{\partial t}, \mathbf{K}_{n,r}(k,y)\right) + \left(\hat{\mathcal{L}}\hat{\mathbf{w}}(k,y,t), \mathbf{K}_{n,r}(k,y)\right) =$$

$$-\epsilon\left(\hat{\mathbf{w}}(k,y,t), \mathbf{K}_{n,r}(k,y)\right) - \left(\hat{\mathbf{S}}(k,y,t), \mathbf{K}_{n,r}(k,y)\right)$$

$$\frac{d\hat{w}_{n,r}(k,t)}{dt} + (\epsilon + i\omega_{n,r})\hat{w}_{n,r}(k,t) = -\hat{S}_{n,r}(k,t)$$

Equation (25) is the transformation to spectral space of the original system (7) and has steady solution

$$\overline{\hat{w}_{n,r}}(k,t) = -\frac{\hat{S}_{n,r}(k)}{\epsilon + i\omega_{n,r}}. \tag{25}$$

When this is inserted into (24), we obtain the steady solution in spectral space

$$\overline{\hat{\mathbf{w}}}(k,y,t) = \sum_{n,r} \overline{\hat{w}_{n,r}}(k)\mathbf{K}_{n,r}(k,y) \tag{26}$$

Taking the inverse Fourier transform of (26) and breaking back into component form, we obtain our final physical space solution.

$$\overline{\mathbf{w}}(x,y,t) \quad = \quad (2\pi)^{-\frac{1}{2}} \int_{-\infty}^{\infty} \overline{\hat{\mathbf{w}}}(k,y,t)e^{ikx}\,dk \tag{27}$$

The solution of our initial value problem consists of a superposition of normal modes. The superposition involves all zonal wavenumbers (integral over k), all meridional normal modes (sum over n and r). It should be noted that typical superpositions of many normal modes result in spatial patterns which differ greatly from individual normal modes.

2.3 Forcing

The dynamical role of the deep convection, in general, can be described as a mass sink in the lower atmosphere and as a source in the upper atmosphere. We parameterize the deep convection (ITCZ) as a mass sink whose shape is gaussian in x and y, assuming that our model represents the lower troposphere.

$$S(x,y) = S_o e^{-x^2/a^2} e^{-(y-y_0)^2/b^2} \tag{28}$$

where y_0 is the center of the Gaussian shaped mass sink, a is its e-folding width in x, and b its e-folding width in y. The factor, $S_o[m/s]$, is the maximum rate of the mass removal and represents the intensity of the deep convection. Realistic measure of $S_o[m/s]$ could be obtained as the projection of the diabatic heating onto the first baroclinic mode.

The Fourier transform of this forcing is

$$\hat{S}(k,y) = 2^{-\frac{1}{2}} S_o a e^{-(y-y_0)^2/b^2} e^{-\frac{1}{4}k^2a^2} \tag{29}$$

Then, using (23), we obtain

$$\begin{aligned}
\hat{S}_{n,r}(k,t) \quad &= \quad \left(\hat{\mathbf{S}}(k,y), \mathbf{K}_{n,r}(k,y)\right) = \int_{-\infty}^{\infty} \hat{S}(k,y,t)\mathcal{H}_{n,r}(k,y)dy \\
&= \quad S_o\sqrt{\pi}abA_{n,r}(2+b^2)^{-\frac{1}{2}} e^{-\frac{1}{4}k^2a^2} e^{-y_0^2/(2+b^2)}. \\
&\left\{-\tfrac{1}{2}(\omega_{n,r}+k)\left(\frac{2-b^2}{2+b^2}\right)^{\frac{n+1}{2}} H_{n+1}\left(\frac{2y_0}{(4-b^4)^{\frac{1}{2}}}\right) + n(\omega_{n,r}-k)\left(\frac{2-b^2}{2+b^2}\right)^{\frac{n-1}{2}} H_{n-1}\left(\frac{2y_0}{(4-b^4)^{\frac{1}{2}}}\right)\right\}
\end{aligned}$$

for $0 < b < 2^{\frac{1}{2}}$ and $n \geq 0$. For the Kelvin mode, $\hat{S}_{-1,2}(k,t)$ can be written as

$$\hat{S}_{-1,2}(k,t) = \frac{A_{-1,2}}{\sqrt{\pi(b^2+2)}} exp\{-(\frac{k^2a^2}{4} + \frac{y_o^2}{b^2+2})\} \tag{30}$$

2.4 Dissipation

The time scales for the kinetic energy dissipation and the radiative cooling are different. We expand the theory such that the dissipation rate can be different between u, v, and h. The time dependent equation becomes

$$\frac{\partial \hat{\mathbf{w}}}{\partial t} + \hat{\mathcal{L}}\hat{\mathbf{w}} = -\epsilon_u(\mathbf{I} - \mathbf{F})\hat{\mathbf{w}} - \hat{\mathbf{S}} \tag{31}$$

where $\mathbf{I}$ is the identity matrix and

$$\mathbf{F} \equiv \begin{pmatrix} 0 & 0 & 0 \\ 0 & 0 & 0 \\ 0 & 0 & 1 - \frac{\epsilon_h}{\epsilon_u} \end{pmatrix} \tag{32}$$

We substitute $\hat{\mathbf{w}}$ with $\sum_{n',r'} \hat{w}_{n',r'}(k)\mathbf{K}_{n',r'}(k,y)$ and take the inner product with $\mathbf{K}_{n,r}(k,y)$. We obtain

$$\frac{d\hat{w}_{n,r}(k,t)}{dt} + (\epsilon + i\omega_{n,r})\hat{w}_{n,r}(k,t) \quad = \quad -\hat{S}_{n,r}(k,t) + \epsilon_u \sum_{n',r'} \hat{w}_{n',r'} \left(\mathbf{F}\mathbf{K}_{n',r'}, \mathbf{K}_{n,r}\right) \tag{33}$$

Applying the relationship (32),

$$\begin{aligned} \frac{d\hat{w}_{n,r}(k,t)}{dt} + (\epsilon + i\omega_{n,r})\hat{w}_{n,r}(k,t) = \\ -\hat{S}_{n,r}(k,t) + (\epsilon_u - \epsilon_h) \int_{-\infty}^{\infty} \sum_{n',r'} \hat{w}_{n',r'} \mathcal{H}_{n',r'} \mathcal{H}^*_{n,r}\, dy \end{aligned} \tag{34}$$

when $(\epsilon_u - \epsilon_h) \ll 1$, the steady state solution is to a good approximation

$$\hat{w}_{n,r} = \hat{w}^{(0)}_{n,r} + \hat{w}^{(1)}_{n,r}(\epsilon_u - \epsilon_h) + \hat{w}^{(2)}_{n,r}(\epsilon_u - \epsilon_h)^2 + \ldots \tag{35}$$

where

$$\hat{w}^{(0)}_{n,r} \quad = \quad -\frac{\hat{S}_{n,r}(k)}{\epsilon_u + i\omega_{n,r}} \tag{36}$$

$$\hat{w}^{(m+1)}_{n,r} \quad = \quad \frac{1}{\epsilon_u + i\omega_{n,r}} \int_{-\infty}^{\infty} \sum_{n',r'} \hat{w}^{(m)}_{n',r'} \mathcal{H}_{n',r'} \mathcal{H}^*_{n,r}\, dy \tag{37}$$

for $m = 0, 1, 2, \ldots$. Thus, the normal modes are coupled in the time dependent equation when the time scale for kinetic energy dissipation and radiative cooling are different. For the special case, $(\epsilon_u = \epsilon_h)$, it is identical to (25).

3 Simple Cases

3.1 Steady Solution to an Idealized Forcing

Equation (26) shows that the model solution is expressed as the infinite sum of the normal modes to represent the full solution. We turncate the solution at $n = 200$ including the first 200 normal modes for the Rossby, Kelvin, and inertial gravity modes. This introduces an error in the final solution. The power spectrum of $\hat{S}_{n,r}$ suggests that including 200 normal modes with reduce the error less than 0.01 %.

We first describe the steady state solution for u, v, h, and w to illustrate the response to the forcing. As a simple representation of ITCZ, we use non-dimensional length scales $a = 1.5$, $b = 0.25$, and $y_o = 0.7$ which are equivalent of $a = 2700[km]$, $b = 450[km]$, and $y_o = 1260[km]$. For dissipation rates, we chose nondimensional parameter $\epsilon_u = 0.1$ and $\epsilon_h = 0.03$ which are equivalent of $\epsilon_u = 0.36[day^{-1}]$ and $\epsilon_h = 0.11[day^{-1}]$. S_o is taken to be $57[m \cdot day^{-1}]$ using the Marshall Island data [2].

Figure 2 shows the steady state solution for u, v, h, and w for this forcing. The geopotential height perturbation has its minimum near the location of the deep convection associated with the cycloninc circulation. The circulation tends to converge near the forcing, and produces intensified upward motion on the order of $50[m/day]$. Outside of the rising region, we have a region of the mild sinking which has two peaks in the north-west of the forcing and the directly south of the forcing. Spatial structure of the sinking motion can be understood as the superposition of the responses from different normal modes.

3.2 Decomposition into Normal Modes

Since the full solution is the sum of all the normal modes, one can take a partial sum to find contributions from individual mode. Throughout this study, the eigenfunctions of the inviscid, free solution are used as the orthonormal basis for the normal mode transformation. These basis are not the eigenfunction of the frictionally-controlled, heat-induced problem. However, the decomposition of the full solution into the "inviscid modes" gives insights into the spatial structure of the solution.

Figure 3 shows the decomposition of the sinking motion into four normal modes; Rossby modes, westward-propagating inertial gravity modes, eastward-propagating inertial gravity modes, and the Kelvin mode. The Rossby modes, the inertial gravity modes, and the Kelvin mode have distinct spatial structure in the vertical motion.

In general, sinking motions associated with the Rossby modes are located at the west of the forcing because Rossby waves propagates to the west. The response of the mixed mode is responsible for the strong sinking motion asymmetric across the equator. The mixed mode is excited when the forcing is asymmetric about the equator.

The sinking motion associated with the inertial gravity modes have two peaks; one to the north, and another to the south of the forcing. The eastward-propagating inertial gravity modes have stronger sinking motion to the south of the forcing. This strong sinking at the south of the forcing is associated with the mixed mode.

The Kelvin mode is always symmetric about the equator and its sinking motion is always located to the east of the forcing because the Kelvin waves propagates to the east.

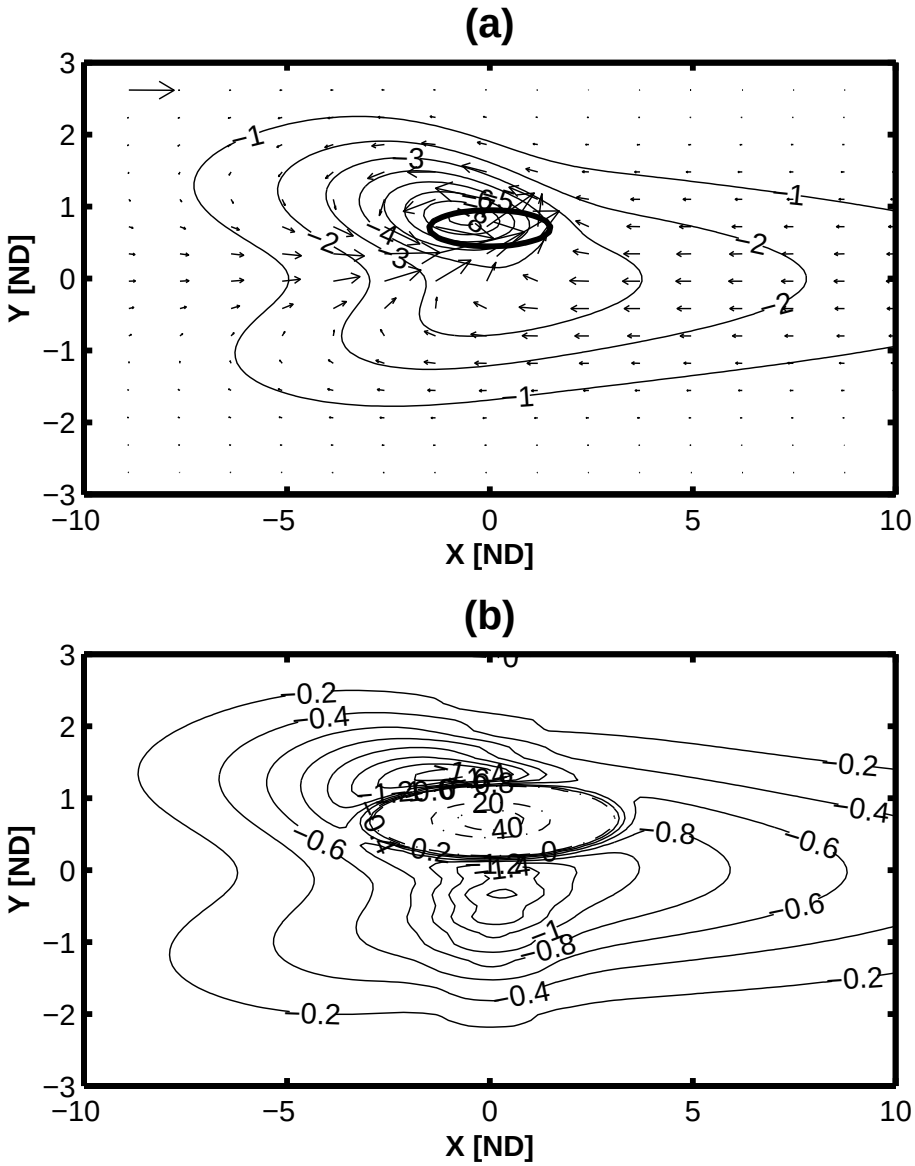

Figure 2: **Steady state solution for u, v, h, and w. (a):** The height perturbation and the wind field. The contour interval is $1[m]$ for height. For the wind field, the reference vector ($1[m/s]$) is drawn at the upper left corner of the domain. **(b):** Vertical motion. The solid contour is sinking motion with the contour interval of $0.2[m/day]$. The dash-dotted lines are rising motion with the contour interval of $20[m/day]$

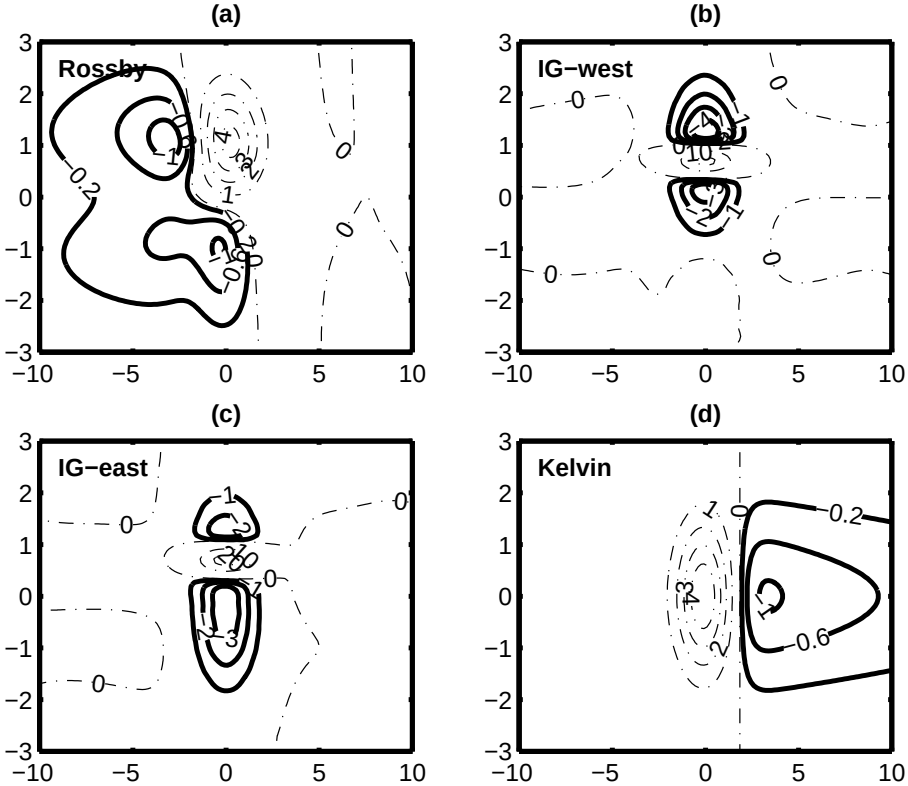

Figure 3: **Decomposition of w into normal modes.** The vertical motion, w, is decomposed into normal modes of four categories. Solid line represents the contour of the sinking motion, and the dash-dotted line represents the contour of the rising motion. **(a):** Rossby modes ($r = 0, n = 0, 1, 2, \ldots$), **(b):** Westward-propagating inertial gravity modes ($r = 1, n = 1, 2, \ldots$), **(c):** Eastward-propagating inertial gravity modes ($r = 2, n = 0, 1, 2, \ldots$), **(d):** Kelvin mode ($r = 2, n = -1$). For the Rossby modes and the Kelvin mode, contour interval for sinking motion is $0.4[m/day]$, and the contour interval for the rising motion is 1 [m/day]. For the inertial gravity modes, contour interval for sinking motion is $1[m/day]$, and the contour interval for the rising motion is 10 [m/day].

The maximum amplitude of the vertical motion of the inertial gravity modes is much stronger and more localized than that of the Rossby modes and the Kelvin mode. Although the Rossby modes and the Kelvin mode are less intense, they have much greater spatial extent. When these four vertical motions are added together, it becomes identical to the total solution shown in Figure 2.

The asymmetric structure of the sinking motion can be understood as following. The east-west asymmetry of the vertical motion is greatly affected by the competition between the Rossby modes and the Kelvin mode. This corresponds to what we call "the Walker Circulation". On the other hand, the north-south asymmetry of the vertical motion is related to the inertial gravity modes. This corresponds to what we call "the Hadley Circulation". To illustrate these idea, we examine the zonally averaged circulation and meridionally averaged circulation.

3.3 Hadley Circulation

Spatially averaged circulation can be s simple indicator for the asymmetric structure of the vertical motion. Figure 4 is the zonally averaged stream function (a) and meridional velocity in the lower troposphere (b). There is a rising motion at the location of the deep convection. The winter branch of the Hadley circulation is much stronger than the summer branch. The sinking motion is wide and intense in the winter hemisphere. This asymmetry in the Hadley circulation can be explained in several ways.

First, Coriolis parameter (equivalent of the inertial stability in the equatorial β-plane) is very small in the vicinity of the equator. The small Coriolis parameter suggests that the deformation radius, $\sqrt{g\overline{h}}/f$, is greater near the equator. Therefore, the spatial scale of the circulation must be greater in the winter hemisphere.

Secondly, the zonally averaged velocities on the equator at steady state is given by

$$\overline{u}^x = 0 \tag{38}$$

$$\overline{v}^x = -\frac{g}{\epsilon_v}\frac{\partial \overline{h}^x}{\partial y} \tag{39}$$

It suggests no zonal flow nearby the equator. Since the convective forcing produces strong meridional gradient of $\overline{h}^x$, the winter branch of the Hadley circulation is enhanced.

Finally, the zonally-averaged meridional velocity, $\overline{v}^x$, is decomposed into normal modes in Figure 4 (b). There is no contribution from Kelvin mode since $v = 0$ always in Kelvin mode. The spatial structure of $\overline{v}^x$ is governed by inertial gravity modes. The contribution from Rossby modes are dominated by the mixed Rossby-gravity mode. The eastward-propagating inertial gravity modes has the strongest intensity in the winter hemisphere because it has contribution from the mixed Rossby-gravity mode as well. The convective forcing which is asymmetric about the equator excites the mixed Rossby-gravity mode and it produces large fraction of the cross-equatorial transport in the zonally averaged circulation.

The north-south asymmetry of the vertical motion is associated with the mixed Rossby-gravity mode, and it has intensified sinking in the winter hemisphere. This is consistent with the satellite image in Figure 1.

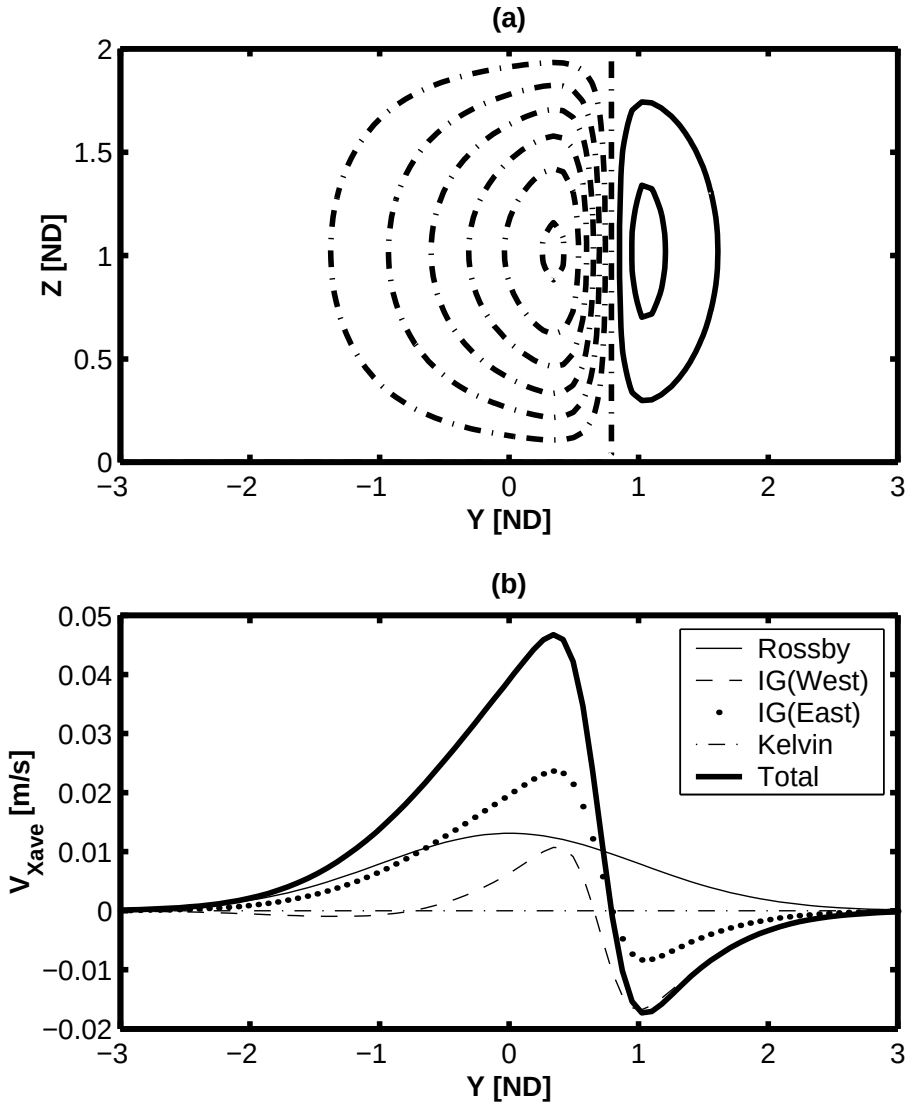

Figure 4: **Hadley Circulation** (a) The meridional stream function. (b) The zonally averaged meridional velocity in the lower layer. The zonal average is first calculated using spectral method. The vertical structure is assumed to be the first baroclinic mode.

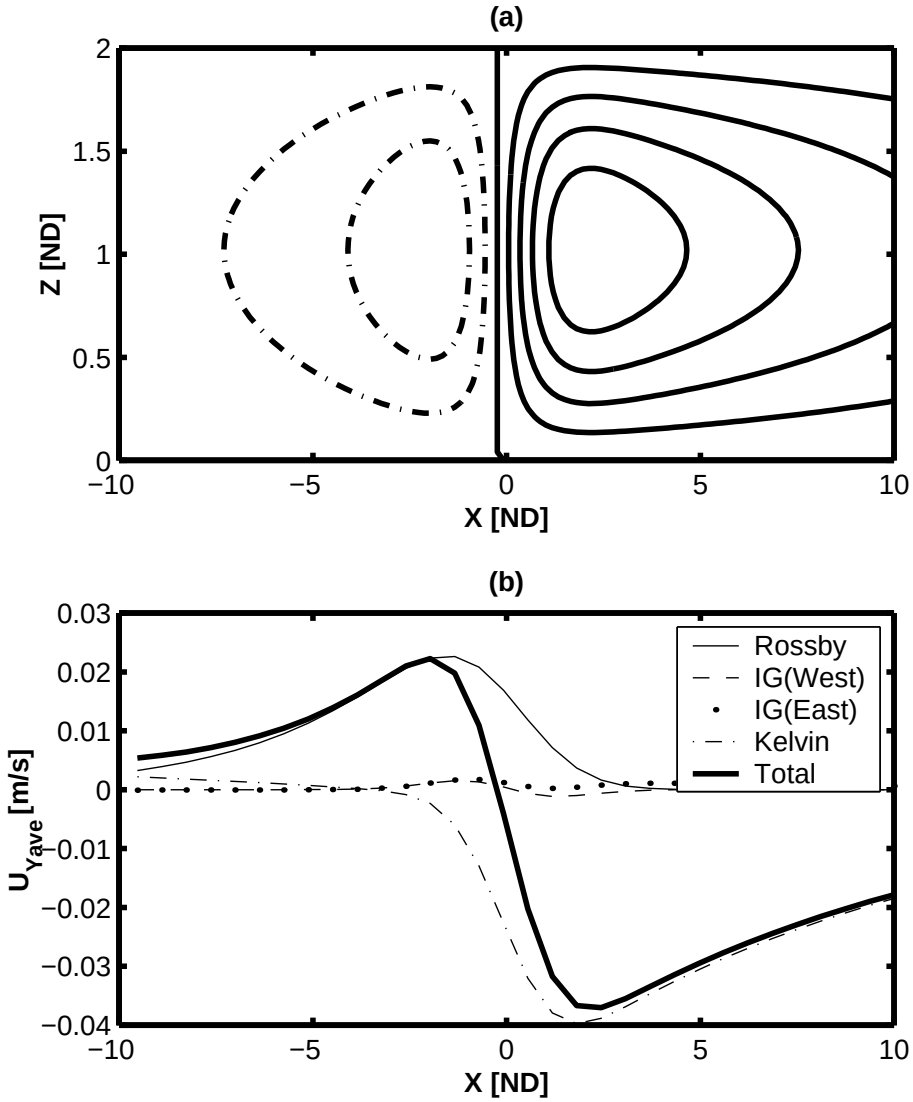

Figure 5: **Walker Circulation** (a) Zonal stream function. (b) Meridionally averaged zonal velocity in the lower layer. The vertical structure for the stream function is given by the first baroclinic mode.

3.4 Walker Circulation

Figure 5 is the meridionally averaged stream function (a) and zonal velocity in the lower troposphere (b). It shows the east-west asymmetry of the Walker circulation. There is a rising motion near the location of the deep convection. The eastern branch of the Walker circulation is stronger than the western branch in this particular example. This asymmetry in the Walker circulation can be explained as the competition between Kelvin mode and Rossby modes.

Figure 5 (b) suggests that the eastern branch is dominated by the Kelvin mode and the western branch is dominated by the Rossby modes. This result is robust with wide range of parameters. It implies that the east-west asymmetry of the Walker circulation reflects the relative intensity of the Rossby modes and the Kelvin mode and its dependence on model parameters.

First, let us consider the Kelvin mode. The projection of the Gaussian-type heating onto the Kelvin mode is shown in Equation (30). It suggests that the forcing has structure such that the intensity of the Kelvin mode decays with y_o. Physically, it means that the forcing projects less onto the Kelvin mode when there is a greater distance between the center of the forcing and the equator because the Kelvin mode is trapped nearby the equator. The eastern branch of the Walker circulation weakens with increasing y_o while a and b are fixed.

Secondly, let us consider the Rossby modes. The response of the Rossby modes to varying y_o is illustrated by considering the potential vorticity equation of the system. The potential vorticity equation can be constructed from Equation (4), (5) and (6).

$$\frac{\partial q}{\partial t} + v = -\epsilon q + yS \tag{40}$$

where $q \equiv \frac{\partial v}{\partial x} - \frac{\partial u}{\partial y} - yh$ is the perturbation potential vorticity in the shallow water system. This PV perturbation is mostly associated with the Rossby modes. It is remarkable that the forcing term in the PV equation (40) is proportional to y. This is due to the increase in the Coriolis term with y. Therefore, the Rossby modes intensifies with increasing y_o. Here, the sensitivity of the Rossby modes has opposite sign from that of the Kelvin mode.

Figure 6 shows the sensitivity of the stream functions to the center of the heating, y_o. Figure 6 (a) clearly shows that the eastern branch weakens and the western branch intensifies as y_o increases. The western branch becomes stronger than the eastern branch when $y_o \sim 1.1$ or greater. Figure 6 (b) confirms the view that the winter hemisphere has stronger sinking motion, and the north-south asymmetry grows with increasing y_o.

4 Somewhat Realistic Solution

The satellite image (e.g. Figure 1) shows quite complicated WV distribution and the time series of the satellite image suggests that it is quite variable. Here, we try to reproduce the large-scale pattern of the dry region in the upper troposphere using the simple model we derived and studied in the previous section. As a first attempt, we study the steady state response of the shallow water system to the multiple convective region. Since the model is linear, the circulation due to the multiple heating can be obtained as the superposition of the circulations due to individual forcing.

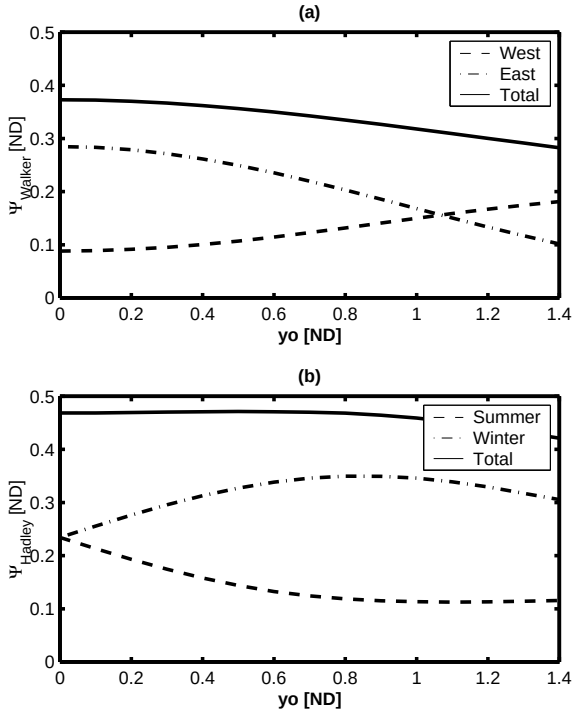

Figure 6: **The sensitivity of the maximum mass transport to the location of the forcing, y_o.** (a) The intensity of the Walker circulation and contributions from its eastern branch and the western branch. (b) The intensity of the Hadley circulation and contributions from its northern branch and the southern branch. The intensity is measured as the maximum value of the stream function.

Table 1: **The size and the location of the deep convection** In the case of the Eastern Pacific in the late July, 2001.

Deep Convection Site	Location (x_o, y_o)	Size (a, b)
A : ITCZ	$(0, 0.7)$	$(1.5, 0.25)$
B : PNG	$(-5, 0)$	$(0.5, 0.5)$
C : SPCZ	$(-1, -1.5)$	$(0.5, 0.5)$

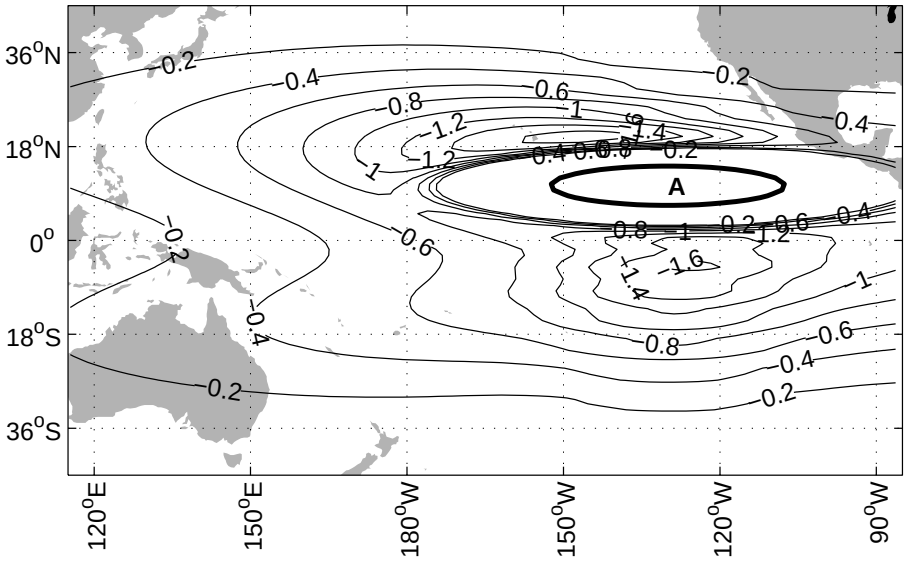

Figure 7: **Steady Solution for the sinking motion due to ITCZ over Eastern Pacific**

Considering the case in the Eastern Pacific in the late July in 2001, (shown in Figure 1), we seem to have two or three sites of convection and they are listed in the Table 4. **(A)**: ITCZ over tropical Pacific is the narrow band of the moist region in the satellite image. This feature is tied to the warm SST over the ocean and often appears around 10N over the Pacific ocean. **(B)**: The deep convection over Papua New Guinea (PNG) is located in the tropical Western Pacific. In the La Nina condition, there is a warm pool in the Western Pacific, and the deep convection is tied to the warm SST. **(C)**: The satellite image suggests that the moist region in the South Pacific which is often called "South Pacific Convergence Zone" (Hereafter, SPCZ). The WV image is more stable in time and space at the deep convection site over Eastern Pacific ITCZ or over PNG. SPCZ is highly variable due to the weather-type baroclinic waves.

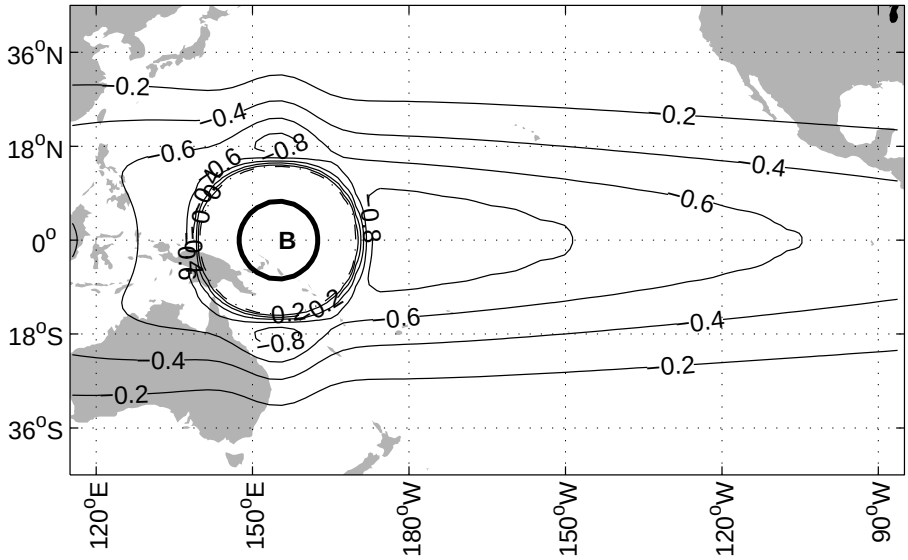

Figure 8: **Steady Solution for the sinking motion due to the deep convection over PNG**

4.1 (A) ITCZ over Eastern Pacific

Figure 7 shows the distribution of the sinking motion at steady state induced by the deep convection over the Eastern Pacific. The pattern suggests that there are two sinking motion maximum. An intense sinking region is located in the southern hemisphere approximately at the same latitude as the forcing (120°W, 8°S). This sinking motion is due to the inertial-gravity modes and the mixed mode. Another intense sinking region is located in the subtropical Eastern pacific around (145°W, 18°N). The spectral decomposition suggests that this is caused by the Rossby mode. The intensity of the latter one is weaker.

4.2 (B) The deep convection over PNG

Figure 8 shows the distribution of the sinking motion at steady state induced by the deep convection over PNG. The pattern suggests that there is a strong response to the east of the convective forcing caused by the Kelvin mode. The sinking motion is symmetric about the equator. There are secondary maximum directly north and south of the forcing induced by the inertial-gravity modes.

4.3 (C) The SPCZ forcing

Figure 9 shows the distribution of the sinking motion at steady state induced by SPCZ. The pattern suggests that there is almost no sinking motion to the east of the forcing. The response of the Kelvin mode is very weak because the forcing is located at greater distance from the equator. The response of the Rossby mode is very strong, creating an intense sinking motion to the west of the forcing. There is an intense response in the mixed mode, which causes the sinking motion in the northern hemisphere. The intensity of the sinking

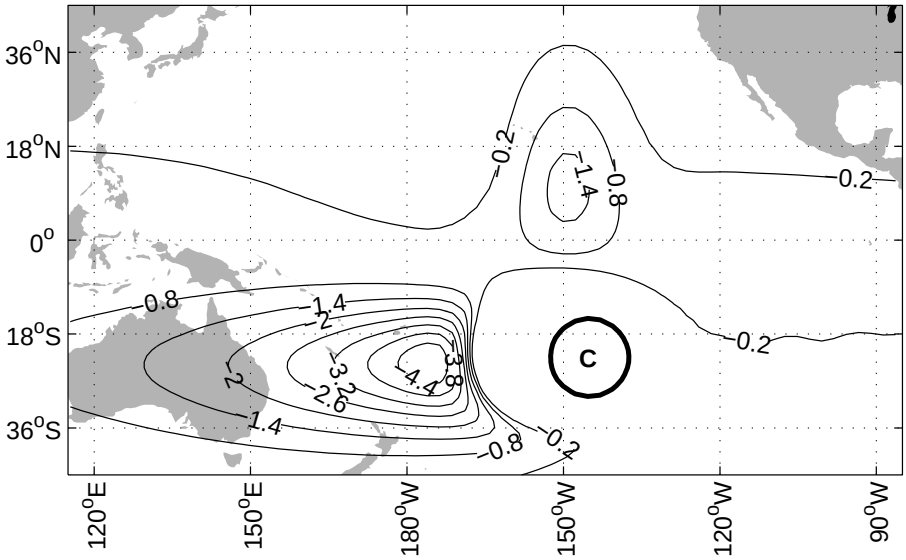

Figure 9: **Steady Solution for the sinking motion due to SPCZ**

motion is much stronger than (A) or (B) partly because of the magnitude of the forcing, S, is prescribed at the same value as (A) and (B). In reality, the magnitude of the convective forcing is much weaker in SPCZ than in ITCZ. Thus, we do not expect to observe this strong sinking motion in the satellite image.

4.4 Response to the multiple heating region

Here, we show the steady state response to the multiple convective region in Figure 10. Since the model is linear, the circulation due to the multiple heating can be obtained as the superposition of the responses to the individual forcing. The intensity of the convective forcing could be different between the forcing (A), (B), and (C). The resulting solution, however, has a robust spatial structure which does not depend of the choice of the relative importance of individual forcing. In Figure 10, the relative intensity of the forcing is prescribed to A:B:C=3:6:1.

The solution for the multiple convective region resembles the satellite image of the black hole of WV remarkably well. The simple model reproduces the intense sinking motion around (120°W, 8°S) which is a combination of the responses to the forcing (A) and (B). This intense sinking motion could explain the formation of the black hole in the winter hemisphere. SPCZ does not contribute to the sinking motion near the black hole.

The solution also agrees with the satellite observation that the relatively dry region in the subtropical Eastern Pacific around (150°W, 20°N).

5 Discussion

Let us summarize the main results.

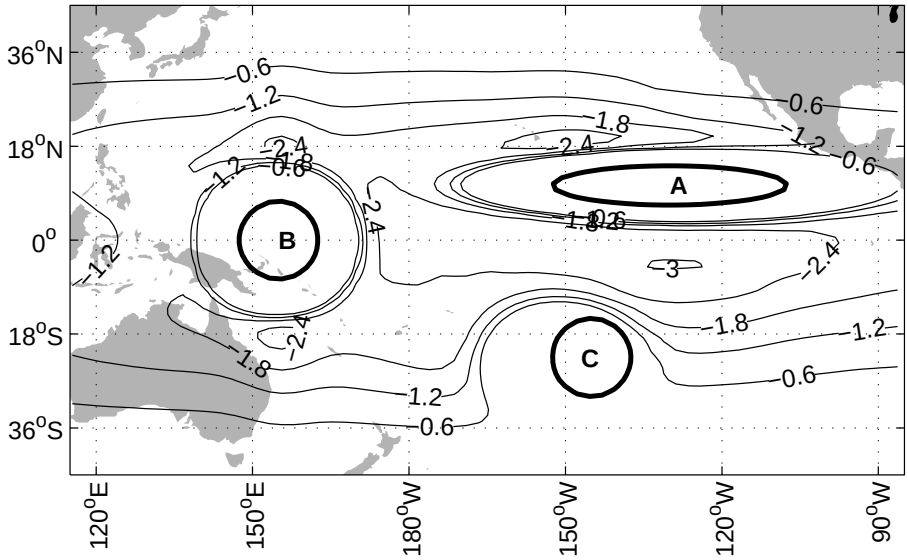

Figure 10: **Steady Solution for the multiple convective region**

- (1) The spectral decomposition into "inviscid normal modes" suggests that the Hadley circulation is mainly sustained by the inertial-gravity modes.
- (2) The asymmetry in the Walker circulation is driven by the competition between the Kelvin mode and the Rossby modes.
- (3) The solutions to the simple, linear shallow water model agrees with the the spatial structure of the upper tropospheric WV satellite images remarkably well.
- (4) The Black Hole of the WV in the tropical Pacific can be understood as the circulation induced by the deep convection over the central Pacific and over Papua New Guinea.

The result (3) and (4) are further tested against several variants of similar experiments with different relative intensity of the convective forcing. Those experiments confirmed that the spatial structure predicted by this simple model is a robust one. It is of interest to examine the sinking motion over the Atlantic ocean and the Indian ocean, which can test the validity of the simple linear theory.

This simple model seems to behave particularly well near the equator where the background flow is relatively weak. The linear assumption breaks down when there is a significant background flow because the model is linearized around the state of rest, which is not applicable in the middle latitudes. Near the location of the convective heating, the flow velocity is also large which causes the linearity to break down.

It can be shown that, in some parameter regime, the potential velocity distribution associated with the steady state solution is unstable to barotropic instability or baroclinic instability [*Gerber et al* [3]]. The dynamical instabilities causes the formation of eddies and the break up of ITCZ. This is also the limitation of the theory based upon the steady state.

Despite the simplicity of the model, this study shows that the linear shallow water model can be used as a conceptual tool for understanding and explaining the upper tropospheric water vapor. It motivates the further investigation of the simple model with emergent questions on the upper tropospheric water vapor. *Rosendal* [8] pointed out the statistical relationship between black holes of water vapor appearing in the winter hemisphere and the development of tropical cyclones in the summer hemisphere.

6 Acknowledgment

The authors are thankful to Joe Keller and Bill Young for helpful comments and discussion. TI is also thankful to Mitsuko Ito, Janet Fields, and all the GFD 2001 fellows for continuous encouragement and support.

References

[1] Dias, P. L. S., W. H. Schubert, and M. DeMaria, "Large-Scale Response of the Tropical Atmosphere to Transient Convection" J. Atmos. Sci. Quart. **40**, 2689 (1983).

[2] Fulton S. and W.H. Schubert, "Vertical Normal Mode Transforms: Theory and Application", Monthly Weather Review, **113**, 647, (1985)

[3] Gerber E.P., T. Ito, and W.H. Schubert, "The Time Evolution of Arid, Black Holes in Upper Tropospheric Water Vapor", in *GFD-2001 volume*, (Woods Hole Oceanographic Institution), (2001)

[4] Gill, A. E., "Some simple solutions for heat induced tropical circulation" Quart. J. Roy. Meteorol. Soc. **106**, 447 (1980).

[5] T. Matsuno, "Quasi-Geostrophic Motions in the Equatorial Area", J. Meteorol. Soc. Japan, **44** 25 (1966).

[6] J. Pedlosky, *Geophysical Fluid Dynamics*, 2nd ed. (Springer Verlag, New York, 1987).

[7] Picon L. and M. Desbios, Relation between METEOSAT Water Vapor Radiance Fields and Large Scale Tropical Circulation Features, Journal of Climate, **3**, 865, (1990)

[8] Rosendal H., "The Black Hole of Water Vapor and Its Use as an Indicator of Tropical Cyclone Development and Intensity Changes", http://members.aol.com/Rosendalhe/black.htm, (1998)

[9] Schmez J. et al., "Monthly Mean Large Scale Analysis of Upper Tropospheric Humidity and Wind Field Divergence Derived from Three Geostationary Satellites" Bulletin of American Meteorological Society, **76**(9), 1578, (1995)